IN SITU SOFT X-RAY SPECTRO-MICROSCOPIC CHARACTERIZATION OF CATALYSTS FOR ELECTROCHEMICAL CO_2 REDUCTION

by

Chunyang Zhang, M.Sc.

A Thesis

Submitted to the School of Graduate Studies

in Partial Fulfillment of the Requirements

for the Degree of

Doctor of Philosophy

McMaster University

ABSTRACT

Carbon dioxide electroreduction (CO_2R) is a promising and sustainable route to generate valuable feedstocks through the electrochemical conversion from CO_2 with electricity generated by renewable energy resources, to reduce greenhouse gas emissions, thereby protecting the global environment. One of the critical challenges for developing practical CO_2R developments is understanding the structures and chemistry of CO_2R electrocatalysts, and then generating fundamental insights to guide the design and optimization of high-performance electrocatalysts. During my Ph.D. studies, synchrotron-based X-ray spectro-microscopy techniques, scanning transmission X-ray microscopy (STXM) and X-ray spectro-ptychography, were used to study nickel-nitrogen-carbon (Ni-N-C) and electrodeposited Cu-based CO_2R electrocatalysts. STXM and ptychography were upgraded to *in situ* characterizations to provide spectroscopic characterization and quantitative, chemically selective imaging of these catalytic materials under CO_2R conditions.

To achieve *in situ* STXM and spectro-ptychography, a micro-fluidic based, liquid-flow electrochemical *in situ* device was developed, fabricated, and implemented. The in situ device is optimized from previous versions developed by Vinod Prabu, past graduate student of Hitchcock group, and the initial concept was provided by Pablo Ingino and Dr. Martin Obst, collaborators at the University of Bayreuth. *In situ* STXM and spectro-ptychography provided a detailed chemical and morphological evaluation of catalyst materials at different applied potentials during electrochemical processes. The *in situ* STXM studies of Cu-based catalysts showed that electrodeposited Cu_2O particles are

converted to metallic Cu with different reaction rates at applied potentials less negative than that for initiation of CO_2R. The *in situ* STXM results show a degree of heterogeneity in the electrochemical response of discrete nanoparticles and metallic Cu as the active catalyst for CO_2 reduction which is structurally relatively stable at CO_2R-relevant potentials within the spatial resolution of STXM. *In situ* spectra-ptychography was used to follow morphological changes of a single Cu-based catalytic particle in the electrochemical regime of CO_2R. Our results show that the Cu particle lost the initial cubic structure and formed irregular dendritic-like structures during the CO_2R process. To the best of my knowledge, this is the first time *in situ* STXM has been applied to CO_2R electrocatalysts under flow liquid and electrochemical conditions and the first report of *in situ* spectro-ptychography studies. In summary, my research has successfully achieved the *in situ* STXM and spectro-ptychography experiments and contributed to an improved understanding of Cu nanoparticle CO_2R electrocatalysts.

ACKNOWLEDGEMENTS

I would like to express my great and deepest thanks to all the people who have supported me throughout my Ph.D. studies.

First and foremost, I am very grateful to my supervisors, Dr. Drew Higgins, and Dr. Adam Hitchcock, for their excellent mentorship, guidance, encouragement, and support over the past four years. Their insights into science, critical thinking, breadth of knowledge, and hard-working attitude played an important role in refining the direction and enhancing the quality of my research. The work experience in Higgin's and Hitchcock's group has become one of the most valuable wealth in my life.

I would like to thank my supervisory committee member, Dr. Charles De Lannoy, for his insightful feedback, research advice, suggestions, and support to enrich the content and rigor of this thesis.

My sincere thanks go to our collaborators: Pablo Ingino, Dr. Martin Obst from the University of Bayreuth; Paul Gatt from the workshop in the Department of Chemical Engineering, Dr Jose Moran-Mirabal and his students in the Department of Chemistry & Chemical Biology, Marcia Reid in the Department of Pathology and Molecular Medicine from McMaster University; Hooman Hosseinkhannazer, Eric Daigle, Alex Lee from the Norcada company. Their support, help, collaboration, and exchange of ideas have contributed immeasurably to the development of this work.

Special thanks to my current and past group members: Haytham Eraky, Vinod Prabu, Dr. Hao Yuan, Dr. Jiatang Chen, Ladan Shahcheraghi, Dr. Fatma Ismail, Dr. Ahmed Abdellah, Wajdi Alnoush, Navid Noor, Storm Gourley and many other members

of the Higgin's and Hitchcock's group, for their assistance, cooperation in the lab and constant support. It's such a wonderful experience to work with all the group members.

I would like to show my appreciation to the Department of Chemical Engineering, the Department of Chemistry & Chemical Biology, and McMaster University for providing me with the resources, facilities, and opportunities for conducting my research. The high research-intensity environment has been instrumental in fostering my growth as a Ph.D. student.

Many thanks to all the beamline scientists and students in different beamlines and synchrotron facilities: Dr. Jian Wang, Dr. Jay Dynes, Dr. Tianxiao Sun, Dr. Jigang Zhou from Canadian Light Source; Dr. Nicolas Mille, Dr. Stefan Stanescu, Dr. Sufal Swaraj, Dr. Rachid Belkhou from Synchrotron Soleil; Dr. Igor Beinik, Dr. Jörg Schwenke, Dr. Claudiu Bulbucan, Dr. Viktoriia Meklesh, Dr. Karina Thånell from MaxIV; Dr. Markus Weigand, Dr. Xianxiao Sun, Thomas Rauch from Bessy-II; Dr. Hendrik Ohldag, Dr. David Shapiro from Advanced Light Source; Dr. Tolek Tyliszcazk, Dr. Anna Mandziak, Dr. Barbara Wolanin, Dr. Krzysztof Matlak from SOLARIS National Synchrotron Radiation Centre. I am grateful for their technical support and expert maintenance of the instruments.

Finally, I would like to thank my family and all my friends. Special thanks to my wife Chen Zhao for her encouragement, support, and love all the time. Also thanks to the marvelous destiny to let me start my research from metallic materials in my undergraduate studies in polymer chemistry and electrochemistry during my master period, organic chemistry when I am working, and finally to the combination of CO_2

reduction electrocatalysis and *in situ* synchrotron-based X-ray techniques in my PhD studies. I am enjoying the research I have done all the way.

Thanks so much to all the people and facilities! While space constraints prevent me from individually acknowledging everyone, I am deeply grateful to everyone for their support, help, and contributions.

TABLE OF CONTENTS

LIST OF FIGURES

Chapter 1

Chapter 2

Chapter 3

Chapter 4

Chapter 5

Chapter 6

Chapter 7

Chapter 8

Chapter 9

LIST OF TABLES

LIST OF ABBREVIATIONS AND SYMBOLS

AEM	Anion-exchange Membrane
ALS	Advanced Light Source
AFM	Atomic Force Microscopy
BESSY-II	Berliner Elektronenspeicherring-Gesellschaft für Synchrotronstrahlung-II
BM	Bend Magnet
CA	Chronoamperometry
CCD	Charge-Coupled Device
CCEM	Canadian Centre for Electron Microscopy
CDI	Coherent diffraction imaging
CE	Counter Electrode
CH_4	Methane
C_2H_4	Ethylene
CLS	Canadian Light Source
CNC	Computer Numerical Control
CO	Carbon Monoxide
CO_2	Carbon Dioxide
CO_2R	Carbon Dioxide Electroreduction
CXRO	Center for X-Ray Optics
Cu	Copper
C_{2+}	Multi-carbon
Δr_n	Width of the Most Outer Zone (Nth) of a Zone Plate
D	Diameter of Zone Plate
DI	Deionized Water
DM	Difference Map
ε	Detector Efficiency
E	Photon Energy
E_{cell}	Thermodynamic Cell Voltage
ePIE	Extended Ptychographic Iterative Engine

$\varepsilon_{Voltage}$	Voltage Efficiency
EPU	Elliptically Polarizing Undulators
f	Focal Length
FE	Faradaic Efficiency
ΔG	Standard Gibbs Free Energy Change
GC	Gas chromatography
ΔH	The Change in Enthalpy
HCOOH	Formic Acid
I	Transmitted Photon Intensity (Flux) in STXM
I_0	Incident Photon Intensity (Flux)
IRAS	Infrared absorption spectroscopy
λ	Wavelength of Light
l	Sample Thickness
M or MW	Molecular Weight
m	Diffraction order of X-ray
MEA	Membrane Electrode Assemblies
MGy	Mega Grays
M_n	Number Average Molecular Weight
M_w	Weight Average Molecular Weight
M–N–C	Metal–nitrogen–carbon
n	Zone number of Zone Plate
NA	Numerical Aperture
NEXAFS	Near Edge X-Ray Absorption Fine Structure
NMR	Nuclear Magnetic Resonance
Ni–N–C	Nickel–nitrogen–carbon
OD	Optical Density
OD1	Optical Density per nm Thickness Material
OER	Oxygen Evolution Reaction
OSA	Order Sorting Aperture

ρ	Sample Density
PCB	Printed Circuit Board
PGM	Plane Grating Monochromator
PDMS	Polydimethylsiloxane
PMMA	Polymethyl Methacrylate
PEM	Proton-exchange membrane
PMMA	Poly(methyl methacrylate)
RE	Reference Electrode
RHE	Reversible Hydrogen Electrode
Res	Spatial Resolution
r_n	Width of the n^{th} Zone of the Zone Plate
SGM	Spherical Grating Monochromator
SEM	Scanning Electron Microscopy
SiNx	Silicon Nitride
SM	Spectromicroscopy
SOLEIL	Synchrotron SOLEIL
STXM	Scanning Transmission X-Ray Microscopy
ΔS	The change in entropy from reactants to products
t	Exposure Time
T	Temperature in Kelvin
TEM	Transmission Electron Microscopy
TEY	Total Electron Yield
TFY	Total Fluorescence Yield
μ	Energy Dependent Mass Absorption Coefficient
V_{Au}	V vs Au reference electrode
V_{cell}	Actual Cell Voltage
V_{RHE}	V vs reversible hydrogen electrode
Ω	Electron Emission Solid Angle
ω	Frequency

WE	Working Electrode
wt%	Weight Percent
XAS	X-ray absorption spectroscopy
XPS	X-ray Photoelectron Spectroscopy
XRD	X-ray Diffraction
ZP	Fresnel Zone Plate
δr_n	Width of the outermost zone

Chapter 1

Introduction

This chapter gives an overview of the thesis, an introduction to electrochemical CO_2 reduction, and motivation to optimize electrocatalysts for higher efficiency and selectivity as well as the development of in situ spectro-microscopic characterization. The significance and applications of this work to electrochemical CO_2 reduction are described. This chapter concludes with a chapter-by-chapter outline of the whole thesis.

1.1 Overview of thesis

Carbon dioxide electroreduction (CO_2R) is a promising and attractive route to electrochemically converted CO_2 gas to generate valuable feedstocks such as hydrocarbon and alcohol products, with the involvement of the electricity generated by renewable energy resources. If this can be achieved, CO_2R can largely reduce the emissions of CO_2 and the reliance on fossil fuels. However, despite much progress in recent years, the poor performance of CO_2 reduction catalysts limits the large-scale application of CO_2R. This motivates people to develop effective strategies to design high-performance catalysts or improve their proprieties, for the development of practical electrochemical CO_2 reduction processes.

In the process of catalyst design and optimization, advanced characterizations are needed to gain an understanding of how the structure and properties of an electrocatalyst influence its performance. Among various techniques, spectro-microscopies are a class of important tools to study electrocatalysts, because they provide both images to directly

visualize the morphology, and, at the same time, spatially-resolved spectroscopic information to identify and map chemical components. In my thesis research, I used two advanced synchrotron-based spectro-microscopic techniques - scanning X-ray transmission X-ray microscopy (STXM) and soft X-ray spectro-ptychography - to study catalytic materials for electrochemical CO_2R. STXM can simultaneously provide microscopic imaging of catalyst morphologies alongside spatially resolved (~50 nm spatial resolution) spectroscopic characterization through near edge X-ray absorption fine structure (NEXAFS) spectroscopy to enable quantitative, chemically selective imaging. X-ray ptychography provides similar spectro-microscopy capabilities as STXM, but with significantly better spatial resolution.

STXM studies of single atomic CO_2R electrocatalysts, nickel–nitrogen–carbon (Ni–N–C) materials with different loadings of Ni, are used to show the advantages of spectro-microscopic characterizations and its importance to catalysts community. Through the chemical mapping and quantification by STXM, the chemical distribution, structure, and amount of the single-atom Ni active sites in Ni–N–C electrocatalysts were elucidated and related to the CO_2R performance. Subsequent X-ray ptychography studies on the same region of Ni–N–C materials studied by STXM, highlighted the significantly improved spatial resolution provided by ptychography. Compared to earlier STXM study, ptychography can efficiently show the chemical components and distributions of very small structures such as nanoparticles and interfaces.

One of the main limitations of the above STXM/ ptychography studies is that the samples were only characterized in dry condition, before or after electrochemical

reactions. These kinds of measurements, which involve removing a sample from operational context, are regarded as *ex situ* characterizations. *Ex situ* characterization is insufficient for providing understanding of the structure and properties of electrocatalyst materials under actual operating conditions, which is crucial for providing scientific insight into structure-property-performance relationships. By contrast, *in situ* studies refer to a category of experiments or measurements that are conducted directly at the location where the phenomenon or reactions occur, which provide information that cannot be obtained by pre- and post-reaction comparisons. This motivated the development of *in situ* STXM and spectro-ptychography as tools to systematically understand the structure and properties of electrocatalysts under operating conditions. To achieve this, an *in situ* micro-fluidic-enabled electrochemical device was developed and used. The *in situ* device used in this thesis is optimized from a previous approach using 3D-printing [Prabu et al., 2018] and the parallel development of a microfluidic approach pioneered by Pablo Ingino and Dr. Martin Obst [Obst et al., 2018]. Details of designs, fabrication, laboratory testing, and improvements of *in situ* devices are present in the thesis.

In situ STXM and spectro-ptychography are used to study Cu-based CO_2R electrocatalysts under reaction conditions. The *in situ* STXM results show that electrodeposited Cu_2O particles are converted to metallic Cu at applied potentials prior to the onset of the CO_2R reaction, indicating that metallic Cu is the active catalyst for CO_2 reduction. At CO_2R-relevant negative potentials, metallic Cu particles are found to be stable chemically and morphologically, within the spatial resolution limits of STXM (~50 nm). However, quantitative chemical mapping by *in situ* spectro-ptychography with a

higher spatial resolution (~20 nm) visualized small morphological changes of a single Cu nanoparticle in the regime of CO_2R. The Cu_2O particles lost their initial cubic structure with conversion to metallic Cu and formed irregular dendritic-like structures with detachment during the subsequent CO_2R process.

1.2 Electrochemical CO_2 reduction

From the beginning of the Industrial Revolution in the late 18th century, the increasing use of fossil fuel - coal and later oil and gas - caused a substantial release of CO_2 into the atmosphere. Since the late 19th century, Earth's average temperature and CO_2 concentration in the atmosphere have both increased dramatically (**Figure 1.1**). [Wu et al., 2017] Especially after the middle 20th century, the CO_2 concentration rapidly increased from 310 to 390 ppm in 60 years from 1950 to 2010, which is a ~25% rise while there is only a ~7% increase from 1890 to 1950. This caused a sharp rise in global temperatures with many wide-ranging problems including the melting of glaciers, extreme weather events, loss of biodiversity, and many other urgent environmental challenges. [Wu et al., 2017. Low et al., 2017]

To mitigate the emissions of CO_2, it is essential to reduce the generation and further accumulation of CO_2 gas. This includes efforts to increase the rate of bio-accumulation of CO_2 through reforestation; increase energy efficiency to minimize energy waste, substantially decrease fossil fuel consumption and associated emissions; transitioning to non-CO_2 emitting, and renewable energy sources; development of new technologies to sustainably recycle and consume CO_2 gas to achieve carbon neutrality.

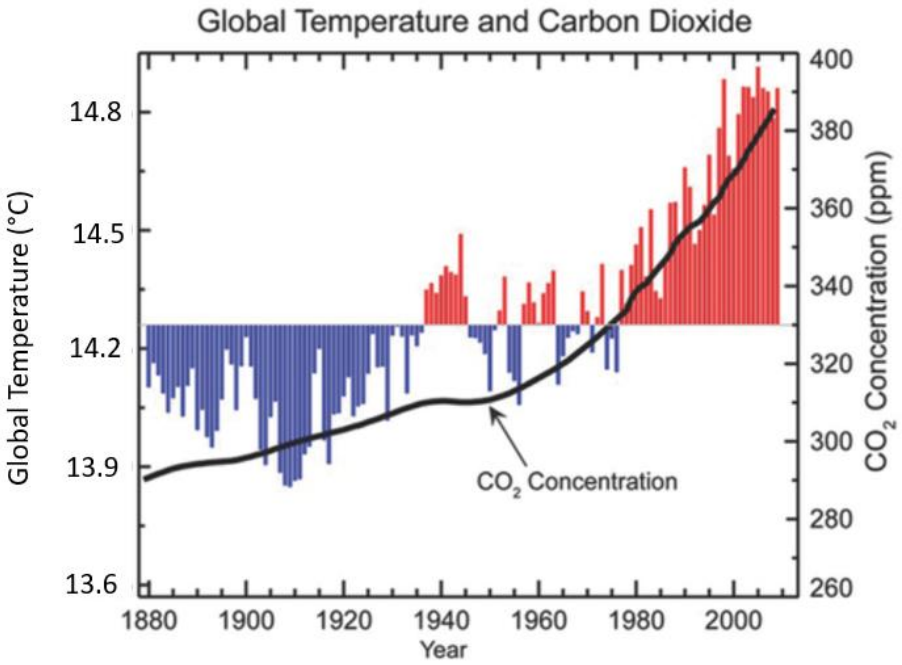

Figure 1.1 Atmospheric CO_2 concentration and corresponding global average temperature since the late 19th century. Red bars indicate temperatures above and blue bars indicate temperatures below the 1901–2000 average temperature. Adopted from the website of the National Ocean and Atmospheric Administration (NOAA).Copyright 2017, NOAA. Re-produce from [Wu et al., 2017]. With permission from WILEY.

Among various efforts to address the climate crisis, CO_2R is important because it offers a sustainable approach to converting CO_2 into useful valuable chemicals, such as CO, hydrocarbon, alcohol, and carbonyl products. These products are significant to chemical industry as chemical feedstock, for the production of plastic and polymers. [De et al., 2019] CO_2 reduction not only reduces the CO_2 emissions to the atmosphere but promotes the effective utilization of CO_2 to reduce the consumption of fossil fuels and achieve efficient carbon cycling. [Hori et al., 2008]

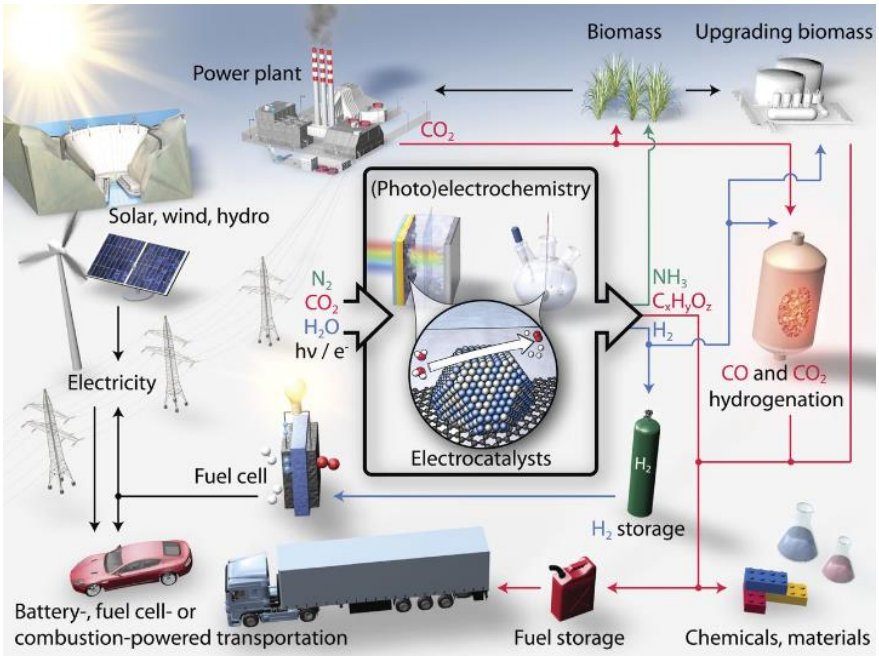

Figure 1.2 Sustainable energy future. Schematic of a sustainable energy landscape based on electrocatalysis. [Seh et al., 2017] With permission from Science.

CO_2 can be reduced through various methods, such as thermal decomposition, photochemical and electrochemical conversions. [Nitopi et al., 2019. Steinberg et al., 1998.] Among these methods, electrochemical CO_2 reduction is a promising and attractive option due to the following advantages: 1. it can be powered by renewable energy sources such as solar or wind power; 2. typically it occurs at mild operating conditions (near-ambient temperature and pressure); 3. it can effectively improve the selectivity to produce desired chemicals by fine-tuning and optimizing the operating conditions such as pH, potential ranges, applied currents, selection of electrode materials and electrolyte; 4. it can be designed to be modular and scalable, making it feasible to

adapt the technology for various applications and production scales. [Seh et al., 2017. Kuhl et al., 2014] This makes CO_2 reduction through electrochemical reactions a promising and sustainable approach to producing carbon-based chemicals and fuels. [Nitopi et al., 2019. De et al., 2020] The practical implementation of CO_2R could be integrated into existing society infrastructure and people's daily life. (**Figure 1.2**)

To achieve CO_2R reaction, overall transformation in an electrolytic cell or electrolyzer is:

$$x\ CO_2 + y\ H_2O \rightarrow C_xH_{2y}O_z + (2x+y-z)\ O_2 \qquad \text{Eqn 1.1}$$

Equation 1.1 is the total reaction of two electrochemical half reactions. Water oxidation (oxygen evolution reaction, OER) happens on the anode:

$$2\ H_2O \rightarrow\ O_2 + 4\ e^- + 4\ H^+ \qquad \text{Eqn 1.2}$$

The CO_2R reaction happens on the cathode:

$$x\ CO_2 + (2y+2x-z)\ H^+ + ne^- \rightarrow C_xH_{2y}O_z + (2x-z)\ H_2O \qquad \text{Eqn 1.3}$$

Although, OER is necessary for the full reaction, this thesis will focus only on the CO_2R half reaction.

To proceed forward the reaction shown in Equation 1.3, a significant amount of electrical power is required to convert input energy to the energy stored in the chemical bonds of the products. Energy efficiency, an important factor for CO_2R, is the percentage of chemical energy stored in the products compared to the total electrical energy input. [Chen et al., 2019. Wen et al., 2020] The energy efficiency of an electrolyzer is typically proportional to the voltage efficiency ($\boldsymbol{\varepsilon_{Voltage}}$), which is presented by:

$$\boldsymbol{\varepsilon_{Voltage} = V_{cell} / E_{cell}} \qquad \text{Eqn 1.4}$$

E_{cell} is thermodynamic cell voltage and V_{cell} is actual cell voltage. Voltage efficiency represents cell efficiency and energy losses in practical conditions.

Because the electricity requirement is a significant portion of the total cost of CO_2R, it can largely affect the cost of products. At present, more than 60% of the product cost is from electricity.[Kibria et al., 2019] Through the optimization of the voltage efficiency, total electricity requirements could be reduced to effectively lower the costs of the products, making CO_2R production of chemical feedstocks practical and potentially profitable.

Table 1.1 shows the equilibrium potentials for a set of possible CO_2R reactions and products with the transfer of 2, 4, 6, or even more electrons and yielding diverse reduction products including carbon monoxide (CO), formic acid (HCOOH), methane (CH_4), ethylene (C_2H_4), and many others. [Singh et al., 2021. Kuhl et al., 2012] The equilibrium potentials are determined solely by thermodynamics and calculated via the Gibbs free energy of reaction using gas-phase thermochemistry data and Henry's Law data:

$$\Delta G=\Delta H-T*\Delta S \qquad \text{Eqn 1.5}$$

ΔG is the standard Gibbs free energy change; ΔS, the change in entropy from reactants to products; ΔH, the change in enthalpy; T, temperature in Kelvin. All the equilibrium potentials are versus reversible hydrogen electrode (RHE), which is widely used to establish a standard hydrogen electrode potential to provide consistent and accurate comparisons across various research studies.

Table 1.1 Electrochemical reactions happening during the CO_2R process with equilibrium potentials and generated products. [Nitopi et al., 2019]

Reaction	E^0/[V vs RHE]	(Product) Name, abbreviation
$2H_2O \rightarrow O_2 + 4H^+ + 4e^-$	1.23	Oxygen Evolution Reaction, OER
$2H^+ + 2e^- \rightarrow H_2$	0	Hydrogen Evolution Reaction, HER
$xCO_2 + nH^+ + ne^- \rightarrow product + yH_2O$		*CO_2 Reduction, CO_2R*
$CO_2 + 2H^+ + 2e^- \rightarrow HCOOH_{(aq)}$	−0.12	Formic acid
$CO_2 + 2H^+ + 2e^- \rightarrow CO_{(g)} + H_2O$	−0.10	Carbon monoxide
$CO_2 + 6H^+ + 6e^- \rightarrow CH_3OH_{(aq)} + H_2O$	0.03	Methanol, MeOH
$CO_2 + 4H^+ + 4e^- \rightarrow C_{(s)} + 2H_2O$	0.21	Graphite
$CO_2 + 8H^+ + 8e^- \rightarrow CH_{4(g)} + 2H_2O$	0.17	Methane
$2CO_2 + 2H^+ + 2e^- \rightarrow (COOH)_{2(s)}$	−0.47	Oxalic acid
$2CO_2 + 8H^+ + 8e^- \rightarrow CH_3COOH_{(aq)} + 2H_2O$	0.11	Acetic acid
$2CO_2 + 10H^+ + 10e^- \rightarrow CH_3CHO_{(aq)} + 3H_2O$	0.06	Acetaldehyde
$2CO_2 + 12H^+ + 12e^- \rightarrow C_2H_5OH_{(aq)} + 3H_2O$	0.09	Ethanol, EtOH
$2CO_2 + 12H^+ + 12e^- \rightarrow C_2H_{4(g)} + 4H_2O$	0.08	Ethylene
$2CO_2 + 14H^+ + 14e^- \rightarrow C_2H_{6(g)} + 4H_2O$	0.14	Ethane
$3CO_2 + 16H^+ + 16e^- \rightarrow C_2H_5CHO_{(aq)} + 5H_2O$	0.09	Propionaldehyde
$3CO_2 + 18H^+ + 18e^- \rightarrow C_3H_7OH_{(aq)} + 5H_2O$	0.10	Propanol, PrOH
$xCO + nH^+ + ne^- \rightarrow product + yH_2O$		*CO Reduction, COR*
$CO + 6H^+ + 6e^- \rightarrow CH_{4(g)} + H_2O$	0.26	Methane
$2CO + 8H^+ + 8e^- \rightarrow CH_3CH_2OH_{(aq)} + H_2O$	0.19	Ethanol, EtOH
$2CO + 8H^+ + 8e^- \rightarrow C_2H_{4(g)} + 2H_2O$	0.17	Ethylene

In addition, CO_2R has large kinetic barriers that must be overcome with excess voltage beyond what is thermodynamically required. One of the main reasons for the slow reaction rate of CO_2R is because of the high activation energy to break the very stable structure of the CO_2 molecule. The C=O double bond in CO_2 has a bond energy of 750 kJ mol^{-1}, which is much more stable than C-C (336 kJ mol^{-1}), C-O (327 kJ mol^{-1}), or C-H (411 kJ mol^{-1}) bond energies in other molecules [Wu et al., 2017] Therefore, CO_2R reactions are thermodynamically uphill reactions and need significant energy to drive the reaction, and also additional activation energy to overcome the kinetic barrier to breaking the C=O bond to initiate the reaction. This excess voltage is referred to as overpotential,

which reduces the voltage efficiency. Lowering the overpotential would increase the energy efficiency of producing chemicals and fuels electrochemically.

1.3 CO_2 reduction electrocatalysts

There are still many fundamental problems and challenges with CO_2 electroreduction [Wu et al., 2017. Sun et al., 2017. Stephanie et al., 2019.]:

1. **Thermodynamics**: the structure of CO_2 molecules with carbon-oxygen double bonds (C=O) is highly stable, so the CO_2R reactions need high activation energies to initiate the chemical reactions and substantial energy inputs to overcome the thermodynamic barrier.
2. **Kinetics**: Even if thermodynamically favorable, reactions can proceed at very low rates due to kinetic limitations as a result of high activation energy barrier.
3. **Mass transport:** The slow rate of CO_2 supply as the feedstock to the CO_2R system, and the slow diffusion of reactants and intermediates involved in the reactions typically are limiting factors.
4. **Competing reactions**: Competing reactions, such as water splitting and oxygen reduction reactions, may happen during the CO_2R reaction to reduce the CO_2R efficiency. In addition, there are multiple possible reaction pathways for CO_2R reactions, leading to the formation of a variety of products, which reduces the selectivity and efficiency of desired CO_2R products.

In the process of addressing these challenges, many factors such as the temperature, pressure, electrochemical parameters (the range of applied potentials, static or pulsed potentials), electrolyte (kinds, pH, and concentration), and others are considered, improved, and optimized to successfully make CO_2 reduction reactions more efficient and economically viable. [Nitopi et al., 2019] Development of high-performance and novel CO_2R electrocatalysts is one of the most crucial factors in greatly improving CO_2R activity and selectivity.

The electrochemical reactions where 2, 4, 6 or even more electrons are transferred to a CO_2 molecule happen on surface of the electrocatalyst. Therefore, the properties of the electrocatalyst largely affect the performance. First, electrocatalysts can improve the kinetics by lowering the activation energy required for the reactions and thereby increase the rate of the desired reaction. One of the primary reasons for the low efficiency and slow reaction rate of CO_2R is due to the significant activation energy input to break the C=O bond to initiate the reactions. With active electrocatalysts, the overpotential can be reduced to increase the energy efficiency of producing CO_2R products. [Wu et al., 2017]

In addition, the electrocatalyst could directly affect the CO_2R reactions and generated products. The CO_2R performance for different metal electrocatalysts is presented in **Table 1.2**. The Faradaic Efficiency here is a measure of the effectiveness of an electrochemical reaction in producing a specific desired CO_2R product compared to the total CO_2R reactions. Faradaic efficiency is the proportion of electrons used in the reduction of CO_2 to a particular product of interest out of the total electrons that were

passed through the electrode during the reaction. The principal and experimental details for determining Faradaic Efficiency are introduced in **Chapter 2** and **Chapter 3**.

Table 1.2 Faradaic Efficiencies of CO_2 Reduction Products on various Metal Electrocatalysts [Hori et al., 2008]

Metal	E [V vs RHE]	J_{total} [mA/cm^2 geo]	CH_4 [%]	C_2H_4 [%]	EtOH [%]	PrOH [%]	CO [%]	$HCOO^-$ [%]	H_2 [%]	Total [%]
Pb	−1.24	−5.0	0	0	0	0	0	97.4	5.0	102.4
Hg	−1.12	−0.5	0	0	0	0	0	99.5	0	99.5
Tl	−1.21	−5.0	0	0	0	0	0	95.1	6.2	101.3
In	−1.16	−5.0	0	0	0	0	2.1	94.9	3.3	100.3
Sn	−1.09	−5.0	0	0	0	0	7.1	88.4	4.6	100.1
Cd	−1.24	−5.0	1.3	0	0	0	13.9	78.4	9.4	103.0
Au	−0.65	−5.0	0	0	0	0	87.1	0.7	10.2	98.0
Ag	−0.98	−5.0	0	0	0	0	81.5	0.6	12.4	94.6
Zn	−1.15	−5.0	0	0	0	0	79.4	6.1	9.9	95.4
Pd	−0.81	−5.0	2.9	0	0	0	28.3	2.8	26.2	60.2
Ga	−0.85	−5.0	0	0	0	0	23.2	0	79.0	102.0
Cu	−1.05	−5.0	33.3	25.5	5.7	3.0	1.3	9.4	20.5	103.5
Ni	−1.09	−5.0	1.8	0.1	0	0	0	1.4	88.9	92.4
Fe	−0.52	−5.0	0	0	0	0	0	0	94.8	94.8
Pt	−0.68	−5.0	0	0	0	0	0	0.1	95.7	95.8
Ti	−1.21	−5.0	0	0	0	0	tr.	0	99.7	99.7

Metal electrocatalysts for CO_2R can be classified into 4 groups: Pb, Hg, Tl, In, Sn, Cd, and Bi produce primarily formate ($HCOO^-$). Au, Ag, Zn, Pd, and Ga produce primarily carbon monoxide (CO); Ni, Fe, Pt, and Ti reduce very little CO_2 and instead almost exclusively reduce water (or protons) to H_2. Cu stands out in uniquely producing a number of hydrocarbons, aldehydes, and alcohols, including CH_4, C_2H_4, ethanol (C_2H_5OH or EtOH), n-propanol ((C_3H_7OH or PrOH). Thus, Cu is the only pure metal that reduces CO_2 to products requiring more than two electron transfers with substantial Faradaic efficiencies. It has been clarified that the >2 e^- transfer for CO_2R reactions using Cu electrocatalysts is due to the special mechanisms of CO_2 bonding to the Cu surface: symmetric coupling (also called top absorption) and asymmetric coupling (also called

bridge absorption). [Shen et al., 2022. Kong et al., 2022] (**Figure 1.3**) The multi-carbon (C_2+) products from CO_2R reactions, are more valuable than CO and $COOH^-$. [De et al., 2019] In particular, C_2H_4, as a key building block for a wide variety of chemical-engineering products. Ethanol can be used as a solvent, a chemical feedstock, and a renewable fuel. Ethylene and ethanol are the two most promising and valuable products from CO_2R and both are major products of Cu electrocatalyszed CO_2R. Therefore, Cu and Cu-based catalysts attract wide attention, and this is why Cu electrocatalysts are the main focus of this thesis.

Other electrocatalysts studied in this thesis are metal–nitrogen–carbon (M–N–C) materials because they have a unique single-atom active site structure and show different CO_2R performance compared with corresponding pure metal. [Varela et al., 2019] For example, pure Fe can only produce H_2, but Fe-N-C can facilitate the generation of CO and CH_4 from the CO_2R process through proton-coupled and proton-decoupled electron transfer pathways. [Ju et al., 2019. Varela et al., 2019].

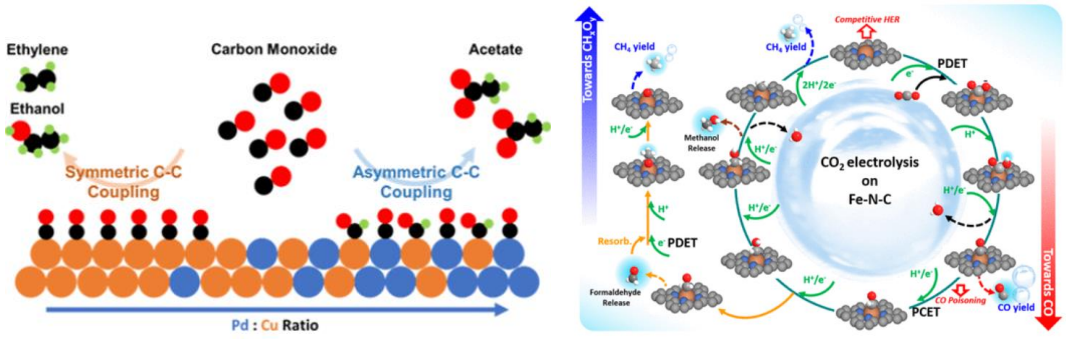

Figure 1.3 Comprehensive reaction network for CO_2 reduction over a) Cu-based catalysts. [Shen et al., 2022]. b) the Fe-N-C catalysts. [Ju et al., 2019]. With permission from the American Chemical Society.

Although judicious choice of CO_2R electrocatalysts can improve CO_2R performance, the low conversion efficiency, and the limited tunability of product distributions currently limit the large-scale application of CO_2R. [De et al., 2019] This can be seen from the CO_2R performance of Cu metal shown in **Table 1.2**. Although the equilibrium potentials to carry out electrochemical reactions to produce methane, ethylene, formic acid, etc. are low, close to 0 V vs reversible hydrogen electrode (V_{RHE}), the practical potential to achieve a reasonable current of -5 mA/cm^2 is -1.05 V_{RHE}. If the applied potential is lower than -1 V_{RHE}, the Faradaic efficiency for overall CO_2R reactions and specific CO_2 products is largely reduced. For example, the overall CO_2R efficiency for pure Cu metal at -0.68 V_{RHE} is ~55%. The Faradaic efficiency of each product is 35% for Ethylene, 3.5% for Propanol, 15% for Ethanol, etc. [Wang et al., 2020] This is due to the need for large overpotential because of high activation energy to break the stable and chemically inert CO_2 molecules, slow reaction rate to need more energy to overcome the kinetic barriers, and unwanted competing reactions to consuming electrons. Even with huge overpotential at -1.05 V_{RHE}, the Faradaic efficiencies for overall CO_2R reactions and efficiency to specific CO_2 products are low: ~80% for overall reactions, 33% for CH_4, 25% for C_2H_4, and <10% for other products. Overall, the huge overpotential, low overall efficiency, and poor selectivity make CO_2R far from large-scale practical application.

Through the design and optimization of high-performance electrocatalysts, the overpotential, efficiency, and selectivity can be improved. The reduction of overpotential can be evident from **Table 1.2** since the potential to reach -5 mA/cm^2 differs among

various metal electrocatalysts. For the generation of substantial CO, the potential to reach -5 mA/cm^2 for Zn metal is -1.15 V_{RHE} while for Au metal it is only -0.65 V_{RHE}, a huge overpotential difference of 0.5 V_{RHE}. To improve the efficiency and selectivity of CO_2R reactions, the development of novel electrocatalysts can achieve a breakthrough in CO2R performance compared to pure metallic electrocatalysts. For example, with Cu alloys, Cu compounds, and nanostructured Cu materials, >60% Faradaic efficiency to specific products, and ~90% for overall CO_2R reaction has been achieved. [Lu et al., 2016. Stephanie et al., 2019. Wu et al., 2017.]

The design and optimization of high-performance electrocatalysts is important to achieve practical electrochemical CO_2 reduction processes. In the process of catalyst design and optimization, understanding the structure and properties of different electrocatalysts is critical. Therefore, studying electrocatalysts using various characterization methods is fundamental to providing critical insights into active sites, structure-activity relationships, mechanistic understanding of the role of the catalyst in the electrochemical reactions, etc.

1.4. *In situ* characterization of CO_2R electrocatalysts

"*In situ*" is a Latin term that means "in place" or "on-site." *In situ* measurements refer to scientific investigations that are conducted while a process or phenomenon is occurring in its native or natural environment without disturbance or interruption. This contrasts with *ex situ* characterization where samples are removed from their reactive environment and analyzed in a controlled laboratory setting.

Many *ex situ* studies can provide fundamental information and important insights for electrocatalysts. For example, scanning electron microscopy (SEM), transmission electron microscopy (TEM), and atomic force microscopy (AFM), these microscopic techniques can provide powerful visualization at various length scales to study the morphology of electrocatalysts, including the shape, size, structure of the catalytic materials, distribution, and surface roughness, etc. [Gong et al., 2021. Li et al., 2019. Kooyman et al., 2017] Spectroscopic characterization, including X-ray absorption spectroscopy (XAS), X-ray photoelectron spectroscopy (XPS), Infrared absorption spectroscopy(IRAS), etc, are typically used to obtain chemical speciation and elemental information about electrocatalysts. [Chou et al., 2020. Wang et al., 2021] These results can help to understand the structure of electrocatalysts and relate the properties to CO_2R performance to understand structure-property-performance relationships, thereby find the best structure for electrocatalysts design and synthesis.

Although *ex situ* characterizations can provide valuable information, the limitation is that the sample materials are studied before and after the operation or reactions, so the morphological/chemical evolution with changing conditions and the actual condition of materials in the process can only be inferred indirectly. [van der Wal et al., 2021. Hwang, et al., 2020.] In electrochemical applications, electrocatalytic "precursors" tend to be either oxidized or reduced under the relevant reaction conditions, and thus the real active sites of the electrochemical reactions are frequently different than the precursor species. [Velasco-Velez et al., 2020. Zhang et al., 2017. Hu et al., 2017] After the reactions, the samples are typically removed from the electrolyte environment and transferred

elsewhere for *ex situ* characterization. In this process, there might be some changes in the samples due to changes in the condition, such as exposure to air and absence of electrolyte. [van der Wal et al., 2021. Wandt et al., 2016] The material transformation under the reaction conditions and the changed environment relative to *ex situ* measurements can lead to misunderstanding. Furthermore, *ex situ* characterization before and after electrochemical reactions make it difficult to achieve an in-depth understanding of the changing structure of the materials and mechanism of the electrochemical reactions. Such information is deduced indirectly from the comparison of as-prepared and post-reaction samples.

The chemical structures present, and the dynamic morphology of Cu-based CO_2R electrocatalysts under reaction conditions are still under debate and thus could be a good example to show the advantages of *in situ* studies.[Timoshenko et al., 2020. Nitopi et al., 2019. Kibria et al., 2019.] The presence of Cu(I) species with subsurface oxygen (such as Cu_2O) during electroreduction has been suggested to improve CO_2R activity and steer the selectivity towards C_2+ products. This has been deduced from theoretical simulation, X-ray Photoelectron Spectroscopy and electron energy-loss spectroscopy.[Cheng et al., 2021, Eilert et al., 2017, Wang et al., 2022.]. However, other studies have refuted the presence of significant amounts of partially oxidized Cu species under the electrochemically reducing conditions required for the reaction from density functional theory (DFT) calculations from thermodynamic/kinetic perspectives, *in situ* grazing incidence X-ray diffraction and secondary-ion mass spectrometry measurements.[Fields et al., 2018. Scott et al., 2019. Lum et al., 2018] Morphological changes also occur in Cu electrocatalysts

under CO_2R reaction conditions that can lead to changes in the properties of the catalyst and, by extension, the resultant CO_2R activity and selectivity. [Grosse. et al., 2021. Arán-Ais et al., 2020.] The morphology and chemical structures present in Cu catalysts change as a direct function of the local reaction environment and applied potential. In addition, nanoparticles of Cu metal and Cu(I) are unstable in air. They tend to be oxidized within a few tens of minutes after removing the Cu materials from electrolyte solution and performing *ex situ* characterization. [Weng et al., 2018. Timoshenko et al., 2020] These issues bring into question the suitability of *ex situ* characterization of as-prepared and post-CO_2R tested materials for establishing catalyst design principles.

1.5. *In situ* soft X-ray spectro-microscopic techniques

There are various *in situ* methods, briefly classified into 3 kinds: 1. microscopic techniques including *in situ* SEM, TEM, etc.[Velasco-Velez et al., 2020, Arán-Ais et al., 2020, Yang et al., 2023]; 2. spectroscopies such as *in situ* XAS, IRAS, etc. [Velasco-Velez et al., 2020. Lee et al., 2020. Chou et al., 2020]; 3. spectro-microscopies such as Infrared (IR) spectro-microscopy, Raman Microscopy, [Wang et al., 2022. Antonio et al., 2014. Paterova et al., 2020] *in situ* STXM and spectro-ptychography, which are the techniques mainly used in the thesis and introduced in detail. [Mefford et al., 2021. Prabu et al., 2018.]

Spectro-microscopies are hybrid techniques that combine the principles of spectroscopy and microscopy to provide spectroscopic information and microscopic imaging simultaneously. Typically, various wavelengths of light (X-rays, infrared, and

ultraviolet) are used to illuminate the sample. Through interactions between the light and the sample, the composition, molecular structure, electronic states, and other relevant properties of the samples are obtained by spectromicroscopy. At the same time, the microscopy aspect is used to image the sample with the same light to provide morphological information.

For *in situ* applications, spectro-microscopic techniques have significant advantages compared with only spectroscopy and only microscopy: 1. providing both spectroscopic data and high-resolution microscopic images simultaneously to correlate spectroscopic information with specific regions of interest on the electrocatalysts; 2. offer the ability to link spectroscopic information with the spatial distribution of chemical species to provide a deeper understanding of local variations and heterogeneities of catalytic materials. 3. real-time observe morphological and spectroscopical changes of electrocatalysts during the CO_2R process. By combining microscopic and spectroscopic information, *in situ* spectro-microscopy provides a comprehensive understanding of catalytic materials.

However, spectro-microscopic techniques are typically more complicated than standalone spectroscopy and microscopy techniques. [Stohr, J et al., 2000] It is very challenging to apply spectromicroscopies to *in situ* applications especially, since additional factors need to be considered. Before I started my Ph.D. in 2019, there were only a few successful cases of *in situ* STXM and no publications for *in situ* spectro-ptychography. Therefore, *in situ* STXM and ptychography were developed and applied to CO_2R electrocatalysts in this thesis.

1.6. A review of the development of *in situ* STXM and spectro-ptychography

The first *in situ* STXM study of electrochemical reactions in a liquid cell was reported in 2005 by Daniel Guay, Adam P. Hitchcock, et al from McMaster University, Canada. [Guay et al., 2005] This work was based on a sealed electrochemical wet cell, consisting of an electrodeposited polyaniline thin film on a thin Au film covered by an overlayer of 1 M HCl solution sitting between two X-ray transparent silicon nitride windows. (**Figure 1.4**) During the *in situ* experiments, cyclic voltammetry and changing potential applied with a constant scan rate were applied to the system and the chemical state of the polyaniline film was reversibly converted between reduced (leucoemeraldine) and oxidized (emeraldine chloride) states.

After that, Benedetto Bozzini, and his colleagues, from Brindisi Fuel Cell Durability Laboratory, Italy, extended the *in situ* STXM studies to a series of electrochemical reactions or phenomenon, such as the electrodeposition of transition metals, [Bozzini et al., 2009a, b], corrosion in fuel cells [Bozzini et al., 2011b], Galvanic coupling [Bozzini et al., 2011c]. In addition, other *in situ* STXM studies on Cu electrodeposition [Hitchcock et al., 2016. Prabu et al., 2018] and Li-ion batteries [Weker et al., 2015. Lim et al., 2016. Chourasia et al., 2022] were reported.

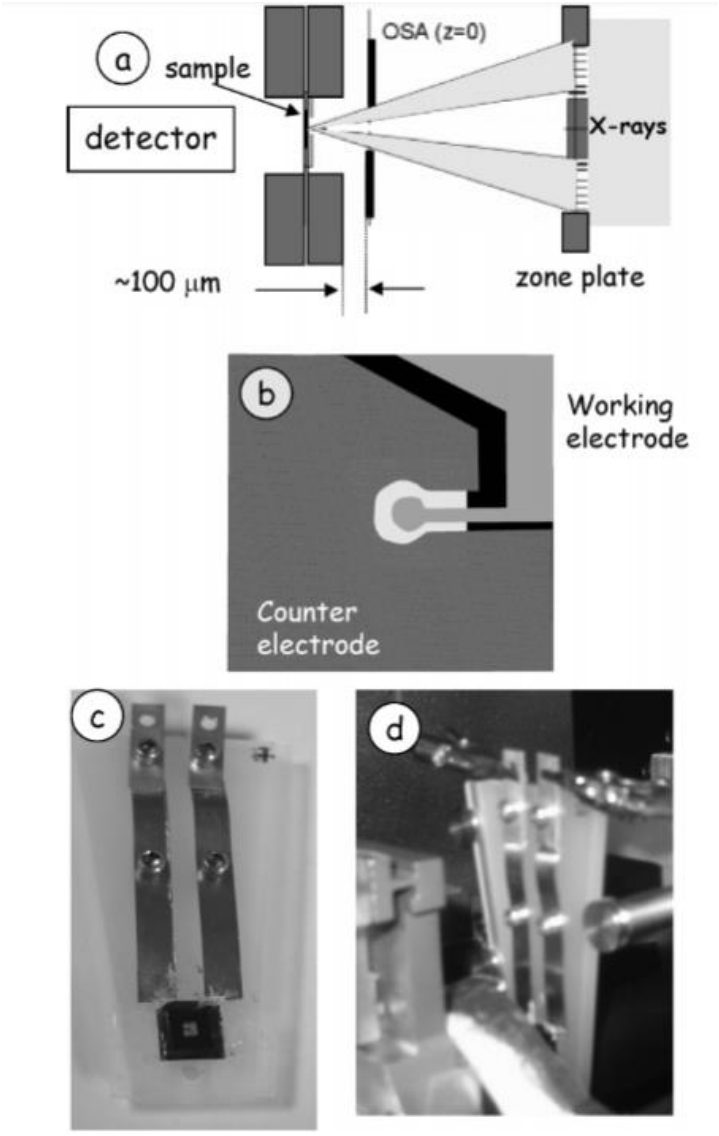

Figure 1.4 Design and photos of the cell used in earlier *in situ* STXM study (a) Schematic of key elements of STXM. (b) Pattern of Au electrodes (10-nm thickness) on a silicon nitride membrane window(1500 x 1500 μm, 75 nm thick) in a Si wafer used for *in situ* electrochemical STXM. (c) Photograph of the sample holder. Electrical contacts are stainless steel spring clips; ridges on the side of the poly(chlorotrifluoroethylene) body provide kinematic relocation of the sample relative to the X-ray beam. (d) Photograph of the holder in beamline 5.3.2 STXM at the ALS. [Guay et al., 2005] With permission from the American Chemical Society.

Table 1.3 lists the important papers or reports about the *in situ* STXM studies on electrochemical reactions, applications or phenomenon. Because this thesis is focusing on *in situ* studies of electrochemical reactions, although there are many excellent *in situ* STXM studies on other research fields such as environmental biofilms [Obst et al., 2018], SnO_2 coated carbon nanotubes [Wang, 2011], NiCo catalysst for dry methane reforming [Beheshti Askari et al., 2020], these papers or reports are not included in Table 1.3.

In situ STXM studies for electrochemical reactions have been greatly developed and at the same time, the device used for *in situ* STXM studies has been improved and optimized. **Table 1.4** lists the important papers or reports about the development of *in situ* devices for STXM. Starting from the earliest *in situ* cell shown in **Figure 1.4**, the *in situ* devices and instrumentations for STXM evolved from a sealed electrochemical wet cell to liquid flow cells with custom designed chips. (**Table 1.4**) In addition to the research scientists involved in the development of the *in situ* devices and instrumentation for STXM, the engineers and research groups in commercial companies have also joined the game, such as Hummingbird, Norcada, etc.

Table 1.3 List of *in situ* STXM studies of electrochemical reactions

Citation	**Important information**
Guay et al., 2005	Electrochemical response of polyaniline film in 1 M HCl solution.
Bozzini et al., 2008	The anodic and cathodic behaviour of Ag in neutral NaCl and $(NH_4)_2SO_4$ aqueous solutions.
Bozzini et al., 2009-a	Ni electrodeposition from ammonium and chloride solutions.
Bozzini et al., 2009-b	Anodic corrosion and cathodic electrodeposition of Ag in aqueous systems
Bozzini et al., 2011-a	Corrosion of Ni electrodes in contact with room-temperature ionic liquids
Bozzini et al., 2011-b	Corrosion of Fe bipolar plates in ionic-liquid-based nano polymer electrolyte membrane fuel-cell
Bozzini et al., 2011-c	Galvanic coupling of Au and Fe in neutral aqueous solutions containing sulphate and fluoride ions,
Bozzini et al., 2012	Mn electrodeposition from a choline chloride/urea eutectic ionic liquid bath
Hitchcock et al., 2016	Cu electrodeposition onto, and stripping from a Au surface in $CuSO_4$ solution.
Lim et al., 2016	Track the reaction dynamics of an electrode material, $LiFePO_4$ during charging and discharging process.
Wu et al., 2017	Study of Mg cathodic electrochemical deposition on Ti and Au electrode
Prabu et al., 2018	Study the evolution of Cu electro-deposited from an aqueous solution of copper sulphate

There are some reports of *in situ* ptychography studies. [Kourousias et al., 2018. Grote et al., 2022] However, to my best knowledge, there is no report for *in situ* spectro-photography prior to this work.

Table 1.4 Papers describing the development of *in situ* STXM devices

Citation	**Important information**
Guay et al., 2005	Electrochemical wet cell with 2 electrode system. Two X-ray transparent silicon nitride windows
Hernández-Cruz et al., 2007	A novel miniature rotation device used in conjunction with *in situ* STXM
Huthwelke et al., 2010	*In situ* cell to study phase transitions and chemical processes on individual aerosol particles
Bozzini et al., 2013	Sealed electrochemical microcell. three-electrode system,
Ohigashi et al., 2016	An azimuthal rotatable sample cell, an electrochemical cell and a controlled humidity cell
Prabu et al., 2018	3D print, liquid flow *in situ* cell with custom designed in situ chips
Förster et al., 2020	Microreactor system for *in situ* at very high humidities and low temperature
Lim et al., 2016	Hummingbird cell. liquid flow *in situ* cell with custom designed chips
http://www.shnti.com:8080/index/product/info/id/67.html https://www.norcada.com/products/in situ-tem/	Norcada cell, liquid flow *in situ* cell with custom designed chips

1.7 Significance of my thesis to electrochemical CO_2 reduction

1. STXM was applied for the first time to study single-atomic Ni-N-C electrocatalysts. The unique capabilities of STXM to achieve spatially resolved imaging and quantitative chemical identification and mapping provided insight into Ni-N-C catalysts, including details about the dependency of the structure and concentration of atomically dispersed active site species as a function of Ni-N-C synthesis.
2. Spectro-ptychography was used to study Ni-N-C materials and compared with STXM. The spatial resolution was improved from ~60 nm (STXM) to ~20 nm (ptychography) This study highlights the added value of spectro-ptychography relative to STXM for studies of electrocatalysts.
3. To achieve *in situ* STXM, a micro-chip based micro-fluidic electrochemical device

enabling controlled, variable electrolyte flow, rapid electrolyte change, and the application of applied potentials in a 3-electrode configuration and coupled instrumentation was developed, fabricated, and utilized. The *in situ* device has some specific advantages relative to existing commercial electrochemical liquid flow devices for synchrotron or electron microscopy. (**Table 1.4**, https://denssolutions.com/, https://www.protochips.com/) It provides stable and reliable electrolyte flow, an electrolyte layer thinner than 2 μm, and full compatibility with the stringent spatial constraints of soft X-ray STXM. It is the only device to my knowledge that is compatible with STXM measurements at the C 1s edge.

4. *In situ* flow electrochemical STXM was used to characterize Cu electrocatalysts during CO_2R conditions. *In situ* STXM studies directly monitor the morphological and chemical structural changes occurring in Cu catalysts under CO_2R conditions by providing quantitative oxidation state analysis and quantitative mapping under the active control of local reaction conditions and electrode potential.
5. *In situ* flow electrochemical spectro-ptychography was achieved for the first time. The spatial resolution was improved by a factor of 3 in comparison with *in situ* STXM at the same sample. The improvements in resolution allowed the observation of small changes happening on a single Cu cubic nanoparticle which could not be detected by *in situ* STXM.

1.8 Outline of the thesis

Chapter 2 describes the fundamentals of STXM and ptychography, including their principles, instrumentation, etc. Chapter 2 concludes with a description of electrochemical tests of CO_2R reactions which identify and quantify gas and liquid CO_2R products and calculate Faradaic efficiencies.

Chapter 3 first describes experimental details for STXM data acquisition and analysis, as well as ptychography data acquisition and analysis. Then sample preparation methods and sample characterizations are presented. This is followed by a detailed description of the design, fabrication process and laboratory testing of the *in situ* device. In the final part of this chapter, experimental details for *in situ* STXM and *in situ* spectro-ptychography studies are presented, in particular how Cu electrodeposition and CO_2R reactions are performed under *in situ* conditions.

Chapter 4 presents the results of *ex-situ* STXM studies of Ni-N-C catalysts which are used to show the advantages of spectro-microscopic characterizations for catalytic materials. Spatially resolved imaging of chemical species and structures of Ni–N–C electrocatalysts by STXM provides the quantification, the chemical structure, and spatial distribution mapping of atomically dispersed Ni active sites. More importantly, the relationship between Ni content/speciation and CO_2R activity/selectivity was identified, illustrating how STXM can be useful in guiding advanced electrocatalysts designs and the importance to catalysis community. This chapter is presented in as-published format.

Chapter 5 describes the *ex-situ* studies of Ni-N-C electrocatalysts by Ni L-edge spectro-ptychography and the comparison with STXM results on the same region. The

spatial resolution of ptychography is significantly improved to ~20 nm, compared to ~60 nm resolution achieved by STXM. Therefore, ptychography can efficiently show the chemical components and distributions of the small nanoparticles that STXM is difficult to study due to low spatial resolution. Some ultra-small interfaces between different chemical species in the particles were identified. This chapter is presented in as-published format.

Chapter 6 presents results and a discussion of *ex-situ* STXM studies for electrodeposited Cu electrocatalysts for CO_2 reduction. First, the reference spectra for various Cu species collected from STXM tests on different Cu samples are used for STXM analysis at the Cu edge. These spectra are fundamental for subsequent *ex situ* and *in situ* studies on Cu electrocatalysts. This is followed by the *ex-situ* STXM studies on electrodeposited Cu layers, dendrites, and Cu nanoparticles before/after CO_2R. The *ex situ* STXM results showed that initial electrodeposited Cu_2O nanoparticles became metallic Cu upon the application of CO_2R conditions. But the lack of direct detection of these Cu materials under electrochemical conditions leaves it unclear what is happening throughout the whole process. This motivated the development of *in situ* STXM and *in situ* spectro-ptychography as tools to systematically understand the structure and properties of electrocatalysts under operating conditions.

Chapter 7 describes the *in situ* STXM studies at the Cu 2p edge on Cu electrocatalysts under CO_2R reaction conditions. The study provides detailed, quantitative results about the changes in the morphology and chemical structure (oxidation state) of the catalyst particles as a function of applied electrode potentials. The initial mixed Cu

and Cu_2O particles are converted to metallic Cu at applied potentials below that for initiation of CO_2R. During this process, Cu_2O particles of various sizes are converted to metallic Cu at different reaction rates and at slightly different electrode potentials, indicating a degree of heterogeneity in the electrochemical response of discrete particles. At CO_2R relevant potentials, only metallic Cu is observed, and the morphology of the particles is fairly stable within the spatial resolution limits of STXM (~ 50 nm), indicating metallic Cu is the active catalyst for CO_2 reduction.

Chapter 8 shows the *in situ* spectro-ptychography results of a single Cu nanoparticle in the electrochemical regime of CO_2R. Because the spatial resolution of spectro-ptychography is improved by a factor of three, compared with STXM, changes of morphology and oxidation states on individual cubic Cu particles as a function of applied potential during CO_2R can be studied. Quantitative chemical mapping demonstrated that, during the CO_2R process, the as-deposited Cu particles underwent morphological changes with conversion to metallic Cu, losing the initial cubic structure and forming irregular dendritic-like structures.

Chapter 9 summarizes the results and proposes future work related to *in situ* STXM at C 1s edge and production of on-electrode samples with ionomer.

Chapter 2

Techniques and principles

This chapter describes the fundamental principles of scanning transmission X-ray microscopy (STXM) and ptychography. For these two synchrotron-based techniques, the beamlines and microscope instrumentation used in this work are presented. Then, the principles of CO_2R reaction testing and Faradaic efficiency are introduced.

2.1 Introduction to STXM

STXM is the primary technique used to study electrocatalysts in this thesis. It is an advanced synchrotron-based spectro-microscopic characterization, which provides high-resolution imaging, spectroscopy and quantitatively chemical mapping. STXM offers detailed information about elemental composition, chemical states (speciation), and electronic properties of a sample from NEXAFS spectra. [Hitchcock et al., 2015. Jacobsen et al., 2019. Hitchcock et al., 2012. H. Ade et al., 2008.] Compared with other spectroscopies and spectro-microscopies, STXM shows many advantages including good spatial resolution, high sensitivity to chemical structure, high energy resolution and lower radiation damage per unit spectral information as compared to analytical electron microscopy. [Wang & Morin et al., 2009. Rightor et al., 1997] This makes STXM a near-ideal tool to study electrocatalytic materials and *in situ* study electrochemical reactions. [Aru, 2021. Kim, 2023]

During my Ph.D. studies, STXMs at 7 the beamlines and 6 synchrotron facilities listed in **Table 2.1** were used. The instrumentation at these 7 beamlines is briefly

compared. Since this thesis is based mainly on results from the ambient STXM on the 10ID-1 Spectromicroscopy (SM) beamline at the Canadian Light Source (CLS) and the STXM on the HERMES beamline at Synchrotron SOLEIL, these instruments are described in detail.

Table 2.1 Properties of STXM microscopes used during my PhD

Beamline	Facility	Ring-E (GeV)	Location	Source	E (eV)	citation
10ID-1	CLS. (3rd gen)	2.9	Saskatoon, Canada	EPU	250-2500	Cutler et al., 2007. Ellis et al., 2011.
HERMES	SOLEIL(3rd gen)	2.75	Paris, France	EPU	70-2500	Belkhou et al., 2015. Coati, A et al., 2017
SoftiMAX	MaxIV (4th gen)	3.0	Lund, Sweden	EPU	275-2500	Tavares, P.F. 2018. Schwenke et al., 2018.
Mystic	Bessy II (3rd gen.)	1.7	Berlin, Germany	EPU	250-750	Hitchcock 2008. Nolle, D. 2012. Beckhoff, B et al., 2000. https://www.wayforlight.eu/beamline/21676
Maxymus		1,7		EPU	150 – 1900	
DEMETER	SOLARIS (4rth gen)	1.5	Kraków, Poland	EPU	100-2000	Wawrzyniak et al., 2021. Kowalski et al., 2021. https://synchrotron.uj.edu.pl/en_GB/linie-badawcze/demeter
11.0.2	ALS (3rd gen.)	1.9	Berkeley, CA, USA	EPU	200-2000	Feggeler et al., 2023. Nichols et al., 2022.

2.1.1 STXM principles

A beam of tunable monochromated X-rays is required for STXM and this is best provided by a synchrotron light source. According to classical physics, any charged particle which moves in a curved trajectory or is accelerated in a straight-line path will emit electromagnetic radiation. Synchrotron radiation is the electromagnetic radiation generated by electrons moving at relativistic velocities in dedicated storage rings with a large radius of curvature from tens to hundreds of meters. [Balerna et al., 2015].

Synchrotron radiation from a bend magnet consists of a continuous electromagnetic spectrum covering energies ranging from microwaves to gamma rays. The X-ray beam brightness can be improved using insertion devices such as undulators and wigglers, which are the main sources at 3rd and 4th generation synchrotron facilities. [Riekel et al. et al., 2009]

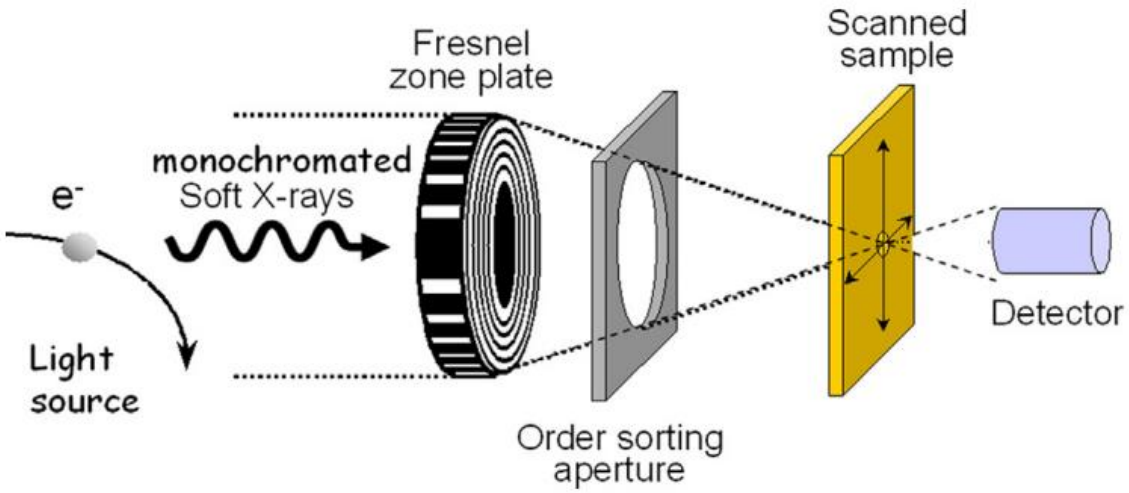

Figure 2.1 Schematic of a scanning transmission X-ray microscope [Hitchcock et al., 2014] With permission from ScienceDirect.

X-rays from the synchrotron are guided into the STXM beamline and subsequently monochromated by beamline optics, and then illuminate a Fresnel zone plate (ZP), as shown in **Fig. 2.1** [Hitchcock et al., 2014] A small fraction (10-15%) of the X-rays are focused by the ZP to a fine point probe of 30 - 50 nm on the sample which is positioned at the ZP focal point. An order sorting aperture (OSA) is used to pass the first-order diffracted X-rays while blocking the un-diffracted light. Images are mode by x-y raster scanning the sample while recording the transmitted X-ray intensity. The X-rays

that pass through the sample are down-converted to visible light by a thin (1-2 μm particle size) P41 phosphor. A high-performance photomultiplier detector is then used to detect the visible photon bursts in single event counting mode. [Hitchcock et al., 2012]

The spatial resolution and signal intensity of a STXM depends on the ZP which is a variable-line-spacing circular diffraction grating, consisting of many concentric X-ray opaque rings with alternating open circular slots fabricated on an X-ray transparent silicon nitride substrate. The setup and distances between each part of STXM are related to the ZP's dimensions and parameters. As shown in Figure **2.2**, [Wang et al., 2008. Attwood et al., 2000] the interference condition of ZP is described by:

$$f^2 + r_n^2 = (f + \frac{mn\lambda}{2})^2 \qquad \text{Eqn 2.1}$$

where f is the focal length (distance along the X-ray propagation direction between the ZP and the focused spot (where the measured sample is located), m is the diffraction order (m = 0, ±1, ±2, ±3, ±4…), λ is the wavelength of the incident X-ray, n is the zone number and r_n is the width of the n^{th} zone of the zone plate. Because the first order light (m=±1) is the most intense, it is typically the one used for STXM measurements. The undiffracted zero order (m=0) light is blocked by the combination of the order OSA and the central stop of the ZP. Higher order X-rays (m>1) are reduced to a certain degree by the OSA and ZP central stop - see Figure **2.2**. [Attwood et al., 2000]

When first-order diffracted light (m=+1) is used in STXM measurements, equation 2.1 can be converted to:

$$r_n^2 = n\lambda f + \frac{n^2\lambda^2}{4} \qquad \text{Eqn 2.2}$$

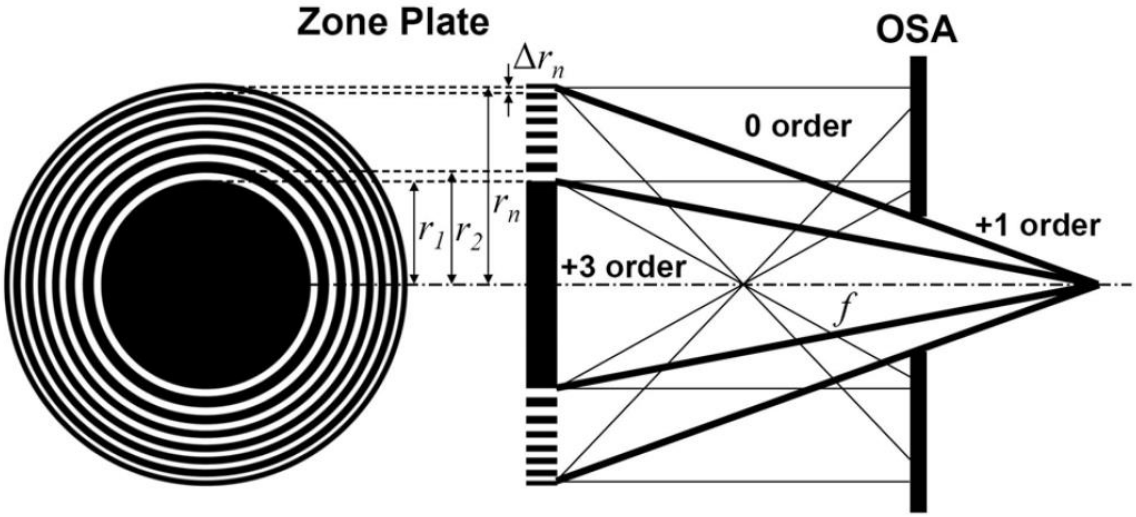

Figure 2.2 Schematic geometry of a zone plate and principles of focusing X-ray in an STXM. (OSA: order sorting aperture) [Wang, 2011]

The second term on the right side of equation 2.2 can be neglected because *f* is on the scale of mm while λ is in on the sub-10 nm scale so that $f >> n\lambda$. The focal length, *f* can thus be approximated as

$$f \approx \frac{r_n^2}{n\lambda} \qquad \text{Eqn 2.3}$$

where r_n is the width of the outermost zone and n is the total number of zones. If the ZP is fabricated with equal area for each zone (which gives even illuminated of each zone), the number of zones in the ZP can be calculated from:

$$n = \pi r_n^2 / 2\pi r_n \Delta r_n = r_n / 2\Delta r_n \qquad \text{Eqn 2.4}$$

where r_n is the radius of the outmost zone and Δr_n is its width ($\Delta r_n = r_n - r_{n-1}$). Then equation 2.3 can be written as:

$$f = \frac{2r_n \Delta r_n}{\lambda} \qquad \text{Eqn 2.5}$$

Thus, the focal length is related to the ZP dimensions and the wavelength of the X-rays. Photon energy (E) is inversely proportional to the wavelength, so equation 2.5 is typically expressed as:

$$f = D\delta r_n E \qquad \text{Eqn 2.6}$$

where D is the ZP diameter and δr_n is the width of the outermost zone. Thus the focal length changes linearly with energy. In order to maintain focus at the sample, the ZP is moved upstream from the sample as the photon energy increases. At the C 1s edge [280-320 eV], the focal length of typical ZP is about 1 mm, and the distance between the OSA and the sample is 250 – 400 μm. This places severe constraints on the design of *in situ* devices since small focal length could make the front side of the *in situ* device hit the OSA and possibly cause damage to STXM instrumentation. ZPs with a larger diameter and larger outer zone width make it easier to perform STXM at low energies, at the expense of difficulty of fabrication and reduced spatial resolution. This information is very important for conducting STXM tests and designing devices for *in situ* STXM. The minimum energy at which STXM has been performed is 50 eV, at the Li 1s edge. [Ohigashi,T. 2020]

In addition, spatial resolution of STXM is directly related to the ZP properties. The simplified equation to calculate diffraction-limited spatial resolution, defined by the

Rayleigh criterion, is given by [Thompson et al., 2001. Howells et al., 2007. Attwood et al., 2000]:

$$\text{Res} = 1.22\Delta r_n \qquad \text{Eqn 2.7}$$

Thus, the spatial resolution (Res) for STXM is determined mainly by the outer zone width of a ZP. However, it is also related to the lateral alignment of the ZP to the X-ray beam, diffraction order, and the zone plate quality. Nanofabrication of ZPs with outer zone widths less than 20 nm is very difficult. The ZPs used in this work had outer zone widths of 25-50 nm, so the spatial resolution of the STXM images is typically 30-60 nm.

2.2 STXM instrumentation

2.2.1 10ID-1 SM beamline and ambient-STXM instrumentation at CLS

The CLS, located at the University of Saskatchewan, Saskatoon is the only synchrotron facility in Canada. It consists of a 250 MeV electron linac, a 2.9 GeV booster ring, and a compact, double-bend achromat lattice storage ring with a circumference of 171 meters.[Cutler et al., 2007. Ellis et al., 2011.] CLS ran in top-up mode since 2021 with a current of 220 mA. Synchrotron radiation ranging from infrared to hard X-ray is generated from the bend magnets of the storage ring. High brightness soft X-rays are generated by Apple type II undulators. [Kaznatcheev et al., 2007] High flux X-rays are generated by superconducting wigglers. There are 18 beamlines, including the 10ID-1 SM beamline which illuminates a photoemission electron microscope (X-PEEM) and two STXMs, the ambient STXM [Kilcoyne et al., 2003. Kaznatcheev et al., 2007.] and the cryo-STXM [Leontowich et al., 2018.]

A schematic diagram and photos of beamline 10ID-1 are presented in **Figure 2.3** [Kaznatcheev et al., 2007. Zhu et al., 2016.] The X-ray beam is generated by an Apple II-type elliptically polarized undulator (EPU), which consists of four magnet assemblies, each movable vertically and horizontally. The beam is horizontally focused and reflected in the vertical direction by the M1 plane mirror. After collimation with a 4-jaw aperture, the beam passes through a plane grating monochromator (PGM), which disperses the X-rays in the vertical direction. The dispersed beam is then focused on to the ambient STXM by the toroidal M3 mirror.

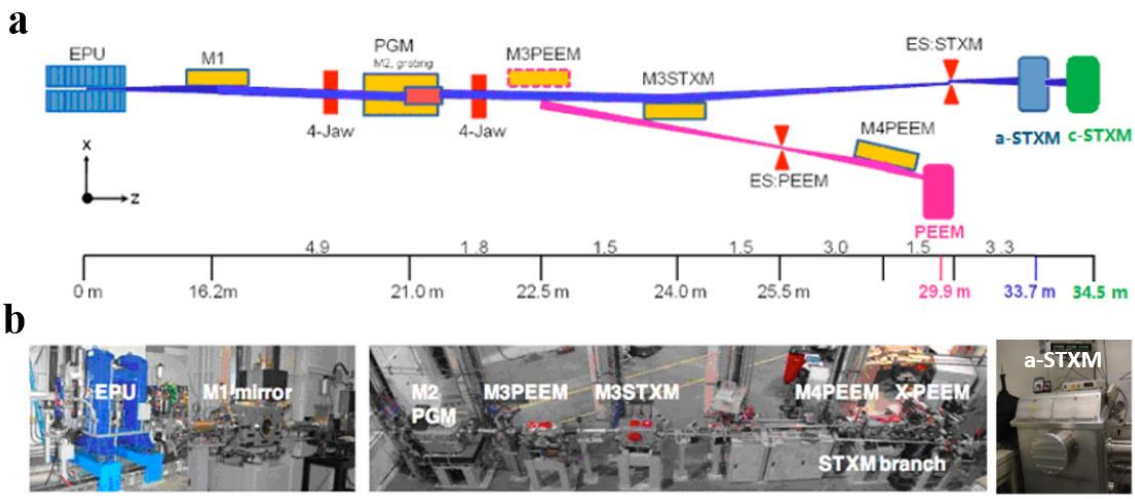

Figure 2.3 a) Schematic diagram [Zhu et al., 2016] and b) photos of 10ID-1 beamline at CLS.[Kaznatcheev et al., 2007] With permission from ScienceDirect.

A vertical exit slit is then used to isolate a specific, narrow band of the X-ray energies with a resolving power between ~3000 to ~10,000. At the same position there is also a horizontal exit slit, such that the combined openings of the horizontal and vertical

slits act as a coherence filter. There is also an in-vacuum fast piezo shutter, which is controlled by the STXM_control software such that X-rays are only hitting the sample when measurements are being made, so as to reduce radiation damage. Many parameters of the beamline and STXM are adjusted to optimize X-ray intensity, stability and to provide X-rays of user-specified energy, polarization and intensity to the STXM.

The external appearance of the ambient-STXM chamber is displayed in **Figure 2.3**. The chamber and all the microscope components are designed to achieve a vacuum of ~ 10^{-6} torr. The ambient STXM is typically pumped to a rough vacuum (0.1 mbar) and then the chamber is filled with 1/6 - 1/3 bar of helium gas for *ex situ* STXM measurements. Compared with air, the helium (He) and vacuum environment provides more photon flux due to lower X-ray absorption, which results in smaller interferometer drifts because of its lower index of refraction. He gas helps keep motors cool due to its high thermal conductivity [Kilcoyne et al.,2003]. For the *in situ* studies, where pumping below 200 mbar may lead to leaks, the air initially present in the STXM tank is typically displaced by opening a pumping fitting and passing 1.1 bar of helium gas into the tank in order to displace the air. This process typically would take 10-15 min, and use ~10 % of a large size He cylinder.

Figure 2.4a is a schematic of the STXM, showing the major components and their directions of motion. The ZP moves only in the z direction. The OSA moves only in the (x, y) directions and its z-position defines the origin of the z-scale. The sample can be moved in (x, y, z), with a set of stepping motor coarse stages (maximum region of 25 x 10 mm) and by an integrated (x,y,z) piezo stage (~60 x 60 x 20 μm). The detector can be

moved in the (x, y, z) directions. The Agilent interferometer system is similar to that of the polymer STXM on beamline 5.3.2.2 at ALS which can meausure the position of the sample (x,y) with ~10 nm precision. [Kilcoyne et al. 2003] A photograph of the key STXM components is presented in **Figure 2.4b**. Only when all the beamline and STXM components are at specific positions through careful spatial adjustments, such as positioning the sample at the ZP focus, can the STXM achieve the best possible resolution and performance.

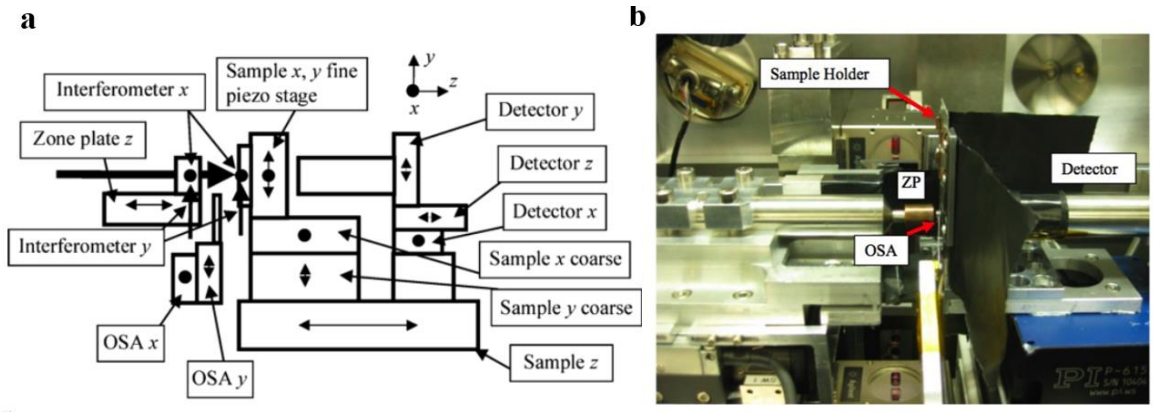

Figure 2.4. **Schematic diagram of STXM microscope** a) Schematic of the STXM components at CLS beamline 10ID1, which is Similar set up with 5.3.2 STXM at ALS [Kilcoyne et al., 2003] b). The layout of ZP, OSA, sample holder, and detector at the ambient STXM at CLS beamline 10ID1. [Courtesy of 10ID-1 CLS STXM manual.] With permission from *Journal of Synchrotron Radiation.*

Various ZPs are used at CLS according to the specific experiments and conditions. A ZP with 35 nm outer zone width, 155 μm outer diameter, and central stop of 80 μm was used for *ex situ* STXM (**chapter 4, 6**) and *in situ* STXM (**chapter 7**). Another ZP

with outer zone width of 50 nm, outer diameter of 300 μm and 90 μm central stop was used for *in situ* STXM at the C 1s edge (**chapter 9**). The longer focal length facilitated the C 1s measurements by operating correctly with a longer distance between the OSA and the sample.

The OSA consists of a Mo sheet with 3 or more small-diameter, laser drilled, circular apertures (usually 50, 60 and 80 μm). The specific OSA used was one that is 10 or 20 μm smaller than the diameter of the ZP central stop (80 or 90 μm). By carefully aligning the OSA with the ZP, only the first-order diffraction light is selected and used for STXM. (**Figure 2.2)**

The STXM samples studied for this thesis are mostly powder samples and nanoparticles. These are electrodeposited (in the case of the *in situ* studies) or mechanically distributed on silicon nitride (SiNx) windows or formvar coated 3 mm diameter TEM grids mounted on trapezoidal Al plates, or on the working electrode (WE) of the chip E of the *in situ* devices. The trapezoidal plates are attached to the kinematic sample holder as shown in **Figure 2.4 b**.

The STXM X-ray detector [Kilcoyne et al. 2003] is a thin phosphor coating on a polymethylmethacrylate (PMMA) light pipe which is coupled to a high-performance photomultiplier with associated electronics and operated in single event counting mode. The detector system responds linearly up to 20 MHz and saturates around 40 MHz. The exit slits are used to reduce the incident intensity below 20 MHz in order to avoid spectral distortion due to detector non-linearity. At the beginning of each run, the (x,y) position of the detector is optimized on the beam (the beam position changes whenever the ZP is

changed). Then the OSA is aligned on the beam, and an OSA_focus scan is used to calibrate the z position of the ZP to ensure that the ZP-z position is correct over a wide range of photon energies.

A 2-D differential laser interferometer system is used to stabilize the (x,y) sample position relative to the ZP (x,y) position. It uses the fine sample piezo stage to position the sample relative to the ZP within ~5 nm, and adjusts it with a response up to 100 Hz. [Kilcoyne et al. 2003, Hitchcock et al., 2012] In the process of the ZP moving several millimeters (as occurs when shifting from the Cu 2p to the C 1s edge), the beam position can move on the order of several hundreds of nanometers due to mis-alignment of the X-ray beam axis and the ZP-z axis [Kilcoyne et al., 2003]. In addition, deviations can also be caused by thermal drift, mechanical instabilities, and other factors. The differential laser interferometer feedback systems in STXMs are typically used to stabilize the region of the sample being scanned. [Kilcoyne et al., 2003] Typically the deviation can be limited to less than a few hundred nm which is good enough for STXM measurements. Deviations of the beam position cause equivalent shifts in the region of the sample scanned. These are removed in a post-acquisition alignment procedure [Hitchcock et al., 2023].

The software “STXM_control”, originally written by Dr. Tolek Tyliszczak and Peter Hitchcock in 1999-2001, and further developed from 2002-2016 by Dr. Tyliszczak, is used for control and data acquisition of the STXM. It controls the beamline (slit sizes, photon energy, polarization, etc) indirectly by issuing commands to the beamline and undulator software. It controls all of the stages in the STXM microscope (the positions for

OSA, ZP, sample ….motor, scanning modes…etc) and has a very flexible menu for STXM optimization and data acquisition. This software is not only used at the CLS ambient STXM, but also at the STXMs at MaxIV, Solaris, Maxymus at Bessy-II, all 5 STXMs at ALS, and STXMs in Japan, Taiwan, and Korea.

2.2.2 HERMES beamline Synchrotron SOLEIL

Synchrotron SOLEIL is a third-generation synchrotron facility located outside of Paris, France. It is a 2.75 GeV storage ring and uses 500 mA currents under top-up mode.[Coati et al., 2017. Sitaud et al., 2012. Giuliani et al., 2009] High-quality beams from infrared to hard X-ray are generated and used by more than 40 beamlines, including the HERMES beamline which provides XPEEM and STXM to users.

A schematic diagram of the HERMES beamline from the source to the end-stations is displayed in **Figure 2.5**. [Belkhou et al., 2015] X-rays of energy from 70 eV to 2.5 keV are generated from two Apple II type undulators on the mid-straight section I10-M of the Synchrotron SOLEIL storage ring. The X-ray beam is reflected by a set of three mirrors in chicane configuration (M1 mirrors) to pass through an exit slit to the plane-grating monochromator. The PGM has a variable line spacing – variable groove depth (VLS–VGD) grating for the low-energy range (70 eV to 1.6 keV). A multilayer grating for high-energy (1.0–2.5 keV) is planned but not yet installed. Downstream of the monochromator exit slit, a toroidal mirror (M4) deflects the beam towards the STXM branch, so that X-ray passes through the ZP slits to enter the STXM end-station.

The STXM instrument at the HERMES beamline was built by Research

Instruments and is an evolution of the mechanical design at the 5.3.2.2 and 11.0.2 STXMs at the ALS. It is similar to the set-up of the CLS ambient-STXM. The software used to control the STXM Is called *pixelator* and was custom written for STXMs at the Swiss Light Source, Diamond, and Bessy-II by *Semafor Informatike and Energie Ag*. SOLEIL acquired a license to the software at a later date, and has very limited access to modify it. Pixelator is modeled on STXM_control. The high level aspects are written in python, as opposed to C++ used in STXM_control.

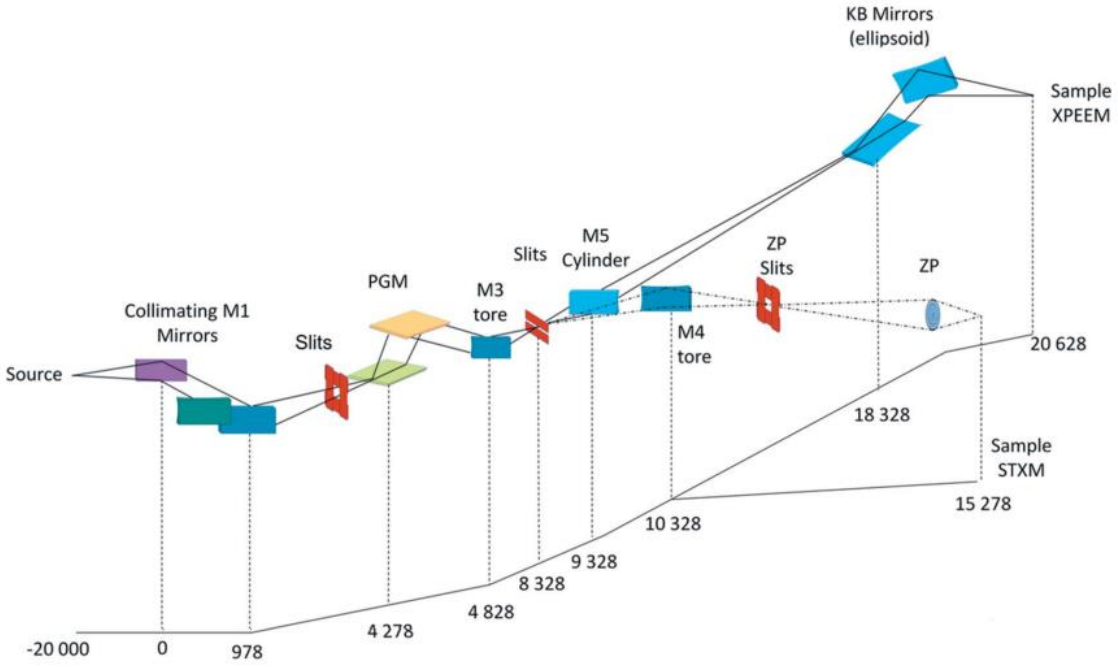

Figure 2.5 Optical layout of the HERMES beamline. The beamline is split into four parts: the source, which includes the two undulators (HU42, HU64); the three first mirrors (M1A, M1B, M1C) installed in a lead-shielded hutch; the monochromator hutch also containing the entrance and exit slits, the monochromator and the switching mirrors (M4, M5); the beamline splits further into two branches in the experimental hutch, where the two end-stations (XPEEM, STXM) are located [Belkhou et al., 2015] With permission from *Journal of synchrotron radiation*.

2.3 Introduction to ptychography

2.3.1 Ptychography principles

The spatial resolution of STXM is determined by the outer zone width of a ZP according to equation 2.7. In principle, when a ZP with smaller outer zone width is used, better spatial resolution can be achieved until it reaches the wavelength-limited resolution of a few nano-meters for soft X-ray STXM. The highest resolution useable ZPs provide ~10 nm [Chao et al., 2012; 2009. Sakdinawat et al., 2010], while the current record for ZP focused spot size is 7 nm [Rosner, B. et al., 2018]. Since the nanofabrication techniques used to make these extremely high performance zone plates are state-of-the-art, it is unlikely that further improvements in ZP will be made, at least in the near future. Typical resolution for STXM is 30-60 nm.

Coherent diffraction imaging (CDI) is a promising approach to increase spatial resolution and reach wavelength-limited resolution. Although the ptychography implementation used in this thesis does use a ZP lens, in principle the spatial resolution achieved by CDI is not dependent on the properties of lenses or other focusing methods. [Miao et al., 2012; Schroer et al., 2008] In X-ray CDI measurements transmission diffraction patterns, from a partially or fully coherent beam impinging on a sample, are measured and then reconstructed into high-resolution images using an iterative computer algorithm.[Miao et al., 1999; 1997., **Figure 2.6]**

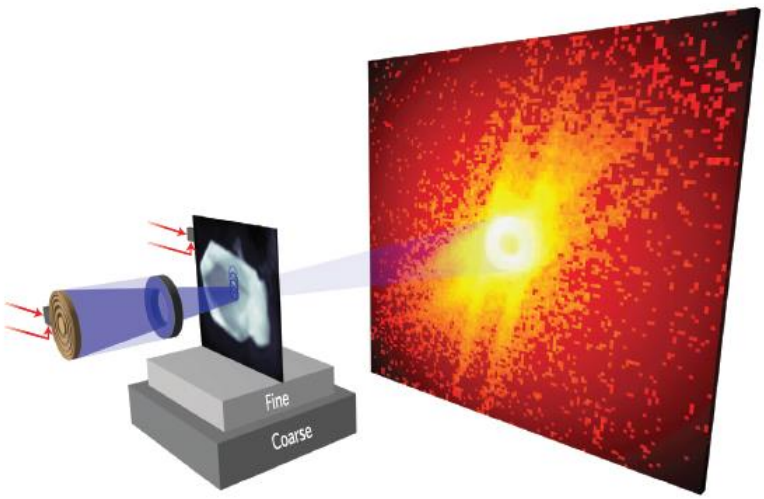

Figure 2.6 Schematic of measurement of coherent diffraction image from one point on a sample. Sets of these DI measured with an overlap of the sampled points constitute a scanned CDI or ptychographic measurement. [Pfeiffer et al., 2018] With permission from *Nature.*

Ptychography is a CDI technique that can be coupled with STXM to have the potential to reach near atomic-scale spatial resolution [Edo et al., 2013]. Ptychography provides similar abilities with STXM to characterize materials spectroscopically and microscopically at the same time, but with much better spatial resolution. Currently, the best spatial resolution achieved by ptychography is 6 nm, measured at 1600 eV using the STXM on ALS beamline 11.0.2. [Shapiro et al., 2014] Although ptychography shows improved performance compared to STXM, as a new technique which was first reported in 2014 using soft X-ray, [Shapiro et al., 2014] it still has many challenges which limit its application, such as uncertainty in the interpretation of the generated data, limited ability to test samples at low X-ray energy (<600 eV) and need of time for the computational reconstruction. So STXM is currently more widely used in synchrotron facilities than

ptychography. Briefly speaking, less than 50% of beamlines with STXM can conduct ptychography measurements, according to my beamtime experience. However, ptychography has been developing rapidly and shows promising prospects in the future. **Figure 2.6** shows a schematic of ptychography diffraction images (DI) measured in a STXM-like apparatus with a beam of partially coherent X-rays.

The interaction of X-rays with an optically thin sample depends on the refractive index of the material(s), which is one of the most important optical parameters showing how much the phase velocity of the light is changed and how much it is attenuated. [Wittwer et al., 2022. Singh, 2002.] Refractive index is a complex, photon energy-dependent quantity and can be represented as:

$$\eta = (1-\delta) - i\beta \qquad \text{Eqn 2.8}$$

where the refractive index decrement δ represents the change in phase velocity compared to that in vacuum, and β describes the attenuation by the material. [Wittwer et al., 2022. Murata et al, 2021.] In equation 2.8, the real part (1 – δ) is the phase and the complex part (β) is the amplitude response of the X-ray interacting with the material. In the ptychography images, the obtained images respectively represent the phase and amplitude signals based on the real and imaginary part of the complex refractive index, called phase and amplitude images. One can think of ptychography as a tool for refractive index mapping. [Wittwer et al., 2022.]

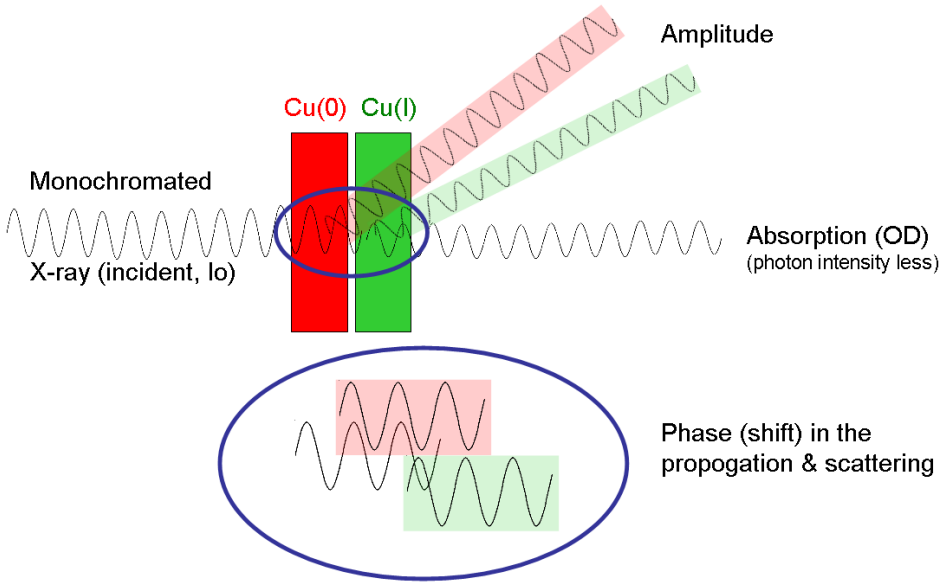

Figure 2.7 Schematic of the physical origin of the X-ray absorption, ptychography amplitude, and ptychography phase signals.

Figure 2.7 sketches the physical origin of the ptychography amplitude and ptychography phase signals. Amplitude signals indicate the attenuation of X-ray intensity after diffraction, which is typically related to X-ray absorption. However, while OD spectra derived from ptychographic amplitude and integrated X-ray transmission signals, both of which represent the X-ray absorption signal, are similar. However, they are not identical, suggesting the relationship between ptychographic amplitude and X-ray absorption signals is more complicated and needs to be clarified. Phase signals show the X-ray shifting in the propagation and scattering process. Phase spectra derived from ptychographic reconstructions are quite different from absorption or amplitude-derived spectra. The physical origin of phase spectra is still not sufficiently understood and the relationships between phase and amplitude spectra are elusive so far. An interesting

question, still incompletely answered in the literature, is, "*Is there additional, independent information from the object phase signals provided by ptychographic reconstruction ?*". A previous Hitchcock group member, Prof. Stephen Urquhart (U. Saskatchewan) is currently mounting a systematic experimental and theoretical study of this question. [Urquhart et al., 2023. Stitsky et al., 2023]

The propagation of an X-ray through a material is a spatial, temporal, and photon energy-dependent quantity that can be described by

$$U = Ae^{i\varphi} \qquad \text{Eqn 2.9}$$

where A is the amplitude at a given position and time, and $e^{i\varphi}$ is a complex propagation/loss function. Upon interaction with a sample, the complex wave field of the coherently scattered light (SC), $U^{SC}(r,\omega)$, is related to the wavefield of the light impinging on the sample (inc), $U^{inc}(r',\omega)$, by

$$U^{\mathrm{sc}}(\boldsymbol{r},\omega) = \int_V F(\boldsymbol{r}',\omega) U^{\mathrm{inc}}(\boldsymbol{r}',\omega) \frac{e^{ik|\boldsymbol{r}-\mathbf{r}'|}}{|\boldsymbol{r}-\mathbf{r}'|} \mathrm{d}\boldsymbol{r}' \qquad \text{Eqn 2.10}$$

where r and r' are time-dependent position vectors of the X-ray before and after the sample, ω is the angular frequency of the light ($\omega = 2\pi\nu$; the photon energy (E) is given by $E=h\nu$) and $e^{ik|r-r'|}/|r-r'|$ is a plane wave description of the light wave. The DI measured in ptychography only measures the amplitude of the scattered X-rays, U^{SC}. The challenge of ptychographic reconstructions is to solve the phase inversion problem [Maiden et al., 2009. Guizar-Sicairos et al., 2021]

Amplitude and phase images of the sample (object) and the incident X-ray beam (probe) can be derived from sets of DI using an iterative algorithm. For a single DI the reconstruction can be described conceptually as outlined in **Figure 2.8**, While this approach uses Fourier transforms (F{p(x) } and F^{-1}{ p(x) }) as propagators, other mathematical functions can be used.

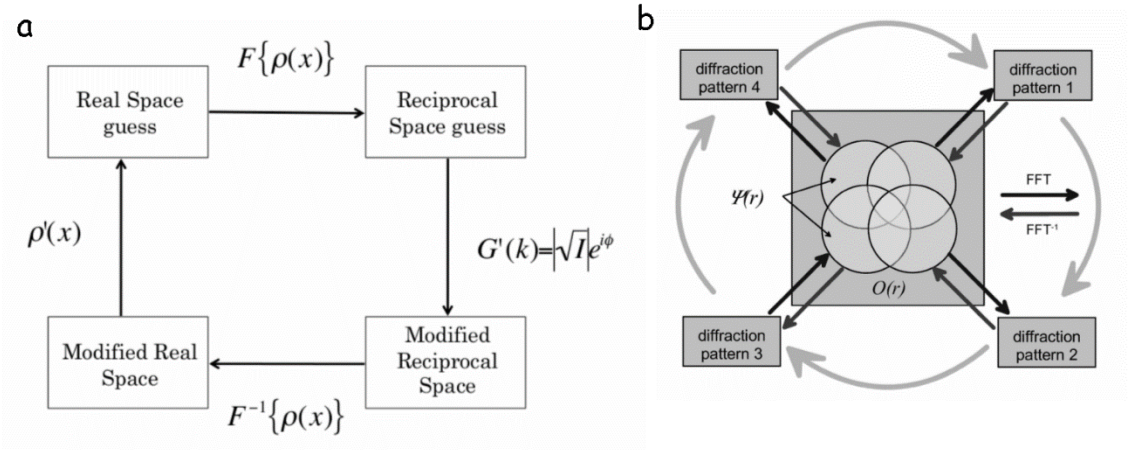

Figure 2.8 Schematic outline of an iterative procedure (**a**) Schematic outline of an iterative procedure to generate the phase and amplitude of an object from a single coherent diffraction image. (**b**) Outline of iterative procedure to generate the phase and amplitude of an object from sets of diffraction images measured with spatial overlap. [M. Rodenburg et al., 2007]. With permission from American Physical Society

In the case of ptychography where multiple diffraction images are measured with spatial overlap, a more extended reconstruction process is required (**Figure 2.9b**). Additional steps are used to constrain the functions describing the sample and the probe in the spatially overlapping regions. Two methods used for such iterative ptychographic reconstruction are (i) the extended Ptychographic iterative engine (ePIE) developed by

Maiden et al. [Maiden et al., 2009] and (ii) the Difference Map (DM) algorithm, developed by Thibault et al. [Thibault et al., 2008]. **Figure 2.9,** taken from the Ph.D. thesis of Shemilt [Shemilt et al., 2014], outlines these two approaches.

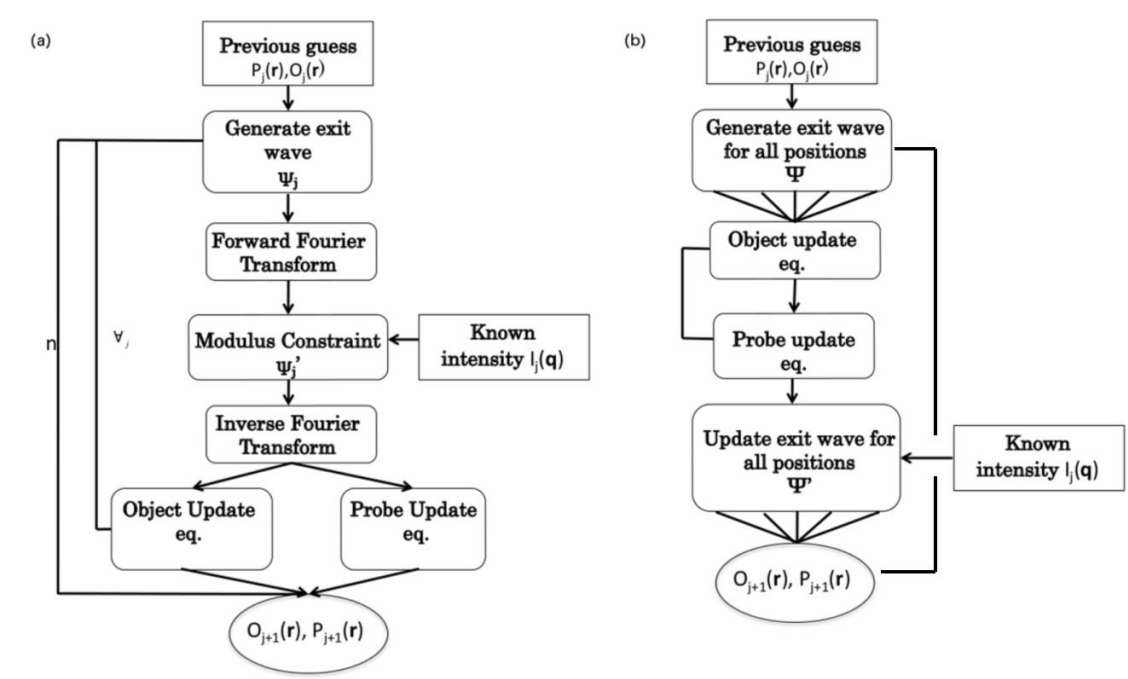

Figure 2.9 Flow diagrams for, (left) the extended Ptychographic Iterative Engine (ePIE), and (right) Difference Method (DM) algorithms for reconstruction of sets of diffraction images recorded over a set of overlapping positions on a sample. The ePIE method works through the set of DI images in a quasi-serial pattern, whereas the DM method carries out the algorithm in a more parallel fashion. In each case, a guess is made of the starting probe properties, while the initial phase of the object is set to a constant. On each iteration, the updated (n^{th}) amplitude prediction of the object is compared with the measured diffraction images, with further constraints in the overlapping spatial regions. The difference is then used to refine the phase and amplitude predictions for the $(n+1)^{th}$ iteration. Typically, a pre-set number of iterations is used, rather than a self-consistent approach (iteration until the difference falls below a user-defined magnitude). [Shemilt et al., 2014]

2.4 Ptychography instrumentation and software

The instrumentation and software used for ptychography differ significantly at different synchrotron facilities. At CLS, except the detector and data analysis software, all the other instrumentation and beamline parameters used for ptychography are the same as those for STXM, which were introduced in **Chapter 2.2.1**. A CCD detector (Andor model DX434, 1024 × 1024 pixels) or a Tucsen Dhyana 95 sCMOS camera is used to record the diffraction images (DI) at overlapping raster scanned spots. MOSAIC is the software used to control the Dhyana camera (https://www.tucsen.com/mosaic-2-3-product/). PyPIE software [Sun, et al., 2021; 2023.] is used to reconstruct sets of the ptychographic DI into amplitude and phase images of the probe and the sample. PyPIE is a CPU-based python program using the ePIE algorithm [Urquhart et al., 2022. Zhang, et al., 2013. Rodenburg, et al., 2004.] and extensively developed by the CLS SM beamline team. Ptychography results from CLS are shown in **Chapter 5**.

For ptychography measurements at Soleil, a modified Dhyana-95 sCMOS camera with ether a coated sensor for E>500 eV (Cu 2p edge) or on uncoated sensor (for E< 500 eV) is used.[Desjardins et al., 2019; 2020.] Ptychographic reconstruction was carried out using the open-source PyNX software [Favre-Nicolin et al., 2020] developed at the European Synchrotron Radiation Facility. Ptychography DI sets are measured using a python acquisition program written by the SOLEIL Hermes beamline team. The ptychography results from SOLEIL are present in **Chapter 8**.

2.5 Introduction to CO_2R tests

This subchapter introduces the fundamental principal and techniques for CO_2R tests to evaluate the CO_2R performance of electrocatalysts.

2.5.1 Electrochemical tests in a 2-compartment electrochemical cell

CO_2R tests can be conducted in various electrochemical cells, [Lobaccaro et al., 2016. Yang et al., 2018] including H-cells, Membrane Electrode Assemblies (MEA) cells. H-cells are a type of experimental setup used in electrochemical studies, particularly in the field of electrocatalysis. H-cells typically consist of two half-cells separated by a proton-exchange membrane (PEM) or anion-exchange membrane (AEM), depending on the specific reaction under investigation. One half-cell contains the working electrode, while the other contains a reference electrode and a counter electrode. H-cells are used to assess the activity and selectivity of catalysts for various electrochemical reactions.[Abdinejad et al., 2021. Weekes et al., 2018] MEAs are specialized assemblies where anode, membrane and cathode are compressed together to form one reactor. MEA are used in electrochemical devices like fuel cells and electrolyzers to facilitate CO_2 reduction reactions and other electrochemical processes.[Chandrashekar et al., 2021] In MEA, CO_2 gas is directly fed to the electrode by diffusion through a porous transport layer to the catalyst surface. The high concentration of CO_2 helps to achieve high current densities for industrial application and scaling up this technology.

In our experiments, the electrochemical tests were set-up and carried out in a custom 2- compartment electrochemical cell, which is close to the H-cell configuration (**Fig. 2.10**). [Kuhl et al., 2012] An ion exchange membrane was used to separate the

working and counter electrode compartments. The Cu electrodeposited Au coated carbon foil support or Ni-N-C materials deposit on coated carbon foil by drop-casting method were used as the working electrode. A platinum foil was used as the counter electrode and a Ag/AgCl electrode calibrated with RHE was used as the reference. A 0.1 M solution of $KHCO_3$ was prepared as electrolyte. The pH of the electrolyte purged with CO_2 was 6.8. During the CO_2 electrolysis process, CO_2 gas regulated by a mass flow controller at 20 standard cubic centimeters per minute (sccm) continuously flowed through both compartments of the cell to supply reactants for CO_2R reactions.

The working, reference and counter electrode are connected to a potentiostat to carry out the electrochemical tests. Chronoamperometry (CA) which is applying of a constant potential to an electrode and monitoring the resulting current as a function of time, is measured for 1 hour at the electrolysis potentials. During this 1 hrs, the current versus time graph is recorded.

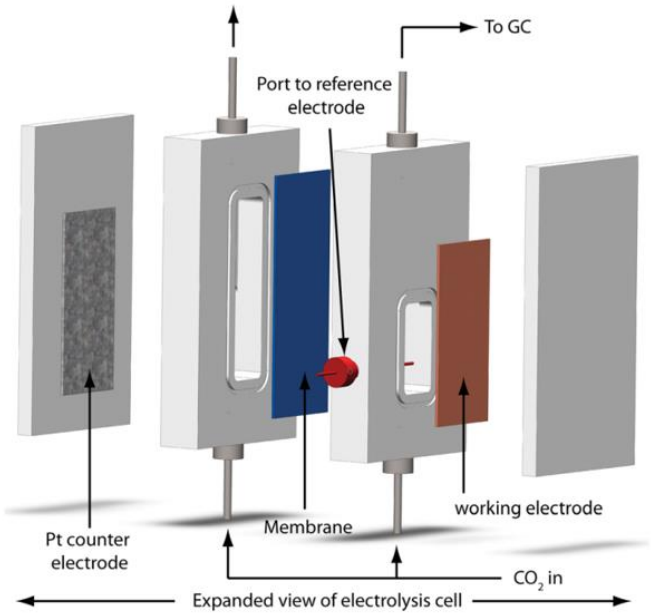

Fig. 2.10 Schematic of the electrochemical cell and experimental setup used in electrolysis experiments. [Kuhl, K.P. et al., 2012] With permission from American Chemistry Society.

2.5.2 Techniques to identify and quantify gas and liquid CO_2R products.

During CO_2 electrolysis at a specific potential, the generated gas products are flowed into the gas chromatography (GC) through the tubing on the top of the electrochemical cell. GC is a versatile gas analytical technique that can separate and quantify components of the mixture of gas CO_2R products including, H_2, CO, CH_4, C_2H_4 and other hydrocarbons. Different gas products are separated based on their differing affinities for a stationary phase in a chromatographic column. [Dierck et al., 2021]. Identification and quantification for CO_2R products can be achieved from the peaks in the chromatogram with specific retention times and the areas of the peaks.

After CO_2 electrolysis, the liquid CO_2R products are in the electrolyte, including

formate and various alcohols. The electrolyte from the compartment is collected and characterized using nuclear magnetic resonance (NMR) spectroscopy to identify and estimate the amount the liquid CO_2R products. NMR is particularly sensitive to the chemical environment of atomic nuclei and can provide detailed structural information about the liquid CO_2R products present in the solution to identify them. Through comparison with internal standards at a specific concentration, the NMR can quantify the relative concentrations of different liquid CO_2R products in a solution.

2.5.3 Calculation of Faradaic efficiency

After the identity and the concentration of gas and liquid products have been determined using GC and NMR techniques, the moles of each CO_2R product are calculated. Then the Faradaic efficiency (FE) for specific products can be calculated according to:

$$FE(\%)= \frac{moles\ of\ the\ product * F * v * electron\ transfer\ per\ mol}{I * 60} \quad \text{Eqn 2.11}$$

where mole of the product is the value estimated from GC or NMR for specific products, F is Faraday constant 96485 C mol^{-1} , v is the flow rate for CO_2 gas (20 sccm), and I is the average current during the 1 hr CA test. The electron transfer per mol is the number of electrons transferring for every mol of specific products generation, which is presented in **Table 1.1.**

After the Faradaic efficiency for each product is calculated, the Faradaic efficiency for overall CO_2R is the sum of the Faradaic efficiencies of all CO_2R products.

Chapter 3

Experimental details

This chapter describes how STXM and ptychography measurements were conducted at various synchrotron facilities and how the data were analyzed. The sample preparation methods used for ex situ STXM and other characterizations are presented. The device used for in situ STXM and ptychography and the experimental procedures for in situ STXM and ptychography are described in detail.

3.1 Summary of experimental runs at synchrotron facilities.

Table 3.1 displays a summary of the experimental runs conducted during 2019-2023 at various synchrotron facilities. Each experimental run is tagged by S / P / F which represents success/ partial success/ failure. Totally around 300 hours beamtime at various facilities were used for the research project. Only a small part of the results are presented in the thesis.

Table 3.1 Summary of experimental runs at various synchrotron facilities.

Time	Synchrotron facilities	Experiments	Evaluation (*)	Chapter
2019-12	CLS	*Ex situ* studies for Ni-N-C and electrodeposited Cu layers/ dendrites	S	4, 6
2020-02	CLS	Preliminarily studies for *in situ* STXM of Cu CO_2R electrocatalysts	S	none
2020-09	CLS	*Ex situ* STXM and ptychography studies for Ni-N-C (remotely)	S	4, 5
2021-02	CLS	*Ex situ* studies for Ni-N-C (remotely)	S	4
2021-08	CLS	*Ex situ* studies for electrodeposited Cu nanoparticles (remotely)	S	6
2021-09	CLS	*In situ* STXM studies of Cu CO_2R electrocatalysts	S	7
2022-03	CLS	*In situ* STXM studies of Cu CO_2R Cu electrocatalysts	P	none
2022-05	MaxIV	*In situ* STXM studies of Cu CO_2R catalysts	S	none
2022-06	CLS	*Ex situ* ptychography studies for Ni-N-C	S	5
2022-06	CLS	*In situ* STXM studies of Ni-N-C and *In situ* STXM studies at C 1s edge	P	9
2022-07	CLS	*In situ* STXM/ ptychography studies using Hummingbird cell	P	none
2022-10	Soleil	*In situ* ptychography studies of Cu CO_2R catalysts	S	8
2022-12	CLS	*Ex situ* Cu, Cu2O, CuO spectroscopy (remotely)	S	6
2023-01	Bessy-II	*In situ* STXM studies of Cu CO_2R catalysts and *in situ* chem-movie	P	none
2023-03	ALS	*In situ* STXM studies of Cu CO_2R catalysts and *in situ* chem movie	F	none
2023-03	MaxIV	*In situ* STXM studies of Ni-N-C	P	none
2023-04	Solaris	*In situ* STXM studies of Cu CO_2 and *in situ* chem-movie	P	none
2023-06	CLS	*In situ* STXM studies of Ni-N-C and *In situ* STXM studies at C 1s edge	P	9

(*) S / P / F indicate success/ partial success/ failure relative to goals defined before the start of the run.

3.2 STXM data acquisition

STXM records transmission signals in different modes, including spectral point scan, single image, multi-energy image sequence (stack) [Jacobsen et al., 2000] **Point scan** measures the transmission spectrum at one or more points on a sample over a user-specified linear or segmental non-linear energy range. The point scan can record spectra efficiently in a few mins. For example, in the Cu electro-deposition part of *in situ* STXM experiments, point scans were used to monitor the Cu^{2+} signal in the electrolyte and estimate the thickness of the electrolyte layer. Point scans over the X-ray energy range of the Cu 2p edge (typically 920 to 965 eV) were measured at the position of SiNx widow on the *in situ* chips and at the position of one of the holes in the *in situ* device to obtain the X-ray spectrum through the electrolyte layer (I) and the X-ray spectrum of the incident (I_o) (**Fig. 3.1 a, b**). The Beer-Lambert equation is then used to generate the optical density (OD) (**Fig. 3.1 c,d**):

$$OD(E) = -\ln(I(E)/Io(E)) \qquad \text{eqn. 3.1}$$

which is the X-ray absorption spectrum of the two silicon nitride (SiN_x) windows and the electrolyte. More generally, a spectrum consists of contributions from n components,

$$OD(E) = \Sigma_i^n \sigma_i(E) \cdot \rho_i \cdot t_i \qquad \text{eqn. 3.2}$$

where $\sigma_i(E)$ is the spectral response, ρ_I is the density and t_i is the thickness of component i. If the material composition and density are known, the X-ray absorption signal is directly related to the thickness. After subtracting the OD of 150 nm SiN_x, which can be predicted from its density (4.3 $g.cm^{-3}$) and elemental response, [CXRO database: https://henke.lbl.gov/optical_constants/] the remaining OD is the X-ray absorption of the

electrolyte. The electrolyte is mostly water so the X-ray absorption properties of H_2O in the 900 – 1000 eV range were used to calculate the thickness of the electrolyte in the window region, which was ~1.6 μm in this case (**Fig. 3.1d).**

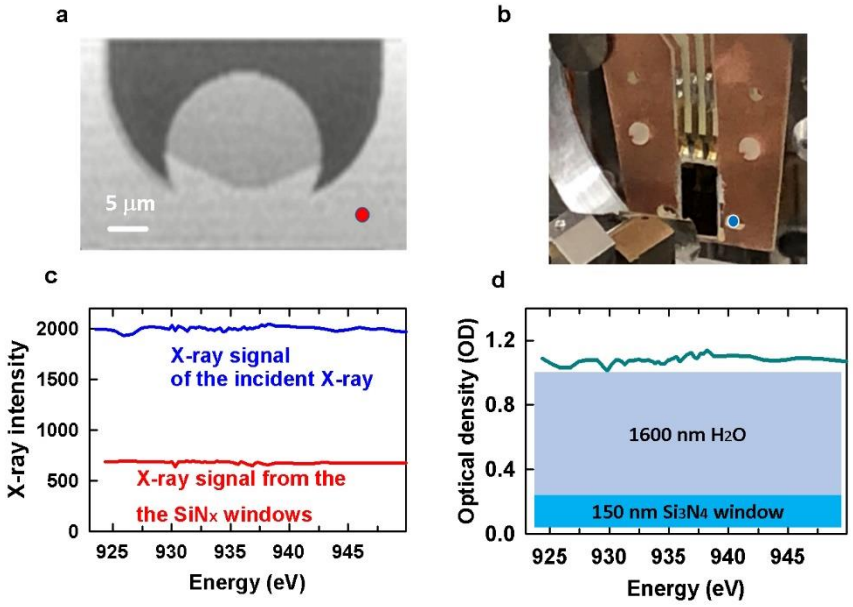

Figure 3.1 Point scan through the *in situ* cell during Cu electro-deposition. (a) STXM transmission image at 960 eV. The red dot indicates where the spectrum through the cell (I) was measured. **(b)** Photo of the *in situ* cell in the STXM. The blue dot indicates the hole through the *in situ* device where the incident flux (I_0) was measured. **(c)** measured X-ray signal of the incident X-ray beam (I_o, blue) and that from the X-ray beam passing through the *in situ* cell off the working electrode (I, red). **(d)** The OD spectrum of the electrolyte and the windows. The calculated OD signal from 1600 nm of water and 150 nm of SiNx is indicated, consistent with an electrolyte thickness of ~1.6 um.

STXM images at a single photon energy were measured by scanning the sample while recording the transmitted X-ray intensity pixel by pixel. (**Fig. 3.1a**) Many

parameters can be adjusted including photon energy, (x, y) position of the center of the image, (Δx, Δy) dimensions of the image, (δx, δy) point spacing in each dimension, and the dwell time at each pixel. A **STXM stack** measures a sequence of **STXM images** collected at various photon energies to provide spatially resolved spectroscopic information about the sample. For example, a 54-energy Cu 2p stack scanned from 920 to 965 eV was used in *in situ* STXM studies on Cu particles, while 143-energies at Ni 2p edge from 836 to 929 eV were used in *ex situ* STXM studies of the Ni-N-C materials.

A **STXM 4-energy stack** (4-E stack) was also used to map chemical species of the sample in an accelerated fashion. To quickly identify the Cu (I) and Cu(0) and quantify their amount, images were measured at 4 specific photon energies - 920 (pre-edge), 933.5 (Cu(I) & Cu(0)), 937 (Cu(0)) and 960 eV (post-edge). 4-energy stack at 927.3 (pre-edge), 930.3(Cu(II)), 933.3 (Cu(I) & Cu(0)), 937.3 (Cu(0)) was used to identify the Cu(II), Cu (I) and Cu(0) and quantify their amount. The signal at these 4 energies provides the same analytical information as a STXM full stack, although with lower statistical precision (**Fig.3.2**).

The photon energy scales of soft-X-ray beamlines are often not accurate and can change between runs, and occasionally even within a single run. To make sure the spectra measured by STXM are correct and accurate, the energy scale of each beamline was calibrated by measuring spectra of appropriate reference gases, including Ne [1s → 3p, 867.05 eV.], SF_6 [F 1s → a_{1g}, 688.3 eV.], CO_2 [C 1s → C 3s, 292.74 eV; C 1s → C 3p, 294.96 eV; O 1s → O 3s, 538.9 eV], N_2 [N 1s → 3s, 406.15 eV; N 1s → 3p, 407.115 eV.][Stierhof et al., 2022, Chen, 1989.]

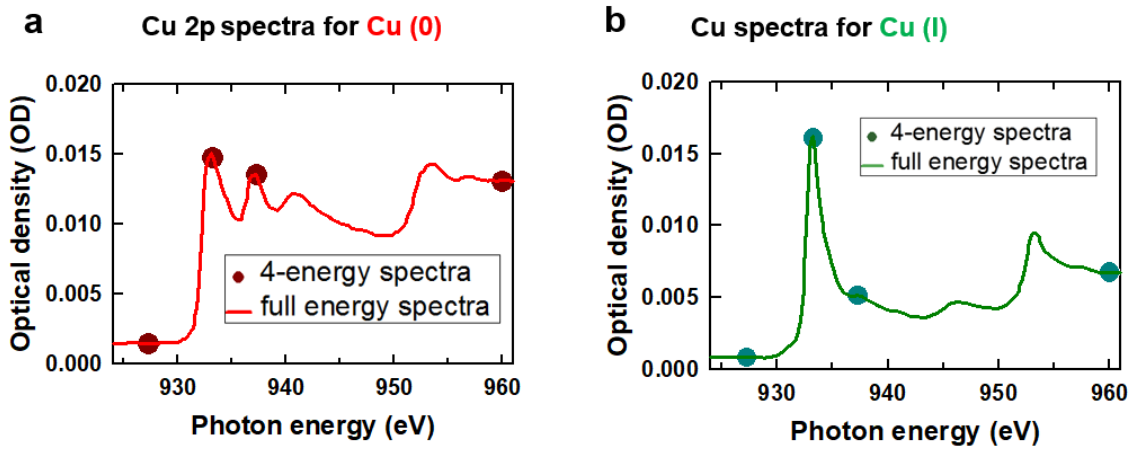

Figure 3.2 Full energy spectra vs 4-energy spectra for **(a)** Cu(0), and **(b)** Cu(I)

3.3 STXM data analysis

All STXM data was analyzed using aXis2000 software. [Hitchcock, 2023] The images in a stack typically drift by a few hundred nm over the 40-80 eV scan range, and therefore the stacks were aligned to ~5 nm registry using a Fourier correlation method. The transmission signal (I) of the aligned stack was converted to an optical density (OD) using the Beer-Lambert Law: $OD(x,y) = -\ln(I/Io)$, where I is the X-ray intensity transmitted through the sample and support, and Io is the incident X-ray intensity measured off the sample but where the X-rays transmit through all other parts of the STXM hardware (optics, windows, zone plate, detector) and the sample support (SiNx window or formvar). After OD conversion, the X-ray absorption spectra (XAS) of selected areas (many pixels, which are not necessarily contiguous, but have similar spectra) were extracted from the STXM stacks using methods described in greater detail below.

The procedures in aXis2000 for fitting single spectra (spectral curve fits) and full stacks (stack fits, where the spectrum at all pixels are analysed) are based on a singular value decomposition (SVD) matrix method. [Koprinarov et al., 2002] The 'stack fit' routine fits the NEXAFS spectrum at each pixel to a user-identified set of reference spectra, which can be derived from the stack itself (internal) or from spectroscopy on well-defined reference compounds (external). The result of a 'stack fit' is a set of component maps (spatial distributions), one for each component, along with a map of a constant signal (no spectral variation), and the residual of the fit. [Hitchcock, 2012] In cases where the set of reference spectra are known to represent all the variation in the stack signal, the stack fit can be performed without the constant component (denoted as an 'SVD fit' in aXis2000). Internal reference spectra (which were extracted from the same STXM stack) or external reference spectra (measured from pure materials) were used at different stages in the data analysis, as explained in more detail in individual chapter presenting *ex situ* and *in situ* results. To quantitatively analyze the data, the reference spectra are converted to an absolute intensity scale, optical density per nm (OD1), by scaling the relative intensity spectra until the pre-edge and far-continuum (>30 eV above the edge) match the elemental response for 1 nm thickness of the known composition and density of the reference material, which is calculated using X-ray parameters from the Centre for X-ray Optics database (https://henke.lbl.gov/optical_constants/). The grayscale of the component maps derived using OD1 reference spectra is an estimate of the thickness of that component at each pixel in the region analyzed. An example of the OD1 reference spectra of various Ni-based materials (scaled

by the elemental response for 1 nm thickness) is presented in **Figure 3.3a. Figure 3.3b** displays the component maps derived from fitting a Ni L23 stack using OD1 reference spectra. The grayscale of each component map is the thickness of that component in nm.

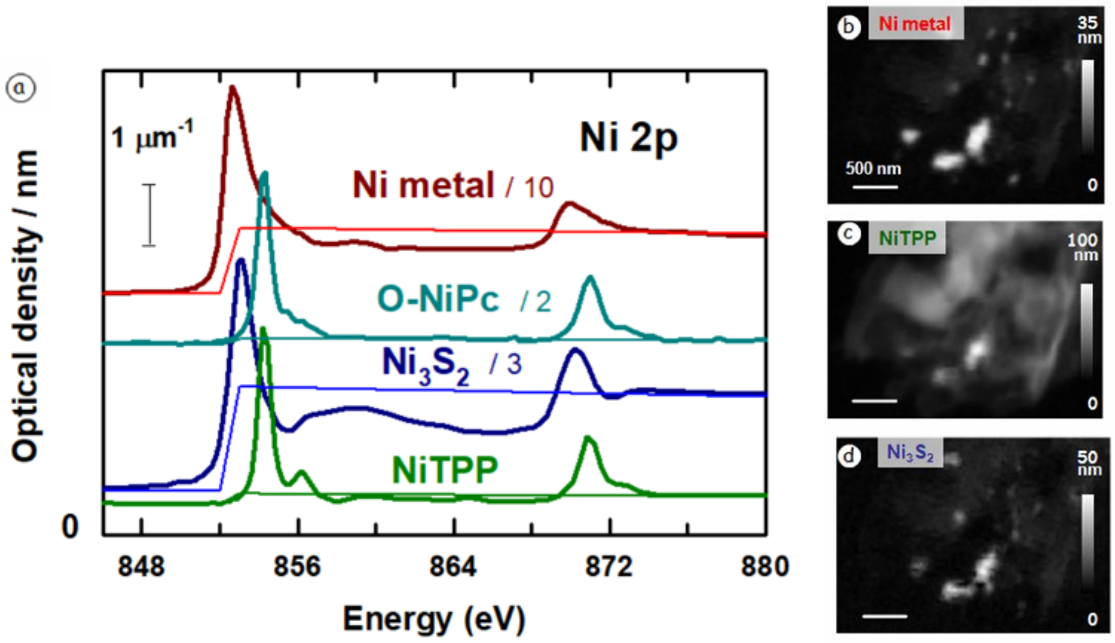

Figure 3.3 An example to show the reference spectra in OD1 and fitting using OD1 spectra. (a) OD1 reference spectra of various Ni-based materials. (b-d) component maps derived from fitting using OD1 reference spectra. grayscale showing the thickness in nm.

Curve fits, which use the same SVD algorithm as used for stack fits, were used to analyze spectra extracted from specific areas of a stack, identified based on morphology and/or spectral similarity. When reference spectra on OD1 intensity scales were used to curve fit a spectrum, the contribution of each spectral component is an estimate of the average thickness (in nm) of that component in the area from which the spectrum was extracted. Volume percent compositions were then estimated by combining the thickness

and areal amounts. The software allows for the quantization of non-contiguous areas, where the pixels of an area are identified from their spectral properties. Outside of the ~20-40 eV region at the onset of a given inner shell edge (the near edge X-ray absorption fine structure, NEXAFS region), the X-ray absorption of any material is only a function of its elemental composition and density. [Hitchcock, 2012] Thus one can convert an X-ray absorption spectrum measured on a relative intensity scale to an absolute intensity scale, by matching the intensity of the pre-edge (e.g. -20 to -5 eV relative to the onset) and post-edge (>30 eV above the onset) NEXAFS regions to that predicted from the elemental composition and density, using tabulated elemental X-ray absorption cross-sections.

3.4 Ptychography data acquisition and analysis

Before each ptychographic measurement, the sample region to be studied is identified and characterized by STXM. Then a statistically precise background signal of the camera is measured with the X-ray beam blocked by an upstream valve. The average background after subtraction of the stable camera background is about 1 electron, giving a dynamic range of over 20,000.

The ptychography measurements are mostly in modes of ptychography image, ptychography full stack, and ptychography 4-E stack, which have a similar definition with the corresponding STXM modes, described in **chapter 3.2**. For these studies arrays of diffraction images are recorded using a defocused X-ray spot with a size of 1 – 3 μm. To obtain the real-space images, ptychographic reconstructions were carried out using either

the PyPIE software package (developed by the CLS SM beamline team [Sun et al., 2021; 2023.]) for CLS data or open-source PyNX software [Favre-Nicolin et al., 2020] (developed by researchers at the European Synchrotron Radiation Facility) for Soleil data.

The reconstruction ptychography images, full stacks and 4-E stacks are similar to the corresponding STXM images, full stacks, and 4-E stack. Because ptychography data acquisition typically takes a long time and ptychographic reconstruction also needs some time, ptychography full stacks are generally recorded with fewer energy points or a reduced energy range. For example, the Cu L_3 ptychography stack used in the *in situ* ptychography study of a single Cu CO_2R catalyst particle consisted of 40 energies from 920 to 946 eV. For the same reason, 4-E stacks are preferred in ptychography studies, since they are much less time-consuming while providing similar chemical mapping as a full stack. To efficiently identify and map the Cu(0), Cu(I), and Cu(II) species, 4-E stacks measured images at 927.3, 930.3, 933.3, and 937.3 eV. (**Fig. 3.4**) The 4-E stack can provide similar chemical information and mapping of the Cu(0), Cu(I), and Cu(II) species as achieved with 40-energy Cu L_3 stack measurements. However, the 4-E stack takes ~20 mins while the 40-energy Cu L_3 stack takes more than 200 mins. In practical ptychography measurements, the Cu L_3 stack was reduced to ~90 mins by measuring a smaller area of the sample.

The analysis of reconstructed ptychography data is similar to data analysis of the STXM using aXis2000 software, consisting of the same steps of alignment, OD conversion, energy calibration, SVD stack fitting, and curve-fitting, which are introduced in **Chapter 3.2**.

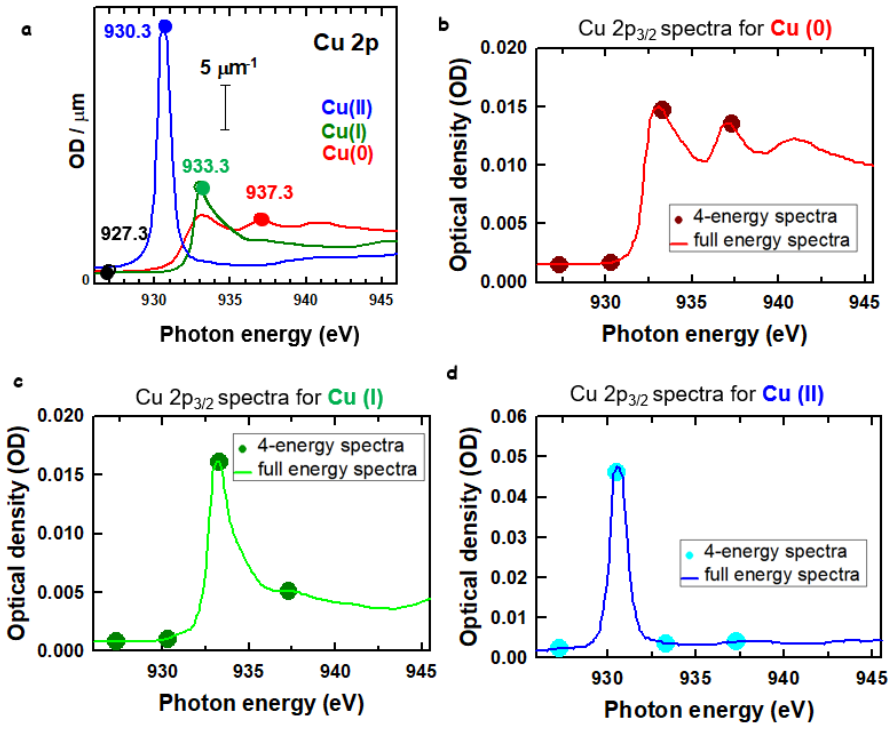

Figure 3.4 Cu L_3 ($2p_{3/2}$) reference spectra of 4 energies and full spectra in ptychography studies. Spectra of Cu metal, Cu_2O, and CuO digitized by Jiang et al. [Jiang et al., 2013]. The intensity has been placed on an absolute scale (optical density per nm at standard density). (a) 4 energies location on the 3 Cu reference spectra were plotted on the same scale. (b) Cu(0). (c) Cu(I). (d) Cu(II). The energies used in the 4-E stack approach are indicated.

3.5 Sample preparation for (*ex situ*) STXM

3.5.1 Synthesis of Ni-N-C materials

The synthesis of the Ni–N–C catalysts was reported elsewhere. [Zhang et al., 2022. Shahcheraghi et al., 2021] The Ni–N–C catalysts were prepared by mixing aniline (1 mL, Sigma-Aldrich), cyanamide (2 g, Sigma-Aldrich), and nickel chloride hexahydrate

($NiCl_2 \cdot 6H_2O$, Sigma-Aldrich) in a 1.5 M HCl solution (200 mL, ACS reagent). This solution was mixed by magnetic stirring, followed by the addition of ammonium persulfate (1.5 g, Sigma-Aldrich) as an oxidant for the polymerization of aniline to polyaniline. The water was evaporated by heating the solution to 80 °C and leaving it stirring overnight. The resulting product was pyrolyzed at 900 °C in Ar for 1 h, acid-washed to remove labile Ni compounds, and then pyrolyzed a second time at 900 °C in Ar for 3 h. The acid washing procedure was to remove any surface-exposed Ni particles that would be active for the hydrogen evolution reaction under CO_2R conditions. [Koshy et al., 2020] The second pyrolysis was to remove any labile residues that remain after the acid wash procedure. In the synthesis, the amount of $NiCl_2 \cdot 6H_2O$ was varied to prepare two different Ni–N–C catalyst materials: sample A, Ni–N–C-high (1.2 g of $NiCl_2 \cdot 6H_2O$), and sample B, Ni–N–C-low (0.08 g of $NiCl_2 \cdot 6H_2O$). A comparison sample N–C (Ni-free) was prepared without the addition of any nickel precursor. Ni_3S_2/C samples were prepared by mixing 20 wt % commercial Ni_3S_2 (Sigma-Aldrich) particles and 80 wt % high-surface-area Vulcan XC-72 (VC, FuelCellStore) powders in a ratio of 20–80 wt %, respectively.

3.5.2 Loading Ni-N-C materials

The Ni-N-C catalysts and reference compound powders were physically deposited from a dry state on either silicon nitride (SiN_x) windows (Norcada Inc), or 3 mm formvar coated Cu TEM grids (TED Pella Inc.). In each case poorly adhering particles and large agglomerates were removed by tapping the edge of the sample substrate on a hard surface.

Figure 3.5 shows the two types of sample mounting used for Ni-N-C samples. These two types of sample mounting methods can be used for most powder samples.

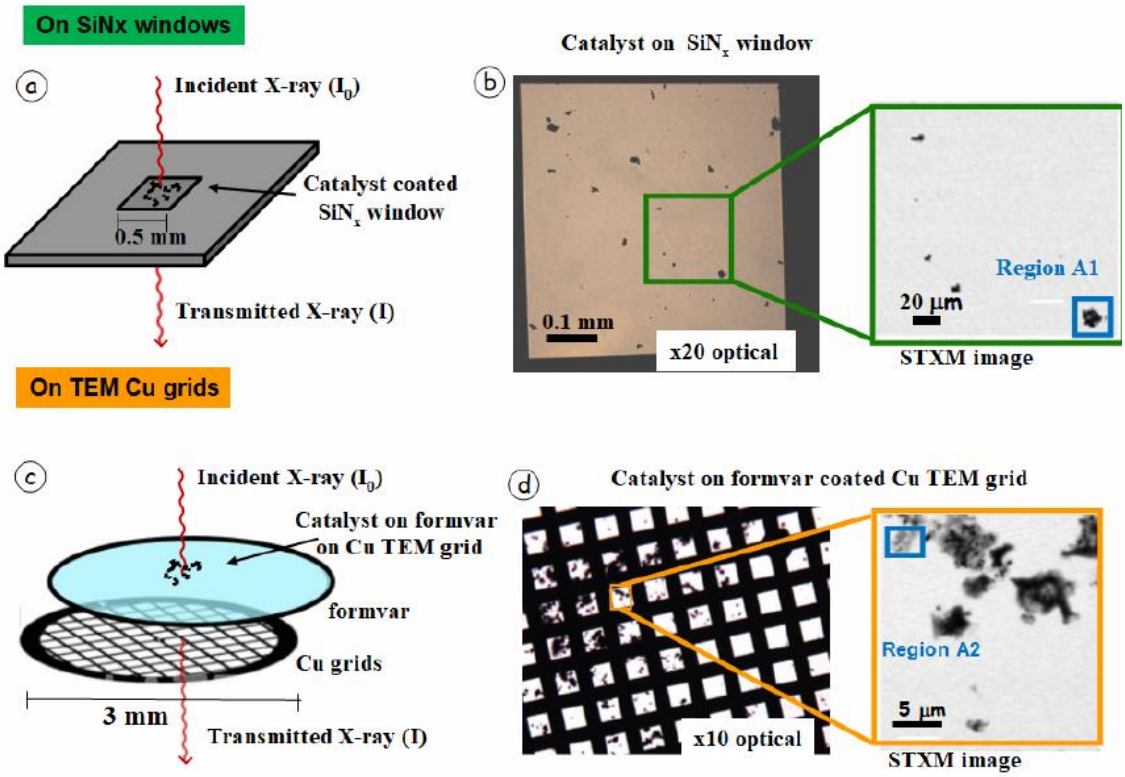

Figure 3.5 Sample mounting used for scanning transmission X-ray microscopy (STXM) measurements. **a)** schematic of SiNx window mounts. **b)** Transmission optical microscopy image (20x) of Ni-N-C-high particles on a SiNx window. The frame is 5 mm x 5 mm, 200 µm thick Si, with a lo-stress 0.5 mm x 0.5 mm, 75 nm thick window pane at the center (Norcada Inc) and STXM image at 395 eV on SiNx windows **c)** schematic of formvar coated TEM 3 mm diameter Cu grid mounts. **d)** Transmission optical microscopy image (10x) of particles Ni-N-C-high on a formvar-coated TEM Cu grids. and STXM image of one square of the TEM Cu grid sample.

3.5.3 Synthesis of electrodeposited Cu layers and dendrites

E*x situ* Cu layers and dendrites samples were prepared in a classic beaker set-up by electrodeposition on to the Au working electrode (WE) on phase 1 electrochemical chip (old design of *in situ* chips, **Fig 3.6 b, and c**) designed by Hitchcock group and produced by Norcada Inc. [Hitchcock et al., 2016]). The Au electrode was connected to a potentiostat as the working electrode (WE), and a full cell assembled using an Ag/AgCl reference electrode (RE) and a Pt wire counter electrode (CE). (**Fig 3.6 a**). The Cu samples were electrodeposited at −0.5 V (vs. Ag/AgCl) for 15 s in an electrolyte of 10 mM $CuSO_4$ and 0.1M H_2SO_4. After the deposition, Cu samples on the chip were dipped in a beaker filled with DI H_2O and air-dried, ready for the STXM studies. **Fig 3.6 d** displays optical images of the *ex situ* samples of Cu layers and dendrites.

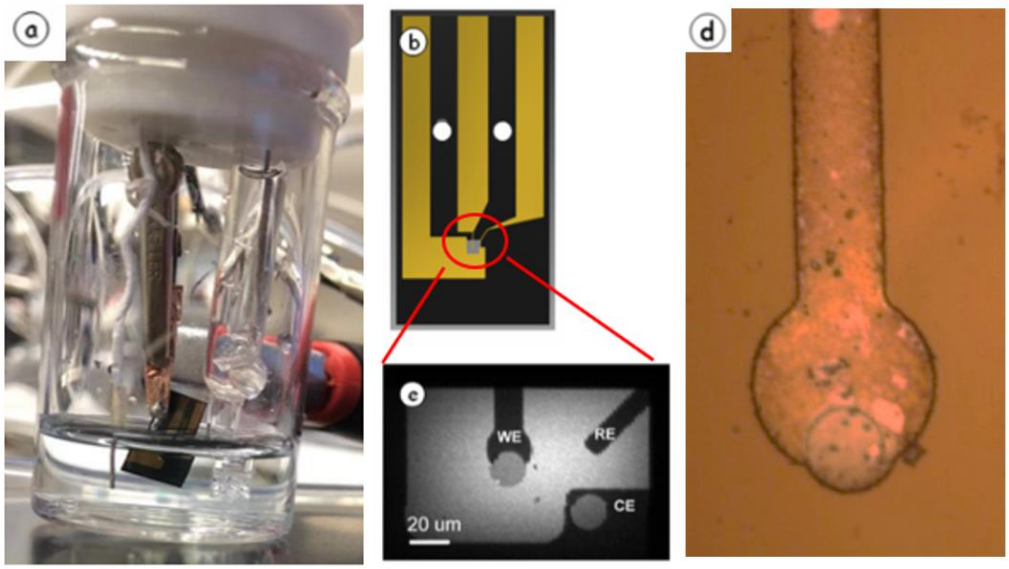

Figure 3.6 *Ex situ* Cu deposition of Cu layers and dendrites a) mini cell used for the *ex situ* electrodeposition **b,c)** schematic diagram **d)** optical images for the deposited Cu layers and dendrites.

The STXM results for the electrodeposited Cu layers and dendrites are shown in **Chapter 6.2**. Because the literature reports that Cu_2O nanoparticles show a better performance than most reported Cu electrocatalysts under comparable conditions, we uesd the synthesis procedure according to the literature to prepare electrodeposited Cu_2O samples as discrete nanostructures and use it in *in situ* experiments.[Arán-Ais et al., 2020]. The details for electrodeposition of electrodeposited Cu_2O nanoparticles are presented in the next sub-chapter.

3.5.4 Synthesis of electrodeposited Cu_2O nanoparticles

To prepare Cu_2O nanoparticles, the electrodeposition process was performed using 3 cycles of cyclic voltammetry (CV) from -0.2 to -0.5 V_{Au} in a mixed solution of 5 mM $CuSO_4$ and 5 mM KCl. (**Fig 3.7 a**) This method is reported by Arán-Ais, et al who used multi-CV runs in 5 mM CuSO4 + 5 mM KCl solution. The role of KCl and Cl^- ions to tune the shape toward Cu_2O cubic particles is discussed in [Arán-Ais et al., 2020].

In the deposition, a 3D-printed device [Prabu et al., 2018] and the phase 1 electrochemical chip was used. **(Fig 3.7 b)**, but without sealing the device. After the electro-deposition and washing using DI H_2O, small particles were observed in optical images **(Fig 3.7 c)**. Through SEM and coupled techniques to preliminarily study the morphology and chemical information of these nanoparticles, the existence of Cu nanoparticles was confirmed and subsequently studied by STXM. The SEM images and STXM results are shown in **Chapter 6.3**.

Using similar methods, 3 cycles of CV from -0.3 to -0.6 V_{Au} in 5 mM $CuSO_4$ and 5 mM KCl solution, Cu nanoparticles were prepared on the phase 1b chips, and then were subjected for 30 mins to CO_2R conditions, -1.0 V_{Au} in 0.1M CO_2 sat' $KHCO_3$ electrolyte for CO_2R. In this way, Cu nanoparticles after the CO_2R process were prepared. STXM results for them are shown in **Chapter 6.4**.

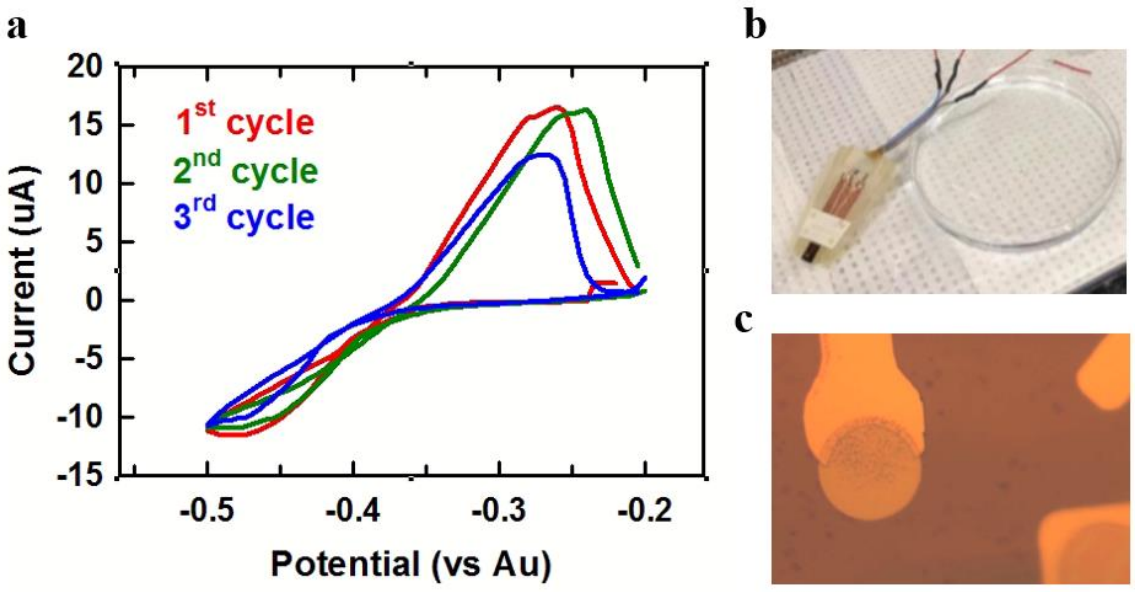

Figure 3.7 ***Ex situ*** **Cu deposition of Cu nanoparticles a)** CV curve of the electrodeposition process b) the setup for electrodeposition c) optical image of the Cu nanoparticles after the depositions.

3.6 Characterization of samples

3.6.1 Optical microscope

Optical microscope uses visible light and a system of lenses to magnify and observe small objects or specimens. An Olympus BX51 optical microscope was used at McMaster University to preview STXM samples on 3 mm TEM grids or Si_3N_4 windows

(such as **Fig 3.5**). In the *in situ* STXM/ptychography projects, the optical microscope is extremely important and is used for the following steps **1**. monitoring the process of electrolyte filling the *in situ* chips to avoid bubbles or broken windows; **2**. sometimes Cu *in situ* deposition and changing the electrolyte from Cu^{2+} electrolyte to HCO_3^- electrolyte is carried out under the optical microscope, before *in situ* STXM/ptychography studies; **3.** in the early studies all the *in situ* experiments were conducted under the optical microscope to practice and collect valuable information for improving techniques and instrumentation. After everything goes well under the optical microscope, the *in situ* experiments can be carried out at in synchrotron facilities to achieve *in situ* STXM/ptychography. These details are shown in **Chapters 3.7-3.9**.

3.6.2 Scanning Electron Microscopy (SEM) and coupled techniques.

Using a beam of high-energy electrons to interact with the specimen and produce detailed images, SEM typically shows a spatial resolution of tens of nm. A TESCAN VP. SEM located in the Electron Microscopy Facility in the Health Science Centre at McMaster University [https://fhs.mcmaster.ca/em/instrumentation.html], was used to identify the morphology of nanostructures of our *ex situ* samples before STXM studies at synchrotron facilities. SEM results are shown in **Chapter 6.**

3.6.3 Transmission Electron Microscopy (TEM) and coupled techniques.

Conventional TEM, high-resolution aberration-corrected transmission electron microscopy (HRTEM), and high-angle, annular dark-field scanning transmission electron

microscopy (HAADF-STEM) imaging along with electron energy loss spectroscopy (EELS) were conducted at the Canadian Centre of Electron Microscopy (CCEM, McMaster University) using an FEI Titan 80-300 HB microscope. TEM works on the principle of transmitting electrons through a thin specimen and then capturing and magnifying those transmitted electrons to create high-resolution images. The TEM and coupled techniques were used to study nanomaterials at sub-nanometer spatial resolution with elemental mapping of the chemical components. The results for TEM and coupled techniques are presented in **Chapter 4**.

3.6.4 CO_2 reduction tests

The principles and methods for electrochemical CO_2R tests in a custom-built two-compartment cell were introduced in **Chapter 2.5**. The detailed experimental process is present here.

First, the working electrode was prepared according to the type of electrocatalyst. **1.** For electrodeposited Cu nanoparticles as electrocatalysts, the working electrodes were prepared by electrodeposition on an Au-coated graphite foil in a solution of 5mM $CuSO_4$ (Sigma-Aldrich) and 5mM KCl (Sigma-Aldrich) through three cycles of CV from 0 V to +0.4 V vs RHE with a scan rate of 20 mV/s. This is identical to the process used to prepare Cu catalysts in the *in situ* STXM cell.[Zhang et al., 2023a] **2.** For the Ni-N-C powder samples as electrocatalysts, the working electrodes were prepared by a drop-casting process. Ten milligrams of Ni-N-C material were suspended in an ink consisting of 1.5 mL of isopropyl alcohol and 0.5 mL of H_2O with 110 μL of a Nafion solution

(Sigma-Aldrich, 5 wt % Nafion in ethanol) and sonicated for 30 min. The suspended ink was drop-cast onto graphite foil (Fisher Scientific) and dried at 70°C for 2 h to obtain the prepared working electrode with an electrode loading of 1 mg/cm^2.

The working electrodes were cut to a 5.7 cm x 5.7 cm shape and assembled into the two-compartment cell. (**Fig 3.8)** The electrolyte compartments of the working and counter electrode were filled with 0.1 M $KHCO_3$ (10 mL), and CO_2 was flown continuously through the catholyte and anolyte chambers at 20 sccm throughout the course of the experiment. A Pt foil was used as the counter electrode and an Ag/AgCl electrode was used as the reference electrode. The catholyte and anolyte chambers were separated by an ion exchange membrane (Selemion AMV, AGC Inc.). Catalysts were tested by chronoamperometric measurements at various electrochemical potentials in the CO_2-saturated 0.1 M $KHCO_3$ (Sigma-Aldrich). The effluent gas from the catholyte compartment was fed to a gas chromatograph (GC, Mandel SRI 8610C) directly. The liquid electrolyte was collected and quantitatively analyzed by nuclear magnetic resonance spectroscopy (NMR, Bruker-Ascend NMR Magnets 300WB) for liquid product identification and quantitation. The liquid and gas product quantitation results were then used to determine Faradaic efficiencies. [Kuhl et al., 2012]

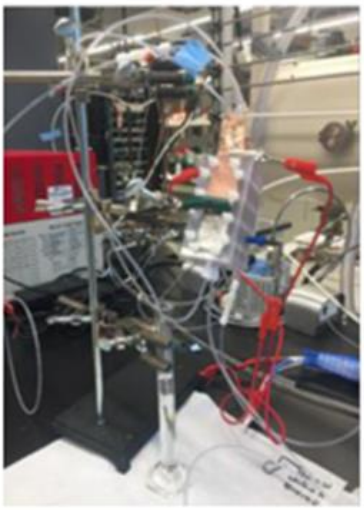

Figure 3.8 photo of the 2-compartment membrane cell.

3.7 Electrochemical device for *in situ* STXM/ ptychography

3.7.1 Design of the *in situ* device

Fig. 3.9 presents the microfluidic-based flow electrochemical device used for *in situ* STXM experiments. The initial concept of this *in situ* device was provided by PhD student Pablo Ingino and Prof. Martin Obst, our collaborators at the University of Bayreuth. [Obst et al., 2018] **Fig. 3.9a** is a photo of the device inside the CLS ambient STXM microscope. The *in situ* device consists of a machined printed circuit board (PCB), a polydimethylsiloxane (PDMS)/glass cell, and a poly(methyl methacrylate) (PMMA) backplate (**Fig. 3.9b-d**). The microfluidic cell contains 4 channels (shown as dotted lines **Fig. 3.9c**) which link the space between the two electrode-equipped chips (Norcada Inc, Edmonton, Canada) to 4 flow tubes (2 inlets, 2 outlets) that can be connected to one or more syringe pumps (New Era Syringe Pump, NE1010, https://www.syringepump.com/) to establish a stable flow of one or more electrolytic fluids. Electrochemical reactions can

then be performed by applying suitable potentials to the three electrodes on base chip E, which are connected to a potentiostat through the PCB traces and a 4-pin connector on the PC board. (**Fig. 3.9e, f**) Spacer chip F has a 0.5 – 1.5 μm spacer defining the height of the flow channel. When the *in situ* device is assembled, the PDMS/glass cell is sandwiched between the PCB and the PMMA plate. The electrical connection of the electrodes to the board is made using Au coated Cu spring clips (**Fig. 3.9b**). This microfluidic-based *in situ* electrochemical device is a major improvement compared to the previously reported 3D-printed device. [Vinod et al., 2018]. In particular it is much more reliable concerning fluid transfer and has fewer problems with leaking. The two inlet and two outlet flow channels facilitate changing electrolytes in minutes rather than hours and are very useful for removing air or gaseous product bubbles. In addition, since the upstream side of the chip-F is flush with the PCB and the catalyst particles are 200-250 μm further downstream, the *in situ* device can be positioned very close to the OSA without contacting it, to achieve *in situ* STXM studies at low energy edges, in particular the C 1s edge, where the gap between the OSA and the focal point of the X-ray beam at the sample has to be <400 μm.

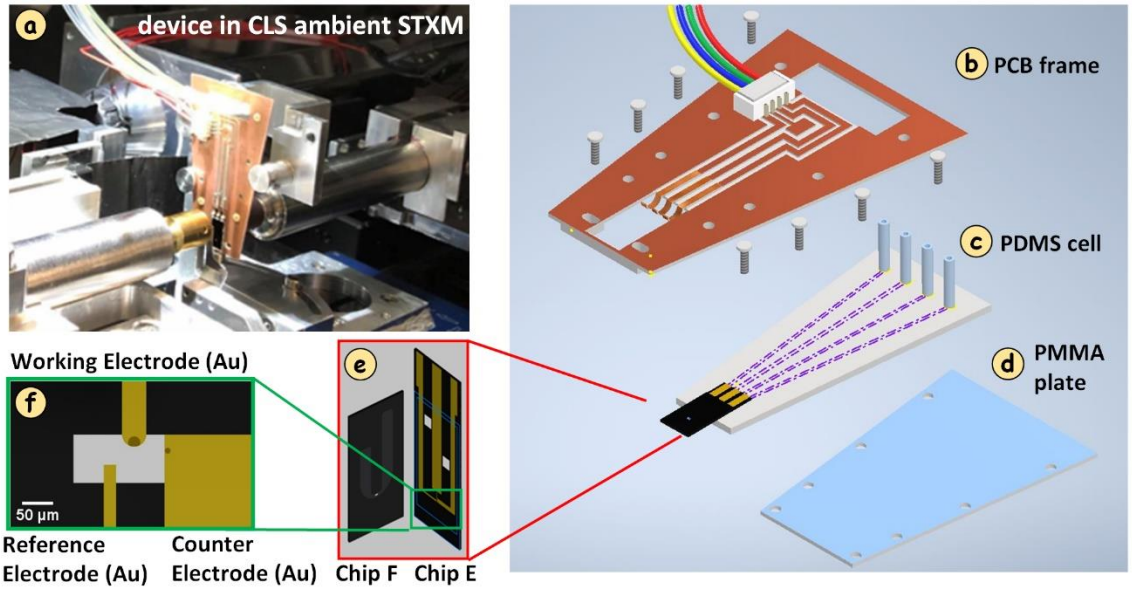

Figure 3.9 Microfluidic-based flow electrochemical device for *in situ* STXM experiments **(a)** Photo of the device inside the CLS ambient STXM. **(b-f)** Details of the device. The Si_3N_4 window area is 240 µm wide and 100 µm high. The thickness of the Si_3N_4 windows is 100 nm (base chip E) and 50 nm (spacer chip F). The areas used for STXM studies (dark circles on WE and CE) are 20 µm in diameter and have a coating consisting of 5 nm Cr and 15 nm Au.

3.7.2 Fabrication of the *in situ* device

The PMMA plate was fabricated using hand tools, to cut the 1.2 mm PMMA (McMaster-Carr) to the desired shape and make positioned holes with screw threads. The *in situ* chips were purchased from Norcada Inc. [Vinod et al., 2018] The PDMS and PC board parts were fabricated at McMaster University through the process described below.

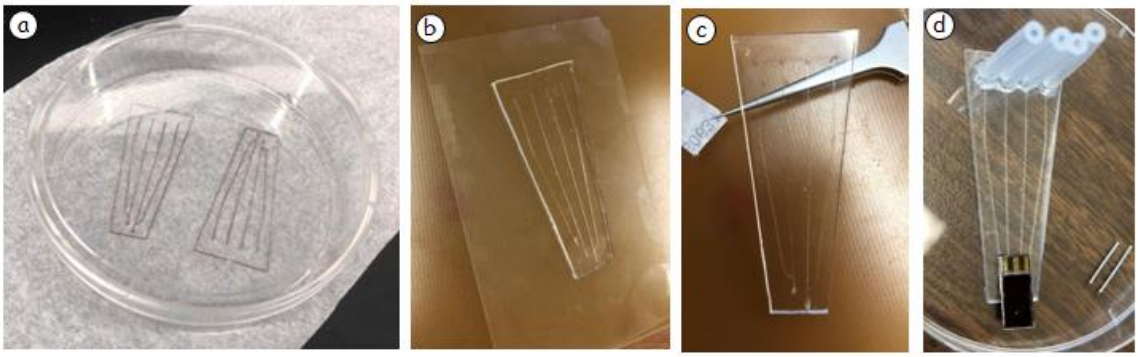

Figure 3.10 Fabrication process for making PDMS part. Pictures of **a)** mold of 4 micro-fluid channels on the petri-dish **b)** PDMS layer in the desired shape **c)** PDMS connected to the cover glass and with holes on the channels **d)** PDMS connected with Silicone tubing and *in situ* chips.

I learned how to make the PDMS part from members of Prof. Jose Moran-Mirabal's group in the Department of Chemistry & Chemical Biology, which has research projects on microfluid techniques. First, the pattern of micro-fluid channels was plotted using the Adobe Illustrator CS6(64 Bit) software and cut on a ByTac PTFE surface protection laminate (thickness of 200 μm) using a Xurography cutting instrument, to obtain the mold for 4 micro-fluid channels. Subsequently, the mold was transferred to a polystyrene petri-dish. (**Fig 3.10a**). A 5 ml mixture of base and curing agent for PDMS (Dow Sylgrard 184, 0.5 kg kit) was poured into the petri-dish with the 4-channel mold. After degassing and curing at 60 C for 2 hours, the 1 mm PDMS layer was peeled from the petri-dish and cut to the desired shape as shown in **Fig 3.10b.** The PDMS layer was plasma bonded (Harrick Plasma PDC32G) to a 0.17 mm cover glass (IHCWorld, **#1.5**) to form the micro-fluidic channels. Subsequently, 0.75 mm diameters holes were punched through the PDMS using the EMS-Core sampling tool (EMS DIASUM, 0.75mm) to open

the channels from the PDMS side. (**Fig 3.10c)** These holes were connected to the silicone tubing (Uxcell, ID 1 mm and OD 2 mm) and *in situ* chips using Silicone Adhesive Sealant (Permatex, 80050) to seal, to make the completed channels for the electrolyte to flow into the cell. (**Fig 3.10d**)

The PC board part was fabricated from a commercial PCB blank (Soddial, 10cm*15cm*1.6mm) using computer numerical control (CNC) machining. First, a 3D model of the PC board part was generated using Autodesk Inventor software (2020 version). (**Fig 3.11a**) After selection of milling tools and adjustment of the sequence for milling various surfaces, the toolpath for cutting the PC board part was simulated using the Autodesk Fusion 360 software (2020 version), as shown in **Fig 3.11 b.** Subsequently, the G-code for controlling the CNC machine to cut the desired shape was generated according to the toolpath. (see **Fig 3.11 c**) A small CNC machine (MySweety 3018 Pro) was purchased and used to test the generated G-code on soft polymer foams. After several cycles of optimizing the 3D model and G-code, 1.6 mm PC boards were milled. Despite the small CNC machine having a slow milling rate, low precision, and low quality of the generated surface, a prototype of the PC board part for the *in situ* cell was fabricated. Then I sent the G-code and 1.6 mm PC boards to Paul Gatt of the Department of Chemical Engineering, to use the advanced CNC machine (Tormach, 770M) in JHE-140 to conduct the milling and cutting process. **Fig 3.11d** shows a photo of the PC board part obtained with high precision and quality.

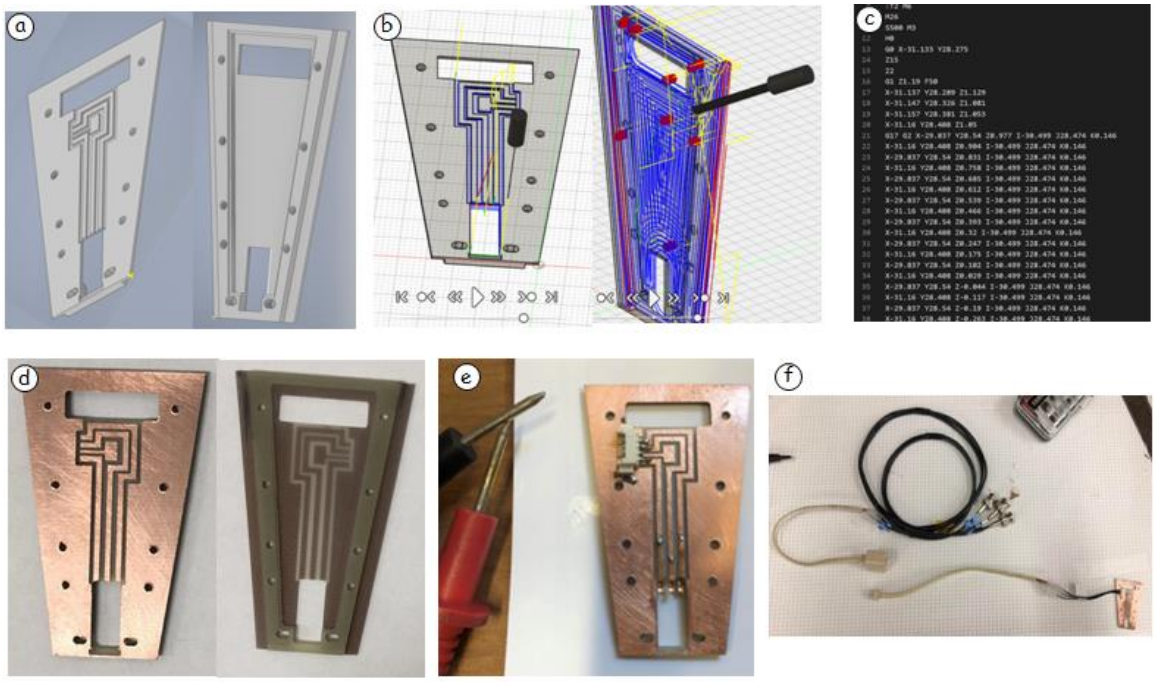

Figure 3.11 Fabrication process for making PCB. Pictures of **a)** 3D model of the PC board part **b)** toolpath for cutting PC board part **c)** G-code for controlling the CNC machines to cut PC board part **d)** obtained PC board part **e)** the PC board part connected with 4-pin connectors and Cu plates **f)** the PC board connected with the electrical wires attached to the potential stat.

Electrical connections to the PC board were achieved by soldering the 4-pin connectors and Cu spring to the Au coated Cu traces on the PC board part. A multimeter (PrimeCables, EM3620) was used to check for continuity and low inter-trace resistance which was typically more than the 1 Gigaohms (above the maximum range of the multimeter). (**Fig 3.11e**) The Au-coated Cu spring touches the top sides of the Au traces on the *in situ* chips. The 4-pin connector is connected to electrical wires using the mating connector (Molex, 1.25 mm pin spacing) which is then attached to the potentiostat, as shown in **Fig 3.11f.** The potentiostat(s) (Ivium-pocketSTAT or Palmsens- EmStat4S)

controlled the potential applied to the WE (relative to the CE, with stabilization by the Au RE pseudo-reference) and measured the currents through software supplied by the potentiostat manufacturer (IviumSoft 4.1121 and PSTrace 5.9) .

3.7.3 Assembly and set up of the *in situ* device.

When the *in situ* device is assembled, the PDMS part with an *in situ* chip is sandwiched between the PC board part and PMMA plate using 4-80 nylon screws. The input and output silicone tubing are connected to Tefzel tubing (IDEX 1517, 1/16" OD x .040" ID) and pre-filled with electrolyte. The Tefzel tubing is connected to a syringe pump, which is used to control the flow rate of electrolyte through the PDMS microfluidic channel and the very narrow pathway inside the chips. Typical flow rate was 10 μL/hour with occasional increase to 50 – 100 μL/hour and / or reversal of flow direction to decrease the electrolyte layer thickness or to clear a bubble.

3.7.4 Laboratory tests of the *in situ* device

In situ experiments were conducted in the lab under an optical microscope to check the fabricated *in situ* devices and collect valuable information for *in situ* procedures, device improvements, and electrochemical behavior. After assembling the *in situ* device and connecting it to a potentiostat (as shown in **Fig. 3.12b**), the input and output silicone tubing were connected to a syringe pump through the Tefzel tubing connection. 5 mM $CuSO_4$ electrolyte was pushed through the PDMS channel and chips at a flow rate of 50 μL/h. The fluid flow and filling process were monitored both visually (examination of the

fluid column in the 4 external tubing) and under optical microscopy (to monitor the fluid inside the windowed area of the *in situ* device. The potentiostat (Ivium-pocketSTAT) was connected to a laptop and operated using the potentiostat software (Iviumsoft 4.11). The setup for *in situ* experiments in the lab is shown in **Fig. 3.12a.**

After everything was set up, cyclic voltammetry (CV) in the potential range -0.3 V_{Au} to +0.3 V_{Au} and -0.6 V_{Au} to +0.5 V_{Au} (V_{Au} versus the Au pseudo reference electrode, i.e. the potential between the RE and CE defines the 0 of the potential scale) with a scan rate of 20 mV/s was used to monitor the Cu electrodeposition on the WE of the *in situ* E chip. The electrodeposition was performed under the optical microscope at 50x magnification.

Fig. 3.12c displays the CV curves and the optical images at various potentials which show morphology changes of the deposited Cu. Before deposition happened, at the open circuit potential (OCP, ~0 V_{Au}) and +0.3 V_{Au} in the 1st CV cycle, there were no Cu particles on the working electrodes. But when the potential was decreased to -0.3 V_{Au}, sub-micron sized Cu particles deposited on the surface and at the edge of the Au WE. When the potential was increased to +0.3 V_{Au} in the 2nd CV cycle, all the Cu particles disappeared. Cu electro-deposition happened at -0.3 V_{Au} in the 2nd cycle. After two CV cycles were finished, the potential was set back to 0 V_{Au}, leaving the Cu particles on the Au WE. There is a reversible Cu deposition and reduction process in this potential range, corresponding to the overall reaction:

$$Cu^{2+}(aq) + 2e^- \rightleftharpoons Cu(s) \qquad \text{eqn. 3.3}$$

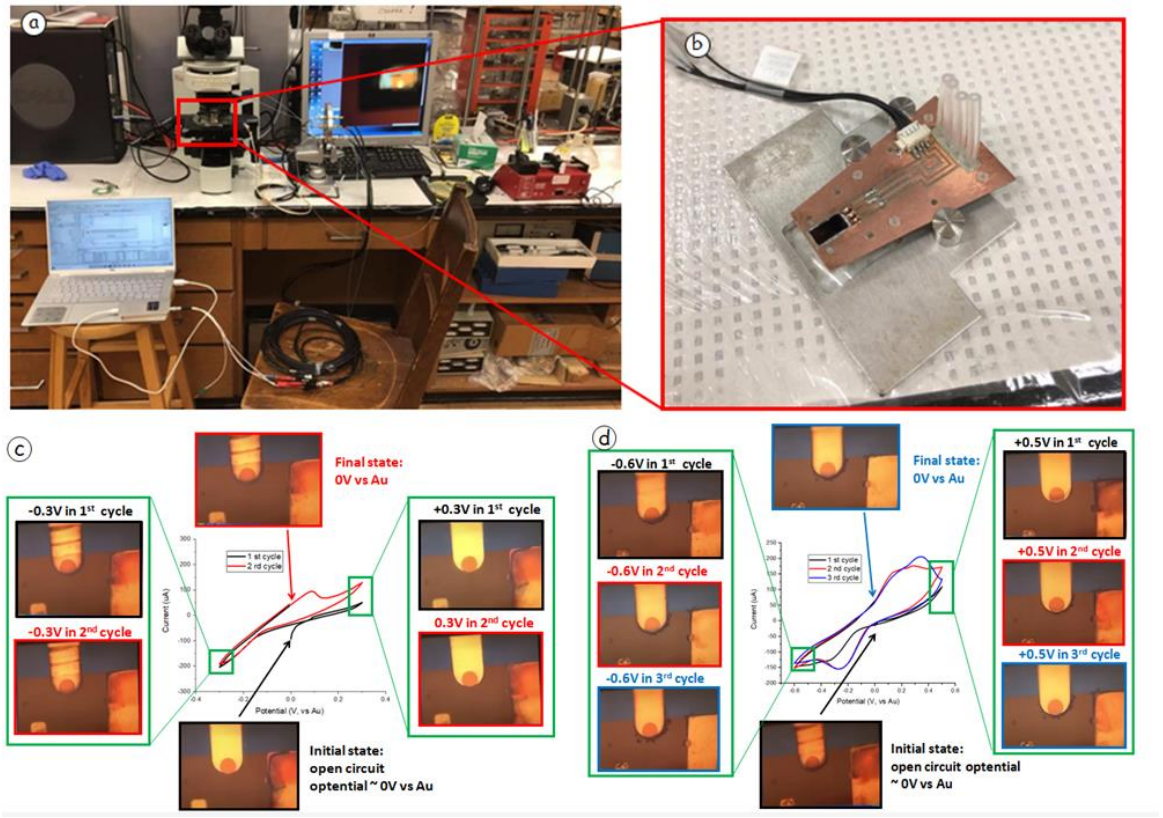

Figure 3.12 Cu electro-deposition in the laboratory tests. a) picture of *in situ* set up under the optical microscope **b)** assembled *in situ* cell **c)** CV curve 1. -0.3 V_{Au} to +0.3 V_{Au} and the microscopic images at indicated potentials **d)** CV curve 2. -0.6 V_{Au} to +0.5 V_{Au} and microscopic images at indicated potentials.

At -0.3 V_{Au}, the reaction shifts to the right and Cu^{2+} ions at the surface of the WE are reduced to form metallic Cu particles (in pure $CuSO_4$ (aq)) or mixed Cu_2O and Cu particles (in mixed $CuSO_4$(aq), KCl (aq)). At the positive potential, the generated Cu particles are oxidized to Cu^{2+}, and the electrochemical reaction shifts back to the left.

In CV curve 2, in the potential range of -0.6V_{Au} to +0.5V_{Au}, the deposited metallic Cu particles had a different morphology. (**Fig. 3.12 d**) In cycle 1 of CV curve 2, from 0 V_{Au} to +0.5V_{Au}, the remaining Cu particles from CV curve 1 were completely reduced. At

-0.6V_{Au} in the 1st cycle, the metallic Cu particles tend to form on the edge rather than on the surface of the working Au electrode. When the potential increased to +0.5V again in the 2nd and 3rd cycles, not all the deposited Cu was oxidized to $Cu^{2+,}$ and some particles were left at the edges. At a potential of -0.6V_{Au} in the 2nd and 3rd cycles, the deposited Cu tended to grow on the Cu particles remaining at the edge of the WE to form dendrites. After 3 cycles in -0.6V_{Au} to +0.5V_{Au}, Cu dendrites grew at the edge of the Au working electrode.

These observations of Cu electro-deposition from dilute $CuSO_4$ solutions are consistent with the literature and previous *in situ* STXM results for Cu electrodeposition. [Arán-Ais et al., 2020. Vinod et al., 2018] The successful utilization of *in situ* devices to carry out Cu electrodeposition with electrochemical and flow control is a milestone for my project. This aspect of the device testing demonstrated that electro-deposition to form sub-micron Cu particles can be achieved. Since the *in situ* electro-deposition was successful in the lab, meant it would also work for *in situ* STXM and ptychography.

3.7.5 Potential calibration of V_{Au} vs V_{RHE}

In order to compare electrochemical results from the *in situ* cell with those from the catalytic reactor and for comparison to the literature [Alnoush et al., 2021], I calibrated the Au pseudo reference in the *in situ* device (V_{Au}) to the RHE scale (V_{RHE}) by comparing CVs of Cu reduction and oxidation measured on the V_{Au} and V_{RHE} scales (**Fig. 3.13**). **Fig. 3.13a,b** displays the CV in CO_2 saturated 0.1M $KHCO_3$ in a 2-compartment electrolyte membrane-separated cell. The working electrode is Cu particles electro-

deposited on an Au-coated graphite foil prepared by physical vapor deposition, as described in section **3.6.4.** A Pt foil was used as the counter electrode and an Ag/AgCl electrode was used as the reference electrode. The Ag/AgCl reference electrode was calibrated versus a homemade RHE, and the potentials are reported versus RHE. The catholyte and anolyte chambers were separated by an ion exchange membrane. The potential range is +0.1 to +0.8 V_{RHE} and the scan rate is 20 mV/s.

Fig. 3.13 c,d displays the CV in CO_2 saturated 0.1M $KHCO_3$ in a 3-electrode (beaker) cell. The working electrode (WE) is electrodeposited Cu on an Au foil. The method for preparing the Cu electrode is described in section **3.6.4**. A Pt foil was used as the counter electrode and an Ag/AgCl electrode was used as the reference electrode. The potential range is +0.25 to +0.7 V_{RHE} and the scan rate is 20 mV/s.

Fig. 3.13 e,f displays the CV in CO_2-saturated 0.1M $KHCO_3$ in an *in situ* cell. The working electrode is the electrodeposited Cu on the WE of the *in situ* cell. Details for the preparation of the Cu electrode are given in section **3.8.** The CE and RE are Au . The potential range is -0.4 to +0.2 V_{Au} and the scan rate is 20 mV/s.

Fig. 3.13 g displays the potential (V_{Au}) versus time (s) under the *in situ* conditions when no potential is applied. i.e. the open circuit potential (OCP) was -48 mV_{Au} ± 4 mV_{Au}. This shows that the Au pseudo reference electrode under *in situ* conditions provides a stable potential reference. To relate the two reference scales, the CV with potentials vs RHE (**Fig. 3.13b**) was compared with the *in situ* CV with potentials vs Au (**Fig. 3.13d**, **h**) This results in a conversion equation:

$$E_{(RHE)} = E_{Au} - 0.40\ V \pm 0.07\ V \qquad \text{eqn. 3.4}$$

The accuracy and reproducibility of Au pseudo reference electrode was checked multiple times by comparing CV curves for Cu redox in CO_2 saturated 0.1 M $KHCO_3$ or $NaHCO_3$. The error ~ ± 0.07 V.

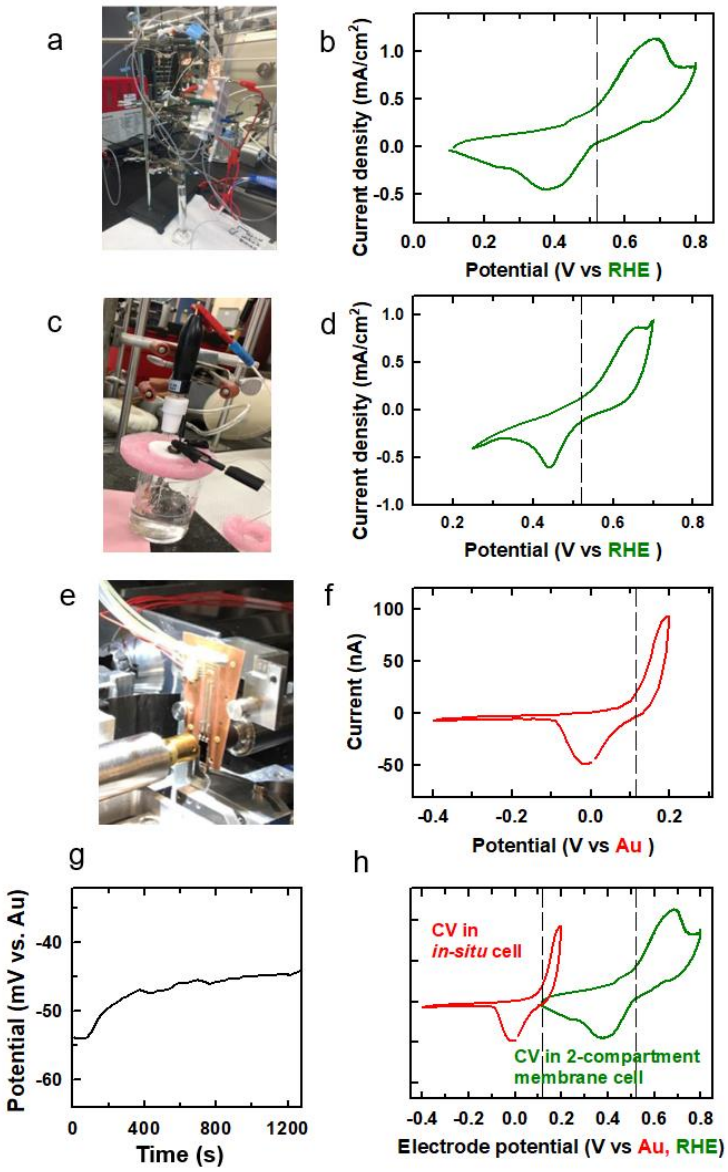

Figure 3.13 The potential difference between V_{RHE} and V_{Au} **a)** photo of 2-compartment membrane cell. **b)** CV measured in the 2-compartment cell. 20 mV/s scan

rate. **c)** photo of 3-electrode (beaker) cell. **d)** CV in beaker cell. **e)** photo of the *in situ* cell. **f)** CV measured in *in situ* cells. **g)** potential (mV_{Au}) vs time (s) under *in situ* open circuit potential (OCP) conditions. **h)** CV is used to derive the relationship of the potential relative to Au (V_{Au}) to that relative to the reversible hydrogen electrode (V_{RHE}) in CO_2 saturated 0.1M $KHCO_3$.

3.8 Experimental details for *in situ* STXM.

3.8.1 Filling electrolyte into *in situ* cell

First, the electrolyte solutions used in *in situ* experiments are prepared and loaded into 1 mL syringes. Bubbles are removed by pushing/withdrawing the syringe. The syringe with the electrolyte is connected to the *in situ* device using tubes. The syringe plunger is pushed manually to fill the tube with electrolyte.

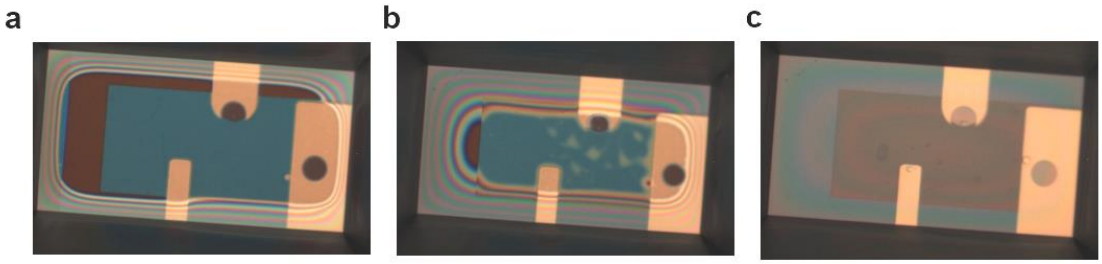

Figure 3.14. Filling the *in situ* cell with electrolyte under an optical microscope. (a), (b), (c) are reflection images ~5 minutes apart (magnification 20x).

Then the filled tubing is connected to the assembled *in situ* device and the syringe is placed into the syringe pump. A flow rate of 25 μl/hr for 10 min is used to slowly fill the *in situ* device with electrolyte. The filling process is always conducted under an

optical microscope, to confirm that the electrolyte fills the window region. (**Fig 3.14**). These procedures verify good electrical connections and steady electrolyte flow with no problems such as liquid leaking, channel blocking due to bubbles, or cable disconnection.

3.8.2 Loading the *in situ* device into the STXM

After the *in situ* device is loaded with electrolyte, and a stable OCP is measured, it is loaded into the STXM. First, the cable to the potentiostat and the connection to syringe pump are disconnected to simplify device insertion into the STXM. The *in situ* device, connected only to the electrolyte tubing, is moved with caution from the optical microscope to the STXM chamber and inserted through a 4.5'' flange. Since these measurements were first made, the fluid line and electrical connections have been modified to be implemented on a 2.75" conflat flange, which enables compatibility with most modern STXMs. In the STXM chamber, the *in situ* device is mounted in the 3-pin sample kinematic holder and then the potentiostat and syringe pump are re-connected. The syringe pump is turned on with a flow rate of 25 μl/hr to keep a stable electrolyte flow through the *in situ* device. The electrolyte tubes and potentiostat cables are organized in the STXM chamber and stabilized using Kapton tape to attach them to a suitable position in the chamber to avoid interfering with STXM operations such as sample scanning.

3.8.3 Initial STXM operation after loading the *in situ* device

After the *in situ* device is loaded in the STXM, the air in the tank is replaced with He gas by displacing the air at a slow rate (~10 min). After achieving a plateau in X-ray transmission, the He gas flow is stopped and the STXM chamber is sealed. Note that this procedure is routine at the CLS ambient STXM, but not possible at some other facilities, due to a minimum vacuum required before the beamline can be opened. STXM imaging was then used to locate the SiN_x window (240 μm x 120 μm) and to make sure there are no bubbles in the 3-electrode area that occasionally occur in the process of moving and loading the *in situ* device into the STXM. The X-ray signal transmitted through the SiN_x windows and electrolyte is measured and compared with the incident X-ray intensity measured in one of the holes in the *in situ* device (**Fig. 2d**) to measure the absorption (optical density, OD) of the electrolyte, which in most spectral regimes is dominated by absorption by the water. Comparison to the known X-ray transmission properties of the SiN_x windows and water allows determination of the thickness of the electrolyte, which was between 2 and 5 μm, depending on the spacer used (0.5, 1, 1.5 μm), syringe pump flow rate, and ID of the electrolyte tubing. An electrolyte layer (as thin as ~1.6 μm) can be achieved. In this work, a 1 μm spacer was used. If the electrolyte layer is too thick (>4 μm), X-rays below ~1000 eV cannot transmit through the electrolyte and thus STXM measurements at the Ni 2p (~830 eV) or Cu 2p (~930 eV) edges cannot be performed. After the liquid thickness is measured and the presence of Cu^{2+}(aq) in the electrolyte is verified, electrochemical experiments are performed on the 3-electrode area through the control of potentials and measurement of currents using a potentiostat.

3.8.4 *In situ* electrodeposition of Cu nanoparticles.

Copper nanoparticles were electrodeposited from a solution of 5mM $CuSO_4$ and 5mM KCl onto the Au WE of the *in situ* micro-chip cell. The electro-deposition solution concentrations and conditions were chosen based on previous reports [Arán-Ais et al., 2020] to target particles in the range of 300 – 500 nm diameter that are relevant for CO_2R and STXM measurements. After setting up the *in situ* device in a STXM, the electrodeposition was carried out by performing three CV cycles between 0 and +0.4 V_{RHE} with a scan rate of 20 mV/s. (**Fig. 3.15**). The as-deposited Cu particles are then characterized using STXM to determine the morphology and chemical (i.e., oxidation state) distributions. STXM measurements at this step should be as fast as possible because some of the Cu particles slowly disappear by dissolution into the 5mM $CuSO_4$ / KCl electrolyte which has a measured pH of 6.1. This could be caused by the slow conversion of Cu(I) to Cu(II) in the mildly acidic environment under open circuit potential conditions (ca. +0.36 V_{RHE}) as Cu(I) is not stable at lower pH values [Beverskog, 1997], followed by Cu(II) dissolution into the electrolyte. (see **Fig. 3.16**). This phenomenon has been observed several times in our *in situ* experiments.

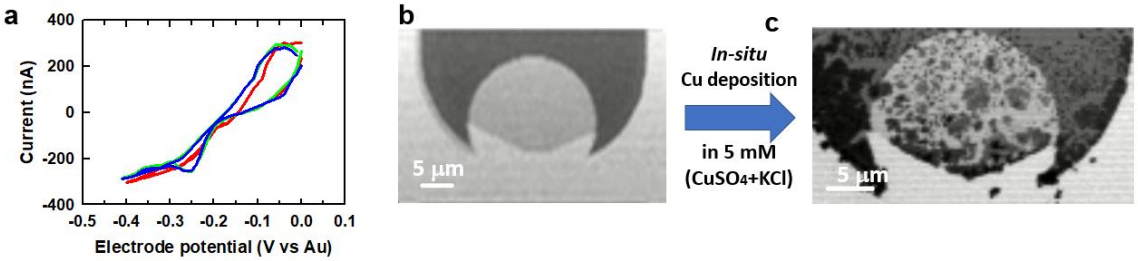

Figure 3.15 *In situ* electrodeposition of Cu particles from a 5 mM $CuSO_4$, 5 mM KCl solution. **(a)** Cyclic voltammetry (3 cycles) **(b)** STXM images at 960 eV before the Cu deposition **(c)** STXM images at 933.5 eV after the deposition of Cu particles. The horizontal bands in the STXM images are an artifact arising from slow (period ~1 s) oscillations of the incident X-ray intensity due to shifts in the position of the electron beam in the CLS ring, which sometimes occurs.

Once a region with particles of a suitable thickness (50 – 200 nm) and size (50 – 600 nm) are identified and the oxidation states determined, (**Fig. 3.16**). the $CuSO_4$/KCl electrolyte is displaced by CO_2 saturated 0.1 M $KHCO_3$ for subsequent *in situ* STXM experiments under CO_2R conditions. The Cu particles are more stable in the CO_2-saturated 0.1 M $KHCO_3$ electrolyte as the pH is close to neutral (pH 6.8). Therefore, changing the electrolyte from $CuSO_4$ /KCl to CO_2 saturated 0.1 M $KHCO_3$ is done as fast as possible to avoid loss of the deposited Cu particles. Part of the "art" of this experiment is to minimize the time between deposition of Cu particles and the change of the electrolyte to CO_2 saturated 0.1 M $KHCO_3$.

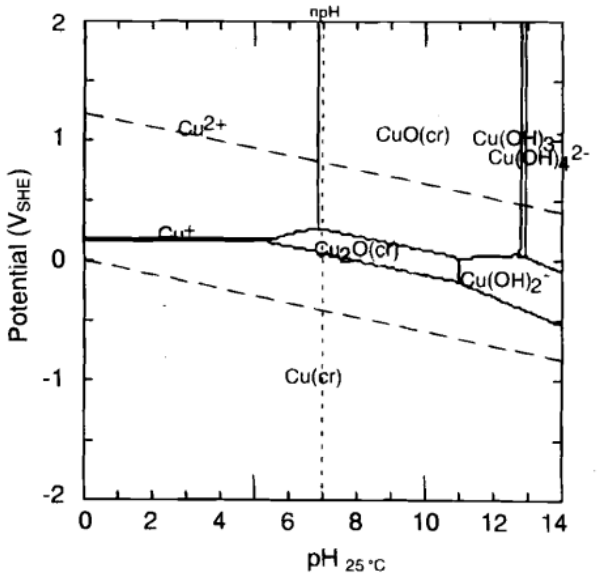

Figure 3.16. Pourbaix diagrams for copper at 25 °C [Beverskog et al., 1997] with permission of IOPScience.

3.8.5 Changing the electrolyte to $KHCO_3$ solution.

The CO_2-saturated 0.1 M $KHCO_3$ or $NaHCO_3$ is prepared just before the *in situ* STXM experiments by bubbling CO_2 gas into 0.1 M $KHCO_3$ solution for 20 mins in a septum sealed vial. After Cu *in situ* electrodeposition, the electrolyte is changed to CO_2 saturated 0.1M $KHCO_3$. Deionized water is first used to flush the $CuSO_4$/KCl out of the *in situ* micro-chip device. Then the CO_2 saturated 0.1 M $KHCO_3$ electrolyte is continuously filled using a 25 μl/hr flow rate. Changing the electrolyte takes around 20 mins. After electrolyte changes, there is no STXM-detectible Cu^{2+} signal in the electrolyte.

3.8.6 *In situ* STXM under CO_2R conditions

In situ STXM measurements were conducted using chronoamperometry (CA) potential sequences. Before all measurements, CA at +0.4V_{RHE} was applied for 30 s (to ensure the catalyst was always in the same starting state) followed by a cathodic step to the electrode potential at which STXM was conducted. STXM measurements were conducted at +0.4, +0.3, +0.2, +0.1, 0, -0.2, -0.4, and -0.6 V_{RHE}. An example of the CA current-time plots is presented in **Fig**. **3.17**. During CA at each potential, the current was continuously recorded. For this study, several STXM measurements were made in a sequence which consisted of (1) STXM image at 933.5 eV; (2) 4-energy stack measurement that enabled differentiation between the different oxidation states of Cu present in the materials; (3) 54-energy Cu 2p stack; and (4) STXM image at 933.5 eV for comparison with the first STXM image measured. In all this took ~43 m at each potential which enabled time-dependent monitoring of morphology and chemical structure changes to the Cu particles under controlled electrode potentials. Potentials more negative than -0.6 V_{RHE} were not applied as bubble formation would often occur, rendering the STXM results unstable. Gas generation by CO_2R to gas phase products or water reduction to H_2 occasionally created large bubbles which occupied the 3-electrode region, leading to a disconnection of the working electrode that stopped the electrochemical reaction. Generally, electrode potentials less negative than -0.6 V_{RHE} did not generate gas bubbles in the *in situ* setup. The *in situ* STXM results are shown in **Chapter 7**.

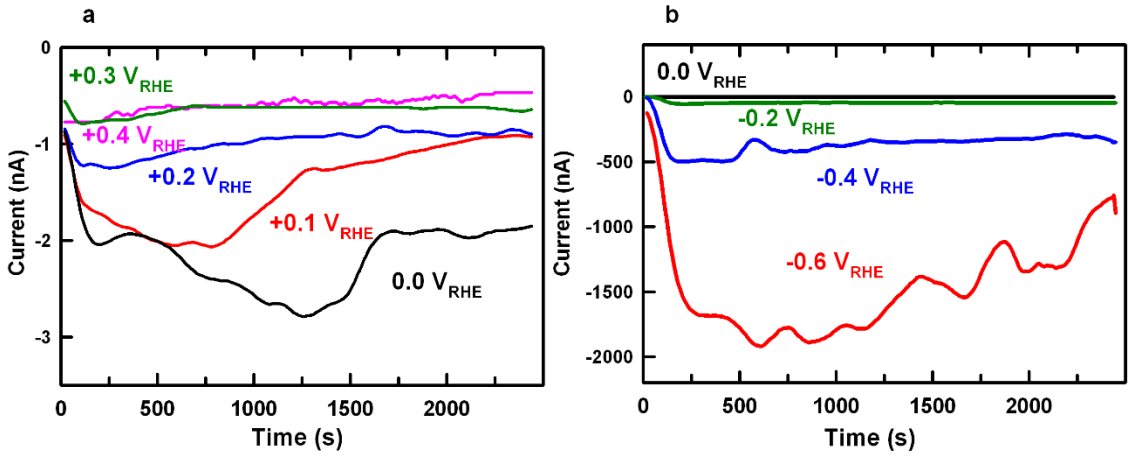

Figure 3.17 Current vs time curve at each potential for *in situ* STXM. (a) +0.4 to 0 V_{RHE}. **(b)** -0.2 to -0.6 V_{RHE}. Note the change in the current scale between (a) and (b).

3.9 Experimental details for *in situ* ptychography

3.9.1 Cu nanoparticle electrodeposition and loading the *in situ* device

The processes of filling the $CuSO_4$ electrolyte, Cu nanoparticle electrodeposition, changing the electrolyte to CO_2 saturated 0.1M $KHCO_3$ and loading the *in situ* device into the STXM are very close to those used for *in situ* STXM shown in **chapter 3.8.1-3.8.5**. The difference is that the Cu nanoparticle electrodeposition and changing the electrolyte to CO_2 are both carried out under the optical microscope, rather than in STXM due to *in situ* ptychography experiments usually taking more time than *in situ* STXM, so there is not enough time to monitor the Cu deposition process by STXM.

3.9.2 Performing *in situ* flow electrochemical measurements by spectro-ptychography.

After the *in situ* device was loaded into STXM chamber and the STXM tank was filled with He gas, STXM imaging was used to find a suitable region of Cu particles. Then four energy (4-E) STXM stack, 4-E ptychography stack, and full ptychography stacks were conducted while chronoamperometry scans at various potentials were sequentially applied. The results of these *in situ* STXM and ptychography measurements are presented and analyzed in **Chapter 8**.

Chapter 4

Chemical Structure and Distribution in Nickel–Nitrogen–Carbon Catalysts for CO_2 Electroreduction Identified by Scanning Transmission X-ray Microscopy

This chapter presents the STXM studies of the nickel–nitrogen–carbon (Ni–N–C) electrocatalysts for CO_2R reactions. Through spatially resolved imaging, identification, and quantification of structures and chemical species in mesoscale regions of Ni–N–C catalysts by STXM, the structure and distribution of the single-atomic sites are clarified, and the relationships between Ni content and CO_2R performance are elucidated.

*Reprinted with permission from the ACS catalysis 12 (**2022**) 8746-8760, Chunyang Zhang, Ladan Shahcheraghi, Fatma Ismail, Haytham Eraky, Hao Yuan, Adam P. Hitchcock, and Drew Higgins, "Chemical Structure and Distribution in Nickel–Nitrogen–Carbon Catalysts for CO2 Electroreduction Identified by Scanning Transmission X-ray Microscopy", Copyright 2022, American Chemical Society.*

The author of this thesis performed all the STXM experiments with the help of Haytham Eraky, Dr. Hao Yuan Prof. A. P. Hitchcock, analyzed all the STXM data, and wrote the publication with assistance in later stages by Prof. A. P. Hitchcock and Prof. Drew Higgins. Ladan Shahcheraghi synthesized the Ni–N–C catalysts. Fatma Ismail and the author tested the CO2 reduction performance of various Ni–N–C catalysts.

The supplement information of the publication is put in Appendix D.

ACS Catalysis

pubs.acs.org/acscatalysis Research Article

Chemical Structure and Distribution in Nickel–Nitrogen–Carbon Catalysts for CO_2 Electroreduction Identified by Scanning Transmission X-ray Microscopy

Chunyang Zhang, Ladan Shahcheraghi, Fatma Ismail, Haytham Eraky, Hao Yuan, Adam P. Hitchcock,* and Drew Higgins*

Cite This: *ACS Catal.* 2022, 12, 8746–8760 Read Online

ACCESS | Metrics & More | Article Recommendations | Supporting Information

ABSTRACT: Atomically dispersed metal–nitrogen–carbon (M–N–C) materials are a class of electrocatalysts for fuel cell and electrochemical CO_2 reduction (CO_2R) applications. However, it is challenging to characterize the identity and concentration of catalytically active species owing to the structural heterogeneity of M–N–C materials. We utilize scanning transmission X-ray microscopy (STXM) as a correlative spectromicroscopy approach for spatially resolved imaging, identification, and quantification of structures and chemical species in mesoscale regions of nickel–nitrogen–carbon (Ni–N–C) catalysts, thereby elucidating the relationship between Ni content/speciation and CO_2R activity/selectivity. STXM results are correlated with conventional characterization approaches relying on either bulk average (X-ray absorption spectroscopy) or spatially localized (scanning transmission electron microscopy with electron energy loss spectroscopy) measurements. This comparison illustrates the advantages of soft X-ray STXM to provide spatially resolved identification and quantification of active structures in Ni–N–C catalysts. The active site structures in these catalysts are identified to be atomically dispersed NiN_x/C sites distributed throughout entire catalyst particles. The NiN_x/C sites were notably demonstrated by spectroscopy to possess a variety of chemical structures with a spectroscopic signature that most closely resembles nickel(II) tetraphenylporphyrin molecules. The quantification and spatial distribution mapping of atomically dispersed Ni active sites achieved by STXM address a target that was elusive to the scientific community despite its importance in guiding advanced material designs.

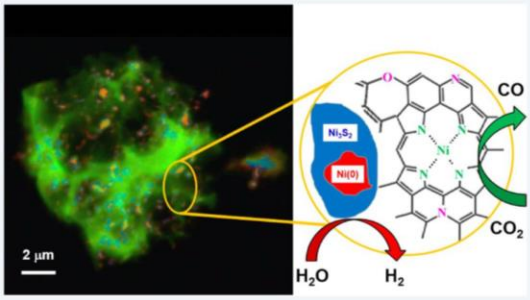

KEYWORDS: *nickel–nitrogen–carbon catalysts, CO_2 electroreduction, X-ray absorption spectroscopy, soft X-ray STXM, STEM-EELS*

1. INTRODUCTION

Nanostructured carbon materials consisting of metal–nitrogen–carbon (M–N–C) species are a promising class of materials for electrocatalytic applications.[1−9] M–N–C materials have attracted great attention as they can be synthesized by straightforward methods that include pyrolyzing a mixture of nitrogen, carbon, and transition-metal-containing precursors, along with their ability to elegantly combine the benefits of heterogeneous and homogeneous catalysts.[10,11] On the heterogeneous side, the catalytically active sites (presumed to be atomically dispersed metal ions coordinated by nitrogen dopants in a MN_x/C configuration[12,13] that is similar in structure to many homogeneous catalysts[14,15]) are embedded in a solid carbon-based framework, so downstream separation of the catalyst from the products is not necessary. Furthermore, the carbon support is highly conductive and no catalyst regeneration is needed, as required for metal-centered homogeneous molecular catalysts that need oxidation or reduction back to their "active" state. On the homogeneous side, M–N–C catalysts in principle can have 100% metal utilization and well-defined active site structures to provide good catalytic activity and selectivity.

M–N–C electrocatalysts first came into prominence with Fe–N–C materials demonstrated as oxygen reduction catalysts in polymer electrolyte membrane fuel cells.[16,17] To date, Fe–N–C materials are the most active nonplatinum group metal catalysts for oxygen reduction in acidic electrolytes due to the presence of an atomically dispersed FeN_x/C active structure that has been identified by a variety of spectroscopy and microscopy techniques.[18−22] More recently, M–N–C research has expanded to other areas, including

Received: March 12, 2022
Revised: June 25, 2022
Published: July 7, 2022

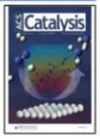

https://doi.org/10.1021/acscatal.2c01255
ACS Catal. 2022, 12, 8746–8760

Scheme 1. Structures of Reference Species and Ni−N−C Samples[a]

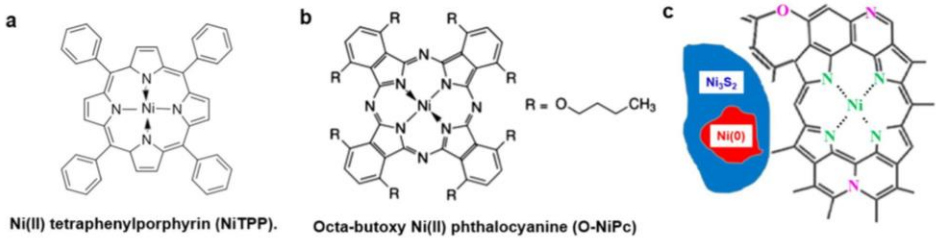

[a](a) Nickel(II) tetraphenylporphyrin (NiTPP), (b) octabutoxy nickel(II) phthalocyanine (O-NiPc), and (c) schematic diagram of the Ni−N−C structure.

catalysis for electrochemical CO_2 reduction (CO_2R).[23] In particular, Ni−N−C electrocatalysts have shown promise for electrochemical CO_2 reduction to CO.[24,25] Scientists have postulated that these catalysts are composed of atomically dispersed NiN_x/C active sites, with a local structure similar to those of Ni(II) porphyrin (such as Ni tetraphenylporphyrin, NiTPP) or nickel(II) phthalocyanine (such as octabutoxy Ni phthalocyanine, O-NiPc), as depicted in Scheme 1a,b.[12,25] The postulated NiN_x/C sites can offer a unique structure for CO_2 adsorption and activation, which reduces the energy barrier for electrochemical CO_2 reduction and exhibits high intrinsic CO_2 reduction activity and selectivity for CO generation.[26,27] Although atomically dispersed MN_x/C moieties have been deemed important for electrocatalytic applications, the identification and characterization of active site structures in M−N−C catalysts prepared by pyrolysis techniques are challenging due to the highly heterogeneous nature of these materials in terms of compositions, phases, and structures that are present.

Many techniques have been used to characterize M−N−C electrocatalysts with the objective of elucidating the structures and properties of catalytically active sites to provide mechanistic insight and inform advanced catalyst designs. Time-of-flight secondary ion mass spectrometry (ToF-SIMS) was the first characterization technique to directly identify species consisting of coordinated Fe, N, and C in oxygen reduction catalysts.[28,29] X-ray absorption spectroscopy (XAS) has also been used widely to characterize the local structure of transition metals and nitrogen atoms in M−N−C catalysts, leading to the elucidation of MN_x/C coordination environments.[30−33] Scanning transmission electron microscopy (STEM) has been used to image single metal atoms in M−N−C catalyst samples. State-of-the-art atomic resolution transmission electron microscopy (TEM) and electron energy loss spectroscopy (TEM-EELS) have provided analytical confirmation of the identity of the single metal atom and provided some insights into the local chemical environment.[34−36]

Prior to this work, characterization using either bulk-averaged or very spatially localized measurements has (i) verified the presence of atomically dispersed MN_x/C sites and (ii) measured the average properties of M−N−C samples and correlated them with the activity/ selectivity/performance of the overall catalyst. Opportunity exists to leverage mesoscale spatial resolution spectroscopy techniques, such as soft X-ray scanning transmission X-ray microscopy (STXM), that will enable a comprehensive understanding of (i) the distribution, content, and properties of different species present in M−N−C catalysts; (ii) how these factors differ with different synthetic strategies; and (iii) the impact of these physicochemical properties on electrocatalytic performance. This comprehensive insight into the heterogeneous compositions and structures of M−N−C materials would help guide the design and optimization of improved performance catalysts for carbon dioxide reduction (CO_2R) and other important electrocatalytic reactions.[37] STXM is a synchrotron-based technique that provides precise chemical speciation through near-edge X-ray absorption fine structure (NEXAFS) spectroscopy[38] and quantitative, chemically selective imaging with sub-40 nm spatial resolution. Here, we use STXM,[39−41] along with XAS and TEM-EELS, to provide a spatially resolved, holistic understanding of the chemical species and structures present in M−N−C materials. Section S1 and Table S1 present a comparison of the advantages and limitations of ToF-SIMS, STEM/EELS, STXM, and XAS.

The samples studied were a series of pyrolyzed, polymer-derived Ni−N−C catalysts that were investigated previously for their oxygen reduction reaction performance and chemical composition.[42] STXM image sequences (stacks) were used to collect spatially resolved NEXAFS spectra at the C 1s, N 1s, O 1s, Ni 2p, and S 2p edges of Ni−N−C materials prepared with different synthetic parameters. These stacks were compared and fit using NEXAFS spectra collected from suitable reference compounds. The Ni 2p results showed the presence of metallic Ni (shown as Ni(0)), as well as trinickel disulfide (Ni_3S_2) and NiN_x/C species. The N 1s and C 1s spectra provided evidence that the local structure of NiN_x/C is closer to that of NiTPP than nickel(II) phthalocyanine, which was the coordination speculated in previous reports.[12,25] Detailed analysis of STXM data on the Ni−N−C catalysts provided quantitative maps of the amount and spatial distributions of the NiN_x/C sites, Ni(0), and Ni_3S_2 on an oxidized carbonaceous matrix, as shown in Scheme 1c. The NiN_x/C structures, which are the active CO_2R catalytic sites, are widely distributed throughout the catalyst structure. The amount of the catalytic NiN_x/C sites in the various Ni−N−C samples was determined from quantitative analysis of the STXM data and used to explain the relative activity and selectivity for CO_2 reduction to CO for different Ni−N−C materials. These insights can be used to inform the design of next-generation M−N−C catalysts. In addition, our work shows that STXM is an excellent tool for electrocatalyst studies since it overcomes the limitations of bulk/average or overly localized techniques. This advantage is particularly important in studies such as M−N−C catalyst development, where the materials are intrinsically highly heterogeneous. This ex situ study thereby validates STXM as

https://doi.org/10.1021/acscatal.2c01255
ACS Catal. 2022, 12, 8746−8760

a powerful tool for characterization of electrocatalyst materials and is an essential step toward in situ electrochemical STXM measurements[43] that our team is currently performing.

2. EXPERIMENTAL METHODS

2.1. Material Synthesis. The synthesis of the Ni−N−C catalysts has been reported previously.[42] Briefly, the Ni−N−C catalysts were prepared by mixing aniline (1 mL, Sigma-Aldrich), cyanamide (2 g, Sigma-Aldrich), and nickel chloride hexahydrate ($NiCl_2{\cdot}6H_2O$, Sigma-Aldrich) in a 1.5 M HCl solution (200 mL, ACS reagent). This solution was mixed by magnetic stirring, followed by the addition of ammonium persulfate (1.5 g, Sigma-Aldrich) as an oxidant for the polymerization of aniline to polyaniline. The water was evaporated by heating the solution to 80 °C and leaving it stirring overnight. The resulting product was pyrolyzed at 900 °C in Ar for 1 h, acid-washed to remove labile Ni compounds, and then pyrolyzed a second time at 900 °C in Ar for 3 h. The acid washing procedure was to remove any surface exposed Ni particles that would be active for the hydrogen evolution reaction under CO_2R conditions.[25] The second pyrolysis was to remove any labile residues that remain after the acid wash procedure. In the synthesis, the amount of $NiCl_2{\cdot}6H_2O$ was varied to prepare two different Ni−N−C catalyst materials: sample A, Ni−N−C-high (1.2 g of $NiCl_2{\cdot}6H_2O$), and sample B, Ni−N−C-low (0.08 g of $NiCl_2{\cdot}6H_2O$). A comparison sample N−C (Ni-free) was prepared without the addition of any nickel precursor. Ni_3S_2/C samples were prepared by mixing 20 wt % commercial Ni_3S_2 (Sigma-Aldrich) particles and 80 wt % high-surface-area Vulcan XC-72 (VC, FuelCellStore) powders in a ratio of 20−80 wt %, respectively.

2.2. Catalyst Testing. The performance of the Ni−N−C-low, Ni−N−C-high, N−C, and Ni_3S_2/C materials for electrochemical CO_2R was tested to gain insight into how the structures and chemical components of the Ni−N−C catalysts impacted the catalytic activity and selectivity. Ten milligrams of material was suspended in an ink including 1.5 mL of isopropyl alcohol and 0.5 mL of H_2O with 110 μL of Nafion (Sigma-Aldrich, 5 wt % Nafion in ethanol) and sonicated for 30 min. The suspended ink was drop-cast onto graphite foil (Fisher Scientific) and dried at 70 °C for 2 h, leading to an electrode loading of 1 mg/cm^2. The catalyst-coated electrodes were used as the working electrode for electrochemical CO_2 reduction and tested in a custom-built two-compartment cell that has been reported previously.[44,45] The geometric area of the working electrode was 5.7 cm^2. The electrolyte compartments of the working and counter electrode were filled with 0.1 M $KHCO_3$ (10 mL), and CO_2 was flown continuously through the catholyte and anolyte chambers at 20 sccm throughout the course of the experiment. A Pt foil was used as the counter electrode and an Ag/AgCl electrode was used as the reference electrode. The Ag/AgCl reference electrode was calibrated vs a home-made reversible hydrogen electrode (RHE). All potentials reported in this manuscript are in terms of vs RHE. The catholyte and anolyte chambers were separated by an ion exchange membrane (Selemion AMV, AGC Inc.). Catalysts were tested by chronoamperometric measurements at various electrochemical potentials in the CO_2-saturated 0.1 M $KHCO_3$. Ni−N−C catalyst materials are known to selectively produce only gas-phase products (CO and H_2),[25,46,47] so gas chromatography (GC) was used for product detection and quantification; liquid product quantification was not performed. A 1 mL sample of the effluent gas from the cathode compartment of the electrochemical cell was fed to a gas chromatography (GC) unit (supplier, SRI; model, 8610C in the multigas configuration #5, equipped with flame ionization and thermal conductivity detectors) for product identification and quantitation to determine faradic efficiencies (FEs). While our setup can also collect liquid products for subsequent analysis by either nuclear magnetic resonance spectroscopy or high-performance liquid chromatography, this was not done in this study as M−N−C catalysts produce almost exclusively gas-phase product, and the faradic efficiency (FE) values were close to 100%.

2.3. STXM Measurements. STXM imaging and spectroscopy were performed using the spectromicroscopy beamline (SM) 10ID1 at the Canadian Light Source (CLS, Saskatoon, Canada). Details of the beamline[48] and STXM,[49] along with operating procedures[40] have been presented elsewhere. Briefly, the monochromatic X-ray beam was focused to a ∼40 nm spot by a Fresnel zone (ZP) plate (Applied Nanotools Ltd.). The sample was positioned at the focal point of the X-ray beam, and STXM images were measured by (x,y) raster-scanning the sample while recording the transmitted X-ray intensity pixel by pixel in a single-photon counting mode using a phosphor/photomultiplier.[50] Spectroscopic information was obtained by recording image sequences (also known as stacks[51]). The energy scale was calibrated by recording spectra of standard gases Ne,[52] N_2,[53] SF_6,[54,54] and CO_2.[53,53] All STXM data was analyzed using aXis2000 software.[55] Detailed information about sample preparation for STXM, a summary of samples investigated, energy-scale calibration, and STXM data analysis can be found in Sections S2−S5, Supporting Information.

2.4. STEM/EELS and XAS Measurements. The catalyst materials were characterized by field-emission transmission electron microscopy (TEM), high-resolution aberration-corrected transmission electron microscopy (HRTEM), and high-angle, annular dark-field scanning transmission electron microscopy (HAADF-STEM) imaging along with EELS using an FEI Titan 80-300 HB microscope at the Canadian Centre of Electron Microscopy (CCEM, McMaster University). The FEI Titan 80-300 HB microscope with an XFEG Source was operated at 200 kV with two hexapole Cs correctors (CEOS) using a 19.1 mrad convergence angle STEM probe and a Fischione HAADF detector. When doing the EELS, the Gatan Quantum GIF with a Gatan K2 Summit direct electron detection camera was used with 55.0 mrad collection semiangle, 0.4 nm/pixel, 0.25 eV/channel dispersion, and 10 ms exposure.

Ensemble-averaged (limited spatial resolution) X-ray absorption spectroscopy (XAS) at the Ni 2p and N 1s edges was performed using the spherical grating monochromator (SGM) beamline 11ID1 at the CLS. To minimize radiation damage, a quick scan protocol was used, with multiple measurements (30 for Ni 2p and 10 for the N 1s) from adjacent 250 μm × 250 μm areas of each sample. The total electron yield (TEY), total fluorescence yield (TFY), and partial fluorescence yield (PFY) signals were measured simultaneously. In all cases, the fluorescence yield spectra were highly distorted by absorption saturation of both incident and fluorescence intensities. Partial ion yields (PFYs) and inverse PFY spectra were also explored, without significant improvement. The reason is that either the Ni−N−C particles were too thick (see the comparison of **A1** and **A2**) or particles overlap in the samples used for the XAS study, where multiple layers of the powder were pressed into the In foil. This

https://doi.org/10.1021/acscatal.2c01255
ACS Catal. 2022, 12, 8746−8760

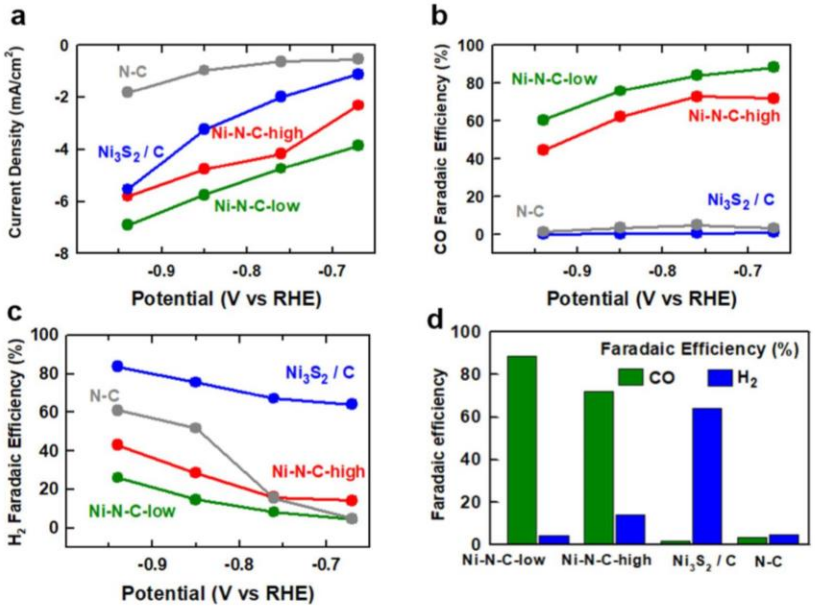

Figure 1. Evaluation of activity and selectivity for electrochemical CO_2 reduction by Ni−N−C-low, Ni−N−C-high, Ni_3S_2/C, and N−C (a catalyst synthesized without Ni). (a) Overall geometric current density. (b) Faradic efficiency toward CO production. (c) Faradic efficiency toward H_2 production. (d) Comparison of CO and H_2 production at −0.67 V vs RHE. Note that in some instances significantly less than 100% faradic efficiencies were reported owing to low current densities that resulted in H_2 concentrations in the effluent from the reactor below the detection limit of the thermal conductivity detector.

demonstrates another major advantage of STXM—the ability to select and measure particles that are sufficiently thin to avoid spectral distortion from absorption saturation. Such particles are also thinner and thus the catalytically active surface sites contribute more than in larger particles. The XAS-TEY results are compared with STXM-derived NEXAFS spectra of the same material to provide an ensemble-averaged confirmation of the STXM results.

3. RESULTS

3.1. Electrochemical CO_2 Reduction Properties. The results of evaluation of the catalytic performance of our Ni−N−C catalysts for electrochemical CO_2 reduction in CO_2-saturated 0.1 M $KHCO_3$ are displayed in Figure 1. At an electrode potential of −0.67 V vs RHE, the Ni−N−C-low sample showed a current density of −3.9 mA/cm^2 (Figure 1a) and a CO faradic efficiency of 88% (Figure 1b). At all potentials investigated between −0.67 and −0.94 V vs RHE, the faradic efficiency of Ni−N−C-low toward CO was >60% and toward H_2 was <25% (Figure 1c), with a decrease in selectivity to CO and an increase in selectivity to H_2 observed at more negative electrode potentials. The Ni−N−C-high sample showed the similar catalytic performance to the Ni−N−C-low sample but with relatively lower activity and lower faradic efficiency (Figure 1d). These trends, including high CO selectivity that diminishes at more negative potentials, are consistent with previous reports on Ni−N−C catalysts and have been attributed to the presence of atomically dispersed NiN_x/C active sites.[56,57] This notion is supported by the electrochemical performance of the N−C (Ni-free) sample, which was found to produce negligible amounts of CO under electrochemical CO_2R conditions (Figure 1b). We also measured the electrochemical CO_2R performance of Ni_3S_2/C as a reference compound, as we had previously identified that the synthesized Ni−N−C materials contain Ni_3S_2 and metallic Ni particles.[42] While metallic Ni would be expected to exclusively produce H_2 under CO_2 reduction conditions,[58,59] it was prudent to determine what impact, if any, the Ni_3S_2 species have on CO_2 reduction activity and selectivity. We tested commercial Ni_3S_2 particles supported on Vulcan XC-72 carbon black (Ni_3S_2/C). This sample demonstrated significantly increased current densities in comparison to Ni−N−C-low at all electrode potentials evaluated (Figure 1a). However, near-negligible amounts of CO were detected (Figure 1b), indicating that Ni_3S_2/C was selective toward the hydrogen evolution reaction (Figure 1c) and not CO_2R. This is consistent with a previous report on transition-metal sulfide catalysts, which were found to be selective only for hydrogen evolution owing to the steep kinetic barrier for a proton−electron transfer to CO_{ads} intermediate species.[60] It should be noted that less than 100% of total faradic efficiencies were measured for N−C and Ni_3S_2/C samples. This is attributed to the low current densities that result in H_2 concentrations in the reactor effluent of <50 ppm, which is lower than the reliable concentration for detection by the thermal conductivity detector in the gas chromatograph used to measure H_2. Taken together, the electrochemical CO_2R testing results indicate that Ni is essential for producing catalysts that are selective for CO production, but the resulting active site species are not Ni_3S_2 or metallic Ni particles.

3.2. STEM/EELS. Results from a HAADF-STEM and STEM-EELS study of the Ni−N−C-low sample are shown in Figure 2. At low magnifications (Figure 2a), the material was found to consist of a carbonaceous matrix decorated with

https://doi.org/10.1021/acscatal.2c01255
ACS Catal. 2022, 12, 8746−8760

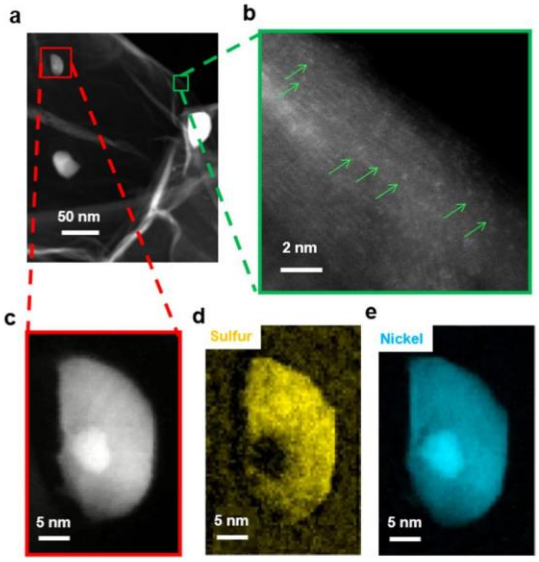

Figure 2. Analysis of the Ni−N−C-low sample by transmission electron microscopy and electron energy loss spectroscopy mapping. (a) Lower-resolution high-angle annular dark-field (HAADF) scanning transmission electron microscopy (STEM) image. (b) Higher-resolution HAADF-STEM image showing graphitic planes, with individual bright (high *Z*-number) atoms indicated by green arrows. (c) STEM image of a particle showing a core−shell structure. STEM electron energy loss spectroscopy (EELS) mapping of (d) sulfur and (e) nickel in this particle.

bright particles. At high magnifications (Figures 2b and S3a), single-atom bright spots (indicating a *Z*-number higher than carbon) were observed throughout the graphitic carbonaceous matrix. These bright spots are interpreted as Ni atoms coordinated to nitrogen atoms within the carbonaceous matrix (in the form of NiN_x/C), as reported previously,[12,25] although without atomic-scale EELS imaging this cannot be stated conclusively. Higher-magnification STEM imaging of a particle shows a core−shell structure (Figure 2c). EELS mapping of sulfur (Figure 2d) and nickel (Figure 2e) indicates that the center of the particle is Ni and the outer shell is nickel-sulfide-based species (Figure 2c). EELS mapping of carbon, nitrogen, and oxygen (Figure S3b) indicates there is a small amount of oxygen in both the particles and the nitrogen-doped carbonaceous matrix. To further understand the chemical environment of Ni, EELS spectra of both the carbonaceous matrix and particle regions are shown in Figure S3c. However, due to the limited energy resolution of the EELS spectra, which is typically ∼1 eV, the chemical species cannot be identified. Therefore, in this work, STXM-derived XAS spectra (energy resolution ∼0.1 eV) are used to clarify the chemical composition of Ni−N−C electrocatalysts and probe the single-atom catalyst hypothesis.

3.3. STXM. *3.3.1. Ni 2p STXM of Ni−N−C-High on SiN_x Windows (**A1** and **A1a** Regions).* Our previous research[42] showed that the Ni−N−C samples (Ni−N−C-high, Ni−N−C-low) used in this study consist of Ni-containing particles distributed throughout a nitrogen-doped carbonaceous matrix, with an increasing quantity of particles observed when higher amounts of nickel chloride were used in the synthesis. The presence of Ni-based particles following acid leaching is likely due to two reasons. First, Ni-based particles can catalyze the formation of a graphitic shell during pyrolysis, which protects them from being exposed to acid.[25] Second, we have found the Ni_3S_2 to be stable through an acid wash, so the Ni_3S_2 shell on the Ni-based particles could prevent their removal during acid washing.[42]

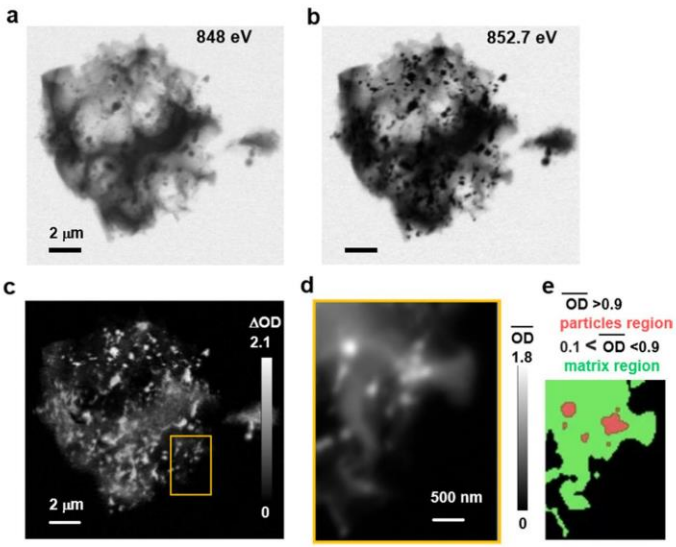

Figure 3. STXM analysis of a Ni−N−C-high structure (**A1** region). (a) Transmission image at 848 eV (Ni 2p pre-edge). (b) Transmission image at 852.7 eV (Ni $2p_{3/2}$ peak). (c) Difference in the optical density, $\Delta OD = OD_{852.7} - OD_{848}$. (d) Average of 143 OD images (Ni 2p stack) recorded in the **A1a** region (yellow rectangle in (c)). (e) Masks used to select spectra of the particles (light red) and matrix (light green).

https://doi.org/10.1021/acscatal.2c01255
ACS Catal. 2022, 12, 8746−8760

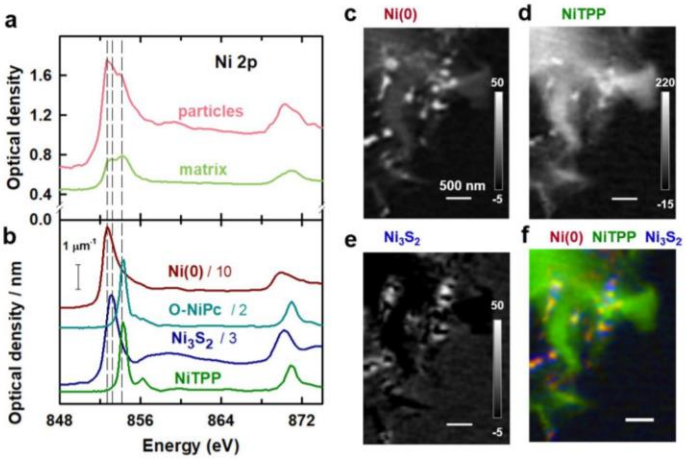

Figure 4. Analysis of the Ni 2p stack of region **A1a** of the Ni−N−C-high sample. (a) Ni 2p X-ray absorption spectra (XAS) of the particles and the carbonaceous matrix of region **A1a** of the Ni−N−C-high sample. (b) XAS spectra of Ni(0) NiTPP, O-NiPc, and Ni_3S_2 on absolute optical density (OD1) scales. Note the scaling used to optimize the visibility of the spectral features. Quantitative component maps of (c) Ni(0), (d) NiTPP, and (e) Ni_3S_2 derived from an SVD fit. The grayscale indicates the thickness based on the use of absolute OD1 reference spectra. (f) Rescaled color-coded composite of the Ni(0) (dark red), NiTPP (dark green), and Ni_3S_2 (dark blue) component maps.

STXM was used to study a Ni−N−C-high particle on a SiN_x window, denoted region **A1** (see Figure S1a−c). STXM transmission images at photon energies of 848 eV (pre-Ni 2p absorption edge) and 852.7 eV (peak of the Ni $2p_{3/2}$ absorption of Ni metal) are shown in Figure 3a,b, respectively. The Ni−N−C-high materials consist of particles ranging in size from tens of nanometers to ~0.5 μm, distributed across the carbonaceous matrix. The heterogeneous morphology observed in the Ni−N−C-high sample is similar to previous TEM observations of the same[42] and similar Ni−N−C materials.[12,25] However, as shown in the previous section, TEM is limited in its ability to provide speciation. Therefore, we have probed these catalysts by STXM spectromicroscopy to perform chemical speciation and investigate the spatial distributions of the species present.

Both the particles and carbonaceous matrix in the Ni−N−C-high show lower contrast at 848 eV, below the onset of the Ni 2p absorption edge (Figure 3a), than at 852.7 eV, the peak of Ni $2p_{3/2}$ absorption (Figure 3b). The change in contrast with photon energy for both morphologies indicates that Ni atoms are present throughout the entire structure. At a photon energy of 848 eV, only large particles are observed throughout the carbonaceous matrix. This is because at 848 eV (Figure 3a) the energy is not high enough to excite the Ni 2p electrons, and therefore, the contrast arises from thickness and composition. At 852.7 eV (Figure 3b), the large particles are much darker and numerous smaller particles appear with high contrast, indicating that the Ni in these particles is in the form of Ni metal.

The STXM transmission images were converted to an OD scale, as shown in Figure S4 and Section S7. Figure 3c displays the difference between the OD images at 852.7 eV (Figure S4d) and 848 eV (Figure S4b), which is referred to as a stack map (ΔOD). Such stack maps identify regions of the sample containing Ni, with the net absorption by Ni directly indicated by the ΔOD value (Figure 3c). Although the highest ΔOD values ($OD_{852.7} - OD_{848}$) are observed at the particles, there is an increase in Ni $2p_{3/2}$ absorption throughout the entire Ni−N−C-high structure, including the carbonaceous matrix. However, on a per-area basis, the Ni $2p_{3/2}$ signal is considerably lower in the carbonaceous matrix than that in the discrete particles.

To investigate the chemical identity and composition of the particles and species in the carbonaceous matrix of the Ni−N−C-high catalyst, a complete Ni 2p stack (143 images from 836 to 929 eV) was recorded. Details of the experimental parameters for each measurement contributing to the figures shown in the paper or the Supporting Information are listed in Table S2. The stack was measured from a thin region of the catalyst particle indicated by the yellow rectangle in Figure 3c (region **A1a**). Figure 3d displays the average X-ray absorption image—i.e., the average of all images in the Ni 2p stack, after alignment and conversion to OD. The grayscale of Figure 3d is the average OD

$$\overline{\mathrm{OD}}(x, y) = \left(\sum_{i=1}^{143} \mathrm{OD}_i(x, y) \right) / 143$$

From Figure 3d, this **A1a** region can be divided into two morphologies: particles ($\overline{\mathrm{OD}} > 0.9$, showing high Ni 2p absorption) and the carbonaceous matrix ($0.1 < \overline{\mathrm{OD}} < 0.9$, showing a relative low Ni 2p absorption). These regions are indicated in Figure 3e. The Ni 2p spectra of the Ni−N−C-high catalyst averaged over the particles (light red) and carbonaceous matrix (light green) are shown in Figure 4a. The spectra for both the particles and carbonaceous matrix are dominated by the Ni $2p_{3/2} \rightarrow 3d$ (852−855 eV) and Ni $2p_{1/2} \rightarrow 3d$ (868−872 eV) resonance regions. Compared with the Ni 2p spectrum of the particles, the carbonaceous matrix has a weaker Ni signal but a higher pre-edge signal relative to the Ni resonance peak intensities. The Ni $2p_{3/2} \rightarrow 3d$ signal of the carbonaceous matrix consists of two peaks of similar intensities at 853.1 and 854.2 eV, respectively. In contrast, the Ni $2p_{3/2} \rightarrow$ 3d signal of the particles is shifted to lower energy and consists of the main peak at 852.7 eV, with a shoulder at 854.2 eV. Since Ni 2p → 3d resonances shift to higher energy as the

https://doi.org/10.1021/acscatal.2c01255
ACS Catal. 2022, 12, 8746−8760

oxidation state of Ni increases,[61−64] these observations suggest that the Ni in the carbonaceous matrix has a higher oxidation state than that of the Ni in the particles.

To interpret the Ni 2p spectra of the Ni−N−C-high catalyst, the spectra of several reference materials were measured by STXM, including metallic Ni, NiTPP, Ni_3S_2, NiO, $NiCO_3$, $NiSO_4(NH_4)_2SO_4$, and O-NiPc (Figure S5). A comparison of the Ni 2p spectra of the Ni−N−C-high catalyst to those of the reference spectra indicates that the main peak at 852.7 eV in the spectra of the particles is due to metallic Ni, which is identified as Ni(0) in the following. The position of the peak at 853.1 eV observed in the particles matches that of the main peak in the spectra of Ni_3S_2, NiO, $NiCO_3$, and $NiSO_4(NH_4)_2SO_4$. Previous X-ray diffraction (XRD) and TEM[42] results showed that there is Ni_3S_2 in the Ni−N−C samples due to the reaction of Ni compounds with the polymerization oxidant, $(NH_4)_2S_2O_8$. Therefore, the peak at 853.1 eV is assigned to Ni_3S_2 particles. The peak at 854.2 eV aligns with the main peak in the Ni 2p spectra of both NiTPP and O-NiPc. NiTPP and O-NiPc are transition-metal-centered macrocyclic molecules in which Ni(II) ions are coordinated by four nitrogen ligands, with a structure similar to those proposed for atomically dispersed NiN_x/C catalysts.[12,25] However, the peaks at 854.2 eV in the spectra of the particle and matrix regions are much broader than the main peak in NiTPP and O-NiPc (Figure S5). This strongly suggests that there is a range of chemical environments of the NiN_x/C single-atom catalyst sites in the Ni−N−C sample, not only the well-defined NiN_4/C structure in NiTPP and O-NiPc (Scheme 1a,b). On the one hand, NiN_x/C sites could exist in various forms. NiN/C, NiN_2/C, NiN_3/C, and NiN_4/C have been proposed for the Ni−N−C materials.[12] On the other hand, although the first coordination shell is similar in NiTPP and O-NiPc, there is ∼0.1 eV difference in the positions of their main $2p_{3/2}$ peak (Table S4). This energy variation has also been observed between Ni(II) phthalocyanine and other Ni(II) porphyrins.[64,65] This indicates that the second coordination shell (eight carbon atoms and four nitrogen atoms around the NiN_4 center in O-NiPc vs 12 carbon atoms around the NiN_4 center in NiTPP and other Ni(II) porphyrins, Scheme 1a,b) affects the chemical and thus catalytic properties of the Ni atoms in NiN_x/C sites. Therefore, in the highly heterogeneous Ni−N−C materials, variation in the surrounding chemical environment of different NiN_x/C sites likely leads to the broad peak at 854.2 eV.

The reference spectra of Ni(0), NiTPP, O-NiPc, and Ni_3S_2 used for analyzing the Ni 2p spectra of the catalysts via STXM measurements are displayed on the OD1 intensity scale in Figure 4b. OD1 scales, which indicate the optical density that 1 nm thickness of a material at a specified density has at specific photon energy, provide quantitative analysis. A comparison of these reference spectra to the spectra of the particles and carbonaceous matrix (Figure 4a) indicates that the particle regions in the Ni−N−C-high sample are primarily comprised of Ni(0) along with Ni_3S_2 and NiN_x/C-type sites, whereas the carbonaceous matrix region is primarily comprised of NiN_x/C-type sites, along with lesser amounts of Ni(0) and Ni_3S_2. To verify the composition of the particle and carbonaceous matrix regions, as well as their distribution throughout the Ni−N−C-high sample, a Ni 2p stack of region **A1a** was analyzed using several different sets of reference spectra. Initially, the internal spectra of the particles and matrix (Figure 4a) were used. The particle and carbonaceous matrix component maps derived from that analysis (Figure S6) identified the particle and matrix regions more precisely than using thresholding of the average Ni 2p $\overline{OD}$ (Figure 3e). While the threshold approach does group spectrally similar regions and provides a statistically meaningful analysis, there is considerable subjectivity with respect to identifying the correct threshold to use for the analysis. To make connections to the spectroscopy of materials with known composition, we have used the high-quality OD1 spectra of the Ni-containing reference species shown in Figure 4b. Due to the similar structure and almost identical energy position, the Ni 2p spectrum of either NiTPP or O-NiPc can be used as the external reference spectrum in the analysis process. Eventually, we selected the NiTPP for analysis because subsequent STXM studies showed that the N 1s and C 1s spectra of NiTPP are closer than O-NiPc to that of the NiN_x/C sites in the Ni−N−C materials (see the Discussion Section). In the fitting procedure, the NiTPP reference spectrum was modified by adding a constant, which accounts for X-ray absorption in the Ni 2p region by carbon- and nitrogen-containing species not directly bonded to Ni.

Figure 4c−e shows the quantitative thickness maps of the Ni(0), NiTPP, and Ni_3S_2 components derived by fitting the Ni 2p stack. Because OD1 reference spectra were used (Section S5), the intensity grayscale indicted on each component map is an estimate of the thickness in nanometer of the indicated species at each pixel. This does not mean that the NiTPP material in the matrix of the Ni−N−C-high sample is a block of that thickness. Rather, it means that the Ni 2p X-ray absorption by NiN_x/C sites in the Ni−N−C-high sample is equivalent to the Ni 2p X-ray absorption of a certain thickness of NiTPP at its standard, bulk density. Figure 4f shows a rescaled color-coded composite of the Ni(0), NiTPP, and Ni_3S_2 component maps, which shows the spatial distribution of the three species relative to each other. In agreement with the qualitative conclusion derived from the fit to the internal spectra of particles and matrix (Figure S6), the analysis presented in Figure 4 shows that the Ni metal is mainly in the particles, but it is also present at a lower level throughout the matrix. Ni_3S_2 is mainly in the shell of the particles and the matrix adjacent to the particles. The NiTPP structure, which is interpreted as NiN_x/C sites, is mainly dispersed throughout the carbonaceous matrix but is also present at enhanced levels adjacent to some of the particles.

The dominant areas of each of the Ni(0), NiTPP, and Ni_3S_2 components were identified by threshold-masking the component maps (Figure 4c−e), as shown in Figure S7a. The component-specific masks were used to extract the average spectrum of the Ni(0), NiTPP, and Ni_3S_2 regions. These spectra were then curve-fit to the external reference spectra to explore the quality of this spectroscopic analysis. Figure S7b compares the internal spectra of each of the masked components to the reference spectra of Ni(0), NiTPP, and Ni_3S_2. The quality of the curve fit analysis (Figure S7c−e and Table S5) supports the validity of the analysis, as shown in Figure 4. Since the external reference spectra are on quantitative OD1 intensity scales, the curve fit results produce a quantitative estimate of the amount of each reference species (Ni(0), NiTPP, and Ni_3S_2) in each of the masked regions. In each case, while the component specified is the largest contributor, the other two components also contribute to varying degrees. This reflects the fact that this is a very heterogeneous material and that each of the Ni species is present in all areas, without a fixed ratio or concentration. This

https://doi.org/10.1021/acscatal.2c01255
ACS Catal. 2022, 12, 8746−8760

quantitative analysis confirms that the particle regions contain a large amount of Ni(0) (average thickness of 30 ± 3 nm), while the matrix contains a very large amount of NiTPP-like species (average thickness of 160 ± 10% nm), which are the NiN_x/C single-atom catalyst sites.

STXM spectromicroscopy of region **A1a** was also performed at the N 1s, C 1s, and O 1s edges. However, most of this region was too thick for X-ray transmission at these lower energies, leading to spectral distortion from absorption saturation. Thus, thinner regions were selected for further measurements to avoid spectral distortions arising from absorption saturation. It is also noted that there was significant spectral distortion from absorption saturation at the N 1s edge for samples supported on SiN_x windows, even when measuring very thin areas with low OD. This was likely due to the N present in the SiN_x membrane. To overcome this problem, subsequent analysis was performed on Ni−N−C catalyst particles deposited on formvar-coated 3 mm TEM Cu grids.

*3.3.2. Ni 2p STXM of Ni−N−C-High on TEM Grids (**A2** Region).* Figure 5a shows an STXM image collected at 852.7 eV from region **A2**, a thin area of the Ni−N−C-high catalyst on a formvar-coated Cu TEM grid (Figure S1d−f). STXM stacks were measured at the Ni 2p, S 2p, C 1s, N 1s, and O 1s edges in this area. Details of the acquisition parameters of each of these stacks are listed in Table S2. The Ni(0), Ni_3S_2, and NiTPP reference spectra (Figure 4b) were used to fit the Ni 2p stack of region **A2**. The component maps for Ni(0), NiTPP, and Ni_3S_2 from that analysis are displayed in Figure S8. Figure 5b presents the rescaled color-coded composite of the Ni(0), NiTPP, and Ni_3S_2 component maps. The spatial distribution of these components in region **A2** is similar to that found in region **A1a**, with the carbonaceous matrix dominated by NiTPP, the dense regions of the particles dominated by Ni metal, and Ni_3S_2 adjacent to or colocated with the Ni metal. The Ni(0), NiTPP, and Ni_3S_2 component maps were threshold-masked (see the insets of Figures 5c and S9a) and Ni 2p spectra of the Ni(0), NiTPP, and Ni_3S_2 regions were generated (see Figures 5c and S9b).

The averaged spectra for these areas and their fits to the external reference spectra are shown in Figure S9c−e with the results summarized in Table S6. The Ni 2p stack analysis indicates that the composition and distribution of Ni species in region **A2** are similar to those in region **A1a** (Figure 4f), which supports the coexistence of Ni(0), NiTPP, and Ni_3S_2 throughout the different morphologies of the Ni−N−C-high sample.

*3.3.3. N 1s, C 1s, O 1s, and S 2p STXM of Ni−N−C-High on TEM Grids (**A2** Region).* In addition to the Ni 2p spectra, Figure 5c plots the S 2p, C 1s, N 1s, and O 1s spectra of the Ni(0), NiTPP, and Ni_3S_2 regions. The stacks at each absorption edge were combined and coaligned to extract spectra of each edge from exactly the same areas. An expanded presentation of the N 1s spectra of the masked areas is given in Figure 5d, along with the reference spectra for O-NiPc, NiTPP, and N−C, which is the nickel-free material synthesized using the same method as for the Ni−N−C catalysts but without the addition of $NiCl_2{\cdot}6H_2O$. The bonding configurations of the nitrogen atoms can be distinguished by the energy position of the absorption peaks observed in the N 1s spectra. The three distinct peaks, N_1 at 398.0 eV, N_3 at 399.4 eV, and N_4 at 401.0 eV in the N−C sample, are assigned to N 1s → π^* transitions of pyridinic, pyrrolic, and graphitic N, respectively.[66,67] There is a fifth, broad peak, labeled N_5, in the range of 406−409 eV,

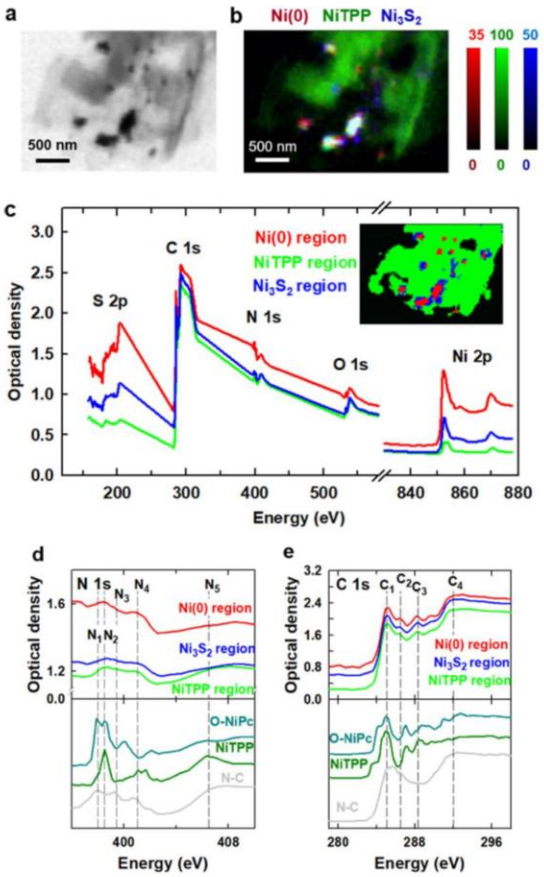

Figure 5. Ni 2p, N 1s, and C 1s results for region **A2** of the Ni−N−C-high sample. (a) STXM transmission image at 852.7 eV. (b) Rescaled color-coded composite of the Ni(0) (dark red), NiTPP (dark green), and Ni_3S_2 (dark blue) component maps derived by a fit of the spectra displayed in Figure 4b to a Ni 2p stack. (c) S 2p, C 1s, N 1s, O 1s, and Ni 2p spectra of Ni(0), NiTPP, and Ni_3S_2 regions. The areas from Ni(0) (red), NiTPP (green), and Ni_3S_2 (blue) regions were generated are indicated in the inset. (d) N 1s spectra of the Ni(0), NiTPP, and Ni_3S_2 regions compared to the N 1s spectra of O-NiPc, NiTPP, and N−C (Ni-free catalyst). (e) C 1s spectra of the Ni(0), NiTPP, and Ni_3S_2 regions compared to the C 1s spectra of O-NiPc, NiTPP, and N−C (Ni-free).

which is attributed to N 1s → σ^*_{C-N} transitions. In the N 1s spectra of the three areas of the Ni−N−C-high sample, two broad peaks are observed at 398.5 eV (N_2) and 401.5 eV (N_4), indicating that higher amounts of Ni lead to different structures of the N-doped carbon materials. According to other spectral studies,[25] the single broad N_2 peak, which is located between the pyridinic (N_1) and pyrrolic (N_3) peaks, exists because the abundant pyrrolic N functionalities coordinating with Ni atoms cause unsaturated pyrrolic nitrogen sites, thus forming a broad convoluted pyridinic/pyrrolic peak, N_2.

The N_2 feature is also observed in the N 1s spectra of NiTPP and O-NiPc. From comparisons with the spectra of reference compounds, the N 1s spectra of the three areas of the Ni−N−C-high sample are close to that of NiTPP, indicating

https://doi.org/10.1021/acscatal.2c01255
ACS Catal. 2022, 12, 8746−8760

the NiN_x/C species has a structure similar to NiTPP. Especially for the Ni(0) and Ni_3S_2 regions, the N 1s spectra exhibit sharper N 1s → π^* features (N_2 and N_4) and relatively lower N 1s → σ^* transitions (N_5). The spectra of NiTPP and O-NiPc showed similar trends with a higher intensity of the N 1s → π^* than N 1s → σ^* transitions, as well as the same peaks (N_2 and N_4) at a similar energy position as in the N 1s spectra of the Ni−N−C-high samples. The N 1s spectrum of the NiTPP region in Ni−N−C-high is similar to that of both NiTPP and N−C. We interpret these observations as follows:

(1) Some N species in the Ni−N−C-high samples are N atoms doped into the carbonaceous matrix created by the pyrolysis of the N-containing polymers. This is confirmed by similar N 1s spectra observed for N−C and the NiTPP region, which is the matrix region in Ni−N−C-high, and strong graphitic N peak (N_4).[66,67] The signal of atomically dispersed NiN_x/C species in the Ni−N−C-high samples is convoluted to a degree with the signal from N doped within the carbon materials, causing the broad N_2 peak to be less obvious in the NiTPP region.

(2) The observation of the N 1s → π^* peaks (N_2 and N_4) and lower intensity of the N 1s→ σ^* transitions (N_5) in the spectrum of the Ni(0) area, along with a comparison to the O-NiPc and NiTPP reference spectra, suggests that the NiN_x/C sites likely aggregate to an extent in the particle regions, which is consistent with the NiN_x/C distribution from the Ni 2p component maps—see Figures 4 and S8 and the quantitative component amounts derived from the Ni 2p spectra (Figures S7, S9 and Tables S5, S6).

(3) The N 1s spectra of the NiN_x/C sites, NiTPP, and O-NiPc are different from each other, indicating the existence of a variety of NiN_x/C structures. The N atoms in the NiN_x/C sites of Ni−N−C-high are closer to those in NiTPP than O-NiPc.

Figure 5e presents the C 1s spectra of the three regions of the Ni−N−C-high sample, in comparison to the C 1s spectra of NiTPP, O-NiPc, and N−C. The C_1 (285 eV) and C_4 (292 eV) spectral features observed in Ni−N−C-high are attributed to C 1s excitations to π^* and σ^* graphitic states, respectively.[66,67] The strong graphitic-like signal indicates that all areas of the catalyst are highly graphitized. The C_3 features in the 287−290 eV region are at positions consistent with C 1s → $\pi^*_{C=N}$ transitions in porphyrins and other compounds with C=N bonds.[65,68] These features are particularly clear in the NiTPP and O-NiPc reference spectra, on account of their well-defined structure. Corresponding transitions are observed in the spectra of all regions in Ni−N−C-high but not in the N−C (Ni-free) sample. This indicates that the nitrogen−carbon chemical environment in Ni−N−C-high, NiTPP, and O-NiPc are similar, which is consistent with an involvement of single Ni atom sites, as postulated for the NiN_x/C structure. The C_2 feature at 286.5 eV, attributed to C 1s → $\pi^*_{C=O}$ transitions, is observed in the spectra of the Ni−N−C-high and N−C samples, indicating the existence of oxygen-containing species in the carbonaceous matrix.

The O 1s spectra for Ni−N−C-high are shown in Figure S10a along with the O 1s reference spectra of N−C and NiO. The O 1s spectra of both Ni−N−C-high and N−C are generally similar, with a sharp O 1s → $\pi^*_{C=O}$ transition (O_1) at 532 eV and a broad band at around 540 eV, which is likely the overlap of σ^*_{C-O} and $\sigma^*_{C=O}$ peaks (O_3). The spectral features of NiO are significantly different, with a sharp peak observed at 534.0 eV (O_2) and a broad peak observed at around 540.0 eV. These distinct spectral differences indicate that there is little or no NiO in the Ni−N−C-high catalysts, and the O 1s signal observes likely arises from oxygen-containing unsaturated functional species in the carbonaceous matrix.

The S 2p spectra of Ni−N−C-high are shown in Figure S10b along with the S 2p spectra from the Ni_3S_2 reference sample. The features at 167.0 eV (S_1) and 181.0 eV (S_2) in the S 2p spectra show there is S in the Ni−N−C-high sample, with spectral similarity to Ni_3S_2, an observation consistent with the presence of Ni_3S_2 in the catalyst as identified previously by XRD.[42] The S 2p features are the strongest in the Ni metal and Ni_3S_2 dominant areas, consistent with our analysis of the Ni 2p stacks.

In summary, for the Ni−N−C-high catalyst sample, the spectral information presented is consistent with a structure consisting of (1) a carbonaceous matrix containing NiN_x/C sites distributed throughout a nitrogen-doped and oxygen functionalized graphitic carbonaceous matrix and (2) dense Ni-metal rich particles surrounded by Ni_3S_2. A representation of the structure for the Ni−N−C-high samples is shown in Scheme 1c.

*3.3.4. STXM of Ni−N−C-Low on TEM Grids (**B1** and **B2** Regions).* To investigate how the morphology and species present in the catalyst depend on the amount of Ni used during synthesis, STXM imaging and spectroscopy at the C 1s, N 1s, O 1s, and Ni 2p edges were performed on the Ni−N−C-low sample (details in Table S2). STXM transmission images at a photon energy of 852.7 eV (above the Ni 2p absorption edge) of two different Ni−N−C-low catalyst particles (regions **B1** and **B2**) are shown in Figure 6a,c, respectively. Ni−N−C-low was found to have very few (in many cases, no) particles throughout the carbonaceous matrix. This is consistent with previous reports, whereby when lower Ni content is used during catalyst synthesis, fewer Ni-rich particles are formed.[25,42] Figure S11 presents the Ni(0), NiTPP, and Ni_3S_2 component maps derived from fitting the Ni 2p stack of

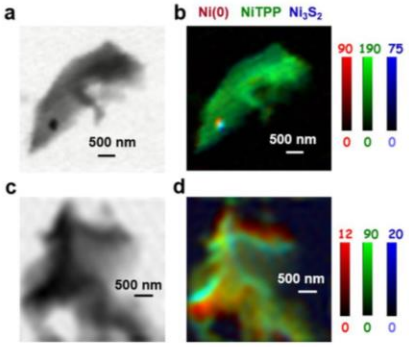

Figure 6. Results for Ni 2p analysis of regions **B1** and **B2** of the Ni−N−C-low sample. (a) STXM transmission image at 852.7 eV of region **B1**. (b) Rescaled color-coded composite of the Ni(0) (dark red), NiTPP (dark green), and Ni_3S_2 (dark blue) component maps for region **B1**. (c) STXM transmission image at 852.7 eV of region **B2**. (d) Rescaled color-coded composite for **B2**.

https://doi.org/10.1021/acscatal.2c01255
ACS Catal. 2022, 12, 8746−8760

region **B1** to the spectra of the reference compounds (Figure 4b). The rescaled, color-coded composites of the Ni(0), NiTPP. and Ni_3S_2 component maps are shown in Figure 6b,d. Masks for the regions of the catalyst dominated by Ni(0), NiTPP, and Ni_3S_2 signals were derived by threshold-masking the component maps for each species in region **B1** (Figure S12a). These masks were then used to extract the Ni 2p, N 1s, O 1s, and C 1s spectra of the Ni(0), NiTPP, and Ni_3S_2 regions of **B1** (Figure S13), which were fit to the reference spectra (Figure S12b–e). Based on the Ni 2p, N 1s, O 1s, and C 1s spectra of the Ni metal, NiTPP, and Ni_3S_2 dominant areas in Ni–N–C-low, the chemical composition of each area in the Ni–N–C-low sample was found to be similar to that in the Ni–N–C-high sample, showing that Ni–N–C electrocatalysts with different Ni contents have a related structure (Scheme 1c) but with fewer Ni-containing particles in the Ni–N–C-low sample. Although the particles consisted of Ni metal and Ni_3S_2, the structure is different from the core–shell structure shown in Figure 2. We speculated that this is because the low spatial resolution of STXM (~40 nm) and low X-ray signal for Ni metal/Ni_3S_2 in a small region made it difficult to completely separate the Ni metal and Ni_3S_2 regions to show the core–shell structure of the particles. The amount of each chemical species present in the matrix and particle areas of both materials was determined quantitatively and directly compared in the next section.

3.4. Quantitative Results from Ni 2p and C 1s Stack Analyses. An advantage of STXM is that the amount of various chemical species present in any region of a sample can be estimated when quantitative OD1 reference spectra are used in the analysis. The average thicknesses of Ni(0), NiTPP, and Ni_3S_2 for nine different regions of the catalyst (five from Ni–N–C-high—**A1a** and **A2**–**A5**—and four from Ni–N–C-low—**B1**–**B4**) were determined by curve-fitting the average spectra to the quantitative OD1 reference spectra shown in Figure 4b. These results are summarized in Figures S14 and S15, while the stack details for each region of the catalysts that were characterized are listed in Table S2. The volumes of each Ni species were calculated from the average thickness and the geometric cross-sectional area of the catalyst regions. Subsequently, the volumes were converted to mass using the density of the corresponding Ni species. Since Ni(0) and Ni_3S_2 are well-defined species, it is straightforward to determine the molar amounts for these two species. However, it was more of a challenge to estimate the amount of NiN_x/C, the NiTPP-like Ni sites, since NiTPP itself is not present in the pyrolyzed Ni–N–C materials. Therefore, the calculated volume and mass of the NiTPP refers to the amount of NiTPP that would have the same X-ray absorption as the NiN_x/C species. The molar amount of Ni in NiN_x/C sites was taken to be that of NiTPP, derived from the mass and volume of NiTPP determined from the curve fit and the area in the NiTPP component maps. To quantitatively compare the amounts of NiN_x/C, Ni(0), and Ni_3S_2 in the Ni–N–C samples, the mole fraction of the Ni atoms present in each of these species was calculated. Furthermore, to understand the absolute content of NiN_x/C sites, the atomic ratio of the Ni atoms in NiN_x/C to the total number of C atoms in the Ni–N–C samples was estimated using the same methods. In this way, although the Ni loading (the amount of all Ni atoms) is different in the different Ni–N–C materials, the concentration of NiN_x/C species in different areas and different samples was determined by comparing the absolute content of NiN_x/C sites to the total number of C atoms. The calculated results for the nine areas are summarized in Table S7. More details of the calculations are presented in Sections S11 and S12.

The atomic fractions of Ni(0), NiN_x/C, and Ni_3S_2 determined from the Ni 2p data and the ratio of the number of Ni atoms in NiN_x/C sites to the total number of C atoms in the Ni–N–C-high samples in regions **A1a**–**A5** of the Ni–N–C-high sample are displayed in Figure S14. The corresponding fractions and ratios for regions **B1**–**B4** of the Ni–N–C-low samples are displayed in Figure S15. The proportions of Ni atoms in Ni–N–C-high and Ni–N–C-low samples that are present in the Ni(0), NiN_x/C, and Ni_3S_2 domains, averaged over all regions, are presented as bar graphs in Figure 7a. For

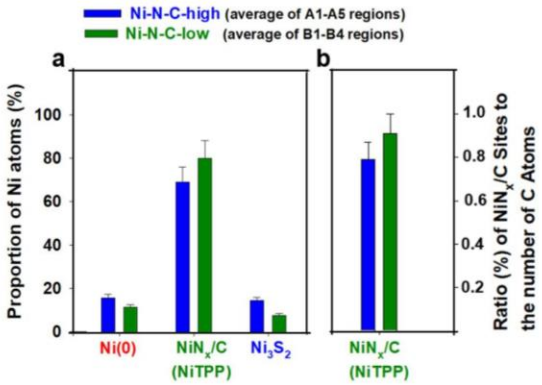

Figure 7. Group bar chart representing the quantitative distribution of different Ni-sites averaged over the five regions of the Ni–N–C-high and four regions of the Ni–N–C-low sample. (a) Total proportion of Ni atoms (out of all the Ni atoms in the sample) present in the domains shown on the *x*-axis, for both catalysts investigated. (b) Ratio of the total number of NiN_x/C sites present in the catalyst divided by the total number of carbon atoms present in the catalyst, providing a quantitative gauge of NiN_x/C species concentration. Values are averaged over the five regions of the Ni–N–C-high and four regions of the Ni–N–C-low sample. The error bars take into account statistical and estimated systematic uncertainties.

Ni–N–C-high, 16 ± 5, 69 ± 7, and 15 ± 5 mol % of the total number of Ni atoms in the catalyst are present in the Ni(0), NiN_x/C, and Ni_3S_2 domains, respectively, In the Ni–N–C-low sample, the average content of Ni(0) and Ni_3S_2 is reduced from 16 to 12 ± 4 mol % and from 15 to 8 ± 3%, respectively, while the mole fraction of NiN_x/C is increased from 69 to 80 ± 8%. The estimated uncertainties include contributions from statistical variation and systematic errors, the largest of which is likely the degree to which the reference materials actually correspond to the species present in the catalysts.

Despite differences in the relative mole fraction of Ni atoms present in NiN_x/C between Ni–N–C-high and Ni–N–C-low, it is advantageous to be able to gauge the quantitative content of NiN_x/C in the catalyst materials. To accomplish this, the atomic ratio of the number of Ni atoms present in NiN_x/C to the total number of C atoms in the Ni–N–C-high and Ni–N–C-low was determined. We define this as the "absolute ratio (%) of NiN_x/C sites". As presented in Figure 7b, relative to the Ni–N–C-high sample, the Ni–N–C-low sample has a slightly higher amount of NiN_x/C sites, with an average value of 0.91 ± 0.09% for the absolute ratio (%) of NiN_x/C sites, compared with an average of 0.79 ± 0.08% for the Ni–N–C-

https://doi.org/10.1021/acscatal.2c01255
ACS Catal. 2022, 12, 8746–8760

high sample. Therefore, the absolute number of NiN_x/C sites increased when using a lower Ni loading during catalyst synthesis, while the absolute amounts of Ni metal and Ni_3S_2 greatly decreased. In addition, the high heterogeneity of Ni−N−C catalysts can be confirmed by the different quantitative results in each region, as shown in Figures S14 and S15. This heterogeneity has often been overlooked by other bulk average and spatially localized measurements. This is especially prominent for Ni−N−C-high, which demonstrates a relatively large fluctuation in the Ni atomic fractions of Ni(0), NiN_x/C, and Ni_3S_2 and the absolute ratio (%) of NiN_x/C sites in the different regions of the catalyst in comparison to Ni−N−C-low. This observation indicates that the presence of dense $Ni(0)/Ni_3S_2$ particles contributes to increasing the heterogeneity of Ni−N−C materials. The resulting high degree of heterogeneity therefore introduces challenges for quantitative estimation of the chemical species present in Ni−N−C-high materials because the calculated results are dependent on the region of the catalyst that is characterized. Although averaging results from multiple regions improves the statistical precision, the preference to select relatively thin catalyst particles to avoid absorption saturation (such as the selection of the **A1a** region in **A1**) could result in the calculated amounts of Ni(0) and Ni_3S_2 being lower than what is actually present in Ni−N−C-high. Thus, the calculated proportions of different species, more specifically the Ni atomic fraction of the NiN_x/C species and the absolute ratio (%) of NiN_x/C Sites, are likely overestimated in Ni−N−C-high, and therefore, the differences between Ni−N−C-high and Ni−N−C-low are likely more pronounced than what is shown in Figure 7a,b.

To make sure our quantitative analysis is reliable, we have compared the spectroscopic results of STXM to ensemble-averaged XAS-TEY spectra—see Section S14, Supporting Information. The similarity of the TEY-XAS and STXM results confirms that, despite measuring an extremely small volume, STXM can measure the average properties of heterogeneous materials. However, a key advantage of STXM is that it probes the chemistry of individual catalyst particles with sub-50 nm spatial resolution, even when the species of interest (i.e., NiN_x/C) contribute only a portion of the overall spectral features. For example, consider the Ni−N−C-high data shown in Figure S17a. When interpreting the TEY-XAS data, the Ni_3S_2 contribution at 853.1 eV could be easily overlooked in an ensemble-averaged XAS study as it is largely overshadowed by the neighboring Ni(0) peak at 852.7 eV. On the contrary, with the spatial resolution of STXM it is possible to identify and differentiate these individual chemical species, which allows for mapping of their chemical signals and distributions throughout the catalyst structure. After using Ni 2p STXM stacks to characterize the spatial distribution of specific species, stacks at other edges can be measured over the same area, thereby gaining a more complete understanding of the chemical properties and how they vary throughout the catalyst (e.g., Figures 5 and S13). More importantly, based on this comprehensive understanding, enabled by location-dependent spectral interpretation, the amount of various chemical species present in the catalysts can be quantified (e.g., Figures 7, S14, and S15). Achieving this level of insight is not possible using ensemble-averaged measurements such as X-ray absorption spectroscopy with limited or no spatial resolution. This comparison demonstrates the significant advantage of STXM for generating fundamental insight into catalyst structures and properties that are essential for guiding advanced material designs.

4. DISCUSSION

These STXM results provide spatially resolved spectral insight into the various chemical species present in these two heterogeneous Ni−N−C catalysts. Metallic Ni(0), Ni_3S_2, and atomically dispersed NiN_x/C species, structurally similar to NiTPP (and O-NiPc), were identified, spatially mapped, and quantified. The atomically dispersed NiN_x/C species were found to be present throughout the entire carbonaceous matrix of the catalyst structure. The observation of these NiN_x/C sites is consistent with previous investigations of Ni−N−C catalysts using various techniques including XAS without spatial resolution[30−33] and STEM-EELS.[12−17] STXM provides an opportunity to image and quantify the distribution of the various Ni-containing species over mesoscale regions of the catalyst structure. The electrochemical CO_2 reduction testing of the Ni−N−C-low catalyst demonstrated a high selectivity toward CO. Based on the fact that Ni_3S_2 and Ni(0) selectively produce hydrogen under CO_2 reduction conditions, the electrochemical results, combined with the STXM analysis, indicate that the activity of the Ni−N−C electrocatalyst for CO_2 reduction to CO arises from the NiN_x/C sites present throughout the entire carbonaceous matrix. The calculated fraction of NiN_x/C sites in the two Ni−N−C catalysts with different Ni contents showed that, as the Ni content in the Ni−N−C electrocatalyst decreased, the amount of NiN_x/C sites increased. This is desirable from an electrocatalytic CO_2R standpoint, as an increased concentration of NiN_x/C provides increased activity and selectivity toward CO production.

A comparison of the Ni 2p, N 1s, and C 1s spectra of the Ni−N−C materials to those of O-NiPc and NiTPP reference compounds showed that a variety of NiN_x/C structures exist in the Ni−N−C catalysts. In the Ni 2p spectra of O-NiPc and NiTPP, the main peaks observed at 854.1 and 854.2 eV, respectively, are quite sharp (Figure S5) due to the well-defined local coordination of Ni in these pure reference compounds. For Ni−N−C (Figure 4), the peak at 854.2 eV is quite broad, likely indicating the existence of NiN_x/C sites with different chemical environments. The high energy of the Ni 2p → 3d transition for NiN_x/C sites is because of a decrease in the effective number of Ni 3d electrons due to the strong Ni 3d−N 2p covalent bonding.[64] With different numbers of N atoms bonding to Ni (NiN/C, NiN_2/C, NiN_3/C, and NiN_4/C have all been proposed for the Ni−N−C materials[12]), the electronic structure of the Ni atom would also vary, causing a shift in the peak location around a mean NiN_4/C peak energy position (~854.2 eV), thereby forming a broad peak.[69] Similarly, different numbers of C atoms in the second shell around the Ni atom in NiN_x/C will affect the Ni 3d electron distributions. For example, the 8 C and 4 N second-shell atoms in O-NiPc will shift the Ni 2p →3d transition to a higher energy than the 12 second-shell C atoms in NiTPP, as is evidenced by a 0.1 eV higher energy in O-NiPc than NiTPP. A comparison of the Ni 2p, N 1s, and C 1s spectra of the NiN_x/C sites to those of O-NiPc and NiTPP indicates that the local coordination of Ni in the NiN_x/C sites is closer to NiTPP than O-NiPc (Scheme 1c). An important and challenging question then arises: what is the impact of different possible $Ni-N_x/C$ sites on catalytic activity?. While it is out of the scope of this work, the scientific community could potentially work toward elucidating this information by

https://doi.org/10.1021/acscatal.2c01255
ACS Catal. 2022, 12, 8746−8760

methods, such as (1) systematic investigations of well-defined model systems such as synthesized Ni-based macrocycles, although structural and electronic differences between such model compounds and catalytic structures in Ni−N−C materials must be taken into account; (2) preparation of structurally homogeneous Ni−N−C catalyst consisting of a single identity of active site structures, that comes with a wide array of synthetic challenges; and (3) computational simulations, such as by density functional theory calculations to understand how the active site structure and surrounding environment of Ni−N_x/C sites impact catalytic activity by tuning adsorption energies with reactive intermediates (i.e., adsorbed *CO)

These results clearly show the power of STXM to perform spatially resolved, mesoscale studies of the morphology and chemical structures using precise spectroscopic characterization at various edges, thereby identifying the chemical species, mapping their spatial distribution, and quantitatively estimating their content. One of the drawbacks of STXM is that measurements are conducted on individual micron or submicron catalyst particles, which, although larger than the sub-nm regions probed by STEM, still may not capture all of the heterogeneity of the global catalyst structure such as that provided by ensemble-averaged XAS measurements that can measure thousands of particles at a time. This limitation can be mitigated by conducting measurements on multiple regions of the catalyst and performing statistical analyses. However, this may not always be necessary as we showed that the Ni 2p spectra collected by STXM on a single catalyst particle had only very subtle differences from bulk-averaged spectra collected by TEY-XAS. Therefore, STXM measurements can largely overcome the issues associated with very spatially localized measurements, such as the nanometer-scale measurements conducted by STEM and related analytical techniques (i.e., EELS). Another limitation of STXM is the spatial resolution, which is much lower than that provided by TEM. To bridge the gap, soft X-ray ptychography[70−74] can be used to significantly improve the spatial resolution of STXM. Ptychography measurements at metal 2p edges in the 600−1100 eV energy range are able to achieve sub-10 nm spatial resolution,[70−72] with a record spatial resolution of 3 nm.[70] Based on very recent work at Soleil,[75] ptychography at energies below 500 eV is now also possible, enabling ptychographic measurements of Ni−N−C catalysts at the N 1s and C 1s edges. Our initial exploration of applying ptychography to catalysts has shown that a spatial resolution of ∼10 nm can be achieved with a similar measurement time to conventional STXM. As an indication of the resolution gains that ptychography can provide, Figure S19 presents a ptychographic amplitude image at 852.7 eV of the **A2** region of the Ni−N−C-high sample, along with an evaluation of its spatial resolution. In addition to ptychography, we are performing in situ STXM characterization of these electrocatalyst materials using a microfluidic flow-electrochemical system developed by our team.[43,76] This will allow determination of the chemical species present and their spatial distribution in catalyst materials under relevant operating conditions, thereby providing better mechanistic understanding and guiding new catalyst designs.[77]

Overall, this work demonstrates that STXM is a very effective tool for studying catalysts such as Ni−N−C, where their highly heterogeneous nature leads to difficulty in characterization by nonspatially resolved methods. The combination of approaches used in this work has led to an improved fundamental understanding of the CO_2−reduction active species in this Ni−N−C CO_2R electrocatalyst.

5. CONCLUSIONS

Gas product analysis measurements showed that lower concentrations of Ni used in the synthesis of Ni−N−C catalysts provide a higher activity for CO_2 reduction and higher selectivity for CO production. To understand this seemingly contradictory observation, we have carried out a comprehensive correlative multi-characterization study. The electrocatalytic properties suggested the existence of atomic NiN_x/C sites. STEM-HAADF imaging showed the presence of atomically dispersed high Z elements (likely Ni) in the carbonaceous matrix of Ni−N−C samples. STXM was applied to further investigate the identity and concentrations of chemical species (especially NiN_x/C sites) present. These materials were found to be highly heterogeneous, consisting of Ni(0) and Ni_3S_2 particles embedded in a carbonaceous matrix with NiN_x/C sites dispersed throughout. The chemical environments, amounts, and spatial distributions of Ni species present in samples prepared with two different Ni loadings were evaluated quantitatively by analyzing sequences of X-ray absorption images at the Ni 2p, N 1s, C 1s, O 1s, and S 2p edges using reference X-ray absorption spectra of Ni(0), NiTPP, O-NiPc, and Ni_3S_2. The results show that, as the Ni loading increases, the amount of Ni(0) and Ni_3S_2 species increases but the amount of NiN_x/C sites decreases. This explains why the Ni−N−C sample prepared with low Ni loading has better electrocatalytic CO_2R performance. In addition, the spectra of the Ni−N−C catalysts showed the existence of a variety of NiN_x/C structures, with the measured spectra being more similar to the spectra of NiTPP than O-NiPc reference compounds. The results provide insight into how the structures, compositions, and spatial distributions of chemical species present in these Ni−N−C electrocatalysts might be modified to achieve higher activity and improved selectivity for CO production via electrochemical CO_2R. This is the first report of using STXM for characterizing atomically dispersed M−N−C catalysts. It has demonstrated the capabilities and advantages of soft X-ray STXM for characterizing atomically dispersed single-atom catalytic sites. In combination with other methods, STXM can generate fundamental insights to guide the design of improved performance Ni−N−C CO_2R catalysts.

■ ASSOCIATED CONTENT

Supporting Information

The Supporting Information is available free of charge at https://pubs.acs.org/doi/10.1021/acscatal.2c01255.

Additional experimental details (images of samples, summary of measurements), data analysis methods, further supporting results (STXM, (S)TEM, and ensemble-averaged total electron yield X-ray absorption spectroscopy), quantitative analysis details, and ptychography results (PDF)

■ AUTHOR INFORMATION

Corresponding Authors

Adam P. Hitchcock − *Chemistry & Chemical Biology, McMaster University, Hamilton, Ontario, Canada L8S*

https://doi.org/10.1021/acscatal.2c01255
ACS Catal. 2022, 12, 8746−8760

4M1; orcid.org/0000-0002-1598-7886; Phone: 905-525-9140; Email: aph@mcmaster.ca

Drew Higgins − *Chemical Engineering, McMaster University, Hamilton, Ontario, Canada L8S 4M1*; orcid.org/0000-0002-0585-2670; Email: higgid2@mcmaster.ca

Authors

Chunyang Zhang − *Chemical Engineering, McMaster University, Hamilton, Ontario, Canada L8S 4M1; Chemistry & Chemical Biology, McMaster University, Hamilton, Ontario, Canada L8S 4M1*

Ladan Shahcheraghi − *Chemical Engineering, McMaster University, Hamilton, Ontario, Canada L8S 4M1*

Fatma Ismail − *Chemical Engineering, McMaster University, Hamilton, Ontario, Canada L8S 4M1*; orcid.org/0000-0003-4270-843X

Haytham Eraky − *Chemistry & Chemical Biology, McMaster University, Hamilton, Ontario, Canada L8S 4M1*

Hao Yuan − *Chemistry & Chemical Biology, McMaster University, Hamilton, Ontario, Canada L8S 4M1;* Present Address: Electrical and Computer Engineering, University of Victoria, Victoria, British Columbia, Canada V8P 5C2

Complete contact information is available at: https://pubs.acs.org/10.1021/acscatal.2c01255

Notes

The authors declare no competing financial interest.

The data sets generated during and/or analyzed during the current study are available from the corresponding author on reasonable request.

■ ACKNOWLEDGMENTS

The authors thank Prof. Daniel Leznoff from Simon Fraser University for providing the reference sample of octa α-octabutoxy Ni phthalocyanine (O-NiPc). This research was supported by the Natural Sciences and Engineering Research Council (NSERC) Discovery program, and the National Research Council of Canada (NRC) Materials for Clean Fuels Challenge program. Measurements were performed using the ambient STXM on beamline 10ID1 and the SGM spectrometer on beamline 11ID1 at the Canadian Light Source (CLS). CLS is supported by the CFI Major Facilities Access program and the University of Saskatchewan. The authors thank staff scientists Jian Wang and Jay Dynes at CLS for their assistance and support of the 10ID1 beamline and STXMs and Jay Dynes for measuring the TEY spectra using the SGM beamline. Electron microscopy imaging was performed at the Canadian Centre for Electron Microscopy (CCEM) at McMaster University. The authors thank Natalie Hamada for her assistance in electron microscopy measurements.

■ REFERENCES

(1) Ju, W.; Bagger, A.; Hao, G.-P.; Varela, A. S.; Sinev, I.; Bon, V.; Roldan Cuenya, B.; Kaskel, S.; Rossmeisl, J.; Strasser, P. Understanding Activity and Selectivity of Metal-Nitrogen-Doped Carbon Catalysts for Electrochemical Reduction of CO2. *Nat. Commun.* **2017**, *8*, No. 944.

(2) Gewirth, A. A.; Varnell, J. A.; DiAscro, A. M. Nonprecious Metal Catalysts for Oxygen Reduction in Heterogeneous Aqueous Systems. *Chem. Rev.* **2018**, *118*, 2313−2339.

(3) Zhang, J.; Xia, Z.; Dai, L. Carbon-Based Electrocatalysts for Advanced Energy Conversion and Storage. *Sci. Adv.* **2015**, *1*, No. e1500564.

(4) Shi, Z.; Yang, W.; Gu, Y.; Liao, T.; Sun, Z. Metal-Nitrogen-Doped Carbon Materials as Highly Efficient Catalysts: Progress and Rational Design. *Adv. Sci.* **2020**, *7*, No. 2001069.

(5) Chen, M.-X.; Zhu, M.; Zuo, M.; Chu, S.-Q.; Zhang, J.; Wu, Y.; Liang, H.-W.; Feng, X. Identification of Catalytic Sites for Oxygen Reduction in Metal/Nitrogen-Doped Carbons with Encapsulated Metal Nanoparticles. *Angew. Chem.* **2020**, *132*, 1644−1650.

(6) Jaouen, F.; Proietti, E.; Lefèvre, M.; Chenitz, R.; Dodelet, J.-P.; Wu, G.; Taek Chung, H.; Marie Johnston, C.; Zelenay, P. Recent Advances in Non-Precious Metal Catalysis for Oxygen - Reduction Reaction in Polymer Electrolyte Fuel Cells. *Energy Environ. Sci.* **2011**, *4*, 114−130.

(7) Xia, C.; Qiu, Y.; Xia, Y.; Zhu, P.; King, G.; Zhang, X.; Wu, Z.; Kim, J. Y.; Cullen, D. A.; Zheng, D.; Li, P.; Shakouri, M.; Heredia, E.; Cui, P.; Alshareef, H. N.; Hu, Y.; Wang, H. General Synthesis of Single-Atom Catalysts with High Metal Loading Using Graphene Quantum Dots. *Nat. Chem.* **2021**, *13*, 887−894.

(8) Franco, F.; Rettenmaier, C.; Sang Jeon, H.; Cuenya, B. R. Transition Metal-Based Catalysts for the Electrochemical CO_2 Reduction: From Atoms and Molecules to Nanostructured Materials. *Chem. Soc. Rev.* **2020**, *49*, 6884−6946.

(9) Li, J.; Jiang, Y.; Wang, Q.; Xu, C.-Q.; Wu, D.; Banis, M. N.; Adair, K. R.; Doyle-Davis, K.; Meira, D. M.; Finfrock, Y. Z.; Li, W.; Zhang, L.; Sham, T.-K.; Li, R.; Chen, N.; Gu, M.; Li, J.; Sun, X. A General Strategy for Preparing Pyrrolic-N4 Type Single-Atom Catalysts via Pre-Located Isolated Atoms. *Nat. Commun.* **2021**, *12*, No. 6806.

(10) Varela, A. S.; Kroschel, M.; Leonard, N. D.; Ju, W.; Steinberg, J.; Bagger, A.; Rossmeisl, J.; Strasser, P. PH Effects on the Selectivity of the Electrocatalytic CO2 Reduction on Graphene-Embedded Fe−N−C Motifs: Bridging Concepts between Molecular Homogeneous and Solid-State Heterogeneous Catalysis. *ACS Energy Lett.* **2018**, *3*, 812−817.

(11) Qu, Y.; Li, Z.; Chen, W.; Lin, Y.; Yuan, T.; Yang, Z.; Zhao, C.; Wang, J.; Zhao, C.; Wang, X.; Zhou, F.; Zhuang, Z.; Wu, Y.; Li, Y. Direct Transformation of Bulk Copper into Copper Single Sites via Emitting and Trapping of Atoms. *Nat. Catal.* **2018**, *1*, 781−786.

(12) Koshy, D. M.; Landers, A. T.; Cullen, D. A.; Ievlev, A. V.; Meyer, H. M., III; Hahn, C.; Bao, Z.; Jaramillo, T. F. Direct Characterization of Atomically Dispersed Catalysts: Nitrogen-Coordinated Ni Sites in Carbon-Based Materials for CO_2 Electroreduction. *Adv. Energy Mater.* **2020**, *10*, No. 2001836.

(13) Xie, X.; He, C.; Li, B.; He, Y.; Cullen, D. A.; Wegener, E. C.; Kropf, A. J.; Martinez, U.; Cheng, Y.; Engelhard, M. H.; Bowden, M. E.; Song, M.; Lemmon, T.; Li, X. S.; Nie, Z.; Liu, J.; Myers, D. J.; Zelenay, P.; Wang, G.; Wu, G.; Ramani, V.; Shao, Y. Performance Enhancement and Degradation Mechanism Identification of a Single-Atom Co−N−C Catalyst for Proton Exchange Membrane Fuel Cells. *Nat. Catal.* **2020**, *3*, 1044−1054.

(14) Sharma, P.; Kumar, S.; Tomanec, O.; Petr, M.; Zhu Chen, J.; Miller, J. T.; Varma, R. S.; Gawande, M. B.; Zbořil, R. Carbon Nitride-Based Ruthenium Single Atom Photocatalyst for CO_2 Reduction to Methanol. *Small* **2021**, *17*, No. 2006478.

(15) Zhang, L.; Wang, Q.; Si, R.; Song, Z.; Lin, X.; Banis, M. N.; Adair, K.; Li, J.; Doyle-Davis, K.; Li, R.; Liu, L.-M.; Gu, M.; Sun, X. New Insight of Pyrrole-Like Nitrogen for Boosting Hydrogen Evolution Activity and Stability of Pt Single Atoms. *Small* **2021**, *17*, No. 2004453.

(16) Chen, Z.; Higgins, D.; Yu, A.; Zhang, L.; Zhang, J. A Review on Non-Precious Metal Electrocatalysts for PEM Fuel Cells. *Energy Environ. Sci.* **2011**, *4*, 3167−3192.

(17) Chung, H. T.; Cullen, D. A.; Higgins, D.; Sneed, B. T.; Holby, E. F.; More, K. L.; Zelenay, P. Direct Atomic-Level Insight into the Active Sites of a High-Performance PGM-Free ORR Catalyst. *Science* **2017**, *357*, 479−484.

(18) Zitolo, A.; Goellner, V.; Armel, V.; Sougrati, M.-T.; Mineva, T.; Stievano, L.; Fonda, E.; Jaouen, F. Identification of Catalytic Sites for Oxygen Reduction in Iron- and Nitrogen-Doped Graphene Materials. *Nat. Mater.* **2015**, *14*, 937−942.

https://doi.org/10.1021/acscatal.2c01255
ACS Catal. 2022, 12, 8746−8760

(19) Bezerra, C. W. B.; Zhang, L.; Lee, K.; Liu, H.; Marques, A. L. B.; Marques, E. P.; Wang, H.; Zhang, J. A Review of Fe−N/C and Co−N/C Catalysts for the Oxygen Reduction Reaction. *Electrochim. Acta* **2008**, *53*, 4937−4951.
(20) Jia, Q.; Ramaswamy, N.; Tylus, U.; Strickland, K.; Li, J.; Serov, A.; Artyushkova, K.; Atanassov, P.; Anibal, J.; Gumeci, C.; Barton, S. C.; Sougrati, M.-T.; Jaouen, F.; Halevi, B.; Mukerjee, S. Spectroscopic Insights into the Nature of Active Sites in Iron−Nitrogen−Carbon Electrocatalysts for Oxygen Reduction in Acid. *Nano Energy* **2016**, *29*, 65−82.
(21) Jia, Q.; Ramaswamy, N.; Hafiz, H.; Tylus, U.; Strickland, K.; Wu, G.; Barbiellini, B.; Bansil, A.; Holby, E. F.; Zelenay, P.; Mukerjee, S. Experimental Observation of Redox-Induced Fe−N Switching Behavior as a Determinant Role for Oxygen Reduction Activity. *ACS Nano* **2015**, *9*, 12496−12505.
(22) Kramm, U. I.; Herranz, J.; Larouche, N.; Arruda, T. M.; Lefèvre, M.; Jaouen, F.; Bogdanoff, P.; Fiechter, S.; Abs-Wurmbach, I.; Mukerjee, S.; Dodelet, J.-P. Structure of the Catalytic Sites in Fe/N/C-Catalysts for O_2 Reduction in PEM Fuel Cells. *Phys. Chem. Chem. Phys.* **2012**, *14*, 11673−11688.
(23) Varela, A. S.; Ju, W.; Strasser, P. Molecular Nitrogen−Carbon Catalysts, Solid Metal Organic Framework Catalysts, and Solid Metal/Nitrogen-Doped Carbon (MNC) Catalysts for the Electrochemical CO_2 Reduction. *Adv. Energy Mater.* **2018**, *8*, No. 1802905.
(24) Li, X.; Bi, W.; Chen, M.; Sun, Y.; Ju, H.; Yan, W.; Zhu, J.; Wu, X.; Chu, W.; Wu, C.; Xie, Y. Exclusive Ni−N4 Sites Realize Near-Unity CO Selectivity for Electrochemical CO_2 Reduction. *J. Am. Chem. Soc.* **2017**, *139*, 14889−14892.
(25) Koshy, D. M.; Chen, S.; Lee, D. U.; Stevens, M. B.; Abdellah, A. M.; Dull, S. M.; Chen, G.; Nordlund, D.; Gallo, A.; Hahn, C.; Higgins, D. C.; Bao, Z.; Jaramillo, T. F. Understanding the Origin of Highly Selective CO_2 Electroreduction to CO on Ni,N-Doped Carbon Catalysts. *Angew. Chem., Int. Ed.* **2020**, *59*, 4043−4050.
(26) Yang, H. B.; Hung, S.-F.; Liu, S.; Yuan, K.; Miao, S.; Zhang, L.; Huang, X.; Wang, H.-Y.; Cai, W.; Chen, R.; Gao, J.; Yang, X.; Chen, W.; Huang, Y.; Chen, H. M.; Li, C. M.; Zhang, T.; Liu, B. Atomically Dispersed Ni(I) as the Active Site for Electrochemical CO_2 Reduction. *Nat. Energy* **2018**, *3*, 140−147.
(27) Yasri, N. G.; Al-Attas, T. A.; Hu, J.; Golam Kibria, M. Electropolymerized Metal-Protoporphyrin Electrodes for Selective Electrochemical Reduction of CO_2. *Catal. Sci. Technol.* **2021**, *11*, 1580−1589.
(28) Lefèvre, M.; Dodelet, J. P.; Bertrand, P. O_2 Reduction in PEM Fuel Cells: Activity and Active Site Structural Information for Catalysts Obtained by the Pyrolysis at High Temperature of Fe Precursors. *J. Phys. Chem. B* **2000**, *104*, 11238−11247.
(29) Lefèvre, M.; Dodelet, J. P.; Bertrand, P. Molecular Oxygen Reduction in PEM Fuel Cells: Evidence for the Simultaneous Presence of Two Active Sites in Fe-Based Catalysts. *J. Phys. Chem. B* **2002**, *106*, 8705−8713.
(30) Zhao, S.; Cheng, Y.; Veder, J.-P.; Johannessen, B.; Saunders, M.; Zhang, L.; Liu, C.; Chisholm, M. F.; De Marco, R.; Liu, J.; Yang, S.-Z.; Jiang, S. P. One-Pot Pyrolysis Method to Fabricate Carbon Nanotube Supported Ni Single-Atom Catalysts with Ultrahigh Loading. *ACS Appl. Energy Mater.* **2018**, *1*, 5286−5297.
(31) Wang, C.; Zhang, H.; Wang, J.; Zhao, Z.; Wang, J.; Zhang, Y.; Cheng, M.; Zhao, H.; Wang, J. Atomic Fe Embedded in Carbon Nanoshells−Graphene Nanomeshes with Enhanced Oxygen Reduction Reaction Performance. *Chem. Mater.* **2017**, *29*, 9915−9922.
(32) Tylus, U.; Jia, Q.; Strickland, K.; Ramaswamy, N.; Serov, A.; Atanassov, P.; Mukerjee, S. Elucidating Oxygen Reduction Active Sites in Pyrolyzed Metal−Nitrogen Coordinated Non-Precious-Metal Electrocatalyst Systems. *J. Phys. Chem. C* **2014**, *118*, 8999−9008.
(33) Zhang, J.; Wang, Z.; Zhu, Z. The Inherent Kinetic Electrochemical Reduction of Oxygen into H_2O on FeN_4-Carbon: A Density Functional Theory Study. *J. Power Sources* **2014**, *255*, 65−69.
(34) Egerton, R. F.; Watanabe, M. Characterization of Single-Atom Catalysts by EELS and EDX Spectroscopy. *Ultramicroscopy* **2018**, *193*, 111−117.
(35) Gao, Y.; Yang, Y.; Schimmenti, R.; Murray, E.; Peng, H.; Wang, Y.; Ge, C.; Jiang, W.; Wang, G.; DiSalvo, F. J.; Muller, D. A.; Mavrikakis, M.; Xiao, L.; Abruña, H. D.; Zhuang, L. A Completely Precious Metal−Free Alkaline Fuel Cell with Enhanced Performance Using a Carbon-Coated Nickel Anode. *Proc. Natl. Acad. Sci. U.S.A.* **2022**, *119*, No. e2119883119.
(36) Li, Y.; Mohd Adli, N.; Shan, W.; Wang, M.; Zachman, M. J.; Hwang, S.; Tabassum, H.; Karakalos, S.; Feng, Z.; Wang, G.; Li, Y. C.; Wu, G. Atomically Dispersed Single Ni Site Catalysts for High-Efficiency CO_2 Electroreduction at Industrial-Level Current Densities. *Energy Environ. Sci.* **2022**, *15*, 2108−2119.
(37) Shi, Q.; Hwang, S.; Yang, H.; Ismail, F.; Su, D.; Higgins, D.; Wu, G. Supported and Coordinated Single Metal Site Electrocatalysts. *Mater. Today* **2020**, *37*, 93−111.
(38) Stöhr, J. *NEXAFS Spectroscopy*, Springer Series in Surface Science; Springer, 1992; Vol. *25*.
(39) Ade, H.; Hitchcock, A. P. NEXAFS Microscopy and Resonant Scattering: Composition and Orientation Probed in Real and Reciprocal Space. *Polymer* **2008**, *49*, 643−675.
(40) Hitchcock, A. P. Soft X-ray Imaging and Spectromicroscopy. In *Handbook of Nanoscopy*; John Wiley & Sons, Ltd., 2012; pp 745−791.
(41) Hitchcock, A. P. Soft X-ray Spectromicroscopy and Ptychography. *J. Electron Spectrosc. Relat. Phenom.* **2015**, *200*, 49−63.
(42) Shahcheraghi, L.; Zhang, C.; Lee, H.-J.; Cusack-Striepe, M.; Ismail, F.; Abdellah, A.; Higgins, D. C. Identifying Activity and Selectivity Trends for the Electrosynthesis of Hydrogen Peroxide via Oxygen Reduction on Nickel−Nitrogen−Carbon Catalysts. *J. Phys. Chem. C* **2021**, *125*, 15830−15840.
(43) Prabu, V.; Obst, M.; Hosseinkhannazer, H.; Reynolds, M.; Rosendahl, S.; Wang, J.; Hitchcock, A. P. Instrumentation for in Situ Flow Electrochemical Scanning Transmission X-Ray Microscopy (STXM). *Rev. Sci. Instrum.* **2018**, *89*, No. 063702.
(44) Kuhl, K. P.; Cave, E. R.; Abram, D. N.; Jaramillo, T. F. New Insights into the Electrochemical Reduction of Carbon Dioxide on Metallic Copper Surfaces. *Energy Environ. Sci.* **2012**, *5*, 7050−7059.
(45) Higgins, D.; Landers, A. T.; Ji, Y.; Nitopi, S.; Morales-Guio, C. G.; Wang, L.; Chan, K.; Hahn, C.; Jaramillo, T. F. Guiding Electrochemical Carbon Dioxide Reduction toward Carbonyls Using Copper Silver Thin Films with Interphase Miscibility. *ACS Energy Lett.* **2018**, *3*, 2947−2955.
(46) Ismail, F.; Abdellah, A.; Lee, H.-J.; Sudheeshkumar, V.; Alnoush, W.; Higgins, D. C. Impact of Nickel Content on the Structure and Electrochemical CO_2 Reduction Performance of Nickel−Nitrogen−Carbon Catalysts Derived from Zeolitic Imidazolate Frameworks. *ACS Appl. Energy Mater.* **2022**, *5*, 430−439.
(47) Leverett, J.; Yuwono, J. A.; Kumar, P.; Tran-Phu, T.; Qu, J.; Cairney, J.; Wang, X.; Simonov, A. N.; Hocking, R. K.; Johannessen, B.; Dai, L.; Daiyan, R.; Amal, R. Impurity Tolerance of Unsaturated Ni-N-C Active Sites for Practical Electrochemical CO_2 Reduction. *ACS Energy Lett.* **2022**, *7*, 920−928.
(48) Kaznatcheev, K. V.; Karunakaran, C.; Lanke, U. D.; Urquhart, S. G.; Obst, M.; Hitchcock, A. P. Soft X-Ray Spectromicroscopy Beamline at the CLS: Commissioning Results. *Nucl. Instrum. Methods Phys. Res., Sect. A* **2007**, *582*, 96−99.
(49) Kilcoyne, A. L. D.; Tyliszczak, T.; Steele, W. F.; Fakra, S.; Hitchcock, P.; Franck, K.; Anderson, E.; Harteneck, B.; Rightor, E. G.; Mitchell, G. E.; Hitchcock, A. P.; Yang, L.; Warwick, T.; Ade, H. Interferometer-Controlled Scanning Transmission X-Ray Microscopes at the Advanced Light Source. *J. Synchrotron Radiat.* **2003**, *10*, 125−136.
(50) Fakra, S.; Kilcoyne, A. L. D.; Tyliszczak, T. Scintillator Detectors for Scanning Transmission X-ray Microscopes at the Advanced Light Source. *AIP Conf. Proc.* **2004**, *705*, 973−976.
(51) Jacobsen, C.; Wirick, S.; Flynn, G.; Zimba, C. Soft X-Ray Spectroscopy from Image Sequences with Sub-100 nm Spatial Resolution. *J. Microsc.* **2000**, *197*, 173−184.

https://doi.org/10.1021/acscatal.2c01255
ACS Catal. 2022, 12, 8746−8760

(52) Hitchcock, A. P.; Brion, C. E. Neon K-Shell Excitation Studied by Electron Energy-Loss Spectroscopy. *J. Phys. B: At. Mol. Phys.* **1980**, *13*, 3269−3273.
(53) Ma, Y.; Chen, C. T.; Meigs, G.; Randall, K.; Sette, F. High-Resolution K-Shell Photoabsorption Measurements of Simple Molecules. *Phys. Rev. A* **1991**, *44*, 1848−1858.
(54) Sodhi, R. N. S.; Brion, C. E. Reference Energies for Inner Shell Electron Energy-Loss Spectroscopy. *J. Electron Spectrosc. Relat. Phenom.* **1984**, *34*, 363−372.
(55) Hitchcock, A. P. aXis2000 Is Written In Interactive Data Language (IDL). It Is Available Free for Noncommercial Use From http://unicorn.mcmaster.ca/aXis2000.html (accessed June 20, 2022).
(56) Varela, A. S.; Ju, W.; Bagger, A.; Franco, P.; Rossmeisl, J.; Strasser, P. Electrochemical Reduction of CO_2 on Metal-Nitrogen-Doped Carbon Catalysts. *ACS Catal.* **2019**, *9*, 7270−7284.
(57) Hu, X.-M.; Hval, H. H.; Bjerglund, E. T.; Dalgaard, K. J.; Madsen, M. R.; Pohl, M.-M.; Welter, E.; Lamagni, P.; Buhl, K. B.; Bremholm, M.; Beller, M.; Pedersen, S. U.; Skrydstrup, T.; Daasbjerg, K. Selective CO2 Reduction to CO in Water Using Earth-Abundant Metal and Nitrogen-Doped Carbon Electrocatalysts. *ACS Catal.* **2018**, *8*, 6255−6264.
(58) Nitopi, S.; Bertheussen, E.; Scott, S. B.; Liu, X.; Engstfeld, A. K.; Horch, S.; Seger, B.; Stephens, I. E. L.; Chan, K.; Hahn, C.; Nørskov, J. K.; Jaramillo, T. F.; Chorkendorff, I. Progress and Perspectives of Electrochemical CO_2 Reduction on Copper in Aqueous Electrolyte. *Chem. Rev.* **2019**, *119*, 7610−7672.
(59) Kuhl, K. P.; Hatsukade, T.; Cave, E. R.; Abram, D. N.; Kibsgaard, J.; Jaramillo, T. F. Electrocatalytic Conversion of Carbon Dioxide to Methane and Methanol on Transition Metal Surfaces. *J. Am. Chem. Soc.* **2014**, *136*, 14107−14113.
(60) Landers, A. T.; Fields, M.; Torelli, D. A.; Xiao, J.; Hellstern, T. R.; Francis, S. A.; Tsai, C.; Kibsgaard, J.; Lewis, N. S.; Chan, K.; Hahn, C.; Jaramillo, T. F. The Predominance of Hydrogen Evolution on Transition Metal Sulfides and Phosphides under CO_2 Reduction Conditions: An Experimental and Theoretical Study. *ACS Energy Lett.* **2018**, *3*, 1450−1457.
(61) Lu, M.; Wang, J.; Fang, H.; Hu, Y.; Zhou, J. Unexpected Phase Separation in Li_{1-x} $Ni_{0.5}Mn_{1.5}O_4$ within a Porous Composite Electrode. *Chem. Commun.* **2018**, *54*, 4152−4155.
(62) Zheng, X.; Zhang, B.; De Luna, P.; Liang, Y.; Comin, R.; Voznyy, O.; Han, L.; García de Arquer, F. P.; Liu, M.; Dinh, C. T.; Regier, T.; Dynes, J. J.; He, S.; Xin, H. L.; Peng, H.; Prendergast, D.; Du, X.; Sargent, E. H. Theory-Driven Design of High-Valence Metal Sites for Water Oxidation Confirmed Using in Situ Soft X-Ray Absorption. *Nat. Chem.* **2018**, *10*, 149−154.
(63) Lenser, C.; Lu, Q.; Crumlin, E.; Bluhm, H.; Yildiz, B. Charge Transfer Across Oxide Interfaces Probed by in Situ X-Ray Photoelectron and Absorption Spectroscopy Techniques. *J. Phys. Chem. C* **2018**, *122*, 4841−4848.
(64) Krasnikov, S. A.; Preobrajenski, A. B.; Sergeeva, N. N.; Brzhezinskaya, M. M.; Nesterov, M. A.; Cafolla, A. A.; Senge, M. O.; Vinogradov, A. S. Electronic Structure of Ni(II) Porphyrins and Phthalocyanine Studied by Soft X-Ray Absorption Spectroscopy. *Chem. Phys.* **2007**, *332*, 318−324.
(65) Kera, S.; Casu, M. B.; Schöll, A.; Schmidt, T.; Batchelor, D.; Rühl, E.; Umbach, E. High-Resolution Inner-Shell Excitation Spectroscopy of H_2-Phthalocyanine. *J. Chem. Phys.* **2006**, *125*, No. 014705.
(66) Yang, H. B.; Miao, J.; Hung, S.-F.; Chen, J.; Tao, H. B.; Wang, X.; Zhang, L.; Chen, R.; Gao, J.; Chen, H. M.; Dai, L.; Liu, B. Identification of Catalytic Sites for Oxygen Reduction and Oxygen Evolution in N-Doped Graphene Materials: Development of Highly Efficient Metal-Free Bifunctional Electrocatalyst. *Sci. Adv.* **2016**, *2*, No. e1501122.
(67) Zhong, J.; Deng, J.-J.; Mao, B.-H.; Xie, T.; Sun, X.-H.; Mou, Z.-G.; Hong, C.-H.; Yang, P.; Wang, S.-D. Probing Solid State N-Doping in Graphene by X-Ray Absorption near-Edge Structure Spectroscopy. *Carbon* **2012**, *50*, 335−338.
(68) Yabuta, H.; Uesugi, M.; Naraoka, H.; Ito, M.; Kilcoyne, A. L. D.; Sandford, S. A.; Kitajima, F.; Mita, H.; Takano, Y.; Yada, T.; Karouji, Y.; Ishibashi, Y.; Okada, T.; Abe, M. X-ray Absorption near Edge Structure Spectroscopic Study of Hayabusa Category 3 Carbonaceous Particles. *Earth, Planets Space* **2014**, *66*, No. 156.
(69) Ikeno, H.; Groot, F. M. F.; de Stavitski, E.; Tanaka, I. Multiplet Calculations of $L_{2,3}$ X-ray Absorption near-Edge Structures for 3d Transition-Metal Compounds. *J. Phys.: Condens. Matter* **2009**, *21*, No. 104208.
(70) Shapiro, D. A.; Yu, Y.-S.; Tyliszczak, T.; Cabana, J.; Celestre, R.; Chao, W.; Kaznatcheev, K.; Kilcoyne, A. L. D.; Maia, F.; Marchesini, S.; Meng, Y. S.; Warwick, T.; Yang, L. L.; Padmore, H. A. Chemical Composition Mapping with Nanometre Resolution by Soft X-Ray Microscopy. *Nat. Photonics* **2014**, *8*, 765−769.
(71) Pfeiffer, F. X-Ray Ptychography. *Nat. Photonics* **2018**, *12*, 9−17.
(72) Liu, D.; Shadike, Z.; Lin, R.; Qian, K.; Li, H.; Li, K.; Wang, S.; Yu, Q.; Liu, M.; Ganapathy, S.; Qin, X.; Yang, Q.-H.; Wagemaker, M.; Kang, F.; Yang, X.-Q.; Li, B. Review of Recent Development of In Situ/Operando Characterization Techniques for Lithium Battery Research. *Adv. Mater.* **2019**, *31*, No. 1806620.
(73) Shapiro, D. A.; Babin, S.; Celestre, R. S.; Chao, W.; Conley, R. P.; Denes, P.; Enders, B.; Enfedaque, P.; James, S.; Joseph, J. M.; Krishnan, H.; Marchesini, S.; Muriki, K.; Nowrouzi, K.; Oh, S. R.; Padmore, H.; Warwick, T.; Yang, L.; Yashchuk, V. V.; Yu, Y.-S.; Zhao, J. An Ultrahigh-Resolution Soft x-Ray Microscope for Quantitative Analysis of Chemically Heterogeneous Nanomaterials. *Sci. Adv.* **2020**, *6*, No. eabc4904.
(74) Yuan, H.; Yuan, H.; Casagrande, T.; Shapiro, D.; Yu, Y.-S.; Enders, B.; Lee, J. R. I.; van Buuren, A.; Biener, M. M.; Gammon, S. A.; Baumann, T. F.; Hitchcock, A. P. 4D Imaging of ZnO-Coated Nanoporous Al_2O_3 Aerogels by Chemically Sensitive Ptychographic Tomography: Implications for Designer Catalysts. *ACS Appl. Nano Mater.* **2021**, *4*, 621−632.
(75) Mille, N.; Yuan, H.; Vijayakumar, J.; Stanescu, S.; Swaraj, S.; Desjardins, K.; Favre-Nicolin, V.; Belkhou, R.; Hitchcock, A. P. Ptychography at the Carbon K-Edge. *Commun. Mater.* **2022**, *3*, No. 8.
(76) Zhang, C.; Ingino, P.; Obst, M.; Shahcheraghi, L.; Yuan, H.; Eraky, H.; Wang, J.; Higgins, D.; Hitchcock, A. P. In-Situ Soft X-Ray Spectromicroscopy Characterization of Electrochemical Processes. *ECS Meet. Abstr.* **2020**, *MA2020-02*, 3176.
(77) Handoko, A. D.; Wei, F.; Jenndy; Yeo, B. S.; Seh, Z. W. Understanding Heterogeneous Electrocatalytic Carbon Dioxide Reduction through Operando Techniques. *Nat. Catal.* **2018**, *1*, 922−934.

https://doi.org/10.1021/acscatal.2c01255
ACS Catal. 2022, 12, 8746−8760

Chapter 5

Atomically dispersed Ni-N-C electrocatalysts, studied by Ni L-edge spectro-ptychography

This chapter presents the spectro-ptychography studies of the Ni–N–C materials and compares the spectro-ptychography with previous STXM results. The ptychography results show a similar chemical mapping with conventional STXM, but the spatial resolution was significantly improved from ~60 nm (STXM) to ~20 nm (ptychography). This work highlights the added value of spectro-ptychography relative to STXM for studies of electrocatalysts.

Reprinted with permission from the Journal of Electron Spectroscopy and Related Phenomena 266 (2023) 147364, Chunyang Zhang, Jiatang Chen, Hao Yuan, Jian Wang, Tianxiao Sun, Drew Higgins, and Adam P. Hitchcock, "Atomically dispersed Ni-NC electrocatalysts, studied by Ni L-edge spectro-ptychography", Copyright 2023, ScienceDirect.

The author of this thesis, Dr. Hao yuan, Dr. Jiatang Chen, Dr. Jian Wang and Prof. A. P. Hitchcock performed the ptychography experiments. Dr. Jiatang Chen, Prof. A. P. Hitchcock and the author analyzed the ptychography data. Tianxiao Sun and Dr. Jian Wang developed the software for the re-construction of ptychography data. Dr. Jiatang Chen wrote the first draft. The author re-wrote and revised the publication, with assistance in later stages by Prof. A. P. Hitchcock and Prof. Drew Higgins.

Journal of Electron Spectroscopy and Related Phenomena 266 (2023) 147364

Contents lists available at ScienceDirect

Journal of Electron Spectroscopy and Related Phenomena

journal homepage: www.elsevier.com/locate/elspec

Atomically dispersed Ni-N-C electrocatalysts, studied by Ni L-edge spectro-ptychography

Chunyang Zhang [a,b], Jiatang Chen [a], Hao Yuan [b,1], Jian Wang [c], Tianxiao Sun [c,d], Drew Higgins [a], Adam P. Hitchcock [b,*]

[a] Dept. of Chemical Engineering, McMaster University, Hamilton, ON L8S 4M1, Canada
[b] Dept. of Chemistry & Chemical Biology, McMaster University, Hamilton, ON L8S 4M1, Canada
[c] Canadian Light Source, Saskatoon SK S7N 2V, Canada
[d] Helmholtz Zentrum Berlin, BessyII, Hahn-Meitner-Platz 1, 14109 Berlin, Germany

ARTICLE INFO

Keywords:
Atomically dispersed Ni electrocatalysts
Spectro-ptychography
Scanning transmission X-ray microscopy
Defocused
Reduced dose

ABSTRACT

Soft X-ray spectro-ptychography of nickel-nitrogen-carbon electrocatalysts containing atomically dispersed Ni-based active sites were measured at the Ni L_3 edge. Samples prepared with two different loadings of Ni precursors were investigated and compared to the results of an earlier study using scanning transmission X-ray microscopy (STXM) [Zhang et al., ACS Catalysis 12 (2022) 8746]. The ptychography data sets were measured using a defocused probe (1–3 μm). The spatial resolution was improved from ~60 nm (STXM) to ~20 nm (ptychography). Spectro-ptychography stacks were measured at 4 component-specific energies (4-E stack) and at many energies across the full Ni L_3 edge (34-E stack). Maps of three key chemical components (Ni metal, Ni_3S_2, and atomically dispersed N-coordinated Ni catalyst sites) were derived by fits of suitable reference spectra to absorption signals derived from the amplitude images from ptychographic reconstruction. The spectro-ptychography 4-E and 34-E stacks gave chemical mapping similar to each other and to the earlier STXM results. The phase signals obtained from the same data set and reconstruction were also found to be analyzable using reference phase spectra extracted from the phase stack, which generated chemical maps similar to those based on ptychography amplitude data. By using a defocused probe, the radiation dose and acquisition times for spectro-ptychography are comparable to conventional STXM, but significantly improved spatial resolution was achieved. This study highlights the added value of spectro-ptychography relative to STXM for studies of electrocatalysts.

1. Introduction

Metal-nitrogen-carbon (M-N-C) nanostructures, commonly referred to as atomically dispersed M-N_x/C catalysts, are a promising class of materials for electrocatalytic applications.[1–4] In particular, nickel-nitrogen-carbon (Ni–N–C) atomically dispersed electrocatalysts have shown activity and high selectivity to generate CO through the electrochemical CO_2 reduction (CO_2R) reaction. [5,6] The catalytic activity of M-N-C materials has been attributed to well-dispersed single metal atoms in the form of nitrogen-coordinated (MN_x) active sites on highly conductive carbon materials. [7,8] Recently we reported a detailed, multi-edge (Ni 2p, S 2p, N 1 s, O 1 s, C 1 s) X-ray spectromicroscopy investigation of Ni-N-C catalysts using scanning transmission X-ray microscopy (STXM) [9], combined with measurements of catalysis performance and electron microscopic characterization. STXM provides a large-scale (tens of microns) overview of the catalyst morphology while achieving chemical mapping at ~50 nm spatial resolution. [10,11] This technique complements much higher spatial resolution methods, such as transmission electron microscopy (TEM) imaging [12] combined with atomic resolution electron energy loss spectroscopy (EELS) [6,13]; and non-spatially resolved methods, such as X-ray absorption spectroscopy (XAS). [14,15].

In our previous work [9] pyrolyzed, polymer-derived Ni-N-C catalysts were analyzed using STXM spectromicroscopy to determine the chemical states present and to quantitatively map their spatial distribution. From the Ni L_{23} near edge X-ray absorption (NEXAFS) spectra,

* Corresponding author.
E-mail address: aph@mcmaster.ca (A.P. Hitchcock).
[1] present address: University of Victoria, Victoria, BC

https://doi.org/10.1016/j.elspec.2023.147364
Received 28 April 2023; Received in revised form 21 June 2023; Accepted 22 June 2023
Available online 1 July 2023

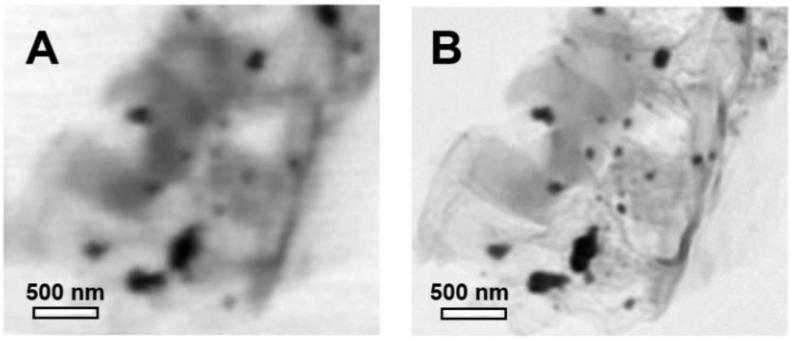

Fig. 1. Comparison of STXM and ptychography images. (a) STXM transmission image at 852.7 eV of the Ni-N-C-high sample [3 ms/pixel, (4 μm)^2 (156)^2 pixels, total acquisition time of 6 min]. (b) Ptychography amplitude image of the same area, at the same photon energy. The diffraction images were measured with a 1.25 μm defocus spot, 32 × 32 spots, with 90% overlap and 3.0 s dwell. Total acquisition time was 29 min.

metallic Ni (referred to as Ni metal in this work), as well as tri-nickel disulphide (Ni_3S_2) and atomically dispersed NiN_x/C species, which were approximated by 5,10,15,20-tetraphenyl- 21 H,23 H-porphine nickel (II) (NiTPP), were identified and mapped. [9] Although STXM spectromicroscopy is very powerful, the spatial resolution achieved with commonly available zone plate lenses is typically 40–60 nm. A significant improvement in spatial resolution can be achieved using ptychography. [16,17] While hard X-ray ptychography is well established, soft X-ray ptychography has only emerged recently. [18–25] Here we have used soft X-ray spectro-ptychography at the Ni L-edge to study the same Ni-N-C catalyst samples previously investigated by STXM, in order to explore the additional information that higher spatial resolution ptychography can provide. The measurements were performed using the ptychography capability recently developed at the ambient-STXM at the Canadian Light Source (CLS). [26–28] The single channel phosphor / photomultiplier detector was replaced by a direct X-ray detecting, charge-coupled device (CCD) camera, which allows imaging of the X-rays coherently scattered from the sample. High-resolution real-space images are generated from the measured coherent diffraction patterns through a ptychography reconstruction software package, PyPIE [26], which is based on the extended ptychographic iterative engine (ePIE) phase retrieval algorithm. [17] The spatial resolution of ptychography is not limited by the properties of focusing optics (indeed ptychography has been referred to as 'lens-less imaging'). It has the potential to reach the far-field optical resolution limit, which is 0.61 * λ/NA where λ is the X-ray wavelength and NA is the numerical aperture – thus of the order of 3 nm at the C K edge and 1 nm at the Ni L edge. Currently, the best spatial resolution achieved by soft X-ray ptychography is ~3 nm at 1500 eV. [18] In this work, a direct comparison of the ptychography and STXM results from the same area of a Ni-N-C catalyst showed a ~3-fold improvement in spatial resolution from ~60 to ~20 nm, while achieving similar chemical mapping. These results reinforce the conclusions previously reached regarding the links between the catalytic activity and morphology of these materials.

2. Experimental methods

2.1. Sample preparation

As described elsewhere [9,29], Ni-N-C catalysts with high-loading Ni content (Ni-N-C-high) and low-loading Ni content (Ni-N-C-low) were synthesized by heat-treating a mixture of aniline (1 mL, Sigma-Aldrich), cyanamide (2 g, Sigma-Aldrich) and different amounts of nickel chloride hexahydrate ($NiCl_2 \cdot 6\ H_2O$,Sigma-Aldrich) [Ni-N-C-high (1.2 g) and Ni-N-C-low (0.08 g)] in a 1.5 M HCl solution (200 mL, ACS reagent). After thorough mixing, ammonium persulfate (1.5 g, Sigma-Aldrich) was added as an oxidant to polymerize the aniline to polyaniline. The resulting product was pyrolyzed at 900 °C in argon for 1 hr followed by an acid washing process to remove surface-exposed labile Ni compounds. A second pyrolysis at 900 °C in argon for 3 hrs was then performed. Reference compounds for spectroscopy analysis included physical vapor deposition Ni metal, 5,10,15,20-tetraphenyl- 21 H,23 H-porphine nickel (II) (NiTPP) (Sigma-Aldrich) and Ni_3S_2 (Sigma-Aldrich).

2.2. STXM measurements and analysis

The catalytic powders were physically deposited in the dry state onto formvar coated 3 mm Cu grids. Poorly adhering particles and large agglomerates were removed by tapping the grid on a hard surface. STXM and spectro-ptychographic imaging were performed at the soft X-ray spectromicroscopy beamline (SM) 10ID-1 at the Canadian Light Source (CLS, Saskatoon, Canada). [30] Spectroscopic information was obtained by recording raster scanned image sequences (also known as stacks [31]). The energy scale of the beamline was calibrated by recording the spectrum of neon gas. [32] STXM images, point spectra, and stacks were analyzed using aXis2000. [33,34] Stacks were first aligned using Fourier cross-correlation procedures, then converted to an optical density (OD) using the Io signal from regions free of the catalyst particles. Chemical maps were obtained by fitting the OD stack to a set of reference spectra recorded from pure materials, as described in detail elsewhere [11].

2.3. Ptychography measurements, reconstruction, and analysis

Diffraction images (DI) at overlapping raster scanned positions were recorded using a CCD detector (Andor model DX434, 1024 × 1024 pixels). In order to convert the focused ~60 nm spot to a defocused spot size of either 1.25 or 3.0 μm diameter, the zone plate position was displaced along the X-ray axis. Dwell times of 1–3 s per diffraction image were used. Although DI of adequate quality can be achieved with sub-second dwell, longer dwells were used so as to have a better duty cycle, which is limited by the ~1 s/image transfer rate of the Andor camera. Sets of ptychographic DI were reconstructed using the PyPIE software package (developed by the CLS SM beamline team [26,28]), which is a CPU-based python program using the extended Python Iterative Engine (ePIE) algorithm. [34–38] Amplitude and phase images of both the object and the probe are generated by the PyPIE iterative reconstruction. The reconstructed amplitude and phase stacks were analyzed using aXis2000 [33,34] in a similar way as for STXM stacks. The amplitude images from the reconstruction are first aligned using Fourier cross-correlation. Following this, an area of the ptycho-amplitude-stack that does not have any catalyst particles is used

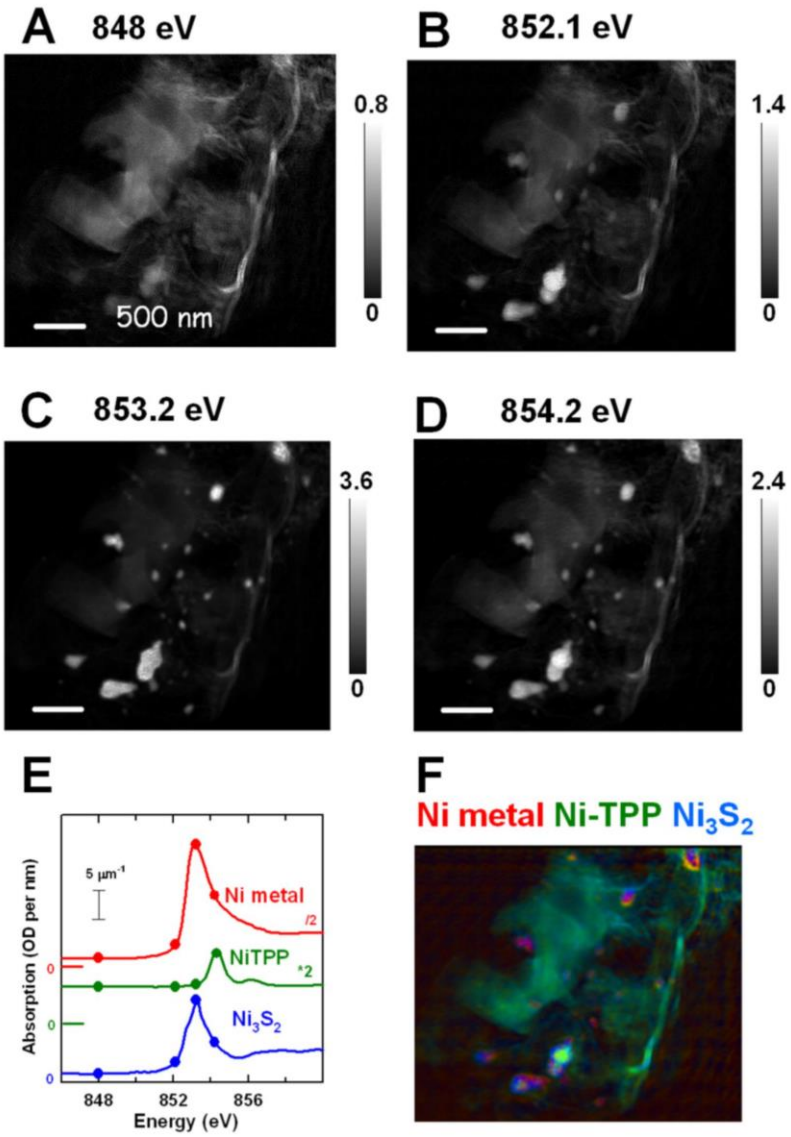

Fig. 2. Chemical mapping of a Ni-N-C-high catalyst aggregate by a 4-energy ptychography stack. Absorption images derived from reconstructed ptychography amplitude images at (a) 848 eV. (b) 852.1 eV (Ni metal). (c) 853.2 eV (Ni_3S_2) (d) 854.2 eV (Ni-TPP). All absorption images are plotted on the indicated grey scales. (e) Reference spectra of Ni metal, Ni-TPP and Ni_3S_2 on an optical density per unit thickness (OD1) scale with offsets, indicated by the color-coded zero of each curve, and scale factor, indicated by the 5 μm^{-1} vertical scale bar. The four energies sampled are indicated. (f) Rescaled color coded composite: Ni metal (red), Ni-TPP (green) and Ni_3S_2 (blue).

as an Io signal in the conversion of the ptycho-amplitude signal to the ptycho-absorption signal. For the phase images, Io normalization was not used [35] since the amplitude of a phase change signal should not be affected by the incident flux. In any case, there is no sharp spectral structure in the incident flux at the Ni L_3 edge. The Io signal does change by a factor of 2 over the energy range measured, which means that Io-normalized phase spectra would be tilted relative to that we present.

3. Results

3.1. Imaging: STXM versus ptychography

Fig. 1a shows a STXM transmission image at 853.9 eV of an agglomerated particle of the high-Ni loading Ni-N-C material. The image was measured using the fully focused spot from a 50 nm outer zone width zone plate. Fig. 1b shows the ptychography amplitude image, generated by reconstructing a ptychography data set measured at 853.9 eV using a 1.25 μm defocused spot size, and 90% overlap (4×4 μm, 32 ×32 samples, 1.7 s/DI). The much higher spatial resolution of the ptychography amplitude image is readily apparent. Some very small Ni nanoparticles (~20 nm) dispersed in the Ni-N-C sample are now observed, which could not be seen in the corresponding STXM image. Lines across sharp features indicate an apparent spatial resolution of 60 ± 10 nm for STXM and 20 ± 5 nm for ptychography. In a preliminary ptychography study of the Ni-N-C sample, a Fourier ring correlation (FRC) determined a half-pitch spatial resolution of 10 nm (see Fig. S19 of ref [9]), consistent with the 20 nm resolution estimated from line profiles across sharp features.

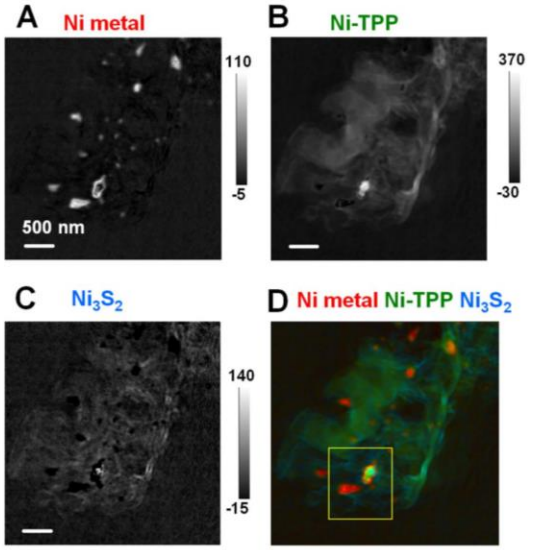

Fig. 3. Chemical mapping of Ni-N-C-high by a 34 energy Ni L_3 spectro-ptychography absorption stack. (a) component map of Ni metal. (b) component map of Ni single atom catalyst, as Ni-TPP. (c) component map of Ni_3S_2. The grey scale limits of each component map are thickness in nm. (d) rescaled colour-coded composite of the 3 component maps. (e) The reference spectra are plotted in Fig. 2e. The yellow box is the region expanded in Fig. 4. The ptychography stack was measured using a 2.0 μm spot to scan over $(4\ \mu m)^2$ area with $(10)^2$ points grid and 80% overlap with a dwell of 2.3 s.

3.2. Spectro-ptychography – amplitude

Fig. 2 presents the results of chemical mapping of the Ni-N-C-high catalyst aggregate by a 4-energy ptychography stack. These energies were chosen to best differentiate the Ni metal, Ni-TPP, and Ni_3S_2 species (see Fig. 2e). As found from the STXM study of the same particle [9], the Ni L_3 spectrum obtained from the carbonaceous region (areas that did not observably contain any particles) is well fit by the Ni L_3 spectrum of Ni-TPP. Meanwhile, the readily visible particles are best fit by a combination of Ni metal and Ni_3S_2, along with some Ni-TPP. Despite measuring only a few energies, the fit quality is excellent. The color-code chemical component maps derived from fitting the 4-E stack show that the nanoparticles mainly consist of Ni metal and Ni_3S_2, while the Ni-TPP signal is strongest in the matrix region. These results are qualitatively in good agreement with those derived from STXM measurements of the same sample [9].

Fig. 3 presents results from fitting a full, 34 energy spectro-ptychography absorption stack. The chemical component maps show the distribution of each Ni species. Ni metal and Ni_3S_2 mostly exist as components of the nanoparticles while the Ni-TPP signal is broadly dispersed in the matrix. This result is very similar to that derived from the 4-energy spectro-ptychography stack (Fig. 2) and that derived from the STXM stack reported in ref [9]. More importantly, since the reference spectra used in the analysis are on an absolute intensity scale – optical density per μm – the grey scale of each component map shown is quantitative, giving thickness in nm.

Fig. 4 is an expanded presentation of the results in Fig. 3, in the region indicated by the yellow box in Fig. 3d, which is a region with several of the larger particles. The particles are clearly a composite of different species, with an exterior dominated by Ni_3S_2 and an interior that is either Ni metal or a combination of Ni metal and Ni-TPP-like Ni-N-C single atom catalyst. A core-shell structure, with a sulfur-rich

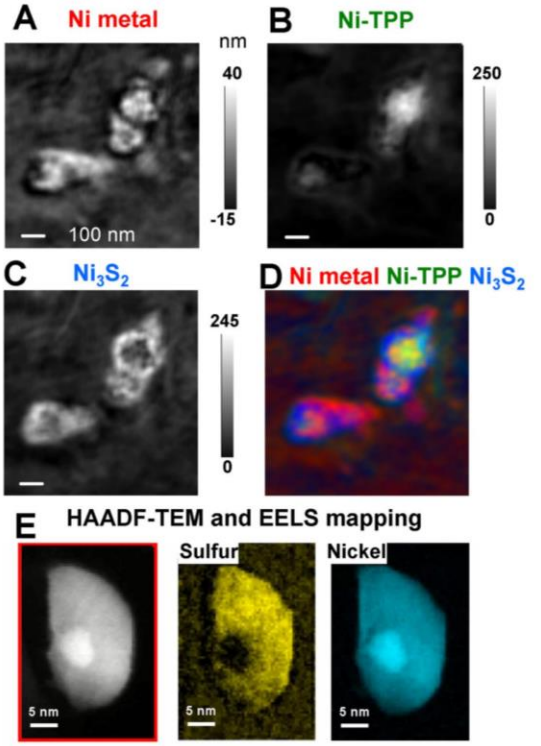

Fig. 4. Chemical mapping of particles in the Ni-N-C-high catalyst aggregate mapped by 4-energy ptychography. Quantitative maps (nm thickness) derived by fitting the 4E stack to the reference spectra (Fig. 2e). (a) Ni metal.(b) Ni-TPP. (c) Ni_3S_2 maps. (d) Rescaled color coded composite of the component maps after removal of pixels with large negative value, in order to better show the distribution of Ni components. Ni metal (red), Ni-TPP (green), Ni_3S_2 (blue). (e) TEM imaging and TEM-EELS sulfur and nickel mapping of an individual particle in the Ni-N-C-low sample. [9].

exterior and a Ni-rich core, had previously been observed by transmission electron microscopy combined with EELS mapping of some particles in the Ni-N-C-low sample, as shown in Fig. 4e (reproduced from Fig. 2 of [9]).

3.3. Spectro-ptychography – phase analysis

Ptychographic reconstruction provides an object scattering phase as well as the object scattering amplitude. A simultaneous analysis of the amplitude and phase signals, combined as an X-ray refractive index signal, would be preferable; an example of that approach has been reported by Farmand et al. [39] Alternatively, one can fit the phase stack to suitable phase reference signals. Although we have not measured phase spectra of the pure reference species by ptychography, we were able to derive these from the phase stack using regions of interest (ROI) defined by the component maps derived from the amplitude/absorption stack (Fig. 3).

Fig. 5 presents the phase spectra of the Ni metal, carbonaceous matrix region (Ni-TPP-like) and Ni_3S_4 extracted from the phase stack derived from the same ptychographic reconstruction of the 34 energy spectro-ptychography stack. The phase spectra have a typical 'derivative-like' shape [38,39]. The scattering phase shift signals from the denser, more crystalline Ni_3S_2 and Ni metal particles are much stronger

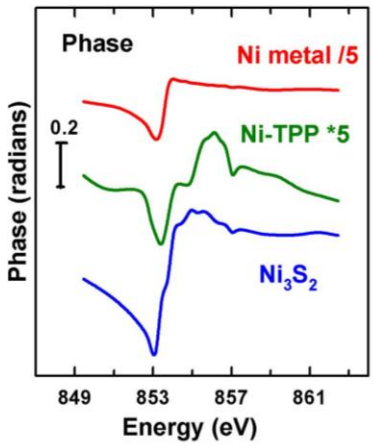

Fig. 5. Phase spectra of Ni metal, Ni-TPP and Ni_3S_2. The phase spectra are extracted from the phase stack for the Ni-N-C-high sample using regions of interest identified from the component maps derived from the analysis of the spectro-ptychography derived absorption stack (Fig. 3). The vertical scale bar, when combined with the indicated multiplicative factors, gives the scale of phase change for each phase-spectral component. The curves are offset for clarity.

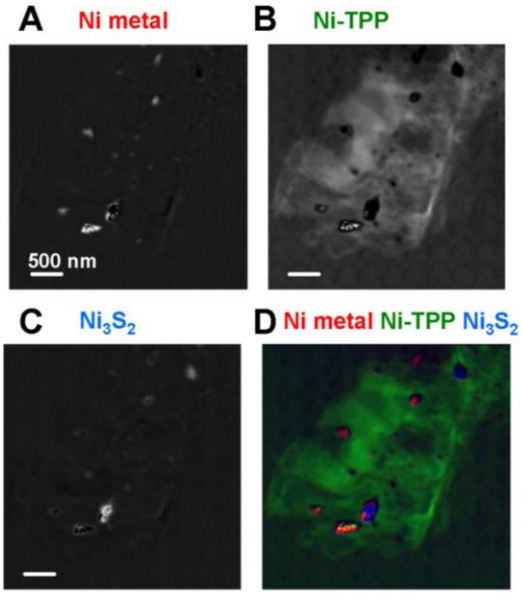

Fig. 6. Chemical mapping of a Ni-N-C-high aggregate by a 34 energy Ni L_3 spectro-ptychography phase stack. Component maps of (a) Ni metal, (b) Ni single atom catalyst, as Ni-TPP. (c) Ni_3S_2, derived by fitting the phase stack (from the same data set for which the absorption ptychography analysis is presented in Fig. 3) to the phase spectra presented in Fig. 5. (d) rescaled color coded composite of the 3 component maps.

than that from the TPP-like single atomic catalyst in the matrix. The first dip in the Ni metal and Ni_3S_2 phase signals occur at 853.1 eV (at the same energy as the absorption maximum in Ni metal but 0.3 eV below

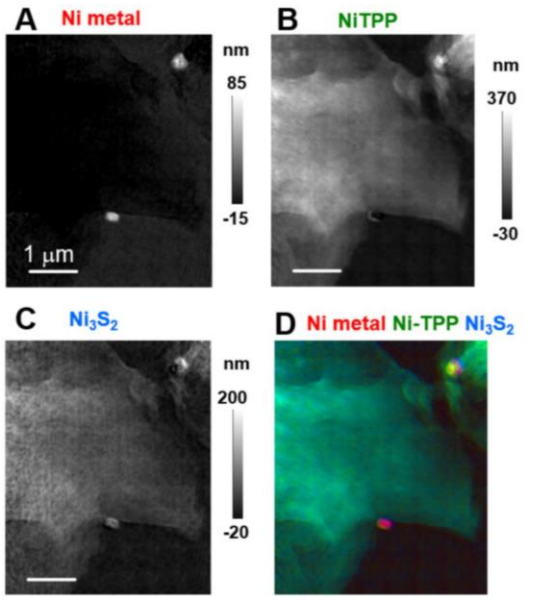

Fig. 7. Chemical mapping of Ni-N-C-low by a Ni L_3 spectro-ptychography absorption stack. Component maps of (a) Ni metal. (b) Ni single atom catalyst, as Ni-TPP. (c) Ni_3S_2, derived from a 34 energy Ni L_3 ptychography stack using 3 μm defocused spot to scan $(6)^2$ μm area with $(10)^2$ pixels and 1.7 s dwell time to achieve 80% overlap. The grey scale limits are thickness in nm. (d) Rescaled color coded composite of the 3 component maps. Reference spectra are plotted in Fig. 2e.

that of Ni_3S_2). The first dip in the phase signal of the carbonaceous matrix occurs at 853.3 eV, which is 0.9 eV below the maximum in the absorption spectrum of Ni-TPP. Chemical mapping based on these phase signals is presented in Fig. 6. In general, the component maps derived from the phase signals are in reasonable agreement with those derived from the ptychography amplitude signals. We note that the intensities in the ptychography phase-derived component maps are qualitative and cannot be related among the 3 species, since the connection between phase spectra and material thickness is not understood. This is in contrast to the quantitative thickness scales provided by analysis of the ptychography amplitude signals in the same way as STXM X-ray transmission signals.

3.4. Ptychography of Ni-N-C-low

In our previous study [9], the Ni-N-C low sample was shown to be a more efficient and selective CO_2 reduction catalyst than the Ni-N-C-high sample. The goal of the STXM study was to identify why. Fig. 7 presents chemical maps of the Ni-N-C-low sample derived from fits of the Ni metal, Ni-TPP, and Ni_3S_2 reference spectra (Fig. 2e) to the absorption images derived from amplitude images generated by reconstruction of a full spectro-ptychographic stack. Qualitatively, the spatial distributions of Ni components in the Ni-N-C-low sample are similar to that of the Ni-N-C-high sample shown in Fig. 3, but there are very few particles compared to the Ni-N-C high sample. In previous STXM studies for Ni-N-C-low samples, the observation of very few particles could have been attributed to the low spatial resolution of STXM such that that particles with size < 50 nm might widely exist but could not be detected. Here, the spectro-ptychographic results with a spatial resolution of ~20 nm, confirm there are very few nanoparticles with size > 20 nm in the Ni-N-C-low material. The spectro-ptychography results show that

the Ni-N-C-low material is quite homogeneous. This is favorable for the design of electrocatalysts and could be one of the reasons why Ni-N-C low shows better catalytic performance.

4. Discussion

Spectro-ptychography, measured using a defocused spot and a high degree of overlap, offers several specific advantages relative to conventional STXM. Radiation damage is frequently a significant limiting factor in high-resolution X-ray microscopy. [40–42] Recently, Mille et al. [24] presented a quantitative dose analysis for soft X-ray ptychography measured using a defocused probe and high overlap, conditions similar to the present study. That analysis showed that defocused spectro-ptychography delivers an appreciably lower dose and much lower dose density compared to STXM. For example, a STXM measurement of a single 4 μm* 4 μm image, using a 40 nm spot size and 2 ms dwell requires an exposure time of 20 s. In contrast, the corresponding ptychographic image measured using 500 ms dwell, 90% overlap and a 1.0 μm spot size (which has over 600 times lower dose density than the STXM conditions) would involve an exposure time of ~500 s. When the 600-fold lower dose density is factored in, the defocused, high-overlap ptychography delivers a dose equivalent to ~1 s of STXM. This ~20-fold lower radiation dose means there is correspondingly lower radiation damage. In addition, the longer dwell time means more X-ray-sample interaction and thus better statistical precision. Also, the long measurement time of each DI (relative to a single point in a full-focused STXM image) reduces the sensitivity of the results to artifacts from mechanical instabilities in the microscope, beamline and storage ring.

While the results presented here demonstrate the improved spatial resolution and statistical precision provided by ptychography, further improvements can be made. The existing CLS ambient STXM platform has relatively poor mechanical stability. A new STXM mechanism has been built and will be installed and commissioned by the end of 2023. The Andor CCD camera used for this study has a relatively slow image transfer speed. A new generation of direct X-ray sensitive sCMOS cameras for the soft X-ray region are now available which have much faster data transfer rates (for example, current generation sCMOS devices can transfer a 1 Mpixel image in 40 ms). Such sCMOS cameras have been used for low energy spectro-ptychography studies [24,25] including a very recent spectro-ptychography study of a Cu carbon dioxide reduction (CO2R) catalyst under in-situ flow electrochemical control conditions [43].

This spectro-ptychography study has provided chemical and morphological information with a significantly superior spatial resolution to that provided by our earlier STXM study. [9] The spectro-ptychography analysis of the few-particle area (Fig. 4), although still at a much lower spatial resolution than the TEM imaging and EELS mapping reported earlier [9], is consistent with the previous conclusion that core-shell particles, with Ni metal surrounded by Ni_3S_2, tend to form with the synthesis conditions for Ni-N-C-high. Lowering the Ni content and reducing the amount of Ni metal-rich nanoparticles increases the homogeneity which was previously shown [9] to improve the Faradaic efficiency for the reduction of CO_2 to CO.

Declaration of Competing Interest

The authors declare that they have no known competing financial interests or personal relationships that could have appeared to influence the work reported in this paper.

Data availability

Data will be made available on request.

Acknowledgments

Research is supported by the Natural Sciences and Engineering Research Council (NSERC) Discovery grant and the National Research Council of Canada's Materials for Clean Fuels Challenge program. Measurements were made using the ambient STXM on beamline 10ID1 at the Canadian Light Source (CLS), which is supported by CFI, NSERC, CIHR, NRC, and the University of Saskatchewan. Electron microscopy was performed at the Canadian Centre for Electron Microscopy at McMaster University.

References

[1] A.S. Varela, W. Ju, A. Bagger, P. Franco, J. Rossmeisl, P. Strasser, Electrochemical reduction of CO_2 on metal-nitrogen-doped carbon catalysts, ACS Catal. 9 (2019) 7270–7284.
[2] A.A. Gewirth, J.A. Varnell, A.M. DiAscro, Nonprecious metal catalysts for oxygen reduction in heterogeneous aqueous systems. Chem. Rev. 118 (2018) 2313–2339.
[3] J. Zhang, Z. Xia, L. Dai, Carbon-based electrocatalysts for advanced energy conversion and storage. Sci. Adv. 1 (2015), e1500564.
[4] Z. Chen, D. Higgins, A. Yu, L. Zhang, J. Zhang, A review on non-precious metal electrocatalysts for PEM fuel cells. Energy Environ. Sci. 4 (2011) 3167–3192.
[5] D.M. Koshy, S. Chen, D.U. Lee, M.B. Stevens, A.M. Abdellah, S.M. Dull, G. Chen, D. Nordlund, A. Gallo, C. Hahn, D.C. Higgins, Z. Bao, T.F. Jaramillo, Understanding the origin of highly selective CO_2 electroreduction to CO on Ni, N-doped carbon catalysts, Angew. Chem. 132 (2020) 4072–4079.
[6] D.M. Koshy, A.T. Landers, D.A. Cullen, A.V. Ievlev, H.M. Meyer III, C. Hahn, Z. Bao, T.F. Jaramillo, Direct characterization of atomically dispersed catalysts: nitrogen coordinated ni sites in carbon-based materials for CO electroreduction, Adv. Energy Mater. 10 (2020), 2001836.
[7] Y. Cheng, S. Zhao, H. Li, S. He, J.-P. Veder, B. Johannessen, J. Xiao, S. Lu, J. Pan, M.F. Chisholm, S.-Z. Yang, C. Liu, J.G. Chen, S.P. Jiang, Unsaturated edge-anchored Ni single atoms on porous microwave exfoliated graphene oxide for electrochemical CO_2, Appl. Catal. B: Environ. 243 (2019) 294–303.
[8] Y. Chen, S. Ji, S. Zhao, W. Chen, J. Dong, W.-C. Cheong, R. Shen, X. Wen, L. Zheng, A.I. Rykov, S. Cai, H. Tang, Z. Zhuang, C. Chen, Q. Peng, D. Wang, Y. Li, Enhanced oxygen reduction with single-atomic-site iron catalysts for a zinc-air battery and hydrogen-air fuel cell. Nat. Commun. 9 (2018) 1–12.
[9] C. Zhang, L. Shahcheraghi, F. Ismail, H. Eraky, H. Yuan, A.P. Hitchcock, D. Higgins, Ni-N-C electrocatalysts for CO_2 reduction studied by scanning X-ray transmission X-ray microscopy, ACS Catal. 12 (2022) 8746–8760.
[10] H. Ade, A.P. Hitchcock, NEXAFS microscopy and resonant scattering: Composition and orientation probed in real and reciprocal space, Polymer 49 (2008) 643–675.
[11] Hitchcock, A.P. Soft X-Ray Imaging and Spectromicroscopy. In Handbook of Nanoscopy Vol. 2, Tendeloo, G. Van, Dyck, V.D., Pennycook, S.J., Eds.; Wiley-VCH Verlag GmbH & Co. KGaA: Weinheim, Germany, 2012, 745–791.
[12] S. Zhao, Y. Cheng, J.-P. Veder, B. Johannessen, M. Saunders, L. Zhang, C. Liu, M. F. Chisholm, R. De Marco, J. Liu, S.-Z. Yang, S.P. Jiang, One-pot pyrolysis method to fabricate carbon nanotube supported Ni single-atom catalysts with ultrahigh loading, ACS Appl. Energy Mater. 1 (2018) 5286–5297.
[13] H.T. Chung, D.A. Cullen, D. Higgins, B.T. Sneed, E.F. Holby, K.L. More, P. Zelenay, Direct atomic-level insight into the active sites of a high-performance PGM-Free ORR catalyst, Science 357 (2017) 479–484.
[14] J. Timoshenko, B. Roldan Cuenya, In situ/operando electrocatalyst characterization by x-ray absorption spectroscopy, Chem. Rev. 121 (2021) 882–896.
[15] H.-T. Lien, S.-T. Chang, P.-T. Chen, D.P. Wong, Y.-C. Chang, Y.-R. Lu, C.-L. Dong, C.-H. Wang, K.-H. Chen, L.-C. Chen, Probing the active site in single-atom oxygen reduction catalysts via operando X-ray and electrochemical spectroscopy, Nat. Commun. 11 (2020) 4233.
[16] F. Pfeiffer, X-ray ptychography, Nat. Photonics 12 (2018) 9–17.
[17] Rodenburg, J.; Maiden, A. Ptychography. *Springer Handbook of Microscopy*; Springer International Publishing: Switzerland, 16 (2019) 819–904.
[18] D.A. Shapiro, Y.-S. Yu, T. Tyliszczak, J. Cabana, R. Celestre, W. Chao, K. Kaznatcheev, K. David, F. Maia, S. Marchesini, Y. Meng, T. Warwick, L. Yang, H. Padmore, Chemical composition mapping with nano-metre resolution by soft X-ray microscopy, Nat. Photonics 8 (2014) 765–769.
[19] A.P. Hitchcock, Soft X-ray spectromicroscopy and ptychography, J. Electron Spectrosc. Relat. Phenom. 200 (2015) 49–63.
[20] X.H. Zhu, A.P. Hitchcock, D.A. Bazylinski, P. Denes, J. Joseph, U. Lins, S. Marchesini, H.-W. Shiu, T. Tyliszczak, D.A. Shapiro, Measuring spectroscopy and magnetism of extracted and intracellular magnetosomes using soft X-ray ptychography, Proc. Natl. Acad. Sci. 113 (2016) E8219–E8227.
[21] J. Wu, X. Zhu, M.M. West, T. Tyliszczak, H.-W. Shiu, D. Shapiro, V. Berejnov, D. Susac, J. Stumper, A.P. Hitchcock, High resolution imaging of polymer electrolyte membrane fuel cell cathode layers by soft X-ray spectro-ptychography, J. Phys. Chem. C. 122 (2018) 11709–11719.
[22] D.A. Shapiro, S. Babin, R.S. Celestre, W. Chao, R.P. Conley, P. Denes, B. Enders, P. Enfedaque, S. James, J.M. Joseph, H. Krishnan, S. Marchesini, K. Muriki, K. Nowrouzi, S.R. Oh, H. Padmore, T. Warwick, L. Yang, V.V. Yashchuk, Y.-S. Yu, J. Zhao, An ultrahigh-resolution soft x-ray microscope for quantitative analysis of chemically heterogeneous nanomaterials, Sci. Adv. 6 (2020) eabc4904.

[23] H. Yuan, H. Yuan, T. Casagrande, D. Shapiro, Y.-S. Yu, B. Enders, J.R.I. Lee, A. van Buuren, M.M. Biener, S.A. Gammon, T.F. Baumann, A.P. Hitchcock, 4D imaging of ZnO-coated nanoporous Al_2O_3 aerogels by chemically-sensitive ptychographic tomography: implications for designer catalysts, ACS Appl. Nanomater. 4 (2021) 621–632.
[24] N. Mille, H. Yuan, J. Vijayakumar, S. Stanescu, S. Swaraj, K. Desjardins, V. Favre-Nicolin, R. Belkhou, A.P. Hitchcock, Ptychography at the carbon K-edge, Commun. Mater. 3 (2022) 8.
[25] J. Vijayakumar, N. Mille, H. Yuan, S. Stenescu, S. Swaraj, K. Desjardins, F. Orsini, V. Favre-Nicolin, E. Najafi, A.P. Hitchcock, R. Belkhou, Soft X-ray spectro-ptychography of boron nitride nanobamboos, carbon nanotubes and permalloy nanorods, J. Synchrotron Radiat. 30 (2023) 746–757.
[26] T. Sun, G. Sun, F. Yu, Y. Mao, R. Tai, X. Zhang, G. Shao, Z. Wang, J. Wang, J. Zhou, "Soft X-Ray ptychography chemical imaging of degradation in a composite surface-reconstructed Li-rich cathode, ACS Nano 15 (2021) 1475–1485.
[27] X. Xia, J. Wang, Y. Hu, J. Liu, A.I. Darma, L. Jin, H. Han, C. He, J. Yang, Molecular insights into roles of dissolved organic matter in Cr(III) immobilization by coprecipitation with Fe(III) probed by STXM-ptychography and XANES spectroscopy, Environ. Sci. Technol. 56 (2022) 2432–2442.
[28] T. Sun, S. Zuo, B. He, X. Yuan, G. Li, J. Zhou, A. Abate, J. Wang, Ionic liquid functionalized tin halide perovskite investigated by STXM and spectro-ptychography, J. Electron Spectrosc. Rel. Phenomena 265 (2023), 147330.
[29] L. Shahcheraghi, C. Zhang, H.-J. Lee, M. Cusack-Striepe, F. Ismail, A. Abdellah, D. C. Higgins, Identifying activity and selectivity trends for the electrosynthesis of hydrogen peroxide via oxygen reduction on nickel–nitrogen–carbon catalysts, J. Phys. Chem. C. 125 (2021) 15830–15840.
[30] K.V. Kaznatcheev, C. Karunakaran, U.D. Lanke, S.G. Urquhart, M. Obst, A. P. Hitchcock, Soft X-ray spectromicroscopy beamline at the CLS: Commissioning results, Nucl. Instrum. Methods Phys. Res. Sect. A: Accel. Spectrom. Detect. Assoc. Equip. 582 (2007) 96–99.
[31] C. Jacobsen, S. Wirick, G. Flynn, C. Zimba, Soft x-ray spectroscopy from image sequences with sub-100 nm spatial resolution, J. Microsc. 197 (2000) 173–184.
[32] A.P. Hitchcock, C.E. Brion, Neon K-shell excitation studied by electron energy-loss spectroscopy, J. Phys. B: At. Mol. Phys. 13 (1980) 3269–3273.
[33] Hitchcock, A.P. aXis2000 is written in Interactive Data Language (IDL). It is available free for non-commercial use from http//unicorn.mcmaster.ca/aXis2000.html (last accessed 23 April 2023.
[34] A.P. Hitchcock, Analysis of X-ray Images and Spectra (aXis2000) – a toolkit for X-ray spectromicroscopists, J. Electron Spectrosc. Rel. Phenomena 266 (2023), 147360.
[35] S.G. Urquhart, X-ray spectro-ptychography, ACS Omega 7 (2022) 11521–11529.
[36] F. Zhang, I. Peterson, J. Vila-Comamala, A. Diaz, F. Berenguer, R. Bean, B. Chen, A. Menzel, I.K. Robinson, J.M. Rodenburg, Translation position determination in ptychographic coherent diffraction imaging, Opt. Express 21 (2013) 13592–13606.
[37] J.R. Fienup, Reconstruction of an object from the modulus of its fourier transform, Opt. Lett. 3 (1978) 27–29.
[38] J.M. Rodenburg, H.M.L. Faulkner, A phase retrieval algorithm for shifting illumination, Appl. Phys. Lett. 85 (2004) 4795–4797.
[39] M. Farmand, R. Celestre, P. Denes, A.L.D. Kilcoyne, S. Marchesini, H. Padmore, T. Tyliszczak, T. Warwick, X. Shi, J. Lee, Y.-S. Yu, J. Cabana, J. Joseph, H. Krishnan, T. Perciano, F.R.N.C. Maia, D.A. Shapiro, Near-edge X-ray refraction fine structure microscopy, Appl. Phys. Lett. 110 (2017), 063101.
[40] J. Wang, G.A. Botton, M.M. West, A.P. Hitchcock, Quantitative evaluation of radiation damage to polyethylene terephthalate by soft X-rays and high energy electrons, J. Phys. Chem. B 113 (2009) 1869–1876.
[41] J. Wang, C. Morin, L. Li, A.P. Hitchcock, X. Zhang, T. Araki, A. Doran, A. Scholl, Radiation damage in soft x-ray microscopy, J. Electron Spectrosc. Rel. Phenom. 170 (2009) 25–36.
[42] I. Martens, L.G.A. Melo, D. Wilkinson, D. Bizzotto, A.P. Hitchcock, Characterization of X-ray damage to perfluorosulfonic acid using correlative microscopy, J. Phys. Chem. C. 123 (2019) 16023–16033.
[43] C. Zhang, H. Eraky, N. Mille, S. Stanescu, S. Swaraj, R. Belkhou, D. Higgins, A. P. Hitchcock, Copper CO_2-reduction electrocatalysts studied by in-situ Soft X-ray spectro-ptychography, Chem. Catal. (2023) (in review).

Chapter 6

Ex situ STXM studies of electrodeposited Cu electrocatalysts for CO_2 reduction

This chapter presents the results of ex situ STXM studies for electrodeposited Cu materials. The results shown in this chapter are foundational for subsequent in situ STXM and in situ spectro-ptychography studies of Cu nanoparticles as CO_2R electrocatalysts. High quality, accurately calibrated reference spectra for Cu metal, Cu_2O, and CuO were measured and tested to verify they can correctly locate and quantify these Cu species from STXM or ptychography spectromicroscopy. The synthesis of electrodeposited Cu materials with different morphology and oxidation state distributions was studied using STXM. Electrodeposited Cu nanoparticles before and after ex situ CO_2R reaction are compared.

6.1 Reference spectra for Cu metal, Cu_2O, and CuO

To systematically study the Cu materials, the X-ray absorption spectra for Cu materials with different oxidation states are studied. The common oxidation states of copper are Cu(0), Cu(I), and Cu(II). Reference spectra were collected from Cu metal, CuCl, and $CuCl_2.2H_2O$ by STXM. [Vinod et al. et al., 2018] **Fig 6.1** shows these Cu 2p X-ray absorption spectra on an absolute OD1 intensity scale. These spectra are similar to the literature spectra of Cu metal, [Magnuson et al., 1997] Cu_2O[Grioni et al., 1992] and CuO [Phillips et al. et al., 2013.] in the literature in terms of shape and energies of the absorption peaks. The main peaks in the Cu $2p_{3/2}$ portion [925-945 eV] occur at 930.6(2)

eV (peak A) for Cu(II), 933.06(8) eV (peak B) for Cu(I), 933.06(8) eV and 933.1(2) eV (peak C) for Cu(0), respectively. [Prabu et al., 2018] In general as an element gets oxidized the X-ray absorption spectral features shift to higher energy with increasing oxidation state due to a lower energy of the core level because the core electrons are more tightly bound due to reduced shielding from the smaller number of valence electrons. However, the main Cu $2p_{3/2}$ peak in Cu(II) spectra is located at significantly lower energy (~3 eV) than the first peak in Cu(0) and Cu(I) due to the unique 3d band structures of these Cu species. For Cu(II), there is a hole in the 3d band ($[Ar]3d^9$) and the sharp peak at 930.6(2) eV is due to Cu $2p_{3/2} \rightarrow$ 3d transitions. But the 3d band of Cu(0) and Cu(I) is full (ground state electron configurations are $[Ar]4s^13d^{10}$ and $[Ar]4s^03d^{10}$) and thus the 2p → 3d transition is forbidden. The first peak in Cu(0) and the main peak in Cu(I) are both Cu $2p_{3/2} \rightarrow$ 4s transitions, located at 933.06(8) eV and occurring at higher core excitation energies than that $2p_{3/2} \rightarrow$ 3d transition in Cu(II) species. The multiple scattering features shown in the region between 936 and 944 eV of the spectrum of Cu metal are due to the well-defined local structure and strong scattering power of Cu atoms.

In subsequent analyses of STXM data of Cu materials using the reference spectra shown in **Fig 6.1**, we found that there were errors when these reference spectra were used. Here, an example of the sensitivity of the analysis of STXM data of Cu nanoparticles using various Cu reference spectra is presented to show the importance of using the correct spectra for Cu metal, Cu_2O and CuO species in STXM analysis.

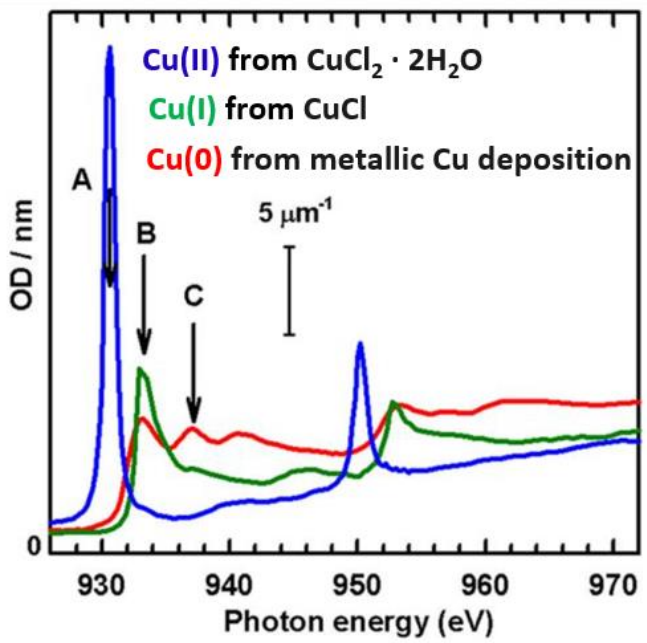

Figure 6.1 Cu 2p reference spectra of Cu(0), Cu(I), and Cu(II), measured from Cu metal, CuCl, and $CuCl_2 \cdot 2H_2O$, respectively. The intensity scale is absolute in terms of the OD/nm thickness at standard densities of the solids (OD1). The arrows labeled A, B, and C indicate the energies previously used to determine Cu(0), Cu(I), and Cu(II). [Vinod et al., 2018] With permission of *American Institute of Physics*

The experimental details for creating Cu nanoparticles and Cu nanoparticles running CO_2R reactions are presented in **Chapter 3.8** and **Chapter 7**. **Fig 6.2** displays the STXM results for Cu nanoparticles subjected to a potential of -0.6 V_{RHE}. **Fig 6.2a** presents a STXM image measured at 933 eV, showing Cu nanoparticles of 100-500 nm in size. The Cu 2p spectrum averaged over all the Cu particles (in the mask region in **Fig 6.2b)** are displayed in **Fig 6.2c**. Compared with the reference spectra in **Fig 6.1**, the Cu nanoparticles are mainly Cu(0). This is reasonable since metallic Cu is

thermodynamically stable under strongly electrochemical reductive conditions such as -0.6 V_{RHE}.

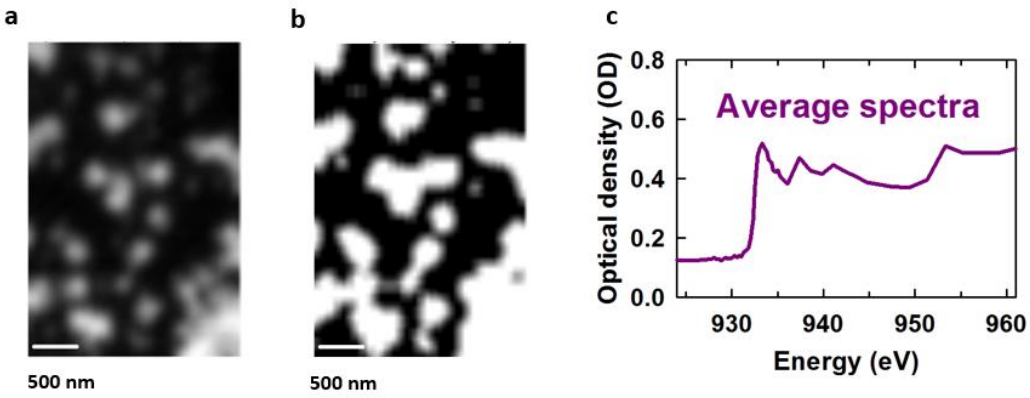

Figure 6.2 a) STXM image of Cu nanoparticles under -0.6 V_{RHE} at 933 eV b) Mask regions used to derive Cu 2p average spectra of all the particles c) Cu 2p average spectra of all the Cu nanoparticles.

The oxidation state distributions of Cu nanoparticles derived using the reference spectra of Cu metal, CuCl, and $CuCl_2.2H_2O$ are presented in **Fig 6.3**. Metallic Cu is the main component in the larger Cu nanoparticles (**Fig 6.3a** and **f**). There is a certain amount of Cu(I) and very little Cu(II) in the Cu particles (**Fig 6.2b** and **c**). To better quantitate the amount of Cu(0) and Cu(I), the average spectra of all the Cu nanoparticles was extracted by threshold masking the average image, and the average spectrum was curve-fit to the reference spectra of CuCl, and $CuCl_2.2H_2O$. The average composition (%, volume ratio) of all the Cu particles was 81% ± 8 % Cu (0) and 19% ± 2 Cu(I) (**Fig 6.4b).** The error is a combination of statistical and estimated systematic uncertainties. However,

that much Cu(I) was very surprising because Cu(I) is not electrochemically stable at a potential of -0.6 V_{RHE}.

To further investigate the possible existence of such a large amount of Cu(I), Cu 2p reference spectra of Cu metal, Cu_2O, and CuO were digitized from the literature [Jiang et al., 2013] and used to analyze the same STXM data.

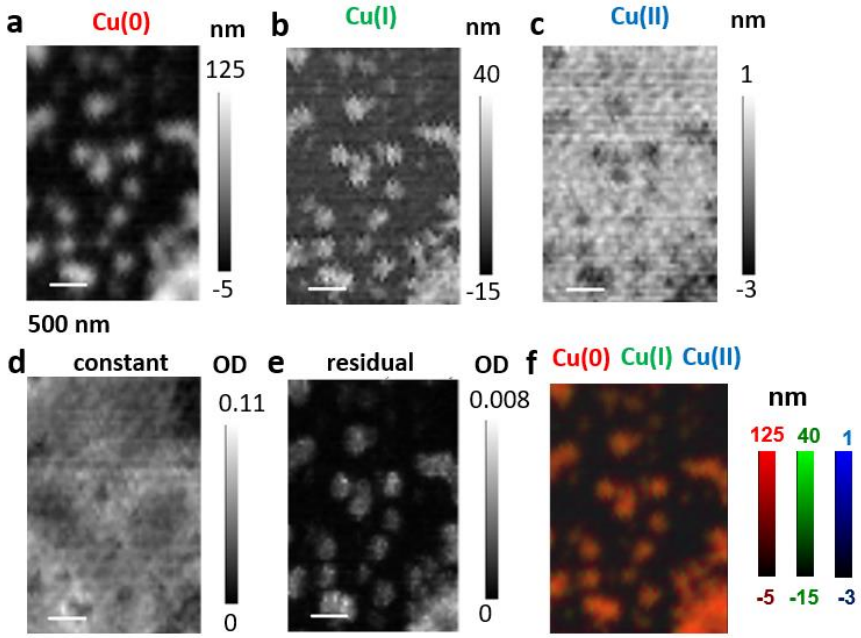

Figure 6.3 Stack-fit analysis of the Cu STXM stack results of Cu nanoparticles under -0.6 V_{RHE} using reference spectra of Cu(0), Cu(I), and Cu(II) from Cu metal, CuCl, and $CuCl_2 \cdot 2H_2O$. [Vinod et al., 2018**]** Quantitative component maps of (a) Cu(0), b) Cu(I), c) Cu(II), d) constant, e) residual, and f) Rescaled color-coded composite of the Cu(0)(red), Cu(I)(green) and Cu(II) (blue)

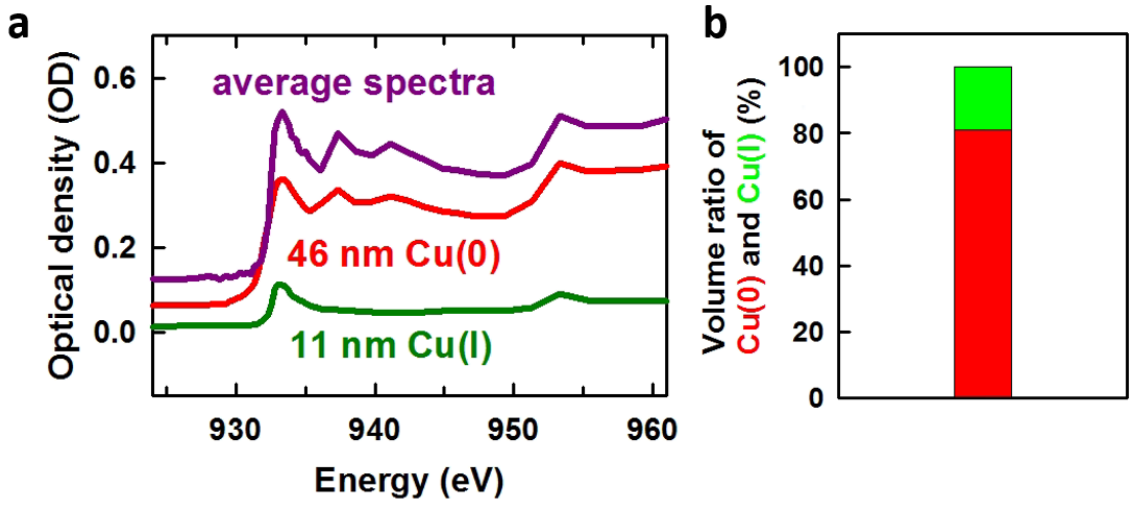

Figure 6.4 Curve-fit analysis of the Cu STXM stack results of Cu nanoparticles under -0.6 V_{RHE} using reference spectra of Cu(0) and Cu(I) from Cu metal, CuCl. [Vinod et al., 2018**]** a) Curve-fit analysis results b) Percentage volume composition of Cu(I) and Cu(0).

When using the digitized Cu metal, Cu_2O, and CuO spectra (shown in **Fig 6.5a)** a different oxidation state distribution was determined, as presented in **Fig 6.5b-g**. Cu(0) is still the main component (**Fig 6.5b** and **g)** but this analysis indicates there is very little Cu(I) in the Cu particles (**Fig 6.5c).** Spectral extraction and curve-fitting using digitized spectra reported volume fractions of 97% ± 10 % Cu (0) and 3% ± 1% Cu(I) (**Fig 6.6).**

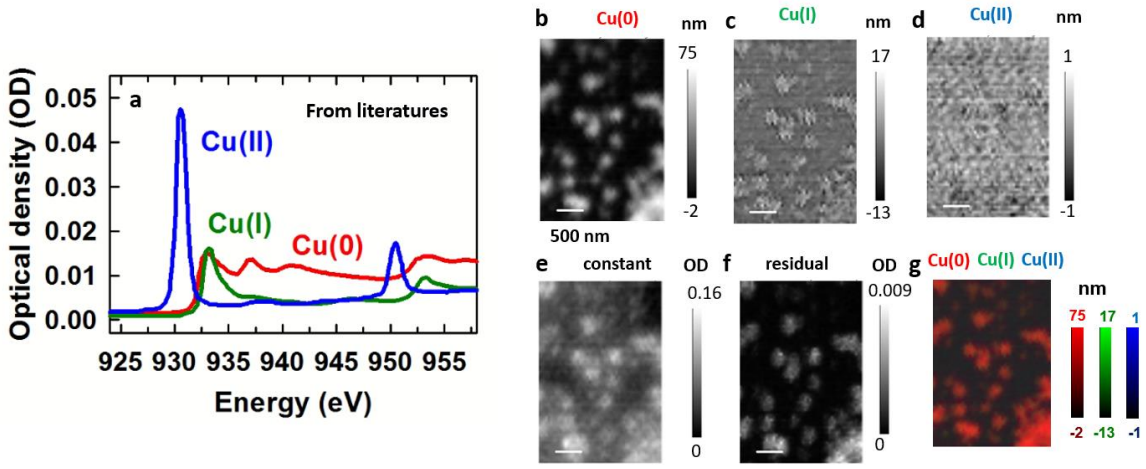

Figure 6.5 Stack-fit analysis of the Cu STXM stack results of Cu nanoparticles under -0.6 V_{RHE} using digitized reference spectra [Jiang et al., 2013] a) the reference spectra of Cu(0), Cu(I), and Cu(II). **[**Jiang et al., 2013**].** Quantitative component maps of (b) Cu(0), c) Cu(I), d) Cu(II), e) constant, f) residual, and g) Rescaled color-coded composite of the Cu(0)(red), Cu(I)(green) and Cu(II) (blue)

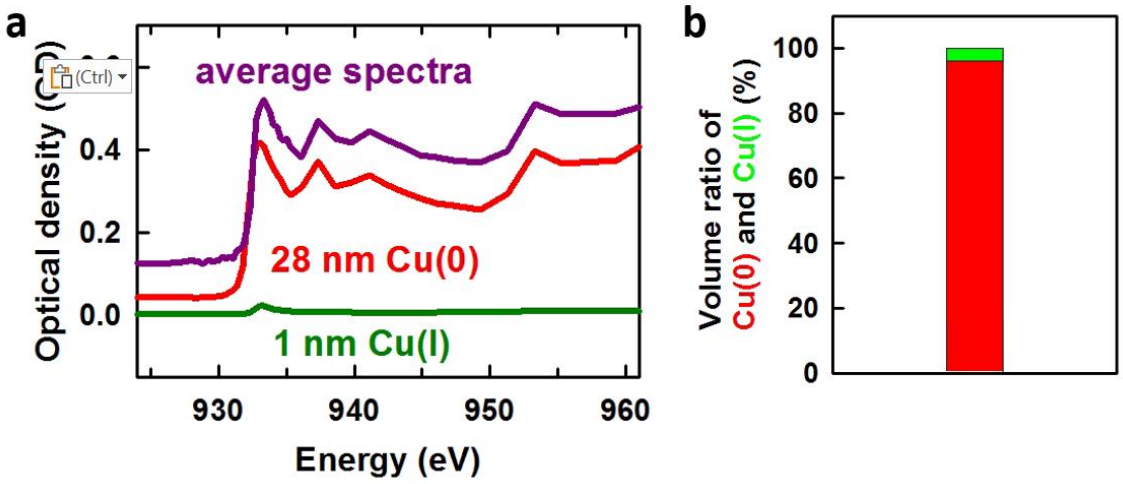

Figure 6.6 Curve-fit analysis of the Cu STXM stack results of Cu nanoparticles under -0.6 V_{RHE} using digitized reference spectra of Cu(0) and Cu(I). [Jiang et al., 2013**]** a) Curve-fit analysis results b) Percentage volume composition of Cu(I) and Cu(0).

Through this comparison it is clear that different choices of reference spectra can modify the outcome of the analysis. Although the reference spectra from [Jiang et al., 2013] and **[**Vinod et al., 2018**]** look similar (**Fig 6.5a** and **Fig 6.1**), the analyzed results are significantly different. Since Cu(I) is thermodynamically unstable under the electrochemical reductive conditions applied (-0.6 V_{RHE}), the results from analysis using reference spectra from [Jiang et al., 2013] are more reasonable. The reference spectra of Cu metal, Cu_2O, and CuO (from [Jiang et al., 2013]) are more appropriate than those of Cu metal, CuCl, and $CuCl_2.2H_2O$ **[**Vinod et al., 2018**]** because of the following issues:

1. The reference spectra of Cu(0), Cu(I), and Cu(II) of [Jiang et al., 2013] are from Cu metal, Cu_2O, and CuO, while that of [Vinod et al., 2018] are measured from electrodeposit Cu, CuCl, and $CuCl_2.2H_2O$. There are minor differences in the X-ray spectra between Cu compounds with O and Cl due to different local environments of Cu atoms. Considering that there is no CuCl or $CuCl_2$ in the Cu nanoparticles under -0.6V_{RHE}, the Cu reference spectra from Cu_2O and CuO are more appropriate.
2. The reference spectrum of Cu metal [Vinod et al., 2018] were measured by Hitchcock group on a bend magnet STXM at the ALS (BL 5.3.2.2) which had poor energy resolution at the Cu 2p edge,. Specifically the lower energy resolution results in a much more gradual onset of the Cu 2p $\rightarrow$ 4s transition at ~932 eV relative to that in spectra measured on the higher energy undulator beamlines used in these studies. The net effect is that the fitting compensates for the incorrect Cu(0) line shape by introducing more Cu(I) which has a sharper rise.

To verify the correct reference spectra of Cu(0), Cu(I), and Cu(II), we measured the Cu 2p spectra of Cu metal, Cu_2O, and CuO on the high energy resolution CLS ambient STXM and Bessy-II Mystic STXM beamlines. These reference spectra are presented in **Fig 6.7a**. They are very similar to the spectra shown in **Fig 6.5a.** [Jiang et al., 2013] The fit results using these reference spectra show similar spatial distributions and amounts of various Cu species (**Fig 6.7b-g**). The curve-fit of the average spectra of all the Cu particles using these reference spectra report a composition 29 nm Cu(0) and 1 nm Cu(I), which correspond to 97% and 3% volume percentages respectively (**Fig 6.8**). The overall results using the reference spectra we collected are close to the results using the spectra digitized from [Jiang et al., 2013].

In subsequent stack-fit and curve-fit analyses to quantify the Cu oxidation states measured in *ex situ* and *in situ* experiments, the reference spectra of Cu metal, Cu_2O, and CuO were used. Generally the results presented in this thesis are based on the spectra from [Jiang et al., 2013] since these spectra were obtained at the beginning of the project, while the reference spectra I recorded were only obtained recently. Indeed the acquisition of independently measured and carefully calibrated Cu 2p reference spectra was motivated due to the anomalously large amount of Cu(I) predicted by analyses using the reference spectra from [Vinod et al., 2018].

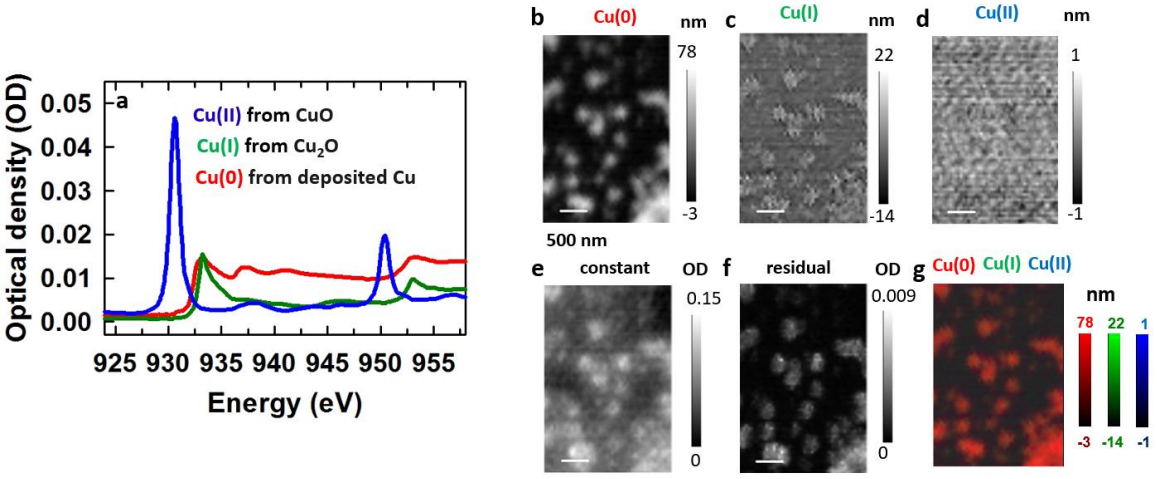

Figure 6.7 Stack-fit analysis of the Cu STXM stack results of Cu nanoparticles under -0.6 V_{RHE} using collect spectra at CLS and Bessy-II a) the reference spectra of Cu(0), Cu(0), and Cu(II) from Cu metal, Cu_2O, and CuO collected at CLS and Bessy-II**.** Quantitative component maps of (b) Cu(0), c) Cu(I), d) Cu(II), e) constant, f) residual, and g) Rescaled color-coded composite of the Cu(0) (red), Cu(I) (green) and Cu(II) (blue)

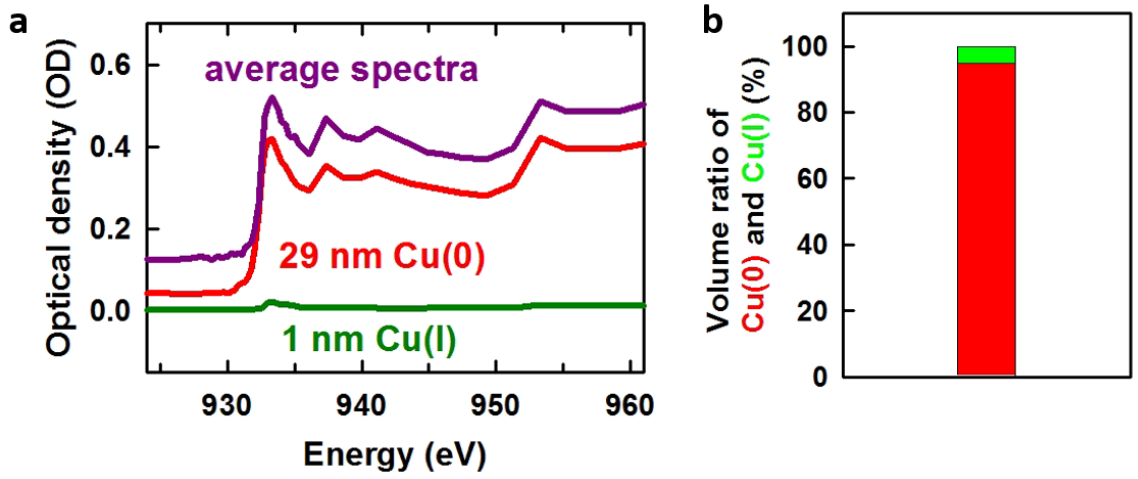

Figure 6.8 Curve-fit analysis of the Cu STXM stack results of Cu nanoparticles under -0.6 V_{RHE} using reference spectra collected at CLS and Bessy-II a) Curve-fit analysis results b) Percentage volume composition of Cu(I) and Cu(0).

6.2 electrodeposited Cu layers and dendrites

The synthesis of the electrodeposited Cu layers and dendrites and optical microscopy of these samples are presented in **Chapter 3.5.3**. **Fig 6.9** displays the *ex situ* STXM results for a sample consisting of electrodeposited Cu layers and dendrites. The image of the *ex situ* Cu sample at 933 eV (**Fig 6.9b**) indicates that a Cu layer was deposited on the Au working electrode, while much thicker Cu dendrites were deposited at the edge of the Au electrode. (**Fig 6.9b**) **Fig 6.9e** shows the maps for Cu metal, Cu_2O, CuO, constant (Au electrode) components, and the residual of the stack-fit using the reference spectra shown in **Fig 6.9a**.[Jiang et al., 2013] The thickness scale (in nm) for each component map is indicated by numbers at the upper and lower right of each map. Color-coded composite maps are shown in **Fig 6.9c** and **Fig 6.9d**. The quantitative STXM mapping shows that a thin layer of Cu_2O is uniformly distributed on the Au electrode surface. A small amount of Cu is present as a thin layer on the Au electrode surface while most of the Cu is in thick dendrites at the edge. The amount of Cu(II) is much less than that Cu(I) and Cu(0) on the electrodeposited Cu samples. It probably occurs because of rapid Cu oxidation in air.

The *ex situ* STXM studies of the electrodeposited Cu samples helped to understand the chemistry and morphology of the sample. The deposits are a mixture of Cu(I) and Cu(0) existing as layers and dendrites, neither of which are favorable for the electrochemical CO_2R performance.

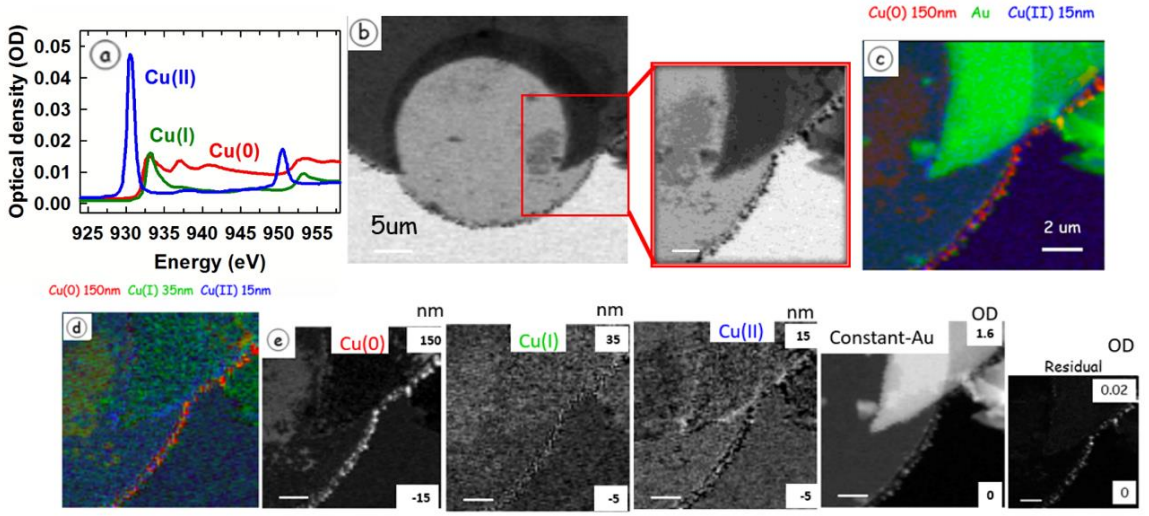

Figure 6.9 Stack-fit analysis of electrodeposited Cu layer and dendrites a) Cu 2p reference spectra of Cu(0), Cu(I), and Cu(II) [Jiang et al., 2013], **b)** STXM image of the *ex situ* Cu sample at 933 eV, **c)** rescaled color-coded composite map of Cu(0) (red), Au electrode (green) and Cu(II) (blue), **d)** rescaled color-coded composite map of Cu(0) (red), Cu(I) and Cu(II) (blue), **e)** component maps for Cu(0), Cu(I), Cu(II), constant (Au electrode) and residual of the fit. [CLS-A1912086]

According to literature, [Arán-Ais et al., 2020. Jiang et al., 2022.] Cu_2O in the nanostructure shows high efficiency and selectivity for CO_2R reactions. It is necessary to understand and shed insight on the state of synthesized Cu_2O particles under CO2R conditions. The Cu_2O nanoparticles were deposited according to the same methods in [Arán-Ais et al., 2020. Grosse et al., 2021] and introduced in the next section.

6.3 Electrodeposited Cu_2O nanoparticles

The synthesis of electrodeposited Cu_2O nanoparticles and the optical microscopy for these samples were presented in **Chapter 3.5.4**. After the sample was prepared, SEM

and EDS were used to check the morphology and elemental composition. **Fig 6.10** displays SEM results for the electrodeposited Cu nanoparticles. **Fig 6.10 a** and **b** present the SEM images of the Cu nanoparticles on various scales, showing well-defined nanoparticle structures.

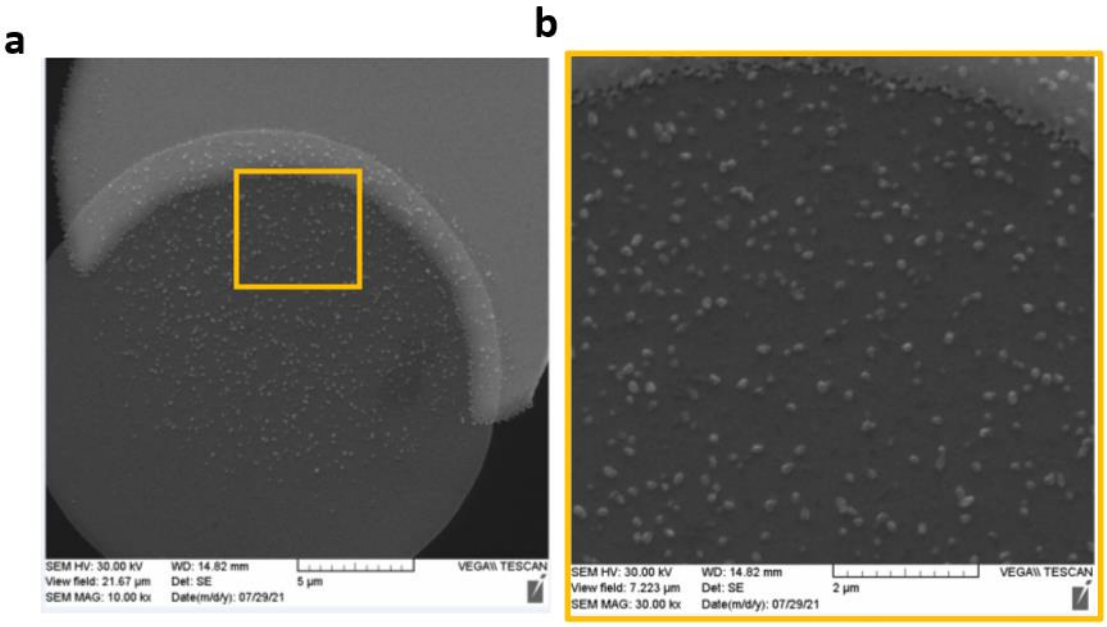

Figure 6.10 SEM for the electrodeposited nanoparticles. a) and b) SEM images of electrodeposited nanoparticles.

Fig 6.11 displays the STXM results for the electrodeposited Cu nanoparticle sample. STXM images of the *ex situ* Cu sample at 933 eV show 100-200 nm diameter Cu particles distributed relatively uniformly on the Au electrode. (**Fig 6.11a,b**), which is in good with SEM results. **Fig 6.11d** shows the maps for Cu(0), Cu(I), Cu(II), constant (Au electrode) components, and the residual of the stack-fit using the literature reference spectra.[Jiang et al., 2013] The thickness scale (in nm) for each component is indicated by numbers at the upper and lower right of each map. Color-coded composite maps are

shown in **Fig 6.11c**. The quantitative STXM mapping shows that these Cu particles mainly consist of Cu(I) with little Cu(0) and Cu(II).

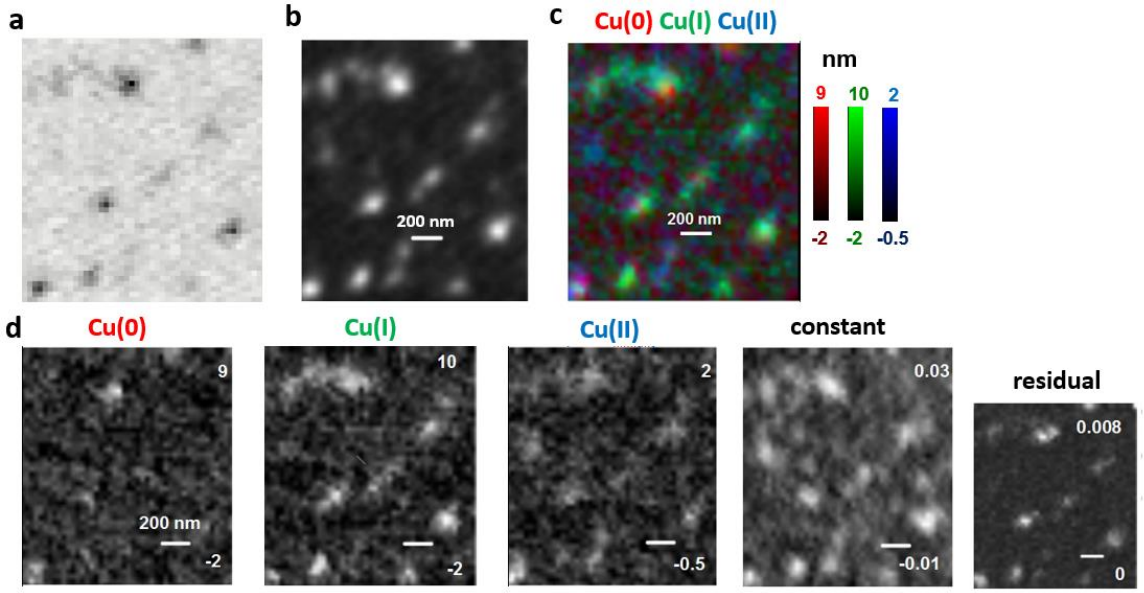

Figure 6.11 Stack-fit analysis of electrodeposited Cu particles a) STXM image of the *ex situ* Cu sample at 933 eV, b) STXM image of the *ex situ* Cu sample after OD conversion at 933 eV **c)** rescaled color-coded composite map of Cu(0) (red), Cu(I) and Cu(II) (blue), **d)** component maps for Cu(0), Cu(I), Cu(II), constant (Au electrode) and residual of the stack-fit using reference spectra.[Jiang et al., 2013] [CLS-A210808009]

6.4 Electrodeposited Cu_2O nanoparticles after CO_2R reactions.

Electrodeposited Cu_2O nanoparticles were prepared by the same method and were used as CO_2R electrocatalysts under -0.6 V_{RHE} for 30 mins. Details of these experiments are presented in **Chapter 3.5.4.** The electrodeposited Cu nanoparticles after CO_2R reactions were characterized using STXM. **Fig 6.12a** presents the STXM images at 933 eV for the Cu nanoparticle sample after CO_2R reactions. A good nanoparticle structure,

with particles in size of 100-200 nm, is observed on the Au working electrode along with dendrites at the edge of the Au electrode (**Fig 6.12 a**) **Fig 6.12c** shows maps for Cu(0), Cu(I), Cu(II), and constant & the residual of the stack-fit using the literature reference spectra.[Jiang et al., 2013] The thickness scale (in nm) for each component is indicated by numbers at the upper and lower right of each map. Color-coded composite maps are shown in **Fig 6.12b**. The quantitative STXM mapping shows that these Cu particles mainly consist of Cu(0) with very little Cu(I) and Cu(II).

A comparison of results of STXM analysis of the Cu nanoparticles before and after CO_2R reaction is shown in **chapters 6.3** and **6.4.** As reported by others [Arán-Ais et al,. 2020], the morphology of the Cu particles changes during the CO_2R process. In addition, the content of Cu(I) decreases and that of Cu(0) increases, and dendrites grow at the edge of working electrodes. Such before / after studies give useful information but do not provide insight into what is happening to the Cu electrocatalysts during CO_2R reaction. *Ex situ* STXM studies before and after the CO_2R reactions show overall changes but one can only speculate the possible chemical and morphological changes occurring during the reaction. This motivated us to develop a device optimized for flow electrochemical *in situ* STXM studies in order to visualize what is happening to the electrocatalytic materials under the reaction conditions. These results are presented in **chapters 7** and **8**.

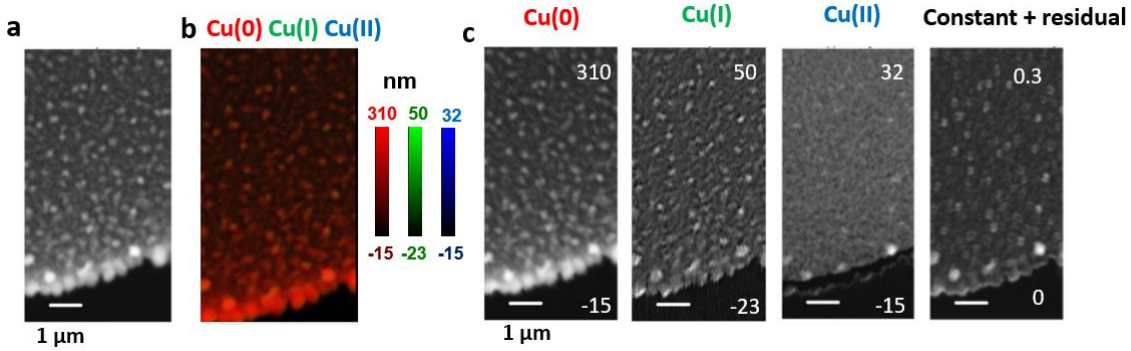

Figure 6.12 Stack-fit analysis of electrodeposited Cu particles after CO_2R.a) STXM image of the *ex situ* Cu sample at 933 eV, b**)** rescaled color-coded composite map of Cu(0) (red), Cu(I) and Cu(II) (blue), **c)** component maps for Cu(0), Cu(I), Cu(II), and residual of the stack-fit using reference spectra.[Jiang et al., 2013][Max_211113016]

Chapter 7

In-situ Studies of Copper-based CO_2 Reduction Electrocatalysts by Scanning Transmission Soft X-ray Microscopy

This chapter presents experimental results of in-situ STXM on electrodeposited Cu-based nanoparticle catalysts during electrochemical CO_2R process. The study provides detailed, quantitative results about the changes in the morphology and chemical structure (oxidation state) of the Cu-based catalytic nanoparticles as a function of applied electrode potentials.

This work has been re-submitted to the ACS Nano (after a major revision according to reviewer's comments) on Aug 31, 2023. The author list is: Chunyang Zhang, Haytham Eraky, Shunquan Tan, Adam P. Hitchcock, and Drew Higgins.

The author of this thesis and Haytham Eraky performed the in-situ STXM experiments. The author and Prof. A. P. Hitchcock analyzed the STXM data. Shunquan Tan and the author tested the CO_2 reduction performance of the Cu catalysts. The author wrote the publication, with assistance in later stages by Prof. A. P. Hitchcock and Prof. Drew Higgins.

The supplement information of the publication is put in Appendix E.

In-situ Studies of Copper-based CO_2 Reduction Electrocatalysts by Scanning Transmission Soft X-ray Microscopy

Chunyang Zhang,[1,2] Haytham Eraky,[2] Shunquan Tan,[1] Adam Hitchcock[2] and Drew Higgins[1*]

1. Chemical Engineering, McMaster University, Hamilton, ON, Canada, L8S 4M1

2. Chemistry & Chemical Biology, McMaster University, Hamilton, ON, Canada, L8S 4M1

Abstract

A micro-fluidic enabled electrochemical device has been developed to investigate electrochemically active nanomaterials under reaction conditions using *in-situ* scanning transmission soft X-ray microscopy (STXM). *In-situ* STXM measurements at the Cu 2p edge were conducted on electro-deposited Cu catalysts under electrochemical CO_2 reduction (CO_2R) conditions. The study provides detailed, quantitative results about the changes in the morphology and chemical structure (oxidation state) of the catalytic nanoparticles as a function of applied electrode potentials. The electrochemically deposited Cu nanoparticles initially contain both Cu(0) and Cu(I). As an increasingly cathodic potential is applied, the Cu(I) species gradually convert to Cu(0) over the potential range of +0.4 to 0 V versus the reversible hydrogen electrode (V_{RHE}). During this process, Cu(I) particles of various sizes are converted to metallic Cu at different reaction rates and at slightly different electrode potentials, indicating a degree of heterogeneity in the electrochemical response of discrete particles. At CO_2R relevant potentials, only metallic Cu is observed, and the morphology of the particles is fairly stable within the spatial resolution limits of STXM (~ 40 nm). We also report *in-situ* STXM studies of a working electrode with relatively thick Cu-based electro-deposits. The spatially resolved chemical analysis identified that Cu-oxide species can persist under CO_2R conditions, but only when the catalytic nanoparticles are electronically isolated from the working electrode and therefore are catalytically irrelevant. In summary, *in-situ* STXM is presented as a technique to gain advanced morphological and spatially-resolved chemical structure insight into electrochemically active nanomaterials, which was used to provide improved understanding regarding Cu nanomaterial catalysts under CO_2 reaction conditions.

* corresponding author: higgid2@mcmaster.ca

TOC graphic/figure

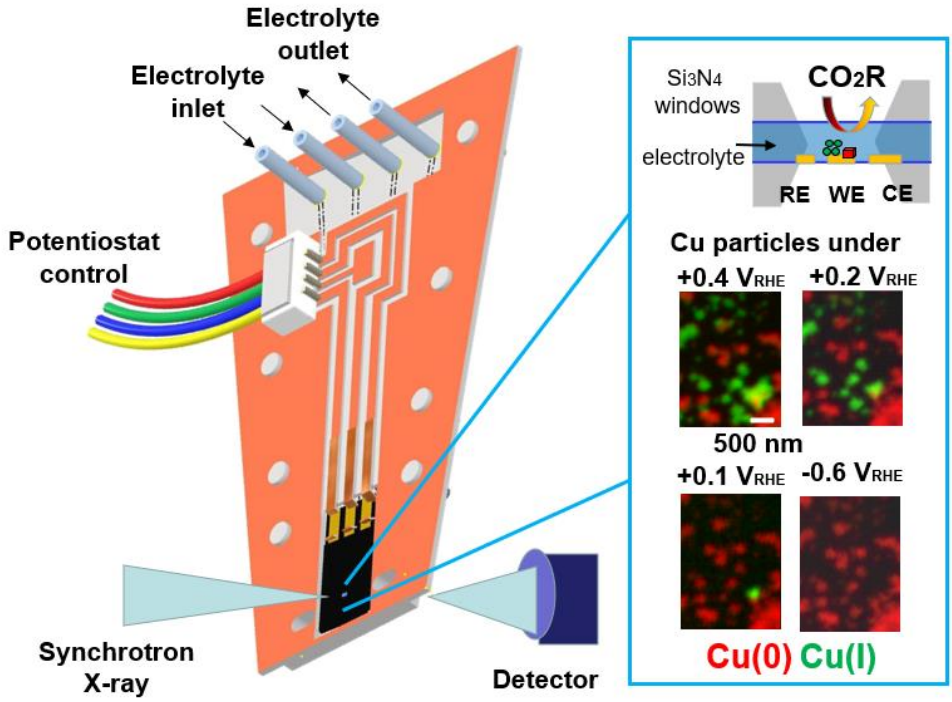

7.1. INTRODUCTION

Carbon dioxide electroreduction (CO_2R) is a promising route to generate valuable fuels and chemical feedstocks through the electrochemical conversion of CO_2 into hydrocarbon, alcohol, and carbonyl products.[1-4] With electricity generated by renewable energy resources such as wind and solar, electrochemical CO_2 reduction has the potential to become a sustainable approach to produce carbon-based chemicals and fuels, which could replace conventional petrochemical processes, thereby reducing greenhouse gas emissions and helping to protect the global environment. Among the different catalysts studied, copper (Cu) is known as the only material that can uniquely convert CO_2 into valuable multi-carbon products (C_{2+}) in appreciable quantities.[5-7] Unfortunately, despite much progress in recent years, the poor conversion efficiency, limited control of product distribution, and low stability of Cu-based electrocatalysts limit large-scale application of CO_2R. [8-9]

Improved understanding of Cu catalysts during electrochemical CO_2R is crucial for the development of high-performance, selective and practical electrocatalysts, yet there remains debate over the nature of active site structure(s) and their evolution under reaction conditions. For example, the presence of oxidized Cu (Cu(I) and/or Cu(II) species) or subsurface oxygen during electro-reduction has been suggested to improve CO_2R activity and steer the selectivity towards C_{2+} products such as ethanol and ethene.[10-12] However, other studies have refuted the presence of non-zero-valent Cu species under the electrochemically reducing conditions required for the reaction.[13-15] Morphological changes of Cu electrocatalysts during the CO_2R process have also been demonstrated, leading to rapid restructuring of catalytic structures which correlate with observed changes in activity and selectivity.[16,17] Overall, the morphology and chemical structures present in Cu catalysts change as a direct function of the local reaction environment and applied potential, which draws into question the suitability of using *ex-situ* characterization techniques to study Cu catalyzed CO_2R processes. This has motivated the development and application of *in-situ/operando* spectroscopy, microscopy and spectro-microscopy techniques to provide real-time and same-position characterization of working catalysts under electrochemical reaction conditions.[18-21] *In-situ* transmission electron microscopy (TEM) has been used as an i*n-situ* method for studying CO_2R electrocatalysts due to its excellent spatial resolution on the order of a few to tens of nanometers that enables imaging of the morphology of an electrocatalyst and how it evolves under reaction conditions.[16,17,22-25] *In-situ* TEM has

also been coupled with select area electron diffraction to identify crystalline phase structures present under reaction conditions.[16,17,22, 23] While TEM instruments are commonly equipped with EELS core level electron energy loss spectroscopy (EELS) capabilities that can provide spatially resolved chemical speciation, conducting EELS under *in-situ* electrocatalysis conditions is challenging due to strong electron-liquid interactions that lead to spectral distortion. This challenge provides opportunity for the development and implementation of alternative techniques that can simultaneously provide spatially resolved imaging of the morphology and chemical structures present in materials under reaction conditions.

In this work, we have used *in-situ* soft X-ray scanning transmission X-ray microscopy (STXM) [26-35] to characterize Cu electrocatalysts in a micro-chip electrochemical cell designed to achieve electrolyte flow under applied electrochemical potentials which closely resemble the conditions experienced by Cu particles in a laboratory-scale CO_2R reactor. STXM is a synchrotron-based spectro-microscopic technique that can simultaneously provide microscopic imaging of catalyst morphologies alongside spatially resolved (~50 nm spatial resolution) [36, 37] spectroscopic characterization through near edge X-ray absorption fine structure (NEXAFS) spectroscopy [36] to enable quantitative, chemically selective imaging. This can overcome some of the limitations of techniques such as *in-situ* diffraction [38] or *in-situ* X-ray absorption spectroscopy [39-41] measurements that provide only bulk-averaged characterization and no morphological insight. It can also complement *in-situ* electron microscopy [16, 17, 22-25, 42, 43] which provides region-specific morphological characterization at extremely high spatial resolution but limited insight into local chemical structures owing to the difficulty of performing high-resolution electron energy loss spectroscopy in the presence of a liquid electrolyte.

By utilizing a microfluidic-based flow electrochemical micro-chip reactor, *in-situ* STXM was used to characterize the morphology and chemical structure(s) present in electrodeposited Cu particles as catalysts under electrochemical CO_2 reduction conditions as a function of time and electrode potential. The micro-fluidic based electrochemical device enabled controlled electrolyte flow and could achieve an aqueous electrolyte thickness < 2 μm [34, 35] to enable soft X-ray transmission-mode measurements. *In-situ* STXM measurements provided a detailed quantitative

evaluation of particle evolution as a function of local chemical environments and applied potential. In this study the electro-deposited Cu particles are initially comprised largely of Cu(I) species that convert to metallic Cu (denoted as Cu metal or Cu(0)) at potentials ~0.2 V more positive than the onset of CO_2R. Significant changes in the particle morphology accompany the reduction of Cu-oxide species into metallic Cu. We also identify conditions where Cu-oxide species persist under reducing electrochemical CO_2R conditions and find that this is an artifact due to electronic isolation of the Cu particles from the working electrode when thick electro-deposits are used. We find no evidence of kinetically or diffusion trapped Cu-oxide species in catalytically relevant particles with electronic connectivity to the electrode. Overall, *in-situ* STXM has enabled spectro-microscopic insight into the behavior of Cu catalysts under CO_2R conditions. The techniques reported here can be readily translated to other electrochemical materials/processes to gain insight into the morphology and spatially resolved chemical structures present in electrochemically active materials.

7.2. RESULTS

7.2.1 Electrochemical CO_2 reduction evaluation.

The catalytic performance of electrodeposited Cu nanoparticles for CO_2 reduction in CO_2-saturated 0.1 M $KHCO_3$ was evaluated in a custom-built 2-compartment electrolyte membrane separated cell that has been reported previously [44, 45] (**Fig. S-1a**), with results displayed in **Fig. 7.1**. Details for catalyst electrode synthesis, experimental details, catalytic efficiency and product distribution measurements are presented in **Section 7.5.1**. At an electrode potential of -0.4 V_{RHE}, the deposited Cu sample showed a current density of -0.18 mA/cm^2 (**Fig. 7.1a**) with the majority of current going towards the production of H_2 with a Faradaic efficiency of 86% (**Fig. 7.1b**). Small amounts of other products (CO, hydrocarbons and alcohols) were detected, suggesting that CO_2R reactions have started to occur but with slow kinetics at this electrode potential. When the potential reached -0.6 V_{RHE}, the overall current density increased to -0.83 mA/cm^2 and there was a larger amount of CO_2R products (29% Faradaic efficiency) compared with at -0.4 V_{RHE}. At -0.8 V_{RHE}, the formation of CO_2R products dominated and the Faradaic efficiency for H_2 production was only 25%. This shows that the CO_2R reactions started to increase the overall reaction rate from -0.6 V_{RHE} and became the main electrochemical reactions at more negative potentials. In general, electrochemical CO_2R on Cu does not occur at appreciable rates at potentials more positive than ca. -0.65 V_{RHE}.[44] In this case, it is important to note that the Cu particles were

electro-deposited on Au, a well-known CO_2 to CO catalyst, to mimic the electrode configuration used for *in-situ* STXM measurements. It is the presence of Au that likely underlies the CO_2R products formed, as Au can produce CO electrochemically that can either be released as a product or subsequently reduced to alcohols and carbonyls by Cu at potentials as positive as -0.4 V_{RHE} [46] via a tandem catalytic reaction scheme.[47, 48]

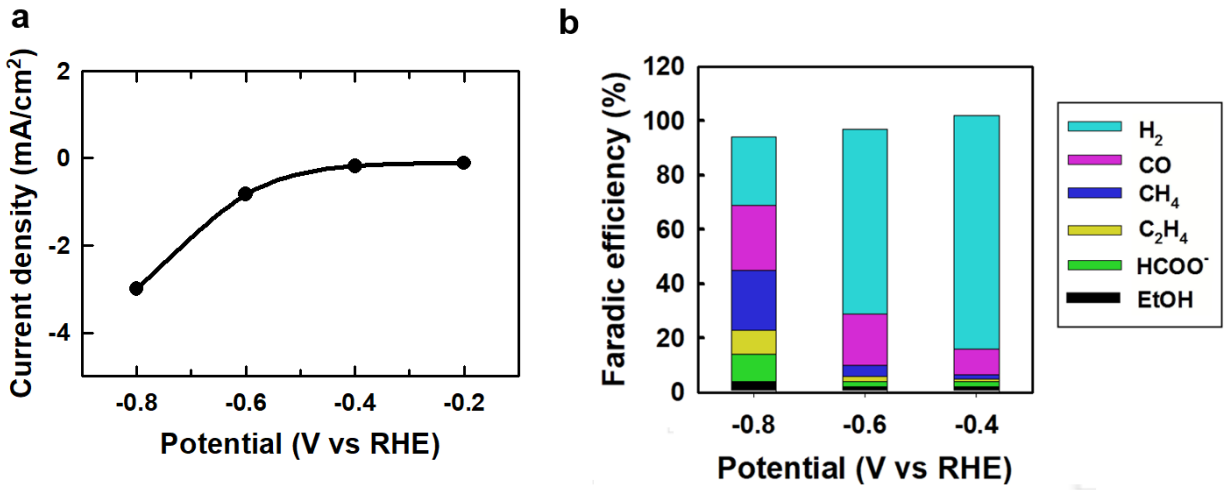

Figure 7.1. Evaluation of activity and selectivity for electrochemical CO_2 reduction by electrodeposited Cu catalysts in CO_2-saturated 0.1 M $KHCO_3$ in a custom-built 2-compartment membrane separated cell. (a) Overall geometric current density. **(b)** Faradaic efficiency towards various products under -0.4, -0.6 and -0.8 V_{RHE}.

7.2.2 *In-situ* STXM experiments in micro-fluidic electrochemical *in-situ* device

All *in-situ* STXM experiments were conducted using a novel micro-fluidic electrochemical *in-situ* device, which differs in several significant ways from existing commercial electrochemical liquid devices. (**Fig. 7.2**, the details are discussed in **Section 7.5.2**) [34, 35] This *in-situ* micro-fluidic device is a major improvement compared to our previously reported 3D-printed device. [30] It is more reliable with respect to electrolyte handling and can provide an electrolyte layer thickness of ~1.6 μm with a continuous flow of 25 μL/h, which provides good ionic conductivity while being thin enough for STXM studies at the Cu 2p edge (**Section S-5, Fig. S-5**). A relatively low flow rate (25 μL/h) was used to avoid bulging of the SiNx window that would result in increased electrolyte thickness. The 25 μL/h flow rate is such that the electrolyte in the electrochemically active area of the *in-situ* cell is changed every ~0.05 s. The two inlet and two outlet flow channels facilitate changing the electrolyte in minutes (rather than hours when

using single inlet/outlets) [30] and are very useful for reducing the inner pressure and removing air or gaseous product bubbles. The light weight of the device, due to the fabrication of components using plastic and polymers rather than steel, improves the stability and reduces vibration in STXMs when the sample is scanned. The *in-situ* micro-chip design includes a working electrode (WE), reference electrode (RE) and counter electrode (CE) that are all observable and measurable within the silicon nitride window area (**Fig. 7.2b, 2c**), as opposed to many *in-situ* electrochemical micro-chip designs that only provide visibility of the working electrode. Imaging all three electrodes is useful for being able to track unexpected electrochemical phenomena and to gain a holistic picture of all electrochemical processes occurring within the system. In this study the electrolyte flow was from the WE to the CE. **Fig. 7.2d** is a picture of the device inside the ambient STXM microscope at the Canadian Light Source (CLS) spectromicroscopy beamline, 10ID-1.

To ensure the local chemical environment present at the surface of the working electrode in our *in-situ* device closely mimics the conditions at the working electrode of the 2-compartment membrane separated cell used for CO_2R activity/selectivity evaluation, cyclic voltammetry (CV) of electrodeposited Cu particles in the two-compartment cell was collected and compared with the CV of electrodeposited Cu (prepared using the same methods) from the *in-situ* device (**Fig. S-1**). Qualitatively, the CV behavior was the same for the two cells, indicating a similar electrochemical reaction environment. Quantitatively the currents from the micro-chip electrode cell were several orders of magnitude lower, which is due to the reduced dimensions (geometric electrode area of ~2200 μm^2 in the *in-situ* cell versus 5.7 cm^2 in the reactor) but the current density was in fact higher (see **Fig. S-If**) . Ultimately, the measurements reported here demonstrate that the electro-deposited Cu catalysts have a very similar electrochemical response and thus similar local reaction environments in our *in-situ* STXM micro-chip reactor as in the two compartment cell used for CO_2R activity/selectivity evaluation. This ensures that the morphological changes and chemical states (oxidation states) observed and mapped by STXM spectro-microscopy are catalytically relevant.

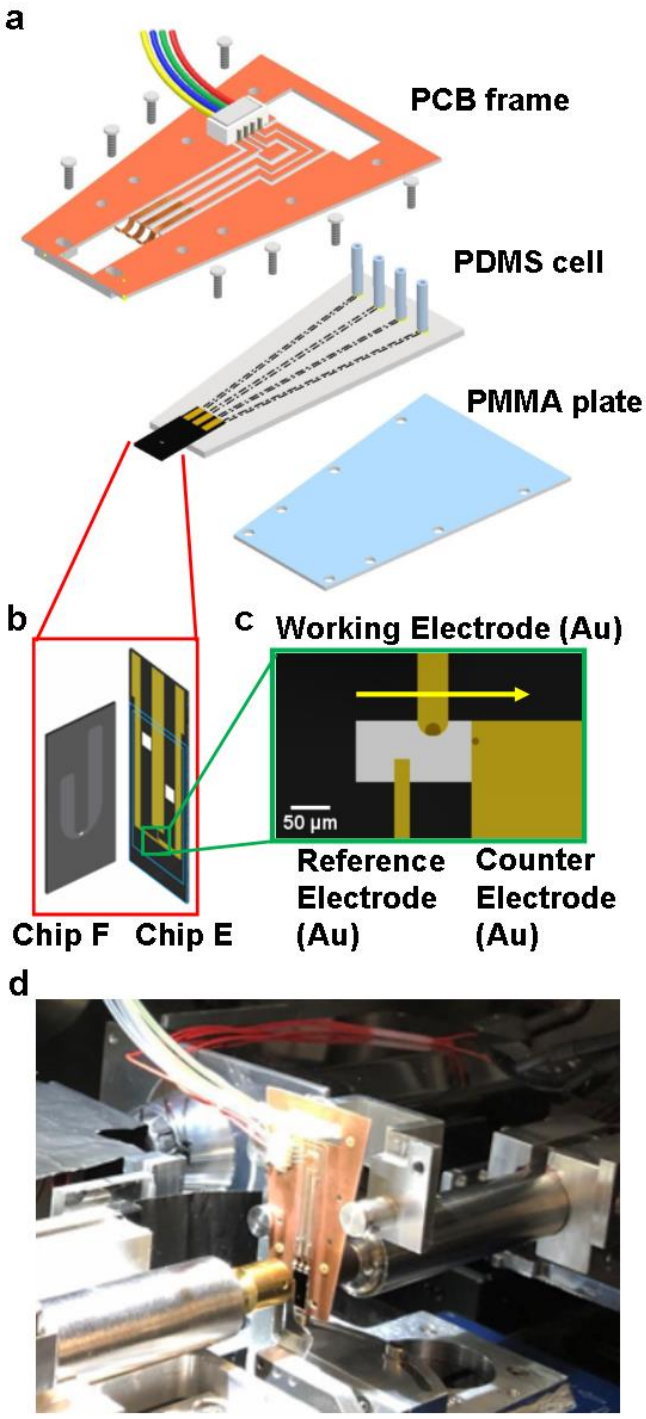

Figure 7.2 Microfluidic-based flow electrochemical device for *in-situ* STXM experiments. Schematics describing **(a)** *in-situ* device consisting of 3 parts: a machined printed circuit board (PCB), a polydimethylsiloxane (PDMS)/glass microfluidic cell equipped with the electrochemical *in-situ* chips (PDMS cell) and a poly(methyl methacrylate) backplate (PMMA plate) **(b)** *in-situ* chips consisting of 2 parts: base chip E containing 3 micro-Au-electrodes and spacer chip F with a pre-deposited 1 µm spacer

defining the height of the electrolyte flow channel within the micro-chip setup. **(c)** 3 micro-Au-electrodes region on base chip E. The Si_3N_4 window area is 240 μm wide and 100 μm high. The thickness of the Si_3N_4 windows are 100 nm (base chip E) and 50 nm (spacer chip F). The areas used for STXM studies (dark circles on working and counter electrodes) are 20 μm diameter and have a coating consisting of 5 nm Cr and 15 nm Au. The arrow indicates the direction of electrolyte flow. **(d)** Photo of the device inside the CLS ambient STXM.

7.2.3 *In-situ* STXM of electrodeposited Cu particles

Cu particles were electrodeposited from a 5 mM $CuSO_4$/KCl solution onto the Au working electrode of the custom-designed *in-situ* STXM device using multiple CV scans as described in **section 7.5.4**. The deposition of Cu-based particles was confirmed by measuring STXM transmission images at 933.5 eV, the peak Cu 2p X-ray absorption energy for both Cu(I) and Cu(0) species. As shown in **Fig. 7.3a**, the electrodeposited Cu typically consisted of particles ranging in size from tens of nm to ~0.8 μm, distributed across the Au-coated working electrode. After Cu particle deposition, a four-energy (4-E) Cu 2p STXM stack was recorded at a region showing well-defined Cu particles (see inset of **Fig. 7.3a**) to identify the composition of the electrodeposited Cu particles. This STXM stack measurement probes the catalyst at four specific photon energies which were carefully chosen to directly identify and map the oxidation states present in the Cu-based particles while enabling significantly accelerated measurements versus recording a stack measurement at closely spaced energy values across the Cu 2p edge. The stack was fit using the reference spectra of Cu(0) and Cu(I) (**Fig. 7.3b**) to generate component maps for each species (**Fig. 7.3c, Fig. 7.3d,** **Fig. S-7**). The component maps were then combined, using rescaling within each color, to generate color-coded component maps such as the one shown in **Fig. 7.3e**. The intensity scales in **Fig. 7.3c** and **7.3d** indicate the thickness in nm of the indicated species. To verify the analyses, spectra of the Cu(0) and Cu(I) regions were extracted and compared with reference spectra (**Fig. S-8**). The extracted spectra from Cu(0) and Cu(I) regions correctly showed that each species was the dominant component.

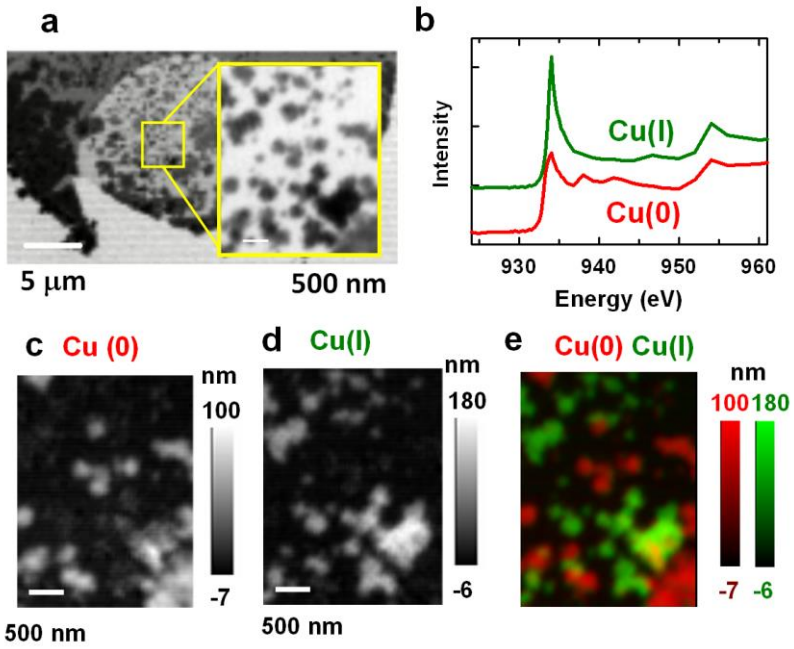

Figure 7.3. Illustration of STXM investigation of *in-situ* electrodeposited copper particles. (a) transmission image at 933.5 eV. **(b)** Cu 2p X-ray absorption spectra of Cu(0) (Cu metal) and Cu(I) from Cu_2O. Quantitative component maps of **(c)** Cu(0), and **(d)** Cu(I), derived from fitting reference spectra to a 4-E stack. **(e)** Color coded composite (rescaled) of the Cu(0) (red) and Cu(I) (green) maps.

7.2.4 Quantitative *in-situ* STXM on Cu particle during CO_2R

After electrodeposition of the Cu particles, the electrolyte was changed from 5 mM $CuSO_4$/KCl to CO_2 saturated 0.1M $KHCO_3$ (**Section 7.5.5**). Chronoamperometry holds at various potentials (+0.4, +0.2, +0.1, 0, -0.1, -0.2, -0.4, -0.6 V_{RHE}) were applied in sequence, with a 30 s hold at +0.4 V_{RHE} applied between each new electrode potential to ensure the catalyst was in the same starting state. **Fig. 7.4a** plots the current density obtained from chronoamperometry as a function of applied potential during the in-situ STXM measurements. **Fig. 7.4b** depicts the electrode potential profile used throughout the process. At each applied potential, two STXM images (image 1 and 2 at 933.5 eV, ~ 3 mins for each), a fast 4-energy STXM stack scan (4-E stack, 920, 933.5, 937 and 960 eV, ~7 mins) and a complete Cu 2p STXM stack scan (full stack, 53 energies from 920 to 965 eV ,~30 min) were conducted. Collecting two STXM images, one at the start of the measurements and one at the end, enabled us to track the morphological changes that occurred over the course of the measurements. The results from the 4-E stack and the full stack showed the evolution of the morphology and oxidation state of the Cu particles on different time scales, with the 4-E stack

covering the first ~3-10 min of the measurements and the full stack covering ~10-40 min after the specified electrode potential was applied.

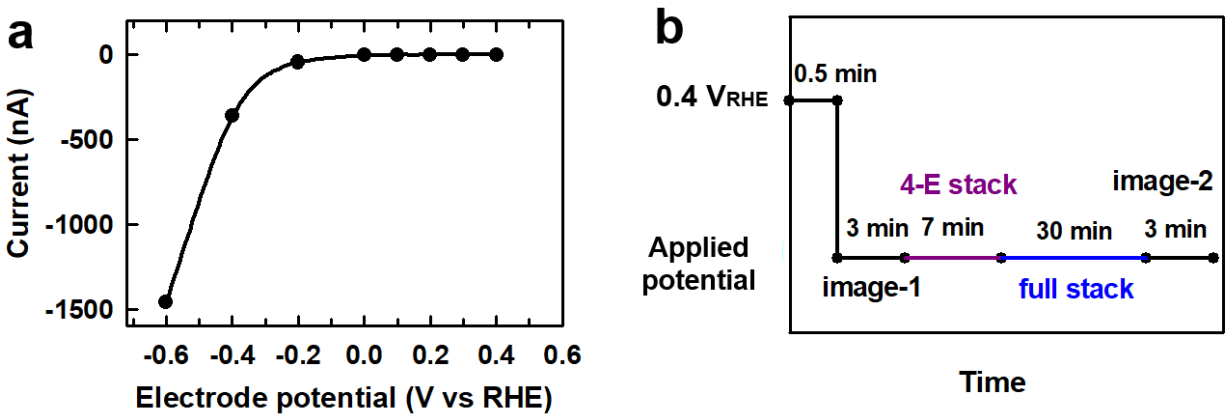

Figure 7.4 *in-situ* STXM studies of Cu particles as a function of potential. (a) Average current at various potentials during chronoamperometric measurements in the *in situ* device. **(b)** Illustration diagram to show the STXM measurements at each applied potential.

Figure 7.5 presents the results collected on the Cu particles under CO_2R conditions following this protocol . It includes **STXM images 1** and **2** alongside colour-coded composite maps of the Cu(0) and Cu(I) species obtained from analysis of the 4-E and the full stacks at potentials ranging from +0.4 to -0.6V_{RHE}. The complete STXM results are presented in **Section S-8, Fig. S-9**. The morphology and oxidation states of the Cu particles were observed during different time periods (0-3, 3-10, 10-40, 40-43 min) under various potentials. From +0.4 to +0.2 V_{RHE}, the Cu(I) particles reduced in size by an extent proportional to their original size. It is easiest to observe the changes of large Cu(I) particles in **region A1** (outlined by a blue square on the 4-E color coded map at +0.4 V_{RHE}). The particles in this region were inter-connected at +0.4 V_{RHE} , but at +0.2 V_{RHE} became smaller in size and more discrete from the Cu agglomerates. For the very small Cu(I) particles outside **region A1**, it was hard to observe size reduction due to the limited spatial resolution. Furthermore, no apparent particle size reduction occurred at the Cu(0) particles. The structural shrinking of Cu(I) particles has been similarly reported by other researchers,[49] most likely arising due to the structural contraction from removal of the oxygen atoms in Cu-oxide. Moreover, from +0.4 to +0.2 V_{RHE}, the amount of Cu(I) present in the particles was reduced to a certain extent. After applying a more reducing potential of +0.1 V_{RHE}, conversion of most of the Cu(I) to metallic Cu(0) was observed, with Cu(I) species found to reduce over a timescale of minutes, as seen by comparing the slightly higher portion of Cu(I) particles present in the 4-E

stack (collected over the first 3-10min of measurement) versus the full stack measurement (collected over the first 10-40min of measurement). These results show that not all of the Cu(I) species convert to metallic Cu at the same time, despite the fact that all particles are nominally experiencing the same applied electrode potential. The Cu(I) species that remained at +0.1 V_{RHE} continued to reduce in size when the electrode potential was reduced to 0 V_{RHE}. No Cu-oxide species were observed after several minutes at this electrode potential. Ultimately, these results demonstrate that the reduction of Cu(I) happens at various times and electrode potentials for different particles, but at electrode potentials from 0 to -0.6 V_{RHE}, only Cu(0) species remain. In addition, after complete reduction to Cu(0) species, the Cu particles largely maintained the same morphology during ~43 mins of CA at -0.6 V_{RHE} under CO_2R conditions.

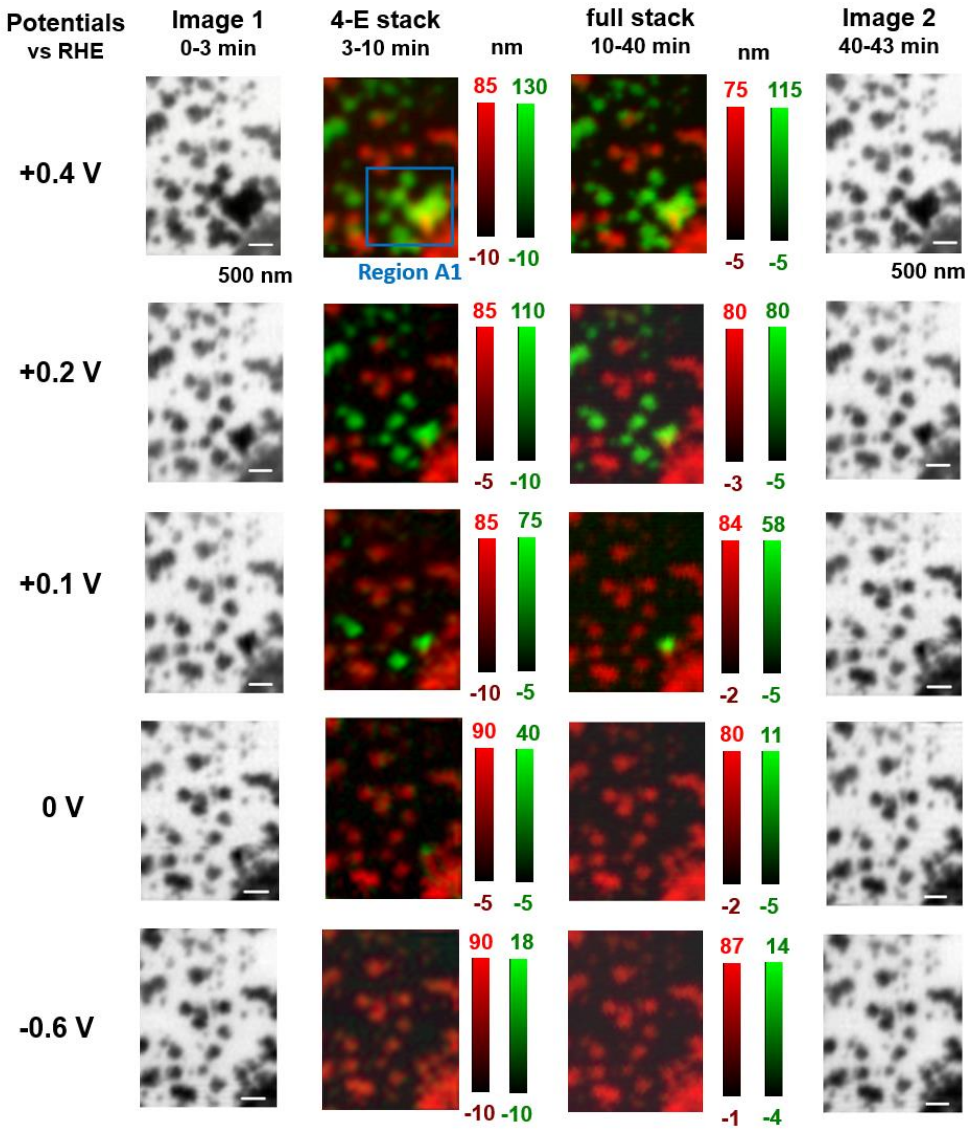

Figure 7.5. Evolution of Cu particle morphology and chemistry with decreasing potential. (Left 1) image 1 at 0-3 min under applied potentials. **(Left 2)** Color coded composites of Cu(0) (red) and Cu(I) (green) maps at the indicated potentials (vs RHE) derived from 4 energy stacks (3-10 min). **(Right 2)** Color coded composites of Cu(0) (red) and Cu(I) (green) maps at the indicated potentials (vs RHE) derived from 54 energy full stacks (10-40 min). **(Right 1)** image 1 at 40-43 min under applied potentials. The dwell time for all *in-situ* STXM measurements was 3 ms/pixel.

Due to the use of OD1 reference spectra (**Fig. 7.3b**), the thickness of the Cu(0) and Cu(I) particles was determined and could be used along with the lateral area to calculate the volume of the Cu(0) and Cu(I) species. **Section S-9, Fig. S-10** shows an example of the calculation of the volume of Cu(0) and Cu(I) at +0.4 V_{RHE} from the full stack results. The calculated volumes at each potential

are shown in **Table S-2**. The volume of Cu species under various potentials from +0.4 to -0.6 V_{RHE} were calculated by the same method, with results shown in **Table S-3**. The volume ratios of Cu(0) and Cu(I) at different time periods after specific potentials were applied are displayed in **Fig. 7.6a**. The Cu(0) particles maintain the same oxidation state at -0.2, -0.4 and -0.6 V_{RHE} (**Fig. 7.6**, **Fig. S-9**), and the volume ratios were calculated from the full stack (10-40 min) at these three electrode potential values. At +0.4 V_{RHE} , the Cu particles were relatively stable, with a composition of 43(±4)% Cu(0) to 57(±6)% Cu(I) during the first 3-10 min of measurement, and 40(±4)% Cu(0) to 60(±6)% Cu(I) during the first 10-40 min of measurement. When the potential was reduced from +0.4 to 0 V_{RHE}, the Cu(I) fraction gradually decreased to < 1%. At all potentials more negative than 0 V_{RHE}, the Cu particles consisted of pure Cu(0) within the measurement precision (>99% Cu(0)).

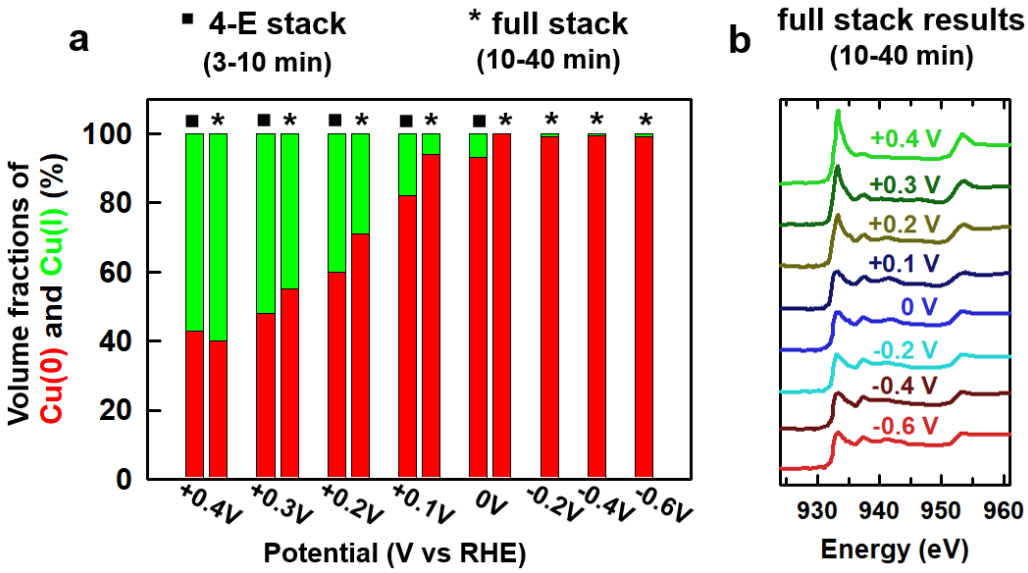

Figure 7.6. Quantitative analysis of composition from Cu 2p spectroscopy. (a) Percentage volume composition of Cu(I) and Cu(0). **(b)** Average spectra of the particles from the 53-energy full stacks at various potentials.

The calculated volumes presented in **Fig. 7.6a** are consistent with the STXM component thickness maps shown in **Fig. 7.6** and **Fig. S-9**. The volumes and volume ratios of Cu(0) and Cu(I) quantitatively show the transition from Cu(I) to Cu(0) during the electrochemical process.

Moreover, this can also be straightforwardly confirmed by examining the average spectrum of all the Cu particles at each of the potentials, as shown in **Fig. 7.6b**. These spectra show that, over the potential sequence, and particularly between +0.2 and 0 V_{RHE}, the particles change from primarily Cu(I) to completely metallic Cu(0).

7.3. DISCUSSION

Our *in-situ* STXM results show that the initially formed, mixed oxidation state Cu particles are converted to exclusively metallic Cu(0) between +0.4 and 0 V_{RHE} − electrode potentials that are several hundred millivolts more positive than where the CO_2R reaction commences. During this reduction process, changes of morphology and oxidation states of the Cu particles were observed during different time periods (0-3, 3-10, 10-40, 40-43 min). Our results show that conversion of some portions of the Cu(I) to Cu(0) is a relatively slow process, continuously occurring over the time period of a few minutes to tens of minutes as the chronoamperometric electrode potential holds are applied. At each potential between +0.4 and 0 V_{RHE}, the Cu(I) particles gradually reduced in size and converted to Cu(0) particles. Moreover, some of the Cu(I) particles completely disappeared during this process rather than converting to metallic Cu, showing there are other reactions in addition to Cu(I)/Cu(0) conversion (see **region A1** in **Fig. 7.5**). Furthermore, some predominantly Cu(I) particles reduced to metallic Cu at different rates at the same electrode potential or did not reduce fully until more negative electrode potentials were applied (**Fig. 7.5**), suggesting each Cu particle can have significantly different electrochemical responses even under the same applied reaction conditions. These observations show complicated conditions that can be encountered when characterizing Cu-based CO_2R catalysts. Others studies have characterized the Cu materials during the CO_2R process using different *in-situ* spectroscopic techniques, and found results similar to **Fig. 7.6b**, whereby Cu (I) decreases and Cu(0) increases as the potential is decreased.[5, 45] However, the use spectro-microscopy in this study gave quantitative oxidation state analysis and mapping at a sub-50 nm spatial scale, thereby probing the process of Cu(0)/Cu(I) conversion and CO_2R with both morphological and chemical information.

At potentials lower than -0.4 V_{RHE} where CO_2R occurs, only Cu(0) species were observed, which we identify as the active site for CO_2R. The Cu(0) particles were stable during the CO_2R reactions with no detectible changes in oxidation state and morphology of particles within the spectral sensitivity and spatial resolution of STXM (~40 nm). According to the calculated Cu

compositions (**Fig. 7.6a**) the particles are >99% Cu(0) at electrode potentials below 0 V_{RHE}. This strongly supports the viewpoint that there are no significant amounts of non-zero-valent Cu species under the electrochemical reducing conditions for CO_2R reaction.[13-15, 49] The results and capabilities of the *in-situ* STXM technique brought us to question the assertion across the literature that non-zero-valent Cu species can persist under CO_2R conditions and impact the catalytic processes.[13-15] While every CO_2R catalyst, electrode and reactor leads to different local chemical reactive environments, we aimed to probe the conditions upon which Cu-oxide species may exist under the CO_2R conditions employed in our *in-situ* setup. To accomplish this, in our early *in-situ* studies, [34] we prepared a working electrode where we did not limit the amount of Cu that was electro-deposited, leading to the formation of micrometer scale deposits extending off the surface of the working electrode. This preparation may more closely mimic the thicker catalyst layers used in CO_2R flow cells or membrane electrode assemblies. A STXM image of this electrode is shown in **Fig. 7.7a**. The chemical mapping of the working electrode after electrodeposition is shown in **Fig. 7.7b**, while **Fig. 7.7c** shows Cu oxidation state maps at 3 different potentials**.** Upon application of potentials of +1.3 and +0.7 V_{RHE}, the system consisted of a mixture of Cu(0), Cu(I) and Cu(II) species, as expected for Cu-based particles under these electrochemical potentials.[50] Interestingly, after applying a negative electrode potential of -0.5 V_{RHE}, a CO_2R relevant electrode potential, a significant portion of the Cu(I) species remained in the electrode structure. More details of these measurements are provided elsewhere.[30] Under these electrochemically reducing conditions the Cu-oxide species persisted, particularly at locations that extended away from the Au-based working electrode. These regions of the catalyst layer remained unresponsive to changes in electrode potential. In contrast, Cu particles in close proximity to the underlying Au-based working electrode were found to interchange between the metallic Cu(0) and Cu-oxide states as a function of electrode potentials that were more negative and more positive than the reversible potential of the Cu(0)/Cu(I) redox pair, respectively. This persistence of Cu-oxide species at potentials as low as -0.5 V_{RHE} contrasts the results shown in **Fig. 7.3**, whereby all Cu species were in metallic form at potentials more negative than 0 V_{RHE}. This observation, combined with the lack of electrochemical response observed for the thick catalyst layer regions, led us to conclude that the Cu-oxide species under CO_2R conditions persist because they are electronically isolated from the electrode and therefore have no relevance on electro-catalytic performance. In particular, there is no oxidation state change for the Cu materials located at the top region while the active Cu materials located at the bottom regions undergoes

oxidation state changes with varying electrode potentials. (**Fig. 7.7c**) Compared to the relatively thick Cu-based layer which more closely mimics the practical catalytic electrodes used CO_2R cells, Cu nanoparticles as the electrocatalysts are favorable due to their superior conductivity and electrochemical activity.

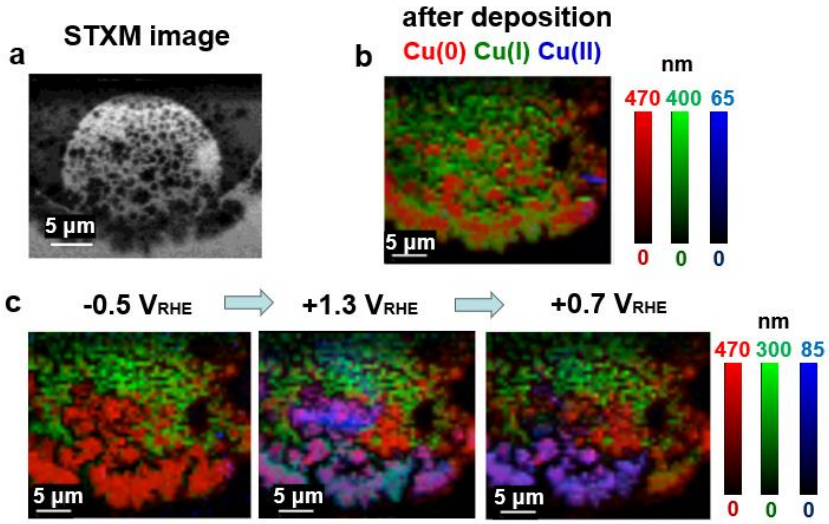

Figure 7.7. *In-situ* STXM to show electronically isolated Cu materials. (a) STXM image (935 eV) for the Cu materials electrodeposited on the whole WE. (**b**) Cu oxidation state maps of Cu(0) (red), Cu(I) (green) and Cu(II) (blue) of electrodeposited thick Cu materials. **(c)** Cu oxidation state maps of Cu(0) (red), Cu(I) (green) and Cu(II) (blue) at -0.5, +1.3 and +0.7 V_{RHE} by sequence. More details are presented in reference [34].

The results presented in this work exemplify one of the significant advantages of *in-situ* STXM over bulk averaged measurement techniques (such as non spatially resolved X-ray absorption spectroscopy). The latter have shown the presence of oxidized Cu species under CO_2R conditions,[14, 15] but cannot provide spatial distinction between regions containing metallic Cu and/or Cu-oxide to validate whether the Cu is electronically active or electronically isolated. The question then arises if small amounts of Cu-oxide can persist under electrochemical CO_2R conditions by being either kinetically or diffusion trapped within the particles. We believe Cu oxides cannot persist if they are electronically active. Other *in-situ* microscopic techniques, including selected area diffraction in (scanning) transmission electron microscope (TEM or STEM), [16, 17, 22] have shown that the nanoscale morphology Cu-based particles can rapidly evolve under CO_2R conditions, rendering it very difficult for subsurface Cu-oxide species to remain protected/entrapped at conditions where, thermodynamically, they are unlikely to persist.[51]

However, based on the limited spatial resolution (~50 nm) of the *in-situ* STXM used in this work, it is difficult to effectively monitor the nanoscale re-construction and evolution of Cu particles during CO_2R reactions, a key limitation of current STXM capabilities. This has motivated us to pursue improving the spatial resolution of *in-situ* soft X-ray spectromicroscopy by performing *in-situ* spectro-ptychography which provides similar chemical mapping to STXM but at ~3 times better spatial resolution.[52, 53] In our recent *in-situ* spectro-ptychography study[53] chemical changes and morphological evolution of a single ~200 nm sized Cu catalyst particle were tracked from formation to CO_2R conditions, demonstrating the ability to significantly improve upon the spatial resolution limits of STXM and advance *in-situ* soft X-ray microscopy beyond the state-of-the-art measurements reported in the present work.

7.4. CONCLUSIONS

In-situ STXM measurements on electrodeposited Cu particles provided detailed, quantitative insight into the morphology and spatially resolved chemical structures present in these catalysts under electrochemical CO_2R conditions. At electrode potentials from +0.4 to 0 V_{RHE}, predominantly Cu(I) particles were converted to metallic Cu. Differences were observed in the electrode potential and/or the rate (time) it took for the particles to become metallic, suggesting that discrete Cu particles have a high degree of heterogeneity in terms of their electrochemical response. However, at CO_2R relevant potentials more negative than 0 V_{RHE}, all of the particles were observed to be completely reduced to metallic Cu within the experimental precision of the measurements (>99%). Very little particle reconstruction was observed, possibly due to the limited spatial resolution capabilities (~40 nm) of the technique. By preparing electrodes with relatively thicker Cu-based electro-deposited catalyst layers, we show that a significant portion of the Cu-species can remain in oxidized form at potentials as low as -0.5 V_{RHE}. These Cu-oxide regions in the catalyst layer were found to remain unresponsive to electrode potential, indicating that they were electronically isolated from the underlying working electrode substrate. Thus, we highlight an advantage of *in-situ* STXM over bulk-averaged *in-situ* measurement techniques in that it can provide spatial and spectroscopic distinction between particles that are electronically connected to the electrode and those that are isolated, rendering them electro-catalytically irrelevant. In this sense, *in-situ* STXM, enabled by our custom designed micro-fluidic electrochemical device, provides a means for achieving advanced understanding of the morphology and nanometer-scale spatially resolved chemical structures present under CO_2R

electrochemical conditions. *In-situ* STXM is suitable for electrocatalysis and energy storage (battery) research. The spatial resolution and other capabilities of the technique can be further improved through technological innovations, such as spectro-ptychography and more rapid data acquisition to better follow electrochemically induced changes. For example we recently demonstrated a 3-fold improvement in spatial resolution with similar chemical sensitivity as STXM and improved sensitivity to morphological changes, by performing *in-situ* spectro-ptychography on this system.[53]

ACKNOWLEDGMENTS

Measurements were made at the ambient STXM on beamline 10ID1 at the CLS. CLS is funded by CFI, NSERC, NRC, CIHR, the Government of Saskatchewan, and the University of Saskatchewan. We thank the beamline staff at CLS-SM (Jian Wang). Thanks to: Martin Obst and Pablo Ingino (University Bayreuth); Paul Gatt and Michael Clarke (Chemical Engineering, McMaster); Prof. Jose Moran-Mirabal and their students (Chemistry & Chemical Biology, McMaster) for assistance with device development and fabrication. This research was supported by the Natural Sciences and Engineering Research Council (NSERC) Discovery Grant program, the National Research Council of Canada (NRC) Materials for Clean Fuels Challenge program and TotalEnergies.

7.5. EXPERIMENTAL SECTION

7.5.1 Catalysis performance characterization.

The activity and selectivity of the Cu particles used in this work towards electrochemical CO_2R was tested. Cu particle coated working electrodes were prepared by electrodepositing a solution of 5mM $CuSO_4$ and 5mM KCl on an Au coated graphite foil by running three cycles of cyclic voltammetry (CV) from 0 V to +0.4 V versus reversible hydrogen electrode (V_{RHE}) with a scan rate of 20 mV/s. This is identical to the process used to prepare Cu catalysts in the *in-situ* STXM cell. The electrodeposited Cu electrode was used as the working electrode for electrochemical CO_2 reduction and tested in a custom-built 2-compartment electrolyte membrane separated cell that has been reported previously.[40, 41] (**Fig. S-1a**) The geometric area of the working electrode was 5.7 cm^2. The electrolyte compartments of the working and counter electrode were filled with CO_2 saturated 0.1M $KHCO_3$ (5 mL). CO_2 was flowed continuously through the

catholyte and anolyte chambers at 20 sccm throughout the course of the experiment. A Pt foil was used as the counter electrode and an Ag/AgCl electrode was used as the reference electrode. The Ag/AgCl reference electrode was calibrated versus a home-made reversible hydrogen electrode (RHE), and the reported potentials are versus RHE. The catholyte and anolyte chambers were separated by an ion exchange membrane (Selemion AMV, AGC Inc). Catalysts were tested by chronoamperometric measurements at various electrochemical potentials, -0.2, -0.4, -0.6 -0.8V_{RHE}. The effluent gas from the catholyte compartment was fed to a gas chromatograph (GC) and the collected electrolyte was tested using nuclear magnetic resonance (NMR) for liquid product identification and quantitation to determine Faradaic efficiencies. CV was conducted to check the potentials of Cu oxidation and reduction peaks in CO_2 saturated 0.1M $KHCO_3$ in the 2-compartment membrane cell. (**Fig. S-1a**).

7.5.2 *In-situ* microfluidic-based electrochemical device.

Figure 7.1 presents the microfluidic-based flow electrochemical device used for *in-situ* flow electrochemical STXM experiments. The *in-situ* device consists of a machined printed circuit board (PCB), a polydimethylsiloxane (PDMS)/glass cell equipped with the electrochemical *in-situ* chips (PDMS cell) and a poly(methyl methacrylate) (PMMA) backplate (PMMA plate) (**Fig. 7.2a**).[34, 35] The microfluidic PDMS cell contains four flow tubes and micro-fluidic channels shown as dotted lines on PDMS cell, which serve as two inlets and two outlets to connect to the assembled *in-situ* micro-chip reactor (**Fig. 7.2b,** Norcada Inc, Edmonton, Canada, https://www.norcada.com). The flow tubes can be connected to one or more fluid circulation devices (we use syringe pumps, but pressure pumps could also be used) to establish a stable flow of one or more electrolytic fluids to the *in-situ* chips. Electrochemical reactions can then be performed by applying suitable potentials to the 3 electrodes on base chip E (**Fig. 7.2c**), which are connected to a potentiostat through the PCB traces and a 4-pin connector on the PC board. Spacer chip F (**Fig. 7.2b**) has a pre-deposited 1 μm spacer defining the height of the electrolyte flow channel within the micro-chip setup. The working electrode, counter electrode and reference electrodes on base chip E are all Au (**Fig. 7.2c**). The darker circles on the working electrode and counter electrode are regions that have been thinned out to reduce X-ray absorption arising from the electrode thickness. The Au reference electrode acts as a pseudo reference electrode, such that all potentials measured are V versus the Au pseudo-reference (V_{Au}). The open circuit potential (OCP) was stable (~ -0.048 ± 0.004 V_{Au}) in CO_2 saturated 0.1M $KHCO_3$ with electrodeposited Cu

on the Au working electrode (**Fig. S-2d**). External CV measurements conducted in a 2-compartment cell using a calibrated Ag/AgCl electrode (**Fig. S-1e**) enabled us to convert from potentials measured relative to the Au pseudo reference electrode to V_{RHE} using the well-defined Cu redox peaks. The calibration yielded a value of: $V_{RHE} = V_{Au} + 0.40$. All potentials reported in this work are relative to RHE, unless stated otherwise.

When the *in-situ* device is assembled, the PDMS/glass cell is kept in place in the machined PCB frame by a PMMA plate. Electrical connections between the on-chip electrodes and Cu traces on the PC board are made using Cu clips soldered to the PCB traces. For the experiments, the *in-situ* microfluidic-based flow electro-chemical device is connected to a potentiostat ((Emstat4, PalmSens) or Ivium PocketStat, https://www.ivium.com/instruments/) to control potential and monitor current while one or more of the fluid lines is connected to a syringe pump (New Era, https://www.syringepump.com/) to establish a stable electrolyte flow rate, typically 10 – 50 μL/hour.

7.5.3 *In-situ* device setup and mounting in STXM.

First, the electrolytes used in *in-situ* experiments are prepared and loaded into 1 mL syringes. Bubbles are removed by pushing/withdrawing the syringe. The syringe with the electrolyte is connected to the *in-situ* device using Tefzel tubes (Idex, www.idex-hs.com) with inner diameter of 0.040" and outer diameter of 1/16") [NB improved performance was found after these experiments by using a narrower 0.010" ID tubing]. The syringe plunger is pushed manually to fill the tubes with electrolyte. Then the filled tubing is connected to the assembled *in-situ* device and the syringe plunger is placed into the syringe pump. A flow rate of 25 μl/hr for 10 min is used to slowly fill the *in-situ* device with electrolyte. The filling process is always conducted under an optical microscope, in order to confirm that the electrolyte completely fills the window region.[**Fig. S-2**]. Once the 3-electrode region (**Fig. 7.2c**) is filled with the electrolyte, the *in-situ* device is connected to the potentiostat. The open circuit potential should be close to ~ +0.35 V_{RHE} and stable within ± 0.004 V, confirming proper connections and electrochemical activity. These procedures verify good electrical connections and steady electrolyte flow with no problems such as liquid leaking, channel blocking due to bubbles or cable disconnection.

Then the *in-situ* device is loaded into the STXM. First, the connections to potentiostat and syringe pump are disconnected to simplify device insertion into the STXM. The *in-situ* device, connected only to the electrolyte tubing, is moved with caution from the optical microscope to the STXM chamber and inserted through a 4.5'' flange. Note, since these measurements were first made, the fluid line and electrical connections have been modified to be implemented on a 2.75" conflat flange, which enables compatibility with most modern STXMs. In the chamber, the *in-situ* device is mounted in the 3-pin sample kinematic holder and then the potentiostat and syringe pump are re-connected. The syringe pump is turned on with a flow rate of 25 μl/hr to keep a stable electrolyte flow through the *in-situ* device. The electrolyte tubes and potentiostat cables are organized in the STXM chamber and stabilized using Kapton tape to attach them to a suitable position in the chamber to avoid interfering with STXM operations such as sample scanning.

After the *in-situ* device is loaded in the STXM, the air in the tank is replaced with He gas by displacing the air at a slow rate (~10 min). After achieving a plateau in X-ray transmission, the He gas flow is stopped and the STXM chamber is closed. Note that this procedure is routine at the CLS ambient STXM, but not possible at some other facilities, due to a minimum pressure requirement. STXM imaging was used to locate the SiN_x window (240 μm x 120 μm) and to make sure there are no bubbles in the 3-electrode area that occasionally occur in the process of moving and loading the *in-situ* device into the STXM. The signal from X-rays transmit through the SiN_x windows and electrolyte is measured and compared with the incident X-ray intensity measured in one of the holes in the *in-situ* device (**Fig. 7.2d**) in order to evaluate the absorption (optical density, OD), which in most spectral regimes is dominated by absorption by the water. Comparison to the known X-ray transmission properties of the SiN_x windows and water allows determination of the thickness of the electrolyte, which was between 2 and 5 μm, depending on the spacer used (0.5, 1, 1.5 μm), syringe pump flow rate, and ID of the electrolyte tubing. A thin electrolyte layer (as thin as ~1.6 μm) can be achieved . In this work a 1 μm spacer was used. If the electrolyte layer is thick (>4 μm), X-ray cannot transmit through the electrolyte and STXM cannot be performed. After the liquid thickness is measured, electrochemical experiments are performed on the 3-electrode area through the control of potentials and current using potentiostat.

7.5.4 Electro-deposition of Cu catalyst particles.

Copper nanoparticles were electrodeposited from a solution of 5mM $CuSO_4$ and 5mM KCl on to the Au working electrode of the *in-situ* micro-chip cell. The electro-deposition solution concentrations and conditions were chosen based on previous reports [16, 17] to target particles in the range of 300 – 500 nm diameter that are relevant for CO_2R and STXM measurements. After setting up the *in-situ* device as described in **Section 7.5.3**, the electrodeposition was carried out by performing three cyclic voltammetry cycles between 0 and +0.4 V_{RHE} with a scan rate of 20 mV/s. This is the same protocol as used in preparing the electrode for the catalyst performance measurements described in **Section 7.5.1**. The as-deposited Cu particles are then characterized using STXM to gain insight into the morphology and chemical structure (i.e., oxidation state) distributions (see **Section S-3, Fig. S-3**). STXM measurements at this step should be as fast as possible because some Cu particles will slowly disappear by dissolution into the 5mM $CuSO_4$ / KCl electrolyte which has a measured pH of 6.1.This could be caused by slow conversion of Cu(I) to Cu(II) in the mildly acidic environment under open circuit potential conditions (ca. +0.35 ±0.004 V_{RHE} under *in-situ* conditions) as Cu(I) is not stable at lower pH values, [54] followed by Cu(II) dissolution into the electrolyte. This phenomenon has been observed several times in our *in-situ* experiments.

Once a region with particles of suitable thickness (50 – 200 nm) and size (50 – 600 nm) is identified and oxidation states determined, the $CuSO_4$/KCl electrolyte is displaced by CO_2 saturated 0.1 M $KHCO_3$ for subsequent *in-situ* STXM experiments under CO_2R conditions. In the CO_2 saturated 0.1 M $KHCO_3$ electrolyte, the Cu particles are more stable as the pH is closer to neutral (pH 6.8). Therefore, changing the electrolyte from $CuSO_4$ /KCl to CO_2 saturated 0.1 M $KHCO_3$ is done as fast as possible to avoid loss of the deposited Cu particles.

7.5.5 *In-situ* STXM under CO_2R conditions

The CO_2 saturated 0.1 M $KHCO_3$ is prepared just before the *in-situ* STXM experiments by bubbling CO_2 gas into 0.1 M $KHCO_3$ solution for 20 mins in a septum sealed vial. After Cu *in-situ* electrodeposition (**Section 7.5.4**) the electrolyte is changed to CO_2 saturated 0.1M $KHCO_3$. Deionized water is first used to flush the $CuSO_4$/KCl out of the *in-situ* micro-chip device. Then the CO_2 saturated 0.1 M $KHCO_3$ electrolyte is continuously filled using a 25 µl/hr flow rate. Changing the electrolyte takes around 20 mins. After electrolyte changes, there is no STXM-

detectible Cu^{2+} signal in the electrolyte. *In-situ* STXM measurements were conducted using a series of chronoamperometry (CA) potential sequences. Before all measurements, CA at +0.4V_{RHE} was applied for 30 s (to ensure the catalyst was always in the same starting state) followed by a cathodic step to the electrode potential at which STXM was conducted. STXM measurements were conducted sequentially (with the +0.4 V_{RHE} for 30s in between each) at +0.4, +0.3, +0.2, +0.1, 0, -0.2, -0.4 and -0.6 V_{RHE}. The CA current-time plots are presented in **Fig. S-4.** During CA at each potential, the current was continuously recorded and several STXM measurements were made in sequence. The sequence consisted of: (1) STXM image at 933.5 eV; (2) 4-energy stack measurement that enabled differentiation between the different oxidation states of Cu present in the materials; (3) 53-energy Cu 2p stack; and (4) STXM image at 933.5 eV for comparison with the first STXM image measured. In all this took ~43 m at each potential which enabled time-dependent monitoring of morphology and chemical structure changes to the Cu particles under controlled electrode potentials. Potentials more negative than -0.6 V_{RHE} were not applied as bubble formation would render the STXM measurements unstable. Gas generation by CO_2R to gas phase products or water reduction to H_2 occasionally created large bubbles which occupied the 3-electrode region, leading to a disconnection of the working electrode that stopped the electrochemical reactions. Generally, electrode potentials less negative than -0.6 V_{RHE} did not generate gas bubbles in the *in-situ* setup. Following CA potentials and STXM measurement, CVs were collected (**Fig. S-1c**).

7.5.6 STXM measurements and analysis

STXM imaging and spectromicroscopy were performed using the spectromicroscopy beamline (SM) 10ID-1 at the Canadian Light Source (CLS, Saskatoon, Canada). Details of the ambient STXM, [55] beamline [56] and operating procedures[36] have been presented elsewhere. Briefly, the monochromatic X-ray beam was focused to a ~40 nm spot by a Fresnel zone plate (ZP). The sample was positioned at the focal point of the X-ray beam. Images were measured by (x,y) raster scanning the sample while recording the transmitted X-ray intensity pixel by pixel in a single photon counting mode using a phosphor/photomultiplier single X-ray counting detector. The energy scale was calibrated by recording the Ne 1s spectrum of Ne gas.[57]

Four types of STXM measurements were used in this work: STXM point scan, STXM image, STXM full stack, and STXM 4-energy (4-E) stack. The **STXM point scan** measures the

transmission spectrum at one or more points on a sample over a user specified photon energy range. In this work, point scans at the Cu 2p edge from 920 to 965 eV were measured at the position of one of the holes drilled through the *in-situ* device to obtain the incident X-ray (I_o) signal (**Fig. S-5a, b**). The difference in the X-ray intensity between the I_o spectrum and that measured through the electrolyte in the cell corresponds to the X-ray absorption by the SiN_x windows and the electrolyte (**Fig. S-5c**). If the material composition and density is known, the net X-ray absorption, given by OD = -ln(I/Io), is directly related to the thickness. After subtracting the OD of 150 nm SiNx, the remaining OD can be considered from the X-ray absorption of the electrolyte. The electrolyte is mostly water so the X-ray absorption properties of H_2O in the 900 – 1000 eV range were used to calculate the thickness of electrolyte in the window region, which was ~1.6 μm (**Section S-5**, **Fig. S-5d**). **STXM images** at a single photon energy were measured by scanning the sample while recording the transmitted X-ray intensity pixel by pixel. A **STXM full stack** involved a sequence of STXM images collected at various photon energies (also known as stacks [36]) to provide spatially resolved spectroscopic information about the sample. In this work, a 53 energy Cu 2p stack spanning 920 to 965 eV (taking a total of ~30 min) was used. A **STXM 4-energy stack** (4-E stack, ~7 min) was also used to conduct chemical speciation of the sample in accelerated fashion. It measured images at 920 (pre-edge), 933.5 (Cu(I)&Cu(0)), 937 (Cu(I)) and 960 eV (post-edge), and provides the same spectroscopic information as STXM full stack (**Fig. S-6**). Further details of the STXM measurements are presented in **Table S-1**.

STXM is typically regarded as a technique which causes limited radiation damage,[58-60] especially relative to analytical electron microscopies.[58-62] Experimental evidence, demonstrating that the results from this *in-situ* STXM study of Cu electrocatalysts are not significantly affected by radiation damage, is presented in Supporting information **Section S-11**.

All STXM data was analyzed using aXis2000 software.[63] The images in a stack typically drift by a few hundred nm over a 40-80 eV scan range. Therefore the stacks were aligned to ~2 nm registry using a Fourier cross-correlation method. The transmission signal (I) of the aligned stack was converted to optical density (OD) using the Beer Lambert Law: $OD_{(x,y)} = -ln(I_{(x,y)}/ I_o)$, where $I_{(x,y)}$ is the X-ray intensity transmitted though the (x,y) point on the sample, and I_o is the incident X-ray intensity measured off the sample but where the X-rays transmit through all other parts of the X-ray path (optics, windows, zone plate, detector) and the sample support (the electrolyte and

150 nm of SiN_x window). After OD conversion, the Cu 2p X-ray absorption spectra (XAS) of selected areas (many pixels, which are not necessarily contiguous, but with similar Cu L_3 spectra) were extracted from the STXM stacks using methods described in greater detail below.

A fitting procedure, based on the singular value decomposition (SVD) matrix method [64], was used to analyze the stacks. The SVD routine fits the NEXAFS spectrum at each pixel to a user-identified set of reference spectra, which can be derived from the spectroscopy of pure reference compounds (external) or to spectra extracted from the measured stack (internal). The result of a SVD fitting is a set of component maps (spatial distributions), one for each component, along with the residual of the fit.[32] For quantitative analysis, the external reference spectra are converted to an absolute intensity scale, optical density per nm (OD1), [33] by scaling the spectrum such that the intensity in the pre-edge and far-continuum (>30 eV above the edge) match the elemental response for 1 nm thickness of the known composition and density of the reference material. The latter are calculated using parameters from the Centre for X-ray Optics database [https://henke.lbl.gov/optical_constants/]. The gray scale of the component maps derived using OD1 reference spectra is an estimate of the thickness of that component at each pixel in the region analyzed. To confirm the validity of the spectro-microscopy fitting procedure, spectra are extracted from specific areas of a stack, identified based on morphology and / or spectral similarity and then subjected to a spectral curve fitting procedure using SVD. When reference spectra on OD1 intensity scales are used in a SVD curve fit, the gray scale of the component maps of each spectral component is an estimate of the average thickness in nm of that component in the area from which the spectra were extracted.

REFERENCE:

1. Wang, P.; Yang, H.; Tang, C.; Wu, Y.; Zheng, Y.; Cheng, T.; Davey, K.; Huang, X. and Qiao, S.Z. Boosting electrocatalytic CO_2–to–ethanol production via asymmetric C–C coupling. *Nature communications* **2022**, *13*, 1-11.
2. Zhang, C.; Shahcheraghi, L.; Ismail, F.; Eraky, H. Yuan, H.; Hitchcock, A.P. and Higgins, D. Chemical Structure and Distribution in Nickel–Nitrogen–Carbon Catalysts for CO_2 Electroreduction Identified by Scanning Transmission X-ray Microscopy. *ACS catalysis* **2022**, *12*, 8746-8760.

3. Chou, T.C.; Chang, C.C.; Yu, H.L.; Yu, W.Y.; Dong, C.L.; Velasco-Vélez, J.J.; Chuang, C.H.; Chen, L.C.; Lee, J.F.; Chen, J.M. and Wu, H.L. Controlling the oxidation state of the Cu electrode and reaction intermediates for electrochemical CO_2 reduction to ethylene. *J. American Chemical Society* **2020**, *142*, 2857-2867.
4. Wei, P.; Gao, D.; Liu, T.; Li, H.; Sang, J.; Wang, C.; Cai, R.; Wang, G. and Bao, X. Coverage-driven selectivity switch from ethylene to acetate in high-rate CO2/CO electrolysis. Nature Nanotechnology **2023,** *18*, 299-306.
5. Yang, Y.; Roh, I.; Louisia, S.; Chen, C.; Jin, J.; Yu, S.; Salmeron, M.B.; Wang, C. and Yang, P. Operando Resonant Soft X-ray Scattering Studies of Chemical Environment and Interparticle Dynamics of Cu Nanocatalysts for CO_2 Electroreduction. *Journal of the American Chemical Society*. **2022**, *144*, 8927–8931.
6. Lu, C.; Li, X.; Wu, Q.; Li, J.; Wen, L.; Dai, Y.; Huang, B.; Li, B. and Lou, Z. Constructing surface plasmon resonance on Bi2WO6 to boost high-selective CO2 reduction for methane. *ACS nano* **2021**, *15*(2), 3529-3539.
7. Wu, Q.; Liu, C.; Su, X.; Yang, Q.; Wu, X.; Zou, H.; Long, B.; Fan, X.; Liao, Y.; Duan, L. and Quan, Z.; 2022. Defect-Engineered Cu-Based Nanomaterials for Efficient CO2 Reduction over Ultrawide Potential Window. *ACS nano* **2023,** *17*, 402-410.
8. Watkins, N.B.; Wu, Y.; Nie, W.; Peters, J.C. and Agapie, T. In Situ Deposited Polyaromatic Layer Generates Robust Copper Catalyst for Selective Electrochemical CO_2 Reduction at Variable pH. *ACS Energy Letters* **2022**, *8*, 189-195.
9. Zhu, C.; Zhao, S.; Shi, G. and Zhang, L. Structure-Function Correlation and Dynamic Restructuring of Cu for Highly Efficient Electrochemical CO2 Conversion. *ChemSusChem*, **2022**, *15***,** .e202200068.
10. Eilert, A.; Cavalca, F.; Roberts, F.S.; Osterwalder, J.; Liu, C.; Favaro, M.; Crumlin, E.J.; Ogasawara, H.; Friebel, D.; Pettersson, L.G. and Nilsson, A. Subsurface oxygen in oxide-derived copper electrocatalysts for carbon dioxide reduction. *The journal of physical chemistry letters*, **2017**, *8*(1), pp.285-290.
11. Wang, H.Y.; Soldemo, M.; Degerman, D.; Lömker, P.; Schlueter, C.; Nilsson, A. and Amann, P. Direct Evidence of Subsurface Oxygen Formation in Oxide-Derived Cu by X-ray Photoelectron Spectroscopy. *Angewandte Chemie* **2022**, *61*, e202111021.
12. Fields, M.; Hong, X.; Nørskov, J.K. and Chan, K. Role of subsurface oxygen on Cu surfaces for CO_2 electrochemical reduction. *The Journal of Physical Chemistry C* **2018**, *122*, 16209-

16215.

13. Scott, S.B.; Hogg, T.V.; Landers, A.T.; Maagaard, T.; Bertheussen, E.; Lin, J.C.; Davis, R.C.; Beeman, J.W.; Higgins, D.; Drisdell, W.S. and Hahn, C. Absence of oxidized phases in Cu under CO reduction conditions. *ACS Energy Letters* **2019**, *4*, 803-804.
14. Lum, Y. and Ager, J.W . Stability of residual oxides in oxide-derived copper catalysts for electrochemical CO_2 reduction investigated with ^{18}O labeling. *Angewandte Chemie*. **2018**, *57*, 551-554.
15. Jiang, P.; Prendergast, D.; Borondics, F.; Porsgaard, S.; Giovanetti, L.; Pach, E.; Newberg, J.; Bluhm, H.; Besenbacher, F. and Salmeron, M. Experimental and theoretical investigation of the electronic structure of Cu_2O and CuO thin films on Cu (110) using x-ray photoelectron and absorption spectroscopy. *The Journal of chemical physics* **2013**, *138*, 024704.
16. Grosse, P.; Yoon, A.; Rettenmaier, C.; Herzog, A.; Chee, S.W. and Roldan Cuenya, B. Dynamic transformation of cubic copper catalysts during CO_2 electroreduction and its impact on catalytic selectivity. *Nature Communications* **2021**, *12*, 6736.
17. Arán-Ais, R.M.; Rizo, R.; Grosse, P.; Algara-Siller, G.; Dembélé, K.; Plodinec, M.; Lunkenbein, T.; Chee, S.W. and Cuenya, B.R. Imaging electrochemically synthesized Cu_2O cubes and their morphological evolution under conditions relevant to CO_2 electroreduction. *Nature communications* **2020**, *11*, 1-8.
18. Handoko, A.D.; Wei, F.; Jenndy, Yeo, B.S. and Seh, Z.W. Understanding heterogeneous electrocatalytic carbon dioxide reduction through operando techniques. *Nature Catalysis* **2018**, *1*, 922-934.
19. Hasa, B.; Zhao, Y. and Jiao, F. In Situ/Operando Characterization Techniques of Electrochemical CO_2 Reduction. *Annual Review of Chemical and Biomolecular Engineering* **2023,** *14*, 1.
20. Zheng, T.; Liu, C.; Guo, C.; Zhang, M.; Li, X.; Jiang, Q.; Xue, W.; Li, H.; Li, A.; Pao, C.W. and Xiao, J. Copper-catalysed exclusive CO2 to pure formic acid conversion via single-atom alloying. *Nature Nanotechnology* **2021**, ***16***, 1386-1393.
21. Li, X.; Yang, X.; Zhang, J.; Huang, Y. and Liu, B. In situ/operando techniques for characterization of single-atom catalysts. *Acs Catalysis* **2019**, *9*, 2521-2531.
22. Yang, Y.; Louisia, S.; Yu, S.; Jin, J.; Roh, I.; Chen, C.; Fonseca Guzman, M.V.; Feijóo, J.; Chen, P.C.; Wang, H. and Pollock, C.J. Operando studies reveal active Cu nanograins for CO_2 electroreduction. *Nature* **2023**, *614*, 262-269.

23. Abdellah, A.; Ismail, F.; Siig, O.; Yang, J.; Andrei, C.; DiCecco, L.; Rakhsha, A.; Salem, K.; Grandfield, K.; Bassim, N.; Black, R.; Kastlunger, G.; Soleymani, L.; Higgins, D. In-Situ Liquid Phase Transmission Electron Microscopy and Electron Diffraction Provides Mechanistic Insight into Electrochemical CO2 Reduction on Palladium/Palladium Hydride Catalysts. *ChemRxiv.* **2023**. This content is a preprint and has not been peer-reviewed.
24. Chee, S.W.; Lunkenbein, T.; Schlögl, R. and Cuenya, B.R. In situ and operando electron microscopy in heterogeneous catalysis—insights into multi-scale chemical dynamics. *Journal of Physics: Condensed Matter* **2021**, *33*, 153001.
25. Hwang, S.; Chen, X.; Zhou, G. and Su, D. In situ transmission electron microscopy on energy-related catalysis. *Advanced Energy Materials* **2020**, *10*,1902105.
26. Guay, D.; Stewart-Ornstein, J.; Zhang, X. and Hitchcock, A.P. In situ spatial and time-resolved studies of electrochemical reactions by scanning transmission X-ray microscopy. *Analytical chemistry* **2005**, *77*, 3479-3487.
27. Bozzini, B.; D'Urzo, L.; Gianoncelli, A.; Kaulich, B.; Kiskinova, M.; Prasciolu, M. and Tadjeddine, A. In situ soft X-ray dynamic microscopy of electrochemical processes. *Electrochemistry Communications* **2008**, *10*, 1680-1683.
28. de Groot, F.M.; de Smit, E.; van Schooneveld, M.M.; Aramburo, L.R. and Weckhuysen, B.M. In-situ scanning transmission X-ray microscopy of catalytic solids and related nanomaterials. *ChemPhysChem* **2010**, *11*, 951-962.
29. Gianoncelli, A.; Kaulich, B.; Kiskinova, M.; Mele, C.; Prasciolu, M.; Sgura, I. and Bozzini, B. Fabrication and testing of an electrochemical microcell for in situ soft X-ray microspectroscopy measurements. *Journal of Physics: Conference Series*. **2013**, *425*, 182010.
30. Prabu, V.; Obst, M.; Hosseinkhannazer, H.; Reynolds, M.; Rosendahl, S.; Wang, J. and Hitchcock, A.P. Instrumentation for in situ flow electrochemical scanning transmission X-ray microscopy (STXM). *Review of Scientific Instruments* **2018**, *89*, 063702.
31. Obst, M.; Ingino, P.; Hitchcock, A.; Prabu, V. and Picard, A. Redox-chemistry of environmental biofilms probed on the submicron scale by *in-situ* electrochemical scanning transmission (soft) X-ray microscopy. *Microscopy and Microanalysis* **2018**, *24*, 502-505.
32. Beheshti Askari, A.; Al Samarai, M.; Morana, B.; Tillmann, L.; Pfänder, N.; Wandzilak, A.; Watts, B.; Belkhou, R.; Muhler, M. and DeBeer, S. *In situ* X-ray microscopy reveals particle dynamics in a NiCo dry methane reforming catalyst under operating conditions. *ACS Catalysis* **2020**, *10*, 6223-6230.

33. Arul, K.T.; Chang, H.W.; Shiu, H.W.; Dong, C.L. and Pong, W.F. A review of energy materials studied by in situ/operando synchrotron x-ray spectro-microscopy. *Journal of Physics D: Applied Physics* **2021**, *54*, 343001.
34. Hitchcock, A.P.; Zhang, C.; Eraky, H.; Shahcheraghi, L.; Ismail, F. and Higgins, D. *In-situ* and Operando Studies with Soft X-Ray Transmission Spectromicroscopy. *Microscopy and Microanalysis* **2021**, *27*, 59-60.
35. Zhang, C.; Eraky, H.; Ingino, P. and Obst, W.; Jian.; Higgins, D.; Hitchcock, AP. *In-situ* STXM Characterization of Cu/Cu_2O Electrocatalysts for CO_2 Reduction. *AIP Conference Proceedings* **2023** accepted.
36. Hitchcock, A. P. Soft X-Ray Imaging and Spectro-microscopy. in *Handbook of Nanoscopy*. **2**, Weinheim, Germany, **2012,** 745–791.
37. Ade, H. and Hitchcock, A.P. NEXAFS microscopy and resonant scattering: Composition and orientation probed in real and reciprocal space, *Polymer* **2008**, *49*, 643-675.
38. Lee, S.H.; Lin, J.C.; Farmand, M.; Landers, A.T.; Feaster, J.T.; Avilés Acosta, J.E.; Beeman, J.W.; Ye, Y.; Yano, J.; Mehta, A. and Davis, R.C. Oxidation state and surface reconstruction of Cu under CO_2 reduction conditions from in situ X-ray characterization. *Journal of the American Chemical Society*, **2020**, *143*, 588-592.
39. Chourasia, A.K.; Pathak, A.D.; Bongu, C.; Manikandan, K.; Praneeth, S.; Naik, K.M. and Sharma, C.S. In Situ/Operando Characterization Techniques: The Guiding Tool for the Development of Li–CO_2 Battery. *Small Methods*, **2022,** *6*, 2200930.
40. Fang, L.; Seifert, S.; Winans, R.E. and Li, T. Understanding synthesis and structural variation of nanomaterials through in situ/operando XAS and SAXS. *Small* **2022**, *18*, p.2106017.
41. Celorrio, V.; Leach, A.S.; Huang, H.; Hayama, S.; Freeman, A.; Inwood, D.W.; Fermin, D.J. and Russell, A.E.; 2021. Relationship between Mn oxidation state changes and oxygen reduction activity in (La, Ca) MnO_3 as probed by in situ XAS and XES. *ACS Catalysis* **2021**, *11*, 6431-6439.
42. Fan, Z.; Zhang, L.; Baumann, D.; Mei, L.; Yao, Y.; Duan, X.; Shi, Y.; Huang, J.; Huang, Y. and Duan, X. In situ transmission electron microscopy for energy materials and devices. *Advanced Materials* **2019**, *31*, 1900608.
43. Huang, H.; Wang, J.; Yang, X.; Hu, R.; Liu, J.; Zhang, L. and Zhu, M. Unveiling the advances of nanostructure design for alloy-type potassium-ion battery anodes via in situ TEM. *Angewandte Chemie*. **2020,** *132*, 14612-14618.

44. Kuhl, K.P.; Cave, E.R.; Abram, D.N. and Jaramillo, T.F. New Insights into the Electrochemical Reduction of Carbon Dioxide on Metallic Copper Surfaces. *Energy Environ. Sci*, **2012**, *5*, 7050−7059 .
45. Higgins, D.; Landers, A.T.; Ji, Y.; Nitopi, S.; Morales-Guio, C.G.; Wang, L.; Chan, K.; Hahn, C. and Jaramillo, T.F. Electrochemical Carbon Dioxide Reduction toward Carbonyls Using Copper Silver Thin Films with Interphase Miscibility. *ACS Energy Lett.* **2018**, *3*, 2947−2955.
46. Wang, L.; Nitopi, S.A.; Bertheussen, E.; Orazov, M.; Morales-Guio, C.G.; Liu, X.; Higgins, D.C.; Chan, K.; Nørskov, J.K.; Hahn, C. and Jaramillo, T.F. Electrochemical carbon monoxide reduction on polycrystalline copper: Effects of potential, pressure, and pH on selectivity toward multicarbon and oxygenated products. *ACS Catalysis* **2018**, *8*, 7445-7454.
47. Morales-Guio, C.G.; Cave, E.R.; Nitopi, S.A.; Feaster, J.T.; Wang, L.; Kuhl, K.P.; Jackson, A.; Johnson, N.C.; Abram, D.N.; Hatsukade, T. and Hahn, C. Improved CO_2 reduction activity towards C2+ alcohols on a tandem gold on copper electrocatalyst. *Nature Catalysis* **2018**, *1*, 764-771.
48. Zheng, Y.; Zhang, J.; Ma, Z.; Zhang, G.; Zhang, H.; Fu, X.; Ma, Y.; Liu, F.; Liu, M. and Huang, H. Seeded growth of gold–copper janus nanostructures as a tandem catalyst for efficient electroreduction of CO_2 to C2+ products. *Small* **2022,** *18*, 2201695.
49. Velasco-Velez, J.J.; Mom, R.V.; Sandoval-Diaz, L.E.; Falling, L.J.; Chuang, C.H.; Gao, D.; Jones, T.E.; Zhu, Q.; Arrigo, R.; Roldan Cuenya, B. and Knop-Gericke, A. Revealing the active phase of copper during the electroreduction of CO_2 in aqueous electrolyte by correlating in situ X-ray spectroscopy and in situ electron microscopy. *ACS Energy Letters* **2020**, *5*, 2106-2111.
50. Reyter, D.; Odziemkowski, M.; Bélanger, D. and Roué, L. Electrochemically activated copper electrodes: surface characterization, electrochemical behavior, and properties for the electroreduction of nitrate. *Journal of the Electrochemical Society* **2007**, *154*, K36.
51. Fields, M.; Hong, X.; Nørskov, J.K. and Chan, K.; 2018. Role of subsurface oxygen on Cu surfaces for CO2 electrochemical reduction. *The Journal of Physical Chemistry C*, *122*(28), 16209-16215. Role of subsurface oxygen on Cu surfaces for CO_2 electrochemical reduction." *The Journal of Physical Chemistry C* **2018,** *122*, 16209-16215.
52. Shapiro, D.A.; Yu, Y.S.; Tyliszczak, T.; Cabana, J.; Celestre, R.; Chao, W.; Kaznatcheev, K.; Kilcoyne, A.D.; Maia, F.; Marchesini, S. and Meng, Y.S. Chemical composition mapping with nanometre resolution by soft X-ray microscopy. *Nature Photonics* **2014,** *8*, 765-769.

53. Zhang, C.; Mille, N.; Eraky, H.; Stanescu, S.; Swaraj, S.; Belkhou, R.; Higgins, D. and Hitchcock, A Copper CO_2 Reduction Electrocatalysts Studied by *In-situ* Soft X-ray Spectro-Ptychography . ChemRxiv. **2023**; This content is a preprint and has not been peer-reviewed.
54. Beverskog, B.; Puigdomenech, I.; Revised Pourbaix Diagrams for Copper at 25 to 300ºC, *J. Electrochemical Society*, **1997**, *144*, 3476.
55. Kilcoyne, A.L.D.; Tyliszczak, T.; Steele, W.F.; Fakra, S.; Hitchcock, P.; Franck, K.; Anderson, E.; Harteneck, B.; Rightor, E.G.; Mitchell, G.E. and Hitchcock, A.P.Interferometer-Controlled Scanning Transmission X-Ray Microscopes at the Advanced Light Source. *J. Synchrotron Radiation* **2003**, *10*, 125−136.
56. Kaznatcheev, K.V.; Karunakaran, C.; Lanke, U.D.; Urquhart, S.G.; Obst, M. and Hitchcock, A.P. Soft X-ray spectromicroscopy beamline at the CLS: Commissioning results. *Nuclear Instruments and Methods in Physics Research Section A: Accelerators, Spectrometers, Detectors and Associated Equipment* **2007**, ***582,*** 96–99.
57. Hitchcock, A. P.; Brion, C. E. Neon K-Shell Excitation Studied by Electron Energy-Loss Spectroscopy. *J. Phys. B: At. Mol. Phys.* **1980**, *13*, 3269−3273.
58. Wang, J.; Botton, G.A.; West, M.M. and Hitchcock, A.P. Quantitative evaluation of radiation damage to polyethylene terephthalate by soft X-rays and high-energy electrons. *The Journal of Physical Chemistry B*, **2009**, 113(7), 1869-1876
59. Zhang, W.; Melo, L.G.D.A.; Hitchcock, A.P. and Bassim, N. Electron beam damage of epoxy resin films studied by scanning transmission X-ray spectromicroscopy. *Micron* **2019**, 120, 74-79.
60. Melo, L.G. and Hitchcock, A.P. Electron beam damage of perfluorosulfonic acid studied by soft X-ray spectromicroscopy. *Micron* **2019**, *121*, 8-20.
61. Martens, I.; Melo, L.G.; West, M.M.; Wilkinson, D.P.; Bizzotto, D. and Hitchcock, A.P. Imaging reactivity of the Pt–ionomer interface in fuel-cell catalyst layers. *ACS Catalysis* 2020, 10(15), 8285-8292.
62. Wu, J.; Melo, L.G.; Zhu, X.; West, M.M.; Berejnov, V.; Susac, D.; Stumper, J. and Hitchcock, A.P. 4D imaging of polymer electrolyte membrane fuel cell catalyst layers by soft X-ray spectro-tomography. *Journal of Power sources* **2018**, 381, 72-83.
63. Hitchcock, A.P. Analysis of X-ray Images and Spectra (aXis2000): a toolkit for the analysis of X-ray spectromicroscopy data, *J. Electron Spectroscopy and Related Phenomena*, **2023**, *266*, 147360.

64. Koprinarov, I.N.; Hitchcock, A.P.; McCrory, C.T. and Childs, R.F. Quantitative Mapping of Structured Polymeric Systems Using Singular Value Decomposition Analysis of soft X-ray Images, *J. Phys. Chem. B* **2002**, *106*, 5358-5364.

Chapter 8

Copper CO_2 Reduction Electrocatalysts Studied by *In situ* Soft X-ray Spectro-Ptychography

This chapter presents experimental results of in-situ spectro-ptychography on Cu nanoparticle catalysts under electrochemical CO_2R conditions. In comparison to STXM, the spatial resolution was improved by a factor of three through measuring patterns of diffracted photons via spectro-ptychography. We present here a detailed study of how individual cubic Cu particles change morphology and oxidation state as a function of applied potential during CO_2R.

This work was accepted by the Cell Reports Physical Science on Sep 25, 2023. The author list is: Chunyang Zhang, Nicolas Mille, Haytham Eraky, Stefan Stanescu, Sufal Swaraj, Rachid Belkhou, Drew Higgins, Adam P. Hitchcock.

The author of this thesis and Prof. A. P. Hitchcock performed all the in-situ STXM and ptychography experiments(in collaboration with beamline scientists at HERMES beamline at Soleil, Nicolas Mille, Stefan Stanescu, Sufal Swaraj and Rachid Belkhou). The author and Haytham Eraky fabricated and prepare the in-situ instrumentations. The author and Prof. A. P. Hitchcock analyzed the STXM and ptychography data. The author wrote the publication, with assistance in later stages by Prof. A. P. Hitchcock and Prof. Drew Higgins.

The supplement information of the publication is put in Appendix F.

Copper CO_2 Reduction Electrocatalysts Studied by *In Situ* Soft X-ray Spectro-Ptychography

Chunyang Zhang,[1,2] Nicolas Mille,[3] Haytham Eraky,[2] Stefan Stanescu,[3] Sufal Swaraj,[3] Rachid Belkhou,[3] Drew Higgins[1*] and Adam P. Hitchcock[2*]

1. Chemical Engineering, McMaster University, Hamilton, ON, Canada, L8S 4M1
2. Chemistry & Chemical Biology, McMaster University, Hamilton, ON, Canada, L8S 4M1
3. Synchrotron SOLEIL, L'Orme des Merisiers, Departementale 128, 91190 Saint-Aubin, France

* co-corresponding author: aph@mcmaster.ca 905-525-9140
* co-corresponding author: higgid2@mcmaster.ca

Highlights:

- *In situ* soft X-ray spectro-ptychography of Cu electrocatalysts under electrochemical CO_2 reduction (CO_2R) conditions
- Spatial resolution improved via spectro-ptychography, showing more insights of the Cu catalysts under the CO_2R conditions compared to *in situ* scanning transmission X-ray microscopy.
- A detailed study of how individual cubic Cu particles change morphology and oxidation state as a function of applied potential under CO_2R conditions
- Quantitative chemical mapping by *in situ* spectro-ptychography showing the Cu(I)/Cu(0) conversion and shape changes of Cu particles during CO_2R

Summary:

A micro-chip based three-electrode electrochemical reactor enabling controlled, variable electrolyte flow, rapid electrolyte change and applied electrode potentials was used for *in situ* soft X-ray spectro-ptychography of Cu particle catalysts under electrochemical CO_2 reduction (CO_2R) conditions. In comparison to scanning transmission X-ray microscopy (STXM), the spatial resolution was improved by a factor of three through measuring patterns of diffracted photons via spectro-ptychography. We present here a detailed study of how individual cubic Cu particles change morphology and oxidation state as a function of applied potential during CO_2R. Quantitative chemical mapping by *in situ* spectro-ptychography demonstrated that as-deposited,

primarily mixed Cu(I) and Cu(0) particles were completely reduced to pure Cu(0) at an electrode potential of -0.2 V_{RHE}, above the potential at which CO_2R commences. At increasingly negative potentials, in the regime of CO_2R, these Cu(0) particles underwent morphological changes, losing the initial cubic structure and forming irregular dendritic-like structures. This initial demonstration of *in situ* soft X-ray spectro-ptychography sheds insight on the morphological and chemical structural changes of Cu particles in the CO_2R regime and paves the way for more detailed *in situ* studies of electrochemical materials and processes.

Graphical abstract:

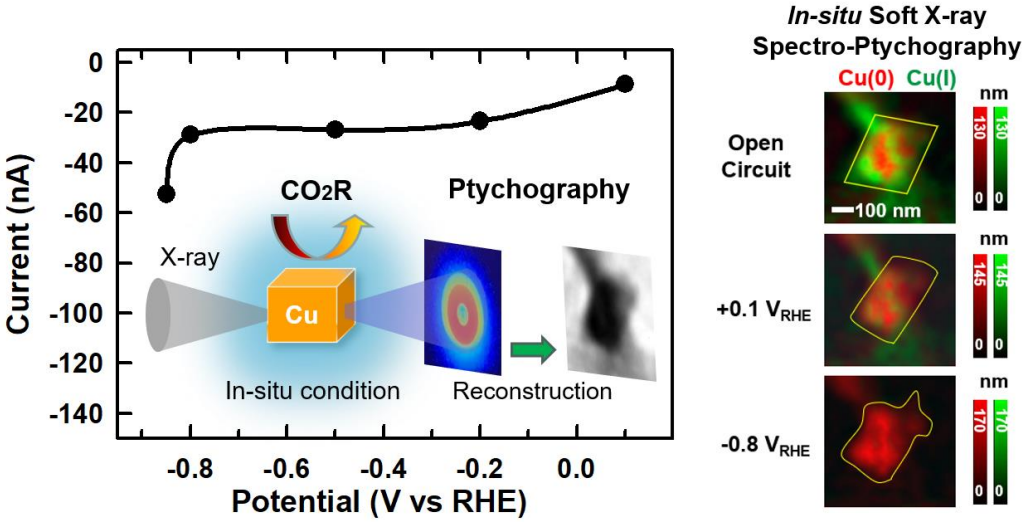

8.1. Introduction

Electrochemical carbon dioxide reduction (CO_2R) using renewable electricity offers a sustainable, carbon neutral approach to produce valuable and societally important hydrocarbon, alcohol, and carbonyl products, provided the CO_2 is generated directly from air capture, or from sustainable sources such as biomass combustion, fermentation, or other routes. [1-3] However, poor energy conversion efficiencies, reaction selectivity and stability of CO_2R electrocatalysts hinder the large-scale deployment of this process.[4,5] Among the various electrocatalysts used for CO_2R, copper is the only material that can uniquely convert CO_2 into valuable multi-carbon products (C_{2+}), such as ethanol or ethylene, at appreciable rates.[6-10] Improved understanding of Cu catalysts for electrochemical CO_2 conversion will provide crucial guidance for the development of next generation, improved performance catalysts and CO_2R device designs. The chemical structures present, and the dynamic morphology of Cu catalysts under reaction conditions, are still under debate.[11-13] For example, the presence of Cu(I) species or subsurface oxygen during electroreduction has been suggested to improve CO_2R activity and steer the selectivity towards C_{2+} products.[14-16]. Other studies have refuted the presence of significant amounts of partially oxidized Cu species under the electrochemically reducing conditions required for the reaction.[17-19] Morphological changes also occur in Cu electrocatalysts under CO_2R reaction conditions that will lead to changes in the properties of the catalyst and, by extension, the resultant CO_2R activity and selectivity.[20, 21] This brings into question the suitability of *ex situ* characterization of as-prepared or post-CO_2R tested materials for establishing catalyst design principles (i.e., morphological, chemical or electrochemical properties of a catalyst that engender optimized activity, selectivity and/or stability). This has motivated the development and implementation of *in situ* characterization methods that enable control of the local reaction conditions and applied electrochemical potentials to gain mechanistic insight into electrochemical CO_2R processes and materials.[6, 22-25] Results from these efforts are crucial for establishing fundamental structure-property-performance relationships which can inform further improvements in Cu-based CO_2R electrocatalyst designs.

Among various *in situ* characterization techniques, spectro-microscopic methods that combine imaging and chemical speciation are particularly useful since they can provide real-time and same-position characterizations to simultaneously monitor changes of oxidation states and morphology under reaction conditions. *In situ* scanning transmission X-ray microscopy (STXM)

is a powerful, synchrotron-based, spectro-microscopic technique that provides microscopic imaging alongside spatially resolved quantitative chemical mapping.[26,27] The chemical sensitivity of the technique is based on near edge X-ray absorption fine structure (NEXAFS) spectroscopy.[28] *In situ* STXM has been used to study charge/discharge processes in battery materials [29-31], the electrodeposition of copper [32], and catalysis of oxygen evolution (OER) and CO_2R reactions.[24, 33, 34] Such studies demonstrate the ability of STXM to provide spatially resolved spectroscopic and microscopic information on the studied materials at different time/potential points during electrochemical processes. However, a major challenge limiting the scientific impact of *in situ* STXM is its limited spatial resolution, typically on the order of 40 - 50 nm because the size of the focused spot depends on the properties of the zone plate. The challenges of zone plate fabrication are such that it is very difficult to improve the spot size beyond ~20 nm [35].

Ptychography provides improved spatial resolution in comparison to STXM by measuring coherent X-ray diffraction images (DI) in transmission at an array of overlapping points on a sample, which is not dependent on the X-ray focused spot size. [36] A mathematical algorithm is then used to reconstruct the set of DI into a real space image.[35-41] Recently, ptychography [36] has been implemented in a number of soft X-ray STXM facilities, including the HERMES beamline at Synchrotron SOLEIL [37, 38], the COSMIC beamline at the Advanced Light Source [39,40], the STXM at the Shanghai Synchrotron Radiation Facility [41], and the spectro-microscopy beamline at the Canadian Light Source.[42] Ptychography is implemented in a STXM by replacing the post-specimen single channel detector with an X-ray sensitive camera, for example, the sCMOS camera [43,44] implemented in the STXM at the HERMES beamline of Synchrotron SOLEIL. For spectro-ptychography, sets of X-ray diffraction images measured with suitable spatial overlap are recorded at a series of photon energies. After suitable reconstruction, the resulting ptychographic amplitude images are converted to ptychography X-ray absorption images (stacks) using the Beer-Lambert Law. The resulting ptychographic absorption stacks can then provide spectroscopy-based chemical analyses similar to conventional STXM X-ray absorption stacks, but with an improved spatial resolution that can be sub-10 nm.[39,40]

Ptychography using hard X-rays (>4 keV) is much more developed than ptychography using soft X-rays (<2 keV), in part because X-ray attenuation is not a significant concern and in part because

of much longer working distances, alleviating constraints on sample and *in situ* reactor designs. [45-52] On the flip side, soft X-ray microscopy is significantly more challenging due to short focal lengths and thus much less space for *in situ* instrumentation, yet soft X-ray spectro-microscopy provides unique opportunities to gain insight into electro-catalytic materials and processes due to the higher chemical sensitivity of 3d transition metal L-edge spectroscopy relative to K-shell spectroscopy, along with the potential to spectroscopically image reaction products or intermediate species, using the carbon K-edge, for example. [37, 53] Despite this promise, soft X-rays are prone to attenuation, leading to challenges in the design and implementation of *in situ* soft X-ray spectro-microscopy methods under electrochemical conditions where photons must transmit through reactor walls, an electrolyte layer and the electro-active materials being characterized. Because of these challenges and the recency of the camera innovations that enable soft X-ray spectro-ptychography [43,44], *in situ* soft X-ray spectro-ptychography has not been reported previously, to the best of our knowledge. This situation presents an opportunity for scientific innovation, one that was explicitly flagged in a recent review article.[45] We note that *in situ* hard X-ray ptychographic imaging of X-ray nucleated, thermally driven growth of Cu_2O particles from a static Cu(acetylacetonitrile)$_2$ solution was reported recently [46]. Although oxidation state changes from Cu(I) to Cu(0) in the temporal evolution of the particles was inferred (and verified by non-spatially resolved spectral studies [54,55]), direct spectroscopy-based, *in situ* evidence of the reduction was not obtained since all measurements were performed at a fixed X-ray energy (15.25 or 8.98 keV). Neither electrochemical processing nor liquid flow was part of that experiment.

In this work, we used *in situ* spectro-ptychography in the soft X-ray region to characterize electro-deposited Cu electrocatalysts under electrochemical CO_2R conditions. By leveraging our custom micro-fluidic reactor design that employs a three-electrode micro-chip electrochemical cell [24, 32, 33], *in situ* soft X-ray spectro-ptychography measurements were conducted under applied electrode potentials in the presence of controlled electrolyte flow. Through direct comparison we demonstrate that the spatial resolution for *in situ* spectro-microscopy measurements is improved three-fold by using spectro-ptychography rather than conventional STXM. Characterization of Cu electrocatalysts under controlled electrochemical CO_2R conditions enabled us to monitor the morphology and spatially-resolved oxidation state changes occurring both within a single Cu particle and multiple Cu particles distributed over a wider region of the electrode surface. The

measurements showed that initially electrodeposited Cu(0)/Cu(I)-based particles are converted to metallic Cu at potentials approaching or below -0.2 V versus the reversible hydrogen electrode (V_{RHE}). At more reducing electrode potentials where electrochemical CO_2R occurs, a single Cu particle was observed to undergo morphological changes from a cubic structure to a dendritic-like particle structure. This study demonstrates that *in situ* soft X-ray spectro-ptychography is an effective approach for attaining fundamental insight into the morphology and chemical structures of electro-catalysts under electrochemical CO_2R conditions.

8.2. Results

In situ spectro-ptychography experiments were conducted using a custom-designed microfluidic device encompassing an electrochemical micro-chip reactor (see Methods section). A brief description of the fundamental physics of ptychography is provided in the Supporting Information section **SI-1, Figs. S-1** to **S-3**. For more extensive details, examples and discussion of ptychography, readers are referred to citations in section **SI-1**. Cu particles were prepared by electrodeposition on the working electrode from a solution of 0.01 M $CuSO_4$ and 0.01 M KCl. After electrodeposition, the electrolyte was changed to CO_2 saturated 0.1M $KHCO_3$ followed by the application of electrode potential to initiate CO_2R. More details are provided in the Methods section. The presentation of results in this manuscript is organized as follows. **Section 8.2.1** compares the results of *in situ* STXM and *in situ* spectro-ptychography measured on electrodeposited Cu catalyst particles which we denote as "**area A**" at open circuit potential (OCP) conditions in CO_2 saturated 0.1M $KHCO_3$. **Section 8.2.2** reports *in situ* spectro-ptychography results for Cu particles on a region of a different electrode surface that was subjected to an applied potential of +0.1 V_{RHE}, which we denote as "**area B**". **Section 8.2.3** reports spectro-ptychography results from an individual Cu particle while subjecting it to a step-wise series of chrono-amperometry holds between OCP and -0.85 V_{RHE}, which is in the range of electrochemical CO_2R. We denote this Cu particle as "**area C**".

8.2.1 Comparing *in situ* STXM and ptychography (area A)

Figure 8.1 compares *in situ* STXM (**Fig. 7.1a**) and *in situ* ptychography (**Fig. 7.1b**) images at 933.3 eV (the peak energy of Cu L_3 absorption of Cu metal and Cu_2O) of deposited Cu particles in **area A** measured at OCP in CO_2 saturated 0.1M $KHCO_3$. The Cu particles range in size from ~300 nm to 1 μm, with the particles better resolved in the ptychography image than in the

STXM image. As outlined in section **SI-2,** the spatial resolution of *in situ* ptychography is estimated to be ~25 ±5 nm from a Fourier ring correlation (FRC) analysis (**Fig. S-4**), which is confirmed by evaluating the abruptness of sharp features in the amplitude images (**Fig. S-5**). This is considerably better than the ~75 ±10 nm spatial resolution of the same features measured from the corresponding *in situ* STXM image. Typically, ptychography can provide up to 5-times improvement in spatial resolution relative to the resolution determined by using a focused probe and single channel, integrated signal detection (i.e., STXM). Perhaps more important is that the quality of the ptychography image in terms of signal-to-noise and sampling is much better than that of STXM. This is in part due to a longer acquisition time and in part to a finer pixel size in the reconstructed images. In this work, each diffraction image was integrated for 60 ms and the reconstruction pixel size was 5.5 nm. In contrast, the STXM measurements used 20 ms sampling and 100 nm pixels. Due to the ptychography measurement conditions used – 1 μm spot size and 80-90% overlap — a given sample area contributes to many diffraction images and these in turn contribute to the signal at each 5.5 nm pixel in the reconstructed amplitude image. In addition, the ptychographic reconstruction partly compensates for scanning artifacts in the STXM, which cause smearing of the boundary of particles and thus lower resolution. Another important point is that, with the use of a defocused spot size (1 μm in this study), the radiation dose is much smaller in spectro-ptychography than a corresponding STXM measurement. As discussed in section **SI-15**, the estimated reduction in dose by using ptychography instead of STXM is a factor of 6.

To investigate the chemical identity and quantify the composition of electrodeposited Cu catalyst particles in **area A**, *in situ* STXM and ptychography images were measured at four photon energies (927.3, 930.3, 933.3, 937.3 eV), which we denote as a four-energy (4-E) stack. These four photon energy values were selected as they allow an unambiguous differentiation of Cu(0), Cu(I) and Cu(II) oxidation states based on the Cu L_3 X-ray absorption spectra of Cu, Cu_2O and CuO (**SI-3**, **Fig. S-6**).[56] At each of the four photon energies the contrast of the particles in the STXM and ptychography images changes significantly (see section **SI-4**, **Fig. S-7**). Analysis with suitable reference spectra [56] is used to map the different Cu oxidation states present within the particles. Although the reference spectra used in this work were those digitized from ref. [56], we have recently re-measured these spectra in STXM, with identical results, and identical analysis outcomes. The average **spectrum** of the Cu particles from the 4-E STXM stack (**Fig. S-7c**) and 4-E spectro-ptychography stack (**Fig. S-7d**) of **area A** indicate the presence of both Cu(I) and

Cu(II) after electro-deposition. The component **maps** for Cu(0), Cu(I) and Cu(II) were derived from fitting (section **SI-5**, **Fig. S-8**). **Figure 8.1c** presents a rescaled colour-coded composite of the STXM-derived Cu(I) and Cu(II) component maps showing that the particles in **area A** are mainly Cu(I) or Cu(II). Cu(0) was detected in **area A**, as shown in **Fig. S-8**. In order to focus on the improvement in spatial resolution afforded by ptychography, we have only included the Cu(I) and Cu(II) signals in the color coded composites (**Fig. 8.1c** and **Fig. 8.1d**).

Ptychography stack measurements were conducted using the same 4-E approach. The resulting amplitude images (**Fig. S-7**) show contrast variations similar to those in the 4-E STXM images (**Fig. S-7a**) but with higher spatial resolution. The 4-E ptychography stack was analyzed to generate Cu(0), Cu(1) and Cu(II) component maps. **Figure 8.1d** presents a rescaled colour-coded composite of the ptychography-derived Cu(I) and Cu(II) component maps. The spatial distributions of Cu(I) and Cu(II) are similar to those derived from STXM, albeit with much higher spatial resolution.

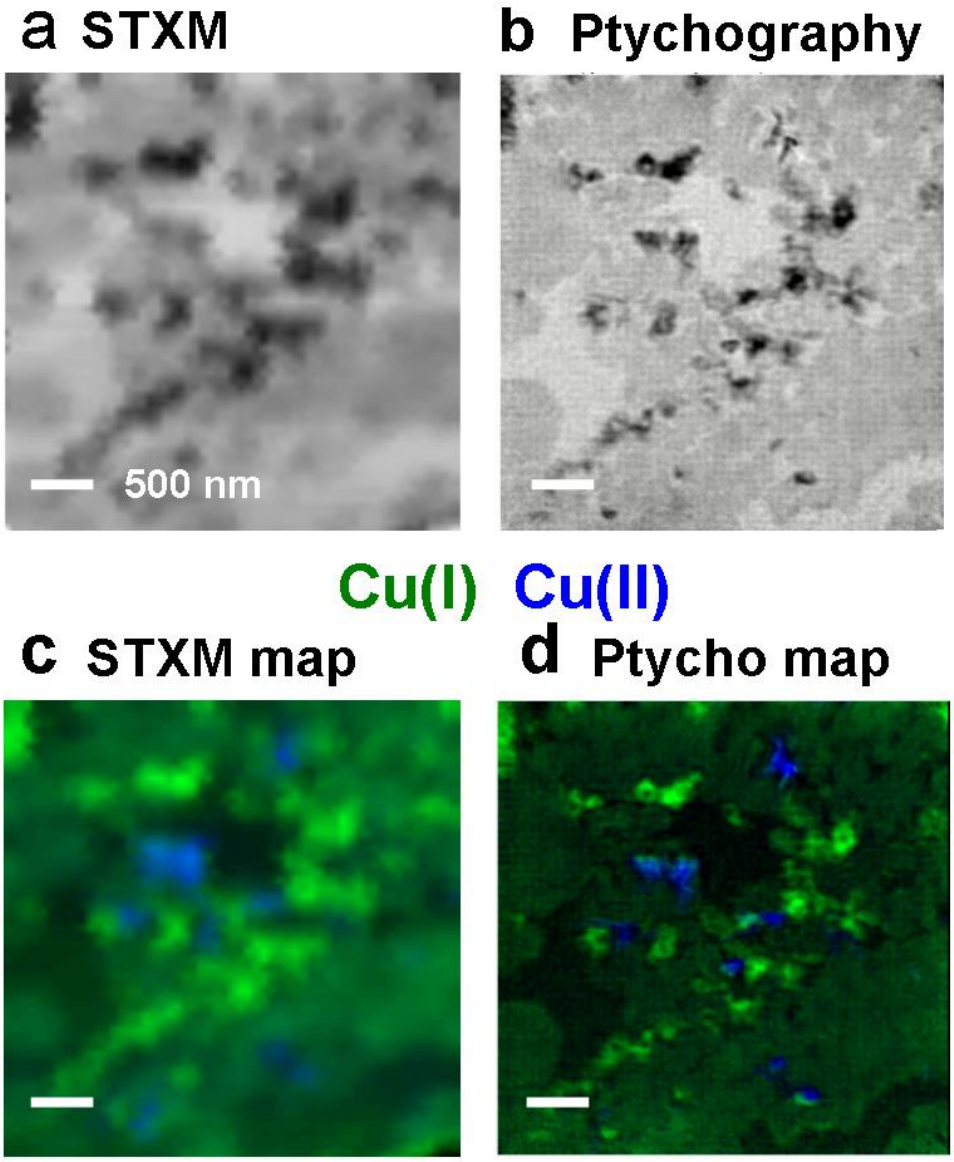

Figure 8.1 Comparison of imaging and chemical mapping by *in situ* STXM and *in situ* ptychography of area A. (a) *In situ* STXM transmission image at 933.3 eV. (b) *In situ* ptychography amplitude image at 933.3 eV. Colour coded composite of Cu(I) (green), and Cu(II) (blue)(component maps, derived from (c) the fit of an *in situ* STXM 4-E stack and (d) the fit of an *in situ* ptychography 4-E stack. All measurements were collected under open circuit potential (OCP) conditions in CO_2 saturated 0.1M $KHCO_3$. Scale bar = 500 nm.

8.2.2 *In situ* spectro-ptychography of Cu particles under CO_2R conditions (area B)

Another electrodeposited Cu-based electrode (**area B**) was prepared *in situ*. After changing the electrolyte to CO_2 saturated 0.1M $KHCO_3$, a Cu L_3 ptychography stack (40 energies from 920 to 946 eV) was measured at an applied potential of +0.1 V_{RHE}. The chrono-amperometry results (current as a function of time) are presented in section **SI-6, Fig. S-9a**. **Figure 8.2** presents the results of analysis of this Cu L_3 spectro-ptychography stack. The stack images were converted to optical densities and fit to quantitative Cu, Cu_2O and CuO reference spectra (**Fig. S-6)** using the singular value decomposition (SVD) matrix method, described in more detail elsewhere.[57] This forward fitting analysis generates quantitative component maps of each chemical species with amplitudes providing the thickness of each species at each pixel in the area measured. Additional details regarding data processing are provided in section **SI-13**. The quantitative maps of Cu(0), Cu(I) and Cu(II) derived from the Cu L_3 spectro-ptychography stack (**Fig. 8.2c-e**). The particles observed in this region range in size from a few tens of nm to ~300 nm (**Fig. 8.2a).** In contrast to **area A**, the particles in **area B** are mainly Cu(0), with a very small amount of Cu(I). There is also a very small amount of Cu(II) more or less uniformly distributed over the electrode. In order to check these results, an alternate, multivariate statistical analysis was applied to this data set, with results presented in section **SI-10**. This analysis reports there are at most 3 statistically significant spectral components. The first two components are pure metallic Cu and a slightly modified metallic Cu due to mixture with a small signal of Cu(I). These 2 signals account for over 99 % of the variance of the data set while the third component is attributed to noise.

To further confirm this analysis, the spectra of the Cu(I) and Cu(0) rich regions were extracted and analyzed to verify the quantitative composition of each region. These spectral analysis results (**Fig. S-9**) are consistent with the mapping analysis. Cu(0) is the largest contributor (> 95%), showing that under +0.1V_{RHE} *in situ* conditions, the majority of Cu(I) and Cu(II) species (such as those observed at OCP in **area A**) were reduced into metallic Cu. **Figure 8.2b** shows the ptychography amplitude spectra of Cu(0), Cu(I) and Cu(II) derived from the spectro-ptychography data.

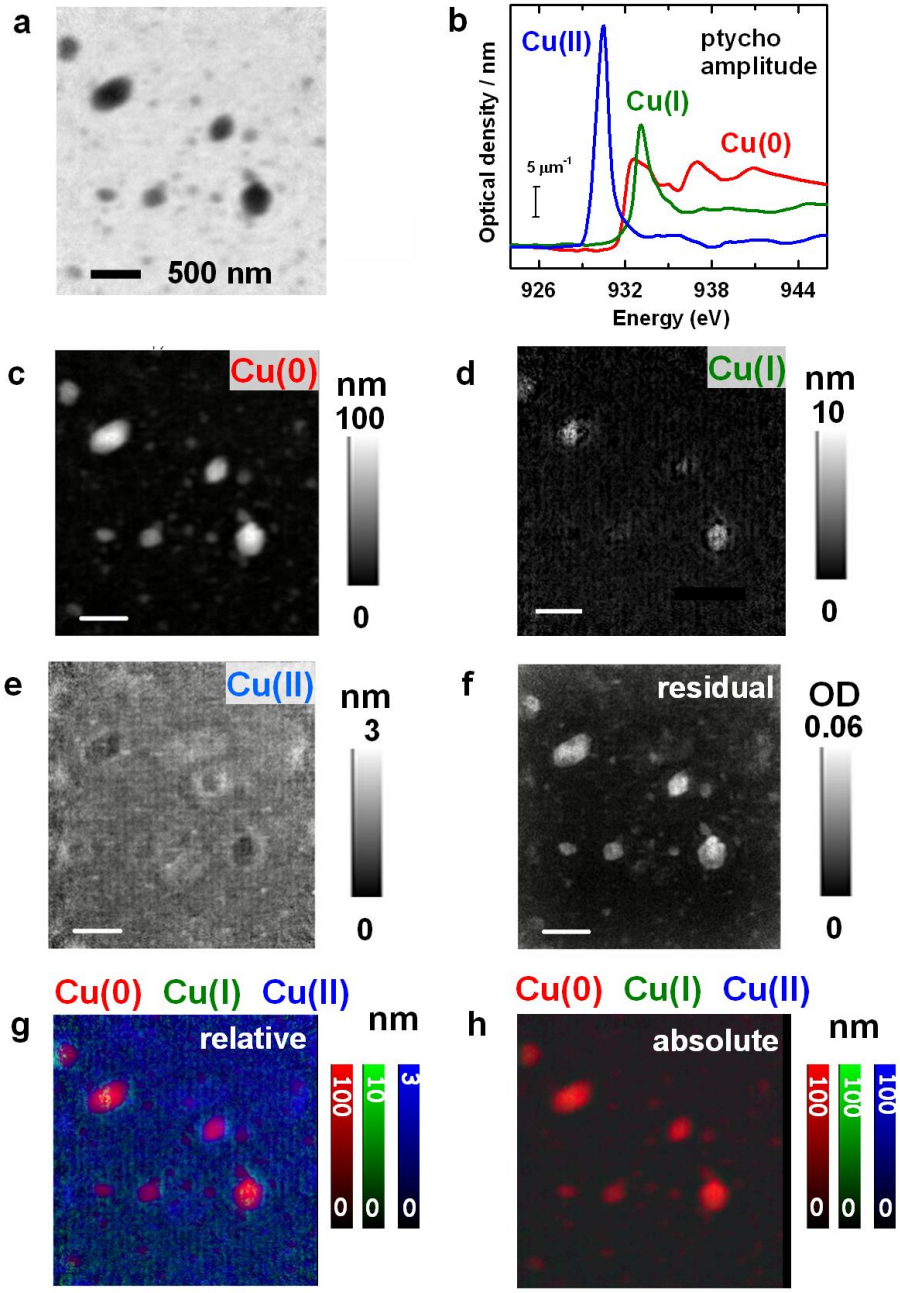

Figure 8.2 Cu L_3 *in situ* spectro-ptychography analysis of area B at +0.1 V_{RHE}. (a) Ptychography amplitude image at 933.3 eV. (b) reference spectra of Cu(0), Cu(I) and Cu(II) from ptychography measurements on OD1 scale, indicated by the 5 μm^{-1} vertical scale bar. Component maps, derived from SVD fit of these reference spectra to the ptychography absorption stack, for (c) Cu(0), (d) Cu(I) and (e) Cu(II). The intensity scales shows thickness in nm. (f) residual of fit. (g) Color coded composite of the component maps, using relative scaling. (h) Color coded component map using absolute scaling. Measurements were conducted in CO_2 saturated 0.1M $KHCO_3$. Scale bar = 500 nm.

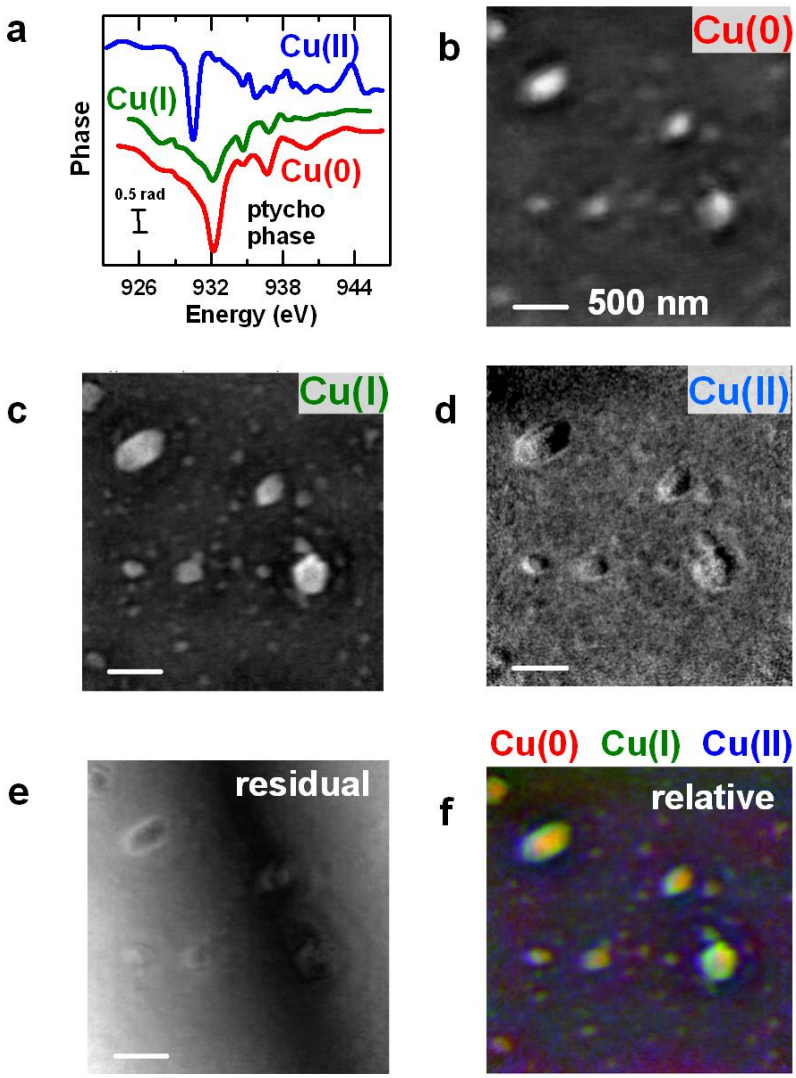

Figure 8.3 Analysis of full Cu L_3 spectro-ptychography phase stack of area B. (a) reference spectra from internal phase stack. (b) Cu metal component map derived from fit of the phase stack to the reference spectra in (3a). (c) Cu(I) component map from phase. (d) Cu(II) component map from phase. (e) residual of fit. (f) Color-coded component map using relative scaling. Scale bar = 500 nm.

In addition to the amplitude signal, which is similar to conventional X-ray absorption, ptychography measurements also provide phase images and thus a phase spectromicroscopy. **Fig. S-10** (section **SI-7**) is a sketch outlining the relationship of X-ray absorption, ptychography amplitude and ptychography phase signals. Phase spectra are quite different from absorption spectra. It is of interest to see if there is complementary, or perhaps even new, information from phase spectroscopy.[45] The phase spectra of Cu(0), Cu(I) and Cu(II) (displayed in **Fig. 8.3a**)

were generated by extracting the signal from the phase stack at the spatial locations of Cu(0), Cu(I) and Cu(II) determined by the analysis of the ptychography absorption stack (**Fig. 8.2**) (i.e., from the same measurement). These phase spectra were used to make an SVD analysis of the Cu L_3 spectro-ptychography phase image stack (**Fig. 8.3**). The spatial distributions of Cu(0), Cu(I) and Cu(II) components **(Fig. 8.3b, 8.3c, 8.3d**) and a relative scale colour coded composite (**Fig. 8.3f**) derived from the phase stack are similar to those derived from the ptychography amplitude stack. The residual of the fit (**Fig. 8.3e**) is rather featureless at the spatial scale of the particles, but it does contain a slowly varying diagonal structure. We interpret this as a result of changes in the phase of the incident probe over the course of the measurement. The probe phase is assumed to be constant in the ptychographic reconstruction. As with the analysis of the amplitude signal, a small amount of Cu(II) is reported from the fit. The phase signal of Cu(II) is quite sharp and occurs ~2 eV below the Cu(0) and Cu(I) phase signals, which means the sensitivity to Cu(II) is very high. The particles consist of Cu(I) and Cu(0), as indicated in the colour-coded composites of component maps derived from both the ptychography amplitude (**Fig. 8.2g**) and ptychography phase (**Fig. 8.3f**) stacks. It is noteworthy that, based only on contrast, the analysis of the phase signals suggests more Cu(I) relative to Cu(0) than determined from the amplitude signals. We think this does not mean there is more Cu(I); rather just that the phase is more sensitive to Cu(I) than to Cu(0). Basically, at this point in the development of soft X-ray ptychography, the relationship between phase spectra and material thickness is not sufficiently understood so as to allow quantitative analysis of phase signals measured by spectro-ptychography. Thus, there is no intensity scale bar for the component maps displayed in Fig.3.

8.2.3 Morphological and chemical changes of a single Cu particle under CO_2R conditions

In situ spectro-ptychography was used to measure the morphology and spatially-resolved oxidation state distributions in a single Cu particle (denoted as **area C**) in CO_2-saturated 0.1M $KHCO_3$ under a series of applied electrode potentials [OCP, +0.1, -0.2, -0.5, -0.8 and -0.85 V_{RHE}] spanning electrochemical CO_2R conditions. After collecting *in situ* spectro-ptychography 4-E stacks or fully sampled Cu L_3 energy stacks at each applied electrode potential, the electrode was returned to OCP (~0.36 V_{RHE}) to return to the same catalyst starting state. **Fig. 8.4a** depicts the electrode potential profile as a function of time utilized during the sequence of measurements. The steady state current measured during the chronoamperometry measurement holds are plotted in **Fig 8.4b**. Supplemental section **SI-8**, **Fig. S-11** displays the current as a function of time at

each potential. We note that Faradaic efficiencies, current densities and product distributions for CO_2R using the same type of electrocatalyst (electrodeposited Cu on Au) were measured in a lab-based 2-compartment electrochemical cell [33]. The similarity of the onset of higher negative currents and unambiguous product-based evidence of CO_2 reduction [33] are direct evidence that the larger negative current observed at electrode potentials below -0.8 V_{RHE} in **Fig.8.4b** is due to CO_2R reactions.

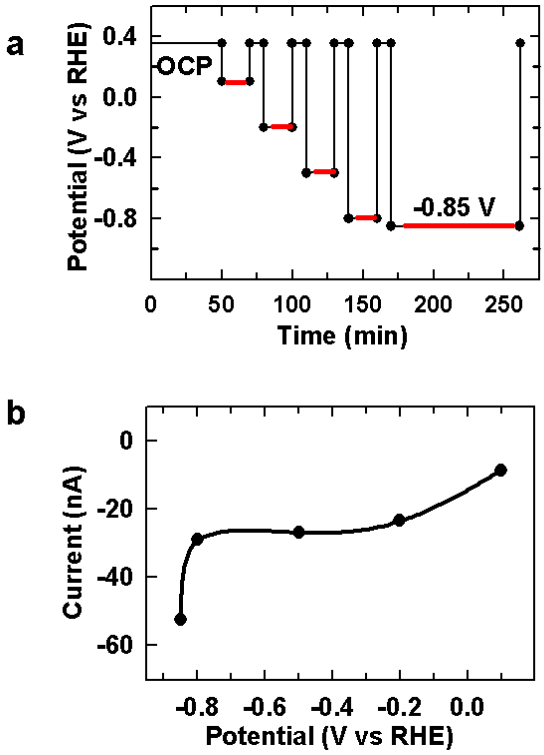

Figure 8.4. Electrochemical tests in area C during *in situ* reduction to CO_2R conditions. (a) the applied electrode potential as a function of time. The red lines indicate when the *in situ* spectro-ptychography measurements were conducted. (b) Steady state currents measured in the *in situ* cell at the indicated applied electrode potentials.

Fig. 8.5a displays a STXM transmission image at 933.3 eV of **area C. Fig. 8.5b** is an expansion in the area of the *in situ* spectro-ptychography studies for a single Cu particle with a pseudo-cubic morphology. **Fig. 8.5c** shows the ptychography amplitude image at 933.3 eV measured from the same area. The improvement in spatial resolution is dramatic (~25 nm in ptychography versus ~75 nm in STXM, **Figs. S-5, S-6**).The edges of the particle are much better defined in ptychography, allowing us to track changes in the particle morphology as a function of electrode

potential under CO_2R conditions. The Cu particle in **Fig. 8.5c** showed a cubic shape prior to applying potential, very similar to the structure of Cu particles reported in the literature prepared by similar methods.[9-12,25, 58, 59]

Ptychography 4-E stacks were used to quantitatively monitor the morphology and chemical changes in the Cu-based particle as a function of potential from +0.1 to -0.8 V_{RHE}. **Fig. 8.5d** to 8.**5g** show ptychography amplitude images at 933.3 eV, collected at the four different electrode potentials indicated in the figure. As the electrode potential becomes increasingly negative and enters the regime of CO_2R (~ < -0.2 V vs RHE), the Cu particles lose their initial cubic structure and grow small, sharp dendrites. The reconstructed 4-E ptychography amplitude stacks were converted to absorption and analyzed by SVD-fitting to obtain quantitative component maps of each Cu species, as shown in section **SI-9**, **Fig. S-12**. The colour-coded composite component maps of Cu(0), Cu(I) and Cu(II) in absolute scaling (showing the thickness of the materials in units of nm) are presented in **Fig. 8.5h** to **Fig. 8.5l**, showing the spatially-resolved distribution of each Cu species under each electrode potential. At OCP, the cubic particle was a mixture of Cu(0) and Cu(I). When more negative electrode potentials were applied, the Cu(I) in the cubic particle converted to Cu(0), with almost all of the Cu(I) being converted to Cu(0) at potentials below -0.2 V_{RHE}.

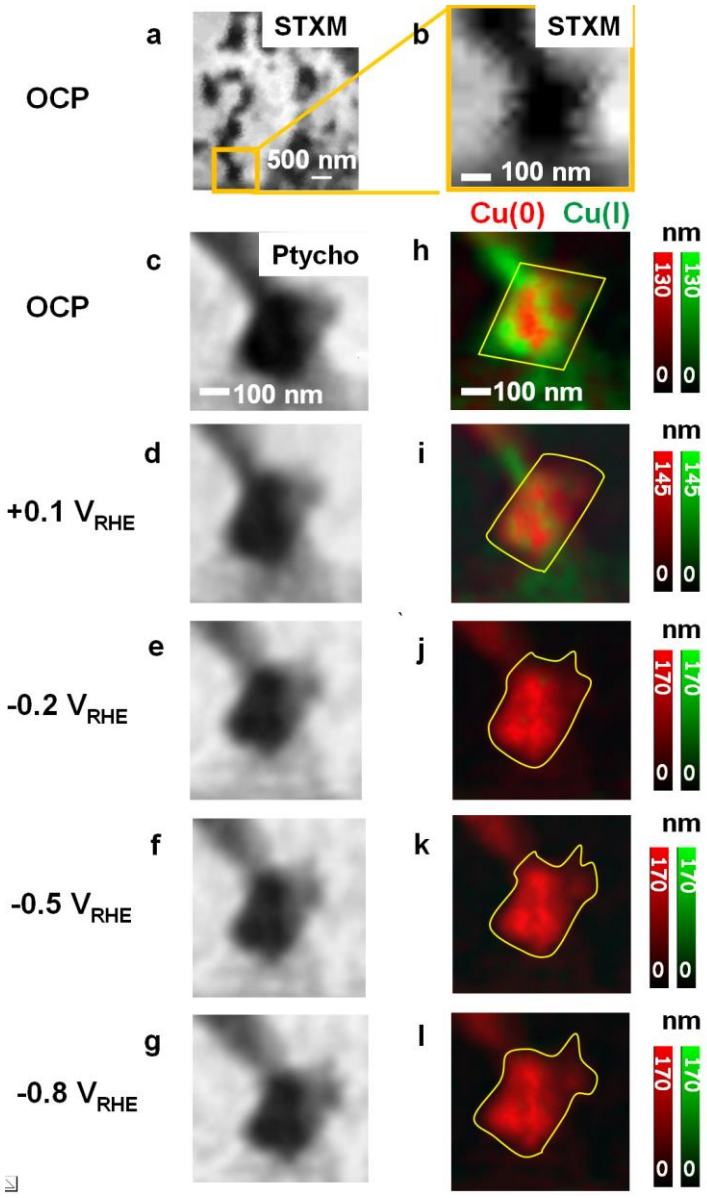

Figure 8.5 ***in situ*** **spectro-ptychography chronoamperometry study**. (a) STXM image of **area C** at 933.3 eV at OCP (b) STXM image of Cu cubic particle at 933.3 eV. Ptychography amplitude images at 933.3 eV of the Cu cubic particle at (c) OCP (d) +0.1V (e) -0.2V (f) -0.5V (g) -0.8V, all potentials versus RHE. Color coded composite of the Cu(0) (red) and Cu(I) component maps of the initially cubic particle using relative scaling derived from spectro-ptychography 4-E stacks measured at (h) OCP (i) +0.1V (j) -0.2V (k) -0.5V and (l) -0.8V vs RHE. The yellow contour lines in (h-l) identify the regions with thickness of Cu(0) higher than 20 nm (see left column of images in **Fig. S.12**).

The average spectrum of the Cu cubic particle (regions of yellow shapes in **Fig. 8.5h** to **Fig. 8.5l**) extracted from the 4-E and fully sampled Cu L_3 spectro-ptychography amplitude stacks as a

function of electrode potential (+0.1 to -0.85 V_{RHE}) are presented in **Fig. S-13**. The evolution of the average spectrum confirms the conversion from Cu(I) to Cu(0) during the electrochemical process. Moreover, the spectra extracted from the Cu(0)-rich and Cu(I)-rich regions were analyzed by SVD using the OD1 (optical density per nm) reference spectra to quantify the composition under various potentials. The results showing the average thickness of each Cu species on the Cu nanoparticles are presented in **Table 8.1**. This spectral-domain analysis confirms the changes of Cu oxidation states during the CO_2R reactions. No statistically significant amounts of Cu(I) were detected at potentials more negative than -0.2 V_{RHE}, verifying that Cu(0) is the oxidation state of the active catalyst under electrochemical CO_2R conditions. The average thickness of Cu(0) gradually reducing could be due to the detachment of Cu materials from the catalytic particles during the CO_2R process, which has been observed in other literature. [20] Our results quantitatively show the Cu detachment during the reactions.

A detailed Cu L_3 ptychography stack was measured during chronoamperometry at -0.85 V_{RHE}, where Cu is very active for the electrochemical conversion of CO_2 into alcohol and hydrocarbon products.[33, 60] Under these electrochemical conditions, bubbles were occasionally observed at or near the working electrode surface, likely due to the formation of gas phase CO_2R products (CO, small hydrocarbons) and/or H_2 evolution from water splitting. An example of a spectro-ptychography measurement under gas evolution conditions is presented in section **SI-11**, **Fig. S-16, SI-video**. Despite the changing position of the liquid interface, it was still possible to conduct spectro-ptychography measurements on the same cubic Cu particle. Quantitative component maps of Cu(0), Cu(I) and Cu(II) and a colour-coded composite of the component maps from processing of the ptychography amplitude stack are presented in section **SI-12**, **Fig. S-17.** The results from the full spectro-ptychography stack are similar to those from the 4-E stack measured at -0.8 V_{RHE} (**Fig. 8.5l** and **Fig S-13)**, thereby verifying the chemical analysis provided by the 4-E stack.

Table 8.1. Compositions of Cu cubic particles under various potentials

	Average thickness (nm) [a]		
Potential (V_{RHE})	Cu(0)	Cu(I)	Cu(II)
OCP	69 ± 5	45 ± 4	<1
+0.1	81 ± 7	19 ± 2	<1
-0.2	83 ± 7	<1	<1
-0.5	76 ± 6	<1	<1
-0.8	78 ± 6	<1	<1
-0.85	60 ± 5	<1	<1

a. The uncertainties combine statistical (±3 %) and estimated systematic uncertainties. The latter were estimated by comparing quantitation of component maps derived from slight but reasonable changes in the analysis procedure.

8.3. Discussion

Individually, *in situ* flow electrochemical STXM and soft X-ray spectro-ptychography are very challenging experimental methods. The combination of controlled *in situ* electrochemical modification of samples and soft X-ray spectro-ptychography has not been reported previously in the scientific literature to the best of our knowledge. In this work, we demonstrate the application of *in situ* spectro-ptychography under controlled electrolyte flow and applied electrode potentials to characterize Cu catalysts under electrochemical CO_2R conditions. This research shows that spectro-ptychography can provide chemically selective imaging under *in situ* conditions with results similar to those from STXM, albeit with superior spatial resolution and image quality. The improved spatial resolution provides increased insight into the morphological changes as the catalyst particles evolve under reducing conditions (**Fig. 8.1, Fig. 8.5**). The combination of improved spatial resolution and the ability to quantitatively map Cu oxidation states with high spatial resolution made it possible to monitor the morphological and chemical state evolution of a single Cu particle under CO_2R conditions.

Using *in situ* spectroscopic [4, 6, 11, 23] or microscopic characterizations [10, 20], some studies have reported the presence of Cu(I) under electro-catalytic CO_2R conditions [3, 10, 14-17], while others report only Cu(0) [18-20]. The quantitative, spectroscopy-based results from our *in situ* spectro-ptychography measurements provide further insight into this issue. As reported in **Table**

8.1, within estimated errors, the particles are 100 ± 7 % Cu(0) at electrode potentials of -0.2V $_{RHE}$ or lower. This strongly supports the viewpoint that non-zero-valent Cu species do not exist under steady-state electrochemical CO_2R conditions.[18-20] After complete conversion of Cu(I) to Cu(0) at -0.2V_{RHE}, there are no further oxidation state changes, but morphology changes continue in the form of dendrite growth (**Fig. 8.5**). This suggests that Cu particles do not change shape under CO_2R as a result of changing oxidation state. Rather the morphology changes are the result of restructuring, reconstruction and re-deposition processes caused by the driving forces associated with the CO_2R reaction itself [20-23, 25]. These results are in good accord with a sub-set of other *in situ* studies of the same type of Cu CO_2R electrocatalysts. [3, 4, 6, 20, 21, 25] In addition, they are supported by the results of a parallel study we have conducted using in situ STXM on a similar electrocatalyst using the same *in-situ* device and protocol including electrodeposition from $CuSO_4$/KCl, followed by changing the electrolyte to CO_2-saturarted $KHCO_3$ and potential dependent chronoamperometry. The in situ STXM measurements were made over a larger area of the electrode and thus a much large number of Cu-based particles. The trends observed in the in situ STXM study are consistent with those reported in this work. [33]

Overall, this study demonstrates *in situ* soft X-ray spectro-ptychography provides sensitive and quantitative chemical speciation with high spatial resolution which gives insight into the complex structural and chemical evolution of CO_2R and other electrocatalysts. In this study we found that *in situ* spectro-ptychography is practical for small areas (< 2 μm). Larger areas, with the required large overlap sampling (>80%, see Methods section), take too long and can generate data sets larger than the SOLEIL HERMES ptycho processing computers can handle. Currently, the upper limit at HERMES for PyNX analysis of a single ptychography data set (1 real space image) is 2500 diffraction images. Thus spectro-ptychography is best suited to studies of detailed changes in small areas. In the context of studies of Cu-based CO_2R electrocatalysis, the 4-E Cu L_3 stack approach is very time efficient, allowing studies of a larger range of *in situ* conditions within a limited time period. We estimate that 4-E stacks save more than 75% of the time compared to 40 energy stacks. This raises the potential of following the kinetics of some changes, as long as the processes occur in the few minute time scale. However it is always useful to measure the detailed energy stacks at selected conditions, both to confirm results from faster 4-E stacks, and to check for unexpected components.

As a final comment, the total elapsed time for spectro-ptychography using defocused spot size (e.g. 1 μm, as used in this work) is not much longer than what would be required to measure STXM of the same area with suitable parameters. Basically the spatial sampling has to be much greater in STXM than in spectro-ptychography in order to sufficiently sample the morphology. The data collection time for spectro-ptycho of area B was 50 minutes. To measure the same area by STXM using a 20 nm spot size and 5 ms/pixel the acquisition time would be 70 minutes (3 x 3 , 150 x 150 pixels, 5 ms/pixel, 34 energies). If the same dwell time as spectro-ptychography was used (60 ms), the time for the analogous STXM measurement would be 64 hours. That long a STXM measurement would deliver an enormous radiation dose. So, for the size of areas studied in this work, ptychography has a slight advantage in elapsed time (ignoring the significant amount of time needed for ptychography reconstruction !!) and huge advantages in terms of (i) much finer pixels in the final reconstructed images, (ii) better spatial resolution, (iii) better statistics, and (iv) greatly reduced radiation dose, and thus less concern about radiation damage. Aside from the effort and computational resources needed to carry out the reconstruction (which is getting easier year-by-year), spectro-ptychography has many advantages relative to conventional STXM.

Acknowledgements

We thank Prof. Martin Obst and his student, Pablo Ingino, (Bayreuth University) for sharing the design of their *in situ* cell and assisting with its optimization. We also thank Paul Gatt and Michael Clarke at McMaster University for CNC machining, and Prof. Jose Moran-Mirabal and his students for their assistance with development of the *in situ* spectro-ptychography device. We thank Dr. Hao Yuan for assistance with the FRC analysis. This research was supported by the Natural Sciences and Engineering Research Council (NSERC) Discovery Grant program, the National Research Council of Canada (NRC) Materials for Clean Fuels Challenge program and TotalEnergies. Measurements were made at the STXM / ptychography end station of the HERMES beamline at Synchrotron SOLEIL. The authors thank synchrotron SOLEIL for the provision of beamtime (proposal No. 20220343).

Declaration of Interests section

The authors declare no competing interests.

8.4. Methods

8.4.1 *In situ* device and instrumentation

A custom-designed microfluidic device encompassing an electrochemical micro-chip reactor [33] was used for these *in situ* studies. The device is presented in more detail in supplementary information, section **SI-13**. The *in situ* device consists of a machined printed circuit board (PCB, **Fig. S-18a**) front frame, a poly(methyl methacrylate) (PMMA) backplate (**Fig. S-18b**) and a polydimethylsiloxane (PDMS)/glass cell equipped with the electrochemical *in situ* chips (**Fig. S-18c**). The electrode equipped *in situ* chip (**Fig. S-18d**), fabricated by Norcada Inc. (https://www.norcada.com), is connected to a potentiostat (Ivium pocketstat, https://www.ivium.com/instruments/) through a 4-pin electrical connector on the PCB frame. The 4 microfluidic channels (shown as dotted lines **Fig. S-18c**) are connected using Tefzel fluoropolymer tubing (Idex, www.idex-hs.com) with inner diameter of 0.0254 cm and outer diameter of 1.5875 cm. One of these tubes is connected to a syringe pump (New Era 1000, https://www.syringepump.com/) for controlled electrolyte flow. The electrochemical reactions were performed using the 3-electrodes on base chip E (**Fig. S-18e**). Spacer chip F has a pre-deposited spacer layer (500 nm or 1 μm thick) defining the height of the flow channel. The 3 electrodes on the base chip E, working/ counter/ reference electrode (WE/CE/RE), are all gold. (**Fig. S-18e**) The darker circles on the WE and CE are regions with thinner Au coating to reduce X-ray absorption from the electrodes. **Fig. S-18a** and **S-18b** show pictures of the assembled device inside the HERMES' STXM chamber with the Dhyana 92 ptychography camera (https://www.tucsen.com/) and associated stray light shield installed.

8.4.2 STXM and Ptychography

8.4.2.1 STXM. The HERMES beamline is described in detail elsewhere [61]. The STXM is commercial, supplied by RI Research Instruments Gmbh (https://research-instruments.de/). The Fresnel Zone Plate (FZP) with an outermost zone width of 25 nm is supplied by Applied Nanotools Inc. (https://www.appliednt.com). The sample is placed on an XYZ piezoelectric stage. The lateral position of the sample relative to the FZP is stabilized to a precision of 5 nm by a differential laser interferometer system [62]. Rectilinear raster scans are used. In STXM mode, the X-rays transmitted through the sample are converted into visible photons by a phosphor and are detected in single event counting mode by a high-performance photomultiplier tube.

8.4.2.2 Ptychography. The set-up for ptychography and the operating procedures are described in detail elsewhere.[35, 36, 39, 40] In this work a modified Dhyana-92 sCMOS camera [43,44] was used. A coated sensor was used, since X-rays above 900 eV are damaging to the uncoated sensor.[43] Before each ptychographic measurement, a statistically precise background is measured with the X-ray beam blocked by an upstream valve. The average background after subtraction of the stable camera background is about 1 electron, giving a dynamic range of over 20,000. A custom holder allows the camera to be mounted on the STXM detector stage with enough positioning flexibility to center the camera on the diffracted image and adjust the sample-to-camera distance as a function of photon energy to ensure fixed-*q* scans. All ptychography measurements were made using a defocused spot, which reduces radiation dose, due to much lower fluence (factor of 400, relative to the fully focused ~50 nm spot). In order to generate a 1.0 μm defocused spot, the zone plate was moved upstream by 18 μm, a distance calculated from dr/dz = D/f where (dr/dz) is the change in the spot size (dr) for a given change in position of the ZP relative to the sample (dz), D is the diameter of the FZP, and f is the focal length given by f = Dδr/E where δr is the outermost zone width (25 nm), and E is the photon energy. Diffraction images were sampled with 80 % or 90 % overlap and a 1.0 μm defocused spot.

8.4.3 *In situ* STXM and Ptychography

The working/ counter/ reference electrode (WE/CE/RE), are gold. All potentials are measured relative to the Au pseudo-reference (V_{Au}) during the experiments. The open circuit potential (OCP) is ~ –0.045 V_{Au} ± 0.01 V_{Au}, showing that stable potentials are achieved using the Au pseudo-reference. The measured potentials versus the Au pseudo-reference were subsequently converted to potential versus the reversible hydrogen electrode (RHE, V_{RHE}), by a conversion of V_{RHE} = V_{Au} + 0.4 V which is determined by comparing cyclic voltammograms (CV) for Cu reduction and oxidation under the *in situ* conditions (versus Au) and under the lab-based conditions (versus RHE) where a Ag/AgCl reference electrode was used to bridge to the RHE scale. The OCP of –0.045 V_{Au} is equivalent +0.355 V_{RHE}.

Details of the procedures used for the *in situ* measurements are presented in **section SI-14**. First, Cu particles are electrodeposited from a mixture solution of 10mM $CuSO_4$ and 10mM KCl on the thin region of the Au working electrode in the *in situ* device. The electrolyte tubes are pre-filled

with $CuSO_4$/KCl solution and connected with the assembled *in situ* device. Then a syringe pump is used to slowly (50 μL/hr) fill the *in situ* device with the electrolyte. The filling process is conducted under an optical microscopy(20x objective), to confirm that the electrolyte completely fills the window region and that the electrolyte layer is of appropriate thickness, as measured by counting Newton rings. For the first *in situ* experiment, the Cu electrodeposition was carried out by performing 3 cycles of cyclic voltammetry in the potential range -0.1 to +0.4 V_{RHE} with a scan rate of 20 mV/s. In this way, Cu particles were deposited on the WE electrode region, as shown by STXM images in **Fig. S-19.** Our goal was to generate cubic particles, as documented using similar, mixed Cu(II) and KCl electrolyte solutions [9,10]. Copper particles having a well-defined cubic structure have been reported to have good efficiency and C_{2+} selectivity for CO_2 reduction.[9-12] The changing morphology in these images (all recorded by STXM at 933.3 eV) is caused by electrochemical changes during the *in situ* measurements. The last spectro-ptychography recorded on **area A** used a fully focused X-ray beam (~50 nm). (The results reported in **Fig. 8.1** were measured before that scan). When the incident flux was increased to >200 MHz by opening the exit slits, the high radiation dose caused X-ray induced reduction of Cu oxide to copper, as evidenced by the square region observed in area A of the electrode that was illuminated under these high flux conditions (region in yellow square in **Fig. S-19b**). After reducing the incident X-ray flux to that used for this study (20 MHz), radiation damage artifacts were not observed (see Fig. **S.20** and **S.21** . **Section SI-15** discusses the issue of radiation damage during these measurements in more detail. It estimates the X-ray doses used to obtain the reported results and provides experimental evidence that the results reported in this *in-situ* spectro-ptychography study of Cu electrocatalysts are not significantly affected by radiation damage.

After *in situ* Cu deposition under the optical microscopy, the electrolyte was changed to CO_2 saturated 0.1M $KHCO_3$, for CO_2R reaction. Millipore Type I Ultrapure water was first used to flush the $CuSO_4$/KCl out of the *in situ* device. The micro-chip reactor was the filled with CO_2 saturated 0.1M $KHCO_3$ electrolyte using the syringe pump with a flow rate of 25 μL/hr. The whole process for changing the electrolyte took around 20 mins.

Different oxidation states were observed in the particles measured in **area A** and **area B**. A possible reason for this is given in supplemental information, section **SI-14**.

After Cu particle deposition and changing the electrolyte to CO_2 saturated 0.1M $KHCO_3$, the *in situ* device was carefully loaded to the STXM instrument chamber. Then the air in the chamber tank is replaced with He gas for STXM and spectro-ptychography measurements. In some cases, the tank is pumped to <1 mbar and the tank backfilled with 0.8 - 1 bar He. In others, a slow flow of He was used to displace the air, without the STXM tank pressure deviating much from 1 bar. Operation at 1 bar, greatly reduced the window bulging that is common when operating *in situ* cells with thin silicon nitride (SiNx) windows. While performing measurements, chronoamperometry at various potentials was applied to the Cu particles on the WE at **areas A, B** and **C**. **Table S-2** summarizes the potentials and measurements of STXM or spectro-ptychography performed to generate the data presented in this paper. When at low potentials or OCP, an electrolyte flow rate of 20 μl/hr is used. While at potentials more negative than -0.5 V_{RHE} where H_2 and CO gas are produced, a faster electrolyte flow rate (50 μl/hr) is applied to remove the gas bubbles from WE region. Between the measurements and prior to changing the potential, the system was returned to open circuit potential +0.355 V_{RHE} (-0.045 V_{Au}) in order to have a standard starting point before applying the next potential in sequence.

8.4.4 Ptychography data processing

The basic principles of scanning coherent diffraction imaging, known as ptychography [36], are outline in **supporting information, section S-1**. Spectro-ptychography [37-39] further extends the basic ptychography imaging method by measuring ptychographic data at a sequence of X-ray energies spanning an X-ray absorption edge of an element of interest, in this case, the Cu L-edge. Ptychographic reconstruction was carried out using the open-source PyNX software [63] developed at the European Synchrotron Radiation Facility. 200 iterations of the Alternate Projection algorithm with a single probe function (AP**200) was used for the initial analysis, which could be performed in ~15 m, about the same time it takes to acquire the next spectro-ptychographic 4-E data set. After the run, the data was re-processed using 800 iterations (AP**800). The increased number of iterations typically reduced the extent of raster grid artifact, and slightly improved spatial resolution. Details of the ptychography acquisition and reconstruction are presented in **Table S-2**.

8.4.5 Spectromicroscopy data processing

Three types of STXM and ptychography measurements were used in this work: image, full stack, 4-energy (4-E) stack. STXM/ ptychography **images** were measured by scanning the sample in a point-by-point mode while recording diffraction images (DI) with 20 - 60 ms acquisition time at each pixel. Spectroscopic information was obtained by recording a **stack**, which is a series of STXM or ptychography image sequences [64], covering a range of photon energies. In this work, a Cu L_3 stack consisted of measurements at 34 or 40 energies from 920 to 946 eV. A 2 μm x 2 μm (20 x 20) pixel, 60 ms/DI ptychography stack took ~ 90 m to measure. When measuring the Cu L_3 STXM stack, using the camera and integrating the full DI, the pixel size was 50 - 100 nm, with a per pixel dwell of 20 ms, which took ~30 m. The **4-E stack** used in this work measured images at 927.3, 930.3, 933.3 and 937.3 eV. This took ~20 m for ptychography and ~15 m for STXM, the 4-E stacks provided similar chemical mapping as a full stack, although the latter gave more complete spectroscopic information.

The STXM and reconstructed ptychography data was analyzed using aXis2000 software.[65] The images in a stack typically drift by a few hundred nm over a 40-80 eV scan range. Therefore, the stacks are aligned to ~2 nm registry using a Fourier cross-correlation method. The transmission signal (I) of the aligned stack is converted to optical density (OD) using the Beer Lambert Law: $OD_{(x,y)} = -ln(I/ I_o)$, where I is the X-ray intensity transmitted though the sample and support, and I_o is the incident X-ray intensity measured off the sample but where the X-rays transmit through all other parts of the X-ray path (optics, windows, zone plate, detector) and the sample support (SiN_x window). After OD conversion, the Cu L_3 X-ray absorption spectra of selected areas (many pixels, which are not necessarily contiguous, but are related by spectroscopy) are extracted from the STXM and ptychography stacks using methods described in greater detail below.

The fitting procedure in aXis2000, which is based on a singular value decomposition (SVD) matrix method [66], was used to analyze the stacks. The SVD stack fitting routine fits the NEXAFS spectrum at each pixel to a user-identified set of reference spectra, which can be derived from the spectroscopy on well-defined reference compounds (external). The result of a SVD stack fitting is a set of component maps (spatial distributions), one for each component, along with the residual of the fit.[26, 27] To quantitatively fit the data, reference spectra were converted to an absolute intensity scale, optical density per nm (OD1), by scaling the relative

intensity spectra so that the signal in the pre-edge and far-continuum (>30 eV above the edge) match the predicted spectrum for 1 nm thickness of the known composition and density of the reference material, which is calculated using elemental parameters from the Centre for X-ray Optics database (https://henke.lbl.gov/optical_constants/). The gray scale of the component maps derived from SVD stack fitting using OD1 reference spectra is an estimate of the thickness of that component at each pixel in the region analyzed. In order to confirm the validity of the spectromicroscopy fitting procedure, spectra are extracted from specific areas of a stack, identified based on morphology and / or spectral similarity and then subjected to a 'curve-fit' procedure in which SVD is used to fit the extracted spectra. When reference spectra on OD1 intensity scales are used in a 'curve-fit', the contribution of each spectral component is an estimate of the average thickness in nm of that component in the area from which the spectra were extracted. Colour-coded composites of the component maps are displayed in both relative and absolute scaling. Relative scaling (e.g. **Fig. 8.2g**), in which the grayscale values of each component are mapped to a 0-255 bit scale for the color representing that component, shows the locations of a component, independent of the amount of the other components. In contrast, in absolute scaling (e,g, **Fig. 8.2h**), the thickness values for each component are displayed such that the 0-255 bit scales of the red, green and blue, are each mapped to the same limits, by default, the minimum and maximum of thickness over all three components.

References

1. Li, X., Wu, X., Lv, X., Wang, J., & Wu, H. B. (2021). Recent advances in metal-based electrocatalysts with hetero-interfaces for CO2 reduction reaction. *Chem Catalysis*, *2* (2), 262-291.
2. Zhang, C., Shahcheraghi, L., Ismail, F., Eraky, H., Yuan, H., Hitchcock, A. P., & Higgins, D. (2022). Chemical Structure and Distribution in Nickel–Nitrogen–Carbon Catalysts for CO2 Electroreduction Identified by Scanning Transmission X-ray Microscopy. *ACS catalysis*, *12*(15), 8746-8760.
3. Chou, T. C., Chang, C. C., Yu, H. L., Yu, W. Y., Dong, C. L., Velasco-Vélez, J. J., ... & Wu, H. L. (2020). Controlling the oxidation state of the Cu electrode and reaction intermediates for electrochemical CO2 reduction to ethylene. *Journal of the American Chemical Society*, *142*(6), 2857-2867.
4. Gibbons, B. M., Wette, M., Stevens, M. B., Davis, R. C., Siahrostami, S., Kreider, M., ... & Jaramillo, T. F. (2020). In situ X-ray absorption spectroscopy disentangles the roles of copper and silver in a bimetallic catalyst for the oxygen reduction reaction. *Chemistry of Materials*, *32*(5), 1819-1827.
5. De Luna, P., Hahn, C., Higgins, D., Jaffer, S. A., Jaramillo, T. F., & Sargent, E. H. (2019). What would it take for renewably powered electrosynthesis to displace petrochemical processes? *Science*, *364*(6438), eaav3506.
6. Yang, Y., Roh, I., Louisia, S., Chen, C., Jin, J., Yu, S., ... & Yang, P. (2022). Operando Resonant Soft X-ray Scattering Studies of Chemical Environment and Interparticle Dynamics of Cu Nanocatalysts for CO2 Electroreduction. *Journal of the American Chemical Society*, *144*(20), 8927-8931.
7. Tabassum, H., Yang, X., Zou, R., & Wu, G. (2022). Surface engineering of Cu catalysts for electrochemical reduction of CO2 to value-added multi-carbon products. *Chem Catalysis*. *2* (7), 1561-1593.
8. Hahn, C., Hatsukade, T., Kim, Y. G., Vailionis, A., Baricuatro, J. H., Higgins, D. C., ... & Jaramillo, T. F. (2017). Engineering Cu surfaces for the electrocatalytic conversion of CO2: Controlling selectivity toward oxygenates and hydrocarbons. *Proceedings of the National Academy of Sciences*, *114*(23), 5918-5923.

9. Timoshenko, J., Bergmann, A., Rettenmaier, C., Herzog, A., Arán-Ais, R. M., Jeon, H. S., ... & Roldan Cuenya, B. (2022). Steering the structure and selectivity of CO2 electroreduction catalysts by potential pulses. *Nature Catalysis*, *5*(4), 259-267.
10. Arán-Ais, R. M., Scholten, F., Kunze, S., Rizo, R., & Roldan Cuenya, B. (2020). The role of in situ generated morphological motifs and Cu (i) species in C2+ product selectivity during CO2 pulsed electroreduction. *Nature Energy*, *5*(4), 317-325.
11. Timoshenko, J., & Roldan Cuenya, B. (2020). In situ/operando electrocatalyst characterization by X-ray absorption spectroscopy. *Chemical reviews*, *121*(2), 882-961.
12. Nitopi, S., Bertheussen, E., Scott, S. B., Liu, X., Engstfeld, A. K., Horch, S., ... & Chorkendorff, I. (2019). Progress and perspectives of electrochemical CO2 reduction on copper in aqueous electrolyte. *Chemical reviews*, *119*(12), 7610-7672.
13. Kibria, M. G., Edwards, J. P., Gabardo, C. M., Dinh, C. T., Seifitokaldani, A., Sinton, D., & Sargent, E. H. (2019). Electrochemical CO2 reduction into chemical feedstocks: from mechanistic electrocatalysis models to system design. *Advanced Materials*, *31*(31), 1807166.
14. Cheng, D., Zhao, Z. J., Zhang, G., Yang, P., Li, L., Gao, H., ... & Gong, J. (2021). The nature of active sites for carbon dioxide electroreduction over oxide-derived copper catalysts. *Nature communications*, *12*(1), 395.
15. Eilert, A., Cavalca, F., Roberts, F. S., Osterwalder, J., Liu, C., Favaro, M., ... & Nilsson, A. (2017). Subsurface oxygen in oxide-derived copper electrocatalysts for carbon dioxide reduction. *The journal of physical chemistry letters*, *8*(1), 285-290.
16. Wang, H. Y., Soldemo, M., Degerman, D., Lömker, P., Schlueter, C., Nilsson, A., & Amann, P. (2022). Direct Evidence of Subsurface Oxygen Formation in Oxide-Derived Cu by X-ray Photoelectron Spectroscopy. *Angewandte Chemie International Edition*, *61*(3), e202111021.
17. Fields, M., Hong, X., Nørskov, J. K., & Chan, K. (2018). Role of subsurface oxygen on Cu surfaces for CO2 electrochemical reduction. *The Journal of Physical Chemistry C*, *122*(28), 16209-16215.
18. Scott, S. B., Hogg, T. V., Landers, A. T., Maagaard, T., Bertheussen, E., Lin, J. C., ... & Chorkendorff, I. (2019). Absence of oxidized phases in Cu under CO reduction conditions. *ACS Energy Letters*, *4*(3), 803-804.
19. Lum, Y., & Ager, J. W. (2018). Stability of residual oxides in oxide-derived copper catalysts for electrochemical CO2 reduction investigated with 18O labeling. *Angewandte Chemie International Edition*, *57*(2), 551-554.

20. Grosse, P., Yoon, A., Rettenmaier, C., Herzog, A., Chee, S. W., & Roldan Cuenya, B. (2021). Dynamic transformation of cubic copper catalysts during CO2 electroreduction and its impact on catalytic selectivity. *Nature Communications*, *12*(1), 6736.
21. Arán-Ais, R. M., Rizo, R., Grosse, P., Algara-Siller, G., Dembélé, K., Plodinec, M., ... & Cuenya, B. R. (2020). Imaging electrochemically synthesized Cu2O cubes and their morphological evolution under conditions relevant to CO2 electroreduction. *Nature Communications*, *11*(1), 3489.
22. Alnoush, W., Black, R., & Higgins, D. (2021). Judicious selection, validation, and use of reference electrodes for in situ and operando electrocatalysis studies. *Chem Catalysis*, *1*(5), 997-1013.
23. Velasco-Velez, J. J., Mom, R. V., Sandoval-Diaz, L. E., Falling, L. J., Chuang, C. H., Gao, D., ... & Schlögl, R. (2020). Revealing the active phase of copper during the electroreduction of CO2 in aqueous electrolyte by correlating in situ X-ray spectroscopy and in situ electron microscopy. *ACS energy letters*, *5*(6), 2106-2111.
24. Hitchcock, A. P., Zhang, C., Eraky, H., Shahcheraghi, L., Ismail, F., & Higgins, D. (2021). In situ and Operando Studies with Soft X-Ray Transmission Spectromicroscopy. *Microscopy and Microanalysis*, *27*(S2), 59-60.
25. Yang, Y., Louisia, S., Yu, S., Jin, J., Roh, I., Chen, C., ... & Yang, P. (2023). Operando studies reveal active Cu nanograins for CO2 electroreduction. *Nature*, *614*(7947), 262-269.
26. Ade, H., & Hitchcock, A. P. (2008). NEXAFS microscopy and resonant scattering: Composition and orientation probed in real and reciprocal space. *Polymer*, *49*(3), 643-675.
27. Hitchcock, A.P., (2012). *Soft X-ray Imaging and Spectromicroscopy* Chapter 22 in Volume II of the Handbook on Nanoscopy, eds. Gustaaf Van Tendeloo, Dirk Van Dyck and Stephen J. Pennycook (Wiley) 745-791.
28. Stöhr, J. (2013). *NEXAFS spectroscopy* (Vol. 25). Springer Science & Business Media.
29. Nelson Weker, J., & Toney, M. F. (2015). Emerging In Situ and Operando Nanoscale X-Ray Imaging Techniques for Energy Storage Materials. *Advanced Functional Materials*, *25*(11), 1622-1637.
30. Lim, J., Li, Y., Alsem, D. H., So, H., Lee, S. C., Bai, P., ... & Chueh, W. C. (2016). Origin and hysteresis of lithium compositional spatiodynamics within battery primary particles. *Science*, *353*(6299), 566-571.
31. Chourasia, A. K., Pathak, A. D., Bongu, C., Manikandan, K., Praneeth, S., Naik, K. M., &

Sharma, C. S. (2022). In Situ/Operando Characterization Techniques: The Guiding Tool for the Development of Li–CO2 Battery. *Small Methods*, *6*(12), 2200930.

32. Prabu, V., Obst, M., Hosseinkhannazer, H., Reynolds, M., Rosendahl, S., Wang, J., & Hitchcock, A. P. (2018). Instrumentation for in situ flow electrochemical scanning transmission X-ray microscopy (STXM). *Review of Scientific Instruments*, *89*(6), 063702.
33. Zhang, C., Eraky, H., Tan, S. Hitchcock, A.P. , Higgins D., *In-situ* Studies of Copper-based CO2 Reduction Electrocatalysts by Scanning Transmission Soft X-ray Microscopy, ACS Nano (submitted 30 Jun 2023 to ACS Nano; revised submitted 30 Aug 2023 (pre-print is online in chemrxiv: 10.26434/chemrxiv-2023-g2rj1)
34. Mefford, J. T., Akbashev, A. R., Kang, M., Bentley, C. L., Gent, W. E., Deng, H. D., ... & Chueh, W. C. (2021). Correlative operando microscopy of oxygen evolution electrocatalysts. *Nature*, *593*(7857), 67-73.
35. Jacobsen, C. (2019). *X-ray Microscopy*. Cambridge University Press.
36. Pfeiffer, F. (2018). X-ray ptychography. *Nature Photonics*, *12*(1), 9-17.
37. Mille, N., Yuan, H., Vijayakumar, J., Stanescu, S., Swaraj, S., Desjardins, K., ... & Hitchcock, A. P. (2022). Ptychography at the carbon K-edge. *Communications Materials*, *3*(1), 8.
38. Vijayakumar, J., Yuan, H., Mille, N., Stanescu, S., Swaraj, S., Favre-Nicolin, V., ... & Belkhou, R. (2023). Soft X-ray spectro-ptychography of boron nitride nanobamboos, carbon nanotubes and permalloy nanorods. *Journal of Synchrotron Radiation*, *30*(4).
39. Shapiro, D. A., Yu, Y. S., Tyliszczak, T., Cabana, J., Celestre, R., Chao, W., ... & Padmore, H. A. (2014). Chemical composition mapping with nanometre resolution by soft X-ray microscopy. *Nature Photonics*, *8*(10), 765-769.
40. Shapiro, D. A., Babin, S., Celestre, R. S., Chao, W., Conley, R. P., Denes, P., ... & Zhao, J. (2020). An ultrahigh-resolution soft x-ray microscope for quantitative analysis of chemically heterogeneous nanomaterials. *Science advances*, *6*(51), eabc4904.
41. Xu, Z., Wang, C., Liu, H., Tao, X., & Tai, R. (2017, June). Low-dose, high-resolution and high-efficiency ptychography at STXM beamline of SSRF. In *Journal of Physics: Conference Series* (Vol. 849, No. 1, p. 012033). IOP Publishing.
42. Xia, X., Wang, J., Hu, Y., Liu, J., Darma, A. I., Jin, L., ... & Yang, J. (2022). Molecular insights into roles of dissolved organic matter in Cr (III) immobilization by coprecipitation with Fe (III) probed by STXM-Ptychography and XANES spectroscopy. *Environmental Science & Technology*, *56*(4), 2432-2442.

43. Desjardins, K., Popescu, H., Mercère, P., Menneglier, C., Gaudemer, R., Thånell, K., & Jaouen, N. (2019, January). Characterization of a back-illuminated CMOS camera for soft x-ray coherent scattering. In *AIP Conference Proceedings* (Vol. 2054, No. 1, p. 060066). AIP Publishing LLC.
44. Desjardins, K., Medjoubi, K., Sacchi, M., Popescu, H., Gaudemer, R., Belkhou, R., ... & Jaouen, N. (2020). Backside-illuminated scientific CMOS detector for soft X-ray resonant scattering and ptychography. *Journal of Synchrotron Radiation*, *27*(6), 1577-1589.
45. Urquhart, S. G. (2022). X-ray Spectroptychography. *ACS omega*, *7*(14), 11521-11529.
46. Grote, L., Seyrich, M., Döhrmann, R., Harouna-Mayer, S. Y., Mancini, F., Kaziukenas, E., ... & Koziej, D. (2022). Imaging Cu2O nanocube hollowing in solution by quantitative in situ X-ray ptychography. *Nature Communications*, *13*(1), 4971.
47. Thibault, P., Dierolf, M., Menzel, A., Bunk, O., David, C., & Pfeiffer, F. (2008). High-resolution scanning x-ray diffraction microscopy. *Science*, *321*(5887), 379-382.
48. Shapiro, D. A., Yu, Y. S., Tyliszczak, T., Cabana, J., Celestre, R., Chao, W., ... & Padmore, H. A. (2014). Chemical composition mapping with nanometre resolution by soft X-ray microscopy. *Nature Photonics*, *8*(10), 765-769.
49. Fam, Y., Sheppard, T. L., Becher, J., Scherhaufer, D., Lambach, H., Kulkarni, S., ... & Grunwaldt, J. D. (2019). A versatile nanoreactor for complementary in situ X-ray and electron microscopy studies in catalysis and materials science. *Journal of synchrotron radiation*, *26*(5), 1769-1781.
50. Hoppe, R., Reinhardt, J., Hofmann, G., Patommel, J., Grunwaldt, J. D., Damsgaard, C. D., ... & Schroer, C. G. (2013). High-resolution chemical imaging of gold nanoparticles using hard x-ray ptychography. *Applied Physics Letters*, *102*(20).
51. Baier, S., Damsgaard, C. D., Klumpp, M., Reinhardt, J., Sheppard, T., Balogh, Z., ... & Grunwaldt, J. D. (2017). Stability of a bifunctional Cu-based core@ zeolite shell catalyst for dimethyl ether synthesis under redox conditions studied by environmental transmission electron microscopy and in situ X-ray ptychography. *Microscopy and Microanalysis*, *23*(3), 501-512.
52. Sun, T., Sun, G., Yu, F., Mao, Y., Tai, R., Zhang, X., ... & Zhou, J. (2020). Soft X-ray ptychography chemical imaging of degradation in a composite surface-reconstructed Li-rich cathode. *ACS nano*, *15*(1), 1475-1485.
53. Wise, A. M., Weker, J. N., Kalirai, S., Farmand, M., Shapiro, D. A., Meirer, F., & Weckhuysen,

B. M. (2016). Nanoscale chemical imaging of an individual catalyst particle with soft X-ray ptychography. *ACS catalysis*, *6*(4), 2178-2181.

54. Kränzlin, N., van Beek, W., Niederberger, M., & Koziej, D. (2015). Mechanistic Studies as a Tool for the Design of Copper-Based Heterostructures. *Advanced Materials Interfaces*, *2*(9), 1500094.
55. Kvashnina, K. O., Butorin, S. M., Modin, A., Soroka, I., Marcellini, M., Guo, J. H., ... & Nordgren, J. (2007). Changes in electronic structure of copper films in aqueous solutions. *Journal of Physics: Condensed Matter*, *19*(22), 226002.
56. Jiang, P., Prendergast, D., Borondics, F., Porsgaard, S., Giovanetti, L., Pach, E., ... & Salmeron, M. (2013). Experimental and theoretical investigation of the electronic structure of Cu2O and CuO thin films on Cu (110) using x-ray photoelectron and absorption spectroscopy. *The Journal of chemical physics*, *138*(2), 024704.
57. Koprinarov, I. N., Hitchcock, A. P., McCrory, C. T., & Childs, R. F. (2002). Quantitative mapping of structured polymeric systems using singular value decomposition analysis of soft X-ray images. *The Journal of Physical Chemistry B*, *106*(21), 5358-5364.
58. Roberts, F. S., Kuhl, K. P., & Nilsson, A. (2015). High selectivity for ethylene from carbon dioxide reduction over copper nanocube electrocatalysts. *Angewandte Chemie*, *127*(17), 5268-5271.
59. Roberts, F. S., Kuhl, K. P., & Nilsson, A. (2016). Electroreduction of carbon monoxide over a copper nanocube catalyst: surface structure and pH dependence on selectivity. *ChemCatChem*, *8*(6), 1119-1124.
60. Higgins, D., Landers, A. T., Ji, Y., Nitopi, S., Morales-Guio, C. G., Wang, L., ... & Jaramillo, T. F. (2018). Guiding electrochemical carbon dioxide reduction toward carbonyls using copper silver thin films with interphase miscibility. *ACS Energy Letters*, *3*(12), 2947-2955.
61. Belkhou, R., Stanescu, S., Swaraj, S., Besson, A., Ledoux, M., Hajlaoui, M., & Dalle, D. (2015). HERMES: a soft X-ray beamline dedicated to X-ray microscopy. *Journal of Synchrotron Radiation*, *22*(4), 968-979.
62. Kilcoyne, A. L. D., Tyliszczak, T., Steele, W. F., Fakra, S., Hitchcock, P., Franck, K., ... & Ade, H. (2003). Interferometer-controlled scanning transmission X-ray microscopes at the Advanced Light Source. *Journal of synchrotron radiation*, *10*(2), 125-136.
63. Favre-Nicolin, V., Girard, G., Leake, S., Carnis, J., Chushkin, Y., Kieffer, J., ... & Richard, M. I. (2020). PyNX: high-performance computing toolkit for coherent X-ray imaging based on

operators. *Journal of Applied Crystallography*, *53*(5), 1404-1413.

64. Jacobsen, C., Wirick, S., Flynn, G., & Zimba, C. (2000). Soft X-ray spectroscopy from image sequences with sub-100 nm spatial resolution. *Journal of Microscopy*, *197*(2), 173-184.
65. Hitchcock, A. P. aXis2000 is written in Interactive Data Language (IDL). It is available free for noncommercial use from http//unicorn.mcmaster. ca/aXis2000. html (*accessed Mar 17, 2023*).
66. Koprinarov, I. N., Hitchcock, A. P., McCrory, C. T., & Childs, R. F. (2002). Quantitative mapping of structured polymeric systems using singular value decomposition analysis of soft X-ray images. *The Journal of Physical Chemistry B*, *106*(21), 5358-5364.

Chapter 9

Summary and future work

This chapter summarizes this thesis. Suggestions are provided for future applications of in situ STXM and in situ spectro-ptychography to energy materials research.

9.1 Summary

In this thesis, advanced synchrotron-based spectro-microscopic techniques, STXM, and ptychography, were used to characterize several CO_2R electrocatalysts. The methods were subsequently upgraded to *in-situ* characterization of electrochemical reactions through the development of an *in-situ* micro-fluidic flow electrochemical cell optimized for soft X-ray STXM microscopes. The research consisted of three parts: *ex-situ* STXM and ptychography studies of electrocatalytic material; development of *in-situ* techniques and related instrumentation; and *in-situ* STXM and ptychography studies of electrocatalysts under CO_2R reactions.

In the area of *ex-situ* STXM and ptychography studies, different electrocatalysts were characterized, including Ni-N-C materials and electrodeposited Cu nanoparticles. Through the STXM measurements of several Ni-N-C materials at the Ni 2p, O 1s, N 1s, C 1s, and S 2p edges, the spectroscopic signature of single-atomic Ni active sites were identified and the local environment of the Ni atoms was elucidated. The spatial distribution of the atomically dispersed Ni was investigated and related to Ni loading and CO_2R performance, providing insights into structure-property-performance relationships

of catalyst or electrode designs. Subsequent *ex situ* ptychography studies on the same Ni-N-C materials, improved the spatial resolution from 60 nm (STXM) to 20 nm (ptychography) which allowed the chemistry of fine morphological features to be clarified. In addition, electrodeposited Cu-based nanoparticles were characterized by *ex situ* STXM before and after the CO_2R process. The chemical changes observed in Cu-based electrocatalysts from Cu_2O to Cu metal during CO_2R reactions motivated development of *in-situ* STXM techniques to provide real-time visualization and monitoring the conversion and performance of the electrocatalyst under CO2R electrochemical conditions. The results sharpened the understanding of CO_2R reactions and the behavior of the catalytic materials in the reaction process. Specifically, it was shown that the initially formed, mixed Cu_2O and Cu nanoparticles were reduced to pure Cu metal at a potential ~0.2 V above the onset of CO_2R, verifying that the catalytically active form is metallic copper.

Development of *in-situ* techniques and related instrumentation was necessary to achieve *in-situ* STXM characterization. The thesis has outlined various aspects of the instrumentation development and verification of its performance at McMaster. These lab-based measurements confirmed our ability to achieve *in-situ* conditions. Subsequently *in-situ* STXM and ptychography measurements of CO_2R catalyzed by electrodeposited copper nanoparticles were carried out at various STXMs. Such studies were used to track morphological and chemical changes of Cu nanoparticles as a function of applied potential. The particles initially electrodeposited were shown to be a mix of Cu and Cu_2O. The Cu_2O was converted to metallic Cu at particle-size-dependent reaction rates at

applied potentials less reducing than 0 V_{RHE}, indicating metallic Cu is the active site for CO_2 reduction. In addition, during the reduction, the size of the nanoparticles was reduced, although this phenomena was only observed for larger particles, due to the limited spatial resolution of STXM (~50 nm). Quantitative chemical mapping by *in-situ* spectro-ptychography demonstrated the morphological changes of a single, ~200 nm x 300 nm Cu nanoparticle which lost its initial cubic structure and formed irregular dendritic-like structures in the regime of CO_2R. These findings contribute to better understanding of morphological and chemical structural changes of Cu electrocatalyst during CO_2R. They demonstrate the ability of *in situ* STXM and *in situ* spectro-ptychography to gain insights into electrochemically active materials under reaction conditions.

9.2 My original contributions to this thesis

- With assistance from Haytham Eraky, Vinod Prabu, Pablo Ingino, Prof. Martin Obst and advice from my supervisors, Prof. Drew Higgins, and Prof. Adam Hitchcock, I developed, fabricated, and tested an improved liquid-flow electrochemical device for *in situ* STXM. (Chapter 3)
- Working with Ladan Shahcheraghi, Fatma Ismail, Haytham Eraky, Dr. Jiatang Chen, Dr. Hao Yuan, Dr. Jian Wang, Dr. Tianxiao Sun, I used *ex situ* STXM STXM and spectro-ptychography to characterize the heterogeneous Ni-N-C electrocatalysts. (Chapter 4, 5)
- Together with Haytham Eraky, I studied the Cu-based CO_2R electrocatalysts using in situ flow electrochemical STXM. These studies showed that Cu metal is the active

sites under CO_2R conditions, helping to resolve an ongoing debate about the possible role of Cu_2O and other oxidized Cu in the catalysts. (Chapter 7)

- In collaboration with beamline scientists at HERMES beamline at Soleil (Nicolas Mille, Stefan Stanescu, Sufal Swaraj and Rachid Belkhou), I performed *in situ* spectro-ptychography measurements of Cu nanoparticle as CO_2R electrocatalysts under reaction conditions. To my knowledge, this is the first ever world-wide achievement of this very challenging technique (Chapter 8).

9.3 Future work

9.3.1 *in-situ* STXM at C 1s edge

In-situ STXM measurement at the C 1s edge is an important target since it has the potential to identify and monitor CO_2R products If *in-situ* STXM measurements with sufficient sensitivity can be conducted at the C 1s edge, *in-situ* identification and quantitation of CO_2R products might be achieved. In this way, *in-situ* STXM might be improved to *operando* STXM. The main challenges to achieving *in-situ* STXM measurements at the C 1s edge include: (i) instrumentation; (ii) electrolyte thickness, (iii) sensitivity. Although product detection has not been achieved, here I estimate the sensitivity required. I show results from some of earlier attempts at C 1s edge measurements and give suggestions to guide future studies.

I assumed that 1.7 g CO_2 gas dissolved in 1 liter CO_2 saturate 0.1 M $KHCO_3$ or $NaHCO_3$ solution, [https://en.wikipedia.org/wiki/Carbon_dioxide#] which is close to the highest solubility of dissolved CO_2 in water at room temperature and pressure due to the

concentration of $KHCO_3$ and $NaHCO_3$ is low. Through the calculation, there is 3.4 $*10^{-12}$ mol of CO_2 in the window region of the in situ cell (240*120*2 μm) or 1.7 $*10^{-12}$ mol/ μm^2. If we consider the CO_2 in form of dry ice (although it is not possible occur, just for easier estimating and showing) with a density of 1.56 g/cm^3, there is ~ 3.3 nm thick CO_2 in the electrolyte in the window region of *in situ* cell and OD is ~0.09 at ~290.3 eV (peak of C 1s $\rightarrow\pi^*$ transition) according to the elemental response for 3.3 nm thickness of the CO_2 dry ice, which is calculated using X-ray parameters from the Centre for X-ray Optics database (https://henke.lbl.gov/optical_constants/). If we assume this CO_2 100% converted to CO_2R products such as CO, C_2H_4, CH_4, C_2H_5OH, the thicknesses and ODs of the strongest C 1s transition for each species are shown in **Table 9.1**.

Table 9.1 The estimated amount of CO_2R products

chemicals	Mol/um^2	Average thickness (nm)	E (eV)	OD	Information
CO_2	1.7 $*10^{-12}$	3.3	290.3	~0.09	Density 1.56 g/cm^3 for CO_2 in solid form.
CO	1.7 $*10^{-12}$	6.0	286.5	~0.12	Density 0.789 g/cm^3 for CO in liquid form.
C_2H_4	8.5 $*10^{-13}$	4.2	284.5	~0.1	Density 0.568 g/cm^3 for C_2H_4 in liquid form
CH_4	1.7 $*10^{-12}$	6.4	-	~0.11	Density 0.424 g/cm^3 for CH_4 in liquid form
C_2H_5OH	8.5 $*10^{-13}$	5.0	-	~0.11	Density 0.789 g/cm^3

Fig.9.1b and **c** present STXM images at C 1s edge at 280 and 320 eV, indicating the ability of visualization of carbon in the electrolyte. **Fig. 9.1d** displays the C 1s spectra of the electrolyte under *in-situ* conditions extracted from a STXM point spectrum

measurement on the 0.1 M CO_2 saturated $KHCO_3$ electrolyte after -0.3 V_{RHE} was applied for ~15 m. The peak at 290 eV is clearly attributed to CO_2 and HCO_3^- ions in the electrolyte, while the double peaks between 295 and 300 eV are clearly due to the K^+ ions in the solution. The C 1s spectrum of the electrolyte shows features between 280 and 290 eV which hint at the presence of CO and C_2H_4. (**Fig. 9.1d)** In order to estimate the amount of each component, the C 1s spectrum of the electrolyte was curve-fit to reference spectra of the postulated species. The results are presented in **Fig.9.1e**. This indicates a large amount of CO_2 and HCO_3^- ions which are from the bicarbonate electrolyte and CO_2 bubbled into the $KHCO_3$ electrolyte to achieve CO_2 saturated solution. This analysis suggests the possible existence of CO and C_2H_4 products, [3 ±1 nm CO and 4 ±1 nm C_2H_4 solid equivalent]. These early results of *in-situ* STXM studies of CO_2R at the C 1s edge suggest there is the potential to obtain meaningful C 1s spectra and quantitatively identify CO_2R products. If successful, this could set the stage for future use of *operando* STXM studies of CO_2 electroreduction reactions.

The unexpected high signal attributed to CO and C_2H_4 products could be a noise artifact. Under the relatively low negative potential applied, which was -0.3 $V_{RHE,}$ the products should be mainly H_2 gas. [**chapter 7**] Generally, CO_2R reactions happen efficiently when the applied potential is more negative than -0.6 V_{RHE}, where CO_2R products dominate. However, when high negative potentials (>-0.6 V_{RHE}) are applied in the *in situ* cell, gas bubbles are generated which can isolate the working electrode from the electrolyte and stop the electrochemical reactions. To solve this problem the mass transfer in the *in-situ* system must be improved to quickly remove the generated gas and

avoid the gas products accumulating to become big bubbles. One suggestion is to try to use two syringe pumps, one pushing from the inlet and one withdrawing from the outlet. This can help to improve mass transfer and balance the inner pressure. The inlet and outlet flow rates must be balanced so as to avoid window bulging.

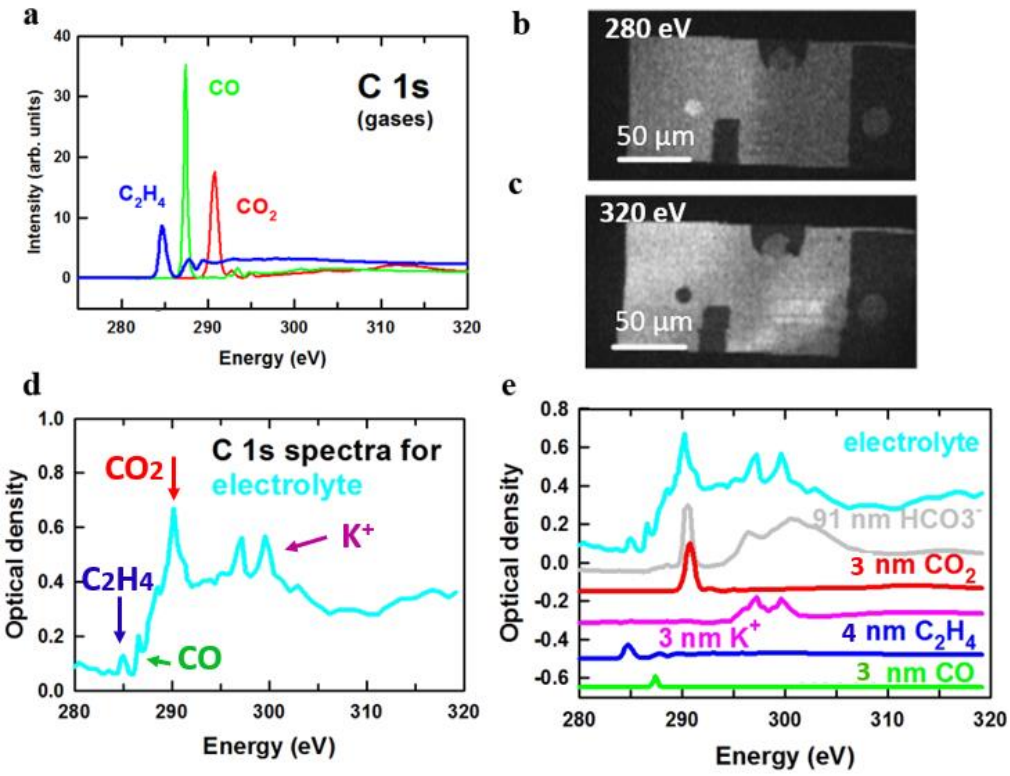

Fig. 9.1 Image and spectra from *in situ* STXM at C 1s edge a) C 1s spectra of CO_2, C_2H_4, and CO [Hitchcock, A.P., 2003]. **b)** STXM transmission image at 280 eV. **c)** STXM transmission image at 320 eV. **d)** the C 1s spectra of 0.1M CO_2 saturate $KHCO_3$ electrolyte measured using *in-situ* STXM. **e)** curve-fit of the C 1s spectrum of electrolyte.

Some suggestions for future studies of *in situ* STXM at C 1s energy are listed:

1. Use the known solubility of CO_2R products in the electrolyte [*J. Chem. Eng. Data* 2012, 57, 3, 78] to evaluate the detection limit of STXM for these CO_2R products.

See **Fig. 9.1** for such an evaluation for CO and ethylene. It is possible when products are at very low concentration, STXM cannot effectively detect them.

2. When high negative potentials are applied, gas bubbles are usually generated. It is possible to conduct STXM tests on the gas bubble to identify the gas products. This was tried at CLS in June 2023. However, due to unstable response at the C 1s edge the collected spectra are not reasonable. Further studies are needed.
3. Figure out how to calculate the efficiency and selectivity of the electrocatalysts according to the obtained thickness of the CO_2R products. Although it is easy to calculate the efficiency and selectivity in lab-based CO_2R tests [**chapter 4, chapter 7**], the CO_2R test experiments in *in-situ* cells on a micron scale device provide additional challenges. For example, the identification and quantification of very small amount of CO_2R products in micro-region is very challenging.
4. Systematically measure the C 1s spectra of more CO_2R products such as CH_4, C_2H_2, EtOH, and understand the features of the spectra of them. This can help to identify the real products from CO_2R reactions.

9.3.2 *in-situ* STXM/ptychography on powder particles with ionomer.

In previous *in-situ* STXM tests, the samples measured were all electro-deposited materials because they can be generated on the *in-situ* Au WE. To increase the scope of studies, I attempted to deposit powder catalysts with ionomer on the WE, which are the most popular kind of electrocatalysts used in lab testing and actual CO_2R cells. STXM and ptychography are suitable to study ionomer and soft polymer materials due to the low

radiation damage. [Wu et al., 2018. Martens et al., 2020]

The Ni-N-C-low powder samples have been thoroughly investigated in **chapters 4** and **5**, and are suitable for *in-situ* STXM studies. **Fig. 9.2** presents some results of this type. First, the powder samples should be deposited on the working electrode of the *in-situ* chips. The method used to deposit the Ni-N-C-low powder sample on the micro-Au WE region on the *in-situ* chip is similar to the method to prepare lab-based test electrodes [**chapter 4**] but with 10 times dilution to decrease the concentration of powders. 1 mg Ni-N-C-low powder sample was suspended in an ink which included 1.5 mL of isopropyl alcohol and 0.5 mL of milli-Q H_2O with 11 μL of a Nafion suspension (Sigma-Aldrich, 5 wt % Nafion in ethanol) and sonicated for 30 min. The suspended ink was drop-cast onto the micro-Au electrode region of an *in-situ* chip using a homemade micromanipulator system under optical microscopy and dried at room temperature. A small amount of Ni-N-C-low particles were deposited on the RE and CE as well as the WE because it is difficult to control where the drop lands. (**Fig. 9.2a**) The size of the particles is very important and should be controlled to less than 3 μm because particles larger than the distance between the E and F chips (**chapter 3**) can break the window. One droplet of nanoparticles deposited on the WE was studied under *in-situ* STXM conditions in 0.1 M CO_2-saturated $KHCO_3$ electrolyte. The STXM image of this particle at 853 eV showed a particle size of ~2 μm. (**Fig. 9.2b**) The Ni 2p spectrum of this particle at -0.2 V_{RHE} is presented in **Fig. 9.2c**,. It is similar to the Ni 2p spectrum obtained from the *ex-situ* STXM stack. [**chapter 4**] One of the challenges is that the Ni 2p spectrum of the particle is very weak – the peak OD is less than 0.15. Another challenge is that there are very few

particles on the WE. Typically one requires more than 10 particles to find one suitable for STXM study. The reason few nanoparticles are deposited is that it is difficult to control the location of particle deposition. If too much Nafion is deposited on the chips, the conductive particles and Nafion can cause shortage between the 3 electrodes. This is why a dilute powder ink is used to deposit just a few Nafion coated particles on the chips.

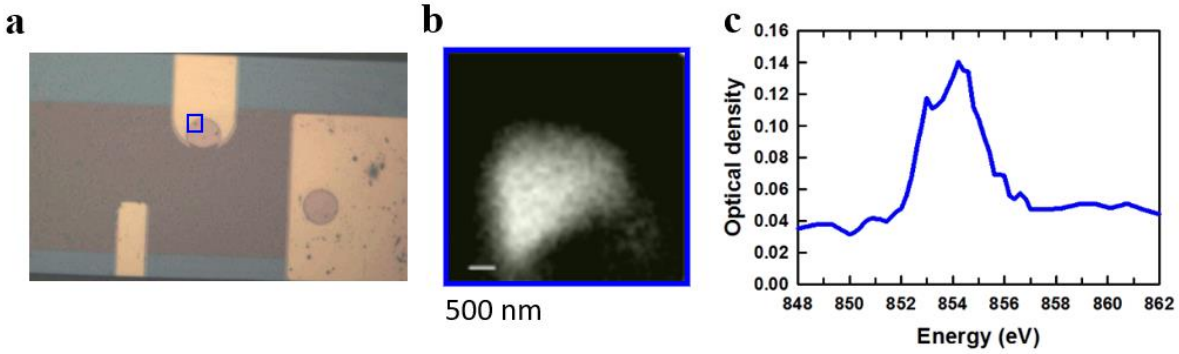

Fig. 9.2 a) Optical image of the 3-electrode region on an *in-situ* chip. b) STXM image of a Ni-N-C-low particle at 853 eV. c) the Ni 2p spectra extracted from the STXM stacks of Ni-N-C-low particle.

To address this problem, we purchased custom-designed mask chips from Norcada. The mask covers all regions of the *in situ* chip E except the WE so that powders or inks are deposited only on the WE. (**Fig. 9.3a)** This can effectively deposit many Ni-N-C-low particles only on the WE, as shown in **Fig. 9.3.b.** After deposition of the powder samples, the mask is removed, and the chip is washed with DI H_2O. However the particles are not stable when filling the electrolyte quickly (**Fig. 9.3c)** or if a bubble is generated (**Fig. 9.3d).** In those cases, most of the Ni-N-C-low particles were removed.

Suggestions for future *in-situ* STXM studies of powder samples include:

1. To stabilize the powder particles, the amount of Nafion as the binder should be

increased in the ink. The ratio between powder sample and Nafion in the ink could be systematically changed to find the optimum for the deposition process. A higher Nafion in the ink is expected to stabilize the particles on the WE and keep them on the WE even when electrolyte is passed quickly at high negative potential.

2. To reduce the thickness of the powder samples, microtoming can be used to cut the particles embedded in a suitable epoxy to a controllable thickness such as 500 nm. If the embedding medium can then be dissolved it may be possible to generate particles with well-defined thickness which can then be deposited on the working electrode for *in-situ* STXM studies. [Wu et al., 2018. Martens et al., 2020.]
3. If the powder samples can be successfully deposited and stabilized, *in-situ* STXM can be studied under various potentials. In this way many novel nanomaterials with known synthesis and well-designed structure can be investigated by *in-situ* STXM.
4. In addition to changes in oxidation states and morphology for Ni-N-C particles under static negative potentials, the amount of single-atomic Ni sites can be monitored real-time during the CO_2R process. This could be important to understand the stability of atomic dispersed Ni during electrochemical reactions and the relationships between the amount of single-atomic Ni and external experimental conditions. This could be an excellent follow-up project to the studies presented in **chapters 4** and **5**.

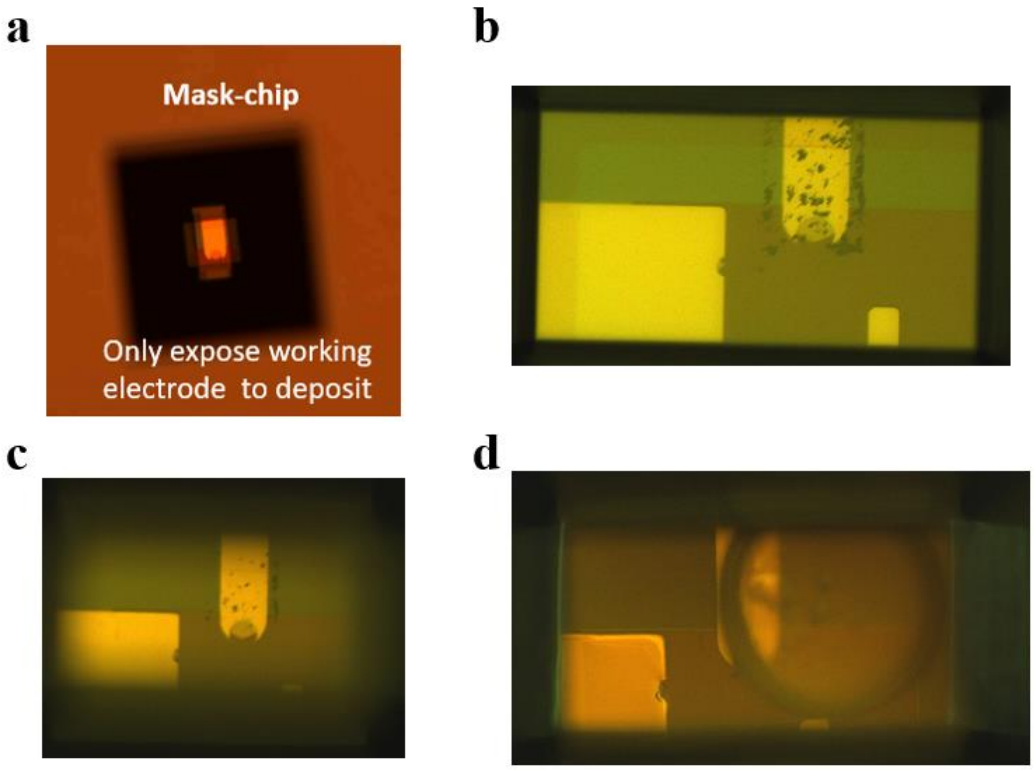

Fig. 9.3 Optical image of **a)** mask *in-situ* chip**. b)** *in-situ* chip after deposition of the powder samples, removing the mask, and washing with DI H_2O **c)** *in-situ* chip after quickly filling the electrolyte. **d)** *in-situ* chip after bubble generation.

In summary, *in-situ* STXM and *in-situ* spectro-ptychography have been systematically developed and applied to in situ studies of candidate CO_2R electrocatalysts. My research has contributed to developing practical instrumentation and methodologies which can be applied in many fields. There is huge potential for further improvements in the future.

REFERENCE

Abdinejad, M., Dao, C., Zhang, X. A., & Kraatz, H. B. (2021). Enhanced electrocatalytic activity of iron amino porphyrins using a flow cell for reduction of CO2 to CO. *Journal of Energy Chemistry*, 58, 162-169.

Ade, H., & Hitchcock, A. P. (2008). NEXAFS microscopy and resonant scattering: Composition and orientation probed in real and reciprocal space. *Polymer*, 49(3), 643-675.

Alnoush, W., Black, R. and Higgins, D., 2021. Judicious selection, validation, and use of reference electrodes for in situ and operando electrocatalysis studies. *Chem Catalysis*, *1*(5), pp.997-1013.

Antonio, K. A., & Schultz, Z. D. (2014). Advances in biomedical Raman microscopy. *Analytical chemistry*, *86*(1), 30-46.

Arán-Ais, R. M., Rizo, R., Grosse, P., Algara-Siller, G., Dembélé, K., Plodinec, M., ... & Cuenya, B. R. (2020). Imaging electrochemically synthesized Cu2O cubes and their morphological evolution under conditions relevant to CO2 electroreduction. *Nature communications*, *11*(1), 3489.

Arul, K. T., Chang, H. W., Shiu, H. W., Dong, C. L., & Pong, W. F. (2021). A review of energy materials studied by in situ/operando synchrotron x-ray spectro-microscopy. *Journal of Physics D: Applied Physics*, *54*(34), 343001.

Attwood, D. (2000). *Soft x-rays and extreme ultraviolet radiation: principles and applications*. Cambridge university press.

Balerna, A., & Mobilio, S. (2015). Synchrotron Radiations: Basics, Methods and Applications. *Introduction to synchrotron radiation. Springer, Berlin*, *799*.

Belkhou, R., Stanescu, S., Swaraj, S., Besson, A., Ledoux, M., Hajlaoui, M., & Dalle, D. (2015). HERMES: a soft X-ray beamline dedicated to X-ray microscopy. *Journal of synchrotron radiation*, *22*(4), 968-979.

Beverskog, B., & Puigdomenech, I. (1997). Revised Pourbaix diagrams for copper at 25 to 300 C. *Journal of The Electrochemical Society*, *144*(10), 3476.

Beheshti Askari, A., Al Samarai, M., Morana, B., Tillmann, L., Pfänder, N., Wandzilak, A., ... & DeBeer, S. (2020). In situ X-ray microscopy reveals particle dynamics in a NiCo dry methane reforming catalyst under operating conditions. *ACS catalysis*, *10*(11), 6223-6230.

Brodu, E., Bouzy, E., & Fundenberger, J. J. (2017). Diffraction contrast dependence on sample thickness and incident energy in on-axis Transmission Kikuchi Diffraction in SEM. *Ultramicroscopy*, *181*, 123-133.

Bozzini, B., D'Urzo, L., Gianoncelli, A., Kaulich, B., Kiskinova, M., Prasciolu, M., & Tadjeddine, A. (2008). In situ soft X-ray dynamic microscopy of electrochemical processes. *Electrochemistry communications*, *10*(11), 1680-1683.

Bozzini, B., D'Urzo, L., Gianoncelli, A., Kaulich, B., Prasciolu, M., Sgura, I., ... & Kiskinova, M. (2009). An in situ synchrotron-based soft X-ray microscopy investigation of Ni electrodeposition in a thin-layer cell. *The Journal of Physical Chemistry C*, *113*(22), 9783-9787. (a)

Bozzini, B., D'Urzo, L., Gianoncelli, A., Kaulich, B., Kiskinova, M., Prasciolu, M., & Tadjeddine, A. (2009, September). Synchrotron-based in situ soft X-ray microscopy of Ag corrosion in aqueous chloride solution. In *Journal of Physics: Conference Series* (Vol. 186, No. 1, p. 012103). IOP Publishing. **(b)**

Bozzini, B., Gianoncelli, A., Kaulich, B., Kiskinova, M., Mele, C., & Prasciolu, M. (2011). Corrosion of Ni in 1-butyl-1-methyl-pyrrolidinium bis (trifluoromethylsulfonyl) amide room-temperature ionic liquid: an in situ X-ray imaging and spectromicroscopy study. *Physical Chemistry Chemical Physics*, 13(17), 7968-7974. **(b)**

Bozzini, B., Mele, C., Gianoncelli, A., Kaulich, B., Kiskinova, M., & Prasciolu, M. (2011). In situ X-ray spectromicroscopy study of bipolar plate material stability for nano-fuel-cells with ionic-liquid electrolyte. *Microelectronic engineering*, *88*(8), 2456-2458. **(c)**

Bozzini, B., Gianoncelli, A., Kaulich, B., Mele, C., Prasciolu, M., & Kiskinova, M. (2012). Electrodeposition of manganese oxide from eutectic urea/choline chloride ionic liquid: An in situ study based on soft X-ray spectromicroscopy and visible reflectivity. *Journal of Power Sources*, *211*, 71-76.

Bozzini, B., Gianoncelli, A., Bocchetta, P., Dal Zilio, S., & Kourousias, G. (2014). Fabrication of a sealed electrochemical microcell for in situ soft X-ray microspectroscopy and testing with in situ co-polypyrrole composite electrodeposition for Pt-free oxygen electrocatalysis. *Analytical chemistry*, *86*(1), 664-670.

Beckhoff, B., Klein, R., Krumrey, M., Scholze, F., Thornagel, R., & Ulm, G. (2000). X-ray detector calibration in the PTB radiometry laboratory at the electron storage ring BESSY II. *Nuclear Instruments and Methods in Physics Research Section A: Accelerators, Spectrometers, Detectors and Associated Equipment*, *444*(1-2), 480-483.

Chao, W., Fischer, P., Tyliszczak, T., Rekawa, S., Anderson, E., & Naulleau, P. (2012). Real space soft x-ray imaging at 10 nm spatial resolution. *Optics express*, *20*(9), 9777-9783.

Chao, W., Kim, J., Rekawa, S., Fischer, P., Anderson, E.H., 2009. Demonstration of 12 nmresolution Fresnel zone plate lens based soft x-ray microscopy. Opt. Express 17, 17669–17677

Chen, C. T., Ma, Y., & Sette, F. (1989). K-shell photoabsorption of the N 2 molecule. *Physical Review A*, *40*(11), 6737.

Cheng, D., Zhao, Z. J., Zhang, G., Yang, P., Li, L., Gao, H., ... & Gong, J. (2021). The nature of active sites for carbon dioxide electroreduction over oxide-derived copper catalysts. *Nature communications*, *12*(1), 395.

Chen, P., Jiao, Y., Zhu, Y. H., Chen, S. M., Song, L., Jaroniec, M., ... & Qiao, S. Z. (2019). Syngas

production from electrocatalytic CO2 reduction with high energetic efficiency and current density. *Journal of Materials Chemistry A*, *7*(13), 7675-7682.

Chou, T. C., Chang, C. C., Yu, H. L., Yu, W. Y., Dong, C. L., Velasco-Vélez, J. J., ... & Wu, H. L. (2020). Controlling the oxidation state of the Cu electrode and reaction intermediates for electrochemical CO2 reduction to ethylene. *Journal of the American Chemical Society*, *142*(6), 2857-2867.

Chourasia, A. K., Pathak, A. D., Bongu, C., Manikandan, K., Praneeth, S., Naik, K. M., & Sharma, C. S. (2022). In Situ/Operando Characterization Techniques: The Guiding Tool for the Development of Li–CO2 Battery. *Small Methods*, *6*(12), 2200930.

Chandrashekar, S., Geerlings, H., & Smith, W. A. (2021). Assessing Silver Palladium Alloys for Electrochemical CO2 Reduction in Membrane Electrode Assemblies. *ChemElectroChem*, 8(23), 4515-4521.

Coati, A., Chavas, L. M. G., Fontaine, P., Foos, N., Guimaraes, B., Gourhant, P., ... & Thompson, A. (2017). Status of the crystallography beamlines at synchrotron SOLEIL⋆. *The European Physical Journal Plus*, *132*, 1-9.

Cutler, J. N., Christensen, C., Kotzer, T. G., Ogunremi, T., Pushparajah, T., & Warner, J. (2007). The Canadian Light Source–A new tool for industrial research. *Nuclear Instruments and Methods in Physics Research Section B: Beam Interactions with Materials and Atoms*, *261*(1-2), 859-862.

Desjardins, K., Popescu, H., Mercère, P., Menneglier, C., Gaudemer, R., Thånell, K., & Jaouen, N. (2019, January). Characterization of a back-illuminated CMOS camera for soft x-ray coherent scattering. In *AIP Conference Proceedings* (Vol. 2054, No. 1). AIP Publishing.

Desjardins, K., Medjoubi, K., Sacchi, M., Popescu, H., Gaudemer, R., Belkhou, R., ... & Jaouen, N. (2020). Backside-illuminated scientific CMOS detector for soft X-ray resonant scattering and ptychography. *Journal of Synchrotron Radiation*, *27*(6), 1577-1589.

De Arquer, F. P. G., Dinh, C. T., Ozden, A., Wicks, J., McCallum, C., Kirmani, A. R., Nam, DH., Gabardo, C., Seifitokaldani, A., Wang,X., Li, Y. C., Li, F., Edwards, J., Richter, L.J., Thorpe, S.J., Sinton, D., Sargent, E.H. (2020). CO_2 electrolysis to multi-carbon products at activities greater than 1 A cm^{-2}. *Science*, *367*(6478), 661-666.

De Luna, P., Hahn, C., Higgins, D., Jaffer, S. A., Jaramillo, T. F., & Sargent, E. H. (2019). What would it take for renewably powered electrosynthesis to displace petrochemical processes?. *Science*, *364*(6438), eaav3506.

Diercks, J. S., Pribyl-Kranewitter, B., Herranz, J., Chauhan, P., Faisnel, A., & Schmidt, T. J. (2021). An online gas chromatography cell setup for accurate CO2-electroreduction product quantification. *Journal of The Electrochemical Society*, 168(6), 064504.

Eilert, A., Cavalca, F., Roberts, F. S., Osterwalder, J., Liu, C., Favaro, M., ... & Nilsson, A. (2017). Subsurface oxygen in oxide-derived copper electrocatalysts for carbon dioxide reduction. *The*

journal of physical chemistry letters, *8*(1), 285-290.

Edo, T. B., Batey, D. J., Maiden, A. M., Rau, C., Wagner, U., Pešić, Z. D., ... & Rodenburg, J. M. (2013). Sampling in x-ray ptychography. *Physical Review A*, *87*(5), 053850.

Ellis, T. H. O. M. A. S., & Hallin, E. M. I. L. (2011). Status of the CLS-New Opportunities for Physics Research in Canada. *Physics in Canada*, *67*, 21-24.

Ezquerra, T. A., Garcia-Gutierrez, M. C., Nogales, A., & Gomez, M. (Eds.). (2009). *Applications of synchrotron light to scattering and diffraction in materials and life sciences* (Vol. 776). Springer.

Favre-Nicolin, V., Girard, G., Leake, S., Carnis, J., Chushkin, Y., Kieffer, J., ... & Richard, M. I. (2020). PyNX: high-performance computing toolkit for coherent X-ray imaging based on operators. *Journal of Applied Crystallography*, *53*(5), 1404-1413.

Feggeler, T., Levitan, A., Marcus, M. A., Ohldag, H., & Shapiro, D. A. (2023). Scanning transmission X-ray microscopy at the Advanced Light Source. *Journal of Electron Spectroscopy and Related Phenomena*, *267*, 147381.

Fields, M., Hong, X., Nørskov, J. K., & Chan, K. (2018). Role of subsurface oxygen on Cu surfaces for CO2 electrochemical reduction. *The Journal of Physical Chemistry C*, *122*(28), 16209-16215.
Förster, J. D., Gurk, C., Lamneck, M., Tong, H., Ditas, F., Steimer, S. S., ... & Pöhlker, C. (2020). MIMiX: a Multipurpose In situ Microreactor system for X-ray microspectroscopy to mimic atmospheric aerosol processing. *Atmospheric Measurement Techniques*, *13*(7), 3717-3729.

Grosse, P., Yoon, A., Rettenmaier, C., Herzog, A., Chee, S. W., & Roldan Cuenya, B. (2021). Dynamic transformation of cubic copper catalysts during CO2 electroreduction and its impact on catalytic selectivity. *Nature communications*, *12*(1), 6736.

Grioni, M., Van Acker, J. F., Czyżyk, M. T., & Fuggle, J. C. (1992). Unoccupied electronic structure and core-hole effects in the x-ray-absorption spectra of Cu 2 O. *Physical Review B*, *45*(7), 3309.

Gianoncelli, A., Kaulich, B., Kiskinova, M., Prasciolu, M., Urzo, B. D., & Bozzini, B. (2011). An in situ electrochemical soft X-ray spectromicroscopy investigation of Fe galvanically coupled to Au. *Micron*, *42*(4), 342-347.

Giuliani, A., Jamme, F., Rouam, V., Wien, F., Giorgetta, J. L., Lagarde, B., ... & Réfrégiers, M. (2009). DISCO: a low-energy multipurpose beamline at synchrotron SOLEIL. *Journal of synchrotron radiation*, *16*(6), 835-841.

Guizar-Sicairos, M., & Thibault, P. (2021). Ptychography: A solution to the phase problem. *Physics Today*, *74*(9), 42-48.

Gong, C., Pu, S. D., Gao, X., Yang, S., Liu, J., Ning, Z., ... & Robertson, A. W. (2021). Revealing the role of fluoride-rich battery electrode interphases by operando transmission electron microscopy. *Advanced Energy Materials*, *11*(10), 2003118.

Grosse, P., Yoon, A., Rettenmaier, C., Herzog, A., Chee, S. W., & Roldan Cuenya, B. (2021). Dynamic transformation of cubic copper catalysts during CO2 electroreduction and its impact on catalytic selectivity. *Nature Communications*, *12*(1), 6736.

Grote, L., Seyrich, M., Döhrmann, R., Harouna-Mayer, S. Y., Mancini, F., Kaziukenas, E., ... & Koziej, D. (2022). Imaging Cu2O nanocube hollowing in solution by quantitative in situ X-ray ptychography. *Nature Communications*, *13*(1), 4971.

Guay, D., Stewart-Ornstein, J., Zhang, X., & Hitchcock, A. P. (2005). In situ spatial and time-resolved studies of electrochemical reactions by scanning transmission X-ray microscopy. *Analytical chemistry*, *77*(11), 3479-3487.

Hernández-Cruz, D., Hitchcock, A. P., Tyliszczak, T., Rousseau, M. E., & Pézolet, M. (2007). In situ azimuthal rotation device for linear dichroism measurements in scanning transmission x-ray microscopy. *Review of scientific instruments*, *78*(3).

Higgins, D., Landers, A. T., Ji, Y., Nitopi, S., Morales-Guio, C. G., Wang, L., ... & Jaramillo, T. F. (2018). Guiding electrochemical carbon dioxide reduction toward carbonyls using copper silver thin films with interphase miscibility. *ACS Energy Letters*, *3*(12), 2947-2955.

Hitchcock, A. P. (2003). Gas phase core excitation database. *http://unicorn. mcmaster. ca/corex/cedb-title. html*.

Hitchcock, A. P. (2012). Soft X-ray imaging and spectromicroscopy. *Handbook of nanoscopy*, 745-791.

Hitchcock, A. P. (2023). Analysis of X-ray images and spectra (aXis2000): A toolkit for the analysis of X-ray spectromicroscopy data. *Journal of Electron Spectroscopy and Related Phenomena*, *266*, 147360.

Hitchcock, A. P., Berejnov, V., Lee, V., West, M., Colbow, V., Dutta, M., & Wessel, S. (2014). Carbon corrosion of proton exchange membrane fuel cell catalyst layers studied by scanning transmission X-ray microscopy. *Journal of Power Sources*, *266*, 66-78. Hitchcock, A.P., 2015. Soft X-ray spectromicroscopy and ptychography. *J. Electron Spectros. Relat. Phenomena* 200, 49–63.

Hitchcock, A. P., & Brion, C. E. (1980). Neon K-shell excitation studied by electron energy-loss spectroscopy. *Journal of Physics B: Atomic and Molecular Physics*, *13*(16), 3269.

Hitchcock, A. P., Dynes, J. J., Johansson, G., Wang, J., & Botton, G. (2008). Comparison of NEXAFS microscopy and TEM-EELS for studies of soft matter. *Micron*, *39*(6), 741-748.

Hitchcock, A. P., & Ishii, I. (1987). Carbon K-shell excitation spectra of linear and branched alkanes. *Journal of Electron Spectroscopy and Related Phenomena*, *42*(1), 11-26.

Hitchcock, A. P., Qin, Z., Rosendahl, S. M., Lee, V., Reynolds, M., & Hosseinkhannazer, H. (2016, January). Electro-deposition of Cu studied with in situ electrochemical scanning transmission x-ray microscopy. In *AIP Conference Proceedings* (Vol. 1696, No. 1). AIP Publishing.

Hitchcock, A. P., Obst, M., Wang, J., Lu, Y. S., & Tyliszczak, T. (2012). Advances in the detection of As in environmental samples using low energy X-ray fluorescence in a scanning transmission X-ray microscope: arsenic immobilization by an Fe (II)-oxidizing freshwater bacteria. *Environmental science & technology*, *46*(5), 2821-2829.

Hori, Y. I. (2008). Electrochemical CO2 reduction on metal electrodes. *Modern aspects of electrochemistry*, 89-189.

Howells, M., Jacobsen, C., Warwick, T., & Van den Bos, A. (2007). Principles and applications of zone plate X-ray microscopes. *Science of microscopy*, 835-926.

Hwang, S., Chen, X., Zhou, G., & Su, D. (2020). In situ transmission electron microscopy on energy-related catalysis. *Advanced Energy Materials*, *10*(11), 1902105..

Hu, C., Ma, Q., Hung, S. F., Chen, Z. N., Ou, D., Ren, B., ... & Zheng, N. (2017). In situ electrochemical production of ultrathin nickel nanosheets for hydrogen evolution electrocatalysis. *Chem*, *3*(1), 122-133.

Huthwelker, T., Zelenay, V., Birrer, M., Krepelova, A., Raabe, J., Tzvetkov, G., ... & Ammann, M. (2010). An in situ cell to study phase transitions in individual aerosol particles on a substrate using scanning transmission x-ray microspectroscopy. *Review of Scientific Instruments*, *81*(11).

Jacobsen, C. (2019). *X-ray Microscopy*. Cambridge University Press.

Jiang, P., Prendergast, D., Borondics, F., Porsgaard, S., Giovanetti, L., Pach, E., ... & Salmeron, M. (2013). Experimental and theoretical investigation of the electronic structure of Cu2O and CuO thin films on Cu (110) using x-ray photoelectron and absorption spectroscopy. *The Journal of chemical physics*, *138*(2).

Jiang, K., Huang, Y., Zeng, G., Toma, F. M., Goddard III, W. A., & Bell, A. T. (2020). Effects of surface roughness on the electrochemical reduction of CO2 over Cu. *ACS Energy Letters*, *5*(4), 1206-1214.

Jiang, P., Prendergast, D., Borondics, F., Porsgaard, S., Giovanetti, L., Pach, E., ... & Salmeron, M. (2013). Experimental and theoretical investigation of the electronic structure of Cu2O and CuO thin films on Cu (110) using x-ray photoelectron and absorption spectroscopy. *The Journal of chemical physics*, *138*(2).

Jiang, Y., Wang, X., Duan, D., He, C., Ma, J., Zhang, W., ... & Xiong, Y. (2022). Structural reconstruction of Cu2O superparticles toward electrocatalytic CO2 reduction with high C2+ products selectivity. *Advanced Science*, *9*(16), 2105292.

Ju, W., Bagger, A., Wang, X., Tsai, Y., Luo, F., Möller, T., ... & Strasser, P. (2019). Unraveling mechanistic reaction pathways of the electrochemical CO2 reduction on Fe–N–C single-site catalysts. *ACS energy letters*, *4*(7), 1663-1671.

Kaznatcheev, K. V., Karunakaran, C., Lanke, U. D., Urquhart, S. G., Obst, M., & Hitchcock, A. P. (2007). Soft X-ray spectromicroscopy beamline at the CLS: commissioning results. *Nuclear*

Instruments and Methods in Physics Research Section A: Accelerators, Spectrometers, Detectors and Associated Equipment, *582*(1), 96-99.

Kibria, M. G., Edwards, J. P., Gabardo, C. M., Dinh, C. T., Seifitokaldani, A., Sinton, D., & Sargent, E. H. (2019). Electrochemical CO2 reduction into chemical feedstocks: from mechanistic electrocatalysis models to system design. *Advanced Materials*, *31*(31), 1807166.

Kilcoyne, A. L. D., Tyliszczak, T., Steele, W. F., Fakra, S., Hitchcock, P., Franck, K., ... & Ade, H. (2003). Interferometer-controlled scanning transmission X-ray microscopes at the Advanced Light Source. *Journal of synchrotron radiation*, *10*(2), 125-136.

Kim, J., Lee, D., Nam, C., Chung, J., Koo, B., Kim, N., & Lim, J. (2023). Energy material analysis via in-situ/operando scanning transmission x-ray microscopy: A review. *Journal of Electron Spectroscopy and Related Phenomena*, *266*, 147337.

Kibria, M. G., Edwards, J. P., Gabardo, C. M., Dinh, C. T., Seifitokaldani, A., Sinton, D., & Sargent, E. H. (2019). Electrochemical CO2 reduction into chemical feedstocks: from mechanistic electrocatalysis models to system design. *Advanced Materials*, *31*(31), 1807166.

Kowalski, G. W., Panaś, R., & Wawrzyniak, A. I. (2021). Insertion devices impact on SOLARIS storage ring optics.

Koprinarov, I. N., Hitchcock, A. P., McCrory, C. T., & Childs, R. F. (2002). Quantitative mapping of structured polymeric systems using singular value decomposition analysis of soft X-ray images. *The Journal of Physical Chemistry B*, *106*(21), 5358-5364.

Koshy, D. M., Chen, S., Lee, D. U., Stevens, M. B., Abdellah, A. M., Dull, S. M., ... & Jaramillo, T. F. (2020). Understanding the origin of highly selective CO2 electroreduction to CO on Ni, N-doped carbon catalysts. *Angewandte Chemie International Edition*, *59*(10), 4043-4050.

Kong, X., Zhao, J., Ke, J., Wang, C., Li, S., Si, R., ... & Geng, Z. (2022). Understanding the effect of* CO coverage on C–C coupling toward CO2 electroreduction. *Nano Letters*, *22*(9), 3801-3808.

Kooyman, P. J. (2017). Development of operando transmission electron microscopy. *Operando research in heterogeneous catalysis*, 111-129.

Kourousias, G., Bozzini, B., Jones, M. W., Van Riessen, G. A., Dal Zilio, S., Billè, F., ... & Gianoncelli, A. (2018). Monitoring dynamic electrochemical processes with in situ ptychography. *Applied Nanoscience*, *8*, 627-636.

Kuhl, K. P., Cave, E. R., Abram, D. N., & Jaramillo, T. F. (2012). New insights into the electrochemical reduction of carbon dioxide on metallic copper surfaces. *Energy & Environmental Science*, *5*(5), 7050-7059.

Kuhl, K. P., Hatsukade, T., Cave, E. R., Abram, D. N., Kibsgaard, J., & Jaramillo, T. F. (2014). Electrocatalytic conversion of carbon dioxide to methane and methanol on transition metal surfaces. *Journal of the American Chemical Society*, *136*(40), 14107-14113.

Lee, S. H., Lin, J. C., Farmand, M., Landers, A. T., Feaster, J. T., Avilés Acosta, J. E., ... & Drisdell, W. S. (2020). Oxidation state and surface reconstruction of Cu under CO2 reduction conditions from in situ X-ray characterization. *Journal of the American Chemical Society*, *143*(2), 588-592.

Leontowich, A. F., Berg, R., Regier, C. N., Taylor, D. M., Wang, J., Beauregard, D., ... & Urquhart, S. G. (2018). Cryo scanning transmission x-ray microscope optimized for spectrotomography. *Review of Scientific Instruments*, *89*(9).

Li, J., Johnson, G., Zhang, S., & Su, D. (2019). In situ transmission electron microscopy for energy applications. *Joule*, *3*(1), 4-8.

Li, S., Chang, Y., Wang, Y., Xu, Q., & Ge, B. (2020). A review of sample thickness effects on high-resolution transmission electron microscopy imaging. *Micron*, *130*, 102813.

Lim, J., Li, Y., Alsem, D. H., So, H., Lee, S. C., Bai, P., ... & Chueh, W. C. (2016). Origin and hysteresis of lithium compositional spatiodynamics within battery primary particles. *Science*, *353*(6299), 566-571.

Lobaccaro, P., Singh, M. R., Clark, E. L., Kwon, Y., Bell, A. T., & Ager, J. W. (2016). Effects of temperature and gas–liquid mass transfer on the operation of small electrochemical cells for the quantitative evaluation of CO 2 reduction electrocatalysts. *Physical Chemistry Chemical Physics*, 18(38), 26777-26785.

Low, Jingxiang, Bei Cheng, and Jiaguo Yu. "Surface modification and enhanced photocatalytic CO2 reduction performance of TiO2: a review." *Applied Surface Science* 392 (2017): 658-686.

Lum, Y., & Ager, J. W. (2018). Stability of residual oxides in oxide-derived copper catalysts for electrochemical CO2 reduction investigated with 18O labeling. *Angewandte Chemie International Edition*, *57*(2), 551-554.

Ma, Y., Chen, C. T., Meigs, G., Randall, K., & Sette, F. (1991). High-resolution K-shell photoabsorption measurements of simple molecules. *Physical Review A*, *44*(3), 1848.

Magnuson, Martin, Nial Wassdahl, and Joseph Nordgren. "Energy dependence of Cu L 2, 3 satellites using synchrotron excited x-ray-emission spectroscopy." *Physical Review B* 56.19 (1997): 12238.

Marchesini, S., Schirotzek, A., Yang, C., Wu, H. T., & Maia, F. (2013). Augmented projections for ptychographic imaging. *Inverse Problems*, *29*(11), 115009.

Martens, I., Melo, L.G., West, M.M., Wilkinson, D.P., Bizzotto, D. and Hitchcock, A.P., 2020. Imaging reactivity of the Pt–ionomer interface in fuel-cell catalyst layers. *ACS Catalysis*, *10*(15), pp.8285-8292.

Mefford, J. T., Akbashev, A. R., Kang, M., Bentley, C. L., Gent, W. E., Deng, H. D., ... & Chueh, W. C. (2021). Correlative operando microscopy of oxygen evolution electrocatalysts. *Nature*, *593*(7857), 67-73.

Maiden, A. M., & Rodenburg, J. M. (2009). An improved ptychographical phase retrieval algorithm for diffractive imaging. *Ultramicroscopy*, *109*(10), 1256-1262.

Nelson Weker, J., & Toney, M. F. (2015). Emerging In Situ and Operando Nanoscale X-Ray Imaging Techniques for Energy Storage Materials. *Advanced Functional Materials*, *25*(11), 1622-1637.

Mille, N., Yuan, H., Vijayakumar, J., Stanescu, S., Swaraj, S., Desjardins, K., Favre-Nicolin, V., Belkhou, R. and Hitchcock, A.P., (2022). Ptychography at the carbon K-edge. *Communications Materials*, *3*(1), p.8.

Miao, J., Sayre, D., Chapman, H.N., (1997). Phase retrieval from the magnitude of the Fourier transforms of nonperiodic objects. *J. Opt. Soc. Am. A* 15, 1662.

Miao, J., Charalambous, P., Kirz, J., Sayre, D., (1999). Extending the methodology of X-ray crystallography to allow imaging of micrometre-sized non-crystalline specimens. *Nature* 400, 342–344

Miao, J., Sandberg, R.L., Song, C., (2012). Coherent X-Ray Diffraction Imaging. IEEE J. Sel. op. Quantum Electron. 18, 399–410

Muller, Daniel J. (2008) AFM: a nanotool in membrane biology." *Biochemistry* 47.31, 7986-7998.

Murata, R., Inoue, K. I., Wang, L., Ye, S., & Morita, A. (2021). Dispersion of complex refractive indices for intense vibrational bands. I. Quantitative spectra. *The Journal of Physical Chemistry B*, 125(34), 9794-9803.

Nitopi, Stephanie, et al. "Progress and perspectives of electrochemical CO2 reduction on copper in aqueous electrolyte." *Chemical reviews* 119.12 (2019): 7610-7672.

Nichols, J.B., Voltolini, M., Gilbert, B., MacDowell, A.A. and Czabaj, M.W., (2022). The hard x-ray nanotomography microscope at the advanced light source. *Review of Scientific Instruments*, *93*(2).

Nolle, D., Weigand, M., Audehm, P., Goering, E., Wiesemann, U., Wolter, C., Nolle, E. and Schütz, G., (2012). Note: Unique characterization possibilities in the ultra high vacuum scanning transmission x-ray microscope (UHV-STXM)"MAXYMUS" using a rotatable permanent magnetic field up to 0.22 T. *Review of scientific instruments*, *83*(4).

Obst, M., Ingino, P., Hitchcock, A., Prabu, V., & Picard, A. (2018). Redox-chemistry of environmental biofilms probed on the submicron scale by in situ electrochemistry scanning transmission (soft) X-ray microscopy. *Microscopy and Microanalysis*, *24*(S2), 502-505.

Ohigashi, T., Nagasaka, M., Horigome, T., Kosugi, N., Rosendahl, S. M., & Hitchcock, A. P. (2016, July). Development of in-situ sample cells for scanning transmission x-ray microscopy. In *AIP Conference Proceedings* (Vol. 1741, No. 1, p. 050002). AIP Publishing LLC.

Paterova, A.V., Maniam, S.M., Yang, H., Grenci, G. and Krivitsky, L.A., (2020). Hyperspectral infrared microscopy with visible light. *Science Advances*, *6*(44), p.eabd0460.

Pfeiffer, F., 2018. X-ray ptychography. *Nature Photonics*, *12*(1), pp.9-17.

Phillips, Courtney L., Tom Z. Regier, and Derek Peak. (2013) Aqueous Cu (II)–organic complexation studied in situ using soft X-ray and vibrational spectroscopies." *Environmental science & technology* 47.24, 14290-14297

Riekel, C., Burghammer, M., Davies, R., Gebhardt, R., Popov, D., (2009). Applications of synchrotron light to scattering and diffraction in materials and life sciences, in: Ezquerra,

Rightor, E.G., Hitchcock, A.P., Ade, H., Leapman, R.D., Urquhart, S.G., Smith, A.P., Mitchell, G., Fischer, D., Shin, H.J. and Warwick, T., (1997). Spectromicroscopy of poly (ethylene terephthalate): comparison of spectra and radiation damage rates in X-ray absorption and electron energy loss. *The Journal of Physical Chemistry B*, *101*(11), pp.1950-1960.

Rodenburg, J. M., & Faulkner, H. M. (2004). A phase retrieval algorithm for shifting illumination. *Applied physics letters*, *85*(20), 4795-4797.

Rodenburg, J.M., (2013). Sampling in x-ray ptychography. *Phys. Rev. A*. 87, 1–8.

Rösner, B., Koch, F., Döring, F., Guzenko, V.A., Meyer, M., Ornelas, J.L., Späth, A., Fink, R.H., Stanescu, S., Swaraj, S. and Belkhou, R., (2018). 7 nm spatial resolution in soft x-ray microscopy. *Microscopy and Microanalysis*, *24*(S2), pp.270-271.

Rodenburg, J. M., Hurst, A. C., Cullis, A. G., Dobson, B. R., Pfeiffer, F., Bunk, O., ... & Johnson, I. (2007). Hard-x-ray lensless imaging of extended objects. *Physical review letters*, *98*(3), 034801.

Prabu, V., Obst, M., Hosseinkhannazer, H., Reynolds, M., Rosendahl, S., Wang, J. and Hitchcock, A.P., (2018). Instrumentation for in situ flow electrochemical Scanning Transmission X-ray Microscopy (STXM). *Review of Scientific Instruments*, *89*(6).

Sakdinawat, A., Attwood, D., (2010). Nanoscale X-ray imaging. *Nat. Photonics* 4, 840–848.

Schroer, C.G., Boye, P., Feldkamp, J.M., Patommel, J., Schropp, A., Schwab, A., Stephan, S.,Burghammer, M., Schöder, S., Riekel, C., (2008). Coherent X-ray diffraction imaging with anofocused illumination. *Phys. Rev. Lett*. 101, 1–4.

Schwenke, J., Thanell, K., Beinik, I., Roslund, L. and Tyliszczak, T., (2018). Soft/MAX-A new Soft X-ray Microscopy and Coherent Imaging Beamline at the MAX IV Facility. *Microscopy and Microanalysis*, *24*(S2), pp.232-233.

Shapiro, D.A., Yu, Y.-S., Tyliszczak, T., Cabana, J., Celestre, R., Chao, W., Kaznatcheev, K.,Kilcoyne, A.L.D., Maia, F., Marchesini, S., Meng, Y.S., Warwick, T., Yang, L.L., Padmore,H.A., (2014). Chemical composition mapping with nanometre resolution by soft X-raymicroscopy. *Nat. Photonics* 8, 765–769.

Shemilt, L. (2014) PhD thesis: “Coherent Diffraction Imaging and Ptychography of Human Metaphase Chromosomes”, University College, London.

Sitaud, B., Solari, P.L., Schlutig, S., Llorens, I. and Hermange, H., (2012). Characterization of radioactive materials using the MARS beamline at the synchrotron SOLEIL. *Journal of nuclear materials*, *425*(1-3), pp.238-243.

Stitsky, J., Wang, J. and Urquhart, S., (2023). Making chemical sense of phase in soft X-ray spectroptychography. *Journal of Electron Spectroscopy and Related Phenomena*, 267, p.147367.

Shahcheraghi, L., Zhang, C., Lee, H. J., Cusack-Striepe, M., Ismail, F., Abdellah, A., & Higgins, D. C. (2021). Identifying Activity and Selectivity Trends for the Electrosynthesis of Hydrogen Peroxide via Oxygen Reduction on Nickel–Nitrogen–Carbon Catalysts. *The Journal of Physical Chemistry C*, *125*(29), 15830-15840.

Scott, S. B., Hogg, T. V., Landers, A. T., Maagaard, T., Bertheussen, E., Lin, J. C., ... & Chorkendorff, I. (2019). Absence of oxidized phases in Cu under CO reduction conditions. *ACS Energy Letters*, *4*(3), 803-804.

Singh, P. and Srivastava, R., (2021). Utilization of bio-inspired catalyst for CO2 reduction into green fuels: Recent advancement and future perspectives. Journal of CO2 Utilization, 53, p.101748.

Singh, S. (2002). Refractive index measurement and its applications. *Physica Scripta*, 65(2), 167.

Seh, Z. W., Kibsgaard, J., Dickens, C. F., Chorkendorff, I. B., Nørskov, J. K., & Jaramillo, T. F. (2017). Combining theory and experiment in electrocatalysis: Insights into materials design. *Science*, *355*(6321), eaad4998.

Shen, H., Wang, Y., Chakraborty, T., Zhou, G., Wang, C., Fu, X., ... & Wang, C. (2022). Asymmetrical C–C coupling for electroreduction of CO on bimetallic Cu–Pd catalysts. *ACS Catalysis*, *12*(9), 5275-5283.

Sodhi, R. N., & Brion, C. E. (1984). Reference energies for inner shell electron energy-loss spectroscopy. *Journal of electron spectroscopy and related phenomena*, *34*(4), 363-372.

Stierhof, J., Kühn, S., Winter, M., Micke, P., Steinbrügge, R., Shah, C., ... & Leutenegger, M. A. (2022). A new benchmark of soft X-ray transition energies of Ne, CO 2, and SF 6: paving a pathway towards ppm accuracy. *The European Physical Journal D*, 76(3), 38.

Steinberg, Meyer. (1998) Production of hydrogen and methanol from natural gas with reduced CO2 emission. *International journal of hydrogen energy* 23.6, 419-425.

Stohr, J., and Simone Anders. (2000): "X-ray spectro-microscopy of complex materials and surfaces." *IBM Journal of Research and Development* 44, 4, 535-551.

Sun, Z., Ma, T., Tao, H., Fan, Q. and Han, B., (2017). Fundamentals and challenges of electrochemical CO2 reduction using two-dimensional materials. *Chem*, 3(4), pp.560-587.

Sun, T.; Sun, G.; Yu, F.; Mao, Y.; Tai, R.; Zhang, X.; Shao, G.; Wang, Z.; Wang, J.; Zhou, J. (2021)

"Soft X-Ray Ptychography Chemical Imaging of Degradation in a Composite Surface-Reconstructed Li-Rich Cathode. *ACS Nano* , 15 1475–1485

Sun, T., Zuo, S., He, B., Yuan, X., Li, G., Zhou, J., Weigand, M., Abate, A. and Wang, J., (2023). Ionic liquid functionalized tin halide perovskite investigated by STXM and spectro-ptychography. *Journal of Electron Spectroscopy and Related Phenomena*, *265*, p.147330.

Tavares, P.F., Al-Dmour, E., Andersson, Å., Cullinan, F., Jensen, B.N., Olsson, D., Olsson, D.K., Sjöström, M., Tarawneh, H., Thorin, S. and Vorozhtsov, A., (2018). Commissioning and first-year operational results of the MAX IV 3 GeV ring. *Journal of synchrotron radiation*, *25*(5), pp.1291-1316.

Timoshenko, J. and Roldan Cuenya, B., (2020). In situ/operando electrocatalyst characterization by X-ray absorption spectroscopy. *Chemical reviews*, *121*(2), pp.882-961.

Thibault, P., Dierolf, M., Menzel, A., Bunk, O., David, C., & Pfeiffer, F. (2008). High-resolution scanning x-ray diffraction microscopy. *Science*, *321*(5887), 379-382.

Thompson, A. C., Attwood, D. T., Gullikson, E. M., Howells, M. R., Kim, K. J., Kirz, J., ... & Winik, H. (2001). X-ray Data Booklet, edited by AC Thompson & D. *Vaughan. Berkeley: Lawrence Berkeley National Laboratory*.

Urquhart, S. G. (2022). X-ray Spectroptychography. *ACS omega*, *7*(14), 11521-11529.

Varela, A. S., Ju, W., Bagger, A., Franco, P., Rossmeisl, J., & Strasser, P. (2019). Electrochemical reduction of CO2 on metal-nitrogen-doped carbon catalysts. *Acs Catalysis*, *9*(8), 7270-7284.

van der Wal, L. I., Turner, S. J., & Zečević, J. (2021). Developments and advances in in situ transmission electron microscopy for catalysis research. *Catalysis Science & Technology*, *11*(11), 3634-3658.

Velasco-Velez, J. J., Mom, R. V., Sandoval-Diaz, L. E., Falling, L. J., Chuang, C. H., Gao, D., ... & Schlögl, R. (2020). Revealing the active phase of copper during the electroreduction of CO2 in aqueous electrolyte by correlating in situ X-ray spectroscopy and in situ electron microscopy. *ACS energy letters*, *5*(6), 2106-2111.

Vijayakumar, J., Yuan, H., Mille, N., Stanescu, S., Swaraj, S., Favre-Nicolin, V., ... & Belkhou, R. (2023). Soft X-ray spectro-ptychography of boron nitride nanobamboos, carbon nanotubes and permalloy nanorods. *Journal of Synchrotron Radiation*, 30(4).

Wandt, J., Freiberg, A., Thomas, R., Gorlin, Y., Siebel, A., Jung, R., ... & Tromp, M. (2016). Transition metal dissolution and deposition in Li-ion batteries investigated by operando X-ray absorption spectroscopy. *Journal of Materials Chemistry A*, *4*(47), 18300-18305.

Wang, H. Y., Soldemo, M., Degerman, D., Lömker, P., Schlueter, C., Nilsson, A., & Amann, P. (2022). Direct Evidence of Subsurface Oxygen Formation in Oxide-Derived Cu by X-ray Photoelectron Spectroscopy. *Angewandte Chemie International Edition*, *61*(3), e202111021

Wang, J., Tan, H. Y., Kuo, T. R., Lin, S. C., Hsu, C. S., Zhu, Y., ... & Chen, H. M. (2021). In situ identifying the dynamic structure behind activity of atomically dispersed platinum catalyst toward hydrogen evolution reaction. *Small*, *17*(16), 2005713.

Wang, L., Higgins, D. C., Ji, Y., Morales-Guio, C. G., Chan, K., Hahn, C., & Jaramillo, T. F. (2020). Selective reduction of CO to acetaldehyde with CuAg electrocatalysts. *Proceedings of the National Academy of Sciences*, *117*(23), 12572-12575.

Wang, L., Wang, H., & Xu, X. G. (2022). Principle and applications of peak force infrared microscopy. *Chemical Society Reviews*, *51*(13), 5268-5286.

Wang, J., Zhou, J., Fang, H., Sham, T. K., Karunakaran, C., Lu, Y., ... & Hitchcock, A. P. (2011). Effect of humidity on individual SnO2 coated carbon nanotubes studied by in situ STXM. *Journal of Electron Spectroscopy and Related Phenomena*, *184*(3-6), 296-300.

Wawrzyniak, A. I., Curcio, A., Guła, K., Knafel, M., Kowalski, G. W., Marendziak, A. M., ... & Wiśniowski, M. (2021). Solaris Storage Ring Performance After 6 Years of Operation.

Wang, J. (2011). *Radiation chemistry by soft X-ray spectromicroscopy*. Ph. D. Thesis, McMaster University, 2008.

Wang, J., Botton, G. A., West, M. M., & Hitchcock, A. P. (2009). Quantitative evaluation of radiation damage to polyethylene terephthalate by soft X-rays and high-energy electrons. *The Journal of Physical Chemistry B*, *113*(7), 1869-1876.

Wang, J., Morin, C., Li, L., Hitchcock, A. P., Scholl, A., & Doran, A. (2009). Radiation damage in soft X-ray microscopy. *Journal of Electron Spectroscopy and Related Phenomena*, *170*(1-3), 25-36.

Weekes, D. M., Salvatore, D. A., Reyes, A., Huang, A., & Berlinguette, C. P. (2018). Electrolytic CO2 reduction in a flow cell. *Accounts of chemical research*, 51(4), 910-918.

Wen, G., Ren, B., Park, M. G., Yang, J., Dou, H., Zhang, Z., ... & Chen, Z. (2020). Ternary Sn-Ti-O Electrocatalyst Boosts the Stability and Energy Efficiency of CO2 Reduction. *Angewandte Chemie International Edition*, *59*(31), 12860-12867.

Weng, Z., Wu, Y., Wang, M., Jiang, J., Yang, K., Huo, S., ... & Wang, H. (2018). Active sites of copper-complex catalytic materials for electrochemical carbon dioxide reduction. *Nature communications*, *9*(1), 415.

Wittwer, F., Hagemann, J., Brückner, D., Flenner, S., & Schroer, C. G. (2022). Phase retrieval framework for direct reconstruction of the projected refractive index applied to ptychography and holography. *Optica*, 9(3), 295-302.

Wu, J., Huang, Y., Ye, W., & Li, Y. (2017). CO2 reduction: from the electrochemical to photochemical approach. *Advanced Science*, *4*(11), 1700194.

Wu, J., Zhu, X., West, M. M., Tyliszczak, T., Shiu, H. W., Shapiro, D., ... & Hitchcock, A. P. (2018).

High-resolution imaging of polymer electrolyte membrane fuel cell cathode layers by soft X-ray spectro-ptychography. *The Journal of Physical Chemistry C*, *122*(22), 11709-11719.

Yang, Y., Louisia, S., Yu, S., Jin, J., Roh, I., Chen, C., ... & Yang, P. (2023). Operando studies reveal active Cu nanograins for CO2 electroreduction. *Nature*, *614*(7947), 262-269.

Yang, W., Dastafkan, K., Jia, C., & Zhao, C. (2018). Design of electrocatalysts and electrochemical cells for carbon dioxide reduction reactions. *Advanced Materials Technologies*, 3(9), 1700377.

Zhang, C., Shahcheraghi, L., Ismail, F., Eraky, H., Yuan, H., Hitchcock, A. P., & Higgins, D. (2022). Chemical Structure and Distribution in Nickel–Nitrogen–Carbon Catalysts for CO2 Electroreduction Identified by Scanning Transmission X-ray Microscopy. *ACS catalysis*, *12*(15), 8746-8760.

Zhang, F., Peterson, I., Vila-Comamala, J., Diaz, A., Berenguer, F., Bean, R., ... & Rodenburg, J. M. (2013). Translation position determination in ptychographic coherent diffraction imaging. *Optics express*, *21*(11), 13592-13606.

Zhang, J., Wu, J., Guo, H., Chen, W., Yuan, J., Martinez, U., ... & Lou, J. (2017). Unveiling active sites for the hydrogen evolution reaction on monolayer MoS2. *Advanced Materials*, *29*(42), 1701955.

Zhu, X. (2016). Studies of magnetotactic bacteria by soft X-ray microscopy. (Doctoral dissertation).

Appendix A

This appendix lists the publications which are published, accepted, in press and in preparation .

Publications (journal articles and conference proceedings)

1. Zhang, C., Mille, N., Eraky, H., Stanescu, S., Swaraj, S., Belkhou, R., Higgins, D. and Hitchcock, A., 2023. Copper CO2 Reduction Electrocatalysts Studied by In-situ Soft X-ray Spectro-Ptychography. (in press)
2. Zhang, C., Eraky, H., Tan, S., Hitchcock, A. and Higgins, D., 2023. In-situ Studies of Copper-based CO2 Reduction Electrocatalysts by Scanning Transmission Soft X-ray Microscopy. (under review)
3. Zhang, C., Eraky, H., Ingino, P., Obst, M.,Wang, J., Higgins, D. and Hitchcock, A.P., 2023 *In-situ* STXM Characterization of Cu/Cu2O Electrocatalysts for CO2 Reduction. *AIP Conference Proceedings.* (accepted)
4. Zhang, C., Chen, J., Yuan, H., Wang, J., Sun, T., Higgins, D. and Hitchcock, A.P., 2023. Atomically dispersed Ni-NC electrocatalysts, studied by Ni L-edge spectro-ptychography. *Journal of Electron Spectroscopy and Related Phenomena*, *266*, p.147364.
5. Zhang, C., Shahcheraghi, L., Ismail, F., Eraky, H., Yuan, H., Hitchcock, A.P. and Higgins, D., 2022. Chemical Structure and Distribution in Nickel–Nitrogen–Carbon Catalysts for CO2 Electroreduction Identified by Scanning Transmission X-ray Microscopy. *ACS catalysis*, *12*(15), pp.8746-8760.
6. Yang, W., Eraky, H., Zhang, C., Hitchcock, A.P. and Zhitomirsky, I., 2022. Scanning transmission X-ray microscopy studies of electrochemical activation and capacitive behavior of Mn 3 O 4 supercapacitor electrodes. *Journal of Materials Chemistry A*, *10*(35), pp.18267-18277.

7. Shahcheraghi, L., Zhang, C., Lee, H.J., Cusack-Striepe, M., Ismail, F., Abdellah, A. and Higgins, D.C., 2021. Identifying Activity and Selectivity Trends for the Electrosynthesis of Hydrogen Peroxide via Oxygen Reduction on Nickel–Nitrogen–Carbon Catalysts. *The Journal of Physical Chemistry C*, *125*(29), pp.15830-15840.
8. Hitchcock, A.P., Zhang, C., Eraky, H., Shahcheraghi, L., Ismail, F. and Higgins, D., 2021. In-situ and Operando Studies with Soft X-Ray Transmission Spectromicroscopy. *Microscopy and Microanalysis*, *27*(S2), pp.59-60.
9. Eraky, H., Zhang, C., Higgins, D. and Hitchcock, A.P., 2023. In-situ Scanning Transmission X-ray Microscopy of MnO2 Supercapacitor Electrodes (in preparation)
10. Eraky, H., Zhang, C., Hitchcock, A.P., 2023. Mn 2p and O 1s X-ray absorption spectroscopy of manganese oxides, J. Electron Spectrosc. Rel. Phenom. (in preparation)
11. Eraky, H., Zhang, C., Ingino, P., Obst, M., Hitchcock, A.P.,2023. Flow Electrochemical Device for In-situ Soft X-ray Scanning Transmission X-ray Microscopy (in preparation)

Appendix B

This appendix lists conference presentations.

1. A.P. Hitchcock, C. Zhang, H. Eraky and D. Higgins, In-situ spectromicroscopy studies of Cu catalysed CO2 electroreduction by soft X-ray STXM and spectro-ptychography, 15th Int. Conf. Electron Spectroscopy and Structure (ICESS), Oulu, Finland, 21-25 Aug 2023.
2. Chunyang Zhang, Haytham Eraky, Drew Higgins, Adam P. Hitchcock, Characterization of Copper Electrocatalysts for CO2 Reduction by In-situ Soft X-ray STXM and Ptychography, Surface Canada, Hamilton, Canada, 14-17 May 2023.
3. Chunyang Zhang, Haytham Eraky, Drew Higgins and Adam P. Hitchcock, In-situ STXM Characterization of Cu/Cu2O Electrocatalysts for CO2 Reduction, 15th Intl Conf X-ray Microscopy (XRM2022) Hsinchu, Taiwan, (virtual) June 19-24, 2022.
4. Chunyang Zhang, Pablo Ingino, Martin Obst, Haytham Eraky, Jian Wang, Drew Higgins and Adam P. Hitchcock, in-Situ Soft X-ray Spectromicroscopy Characterization of Electrochemical Processes, PRiME, Electrochemical Society meeting, (Honolulu, HI, Oct 2020.

Appendix C

This appendix lists all the software packages used for this thesis.

1. aXis2000

aXis2000 is a freeware program written in Interactive Data Language (IDL) by Adam Hitchcock, and it is available from http://unicorn.mcmaster.ca/aXis2000.html. It was used for the spectromicroscopy data analysis: images, stack and spectral analyses. [Hitchcock, A. P. (2023). Analysis of X-ray images and spectra (aXis2000): A toolkit for the analysis of X-ray spectromicroscopy data. *Journal of Electron Spectroscopy and Related Phenomena*, *266*, 147360.]

2. Sigma Plot 2000

Sigma Plot 2000 (by Jandel Scientific) was used for graphical representations and regression analysis.

3. STXM_Control

This software was initially written by Dr. Tolek Tyliszczak and Peter Hitchcock, and extensively further developed from 2002-2006 by Dr. Tyliszczak, especially the pattern generation function. It controls the beamline (slit sizes and monochromator) and the STXM microscope, and acquires the data.

4. IviumSoft

IviumSoft is a user interface for single and multichannel instrument control, electrochemical method selection and composition, data display and analysis for Ivium-pocketSTAT potentiostat.[https://www.ivium.com/software/]

5. PSTrace

PSTrace is the software to control the Palmsens-EmStat4S potentiostat [https://www.palmsens.com/software/ps-trace/].

6. Autodesk Inventor and Autodesk Fusion 360

Autodesk Inventor and Autodesk Fusion 360 are both computer-aided design (CAD) and computer-aided manufacturing software applications developed by Autodesk, a well-known software company in the design and engineering industry.

Autodesk Inventor is a professional-grade CAD software providing a comprehensive set of tools for creating parametric 3D models, assemblies, and detailed drawings.

Autodesk Fusion 360 is a cloud-based design and manufacturing platform offers parametric 3D modeling, similar to Inventor, allowing users to create and edit complex designs. Additionally, Fusion 360 integrates computer-aided manufacturing tools, enabling users to generate toolpaths and G-code for CNC (computer numerical control) machining.

Appendix D

This appendix shows the Supporting Information for Chapter 4.

Supporting Information for

Chemical Structure and Distributions in Nickel-Nitrogen-Carbon Catalysts for CO_2 Electroreduction Identified by Scanning Transmission X-ray Microscopy

Chunyang Zhang,[1,2] Ladan Shahcheraghi,[1] Fatma Ismail, [1] Haytham Eraky,[2] Hao Yuan,[2,#]
Adam P. Hitchcock[2*] and Drew Higgins[1*]

1. Chemical Engineering, McMaster University, Hamilton, ON, Canada, L8S 4M1

2. Chemistry & Chemical Biology, McMaster University, Hamilton, ON, Canada, L8S 4M1

* co-corresponding author: aph@mcmaster.ca 905-525-9140
* co-corresponding author: higgid2@mcmaster.ca

present address: Electrical and Computer Engineering, U. Victoria, Victoria, BC, Canada

Table of Contents

Section S1 Overview of STXM samples

Figure S1 shows the two types of sample mounting used in this study. All materials are in the form of partially aggregated powders, except metallic Ni, which was measured as a physical vapour deposition (PVD) thin film. Samples were prepared by attaching the support with tape or epoxy to the trapezoidal STXM sample plate (not shown in **Fig. S1**), then dropping a spatula tip (<1 mg) on the support, then sharply tapping the STXM plate against a hard surface to detach weakly adhering large aggregates.

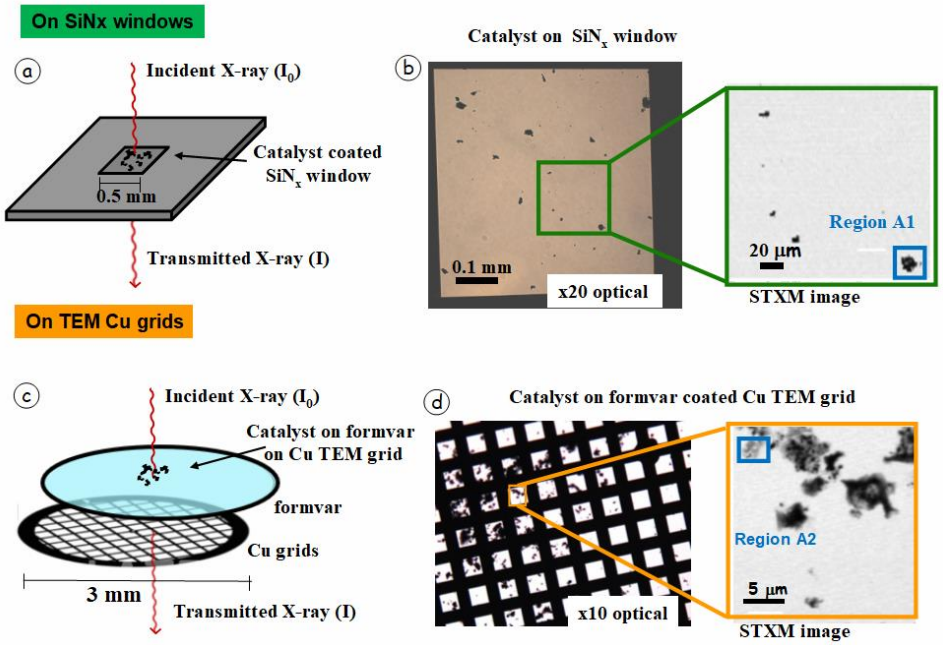

Figure S1 Sample mounting used for scanning transmission X-ray microscopy (STXM) measurements. **a)** schematic of SiNx window mounts. **b)** Transmission optical microscopy image (20x) of Ni-N-C-high particles on a SiNx window. The frame is 5 mm x 5 mm, 200 µm thick Si, with a lo-stress 0.5 mm x 0.5 mm, 75 nm thick window pane at the center (Norcada Inc) and STXM image at 395 eV of region **A1** on SiNx windows **c)** schematic of formvar coated TEM 3 mm diameter Cu grid mounts. **d)** Transmission optical microscopy image (10x) of particles Ni-N-C-high on a formvar-coated TEM Cu grids. and STXM image of one square of the TEM Cu grid sample, containing region **A2.**

Section S2 Summary of samples investigated

Table S1. Details of the Ni-N-C samples and conditions of the measurements for each sample

Code	sample	substrate	edge	time	Pixel (nm)	# pixel	E- range (eV)
A1	Ni-N-C-high	SiNx	Ni 2p	2019-July	65	300*267	847.6, 852.2
A1a	Ni-N-C-high	SiNx	Ni 2p	2019-July	45	87*69	836-929
			O 1s	2019-July	45	87*69	524-568
			N 1s	2019-July	60	55*55	394-432
			C 1s	2019-July	60	51*51	278-320
A2	Ni-N-C-high	TEM grid	Ni 2p	2021-Jan	35	100*70	842-878
			O 1s	2021-Jan	35	100*70	524-568
			N 1s	2021-Jan	35	100*70	394-422
			C 1s	2021-Jan	35	100*70	278-320
			S 2p	2020-Sep	80	45*32	158-205
A3	Ni-N-C-high	TEM grid	Ni 2p	2020-Aug	80	75*75	842-900
A4	Ni-N-C-high	TEM grid	Ni 2p	2020-Aug	30	83*83	842-920
			C 1s	2020-Aug	35	72*72	278-320
A5	Ni-N-C-high	SiNx	Ni 2p	2019-July	30	103*100	840-892
			C 1s	2019-July	35	91*85	278-320
B1	Ni-N-C-low	TEM grid	Ni 2p	2020-Sep	66	60*60	842-878
			O 1s	2020-Sep	90	44*44	524-568
			N1s	2020-Sep	66	60*60	394-422
			C 1s	2020-Sep	90	44*44	278-320
B2	Ni-N-C-low	TEM grid	Ni 2p	2021-Feb	66	60*60	842-890
B3	Ni-N-C-low	TEM grid	Ni 2p	2021-Jan	35	70*70	842-878
			C 1s	2021-Jan	50	50*50	278-320
B4	Ni-N-C-low	SiNx	Ni 2p	2019-Dec	90	78*78	840-892
			C 1s	2019-Dec	90	78*78	278-320

Section S3 STXM energy calibration

We found that comparison of our spectra with results reported in the literature [1-6] was challenging due to often incomplete details regarding how the energy scales were calibrated in different studies. Especially for the Ni 2p edge, the energy of the maximum of the Ni $2p_{3/2} \rightarrow 3d$ transition in Ni metal varied by over 1 eV in the literature [6-9]. In this work, the Ni 2p spectra were calibrated by including a few torr of Ne gas in the STXM tank, such that the sharp Ne $1s \rightarrow 3p$ transition at 867.05 eV [1] was included in the same data set and thus could provide accurate calibration. Other edges were calibrated using appropriate gases whose spectra were recorded within the same injection as key catalyst or reference compounds. **Table S2** summarizes all the gas calibration features used, along with references to their calibration. **Table S3** reports the energies of the Ni $2p_{3/2} \rightarrow 3d$ peaks for the catalyst and reference compounds, in order to evaluate reproducibility.

We note that the spectromicroscopy beamline at the Canadian Light Source (CLS SM) has issues with monochromator energy scale stability which can lead to energy scale shifts between injections (typically every 8 hours), and sometimes even within a single injection. One source of this instability is slackness in the mechanical linkage driving the angle of the plane grating. A backlash protocol, consisting of slewing to 50 eV below the start energy of a spectral scan, was implemented to reduce that problem. In addition, since the optical path of the CLS SM beamline does not include an energy defining entrance slit, the energy scale can shift if there are deviations of more than 1 μm in the vertical position of the electron beam in the storage ring. Due to these factors, we occasionally found that the energy scales of the Ni 2p data sets differed by up to 1.5 eV. In the early stages of this work, energy calibration with gas standards was only performed at the start of the STXM measurements. In later runs, we calibrated before and after critical STXM measurements and used Ne gas as internal standard for Ni 2p STXM stacks (Ni metal, Ni-N-C-high), which gave more reliable results (>±0.1 eV variation). We were careful about calibrating the Ni 2p spectrum of Ni metal. Ultimately, for the critical Ni 2p analysis, we determined a value of 852.7(1) eV for Ni metal [Ni(0)] and used it as an internal standard. This is close to the energy of the Ni $2p_{3/2} \rightarrow 3d$ peak for Ni metal reported by two other groups.[8, 10] We strongly encourage researchers to provide details of the energy scale calibration to enable information sharing and cross-study comparisons in the future.

Table S2 Gaseous species energy calibration

Edge	Species	Feature	Energy (eV)	ref
Ne 1s	Ne gas	Ne 1s $\rightarrow$ 3p	867.05 (8)	11
F 1s	SF_6 gas	F 1s $\rightarrow a_{1g}$	688.3 (1)	12
C 1s	CO_2 gas	C 1s $\rightarrow$ C 3s C 1s $\rightarrow$ C 3p	292.74 (5) 294.96 (5)	13
O 1s	CO_2 gas	O 1s $\rightarrow$ O 3s	538.9 (1)	14
N 1s	N_2 gas	N 1s $\rightarrow$ 3s N 1s $\rightarrow$ 3p	406.15(2) 407.115 (5)	15

Table S3 Reproducibility of peak positions in catalyst and reference compound samples

samples	file	Ni (0)	Ni_3S_2	NiN_x/C	Ni(2+)
Ni metal (PVD)	A210807022	852.64 eV	-------	-------	--------
Ni metal (PVD)	A210125033	852.77 eV	---------	----------	-------
Ni-N-C-high	A210807037	852.71 eV	852.99 eV	854.19 eV	----------
Ni-N-C-high	A210120064	852.8 eV	853.1 eV	854.2 eV	--------
Ni-N-C-high	A190712097	852.75 eV	853.15 eV	854.15 eV	------
NiTPP	A210125029	----------	---------	854.08 eV	-------
Ni_3S_2	A210202019	--------	853.1 eV	----------	--------
O-NiPc	A210918047	--------	--------	854.20 eV	------
NiO	A200802045	---------	--------	-------	853.03 eV
$NiCO_3$	A200801005	---------	--------	-------	853.25 eV
$Ni(NH_4)_2(SO_4)_2$	A200801017	---------	--------	-------	853.35 eV

Section S4 Generation of quantitative Ni 2p reference spectra for fitting

Outside of the ~20-40 eV region at the onset of a given inner shell edge (the near edge X-ray absorption fine structure, NEXAFS region), the X-ray absorption of any material is only a function of its elemental composition and density.[16] Thus one can convert an X-ray absorption spectrum measured on a relative intensity scale to an absolute intensity scale, by matching the intensity of the pre-edge (e.g. -20 to -5 eV relative to the onset) and post-edge (>30 eV above the onset) NEXAFS regions to that predicted from the elemental composition and density, using tabulated elemental X-ray absorption cross-sections. [17] **Figure S2** shows the OD1 Ni 2p spectra of the 4 Ni materials used to analyze the Ni-N-C catalyst samples.

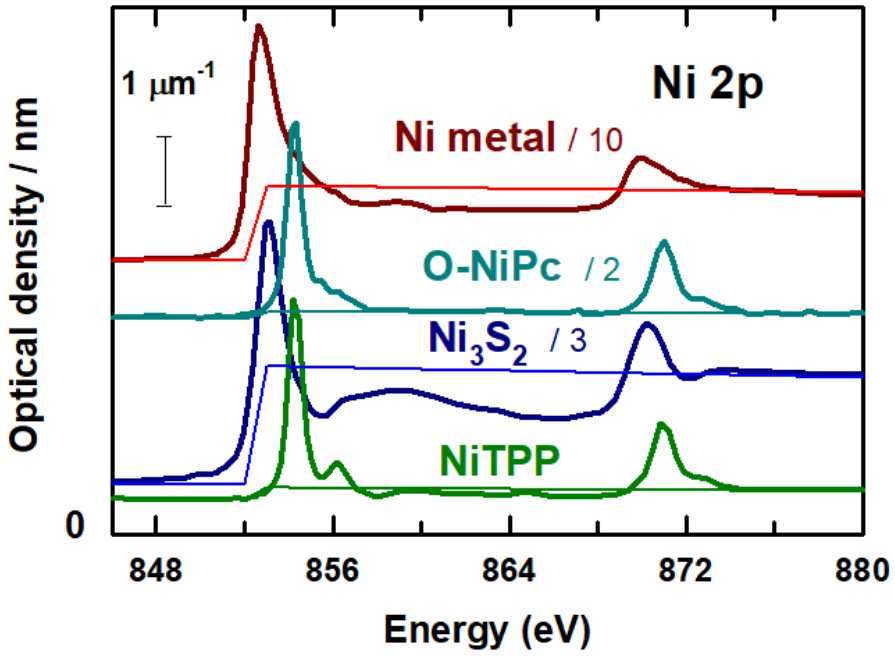

Figure S2 The quantitative Ni 2p spectra of metallic nickel (Ni(0)) (dark red), Ni_3S_2 (dark blue), O-NiPc (dark cyan) and NiTPP (dark green) on OD1 intensity scales. The step curve with corresponding color is the calculated X-ray absorption for 1 nm of elemental composition of Ni , Ni_3S_2, NiTPP ($C_{44}H_{28}N_4Ni$) and O-NiPc ($C_{64}H_{80}N_8NiO_8$), based on the response tabulated in the CXRO data base[17] and the known density of these materials (8.9 $g.cm^{-3}$ for Ni(0) [18] , 1.6 $g.cm^{-3}$ for NiTPP and O-NiPc (assume the density of NiTPP and O-NiPc same with Ni phthalocyanine) [19], and 5.8 $g.cm^{-3}$ for Ni_3S_2 [20]).

Section S5 STEM/EELS results for C, N, O of Ni-N-C low sample

Figure S3a presents EELS mapping of C, N, O of the particle shown in **Fig. 2**

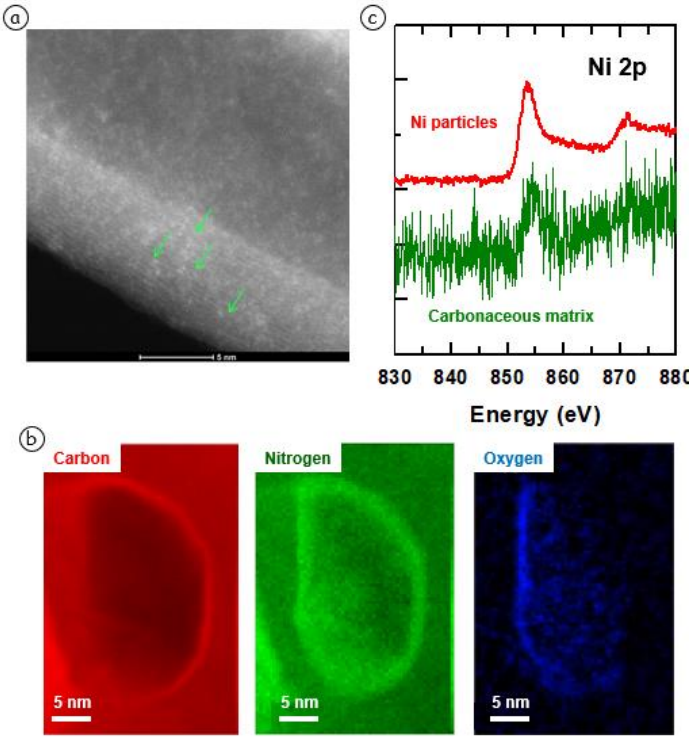

Figure S3 a) Higher resolution HAADF-STEM image. b) EELS mapping for Ni-N-C-low particles region. c) EELS spectra for Ni particles region and carbonaceous matrix region.

Section S6 Ni-N-C-high detailed analysis

S6-a Ni-N-C-high detailed analysis of areas A1 and A1a

Figure S4 illustrates the conversion of measured transmission STXM images to the corresponding optical density (OD) images using the Beer-Lambert law:

$$OD(x,y) = -\ln(I(x,y)/I_o)$$

where I(x,y) is the transmitted intensity at pixel (x,y) and Io is the incident flux, measured off the sample, but through all other components of the STXM (all optics, windows, the sample support and the detector.

Fig. 3c (main manuscript) presents the difference, $\Delta OD = OD_{852.7} - OD_{848}$, which is called a **stack map**. It is a map of the Ni content present in aggregate **A1**.

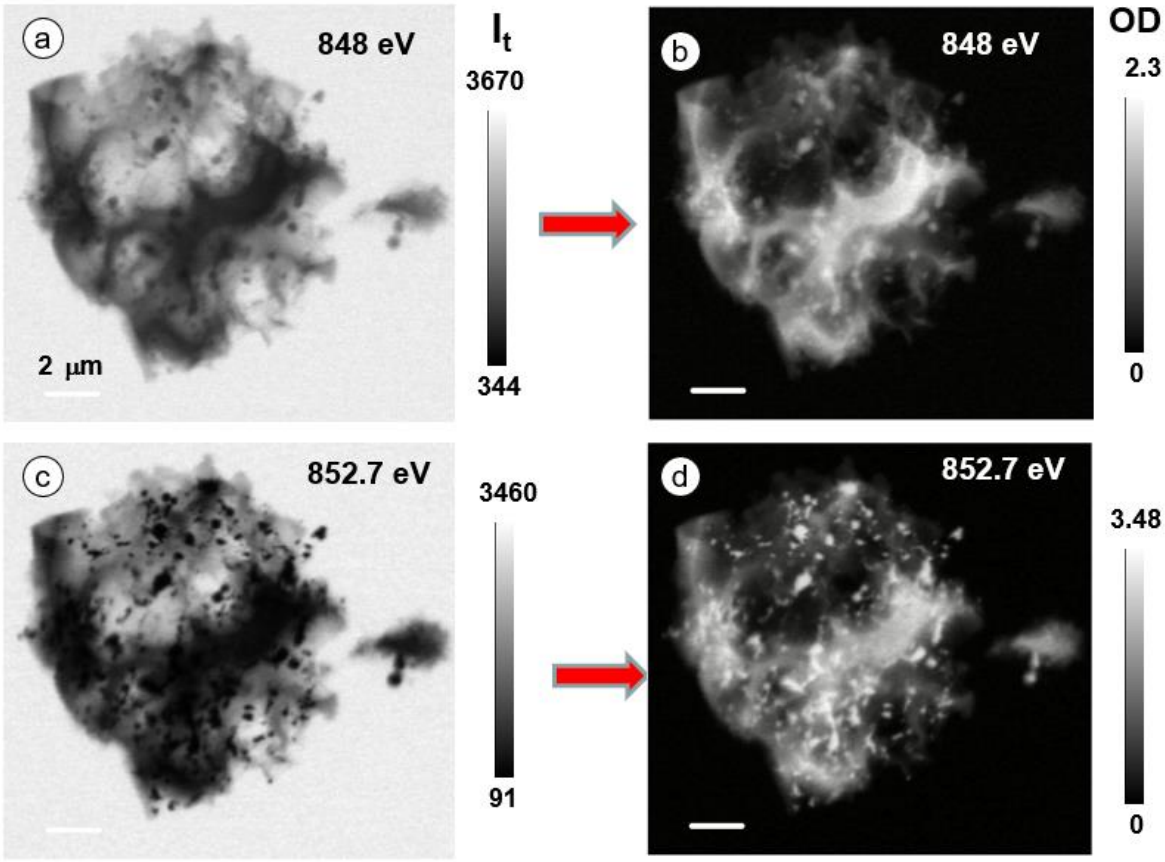

Figure S4 optical density (OD) conversion for region **A1** on SiNx window **a, b)** at 848 eV, **c, d)** at 852.7 eV.

Figure S5 compares the optimized Ni 2p spectra of the particles and matrix (i.e. from the masked regions in **Fig. 3e**) to the Ni 2p spectra of 7 reference compounds, which, from the perspective of the catalyst synthesis, are candidates for being present in the catalyst. Careful examination shows a good alignment of the low energy Ni $2p_{3/2}$ peak in the particle spectrum with the Ni $2p_{3/2}$ peak in Ni metal, the low energy Ni $2p_{3/2}$ peak in the matrix spectrum with the Ni $2p_{3/2}$ peak in Ni_3S_2 and the higher energy Ni $2p_{3/2}$ peak in the matrix spectrum with the Ni $2p_{3/2}$ peak in Ni-TPP. Corresponding alignments are also present in the Ni $2p_{1/2}$ spectral region. Based on these observations we explored the use of the spectra of Ni metal [Ni(0)], Ni-TPP and Ni_3S_2 to interpret the Ni 2p spectra of the catalysts studied, as presented in the paper.

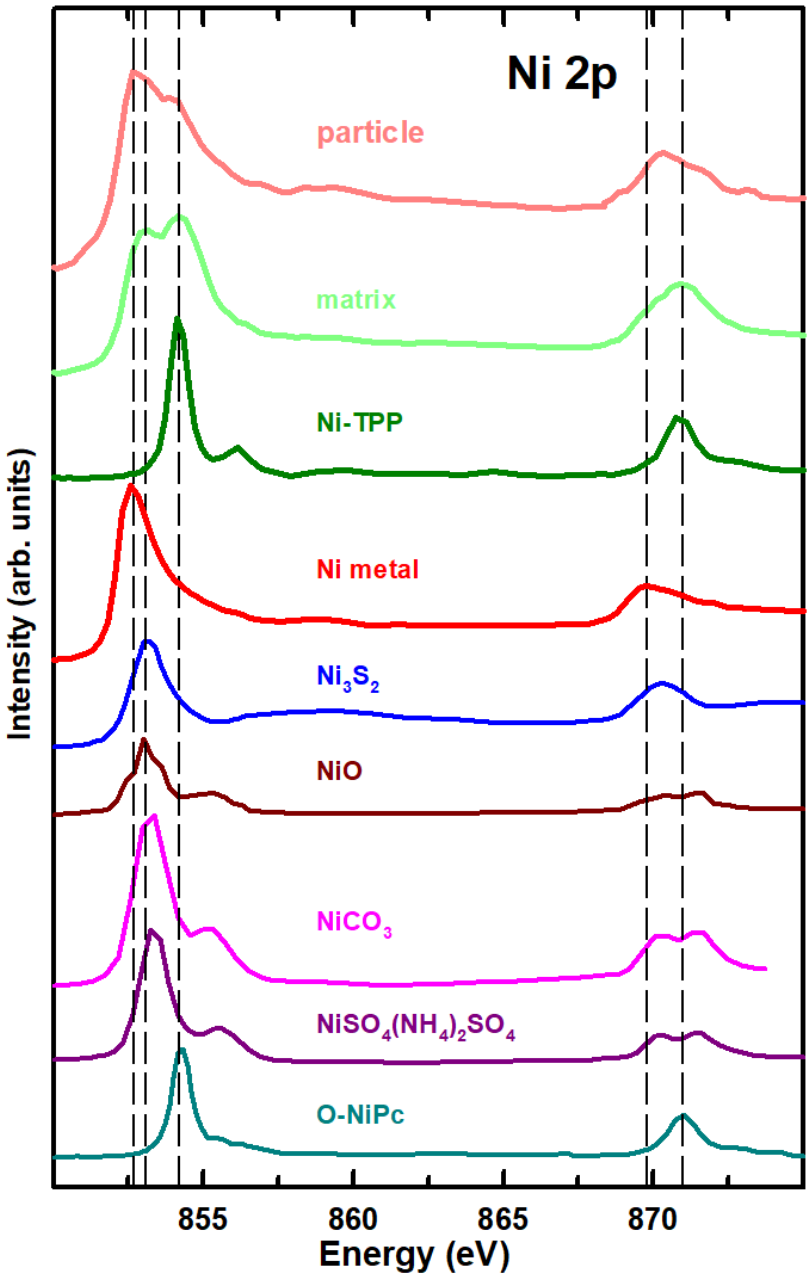

Figure S5 Optimized Ni 2p spectra of particles (light red) and matrix (light green) in region **A1a**, compared with reference spectra of NiTPP, Ni(0), Ni_3S_2, NiO, $NiCO_3$, Ni ammonium sulphate and O-NiPc. The vertical lines indicate correlation of positions in the Ni-C-N catalyst with features in the spectra of the reference compounds.

Figure S6 summarizes the analysis of the Ni 2p stack of region **A1a** of the Ni-N-C-high sample using internal spectra extracted from the Ni 2p stack. While this does provide one possible interpretation of the data, it is not optimal because of the relatively high and structured residual, which suggests a third component may give an improved fit, the chemical identity is not defined and the analysis at this stage is only qualitative. In order to go further, it is useful to compare the optimized particle and matrix spectra with the Ni 2p spectra of possible species present.

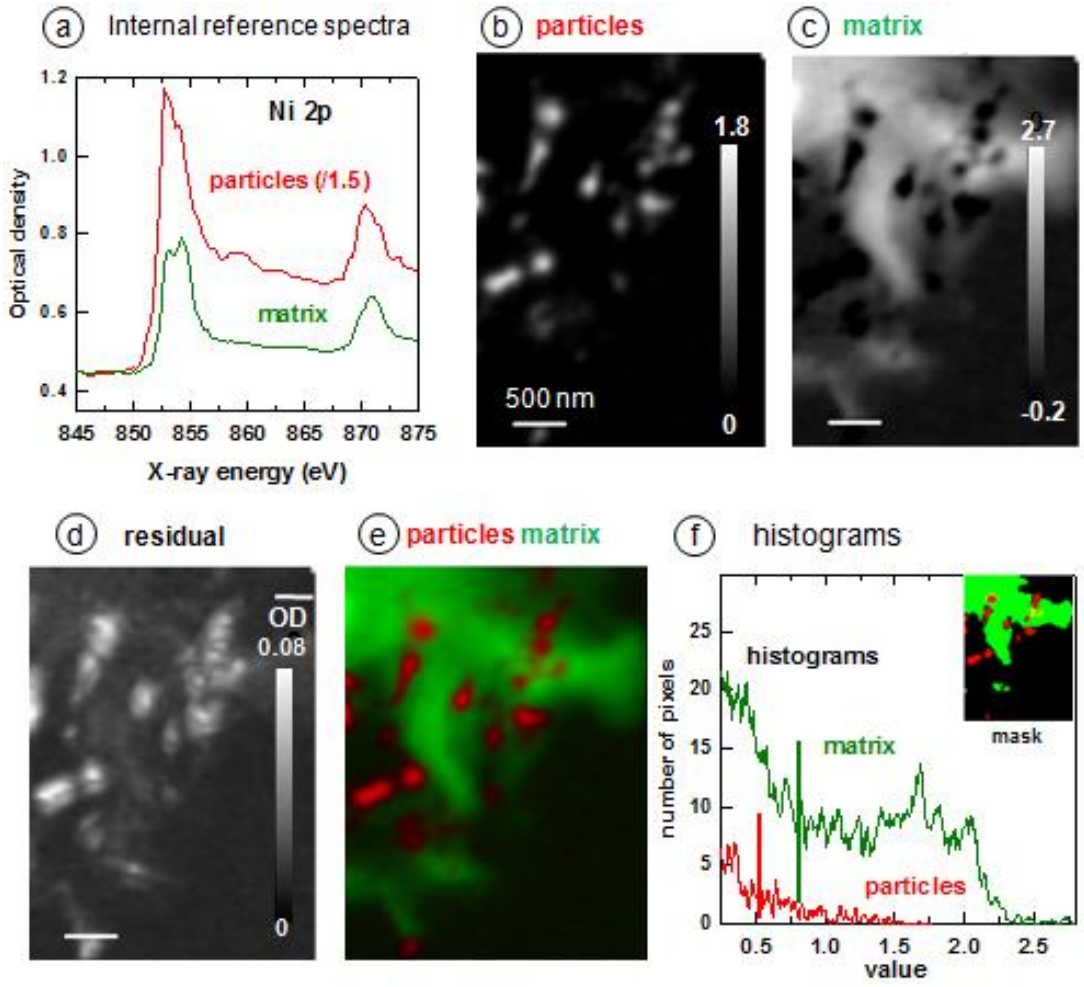

Figure S6 SVD analysis of the Ni 2p stack of region **A1a** of the Ni-N-C-high sample using internal reference spectra. **a)** Spectra of particles and matrix from arbitrarily selected areas. **b)** component map of the particles. **c)** component map of the matrix region. The grayscales in **(b, c)** are in multiplicative units of the reference spectra. **d)** residual of the fit. **e)** color coded composite of the particle (red, a) and matrix (green, b) maps. **f)** histogram of pixel values in the component maps. The vertical lines indicate the thresholds used. All pixels above these values form 0/1 masks (displayed as the insert) which is used to extract optimized spectra of the particles and matrix.

Figure S7 presents a verification of the analysis of the Ni 2p stack of region **A1a** of the Ni-N-C sample, as a linear combination of Ni(0), Ni-TPP and Ni_3S_2 components, as presented in **Fig. 5** of the paper. **Table S4** summarizes the quantitative results for this curve fit analysis.

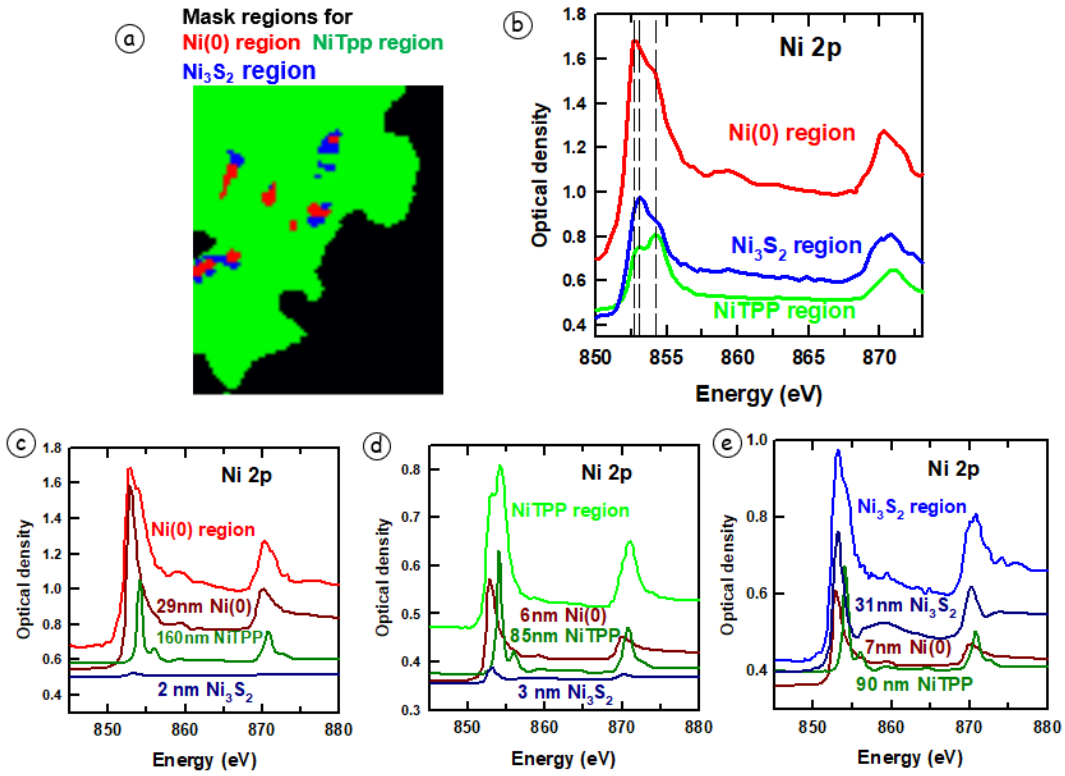

Figure S7 Spectral domain representation of the 3 component (Ni(0), NiTPP, Ni_3S_2) SVD analysis of the Ni 2p stack of region **A1a** of the Ni-C-N-high catalyst. **a)** shows the masked regions for Ni(0), NiTPP, Ni_3S_2. **b**) the internal spectra for the regions of Ni(0), NiTPP, Ni_3S_2. **(c)** curve fit of the Ni(0) region. **d**) curve fit of the NiTPP region. **e**) curve fit of the Ni_3S_2 region.

Table S4 Results of SVD curve fit analysis of region **A1a** of the Ni-N-C sample

	Species (average thickness in nm)			
area	Ni(0)	Ni-TPP	Ni_3S_2	χ^2
Ni(0) region	29	160	2	0.06
NiTPP region	6	85	3	0.02
N_3S_2 region	7	90	31	0.02

S5-b SVD analysis of Ni 2p stack of region A2 of Ni-N-C-high

Figure S8 presents the SVD analysis of Ni 2p stack of region **A2** of Ni-N-C-high using optical density per nm (OD1). In order to account for the significant part of the matrix where there is C-N-O but no Ni, a constant value of 0.003 was added to the OD1 spectrum of NiTPP, so that the relative proportions of pre-edge and Ni 2p signal were similar to that in the spectrum of the matrix.

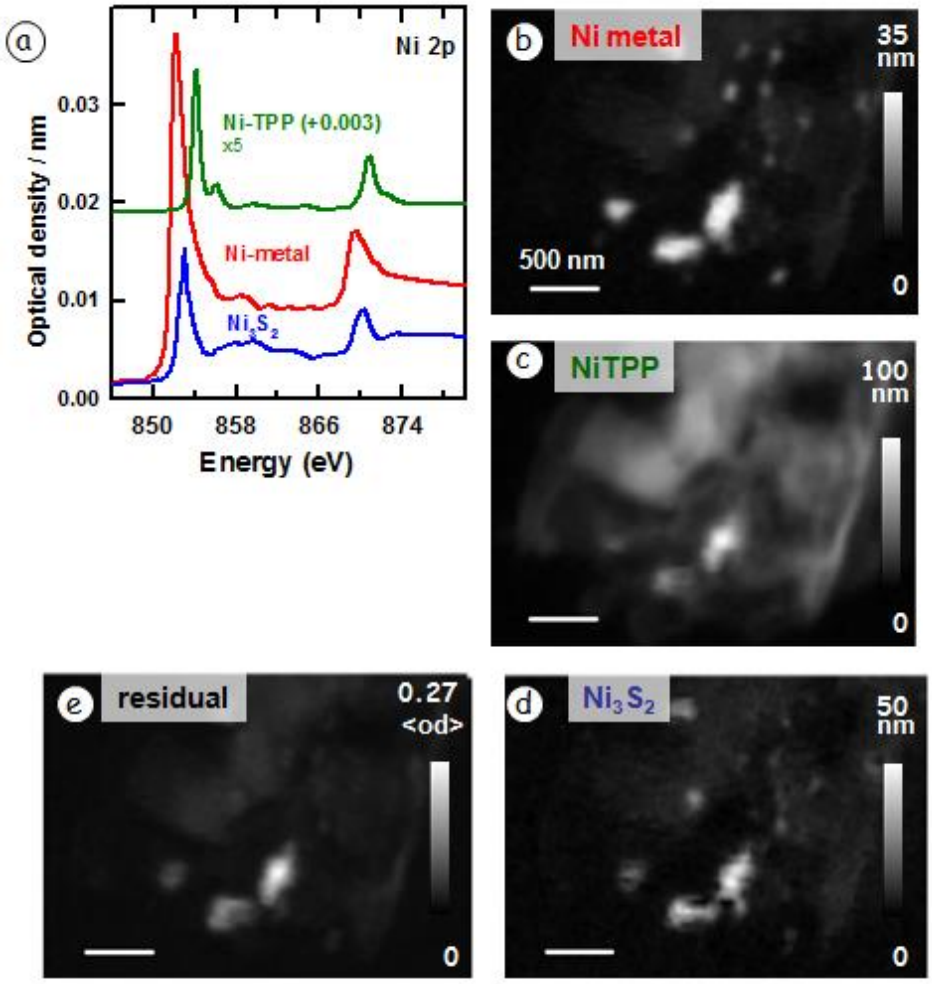

Figure S8 SVD analysis of Ni 2p stack of region **A2** of Ni-N-C-high. (**a**) OD1 spectra of Ni metal, Ni-TPP* and Ni_3S_2 used to fit the stack. The NiTPP reference spectrum is the OD1 spectrum of Ni-TPP with an additional 0.003 added, to account for the fraction of the matrix region which has C-N-O signal but not Ni 2p signal. **b)** component map of the Ni metal. **c)** component map of the Ni –TPP*. **d)** component map of Ni_3S_2. **e)** Residual of fit. See **Fig. 4b** for the color coded composite

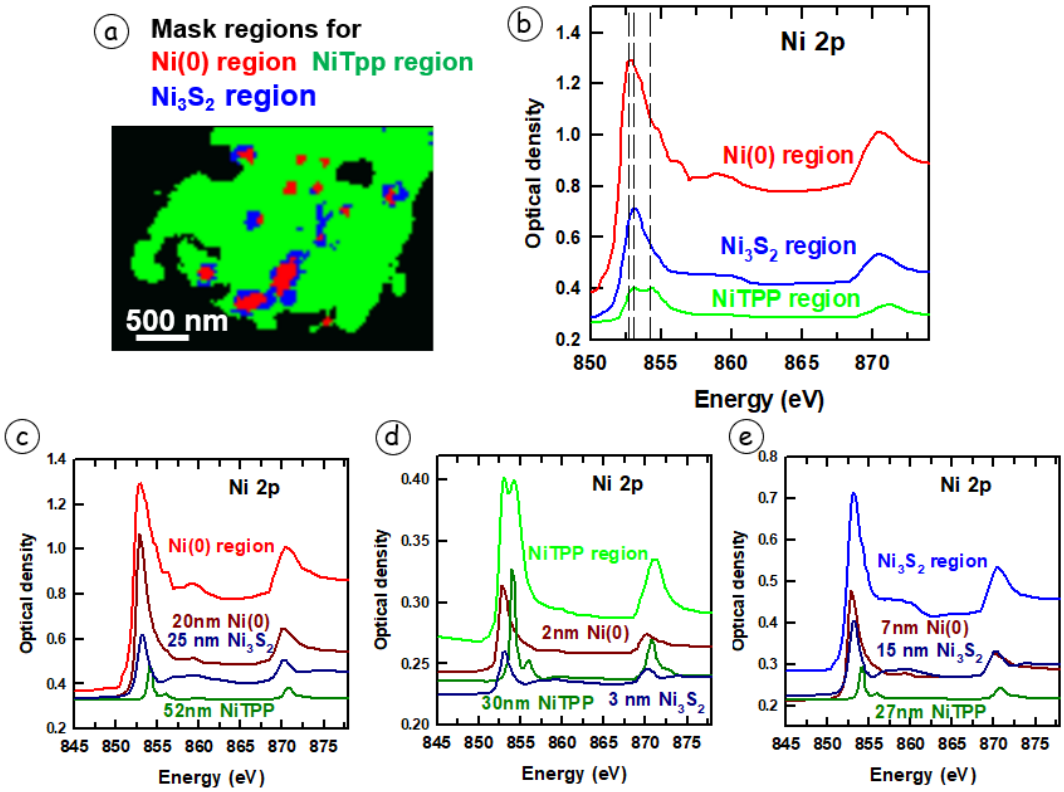

Figure S9 Spectral domain representation of the 3 component (Ni(0), NiTPP, Ni_3S_2) SVD analysis of the Ni 2p stack of region **A2** of the Ni-C-N-high catalyst. **a)** Masked regions the Ni(0) (red), NiTPP (green) and Ni_3S_2 (blue) regions. **b**) the internal spectra for the regions of Ni(0), NiTPP, Ni_3S_2 **c**) curve fit of the Ni(0) regions. **d**) curve fit of the NiTPP regions. **e**) curve fit of the Ni_3S_2 regions.

Figure S9 presents verification of the analysis of the Ni 2p stack of region **A2** of the Ni-N-C sample, as a linear combination of Ni(0), Ni-TPP and Ni_3S_2 components . **Table S5** presents the numerical results.

Table S5 Results of SVD curve fit analysis of region A2 of the Ni-N-C sample

	Species (average thickness in nm)			
area	Ni(0)	Ni-TPP	Ni_3S_2	χ^2
Ni region	20	52	25	0.23
NiTPP region	2	30	3	0.03
N_3S_2 region	7	27	15	0.03

Section S7 O 1s and S 2p results for area A2 of the Ni-N-C-high sample.

Figure S10 present the O 1s and S 2p results for area **A2** of the Ni-N-C-high sample.

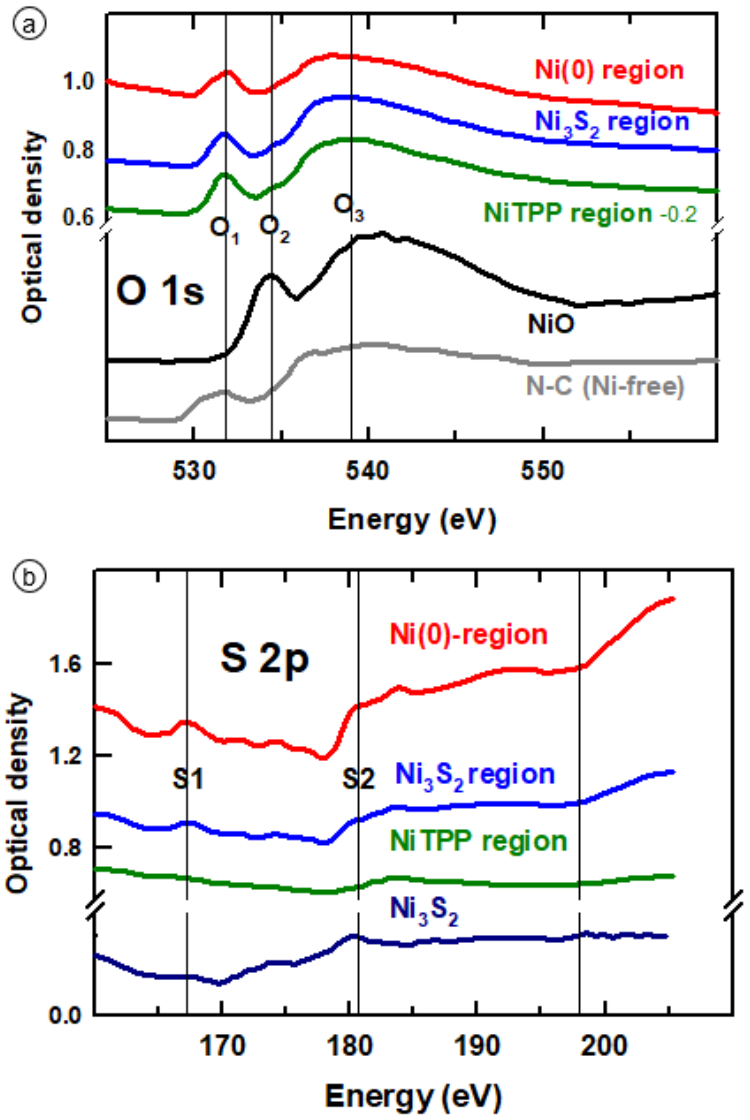

Figure S10 O 1s and S 2p results for area **A2** of the Ni-N-C-high sample. **a)** O 1s spectra of Ni(0) dominant, NiTPP dominant and Ni_3S_2 dominant areas from the O 1s stack of the **A2** region compared to the reference spectra of Ni(0), NiTPP and Ni_3S_2. **b)** S 2p spectra of Ni(0) dominant, NiTPP dominant and Ni_3S_2 dominant areas from the S 2p stack of the **A2** region

Section S8 Analysis of Ni 2p stack of region B1 of the Ni-N-C-low sample

Figure S11 presents the results of an SVD analysis of Ni 2p stack of region **B1** of the Ni-N-C-low sample.

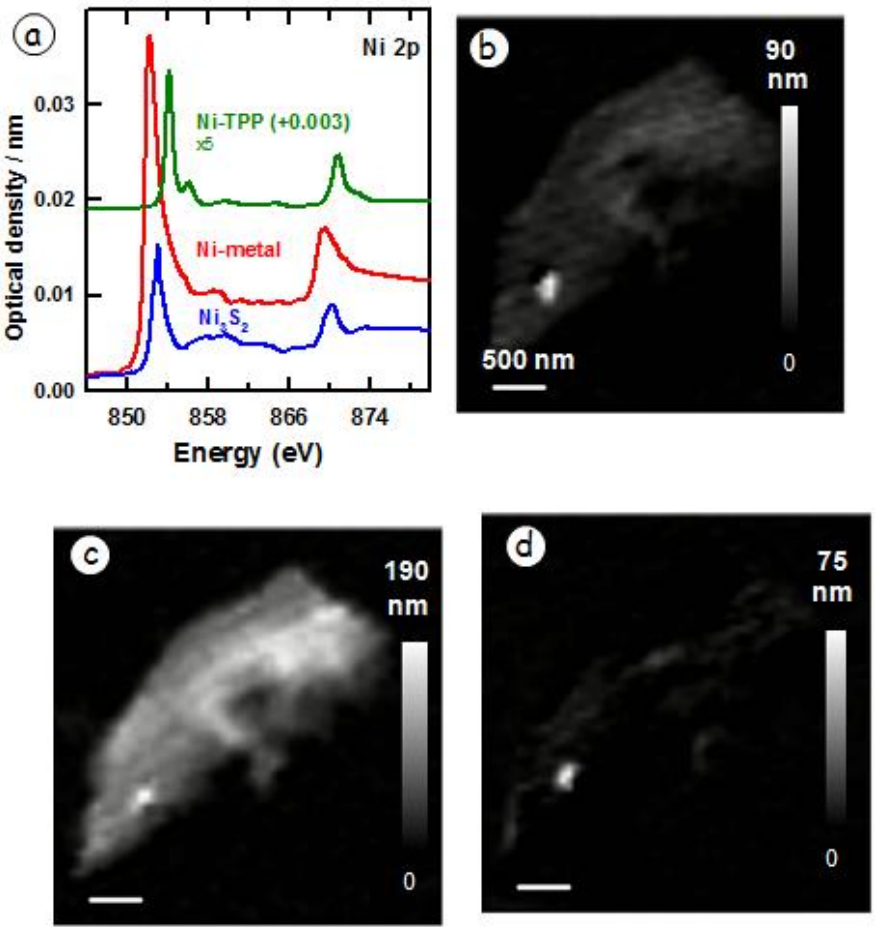

Figure S11 SVD analysis of Ni 2p stack of region **B1** of Ni-N-C low. (**a**) OD1 spectra of Ni metal, Ni-TPP* and Ni_3S_2 used to fit the stack. The NiTPP reference spectrum is the OD1 spectrum of Ni-TPP with an additional 0.003 added, to account for the fraction of the matrix region which has C-N-O signal but not Ni 2p signal. **b)** component map of the Ni metal. **c)** component map of the NiTPP. **d)** component map of Ni_3S_2. **e)** Residual of fit. See **Fig. 6b** for the color coded composite

Figure S12 presents a spectral domain check on the SVD analysis of the Ni 2p stack of region **B1** of Ni-N-C low.

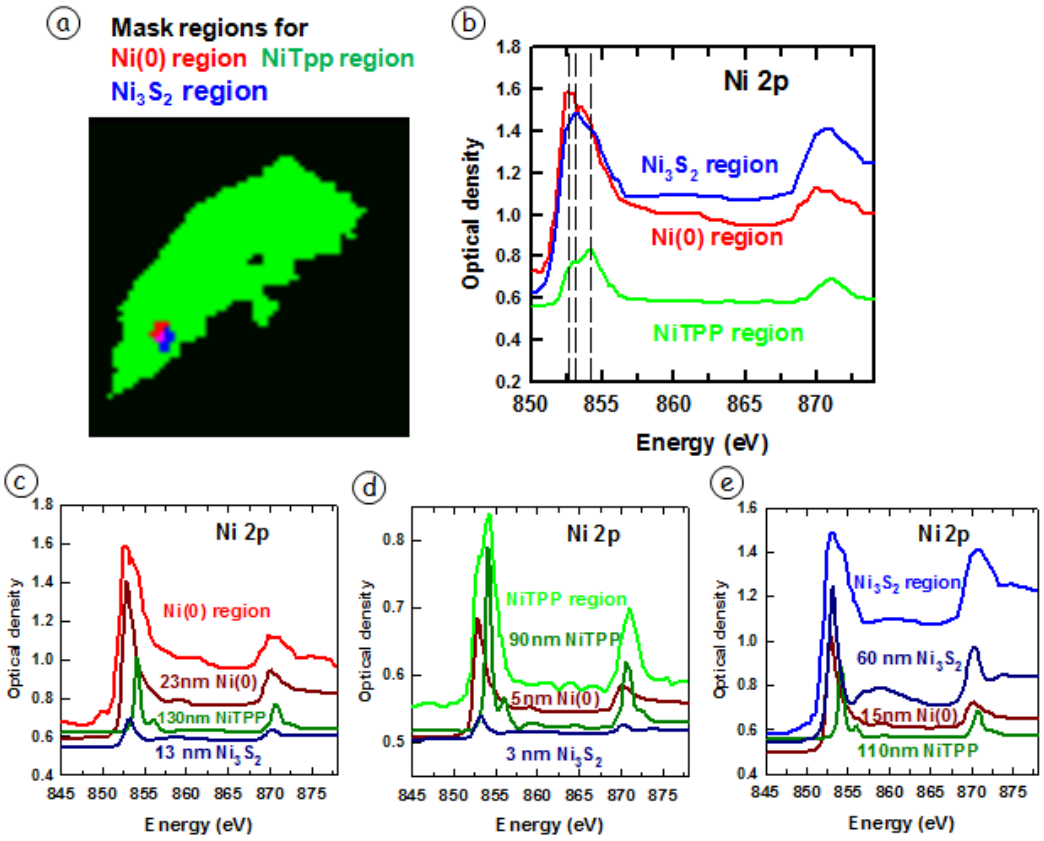

Fig. S12 Spectral domain representation of the 3 component (Ni(0), NiTPP, Ni_3S_2) SVD analysis of the Ni 2p stack of region **B1** of the Ni-C-N-low catalyst. **a)** Masked regions the Ni(0) region (red), NiTPP region (green) and Ni_3S_2 region (blue). **b**) the internal spectra for the regions of Ni(0), NiTPP, Ni_3S_2 **c**) SVD curve fit of the Ni(0) region. **d**) SVD curve fit of the NiTPP region. **e**) SVD curve fit of the Ni_3S_2 region.

Section S9 Analysis of all edges of region B1 of the Ni-low sample.

Figure S13 presents the combined Ni 2p, O 1s, C 1s and O 1s spectra data for the region **B1** of the Ni-C-N-low catalyst. Should be mentioned that some area in B1 was absorption saturation at the N 1s edge. The N 1s spectra shown in Fig.S22-c was adjusted according to N 1s spectra of the un-saturation area in B1 region.

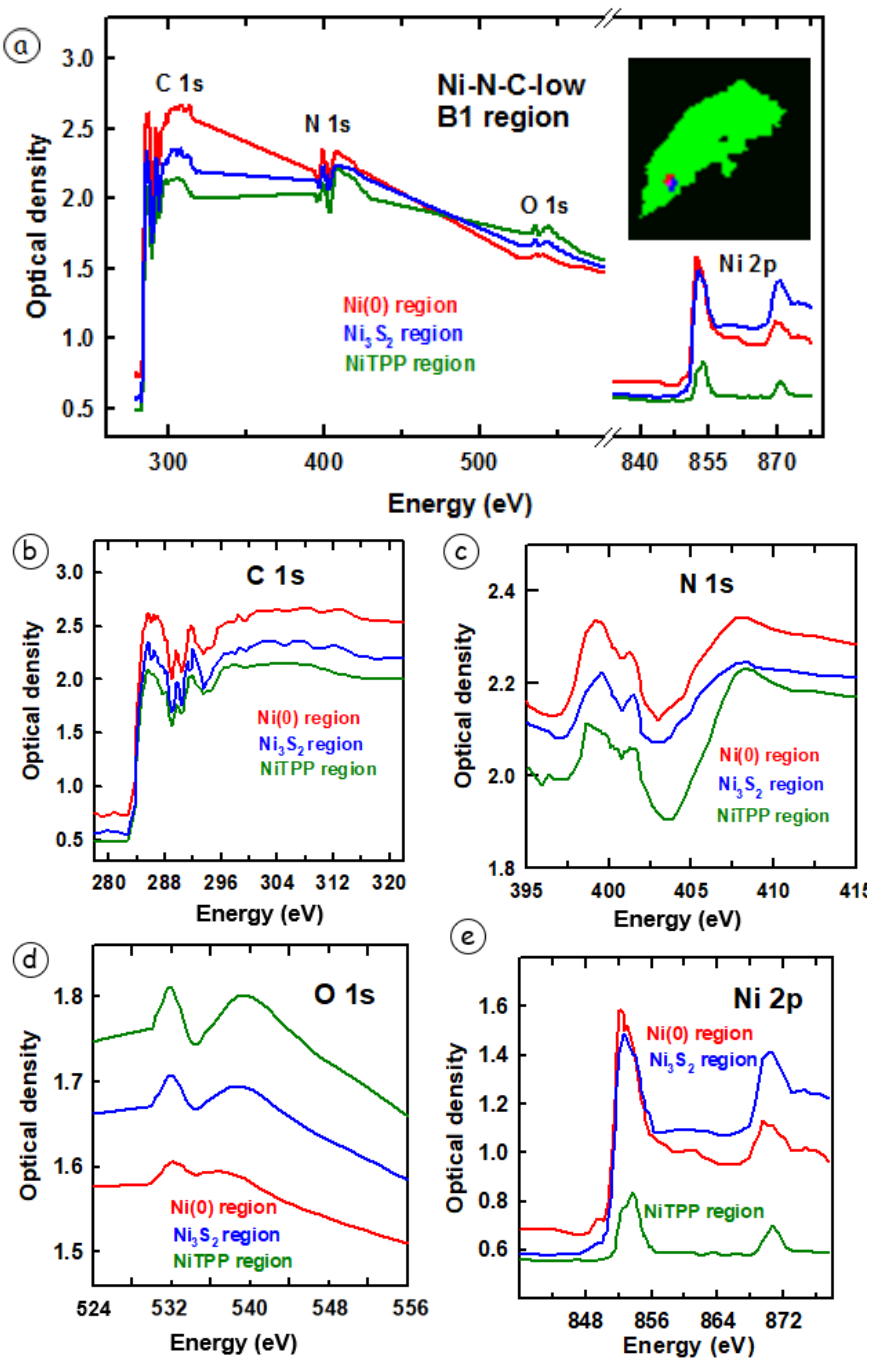

Fig. S13 a) the spectra for a) Ni 2p, N 1s, O 1s, C1s edge of extraction area for regions of Ni(0) (red), NiTPP (green) and Ni_3S_2 (blue). **Insert**: the color coded (rescaled) composite of extraction area for dominant Ni(0) (red), NiTPP (green) and Ni_3S_2 (blue) in region **B1**. The spectra of **b)** Ni 2p **c)** N 1s, **d)** C 1s, **e)** O 1s at the regions of Ni(0) (red), NiTPP (green) and Ni_3S_2 (blue).

Section S10 Analysis of other regions of the Ni-N-C high sample

Figure S14 presents a summary of the Ni 2p analysis of all the regions of Ni-N-C-high sample studied (**A1a-A5**) Mole fractions of Ni(0), NiTPP, Ni_3S_2 and amounts of carbon in 5 different particles of the Ni-N-C-high catalyst sample. Rescaled color coded composites of the component maps from analysis of Ni 2p stacks of each region are indicated.

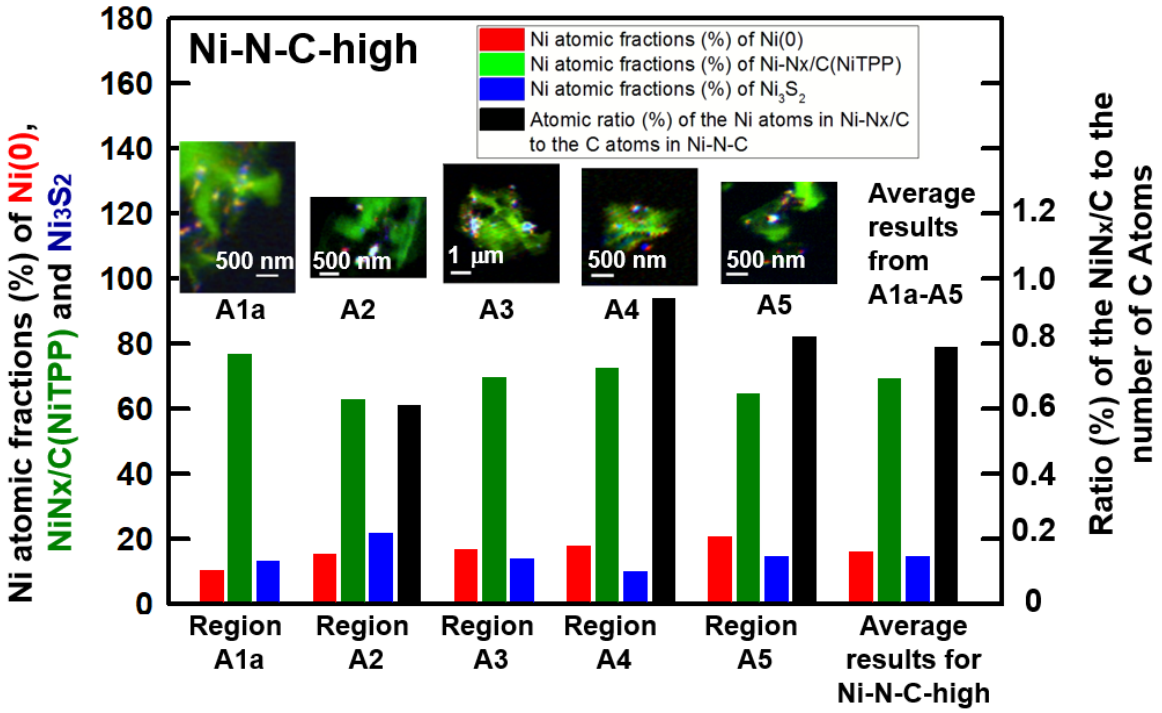

Fig. S14 Overview of analyses of regions **A1a, A2, A3, A4**, and **A5** of the Ni-N-C-high sample

S11 Analysis of other regions of the Ni-N-C-low sample

Figure S15 presents a summary of the Ni 2p analysis of all the regions of Ni-N-C-low sample **B1-B4**. **(b)** Mole fractions of Ni(0), NiTPP, Ni_3S_2 and amounts of carbon in 5 different particles of the Ni-N-C-low catalyst sample. Rescaled color coded composites of the component maps from analysis of Ni 2p stacks of each region are indicated.

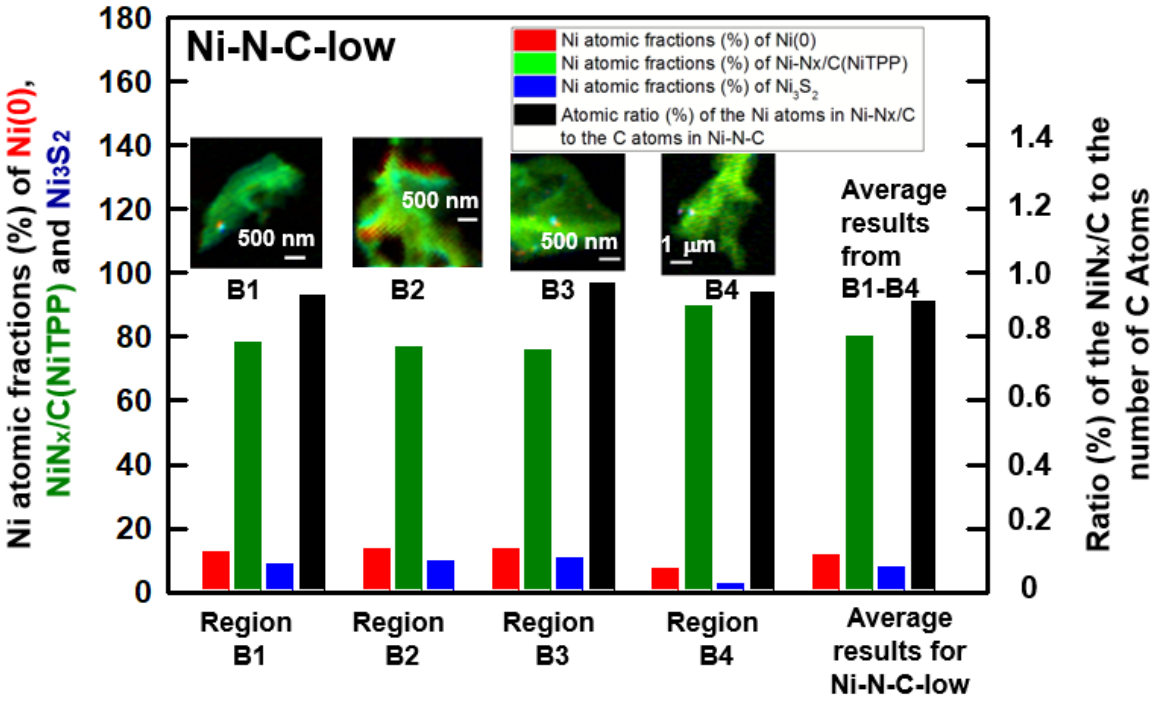

Fig. S15 Overview of analysis of regions **B1, B2, B3**, and **B4** of the Ni-N-C-low sample

S12 Quantitative results from STXM analysis of the Ni-high and Ni-low samples

Table S6 presents the results of the curve fit to the average Ni 2p spectra of regions **A1-A5** of the Ni-N-C-high sample and **B1-B4** of the Ni-N-C-low sample.

Table S6 Quantitative results from curve fits of the Ni(0), Ni_3S_2 and NiTPP reference spectra to the average Ni 2p spectra of regions **A1-A5** of the Ni-N-C-high sample and **B1-B4** of the Ni-N-C-low sample.

Sample	Sample region	Area of extraction (um2)	Calculation from the Ni 2p STXM stacks															Calculation from the C 1s STXM stacks			Atomic ratio of the Ni atoms in NiN_x/C to the C atoms in the Ni-N-C samples
			Volume of Ni species (um3)				Mass of Ni species (10^-15 g)				Mol of Ni atoms in each Ni species (10^-15 mol)				Ni atomic fractions in each Ni species			Volume of graphite carbon (um3)	Weight of graphite carbon (10^-15 g)	Mol of carbon atoms (10^-15 mol)	
			Ni(0)	NiTPP	Ni3S2	Total	Ni(0)	NiTPP	Ni3S2	Total	Ni(0)	NiNx/C (NiTPP)	Ni3S2	Total	Ni(0)	NiNx/C (NiTPP)	Ni3S2				
Ni-N-C-high	A1a	38.44	0.22	3.6	0.26	4.1	25.0	2256.0	44.4	2325.4	0.43	3.2	0.56	4.2	**10%**	**77%**	**13%**	-	-	-	**-**
	A2	18.49	0.072	0.63	0.091	0.80	8.10	396.4	15.6	420.10	0.14	0.56	0.20	0.90	**15%**	**63%**	**22%**	2.53	1118.4	93.2	**0.61%**
	A3	144	1.4	12.7	1.1	15.2	158	7947	181.2	8286.8	2.7	11.3	2.3	16.3	**16%**	**70%**	**14%**	-	-	-	**-**
	A4	1.21	0.005	0.046	0.0025	0.54	0.58	28.6	0.44	29.6	0.01	0.04	0.005	0.06	**18%**	**72%**	**10%**	0.12	52.2	4.4	**0.94%**
	A5	7.29	0.026	0.17	0.016	0.21	2.9	107.5	2.8	113.2	0.05	0.15	0.035	0.24	**21%**	**65%**	**14%**	0.51	224.8	18.7	**0.82%**
	Average Ni-N-C-high	-	-	-	-	-	-	-	-	-	-	-	-	-	**16%**	**69%**	**15%**	-	-	-	**0.79%**
Ni-N-C-low	B1	16.81	0.087	1.2	0.055	1.3	9.8	935.4	9.6	754.8	0.17	1.1	0.12	1.3	**12%**	**79%**	**9%**	3.0	1338.9	111.6	**0.93%**
	B2	53.29	0.25	3.0	0.15	3.4	27.5	1881.8	26.6	1936.0	0.47	2.7	0.33	3.5	**13%**	**77%**	**10%**	-	-	-	**-**
	B3	30.25	0.19	2.3	0.14	2.6	21.4	1442.5	23.5	1487.4	0.36	2.1	0.29	2.7	**13%**	**76%**	**11%**	5.7	2520.4	210.0	**0.97%**
	B4	169	0.42	10.9	0.14	11.4	47.5	6791.7	23.3	6862.5	0.81	9.7	0.29	10.8	**7%**	**90%**	**3%**	31.3	13847.1	1152.8	**0.84%**
	Average Ni-N-C-low	-	-	-	-	-	-	-	-	-	-	-	-	-	**12%**	**80%**	**8%**				**0.91%**

S13 Total electron yield (TEY) X-ray absorption spectroscopy (XAS) measurements

Figure S16 presents the results of total electron yield (TEY) X-ray absorption spectroscopy (XAS) measurements for the Ni-N-C-high, -N-C-low samples and other reference samples at the Ni 2p, N 1s and C 1s edges. In general, there is good agreement between the shapes of the TEY spectra and the OD spectra measured with STXM.

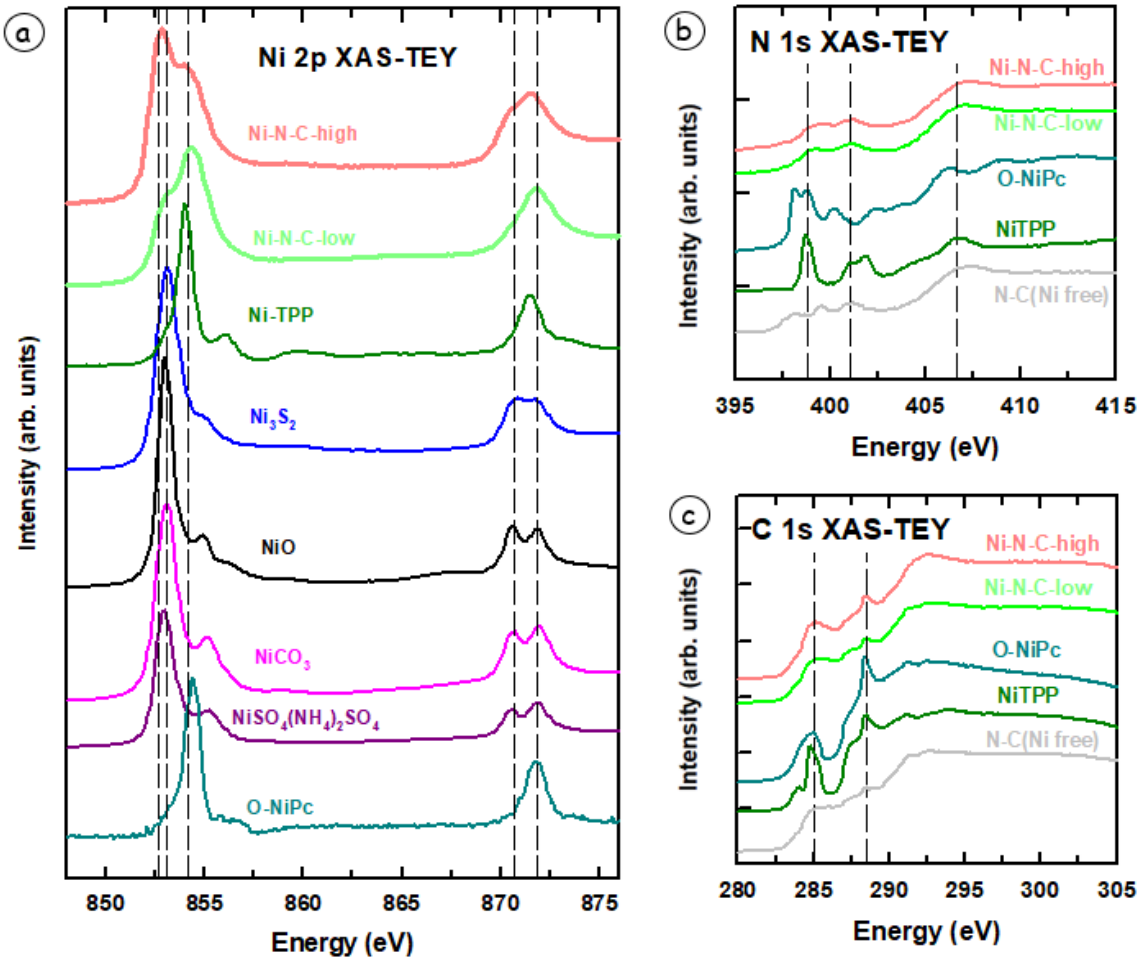

Fig. S16 Total electron yield (TEY) X-ray absorption spectroscopy (XAS) measurements for the Ni-N-C-high, -N-C-low samples and other reference samples at **a)** Ni 2p, **b)** N 1s and **c)** C 1s edge.

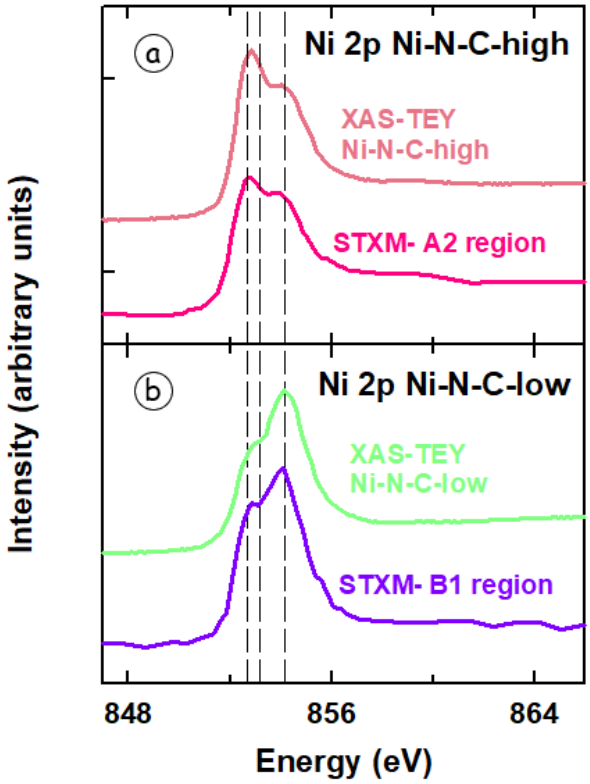

Fig. S17 Comparison for XAS and STXM results of Ni-N-C materials at Ni 2p edge. (a) Ni 2p XAS-TEY spectra of the Ni-N-C-high sample compared with the average STXM spectra of the Ni-N-C-high sample (**A2**). **(b)** Ni 2p XAS-TEY spectra of the Ni-N-C-low sample compared with the average STXM spectra of the Ni-N-C-low sample (**B1**). The dashed lines are the positions of the main $2p_{3/2} \rightarrow 3d$ peaks of Ni(0) at 852.7 eV, Ni3S2 at 853.1 eV, and NiN_x/C at 854.2eV. The intensities of each spectrum are scaled so the difference in signals ate 864 eV and 848 are the same for each data set. Offsets are used for clarity.

Figure S17 compares the XAS-TEY and STXM Ni 2p spectra of the Ni-N-C materials. There is good agreement between the shapes of the XAS-TEY spectra and the OD spectra measured with STXM.

Table S7 present the numerical results from a compositional analysis of the XAS-TEY spectra of the Ni-N-C-high and Ni-N-C-low samples. The reference spectra used for the fitting were those presented in **Fig. 4b**.

	Ni species (fraction of total signal)		
sample	Ni(0)	NiTPP	Ni_3S_2
Ni-N-C-high	27%	54%	19%
Ni-N-C-low	9	78%	13%

Table S7 Results of SVD curve fit analysis of XAS-TEY of the Ni-N-C samples

Figure S18 presents a group bar chart representing the quantitative distribution of different Ni-sites of the Ni-N-C-high and Ni-N-C-low sample calculated from XAS-TEY results.

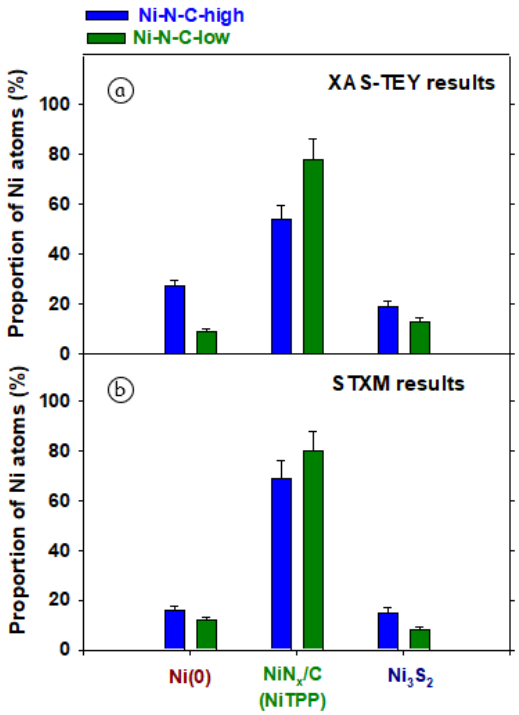

Fig. S18 Group bar chart representing the quantitative distribution of different Ni-sites of the Ni-N-C-high and Ni-N-C-low sample from (a) XAS-TEY results and (b) STXM results. Represents the total proportion of Ni atoms (out of all the Ni atoms in the sample) present in the configuration shown on the x-axis for both catalysts investigated.

S14 Ptychography image of area A2 of the Ni-N-C-high sample

Figure S19a presents the ptychography amplitude image of area **A2** of the Ni-N-C-high sample at 852.7 eV, while **Fig. S19b** is an estimation of a spatial resolution of 10 nm (half pitch) from a Fourier ring correlation (FRC) analysis.

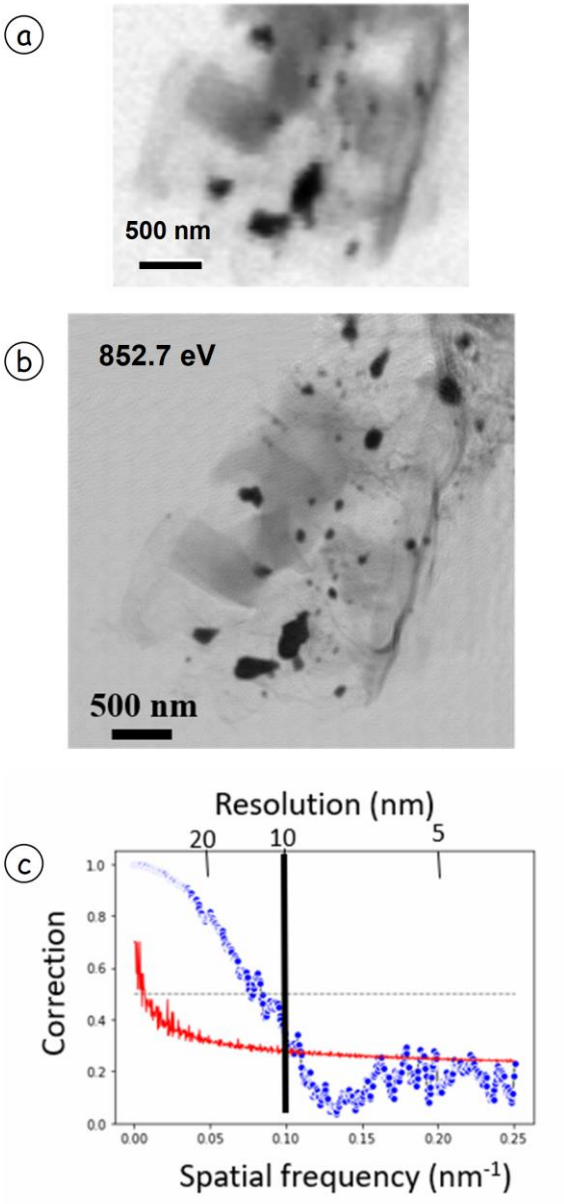

Figure S19 a) STXM images of region **A2** of the Ni-n-C high sample. **b)** Ptychography amplitude image of the Ni-N-C-high at A2 at 852.7 eV **c)** spatial resolution estimated from a Fourier ring correlation (FRC) analysis.

S15 Comparison of advantages and limitations of STEM/EELS, STXM, XAS

Table S8 present the comparison of advantages and limitations of STEM/EELS, STXM, XAS

	Spatial resolution	Energy resolution	Advantages	Limitations
STEM/EELS (Scanning transmission electron microscopy with electron energy loss spectroscopy)	Atomic resolution	Typically ~1 eV	Very high spatial resolution	Spatially localized measurements. Low energy resolution.
STXM (Scanning transmission X-ray microscopy)	Sub-40 nm	~0.1 eV	High energy resolution with spatial resolution. Quantitative analysis.	Relatively low spatial resolution.
XAS (X-ray absorption spectroscopy)	None	~0.1 eV	High energy resolution. Bulk ensemble. Quantitative analysis.	No spatial resolution.

References

1. Lu, M. et al. Unexpected phase separation in Li_{1-x} $Ni_{0.5}$ $Mn_{1.5}$ O_4 within a porous composite electrode. *Chemical Communications* **54**, 4152-4155 (2018).
2. Zheng, X. et al. Theory-driven design of high-valence metal sites for water oxidation confirmed using in situ soft X-ray absorption. *Nature chemistry* **10**, 149-154 (2018).
3. Lenser, C. et al. Charge transfer across oxide interfaces probed by in situ X-ray photoelectron and absorption spectroscopy techniques. *The Journal of Physical Chemistry C* **122,** 4841-4848 (2018).
4. Huang, W. et al. Application of Synchrotron Radiation Technologies to Electrode Materials for Li-and Na-Ion Batteries. *Advanced Energy Materials* **7**, 1700460 (2017).
5. Zhong, J. et al. Probing solid state N-doping in graphene by X-ray absorption near-edge structure spectroscopy. *Carbon* **50**, 335-338 (2012).
6. Liang, X. et al. Hydrothermal synthesis of highly nitrogen-doped few-layer graphene via solid–gas reaction. *Materials Research Bulletin* **61**, 252-258 (2015).
7. Regan, T. J. et al. Chemical effects at metal/oxide interfaces studied by x-ray-absorption spectroscopy. *Physical Review B* **64**, 214422 (2001).
8. Senkovskiy, B. V. et al. Electronic structure of Ti–Ni alloys: An XPS and NEXAFS study. *Journal of alloys and compounds* **537**, 190-196 (2012).
9. Furlan, A. et al. Crystallization characteristics and chemical bonding properties of nickel carbide thin film nanocomposites. *Journal of Physics: Condensed Matter* **26**, 415501 (2014).
10. Krasnikov, S. A. et al. An X-ray absorption and photoemission study of the electronic structure of Ni porphyrins and Ni N-confused porphyrin. *Journal of Physics: Condensed Matter* **20**, 235207 (2008).
11. Hitchcock, A. P. et al. Neon K-shell excitation studied by electron energy-loss spectroscopy. *Journal of Physics B* **13**, 3269 (1980).
12. Sodhi, RNS. et al. Reference energies for inner shell electron energy-loss spectroscopy. *Journal of electron spectroscopy and related phenomena* **34**, 363-372 (1984).
13. Ma, Y. et al. High-resolution K-shell photoabsorption measurements of simple molecules. *Physical Review A* **44**, 1848 (1991).
14. Hitchcock, A. P. et al. Carbon K-shell excitation spectra of linear and branched alkanes. *Journal of Electron Spectroscopy and Related Phenomena* **42**, 11-26 (1987).
15. Chen, C.T. et al. K-shell photoabsorption of the N2 molecule. *Physical Review A* **40**, 6737 (1989).
16. Hitchcock, A. P. et al. Soft X-Ray Imaging and Spectromicroscopy. In *Handbook of Nanoscopy*. **2**, Weinheim, Germany, 745–791 (2012). https://doi.org/10.1002/9783527641864.ch22
17. https://henke.lbl.gov/optical_constants/
18. https://www.britannica.com/science/nickel-chemical-element
19. Issa, S. et al. The evolution of gamma-rays sensing properties of pure and doped phthalocyanine. *Progress in Nuclear Energy* **100**, 276-282 (2017).
20. https://www.americanelements.com/nickel-sulfide-12035-72-2

Appendix E

This appendix shows the Supporting Information for Chapter 7.

Supporting Information for

In-situ Studies of Copper-based CO_2 Reduction Electrocatalysts by Scanning Transmission Soft X-ray Microscopy

Chunyang Zhang,[1,2] Haytham Eraky,[2] Shunquan Tan,[1] Adam Hitchcock[2] and Drew Higgins[1*]

1. Chemical Engineering, McMaster University, Hamilton, ON, Canada, L8S 4M1

2. Chemistry & Chemical Biology, McMaster University, Hamilton, ON, Canada, L8S 4M1

Table of Contents

Section S-1 Comparison of *in-situ* and reactor CV: calibration of V_{Au} versus V_{RHE}

Fig. S-1a,b displays the cyclic voltammetry (CV) in CO_2 saturated 0.1M $KHCO_3$ in a 2-compartment electrolyte membrane separated cell. The working electrode is Cu particles electro-deposited on a Au-coated graphite foil prepared by physical vapor deposition. The details for the preparation of Cu electrode are provided in **section 6.1.** A Pt foil was used as the counter electrode. A Ag/AgCl electrode was used as the reference electrode. The Ag/AgCl reference electrode was calibrated versus a home-made reversible hydrogen electrode (RHE), and the potentials are reported versus RHE. The catholyte and anolyte chambers were separated by an ion exchange membrane (Selemion AMV, AGC Inc). The potential range is +0.1 to +0.8 V_{RHE} and scan rate is 20 mV/s.

Fig. S-1c,d displays the CV in CO_2 saturated 0.1M $KHCO_3$ in a 3-electrode (beaker) cell. The working electrode (WE) is the electrodeposited Cu on the Au foil. The method for preparing the Cu electrode is the same Cu electrodeposition on the Au-coating graphite foil, shown in **section 6.1**. A Pt foil was used as the counter electrode (CE) and a Ag/AgCl electrode was used as the reference electrode (RE). The potential range is +0.25 to +0.7 V_{RHE} and scan rate is 20 mV/s.

Fig. S-1e,f displays the CV in CO_2 saturated 0.1M $KHCO_3$ in an *in-situ* cell. The working electrode is the electrodeposited Cu on the micro-working electrode of the *in-situ* cell. Details for the preparation of Cu electrode are in **section 6.4.** Au micro-electrodes are used as the counter electrode and the reference electrode. The potential range is -0.4 to +0.2 V_{Au} and scan rate is 20 mV/s. The CV measured under *in-situ* conditions **(Fig. S1f)** was stopped at +0.2 V_{RH} , resulting in a narrow anodic peak compared to the other two CV curves, in order to avoid oxidizing the Cu particles all the way to Cu(II) ions which readily dissolve into the electrolyte. The current density was estimated by dividing the measured current by the estimated electrode area of 2200 μm^2 (the geometrical area of the Au working electrode including all of the round region and a rectangle region at the top of the WE). [S1] [**Figure S-2].** All other areas of the working electrode are coated with an insulating layer. [S1] Compared to the current densities measured by CV in a beaker cell and in the 2-compartment membrane cell, the *in-situ* CV current density is ~4 times larger. This could be due to the actual surface area being larger than the estimated area. It may also reflect additional active surface area at the sides or interior of the particles.

Fig. S-1g displays the potential (V_{Au}) versus time (s) under the *in-situ* condition when no potential is applied, which is the open circuit potential (OCP) between the working electrode and reference electrode. The OCP was -48 $mV_{Au} \pm 4$ mV_{Au}. This shows that the Au pseudo reference electrode under *in-situ* conditions provides a stable potential reference.

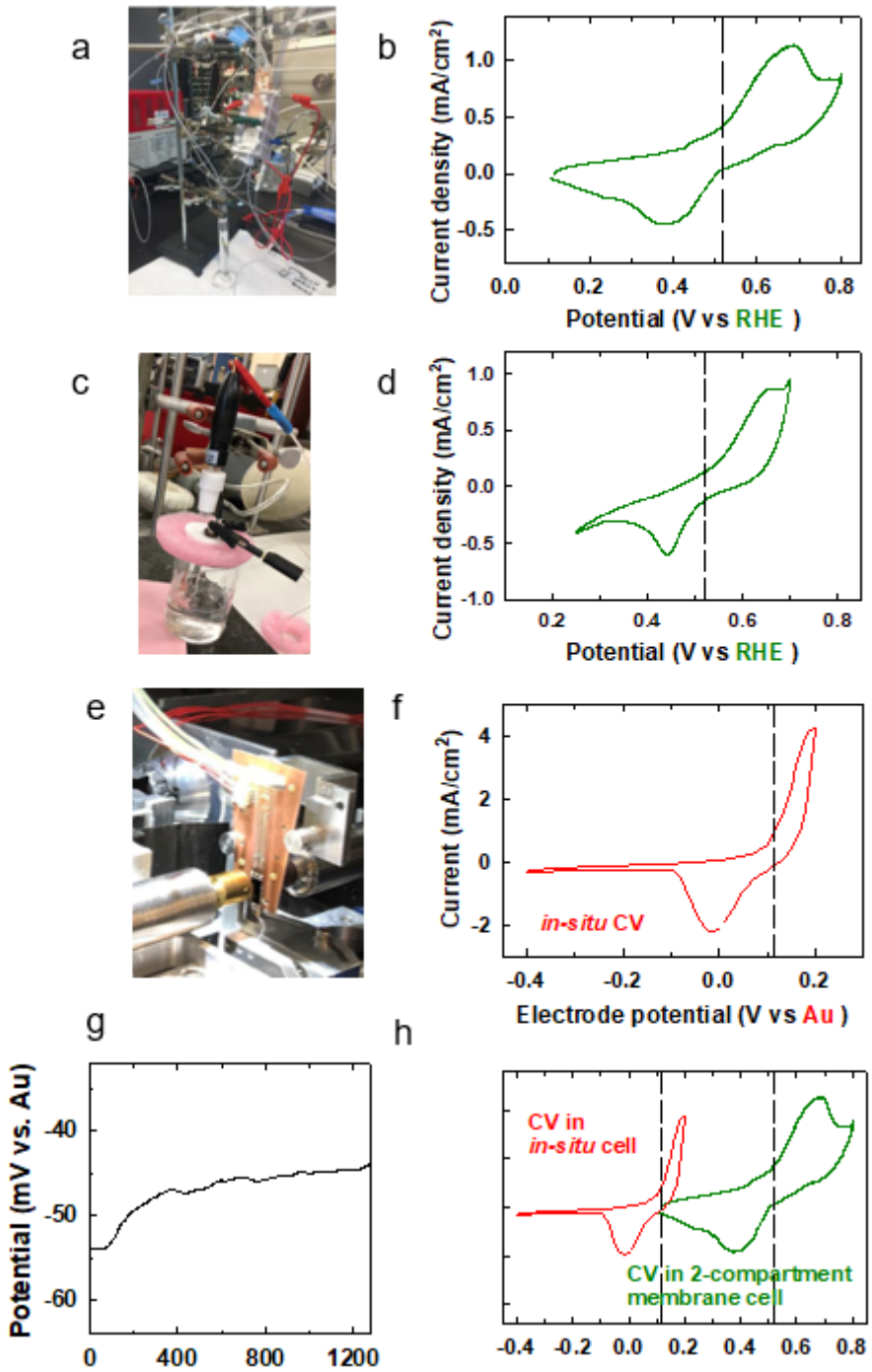

Figure S-1 CV of electrodeposited Cu in: a) photo of 2-compartment membrane cell. **b)** CV measured in 2-compartment cell. 20 mV/s scan rate. **c)** photo of 3-electrode (beaker) cell. **d)** CV in beaker cell. **e)** photo of *in-situ* cell. **f)** CV measured in *in-situ* cell. **g)** potential (mV_{Au}) vs time (s) under *in-situ* open circuit potential (OCP) conditions. **h)** CV used to derive the relationship of the potential relative to Au (V_{Au}) to that relative to the reversible hydrogen electrode (V_{RHE}) in CO_2 saturated 0.1M $KHCO_3$.

Due to the use of a Au pseudo reference in the *in-situ* STXM experiments, the potentials vs Au were converted to the RHE scale for convenience in comparing to literature. In order to relate the two reference scales, the CV with potentials vs RHE (**Fig. S-1b**) can be compared with the *in-situ* CV potentials vs Au (**Fig. S-1d**) to relate the two scales. (**Fig. S-1h**) This results in a conversion equation in this work:

$$\mathbf{E_{(RHE)} = E_{Au} - 0.40\ V} \qquad \text{(Eqn. S1)}$$

The accuracy and reproducibility of Au pseudo reference electrode was checked multiple times by comparing CV curves for Cu redox in CO_2 saturated 0.1 M $KHCO_3$ or $NaHCO_3$. The difference between the Au pseudo reference electrode and RHE observed via CVs was -0.43 ± 0.07 V. In addition, we have checked this result by measuring Au and RHE reference CVs for 0.1 M Fe(II) / Fe(III) cyanides solutions, which showed a shift of 0.5 ± 0.1 V.

All potentials shown in the manuscript and Supporting Information (SI) are converted to RHE using Eqn. S1, unless stated otherwise.

Section S-2 The electrolyte filling process under optical microscopy

Figure S-2 displays the process of filling the electrochemical cell used for *in-situ* STXM measurements with the electrolyte, as observed by optical microscopy.

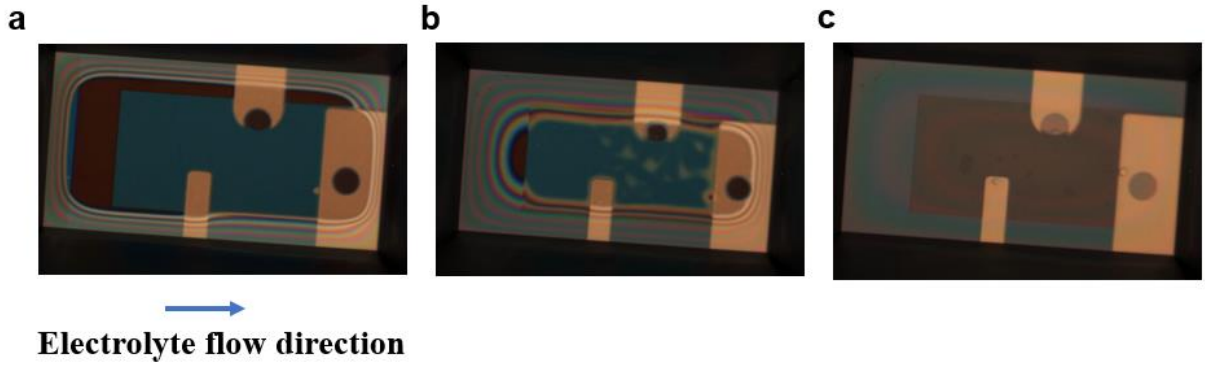

Figure S-2 Filling the *in-situ* cell with a solution of 5mM $CuSO_4$ and 5mM KCl under an optical microscope. **(a), (b), (c)** are reflection images ~5 minute (m) apart (magnification 20x).The direction for the electrolyte flow is shown as the arrow in **(a)**

Section S-3 Details of *in-situ* electrodeposition of Cu particles

Figure S.3 displays details of the *in-situ* deposition of Cu particles on the Au working electrode (WE) in the *in-situ* cell. **Fig. S-3a** shows the 3 cycle cyclic voltammetry curves for Cu deposition. The STXM

images before and after the Cu deposition on Au working electrode are shown in **Fig. S-3b** and **Fig. S-3c.**

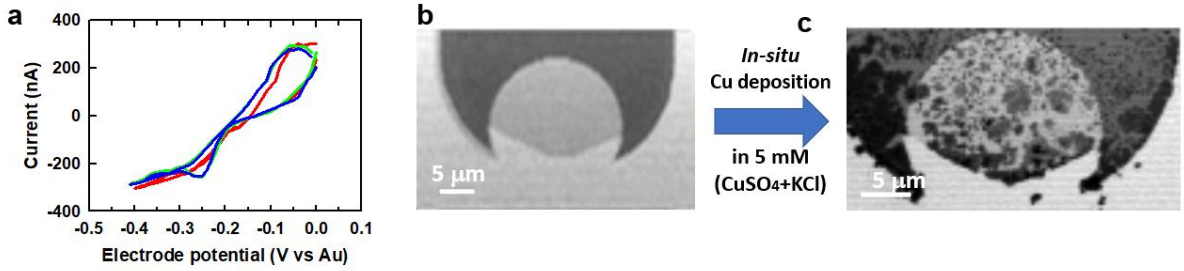

Figure S-3 ***in-situ*** **electrodeposition of Cu particles from a 5 mM $CuSO_4$, 5 mM KCl solution**. **(a)** Cyclic voltammetry (3 cycles) **(b)** STXM images at 960 eV before the Cu deposition **(c)** STXM images at 933.5 eV after the deposition of Cu particles. The horizontal bands in the STXM images (**Fig. S-3b, S-3**c) are an artifact arising from slow (period ~1 s) oscillations of the incident X-ray intensity due to shifts in the position of the electron beam in the CLS ring, which sometimes occur.

Section S-4 Chronoamperometry (CA) current-time plots at indicated potentials.

Figure S-4 plots the currents measured as a function of time during the chronoamperometry scans at increasingly negative potentials. There is a current transient at the beginning of each scan which is associated with the transition from the 30 second open circuit hold prior to each measurement.

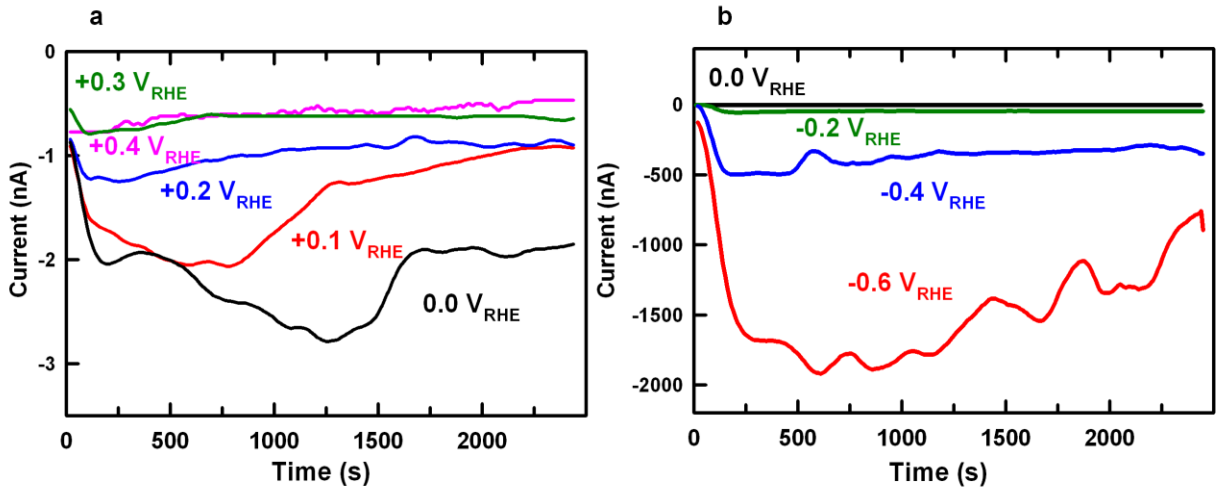

Figure S-4 Current vs time curve at each potential. (a) +0.4 to 0 V_{RHE}. **(b)** -0.2 to -0.6 V_{RHE} . Note the change in the current scale between (a) and (b).

Section S-5 Calculating the electrolyte thickness.

Figure S-5 shows how the electrolyte thickness is calculated. The positions for measuring the X-ray signal through the cell (electrolyte and SiNx windows) and through an empty hole in the *in-situ* device are shown in **Fig. S-5a** and **Fig. S-5b**. **Fig. S-5c** compares the X-ray signal of the incident X-ray with that from the SiNx windows. **Fig. S-5d** plots the OD spectrum of the electrolyte, indicating the contributions from150 nm of SiNx windows and ~1.6 μm of the electrolyte, which is dominated by the absorbance by water.

Section S-6 Details of STXM measurements and analysis

Figure S-6 displays the details for the comparison between the full energy spectra and 4-energy spectra. The comparison of full (53 energy) spectra vs 4-energy spectra for Cu(0) (**Fig. S-6a**) and Cu(I) (**Fig. S-6b**) shows that the 4-energy spectra provides the same chemical information as full energy spectra. Therefore, 4-E stack was used to obtain the same information as a full energy stack to save time.

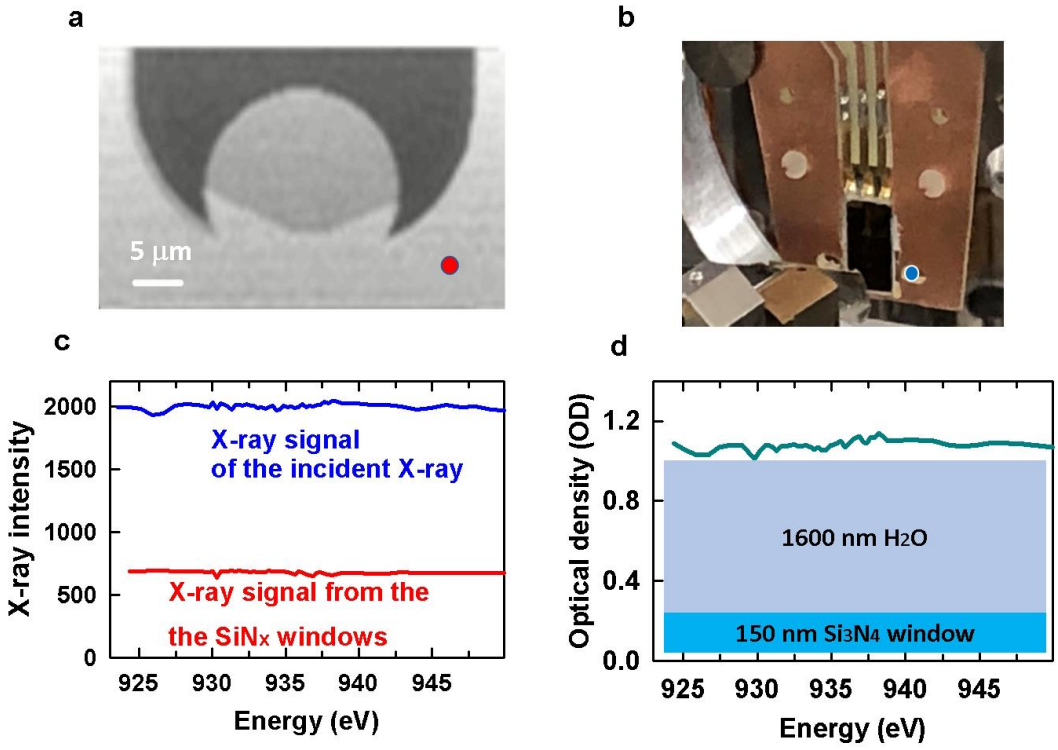

Figure S-5 Estimating the thickness of the electrolyte layer. (a) STXM transmission image at 960 eV. The red dot indicates where the electrolyte spectrum was measured. **(b)** Photo of the in situ cell in the STXM. The blue dot indicates the hole through the *in-situ* device where the incident flux was measured. **(c)** comparison between the X-ray signal of the incident X-ray beam (blue) and that from the X-ray beam passing through the electrolyte region of the cell (red), which includes 150 nm of SiNx windows. **(d)** The OD spectrum of the electrolyte and the windows. The OD signal from 1600 nm of water and 150 nm of SiNx are indicated, consistent with an electrolyte thickness of ~1.6 μm.

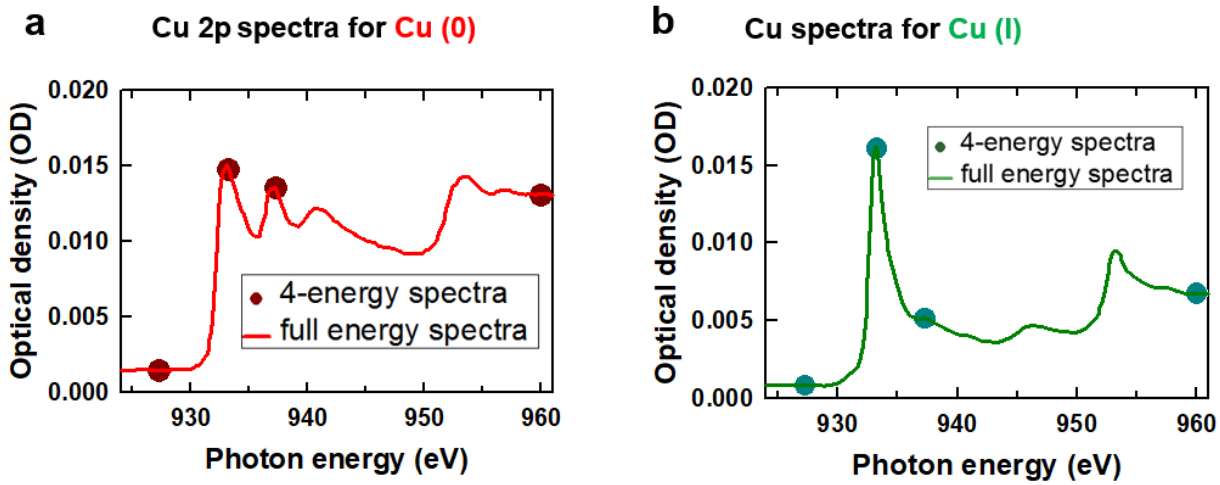

Figure S-6 Full energy spectra vs 4-energy spectra for **(a)** Cu(0), and **(b)** Cu(I)

Table S.1 Summary of main STXM measurements reported in this paper. A dwell of 3 ms/pixel and a flow rate of 25 μL/h was used for all measurements.

Sample/Region	Fig #	Type	File	Size (μm)	Size (pixels)	Energy (eV)	#E	V_{RHE}
SiN_x window	Fig. S-5	Point scan	A210919005	0.04	1	924-950	50	OCP
Empty hole on device	Fig. S-5	Point scan	A210919008	0.04	1	920-965	53	OCP
Whole WE (before Cu deposition)	Fig. S-3	image	A210919020	40 x 30	80*60	960	1	OCP
Whole WE (after Cu deposition)	Fig. S-3, Fig. 3a	image	A210919059	30 x 15	120*60	960	1	OCP
Region for particle	Fig. 3a	image	A210915066	2.9 x 3.7	87*110	933.5	1	OCP
Region for particle	Fig. 3b, 3c	4-E stack	A210915065	2.9 x 3.7	87*110	920-960	4	OCP
Region for particle	Fig. 5	image	A210915067	2.8 x 3.6	84*96	933.5	1	+0.4
Region for particle	Fig. 5	4-E stack	A210915068	2.8 x 3.6	56*72	920-960	4	+0.4
-	Fig. 5	Full stack	A210915069	2.8 x 3.6	56*72	920-965	53	+0.4
-	Fig. 5	image	A210915070	2.8 x 3.6	56*72	933.5	1	+0.4
-	Fig. 5	4-E stack	A210915073	2.8 x 3.6	56*72	920-960	4	+0.3
-	Fig. 5	Full stack	A210915074	2.8 x 3.6	56*72	920-965	53	+0.3
-	Fig. 5	4-E stack	A210915078	2.8 x 3.6	56*72	920-960	4	+0.2
-	Fig. 5	Full stack	A210915079	2.8 x 3.6	56*72	920-965	53	+0.2
-	Fig. 5	4-E stack	A210915082	2.8 x 3.6	56*72	920-960	4	+0.1
-	Fig. 5	Full stack	A210915083	2.8 x 3.6	56*72	920-965	53	+0.1
-	Fig. 5	4-E stack	A210915086	2.8 x 3.6	56*72	920-960	4	0
-	Fig. 5	Full stack	A210915087	2.8 x 3.6	56*72	920-965	53	0
-	Fig. S-9	4-E stack	A210915090	2.8 x 3.6	56*72	920-960	4	-0.2
-	Fig. S-9	Full stack	A210915091	2.8 x 3.6	56*72	920-965	53	-0.2
-	Fig. S-9	4-E stack	A210915094	2.8 x 3.6	56*72	920-960	4	-0.4
-	Fig. S-9	Full stack	A210915095	2.8 x 3.6	56*72	920-965	53	-0.4
-	Fig. 5	4-E stack	A210915098	2.8 x 3.6	56*72	920-960	4	-0.6
Region for particle	Fig. 5	Full stack	A210915099	2.8 x 3.6	56*72	5920-965	53	-0.6

Section S-7 STXM analysis of electrodeposited Cu particles

Figure S-7 displays the details for SVD fitting analysis of the 4-energy stack of deposited Cu particles. The component maps of Cu(0) (**Fig. S-7a**) and Cu(I) (**Fig. S-7b**) show the distribution of Cu(0) and Cu(I), with the gray scale bar showing the thickness. The residual map (**Fig. S-7c**) shows the residual signal (averaged over all energies) of the fit. The small and unstructured residual (maximum OD is 0.15, <10% of the total OD signal) indicates a high quality SVD fit. **Fig. S-7d** is the colour-coded composite map showing Cu(0) in red and Cu(I) in green. **Figure S-8** displays the spectra of Cu(0)-rich and Cu(I)-rich regions extracted from the 4-E stack. **Figure S-8a** shows the regions to collect the spectra, generated from **Fig. S-7d**. **Figure S-8b** and **Fig. S-8c** show the spectra of the Cu(0)-rich region and Cu(I)-rich region, compared to the Cu(0) and Cu(I) reference spectra.

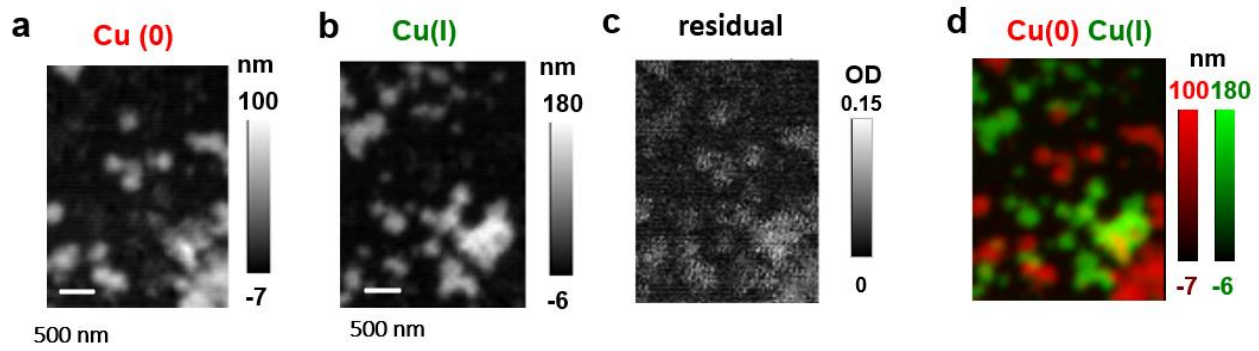

Figure S-7 Analysis of the 4-energy stack of deposited Cu particles. Component maps of (a) Cu(0), (**b**) Cu(I), (c) residual, and (d) colour-coded composite map.

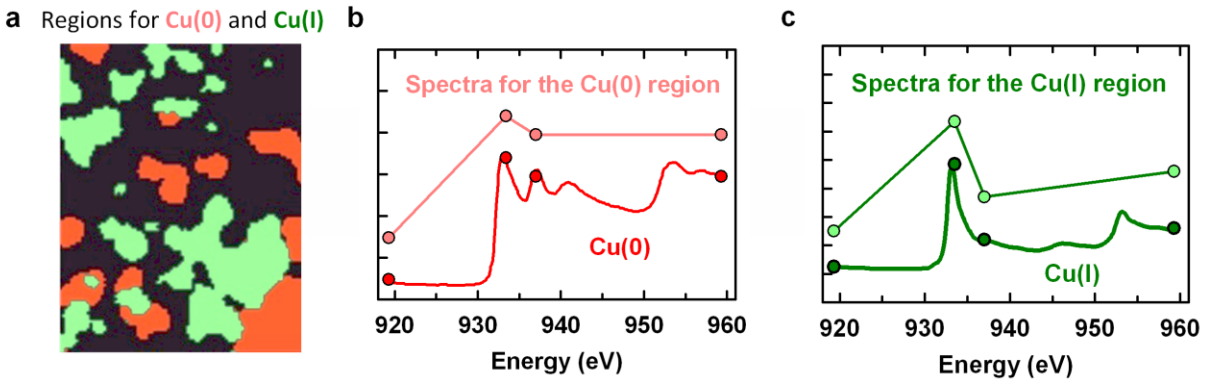

Figure S-8. Verification of the analysis of 4-energy stack of deposited Cu particles. (a) Regions for the Cu(I) and Cu(0) areas derived by component maps **(b)** extracted spectra from the Cu(0) region compared with Cu(0) reference spectra. **(c)** extracted spectra from the Cu(I) region compared with Cu(I) reference spectra.

Section S-8 STXM results at applied potentials from +0.4 to -0.6V_{RHE}

Figure S-9 displays the details for the various STXM results: 2 STXM images (image 1 and 2, 933.5 eV, ~ 3 mins for each), a fast 4-energy STXM stack (4-E: 920, 933.5, 937 and 960 eV, ~7 mins) and a complete Cu 2p STXM stack (full stack, 53 energies from 920 to 965 eV ,~30 min) at potentials from +0.4 to -0.6 V_{RHE}.

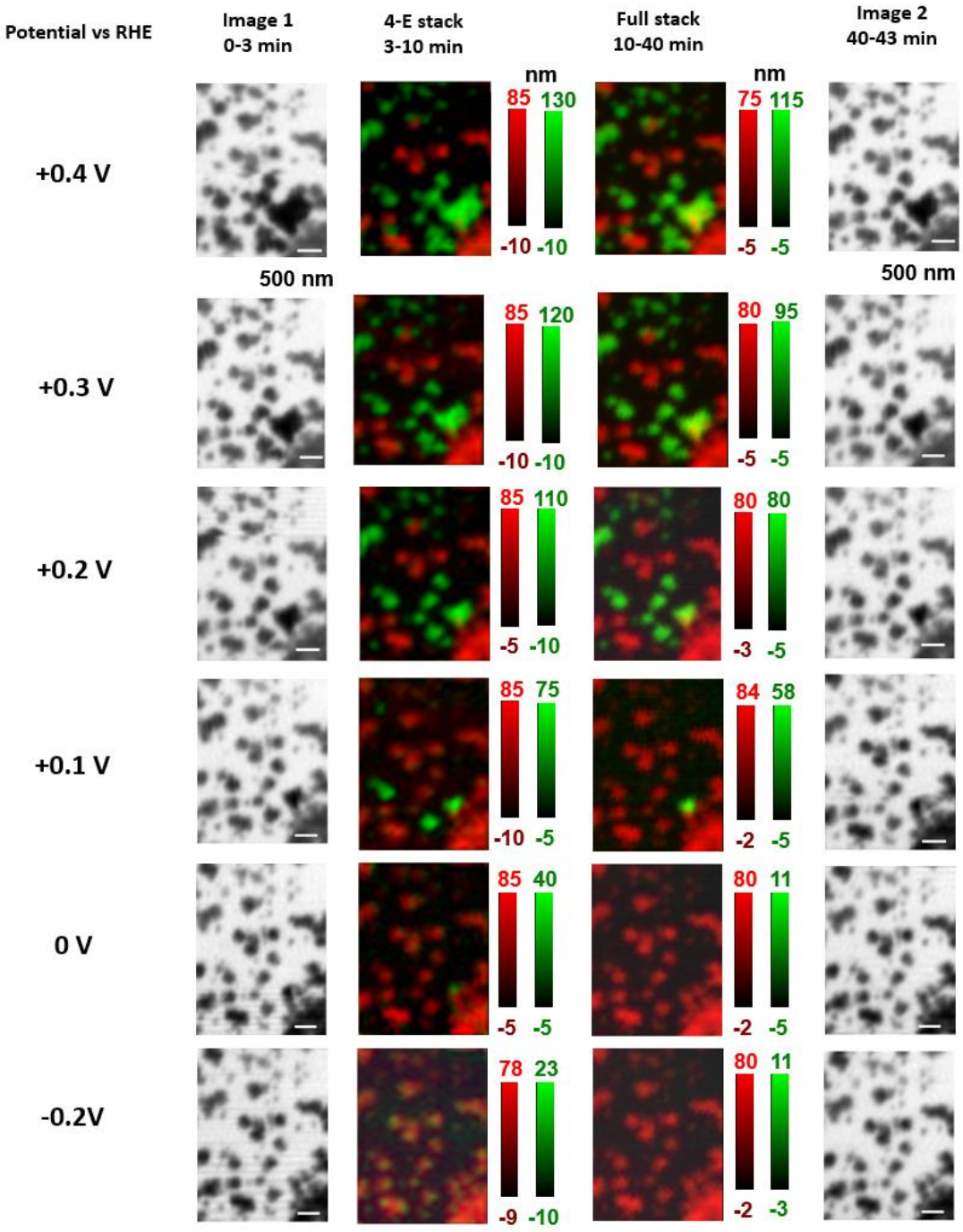

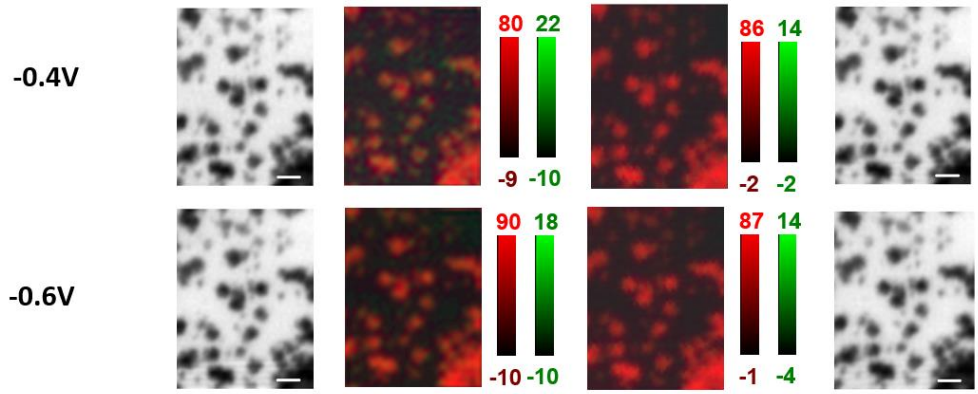

Figure S-9 Cu particle morphology and chemistry under various potentials. (Left 1) image 1 at 0-3 min under applied potentials. **(Left 2)** Color coded composites at the indicated potentials (vs RHE) derived from 4 energy stacks (3-10 min). **(Right 2)** Color coded composites at the indicated potentials (vs RHE) derived from 54 energy full stacks (10-40 min). **(Right 1)** image 1 at 40-43 min under applied potentials.

Section S-9 Sample calculation of volume of Cu(0) and Cu(I) at +0.4 V_{RHE}.

Figure S-10 displays the details for the calculation of the volume of Cu(0) and Cu(I) from the full stack at +0.4 V_{RHE} . First, the region to collect spectra (**Fig. S-10a**) was identified by threshold masking the component maps. Then the average spectra of Cu(0) region and Cu(I) region were extracted from the full stack at +0.4 V_{RHE} and shown in **Fig. S-10b**. The average spectra of Cu(0) and Cu(I) regions were analyzed using SVD curve-fitting to calculate the composition in terns of an average thickness; the results are shown **Fig. S-10c** and **Fig. S-10d**. These values were combined with the area of the Cu(0) and Cu(I) regions to determine a total volume, and volume ratio, of Cu(0) and Cu(I) as a function of the potential. The results for +0.4 V_{RHE} are summarized in **Table S.2**. A similar compositional analysis was carried out from the STXM results at all potentials, as further described in **section S-10**.

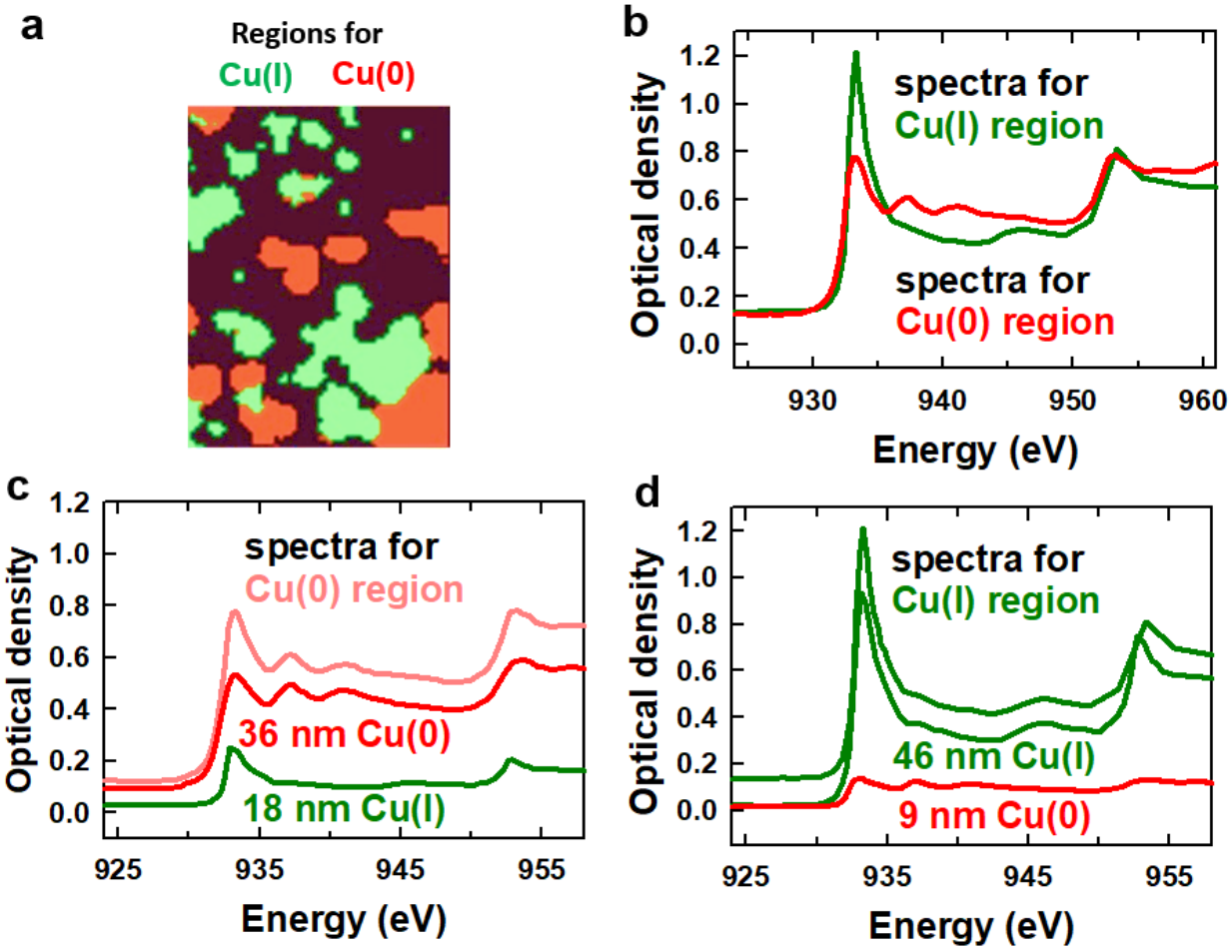

Figure S-10 Analysis of the STXM full stack of particles at +0.4 V_{RHE}. (a) regions for Cu(I) and Cu(II) from the component maps. **(b)** the average spectra of region Cu(0) and Cu(I). **(c)** Composition of average spectra from Cu(0) region using SVD curve-fitting. **(d)** Composition of average spectra from Cu(I) region using SVD curve-fitting.

Table S.2 Volume compositional analysis for the full stack at +0.4 V_{RHE}.

Regions	Area	Average thickness	Volume of **Cu(0)** (μm^3)	Volume of **Cu(I)** (μm^3)
Cu(0) region	2.1 μm^2	36 nm Cu(0) 18 nm Cu(I) Residual 0.035(OD)	$76*10^{-3}$	$38*10^{-3}$
Cu(I) region	2.3 μm^2	9 nm Cu(0) 46 nm Cu(I) Residual 0.053(OD)	$21*10^{-3}$	$106*10^{-3}$
			Cu(0)	**Cu(I)**
Total volume (μm^3)			$96*10^{-3}$	$144*10^{-3}$
Volume Ratio			**40%**	**60 %**

a. The uncertainty of ± 10 % is estimated from a combination of statistical and systematic uncertainties.

Section S-10 Volume composition of Cu(0) and Cu(I) at various potentials

First, Cu(I)-rich and Cu(0)-rich regions were identified by threshold masking the component maps from STXM full stack at +0.4 V_{RHE} shown in **Fig. 5**, as shown in **Fig. S-10a.** The average spectra of Cu(I)-rich and Cu(0)-rich regions from STXM full stack at +0.4 V_{RHE} were then extracted and compared in **Fig. S-10b**. The average thickness of Cu(I) and Cu(0) in each region was determined by SVD curve fitting the average spectra to the quantitative OD1 reference spectra (**Fig. 3b**), as shown in **Fig. S-10c** and **Fig. S-10d**. Subsequently the volumes of each Cu species were calculated from the average thickness and the geometric cross-sectional area of the catalyst regions. These results are summarized in **Table S-3**.

Table S.3 Volumes of Cu(0) and Cu(I) at various potentials.

Potentials (V_{RHE})	STXM measurements	Total volume of Cu(0) (10^{-3} *μm^3)	Total volume of Cu(I) (10^{-3} μm^3)	Volume Ratio of Cu(0)	Volume Ratio of Cu(I)
+0.4	4-E stack	112	150	43%	57%
	Full stack	96	144	40%	60%
+0.3	4-E stack	111	123	48%	52%
	Full stack	107	88	55%	45%
+0.2	4-E stack	102	67	60%	40%
	Full stack	106	44	71%	29%
+0.1	4-E stack	96	22	82%	18%
	Full stack	115	6	94%	6%
0	4-E stack	123	9	93%	7%
	Full stack	119	0.1	99.9%	0.1%
-0.2	Full stack	120	1	99.1%	0.9%
-0.4	Full stack	128	0.6	99.5%	0.5%
-0.6	Full stack	123	1.2	99.0%	1%

a. The uncertainty of ± 10 % is estimated from a combination of statistical and systematic uncertainties.

Section S-11 Evaluating radiation dose and possible radiation damage.

S-11.1 Evaluating radiation dose

Methods to evaluate the dose delivered in a STXM measurement have been reported elsewhere[S2 S3, S4] and have been used to estimate the dose delivered in the measurements reported in this work. Briefly, the dose delivered by STXM in units of MGy is given by [S2]

$$a(STXM) = \frac{I_0(1 - e^{-OD})Et}{\varepsilon V \rho} \times 1.60 \times 10^2 \qquad \text{(Eqn. S2)}$$

where I_0 is the incident flux (number of photons per second), E is the exposure energy in eV, t is the

exposure time in milliseconds (ms), ε is the detector efficiency (measured to be 80% at the Cu 2p edge)[S5], V is the volume of the exposed region, ρ is the sample density (g/cm^3), and OD is the optical density of the exposed region at the energy of irradiation. Based on eqn. S2 and the experimental parameters summarized in **Table S.4,** he dose for the 54E in-situ STXM full stacks is ~110 MGy. The average dose for 4E STXM stacks is ~10 MG.

Table S4 Estimating dose for *in-situ* full 54- E STXM stack

symbol	A210915069- mostly Cu(I)	A210915099- mostly Cu metal	comments
I_0	6 MHz	11 MHz	-
OD	0.55	0.45	OD average over energy range measured
E	933 eV	933 eV	
t	162 ms	162 ms	Although the measurements took a long elapsed time (~30 min)s, the actual time the beam was on any given spot of the sample was quite small, (3 ms dwell/pixel ; 54 images = 162ms
ε	0.8	0.8	[S5]
V	100000 nm^3	110000 nm^3	Different density and thickness
ρ	7 g/cm^3	9 g/cm^3	
Dose	**108 MGy**	**120 MGy**	Average is ~110 MGy

2. Evidence that there is no damage from *in-situ* STXM

Before the STXM measurements reported in this paper, several STXM 4E-stack and full stack measurements were made on a different region in the same cell, with results shown in **Figure S-11**. No significant change in morphology or oxidation state distributions were detected by 4E stack analysis before and after a 54-E stack. The subsequent *in-situ* STXM experiments were not performed in this region because some Cu particles dissolved after applying high positive potentials. The Cu particles were re-deposited on the working electrode and the study was performed in the region shown in the paper.

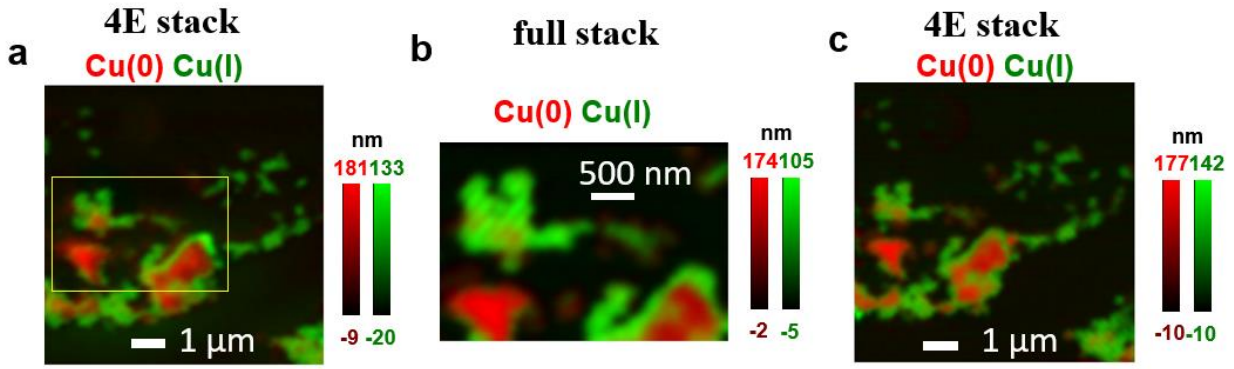

Figure S-11 Chemical maps measured in sequence on a different region in the same cell under *in-situ* conditions, prior to the studies reported in the manuscript. (a) 4-E stack, A210919045. The yellow frame is the region for full stack **(b)** Full stack**,** 210919046. **(c)** 4-E stack, 210919048.

In addition, after all the *in-situ* STXM measurements shown in the paper (**Fig. 5**), a 4-E stack was measured on a larger region of the electrode, which included adjacent areas which had never been exposed to the X-ray beam (**Figure S-11).** The same morphology and similar oxidation state distributions were found between the area that had been illuminated by STXM measurements and the particles in the un-exposed surrounding area, suggesting there was negligible beam damage on Cu electrocatalysts during *in-situ* STXM measurements.

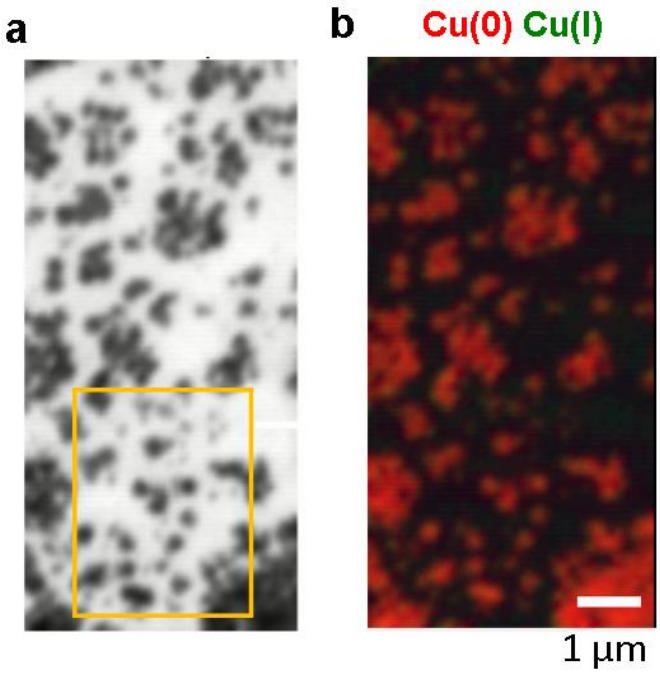

Figure S-12 Chemical maps from a larger region after all the *in-situ* STXM measurements were made in the area indicated by the yellow box. (a) STXM image at 933.5 eV. The yellow frame is the region of all in-situ STXM measurements. **(b)** color-coded components map for the larger region.

3. Evaluation of possible damage at higher STXM doses (ex-situ, dry)

To further address the radiation damage issue, we intentionally exposed a square region of Cu metal, Cu_2O and CuO to much larger doses. If damage occurred, changes would be visible at specific energies and/or in the derived chemical maps in the region heavily dosed. Despite intentional doses greater than 5000 MGy (more than 7 times larger dose than the total beam dose used for the measurements reported in **Fig, 5** and **6**, no changes beyond statistical variations were observed – see **Figs. S-13** and **S-14.**

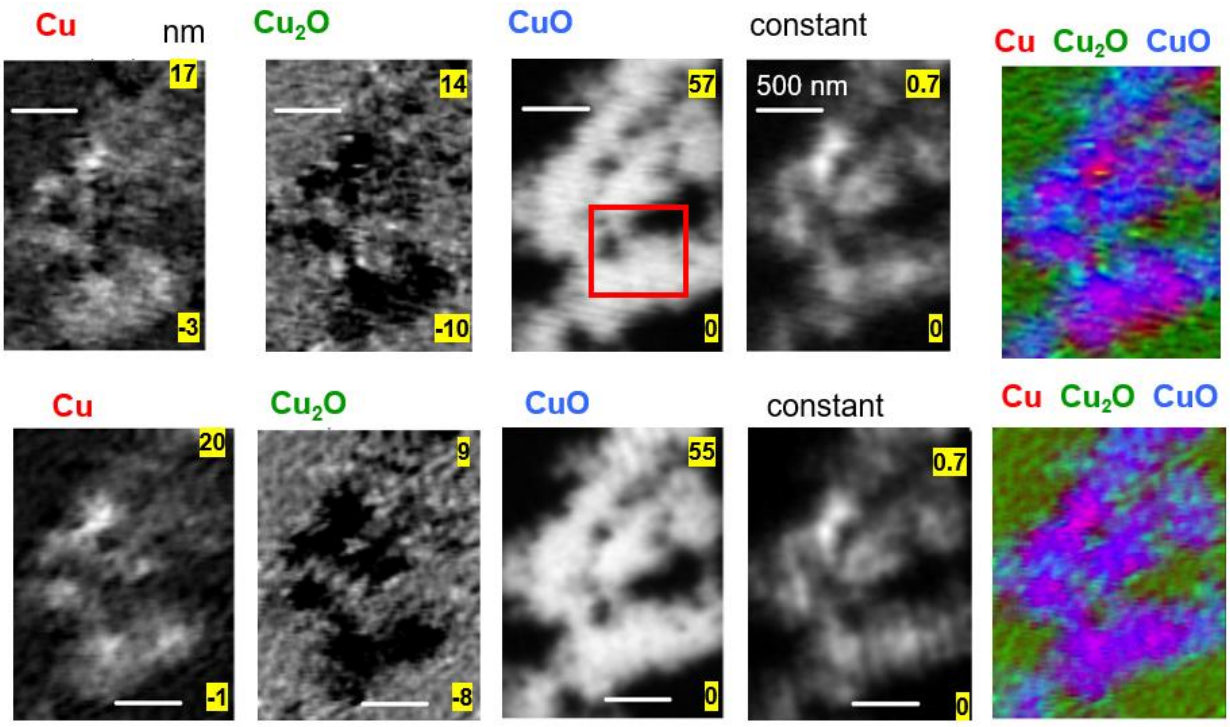

Figure S-13 Chemical maps before (upper panels) and after (lower panels) an intentional dose of **~5000MGy** in a 0.6x0.6 μm area of a region of Cu metal, Cu2O, and CuO (dosed area indicated by the red square)

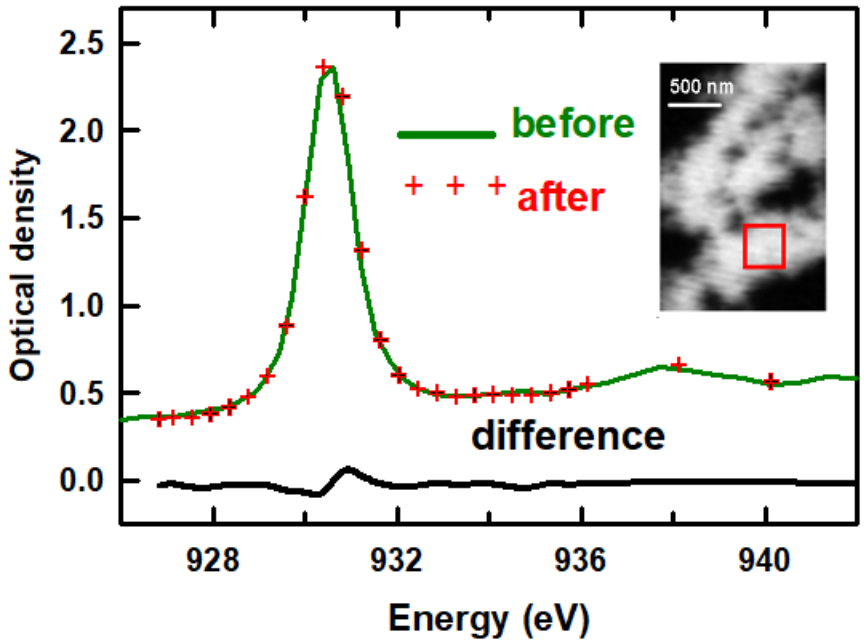

Figure S-14. Comparison of Cu L_3 spectra of the area of added dose before and after the**~5000MGy** dose.

References:

S1. Prabu, V.; Obst, M.; Hosseinkhannazer, H.; Reynolds, M.; Rosendahl, S.; Wang, J. and Hitchcock, A.P. Instrumentation for in situ flow electrochemical scanning transmission X-ray microscopy (STXM). *Review of Scientific Instruments* **2018**, *89*, 063702

S2. Wang, J.; Botton, G.A.; West, M.M. and Hitchcock, A.P. Quantitative evaluation of radiation damage to polyethylene terephthalate by soft X-rays and high-energy electrons. *The Journal of Physical Chemistry B,* **2009**, *113*, 1869-1876.

S3. Berejnov, V.,Rubinstein, B., Melo. L.G.A. and Hitchcock, A.P. First principles X-ray absorption dose calculation for time dependent mass and optical density, J. Synchrotron Radiation **2018** *25*, 833-847.

S4. Berejnov, V., Rubinstein, B., Melo, L.G.A. and Hitchcock, A.P. Calculating Absorption Dose When X-ray Irradiation Modifies Material Quantity and Chemistry, J. Synchrotron Radiation, **2021** *28*, 834-838,

S5. Kilcoyne, A.L.D.; Tyliszczak, T.; Steele, W.F.; Fakra, S.; Hitchcock, P.; Franck, K.; Anderson, E.; Harteneck, B.; Rightor, E.G.; Mitchell, G.E. and Hitchcock, A.P .Interferometer-Controlled Scanning Transmission X-Ray Microscopes at the Advanced Light Source. *J. Synchrotron Radiation* **2003**, *10*, 125−136.

Appendix F

This appendix shows the Supporting Information for Chapter 8.

Supplementary Information

Copper CO_2 Reduction Electrocatalysts Studied by *In Situ* Soft X-ray Spectro-Ptychography

Chunyang Zhang,[1,2] Nicolas Mille,[3] Haytham Eraky,[2] Stefan Stanescu,[3] Sufal Swaraj,[3] Rachid Belkhou,[3] Drew Higgins[1*] and Adam P. Hitchcock[2*]

1. Chemical Engineering, McMaster University, Hamilton, ON, Canada, L8S 4M1

2. Chemistry & Chemical Biology, McMaster University, Hamilton, ON, Canada, L8S 4M1

3. Synchrotron SOLEIL, L'Orme des Merisiers, Saint-Aubin, Departementale 128, 91190 Saint-Aubin, France

Contents

Section SI-1 X-ray refraction, CDI, and basic concepts of ptychographic reconstruction

A number of reviews of X-ray ptychography have been published [**S.1 – S.6**]. The following is a distillation of these. Ptychography is a scanned coherent diffraction imaging (CDI) method which consists of measuring diffraction images (DI) generated when a beam of partially or fully coherent X-rays passes through an optically thin sample (OD < 2). The DI are typically measured using a high performance camera with single X-ray photon/pixel sensitivity, placed downstream from the sample (**Fig. S.1**).

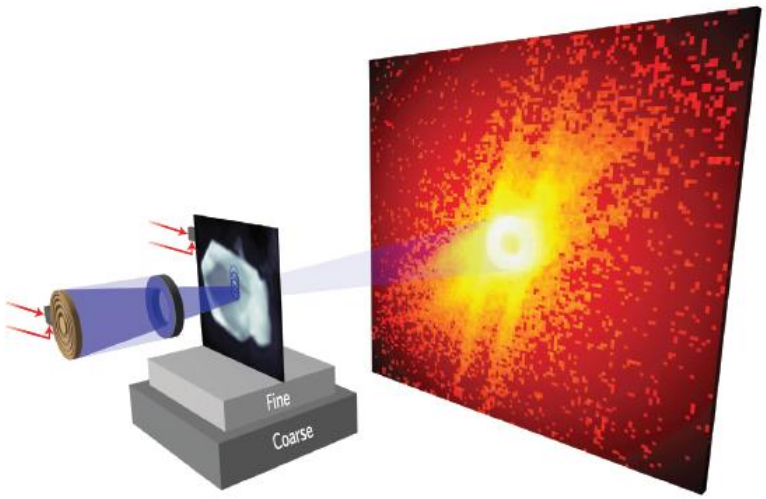

Fig. S.1 Schematic of measurement of coherent diffraction image (DI) from one point on a sample. Sets of these DI measured with overlap of the sampled points constitutes a scanned CDI or ptychographic measurement. Reproduced with permission from *Nature Photonics* **8**, 765-769 (2014).

The interaction of X-rays with an optically thin sample depends on the refractive index of the material(s), η, which is a complex, photon energy dependent quantity

$$\eta = (1-\delta) - i\beta \qquad \text{Eqn SI-1.1}$$

where the real part (1 – δ) is the phase and the complex part (β) is the amplitude response of the X-ray interacting with the material. The propagation of an X-ray through a material is a spatial, temporal and photon energy dependent quantity that can be described by

$$U = Ae^{i\varphi} \qquad \text{Eqn SI-1.2}$$

where A is the amplitude at a given position and time, and φ is a complex propagation/loss function, which contains η. Upon interaction with a sample, the complex wavefield of the coherent scattered light (SC), $U^{SC}(r,\omega)$, is related to the wavefield of the light impinging on the sample (inc), $U^{inc}(r',\omega)$, by

$$U^{\mathrm{sc}}(\boldsymbol{r},\omega) = \int_V F(\boldsymbol{r}',\omega) U^{\mathrm{inc}}(\boldsymbol{r}',\omega) \frac{e^{ik|r-\mathbf{r}'|}}{|\boldsymbol{r}-\mathbf{r}'|} \mathrm{d}\boldsymbol{r}' \qquad \text{Eqn SI-1.3}$$

where r and r' are time dependent position vectors of the X-ray after and before the sample, ω is the angular frequency of the light ($\omega = 2\pi\nu$; the photon energy (E) is given by $E=h\nu$) and $e^{ik|r-r'|}/|r-r'|$ is a plane wave description of the light wave. The DI measured in ptychography only measure the amplitude of the scattered X-rays, U^{SC}. The challenge of ptychographic reconstructions is to solve the phase inversion problem [**S.4, S.6**].

Amplitude and phase images of the sample (object) and the incident X-ray beam (probe) can be derived from sets of DI using an iterative algorithm. For a single DI the reconstruction can be described conceptually by (**Fig. S.2a**), While this approach uses Fourier transforms ($F\{\rho(x)\}$ and $F^{-1}\{\rho(x)\}$) as propagators, other mathematical functions can be used.

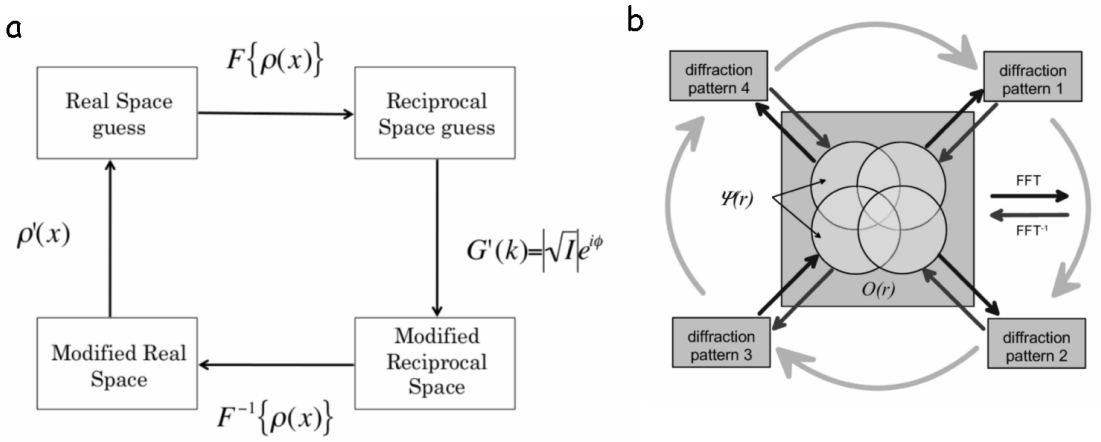

Figure S.2 (**a**) Schematic outline of an iterative procedure to generate the phase and amplitude of an object from a single coherent diffraction image. (**b**) Outline of iterative procedure to generate the phase and amplitude of an object from sets of diffraction images measured with spatial overlap. (Figure reprinted with permission from J. M. Rodenburg, A. C. Hurst, A. G. Cullis, B. R. Dobson, F. Pfeiffer, O. Bunk, C. David, K. Jefimovs, and I. Johnson *Phys. Rev. Lett.* 98, 034801 (2007) **[S.3]**, copyright 2007 by the American Physical Society).

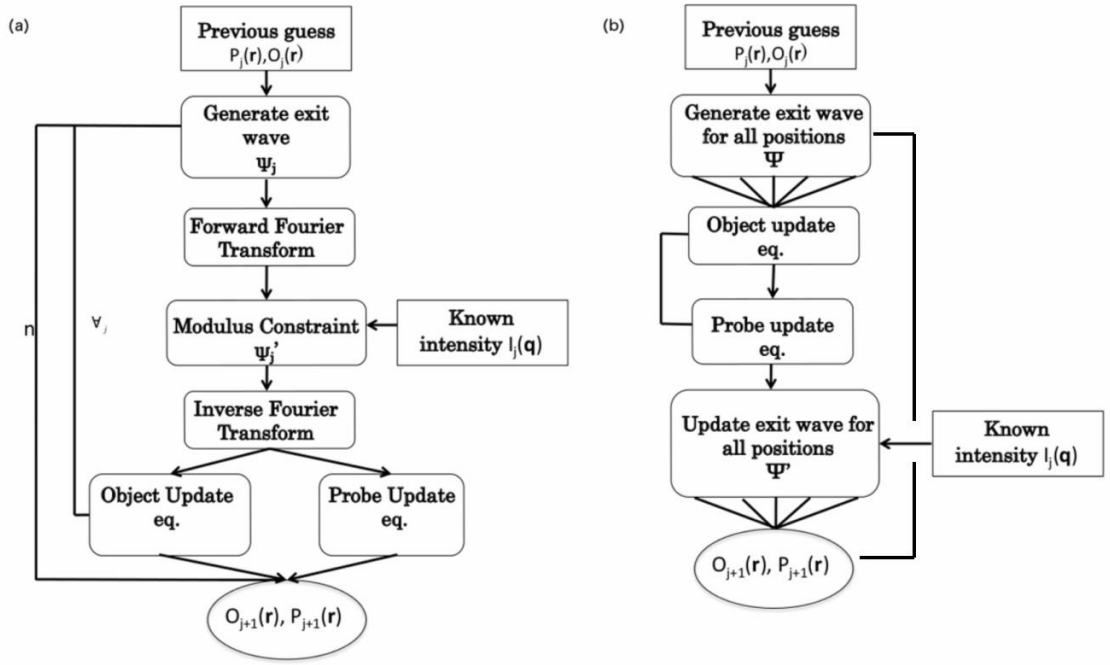

Figure S.3 Flow diagrams for, (left) the extended Ptychographic Iterative Engine (ePIE), and (right) Difference Method (DM) algorithms for reconstruction of sets of diffraction images recorded over a set of overlapping positions on a sample. The ePIE method works through the set of DI images in a quasi-serial pattern, whereas the DM method carries out the algorithm in a more parallel fashion. In each case a guess is made of the starting probe properties, while the initial phase of the object is set to a constant. On each iteration, the updated (n^{th}) amplitude prediction of the object is compared with the measured diffraction images, with further constraints in the overlapping spatial regions. The difference is then used to refine the phase and amplitude predictions for the $(n+1)^{th}$ iteration. Typically a pre-set number of iterations is used, rather than a self consistent approach (iteration until the difference falls below a user-defined magnitude). Adapted from Figure 2.6 of **S.5**, with permission from the author.

In the case of ptychography where multiple diffraction images are measured with spatial overlap, a more extended reconstruction process is required (**Fig. S.2b**). Additional steps are used to constrain the functions describing the sample and the probe in the spatially overlapping regions. Two methods used for such iterative ptychographic reconstruction are (i) the extended Ptychographic iterative engine (ePIE) developed by Maiden et al. [**S.4**] and (ii) the Difference Map (DM) algorithm, developed by Thibault et al. [**S.2**]. **Figure S.3,** taken from the PhD thesis of Shemilt [**S.5**], outlines these two approaches. In this work an alternating projection (AP)

reconstruction method implemented in PyNX [**S.7**] was used, since it was found to be more stable and provide more rapid convergence than DM method implemented in PyNX.

Section SI-2 Estimation of spatial resolution of STXM and ptychography

Figure S.4 presents results of spatial resolution evaluation using the Fourier ring correlation (FRC) method [**S.8**]. Ptychographic reconstructions using large degrees of overlap introduce a large degree of correlation among the signal at adjacent spatial points. Thus inaccuracies could be introduced by using the even / odd pixel index method of using FRC to evaluate spatial resolution from a single ptychographic reconstructed image. In order to avoid such artifacts, we have used 2 independently measured ptychographic data sets from the same spatial region. These images are displayed as **Fig. S.5a** and **S.5b**. The pixel size in these images is 5.5 nm. The FRC applied to these two images is presented in **Fig. S.5c**. Using the half-bit criterion, probably the most common metric used in soft X-ray ptychography, a spatial resolution of 7 nm (half-pitch) or 14 nm (full pitch) is estimated. The more conservative half-height criterion results in a spatial

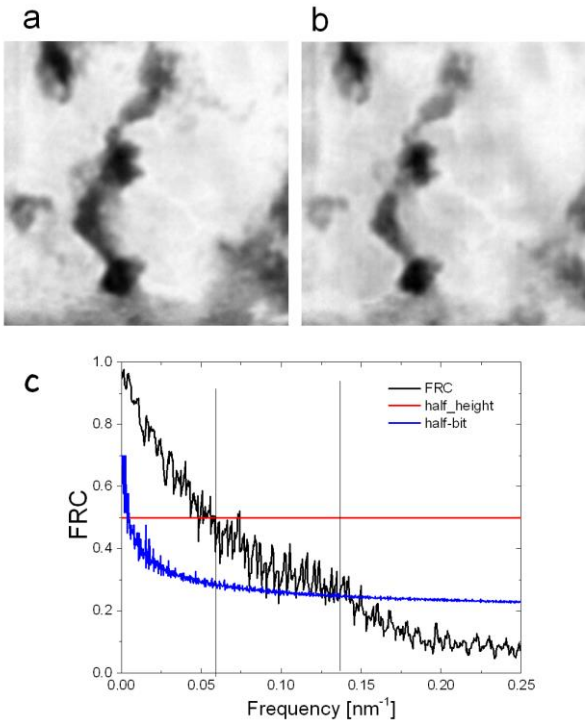

	Spatial Resolution (nm)	
Type	half-bit	0.5 (half-height)
Half-pitch:	7	16
Full-pitch:	14	32

Fig. S.4 Fourier ring correlation (FRC) analysis of the spatial resolution of the cubic particle in **area C**. (a) first image. (b) second image (from same area). (b) FRC plot.

resolution of 16 nm (half-pitch) or 32 nm (full pitch). Thus, we conservatively estimate the spatial resolution of the *in situ* spectro-ptychography as 25 ± 5 nm.

Figure S.5 plots line profiles across abrupt features in the ptychography and STXM images of **area C**. The abruptness of the profile across the STXM image (**Fig. S5a**) is 80±10 nm, while that for the profile across the ptychography image (**Fig. S5c*)*** is 37±4 nm, as measured from the 20 % to 80 % intensity levels.

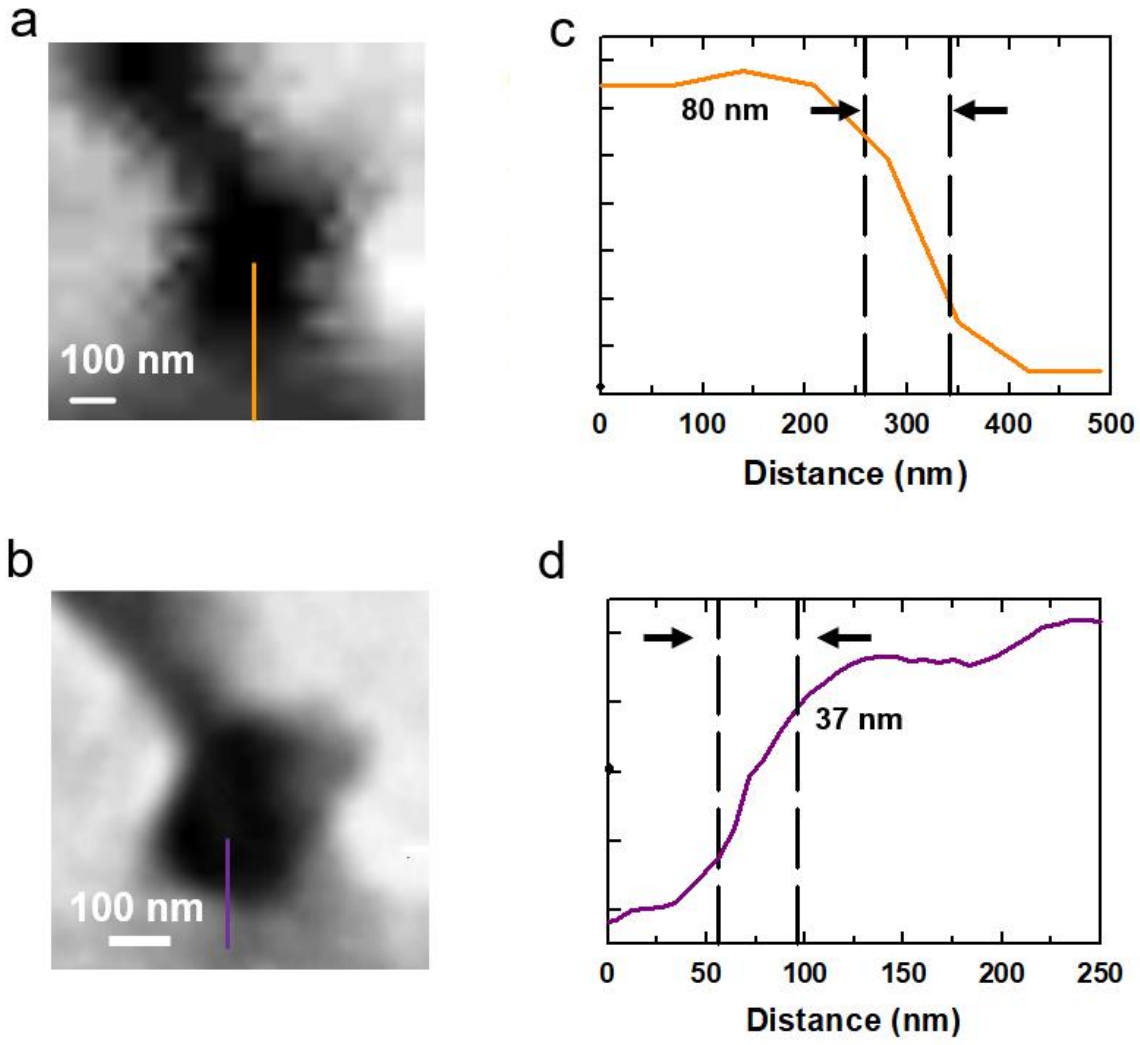

Figure S.5 Estimation of spatial resolution from a knife-edge measurement (line profile across a high contrast boundary) in **area C**. (a) *In situ* STXM image at 933.3 eV. (b) *In situ* ptychography amplitude image at 933.3 eV. (c)) Line profile across the orange line. The abruptness of the rise in optical density (20% – 80 %) is 80 ± 10 nm. (d). Line profile across the purple line. The abruptness of the rise in optical density (20% – 80 %) is 37 ± 4 nm.

Section SI-3 Cu L_3 ($2p_{3/2}$) reference spectra

Figure S.6 presents the Cu L_3 reference spectra of Cu metal, Cu_2O and CuO used for generating quantitative component maps from the absorption stacks and spectra derived from spectro-ptychography amplitude image sequences. These spectra were digitized carefully from the paper by Jiang et al. [**S.9**]. The dots indicate the 4 energies used to produce chemical mapping from the 4-E stack measurements. By carefully selecting energies which best differentiate the 3 oxidation states, we found that the 4-E stack can provide similar chemical information and mapping of the Cu(0), Cu(I) and Cu(II) species as achieved with 40-energy stack measurements.

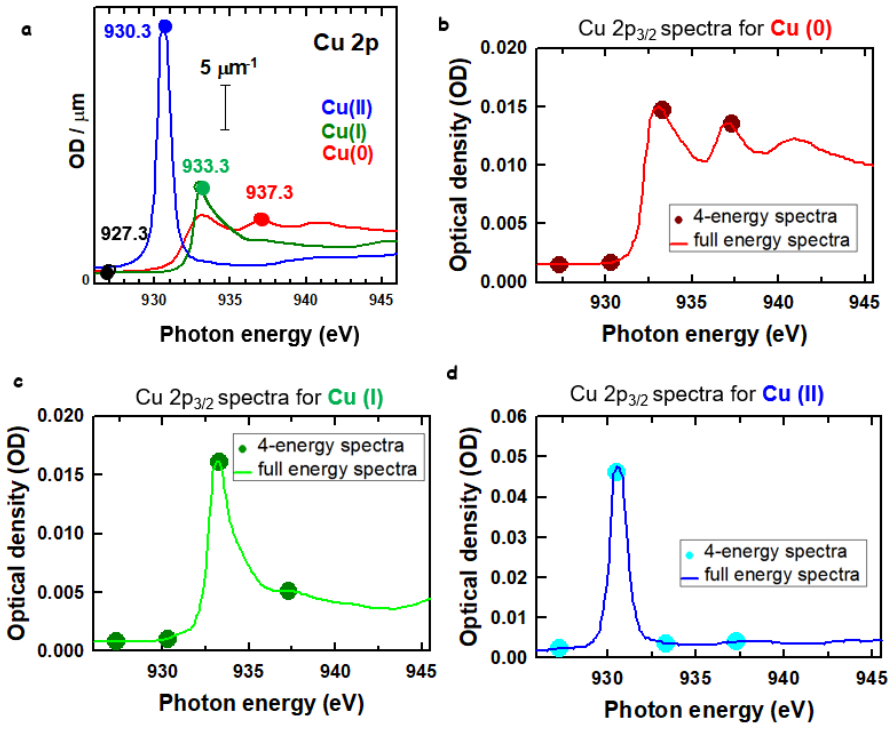

Fig. S.6 Cu L_3 ($2p_{3/2}$) reference spectra. Spectra of Cu metal, Cu_2O and CuO digitized from Jiang et al. [**S.9**]. The intensity has been placed on an absolute scale (optical density per nm at standard density) [**S.10**]. (a) 4 energies location on the 3 Cu reference spectra plotted on the same scale. (b) Cu(0). (c) Cu(I). (d) Cu(II). The energies used in the 4-E stack approach are indicated.

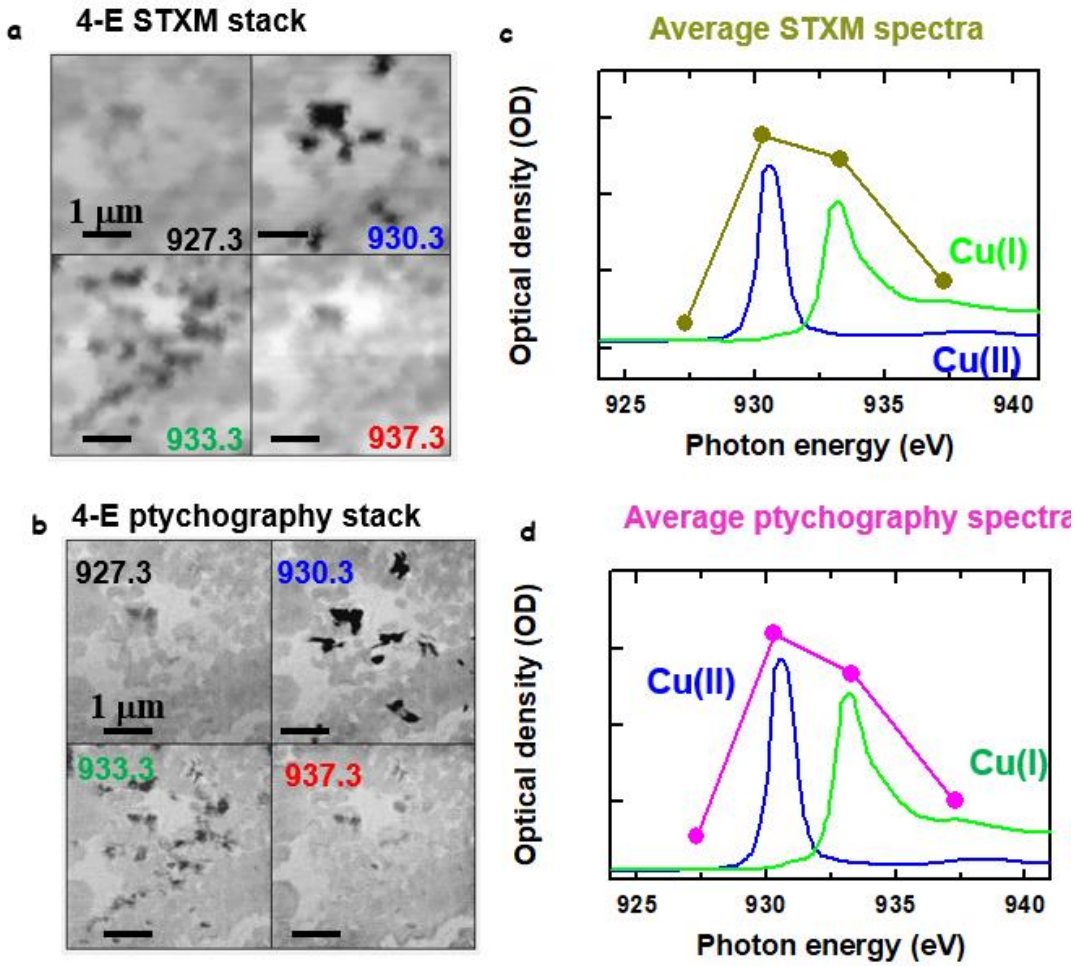

Fig. S.7 4-E STXM and spectro-ptychography stacks of area A. (a) STXM transmission images at 4 E. (b) Spectro-ptychography amplitude images at 4 E. (c) average STXM 4-E spectra of the Cu particles in **area A** compared to Cu(I) and Cu(II) spectra. (d) average spectra-ptychography 4-E spectra of the particles in **area A** compared to Cu(I) and Cu(II) spectra.

Section SI-4 STXM and spectro-ptychography 4-E stacks of area A

Figure S.7 presents the 4 energy (4-E) STXM transmission images (**Fig. S.7a**) and the 4-E spectro-ptychography amplitude transmission images (**Fig. S.7b**) of **area A**. The spectral signals averaged over all particles in **area A** are displayed in **Fig. S.7c** and **Fig. S.7d.** Comparison to the reference spectra indicate these particles are a combination of Cu(I) and Cu(II). **Figure S.8** displays the component maps for Cu(I) and Cu(II) derived by singular value decomposition (SVD) of the STXM (**Fig. S.8a-c**) and spectro-ptychography (**Fig. S.8d-f**).

Section SI-5 Analysis of the STXM and spectro-ptychography 4-E stacks of **area A**

Figure S.8 presents an SVD fit analysis of the STXM and ptychography 4-E stack of **area A.** Using suitable, quantitative reference spectra (**Fig. S.6**) , OD (STXM) or absorption images derived from reconstructed amplitude images are reduced to a set of chemical component maps by the singular valued decomposition (SVD) procedure, which is described in detail in **section SI-13**.

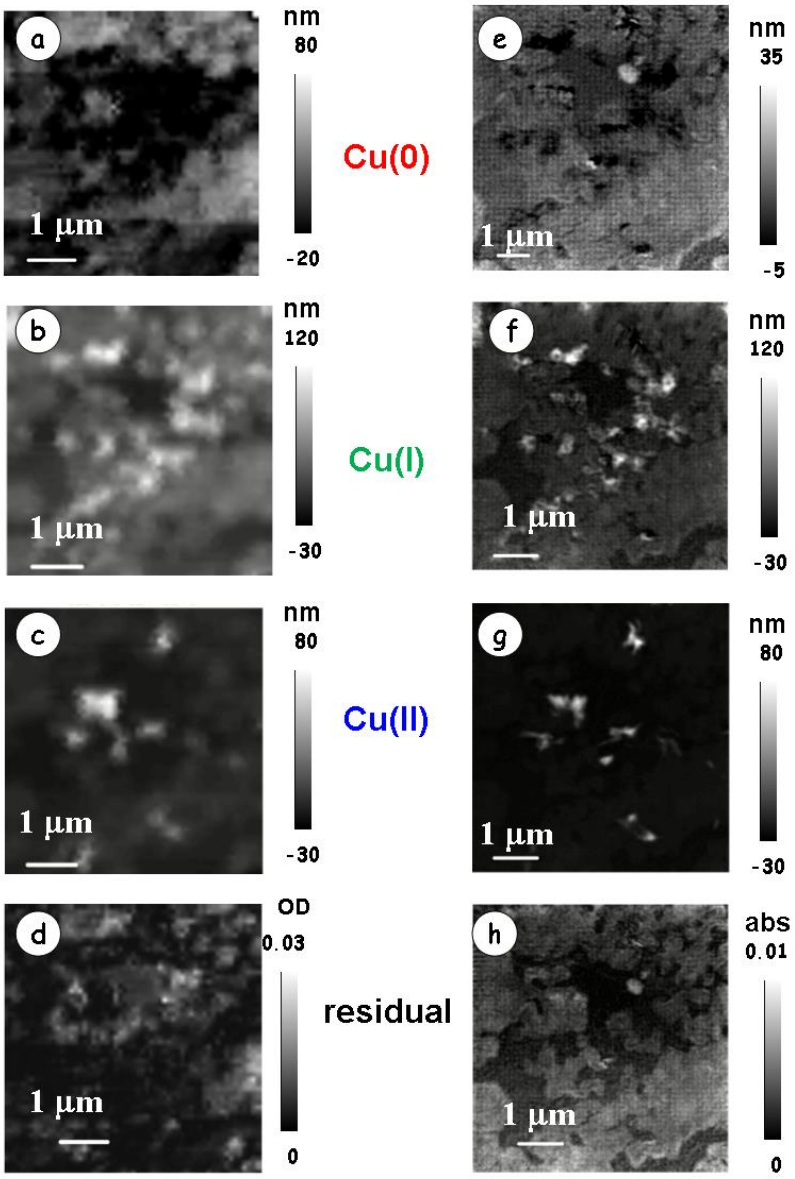

Fig. S.8 SVD fitting analysis of 4-E STXM and 4E spectro-ptychography stacks for area A (a) Cu(0), (b) Cu(I), (b) Cu(II) component maps and (d) residual map from SVD analysis of the 4-E STXM stack. (e) Cu(0), (f) Cu(I), (g) Cu(II) component maps and (h) residual map from SVD analysis of the 4-E spectro-ptychography stack.

Section SI-6 Analysis of spectro-ptychography full (40-E) stacks of area B

Figure S.9 presents details of the analysis of the ptychography full stack of **area B**. **Figure S.9a** plots the chronoamperometry (current vs time) graph when +0.7 V_{RHE} was applied. There is a pulse-like structure superimposed on the current versus time chronoamperometry signal. This is due to a combination of a small X-ray induced current (XBIC) and the use of a shutter to block the X-ray beam while the photon energy is changed, which takes ~15 s. During the time the X-ray beam is off the current changes by the amount induced by the X-ray beam. Once the shutter is re-opened and the ptychography measurements start, the XBIC signal is again observed. The ~85 s taken to measure the ptychography image at each energy matches the scan parameters used (900 diffraction images (DI), 60 ms dwell/DI plus ~30 ms to readout each DI image). This type of XBIC signal has been reported in other X-ray measurements, and in fact has been used as an imaging signal [S11].

Figure S.9b shows the regions from which Cu(I)-rich and Cu(0)-rich spectra (**Fig. S.9c**) were extracted. **Figure S.9d** shows the spectral decomposition of the spectrum of the Cu(0)-rich selected area. **Figure S.9e** shows the spectral decomposition of the spectrum of the Cu(I)-rich selected area.

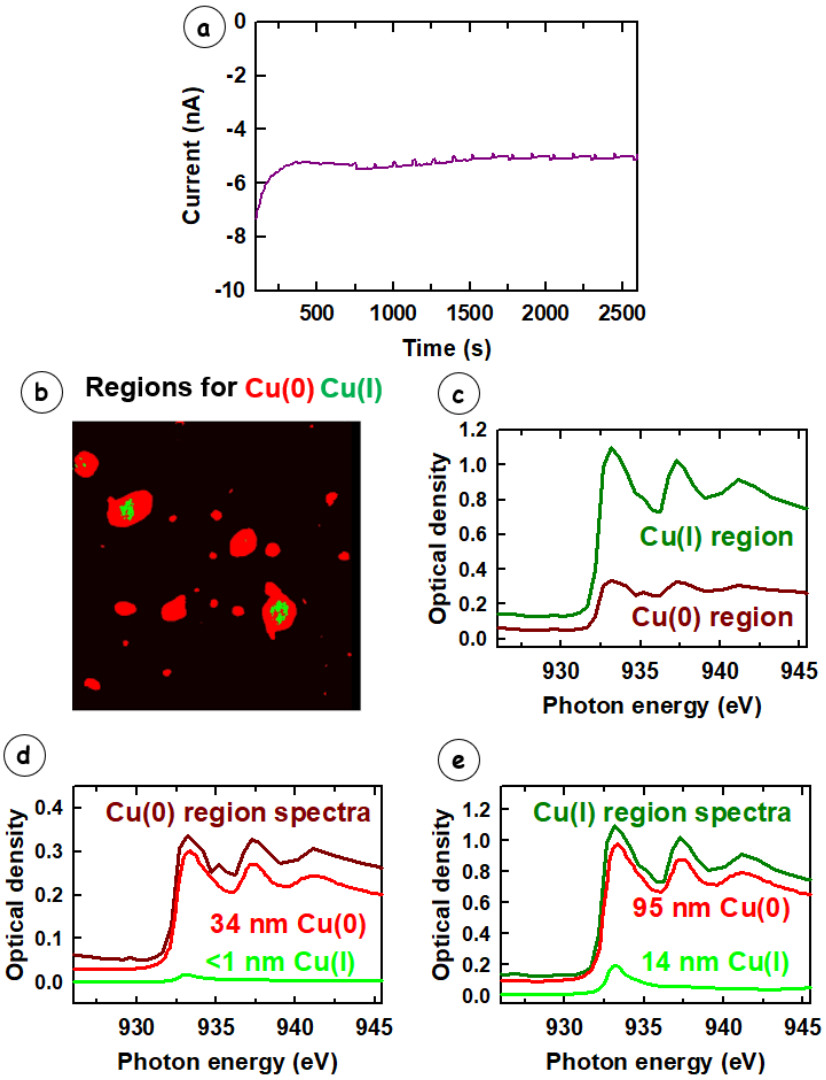

Fig. S.9 Analysis of the ptychography amplitude full stack of area B. (a) current vs time graph at the +0.1V vs RHE (b) regions for Cu(I) and Cu(II) from the component maps. (c) the average spectra of masked Cu(0)-rich and Cu(I)-rich regions. (d) decomposition of average spectra from the masked Cu(0)-rich region using SVD curve-fitting. (e) decomposition of average spectra from Cu(I) region using SVD curve-fitting.

Section SI-7 Physical basis of X-ray absorption, ptychography amplitude and ptychography phase signals

Figure S.10 sketches the physical origin of the X-ray absorption, ptychography amplitude and ptychography phase signals. Absorption spectra derived from ptychographic amplitude and integrated X-ray transmission signals are similar, but not the same. Phase spectra derived from ptychographic reconstructions are quite different than absorption or amplitude-derived spectra. An interesting question, still incompletely answered in the literature, is, "*Is there additional, independent information from the object phase signals provided by ptychographic reconstruction ?*".

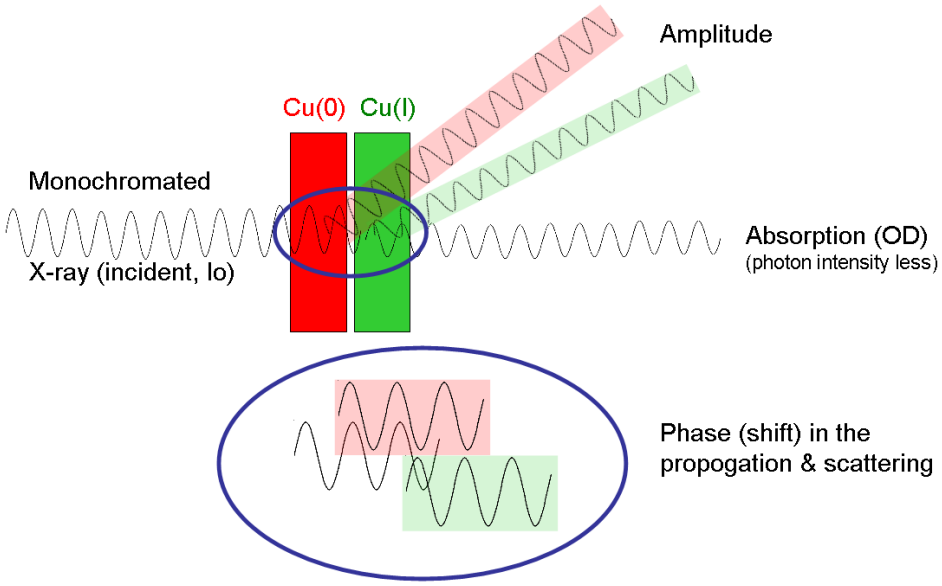

Fig. S-10 Schematic of the physical origin of the X-ray absorption, ptychography amplitude, and ptychography phase signals.

Section SI-8 Chronoamperometry at potentials from +0.1 to -0.85 V_{RHE}

Fig. S.11 shows the chronoamperometry current curve at five potentials from +0.1 to -0.85 V_{RHE}. Only the parts of the current response after it became stable are plotted.

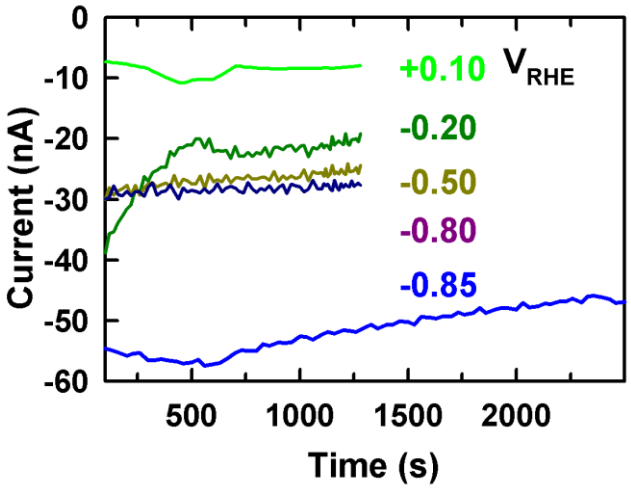

Fig. S.11 Current versus time curve at each potential. +0.1 to -0.85 V_{RHE}

Section SI-9 Spectro-ptychography 4-E stacks of area C at 5 potentials

Figure S.12 displays the Cu(0), Cu(I) and Cu(II) component maps of **area C** at 5 potentials [OCP, +0.1, -0.2 , -0.5 and -0.8 V_{RHE}] derived from SVD fitting of the absorption images at 4 energies, derived from the 4-E ptychography amplitude stacks, analyzed through SVD-fitting using the OD1 reference spectra of Cu(0), Cu(I) and Cu(II) under various indicated potentials.

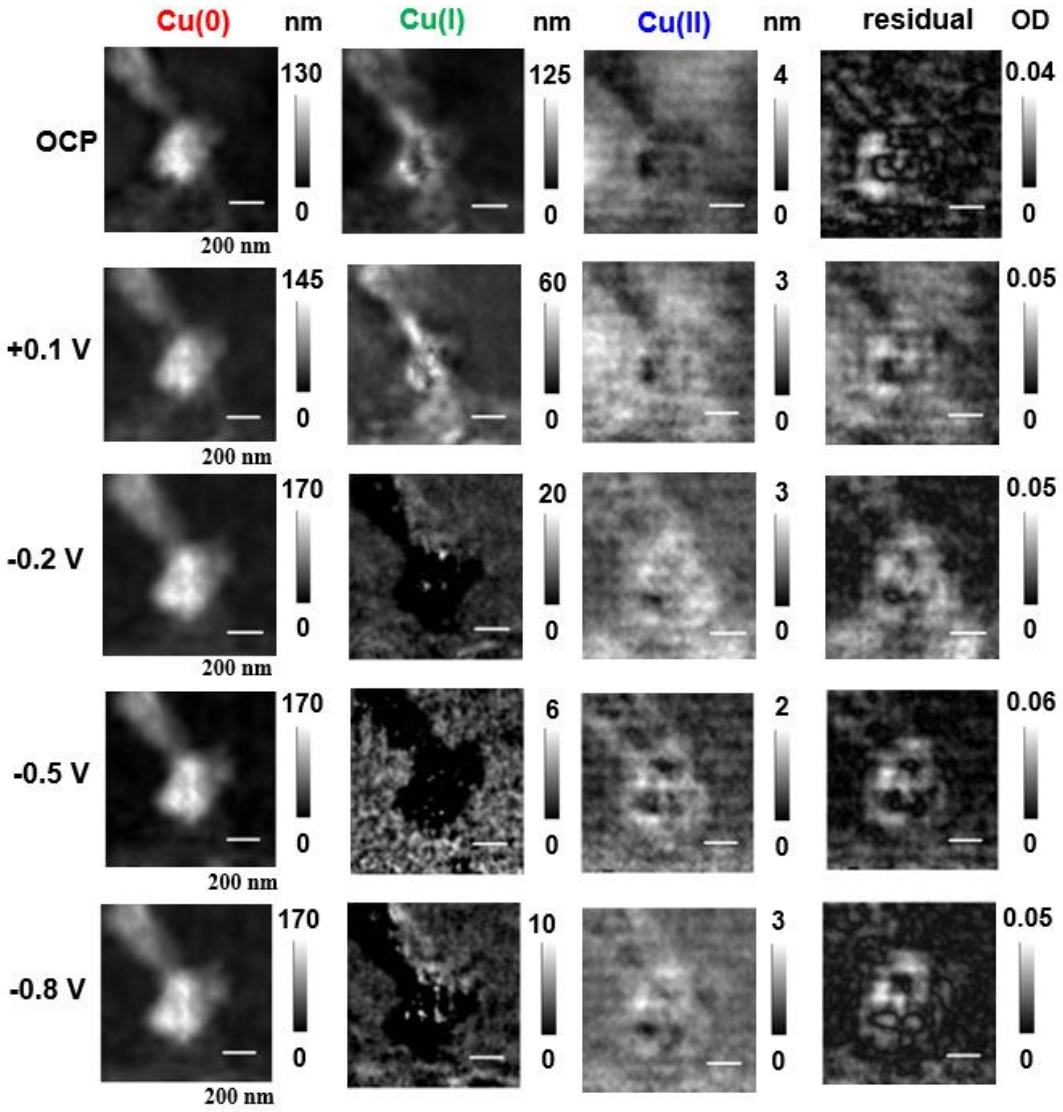

Fig. S.12 results for 4-energy ptychography amplitude stacks of **area C** analyzed through SVD-fitting using the OD1 reference spectra of Cu(0), Cu(I) and Cu(II) at the indicated potentials.

Figure S.13 plots the 4E spectra for the 5 potentials (averaged of the particle regions), along with the spectrum extracted from the full 34 energy stack with an applied potential of -0.85 V_{RHE}. The change in slope between 933 and 937 eV between -0.2V and -0.5V indicates the reduction of the Cu(I) between these 2 potentials.

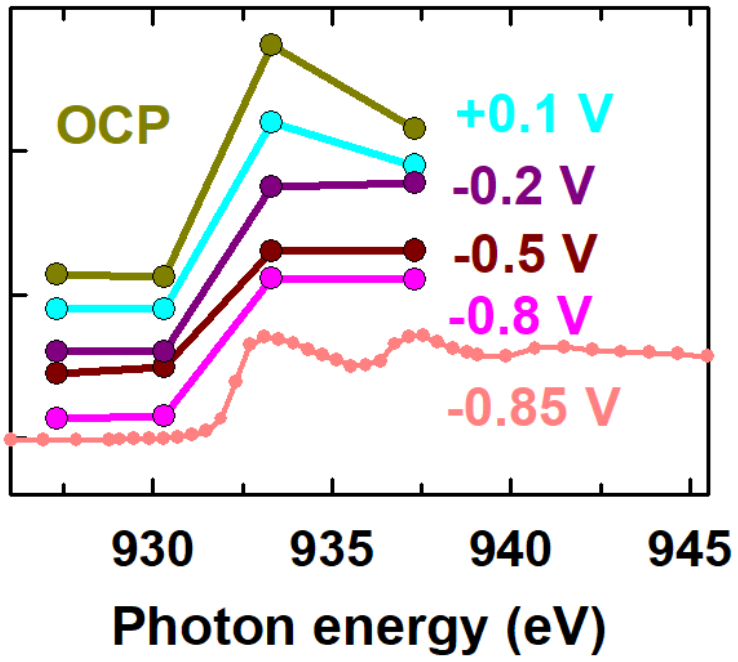

Fig. S.13 extracted average spectra from 4-E and 34-E stack ptychography amplitude from the Cu cubic particle at each potential.

Section SI-10 Multivariate statistical analysis of ptychography stack at +0.1V_{RHE}

In addition to forward fitting (least squares analysis), multivariate statistical methods [S.12 – S.14] were applied to the spectro-ptychography stack measured in area B. **Figure S.14** presents the eigenvalue analysis of the absorption stack derived from the reconstructed ptycho amplitude stack, measured at +0.1V_{RHE} and an average current of 5 nA. This suggests there could be 4 statistically significant spectral components. In order to check this and to get a rotation of the PCs into a "cluster space" where the spectra are more clearly XAS, a PCA_GUI cluster analysis was performed. The results of this analysis are presented in **Fig. S.15**. The statistical evaluation reports that there only 3 statistically significant spectral components, despite using the first four PCs in the cluster analysis. Further the first component is representative of 97 % of all pixels, while the second cluster component, which is a spectrum of Cu metal with a small amount of Cu(I) at the center of the thickest particles, is only ~3 % of the pixels. The 3rd component (<1% of the pixels) is clearly noise. Thus the statistical analysis unequivocally supports the conclusion drawn from the forward fitting analysis presented in the manuscript, namely, that even at +0.1V_{RHE}, higher potential than the onset of CO_2R, the particles are mostly Cu metal.

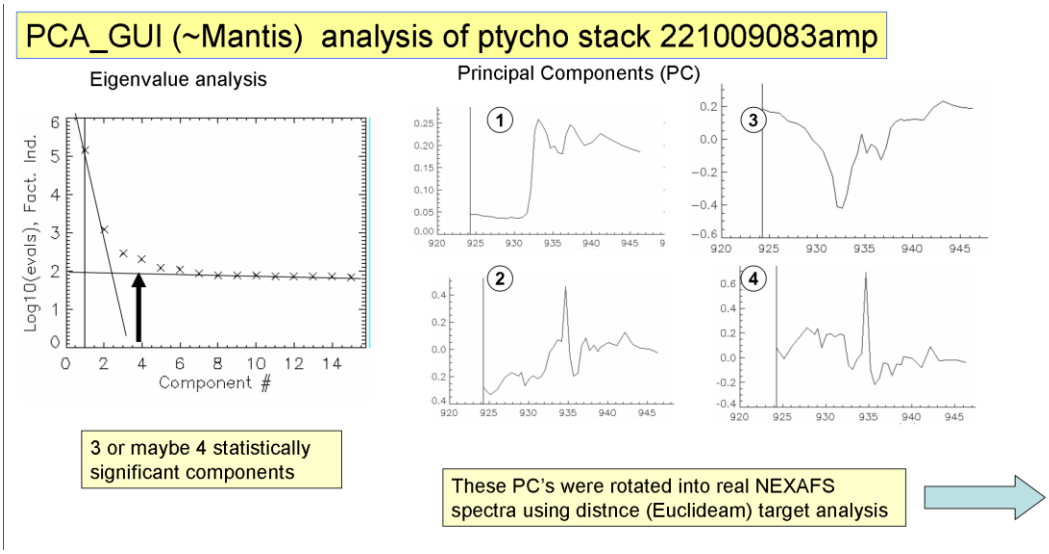

Fig. S.-14 (left) logarithmic display of the eigenvalues (orthoganalized contributions). Typically the statistically significant PCs are those above the extrapolation of the trend at large PC# (low contributions which are patterns of noise). PC components 1, 2, 3, 4 are candidates for statistically significant signals. (right) the first 4 PC spectra (eigenfunctions). Only the first one is "NEXAFS-like", and is clearly identified as the Cu L_3 spectrum of Cu metal. The second (largest deviation of average spectrum from PC1 looks like a damped inverted Cu metal spectrum.

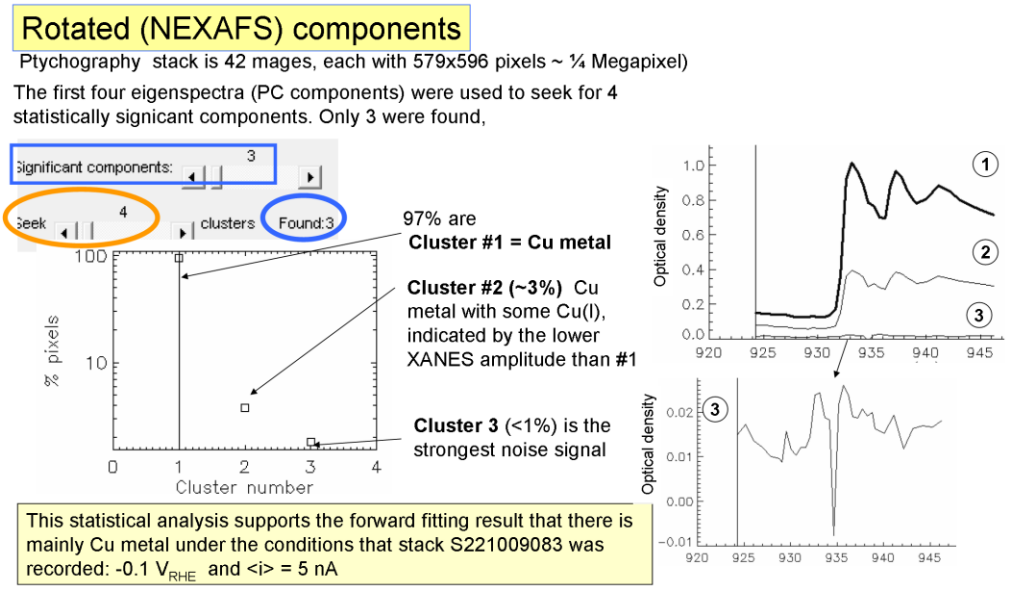

Fig. S-15 (upper left) report of the cluster analysis. (lower left) plot of %-pixels corresponding to the three statistically significant cluster components. (upper right) Plot of the first 3 component spectra on the same OD scale. (lower right) expanded scale plot of the 3rd cluster component.

Section SI-11 Bubble formation during Cu L_3 spectro-ptychography stack of area C with -0.8 V_{RHE} applied

Fig. S.16 presents images taken from the full spectro-ptychography stack measured with -0.85 V_{RHE} applied. A bubble formed during the measurements. Despite the continuous change of electrolyte level during the measurement (see supplementary movie, **SI-video-areaC-bubble_48ampb2a4odc.gif**), the ptychography data reconstructed very well. At this potential there is possibility of water splitting, generating H_2. Alternatively the bubble could have been CO, generated by CO_2 reduction. If C 1s measurements could be made from the bubble, these two alternatives could be distinguished.

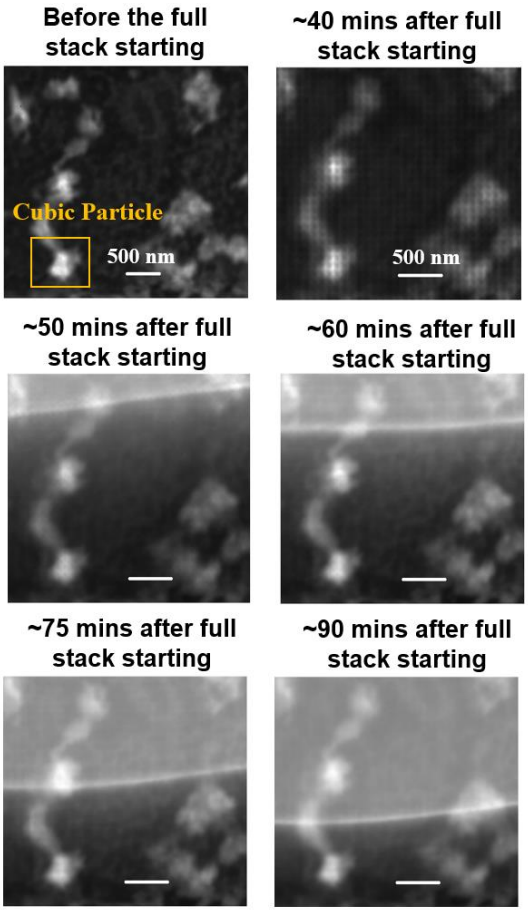

Fig. S.16 Absorption images from amplitude images reconstructed from spectro-ptycho stack S221008048, with potential fixed at -0.85 V_{RHE}. Interpretation is bubble generation either water splitting (H_2) or CO_2 reduction (CO or other product gases).

Section SI-12 Chemical maps derived from full spectro-ptychography stack of area C

Figure S.17 shows the SVD fitting analysis of ptychography amplitude full stack for the Cu cubic particle measured at -0.85V RHE.

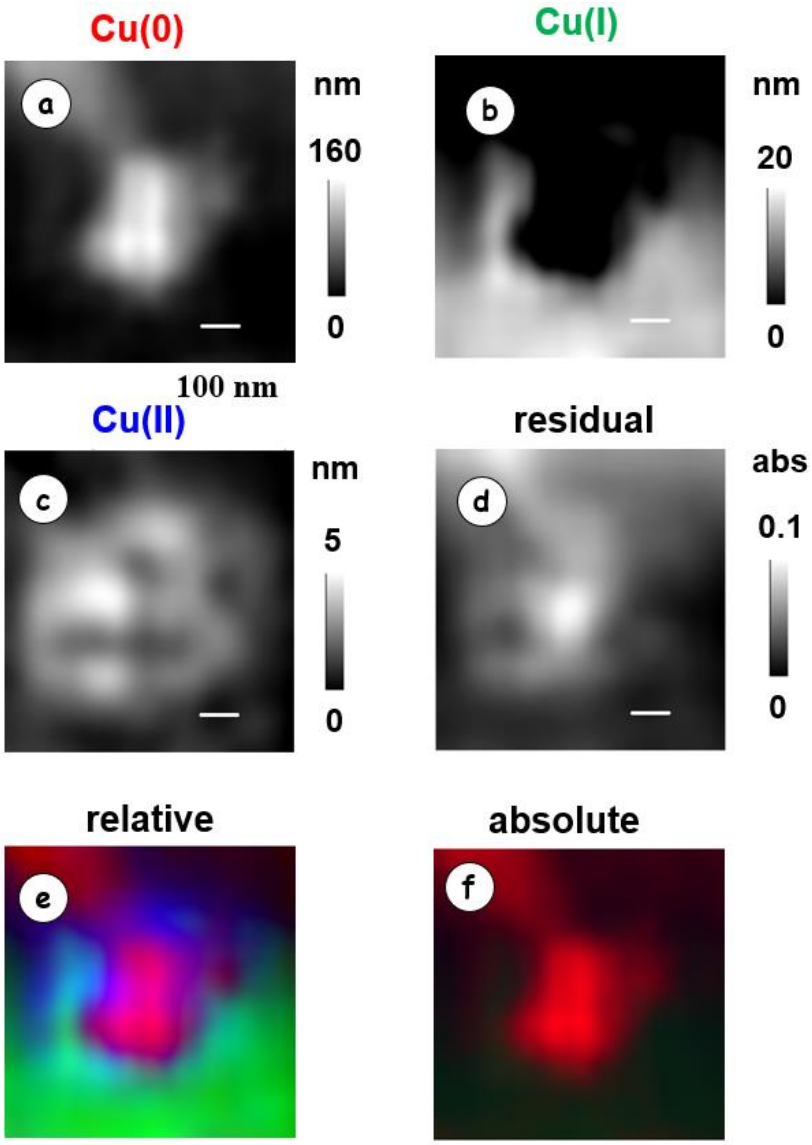

Fig. S.17 SVD analysis of ptychography amplitude full stack for Cu cubic particle (area C) under -0.85V$_{RHE}$. Component maps of (a) Cu(0). (**b**) Cu(I), (**c**) Cu(II). (d) residual. Colour-coded component map using (e) relative scaling and (f) absolute scaling. The data has been subjected to a 9-point Savitsky-Golay 2D smooth to remove raster-scan artefacts (original pixel size is 5 nm).

Section SI-13 Details of the *in situ* flow electrochemical device

Fig. S-18 displays the microfluidic-based flow electrochemical device for *in situ* STXM and ptychography experiments. The *in situ* device consists of a machined printed circuit board frame (PCB, **Fig. S-18a**), a poly(methyl methacrylate) (PMMA) backplate (**Fig. S-1*8*b**), a polydimethylsiloxane (PDMS)/glass cell (**Fig. S-18c**), and a set of custom electrode-equipped Si / SiN_x / Au chips (Norcada Inc) (**Fig. S-18d**). The PCB frame is machined at the Chemical Engineering department in McMaster University. The PMMA backplate and PDMS/glass cell are prepared in the Hitchcock laboratory (Chemistry & Chemical Biology, McMaster University). The PCB frame provides mechanical support for the PDMS/glass/electrode assembly, and electrical connections. Au coated Cu spring clips soldered to the PCB traces are used to electrically connect the 3 Au electrodes - (working/ counter/ reference electrodes (WE/CE/RE) - on the *in situ* chip to a potentiostat via a 4-pin connector and cable. The PCB frame is attached to the PMMA backplate by 8 nylon screws. The PDMS /glass cell is sandwiched between the assembled PCB frame and the PMMA backplate. The PDMS layer contains 4 channels (dotted lines, **Fig. S-18c**) which connect flow channels in the *in situ* chips to 4 flow tubes (2 inlet, 2 outlet). The flow tubes can be connected to one or more fluid circulation devices, such as syringe or pressure pumps, to establish a stable flow of electrolytic fluid into the *in situ* chips. The *in situ* chips are purchased from Norcada Inc (Edmonton, Canada, https://www.norcada.com) There are 3 Au electrodes on **base chip E** (**Fig. S-18e**). **Spacer chip F** has a spacer layer (500 nm, 1 μm or 1.5 μm thick) defining the height of the flow channel. In this work we used a 1 μm spacer layer. The SiN_x window area is 240 μm wide and 100 μm high. The SiN_x windows have a thickness of 100 nm (base chip E) and 50 nm (spacer chip F). The areas typically used for electrocatalysis studies (dark circles on WE and CE, **Fig. S-18e**) are 20 μm diameter and have a coating consisting of 5 nm Cr and 15 nm Au.

Section SI-14 Detailed *in situ* procedures and summary of measurements.

Cu nanoparticle electrodeposition: The 4 electrolyte tubes were pre-filled with a solution of 10 mM $CuSO_4$ and 10 mM KCl and then connected to the 4 channels of the assembled *in situ* device. A syringe pump (New Era N1000) was used in push mode with a flow rate 25 μl/hr for 10 mins to fill the *in situ* device with electrolyte from the inlet channels. The filling process was monitored under an optical microscope (20x objective) to confirm that the electrolyte completely filled the window region and the cell was free of bubbles.

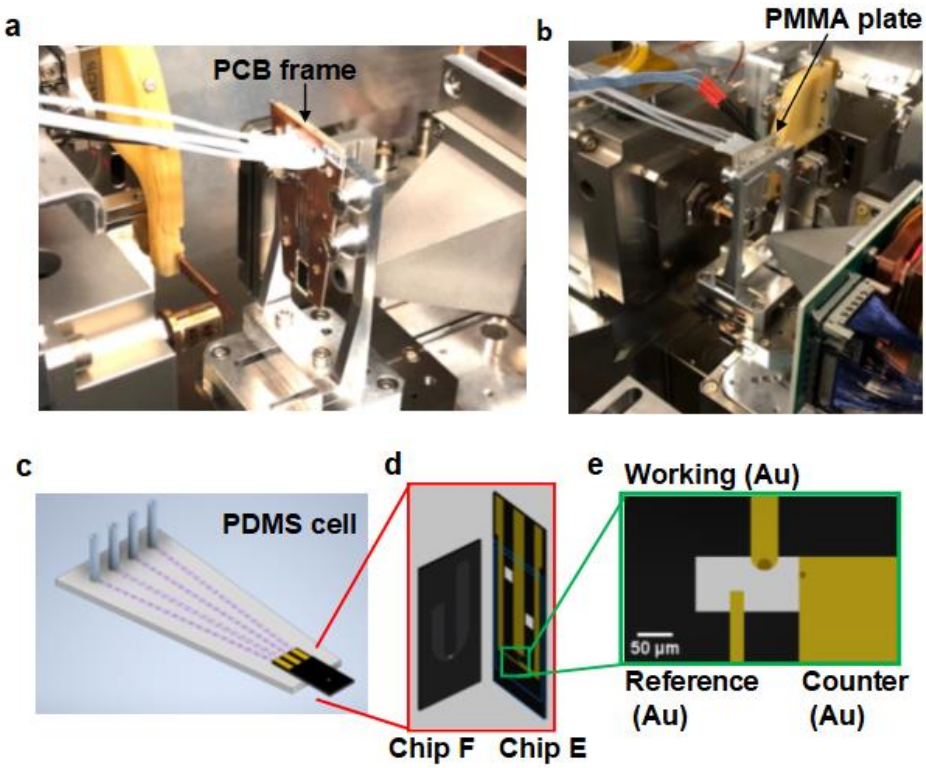

Fig. S-18 ***in situ*** **flow electrochemical device for soft X-ray STXM and ptychography**. Photograph of the assembled device inside the HERMES' STXM chamber: **(a)** front side; **(b)** back side. Schematics of **(c)** PDMS/glass cell; **(d)** in situ chips; **(e)** the 3-electrodes region on in situ chip E.

Figure S-19a is a reflection optical image of the window area of the device after filling the $CuSO_4$/KCl electrolyte. Once the 3-electrode region was filled with the electrolyte, a potentiostat (either an Ivium pocketstat or an Emstat 4s) was connected to the *in situ* device via the 4-pin connector. The open circuit potential (OCP) was stable and around -0.045 V_{Au} (equivalent to +0.355 V_{RHE} Then 3 cycles of cyclic voltammetry (CV) in the potential range -0.5 to 0 V_{Au} (-0.1 to +0.4 V_{RHE}) with a scan rate of 20 mV/s were performed. **Fig S-19b** is a reflection optical image of the window area after the electrodeposition. The Cu particles in **area A** and **area B** were electrodeposited in two different *in situ* cells using this procedure.

Changing the electrolyte to CO_2 saturated 0.1M $KHCO_3$: Millipore filtered, deionized water was first used to flush the $CuSO_4$/KCl out of the *in situ* device using the syringe pump with a flow rate 25 µl/hr for 5 min. Then the water in the cell was replaced with CO_2 saturated 0.1M $KHCO_3$ electrolyte using the syringe pump with 25 µl/hr flow for 15 min. This process was also conducted under the optical microscopy to ensure the window region was free of bubbles and the

Cu deposit was largely unchanged. Note that, although the process above was followed for these *in situ* ptychography measurements, we have also loaded an empty cell into the STXM and performed the electrodeposition and exchange of electrolytes inside the STXM (with the sample retracted in case of leaks).

Loading the *in situ* device into the STXM: First, the potentiostat and syringe pumps were disconnected to simplify device insertion into the STXM. The *in situ* device, connected only to the 4 electrolyte silicone tubes, was moved carefully from the optical microscope into the STXM chamber. In the chamber, the edges of the *in situ* device were engaged with the 3-pins of the trapezoidal kinematic holder. Once the device was firmly in position, the potentiostat cables were re-connected. A 2-sided 9 pin D-subminiature ("DB9") connector welded into a 2-3/4" (70 mm OD) conflat flange was used for electrical connection through the STXM vacuum chamber wall. The fluid lines were passed through 4 holes in the same flange and sealed with epoxy.After loading the device, the syringe pump was connected and operated at a flow rate of 25 μl/hr to keep a stable electrolyte flow. The electrolyte tubes and potentiostat cables were organized in the STXM chamber and stabilized using Kapton tape to attach them to a suitable position in the chamber to avoid interfering with STXM operations such as sample scanning. After the *in situ* device was loaded in the STXM, the air in the tank was changed from air to He gas by displacing the air at a slow rate (~10 min), maintaining the chamber pressure slightly above 1 bar. Replacing air with He was directly monitored using the intensity of transmitted X-rays. After achieving a plateau in X-ray transmission, the He gas flow was stopped and the STXM chamber was sealed.

Performing *in situ* flow electrochemical measurements by spectro-ptychography: STXM images were used to find a region consisting of Cu particles. Region A was found and studied. A four energy (4-E) STXM stack and a 4-E ptychography stack were conducted at area A with applied potentials (OCP). Then a full ptychography stack was measured on region A using an elevated flux (slits of 15 μm x 15 μm) in an attempt to get stronger ptychography signals. This ptychography stack on **area A** took ~90 min with X-ray intensity of much more than 50 MHz/s (that was the intensity observed by the phosphor/PMT STXM detector, but that detector is known to be saturated at 50 MHz). The high dose caused radiation damage in the form of X-ray induced reduction, as observed by the square in image **Fig. S-19d**. After this was observed, the X-ray beam intensity was reduced to ~20 MHz/s by closing the exit slits to 5 μm x 5 μm. Analyzable ptychography diffraction images were still obtained. All subsequent experiments were performed

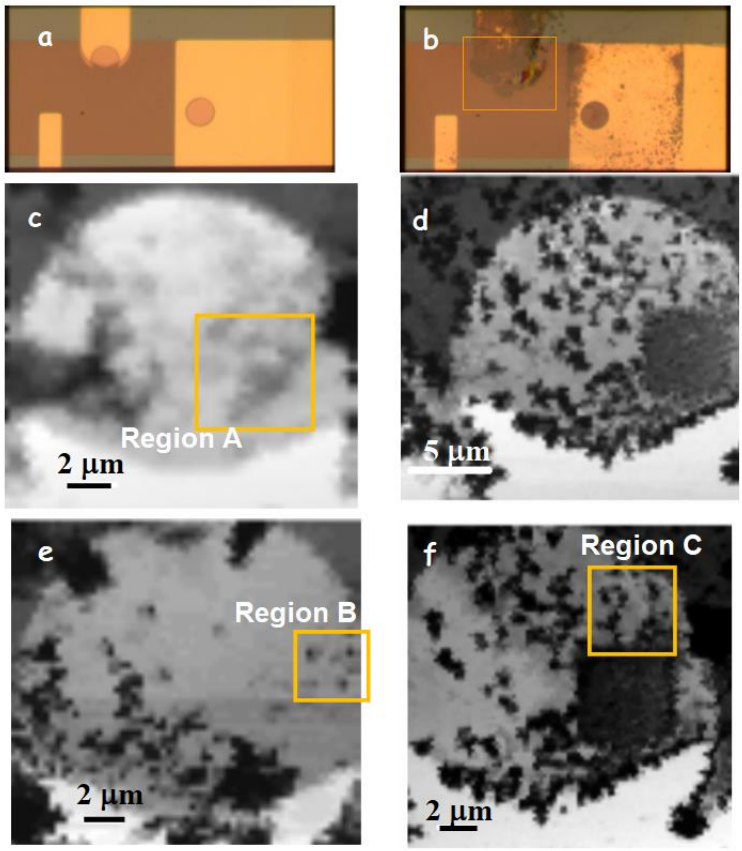

Fig. S-19 Images of the in situ cell. (a) Reflection optical image after filling with 10 mM $CuSO_4$ / 10 mM KCl electrolyte. (b) Reflection optical image after Cu electrodeposition. (c) STXM image at 933.3 eV prior to study of **area A**. (d) STXM image at 933.3 eV after STXM and ptychography study of **area A**. (e) STXM image at 933.3 eV prior to study of **area B**. (f) STXM image at 933.3 eV prior to study of **area C**.

with 20 MHz flux, without observable radiation damage, as is discussed in section. **SI-19,** and **Figs S.20** and **S.21**.

Since **area A** was damaged, the Cu particles were deposited again according to the above Cu nanoparticle electrodeposition process. **Area C** was found, showing well-defined Cu particles. 4E stack or full stack at Cu $2p_{3/2}$ edge were measured from area C while chronoamperometry scans at various potentials [OCP, +0.1, -0.2, -0.5, -0.8 and -0.85 V_{RHE}] were sequentially applied. The potential was returned to OCP (+0.355 V_{SHE}) between measurements. After the tests on **area A** and **area C**, another *in situ* cell (cell 2) was used. First the Cu deposition were conducted according to the above Cu nanoparticle electrodeposition process. **Area B**, consisting of many well defined Cu particles, was found. Chronoamperometry was performed under reducing conditions (-0.3 V_{Au}, +0.1 V_{RHE}) while recording a full Cu $2p_{3/2}$ ptychography stack on **area B**.

The *in situ* conditions for Cu particles:

The electrodeposited Cu particles are not stable under *in situ* conditions and the oxidation states of Cu could change with different local electrochemical conditions. First, Cu metal and Cu_2O are not thermodynamically stable relative to CuO at potentials above +0.2 V (vs Standard Hydrogen Electrode, SHE) according to the Pourbaix diagram for Cu in aqueous solution at 25 °C [S.15]. Thus the Cu(0) and Cu(I) species generated by electro-reduction should ultimately become CuO, which is water-insoluble. The fact that particles with large Cu(0) and Cu(I) content are observed after completing electrodeposition, is related to slow kinetics for oxidation.

Second, with different electrochemical histories, the Cu particles are shown in different chemical conditions. Although the Cu particles are electrodeposited on **areas A**, **B**, **C** by the same method shown in **Section SI-14**, the different conditions when STXM and ptychography measurements were conducted and different electrochemical environments can change the Cu particles. For **area A**, the time from electrodeposition to the measurement was quite long (~8 hours) due to various technical issues. During this period the cell was filled with a 0.1 M $KHCO_3$ solution with an open circuit potential of +0.4 V_{RHE}. This gave time for the oxidation to occur, resulting in the observation of more Cu(I) and Cu(II) particles (see **Fig. 1**). The STXM and ptychography measurements on **area B** were made immediately after changing the electrolyte to $KHCO_3$ so there was insufficient time for the as-deposited particles to be oxidized. When ptychography measurements were tested on **area B**, an +0.1 V_{RHE} was applied, and most Cu particles were electrochemically reduced to metallic Cu (see **Fig. 2**). **Area C** is in the same in situ device as

Area A, but under different conditions. After *in situ* STXM/ptychography measurements on **Area A** which caused radiation damage, **Area C** was then found and measured in **Fig. 5**.

Section SI-15 Evaluating radiation dose and possibility of radiation damage

Although radiation damage was observed in **area A** (**Fig. S.19d**) due to a long measurement and too high an X-ray intensity, this was caused by a stack measured **after** the 4E ptychography stacks shown in **Fig. 1** were measured. After the image in Fig. 19.d was measured, the slits were reduced until the incident flux was 20 MHz, the value that was used for all subsequent measurements. Here we evaluate the dose and present evidence that no further damage was observed.

S-15.1 Evaluating radiation dose for ptychography measurements.

The dose delivered in a spectro-ptychography measurement depends on the rate of X-ray absorption per unit area and the length of time the beam is on a given area.[S16, S17] Briefly, the dose in units of MGy is given by [S16]

$$a(STXM) = \frac{I_0(1 - e^{-OD})Et}{\varepsilon V \rho} \times 1.60 \times 10^2 \qquad \text{(Eqn. SI-2)}$$

where I_0 is the incident flux (number of photons per second), E is the exposure energy in eV, t is the exposure time in milliseconds (ms), ε is the detector efficiency, V is the volume of the exposed region, ρ is the sample density (g/cm^3), and OD is the optical density of the exposed region at the energy of irradiation.

The estimated dose for 4E in situ ptychography stacks is 70 MGy and for 34E ptychography stacks is 1020 MGy using the parameters listed in **Table S.1**.

Table S.1 Parameters for estimating dose for in situ spectro-ptychography stacks

symbol	4E stack	34E stack	comments
I_0	20 MHz	20 MHz	-
OD	0.23	0.3	average over E/s measured
E	933 eV	933 eV	-
t	320 ms	3.2s	Although the measurements took a long elapsed time (~90 min for full stack and ~20 min for 4E stack), the actual time the beam was on any

			given spot of the sample was quite small (60 ms dwell/pixel)
ε	0.8	0.8	-
diameter (μm)	1	1	-
Thickness (nm)	75	35	-
V	$7.5*10^6$ nm^3	$3.5*10^6$ nm^3	From Table 1 and Fig. 5. Different density and thickness
ρ	7 g/cm^3	9 g/cm^3	
Overlap factor	100	100	1 μm spot stepped 0.1 μm, in 2-D
Calculated dose	**70 MGy**	**1020 MGy**	

4E-stack : 221008037 (mostly CuO) 34-E stack: 221008048 (mostly Cu)

For comparison, if the same area was measured by conventional STXM with the fully focused 50 nm spot size, 20 nm step size and 20 ms/point, the estimated doses would be 450 MGy for a 4E stack and 6,500 MGy for a 42-E stack. Thus spectro-ptychography using a 1 μm defocused spot size delivers about 6 times lower dose than STXM, while at the same time giving better statistical precision and much better spatial resolution.

2. Evidence that there is negligible damage from *in situ* spectro-ptychography

Color coded composites of component maps derived from 4E spectro-ptychography stacks measured before and after a full ptychography stack (area B, **Fig. 2**) are shown in **Figure S-20**. No significant change in morphology or oxidation state distributions were detected.

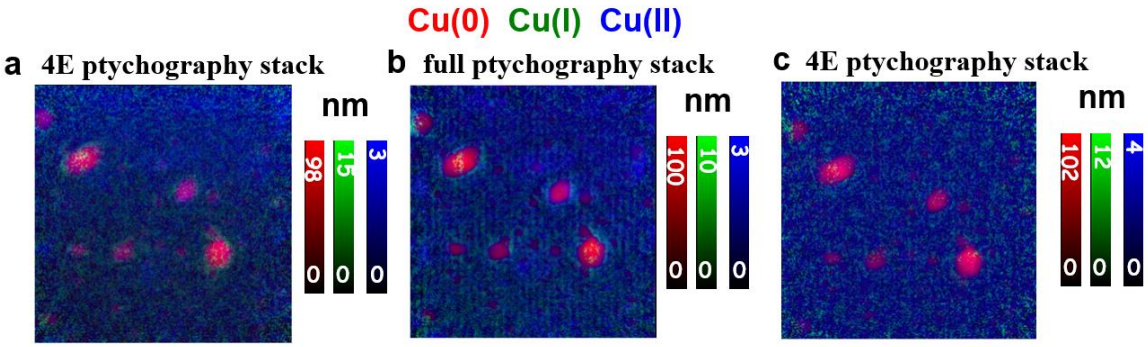

Figure S-20 Check for radiation damage, by measuring 4E stacks before and after a 42E stack under *in situ* condition (-05 V_{Au}, 5 nA). Color coded composites of component maps derived from **(a)** 4-E ptychography, 2022109082. **(b)** Full stack**,** 2022109083. **(c)** 4-E stack, 2022109086.

In addition, after completing all the *in situ* ptychography measurements on area C (**Fig. 5**), a 4-E stack was measured on a larger region which included adjacent areas which had never been exposed to the X-ray beam (**Figure S-21).** The same morphology and similar oxidation state

distributions were found between the area that had been illuminated by ptychography measurements and the particles in the un-exposed surrounding area, indicating there was negligible beam damage on Cu electrocatalysts during *in situ* ptychography measurements.

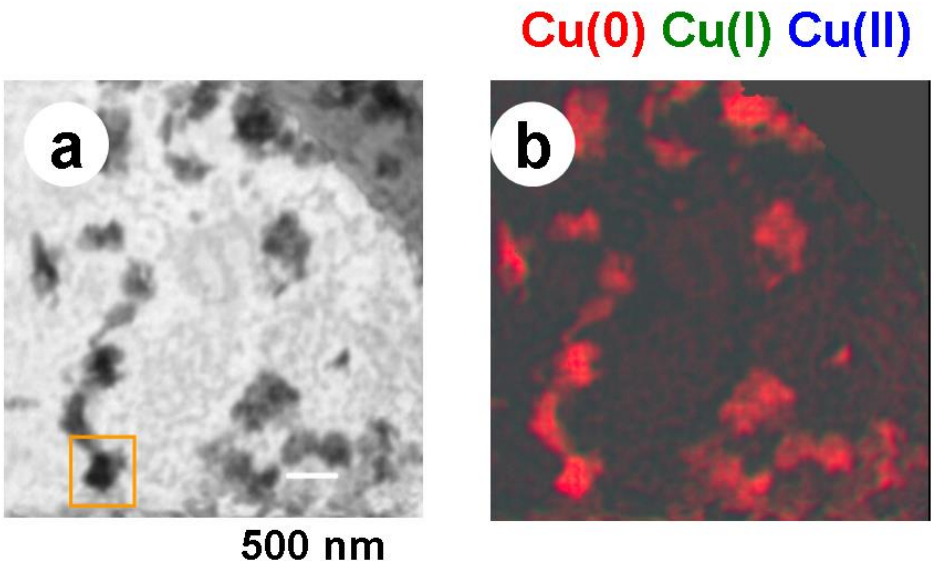

Figure S-21 Check for damage after measurements in area C. (a) STXM image at 933.5 eV. The yellow frame is the region of the *in situ* ptychography measurements on area C (**Fig. 5**). **(b)** color-coded composite of the component maps derived from 4E spectro-ptychography stack measured over a larger region after all the chronoamperometry and stacks were completed.

References

S.1. Pfeiffer, F. X-ray Ptychography. *Nature Communications* **12**, 9-17 (2018)

S.2. Thibault, P. et al. High-resolution scanning x-ray diffraction microscopy. *Science* **321**,379 (2008).

S.3. J. M. Rodenburg, et al. Hard-X-Ray Lensless Imaging of Extended Objects, *Phys. Rev. Lett.* **98**, 034801 (2007).

S.4. A. Maiden, A. Rodenburg, J. M. An improved ptychographical phase retrieval algorithm for diffractive imaging. *Ultramicroscopy* **109**, 1256–1262 (2009).

S.5. Shemilt, L. (2014) PhD thesis: "Coherent Diffraction Imaging and Ptychography of Human Metaphase Chromosomes", University College, London.

S.6. Guizar-Sicairos, P. Thibault, P. Ptychography: A solution to the phase problem, *Physics Today* **74**, 9, 42 (2021).

S.7. Marchesini, S. et al. Augmented projections for ptychographic imaging, *Inverse Problems* **29**, 115009 (2013).

S.8. Banterle, N. Bui et al. Fourier ring correlation as a resolution criterion for super-resolution microscopy, *J. Struct. Biol*. **183**, 363-367 (2013).

S.9. Jiang, P. et al. Experimental and theoretical investigation of the electronic structure of Cu_2O and CuO thin films on Cu (110) using x-ray photoelectron and absorption spectroscopy. *J. Chemical Physics* **138**, 024704 (2013).

S.10. Hitchcock, A.P. *Soft X-ray Imaging and Spectromicroscopy* Chapter 22 in Volume II of the Handbook on Nanoscopy, eds. Gustaaf Van Tendeloo, Dirk Van Dyck and Stephen J. Pennycook (Wiley, 2012) pp 745-791

S.11. Ossig, C., Nietzold, T., West, B., Bertoni, M., Falkenberg, G., Schroer, C. G., & Stuckelberger, M. E. (2019). X-ray beam induced current measurements for multi-modal x-ray microscopy of solar cells. *JoVE (Journal of Visualized Experiments)*, (150), e60001.

S.12. Lerotic et al., J. Cluster analysis in soft X-ray spectromicroscopy: Finding the patterns in complex specimens. J. Electron Spectroscopy and Related Phenomena. **144–147**, 1137-1143 (2005).

S.13. Lerotic M, Jacobsen C, Schäfer T, Vogt S. Cluster analysis of soft X-ray spectro-microscopy data. Ultramicroscopy **100**, 35-57 (2004)

S.14. Lerotic M, Mak R, Wirick S, Meirer F, Jacobsen C. MANTiS: a program for the analysis of X-ray spectromicroscopy data. J. Synchrotron Rad. **21**, 1206–1212 (2014)

S.15. Brandt, Iuri Stefani, et al. Electrodeposition of Cu_2O: growth, properties, and applications. *Journal of Solid State Electrochemistry* **21**,1999-2020 (2017).

S.16. Wang, J, et al. Quantitative evaluation of radiation damage to polyethylene terephthalate by soft X-rays and high-energy electrons. *The Journal of Physical Chemistry B* **113**, 1869-1876 (2009).

S.17. Berejnov, V., et al. Calculating Absorption Dose When X-ray Irradiation Modifies Material Quantity and Chemistry, J. Synchrotron Radiation **28,** 834-838 (2021).

Table S.2 Summary of ptychography measurements reported in this paper

Note: Area A and **area C** are different areas on the same *in situ* device, but with a different electrochemical history.
Area B is from a different *in situ* device, but using a similar deposition protocol as used for **Area A**.

Area	Fig #	Type	File (202210xxx) (day)###	Size (μm, pixel)	Flow (μL/h)	V vs RHE [@]	algorithm[#]	Maxsize[$]	Thresh[&]	Det. Dist[^] (mm)	Defocus[!] (μm)	Acquisition time (min)
A	Fig. 1	STXM	7-024	6 *6; 60*60	20	OCP	NA					25
A	Fig. 1	ptycho	7-029	5 *5 ; 50*50	20	OCP	AP**800	1100	10	52.25	-25	30
B	Fig. 2,3	ptycho	9-083	3 *3, 30*30	20	+0.10	AP**200	1100	10	54.9	-26	90
C	Fig. 5	STXM	8-036	5 *5 , 100*100	20	OCP	NA					20
C	Fig. 5	ptycho	8-037	0.5*0.5 ,10*10	20	OCP	AP**500	1100	5	52.07	-18	20
C	Fig. 5	ptycho	8-038	0.5*0.5 ,10*10	20	+0.10	AP**500	1100	5	52.07	-18	20
C	Fig. 5	ptycho	8-040	0.5*0.5 ,10*10	20	-0.20	AP**500	1100	5	52.07	-18	20
C	Fig. 5	ptycho	8-041	0.5*0.5 ,10*10	50	-0.50	AP**500	1100	5	52.07	-18	20
C	Fig. 5	ptycho	8-042	0.5*0.5 ,10*10	50	-0.80	AP**500	1100	5	52.07	-18	20
C	Fig. 5	ptycho	8-048	0.5*0.5 ,10*10	50	-0.85	AP**500	1100	5	52.07	-18	100

adaptq = hard was used for all reconstruction. This means the camera is moved at each photon energy so the Q-range of the diffraction image (DI) was the same at all energies of a stack. (There is a software correction, but moving the camera is better)

bin = 1 for all reconstructions.

[@] **nc** = not connected

AP – alternate projection mode of PyNX, # after ****** is # of iterations.

Note there is no test for convergence, as typically done in self-consistent field quantum chemical calculations.

$ **maxsize:** camera images are 2000 x 2000 (11 μm pixels). Maxsize = 1300 gives good reconstruction for strong scatterers like Siemen's stars (Au), but maxsize=1100 was better for these reconstructions.

& **threshold** is applied AFTER background subtraction.

^ **Detector distance** Physical distance from the sample to the sensor in the camera

! **Defocus** This is the change in the ZP-z position used to get the desired spot size. Sign is important